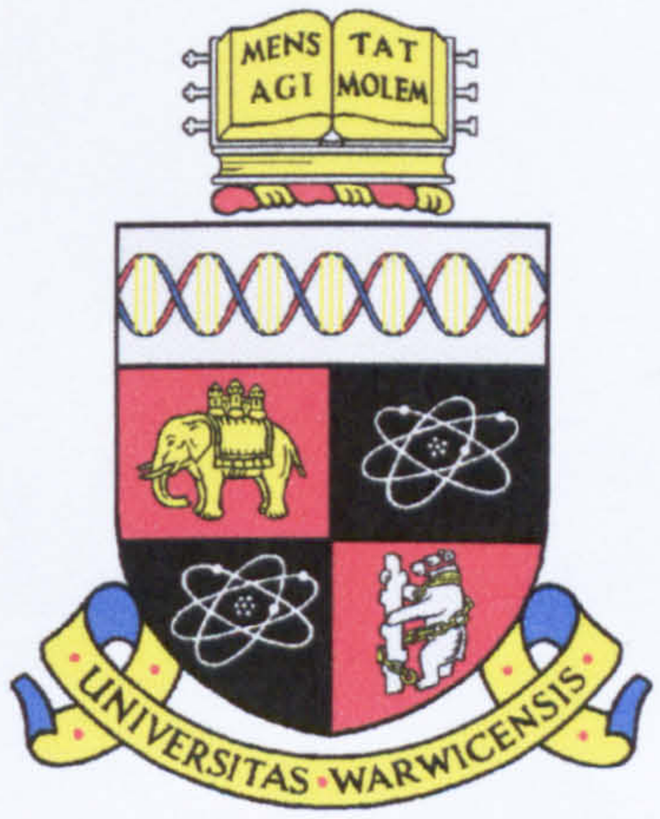

Low-power silicon planar micro-calorimeter employing nanostructured catalyst

by

Siu Man Lee

School of Engineering

University of Warwick

A thesis submitted to the University of Warwick

for the degree of Doctor of Philosophy

December 2002

THESIS CONTAINS CD/DVD

Contents

Appendices

Acknowledgements

I would like to express my deepest appreciation to my academic supervisor, Prof. Julian W. Gardner for his excellent supervision and guidance. I would also like to thank Dr. James A. Covington for his proof reading and advice. I wish to thank the following people for their assistance throughout this research:

University of Warwick, UK

Mr. Frank Courtney (Technician in Sensors Research Laboratory) for his technical support; Mr. Huw Edwards (Technician) for his guidance on the vacuum system. Dr. David C. Dyer for his expert advice on electronics systems and instrumentation.

University of Southampton, UK

Prof. Phillip N. Bartlett, Dr. Yu May Tan and Mr. Jan Marwan for the electrochemical deposition of the nanoporous palladium catalyst.

City Technology Ltd., UK

Dr. Martin Willett and Dr. Stephane Leclerc for their financial support of this project.

Institute of Microtechnology, University of Neuchâtel, Switzerland

Dr. D. Briand for the silicon wafer processing of the two device generations.

Apart from the academic and technical support, I would like to express my gratitude to my family, especially my mother Mdm. Mo Chi Tam, for their continuous support and encouragement. A special thank to Miss Sarah S. L. Kwan for her prayers and understanding, particularly during preparation of this thesis. I would like to take this chance to show my greatest appreciation to my Uncle Mr. Kong Ah Tam for his enlightenment. Finally, I wish to thank Dr. Stephen K. C. Tam and his wife Mrs. Y. S. Tam; Mr. Kong Ting Tam and his wife Mrs. Connie S. H. Tam; Mrs. Y. K. Kwan for their psychological support.

Declaration

The work described in this thesis is entirely original and my own, except where otherwise indicated. I also confirm that this thesis has not been submitted for a degree at another university.

Part of this work has been presented at international conferences:

[1] S. M. Lee, J. W. Gardner, D. C. Dyer, Silicon planar pellistor employing nanostructured films and a micro-hotplate, *Proceeding the euspen nanotechnology workshop and joint Warwick-Tokyo Nanotechnology Symposium*, Warwick University, UK, 18th to 21st September 2000.

[2] S. M. Lee, J. W. Gardner, D. C. Dyer, Silicon planar pellistor employing nanostructured films and a micro-hotplate, Poster Presentation in the euspen nanotechnology workshop and joint Warwick-Tokyo Nanotechnology Symposium, Warwick University, UK, 18th to 21st September 2000.

[3] J. W. Garnder, S. M. Lee, P. N. Bartlett, S. Guerin, D. Briand and N. F. de Rooij, *Technical digest of Transducer'01 and EurosensorsXV*, The 11th international conference solid-state sensors and actuators, Munich, Germany, 10th to 14th June, 2001.

[4] S. A. A. Leclerc, M. J. Willett, S. M. Lee, J. W. Gardner, J. Marwan, P. N. Bartlett, Optimisation of mesoporous catalyst for combustible gas sensor application, *Proceeding of International Meeting on Chemical Sensors*, Boston, Massachusetts, USA, 7th – 10th July, 2002.

[5] S. A. A. Leclerc, M. J. Willett, S. M. Lee, J. W. Gardner, J. Marwan, P. N. Bartlett, Novel combustible gas sensors employing micromachined silicon substrates and nanostructured catalysts, *Proceeding of International Meeting on Chemical Sensors*, Boston, Massachusetts, USA, 7th – 10th July, 2002.

[6] P. N. Bartlett, S. Guerin, J. Marwan, J. W. Gardner, S. M. Lee, M. J. Willett and S. A. A. Leclerc, A micromachined planar pellistor using an electrochemically deposited nanostructured catalyst, *Proceedings for the Symposium on Microfabricated Systems and MEMs – V*, Spring meeting of the Electrochemical Society, Philiadelphia, USA, 17th – 22nd May, 2002.

Part of the work contained in this thesis is being published in the scientific literature:

[7] S. A. A. Leclerc, M. J. Willett, S. M. Lee, J. W. Gardner, J. Marwan, P. N. Bartlett, Novel combustible gas sensors employing micromachined silicon substrates and nanostructured catalysts, submitted to *Sensors and Actuators B*.

[8] S. M. Lee, D. C. Dyer, J. W. Gardner, Design and optimisation of a high-temperature silicon micro-hotplate for nanoporous palladium pellistors, *Microelectronics Journal,* 34, pp 115-126, 2003.

[9] S. M. Lee and J. W. Gardner, Pulse mode operation for a high-temperature silicon micro-calorimeter for ultra-low power application (in preparation).

Summary

This thesis describes the development of silicon planar micro-calorimetric gas sensors employing a nanostructured palladium (Pd) catalyst. Present commercial, bead-type calorimetric sensors have been manufactured for nearly forty years and are used in many applications, such as mining, water treatment and emergency services, with an estimated European market value of €221M by 2004. However, recent advances in both silicon micro-machining and nanomaterials have created the technologies necessary to transform the present labour-intensive fabrication process into a new low-cost batch production. In addition, a reduction in power consumption, improved sensitivity and increased poisoning resistance of the sensor can also be achieved.

Here, two generations of micro-calorimeter have been designed and fabricated comprising a silicon membrane structured micro-hotplate that can reach up to a temperature of 870°C without failure and an ultra-high surface area nanoporous Pd catalyst (about 20 m^2/g), typically 25 nm thick, deposited electrochemically on top of a gold electrode above the micro-heater. The exothermic reaction caused by the target gas (e.g. methane) interacting with the Pd catalyst results in an increase in the temperature and so resistance of the micro-heater. A Wheatstone bridge interface circuit is normally used to detect and measure the fractional resistance change.

Full 3-D thermo-mechanical simulations have been performed employing experimental data in order to establish a simulation database for future developments. The differences between simulated and experimental results were found to be as low as 4.6%. The response of the sensors has been characterised in both continuous powering mode and pulse modulation powering mode. Device power consumption is only 50 mW at 500°C in continuous mode, which is up to 100 mW lower than that for commercial sensors. Typical response times of 2 ms have been measured and so further power saving can be achieved when the sensors are operated in a pulse mode, e.g. 50% duty-cycle at 10 Hz. Hence, an overall power saving of 75% could be achieved compared to commercial product. Infrared thermography revealed that a centre hot spot, commonly found with meander style micro-heaters, has been eliminated by the new drive-wheel micro-heater design. The sensitivity of the sensors has also been improved, up to a factor of 4 at 500°C ($(60\ mV/mm^2)/\%CH_4$), by the nanoporous catalyst and by heating it more isothermally. Furthermore, improvements have also been found on the poisoning resistance. Therefore, the potential commercialisation of the micro-calorimeter is very promising.

List of symbols and prefixes

Symbol	Meaning
a	Length of the active area for a device
A	Surface area
$A.R.$	Aspect Ratio
$A_{catalyst}$	Geometrical area of the catalyst
A_{chip}	Area of the die
A_{cross}	Cross-sectional area
A_{heater}	Area of the heater
C	Electrical capacitance
c_p	Specific heat capacity at constant pressure
C_{th}	Thermal capacitance
f_c	Corner frequency (3 dB point)
f_{off}	Cut-off frequency
G''	Thermal conductivity of the gas
G_{con}	Gas concentration
H	Heat source
i	Current (D.C.)
i_{fall}	Integral of the current transient at falling edge
i_{rise}	Integral of the current transient at rising edge
I	Constant current (D.C.)
I_{tran}	Total current in the transient
ℓ	Nusselt length
L	Length of the micro-heater track
Nu	Nusselt Number
P	Power consumption
P_{air}	Power consumption in air
P_{idle}	Power consumption of the device at idle voltage (150°C)
P_{mem}	Power loss in the membrane
P_{osc}	Power consumption of the device during oscillation
P_{rad}	Radiative power loss

Symbol	Meaning
P_{tol}	Total power consumption of a device
P_{tran}	Power consumption of the device in the transient
R_{162g}	Micro-heater resistance for SRL 162g
R_{500}	Resistance of the micro-heater at 500°C
R_a	Resistance of the current sensing resistor
R_b	Balancing resistor in a Wheatstone bridge circuit
R_H	Resistance of the micro-calorimeter
R_{heater}	Resistance of the micro-heater
R_{new}	Resistance of a new micro-heater design
R_o	Base-line resistance
R_s	Resistance of the sensor
R_{sheet}	Sheet resistance
R_T	Device resistance at a specific temperature (T)
R_{th}	Thermal resistance
S_T	Thermal sensitivity of the sensor
S_V	Voltage sensitivity of the sensor
t	Thickness of a material
T	Temperature
t_d	Dead time of a chamber or gas test system
T_o	Ambient temperature
u	Length of the membrane for a device
V_{162g}	Voltage for SRL 162g to operate at 500°C above ambient
V_{air}	Sensor output in air
V_{bridge}	Supply voltage to the Wheatstone bridge circuit
V_{gas}	Sensor output in the presence of target gas
V_h	Supply voltage to the micro-heater
V_{in}	Constant voltage supply
V_{new}	Voltage for a new device to operate at 500°C above ambient
V_o	Voltage output signal from an interface circuit
V_{out}	Output voltage from interface circuit in chemical characterisation
V_p	Voltage across a sensor

Symbol	Meaning
V_s	Supply voltage
V_{ss}	Main supply voltage to electronic system
V_{T500}	Voltage required for a device to reach 500°C above ambient
W	Width of the micro-heater track
Greek	
α	Temperature coefficient of resistance
Δ	Difference
ε	Emissivity
ϕ	Flow-rate (volumetric)
φ	Micro-heater track coverage
κ	Thermal conductivity
λ_∞	Mean-free path of a material with infinite thickness
ν	Local fluid-flow velocity
π	Constant
ρ	Density
ρ_∞	Resistivity of a material with infinite thickness
σ	Stefan-Boltzmann constant
$\tau_{electric}$	Electrical time constant of a device
τ_{fall}	Device time constant (falling edge)
τ_{rise}	Device time constant (rising edge)
τ_{th}	Thermal time constant of a device
$\tau_{thermal}$	Thermal time constant of a device
υ_a	Average velocity
Mathematical	
=	Is equal to
≈	Is approximately equal to
±	Plus or minus
°	Degrees in angle or temperature

Symbol	Meaning
Prefix	
n	Nano – (10^{-9})
μ	Micro – (10^{-6})
m	Milli – (10^{-3})
c	Centi – (10^{-2})
k	Kilo – (10^{3})
M	Mega – (10^{6})

List of abbreviations

Abbrev.	Meaning
3-D	Three dimensional
A.C.	Alternating current
A/D	Analogue / Digital
ADC	Analogue-to-Digital Converter
APCVD	Atmospheric pressure chemical vapour deposition
CCD	Charge Coupled device
CMOS	Complementary Metal Oxide Semiconductor
CNC	Computer Numerical Control
CTL	City Technology Ltd.
CVD	Chemical Vapour Deposition
D.C.	Direct Current
DRIE	Deep Reactive Ion Etching
EPSRC	Engineering and Physical Sciences Research Council
FEM	Finite Element Method
GC	Gas Chromatography
HCPA	Hexachloroplatinic Acid
HMDS	Hexamethyldisiloxane
IC	Integrated Circuit
IMT	Institute of Microtechnology (Neuchâtel)
IR	Infrared
ISE	Integrated System Engineering
KOH	Potassium Hydroxide
LCD	Liquid Crystal Display
LED	Light Emitting Diode
LEL	Lower Explosive Limit
LIGA	Lithographie, Galvanoformung, Abformung
LPCVD	Low Pressure Chemical Vapour Deposition
MBE	Molecular beam epitaxy
MHR	Membrane-to-Heater Ratio

Abbrev.	Meaning
MOSFET	Metal Oxide Semiconductor Field Effect Transistor
PC	Personal Computer
PCB	Printed Circuit Board
PECVD	Plasma Enhanced Chemical Vapour Deposition
PVD	Physical vapour deposition
RIE	Reactive Ion Etching
SCE	Saturated Calomel Electrode
SRL	Sensors Research Laboratory
TCR	Temperature Coefficient of Resistance
TEM	Tunnelling Electron Microscope
TO	Transistor Outline
UV	Ultra-Violet
V-I	Voltage – Current
VPE	Vapour-phase epitaxy

To my mother, Mdm. Mo Chi Tam

and my Uncle, Mr. Kong Ah Tam

"Unless the LORD builds the house, its builders labour in vain. Unless the LORD watches over the city, the watchmen stand guard in vain."

Bible, Psalm 127: 1-2.

Glory and praise to my LORD, Amen.

Chapter 1

Introduction

This chapter describes a historical overview of the technology for the detection of atmospheric methane. It covers the five principal methods of methane detection, namely calorimetric sensing, chemoresistive sensing, spectroscopic detection, electrochemical sensing and piezoelectric resonant detection. The characteristics of these various detection methods have been explored. Improvements of commercial calorimetric gas sensors have been identified. Recent developments of silicon-based micro-calorimeter are studied. An introduction to the novel nanostructured Pd catalyst and micromachining technology is also provided, discussing the basics of the technology relevant to this research. Finally, the research objectives and an outline of this thesis are given.

1.1 Methane detection

The mining industry was one of the first important applications for methane (CH_4) detection. This is a critical safety requirement because it is one of the hazardous gases existing naturally that cannot be detected by the human olfactory senses. It becomes explosive when it is accumulated above the Lower Explosive Limit (LEL), i.e. 5% in air. A primitive safety measure was initially employed by igniting the accumulating CH_4 before the concentration reached the LEL. This method required a miner, covered in a wet blanket, to travel to all susceptible shafts with a candle on a stick, at the beginning of every shift [1.1]. Later, a monitoring technique was developed, that used an oil lamp where the flame changed colour in the presence of methane [1.2]. However, these techniques are obviously primitive, inaccurate and dangerous. Therefore, modern methane sensing techniques have been developed to improve sensitivity, accuracy and reliability. The sensor or transducer converts the concentration of methane into electrical signals which can be interpreted by the user.

Furthermore, applications for the methane detection have been broadened and are no longer confined to the mining industries. The major application areas include oil and

gas, mining, water treatment, waste treatment, paint manufacturing, fire and emergency services, food industry and land fill [1.3]. The European industrial gas sensor market was worth €154.3 million in 1997 and it is expected to rise to €221.0 million in 2004 [1.4]. The demand in North America is even greater, reaching €282.6 million in 2003 [1.5].

This section introduces the major methane sensing techniques, namely the calorimetric, chemoresistive, spectroscopic, electrochemical and piezoelectric resonating systems. Although other methods, such as standard gas chromatography (GC), are also available, they tend to be complicated and expensive. Hence, they are less significant in sensor applications. A comparison of the market maturity for various sensing techniques is shown in Appendix 1.

1.1.1 Calorimetric sensor

Calorimetric sensors oxidise methane at high temperature (e.g. 500°C), causing an increase in the temperature of a resistive sensing element. The sensor usually uses Platinum (Pt) or Palladium (Pd) as the catalyst. The resistance change is a function of the gas concentration up to 90% because the oxidation requires a minimum of 10% oxygen in the reaction.

A pellistor is a type of calorimetric sensor that is used to detect combustible gases, such as methane, in normal atmosphere and convert it into an electrical signal. Early designs comprised of bare coils of platinum wire operating between 800°C and 1000°C. However, the platinum wire evaporates rather quickly at such temperature. Therefore, Baker (patented in 1959) introduced a catalyst to reduce the operating temperature without affecting the sensitivity and prolonging the lifetime of the sensor up to a minimum of 100 hours [1.6].

Commercial pellistors are comprised of a platinum coil encapsulated with alumina and coated with a layer of sintered porous palladium catalyst to form a small bead. This bead is suspended between two metal pins inside a protective metal can, as shown in Figure 1.1(a). A voltage is applied across the coil to raise its temperature to about 500°C. The high temperature causes the gas to combust and so raises the temperature of the bead. The corresponding increase in the electrical resistance of the platinum coil is measured using a Wheatstone bridge circuit with a second inert pellistor acting as a balance arm, as shown in figure 1.1(b). A trimming resistor is included to create a match pair between the detector and the compensator. Furthermore, a zero set

variable resistor is used to allow the Wheatstone bridge output to be adjusted to zero. Detailed analysis about this interface circuit is explained in Chapter 4.

The output from a commercial pellistor is typically 50 mV for each percent of methane in air [1.8], but requires a high power consumption of 100 to 500 mW per element. The relatively high output magnitude allows the output signal to be detected without additional amplification. This was one of the most attractive features at the time because of its simplicity and low-cost.

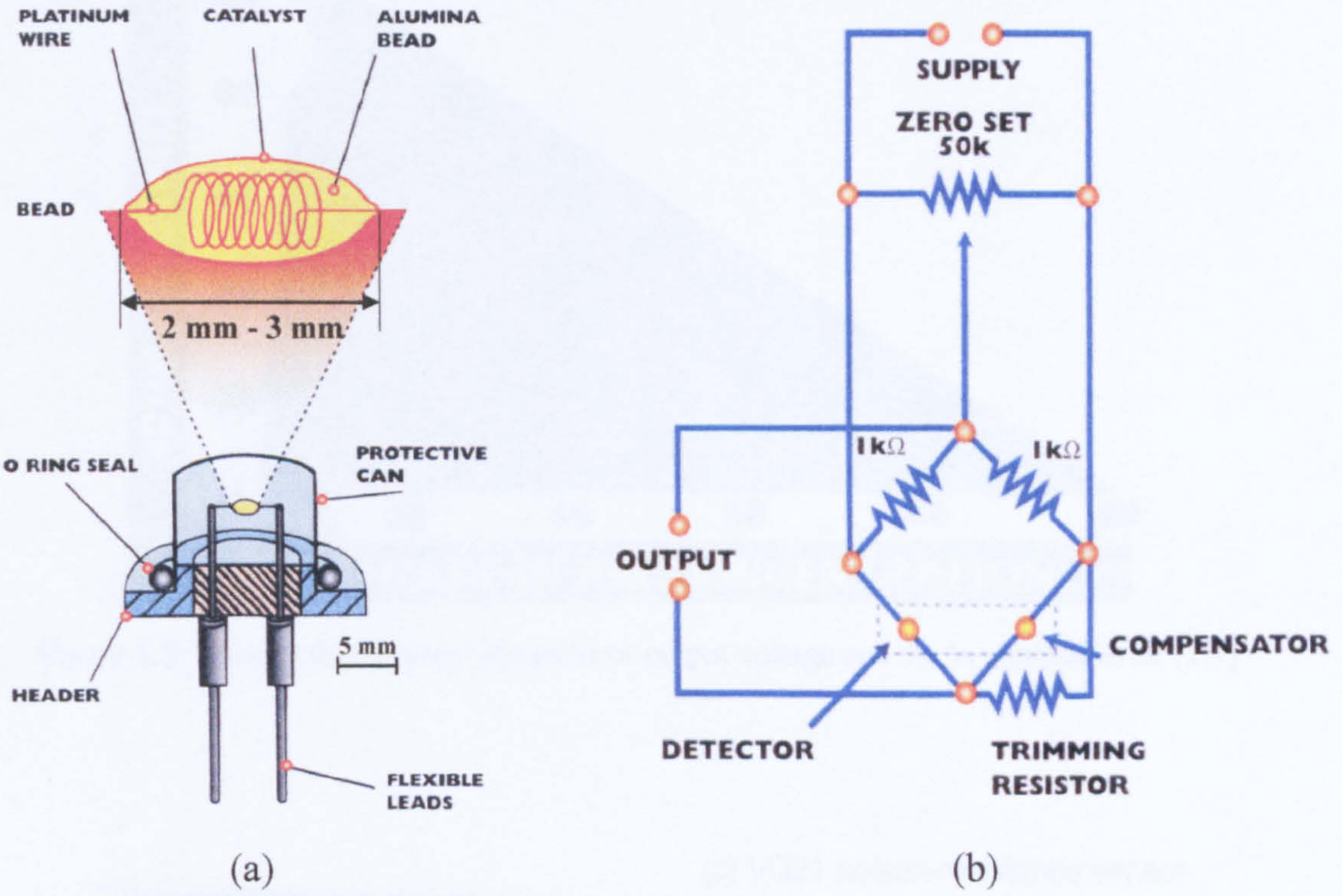

Figure 1.1: (a) The construction of commercial pellistor [1.7]. (b) The common Wheatstone bridge interface circuit including the sensor (detector), compensator, trimming and zero set resistor [1.9].

Pellistors usually measure in the range from 0% to 100% of the LEL for a given combustible gas. The output from the pellistor will continue to rise when the concentration of the gas exceeds this limit. However, the gas is likely to be ignited by the heated pellistor bead which leads to an unstable signal output. Further increases of concentration will cause incomplete combustion because of the reducing level of oxygen and the output will begin to fall. The device output will eventually become zero when the concentration of the combustible gas reaches 100%. An example of the relation between the output voltage and the methane concentration is shown in figure 1.2 [1.9].

Various companies have manufactured conventional pellistors for more than three decades and millions of units have been sold. However, the manufacturing process is very labour-intensive which leads to high unit cost, about € 40. The platinum wire coil is wound manually but even the shape of the coil can influence the performance. Therefore, the match pellistor pair has to be identified individually by a trial and error method. Alternative technologies had been sought by manufacturers to produce pellistors in high volume at lower unit cost, as described in section 1.2.

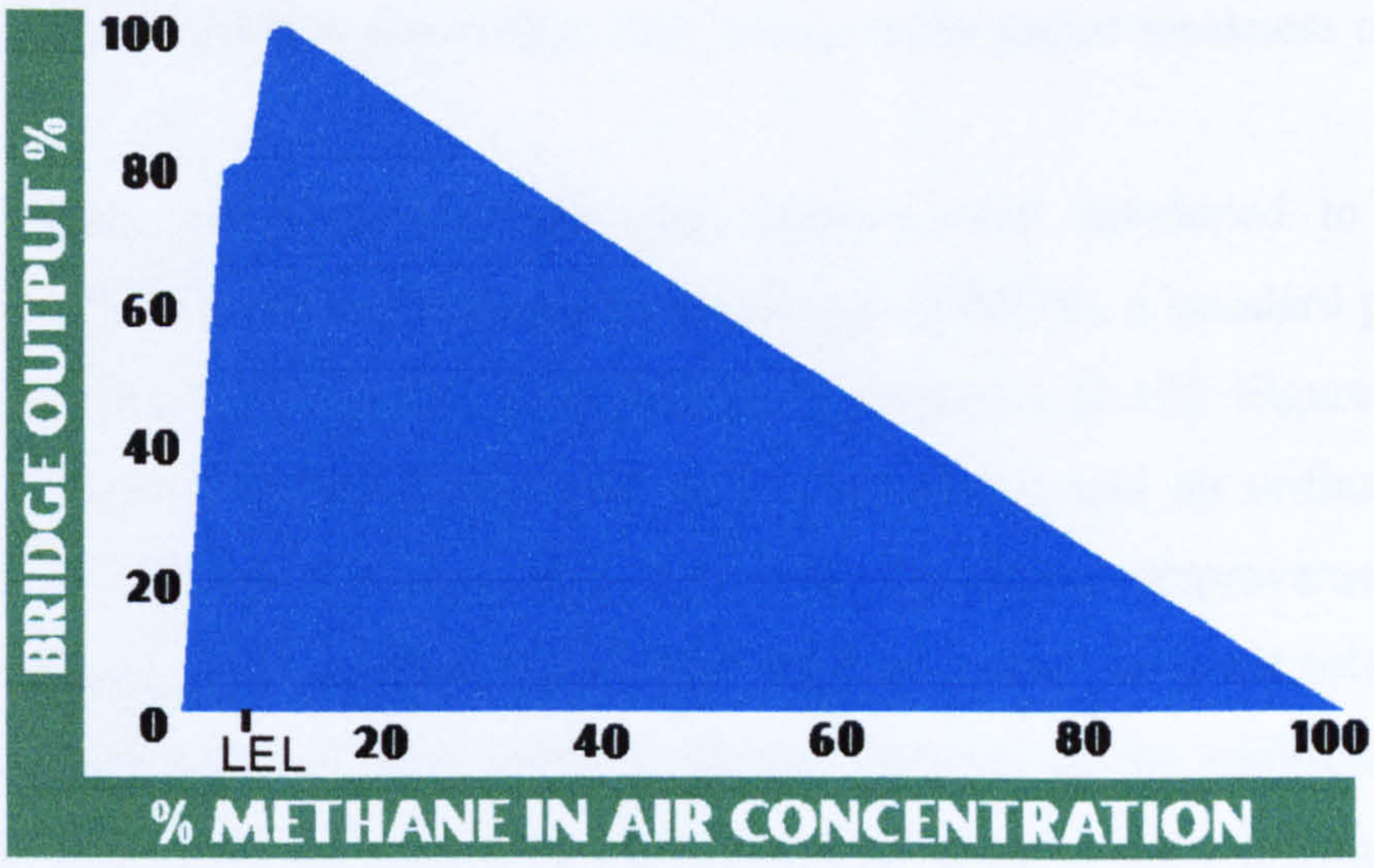

Figure 1.2: Relationship between the pellistor output voltage and the % methane in air [1.9].

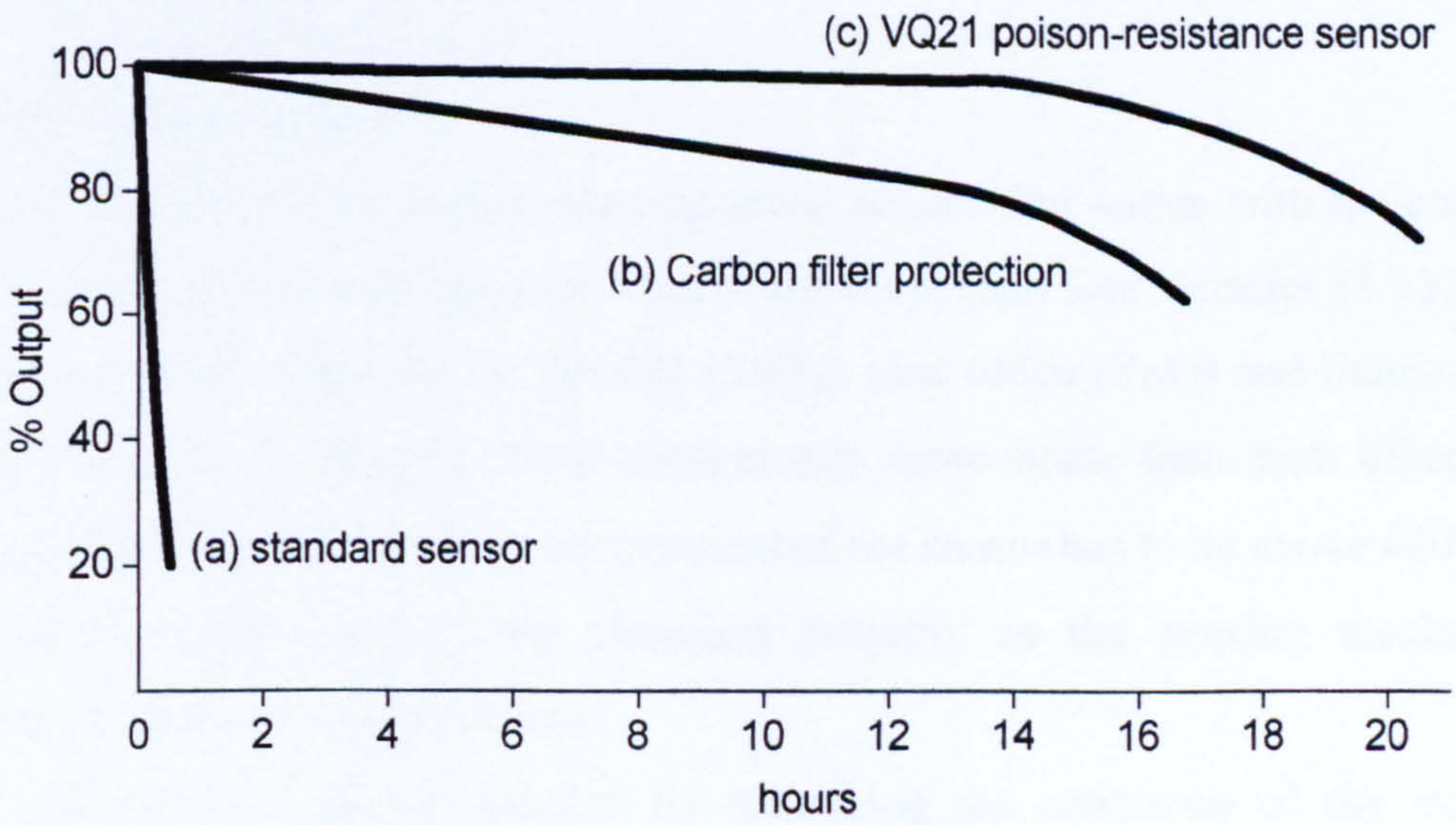

Figure 1.3: The effect of 10 ppm HMDS on (a) a standard sensor, (b) the same sensor protected by an activated carbon filter and (c) sensor type VQ21 by EEV Ltd., the HMDS poison-resistance device [1.3].

Despite the high power consumption and labour intensive production, pellistors usually require little attention and can continuously operate for up to 10 years [1.10]. However, the life expectancy of the sensor can be significantly shortened in the presence of catalyst poisons. These poisons include silicone compounds used in electrical insulation or foam thermal insulation, and leaded petrol fumes [1.11]. The poisoning chemical causes an unrecoverable loss of sensitivity. Activated carbon filters were incorporated into the packaging to provide certain level of poison resistance [1.11]. Unfortunately, this method limited the type of flammable gas detectable because only the smaller gas molecules could pass through without absorption. This becomes the major weakness of this type of sensor.

Therefore, special poison resistance sensors were developed to increase the poison resistance of pellistors. Hexamethyldisiloxane (HMDS), a standard poisoning test gas was employed to justify the level of poison resistance [1.12]. Figure 1.3 shows a comparison between different measures against poisoning and an ordinary sensor. It indicates that the various measures provided significant improvement over the unprotected sensor, up to a factor of 10^2. Nevertheless, poison resistant pellistors require higher power consumption than ordinary devices because of the additional amount of catalyst. Furthermore, the poison gas concentration used in the experiment was very small and the sensitivity of the device will decline by 50% in a day, even with the highest resistance devices. Improved poison resistance sensors are desirable to enhance reliability.

1.1.2 Chemoresistive sensor

Electrical conductivity of semiconducting metal oxides that varies with the composition of the gaseous atmosphere has been known for more than four decades [1.13]. Typical gas sensing metal oxides are tin dioxide (SnO_2), zinc oxide (ZnO) and titanium dioxide (TiO_2). However, methane is thermodynamically more stable than most other reducing gases and therefore the operating temperature of the sensor has to be above 400°C [1.15]. The sensors which employ this chemical property as the sensing mechanism are classified as chemoresistive sensors.

This type of sensor operates by measuring the resistance of the metal oxide sensing layer. The electrical conductance of the sensing layer increases significantly in the presence of combustible gas, such as methane. A platinum heater coil is usually used

to elevate the sensor temperature to between 400°C and 700°C, depending on the specific application and the composition of the metal oxide catalyst. Wheatstone bridge circuitry is a common interface for this type of sensor, although more sophisticated circuitry may be employed for temperature and humidity compensation purposes.

Chemoresistive sensors have been manufactured for more than three decades. A wide range of products for various applications has been fabricated, as shown in figure 1.4. The sensing material for commercial products is typically sintered tin dioxide (SnO_2) while additional materials (e.g. alumina) may also be included to reduce output degradation due to high humidity content [1.15].

In addition, Komatsu in 1984 suggested a new design of chemoresistive sensor, known as the semistor [1.17]. Instead of using a separate heater, the sintered SnO_2 is directly coated onto the platinum heater coil which becomes a multiple electrode, as shown in figure 1.5. As the electrical conductance of the SnO_2 becomes reduced in the presence of the target gas, the coil is partially shorted. This results in a significant drop of coil resistance. Interfaced with a Wheatstone bridge circuit, the response of the new design is shown in figure 1.6(a). The selectivity of the sensor can be improved by an additional filter coating on top of the metal oxide layer, as shown in figure 1.6(b).

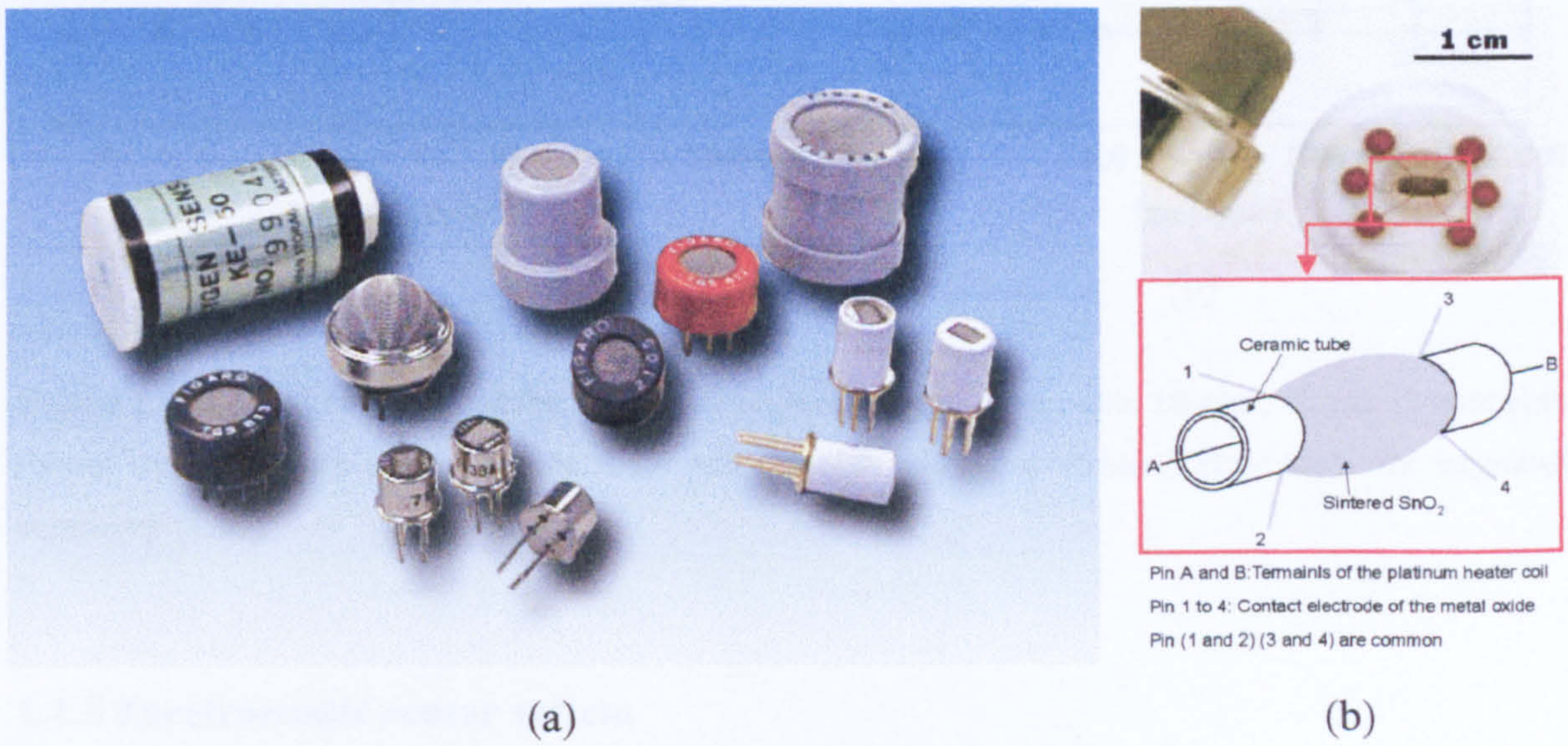

Figure 1.4: (a) Commercial chemoresistive sensors for various target gases in different packages. (b) A packaged sensor (TGS 800 series) and its pin configuration. Manufactured by Figaro Engineering Inc. Japan.

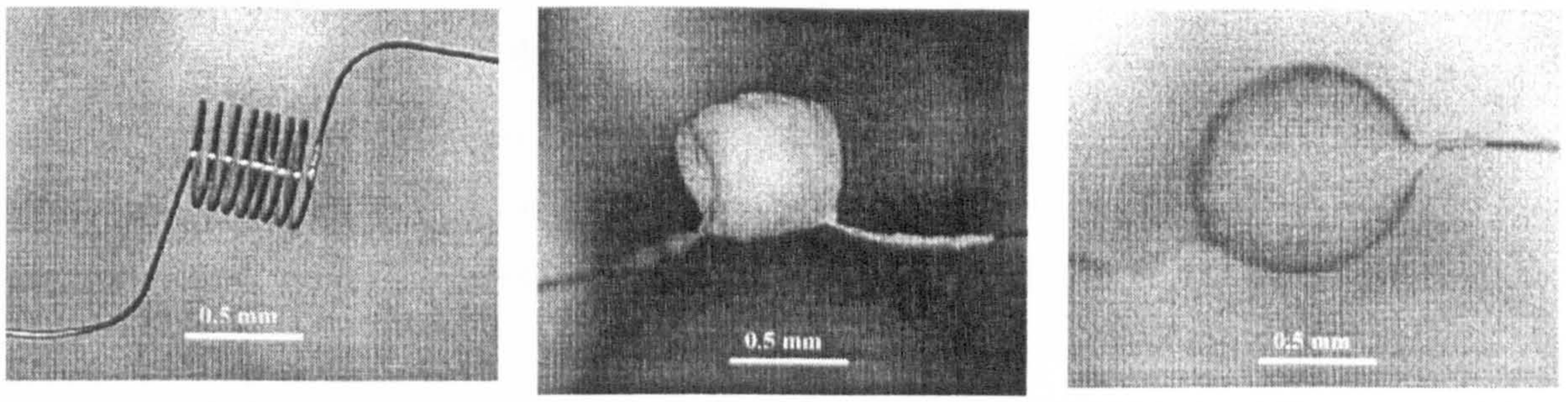

(a) (b) (c)

Figure 1.5: Construction of the new chemoresistive combustible gas sensor design (semistor) [1.16]. (a) The bare coil, (b) initial SnO_2 coating and (c) final coating.

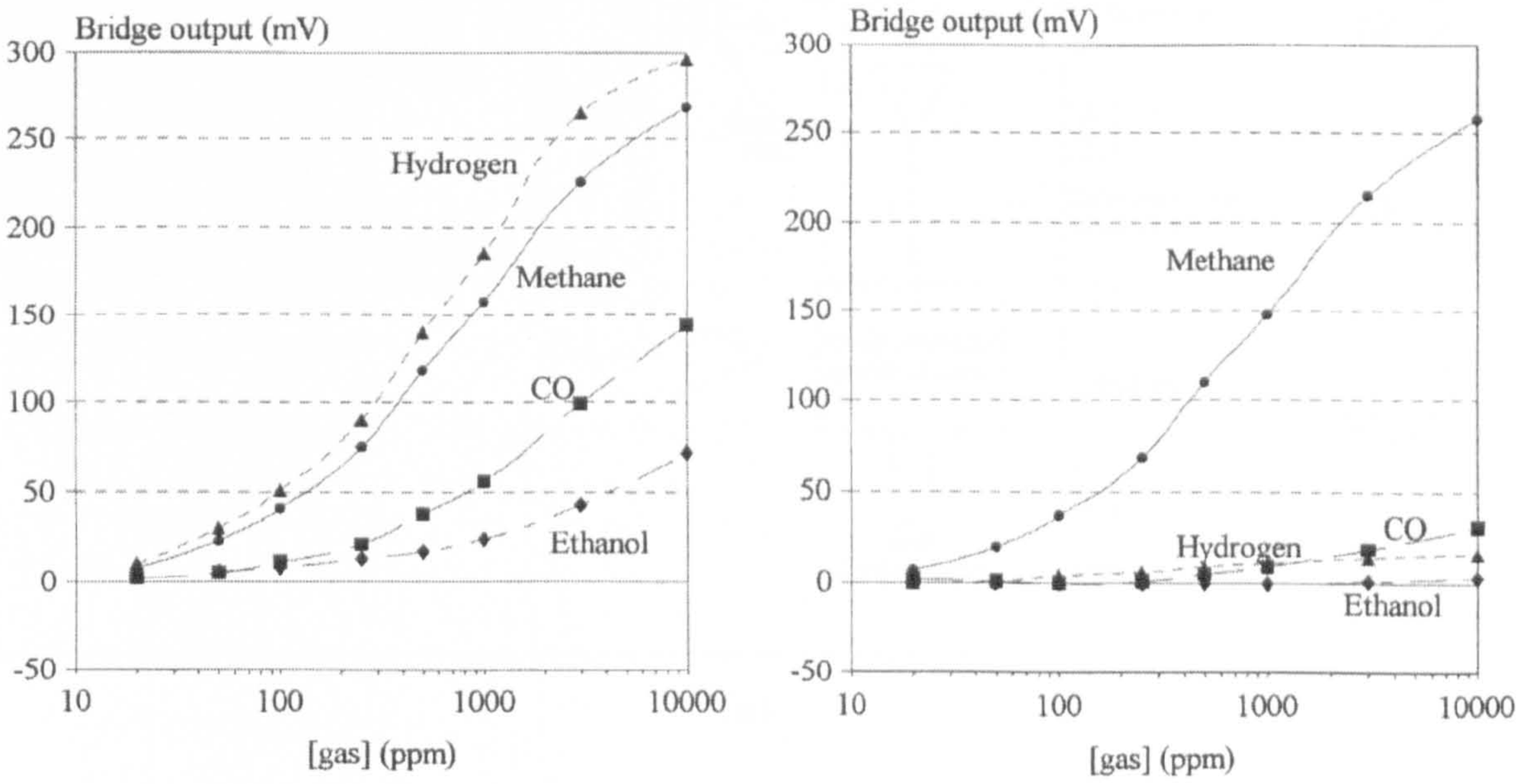

(a) (b)

Figure 1.6: Typical responses of the new chemoresistive sensor design with 10-turn, 10 μm Pt wire coils coated with (a) only polycrystalline SnO_2 and (b) with additional Pt-based filter layer for improved selectivity [1.16].

1.1.3 Spectroscopic sensor system

An alternative detection technique is to measure the spectroscopic absorption of a combustible gas molecule, such as methane. Typically, this system operates in the mid-infrared range (wavelength of 1 μm – 5 μm) [1.18]. Figure 1.7(a) illustrates the basic principle and the output signal analysis [1.19]. As the infrared source (incandescent lamp or IR LED) illuminates a volume of gas in a permeable gas cell, the target gas absorbs

certain wavelengths while others pass through completely unattenuated. An infrared detector is used to measure the amount of absorption which is related to the type and concentration of the target gas. The intensity of the IR source is monitored by a reference detector to provide a benchmark for the absorption measurement. IR detectors are interfaced with a microprocessor for the required computation.

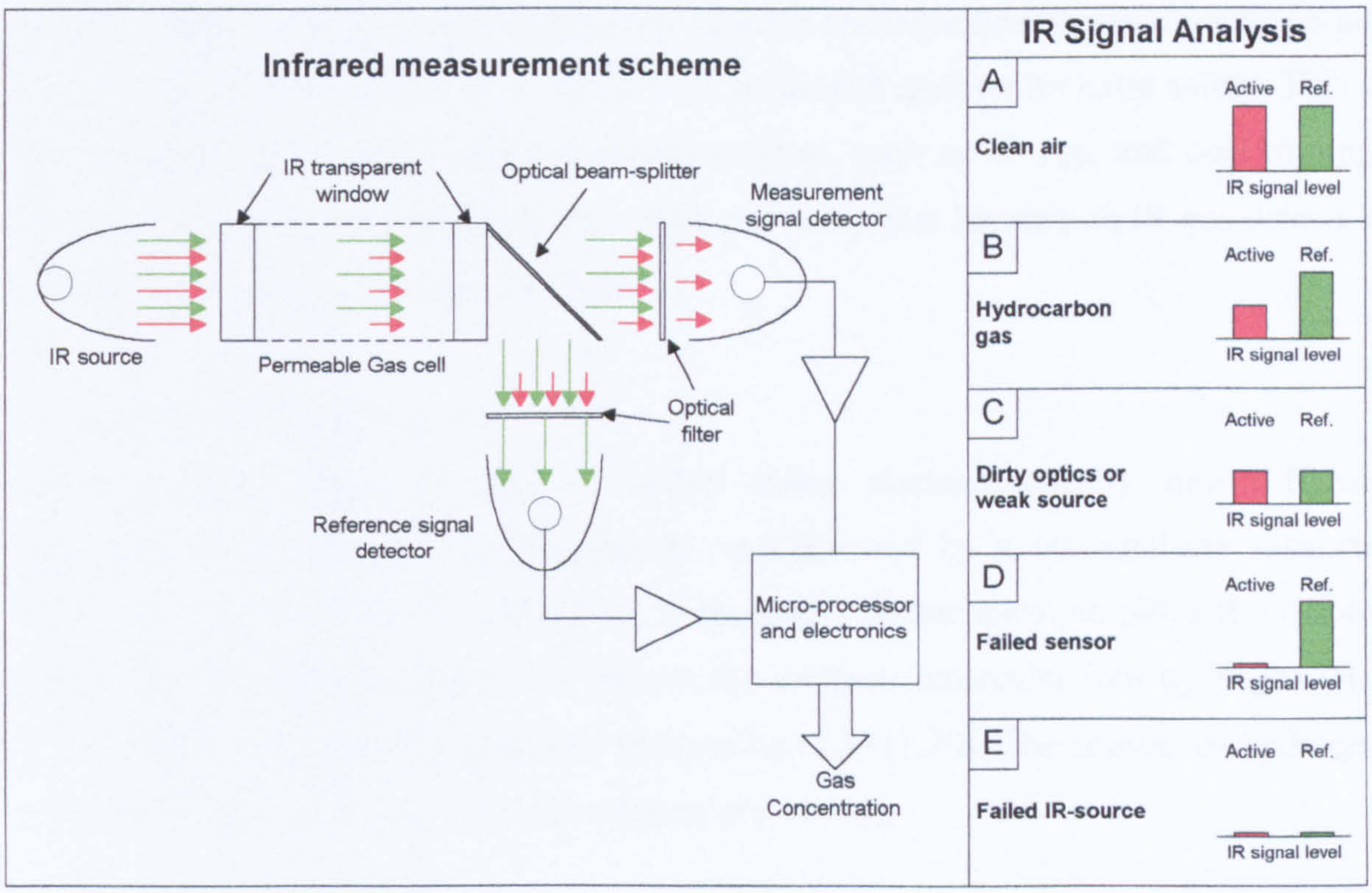

(a)

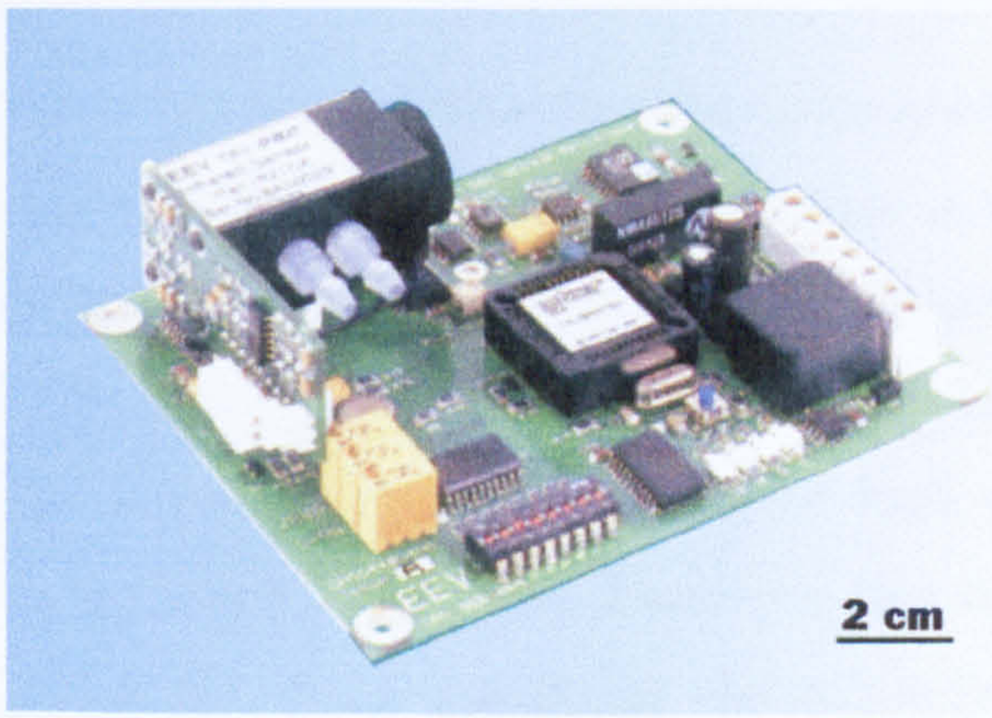

(b)

Figure 1.7: (a) A schematic diagram of a typical IR spectroscopic gas sensor system. The sub-diagram indicates the fault analysis strategy [1.19]. (b) A commercial IR spectroscopic gas sensor module interfaced with micro-controller, manufactured by EEV Ltd. UK [1.9].

Although the sensitivity of the system can be affected by temperature, pressure, contaminated optics, aging component and humidity, it allows automatic failure detection, as shown in the sub-diagram in figure 1.7(a). Furthermore, a recent study indicates that silica optical-fibre can be used in the IR transmission [1.18]. Therefore, this spectroscopic gas sensor can perform remote sensing in a large-scale safety detection network (up to tens of kilometre squares) and with a large number of interrogation points, without suffering from signal degradations. In addition, these interrogation points do not require any power input and so it is free from accidental ignition for extra safety. This is particularly appreciated in energy exploration areas, such as oil rigs and coal mining. However, a major disadvantage of this technique is the cost because an IR gas detection system could cost a few thousands Euros.

1.1.4 Electrochemical sensor

Methane (CH_4) molecules can be broken down electrochemically into different chemicals. The product of the reaction is then detected by a non-methane sensitive sensor. Research at Delft University of Technology, Netherlands, employs the carbon dioxide (CO_2) reforming reaction to reduce the methane molecules into hydrogen (H_2) and carbon monoxide (CO), as shown in equation (1.1) [1.20]. The amount of hydrogen generated is proportional to the concentration of methane.

$$CH_4 + CO_2 \rightarrow 2CO + 2H_2 \qquad (1.1)$$

The detection principle of this sensor is based on the difference in catalyst activity of two different metals that are involved in the reforming reaction. A schematic diagram of the sensing element is shown in figure 1.8. It comprises a proton-conducting solid electrolyte which is sandwiched by two different electrodes, namely the working electrode and counter electrode. The working electrode has a very high catalytic activity toward methane, compared to the counter electrode. Therefore, this creates an electrochemical potential difference across the proton-conducting electrolyte that can be measured by a voltmeter. Other reduction methods are also available to transform methane into other detectable products.

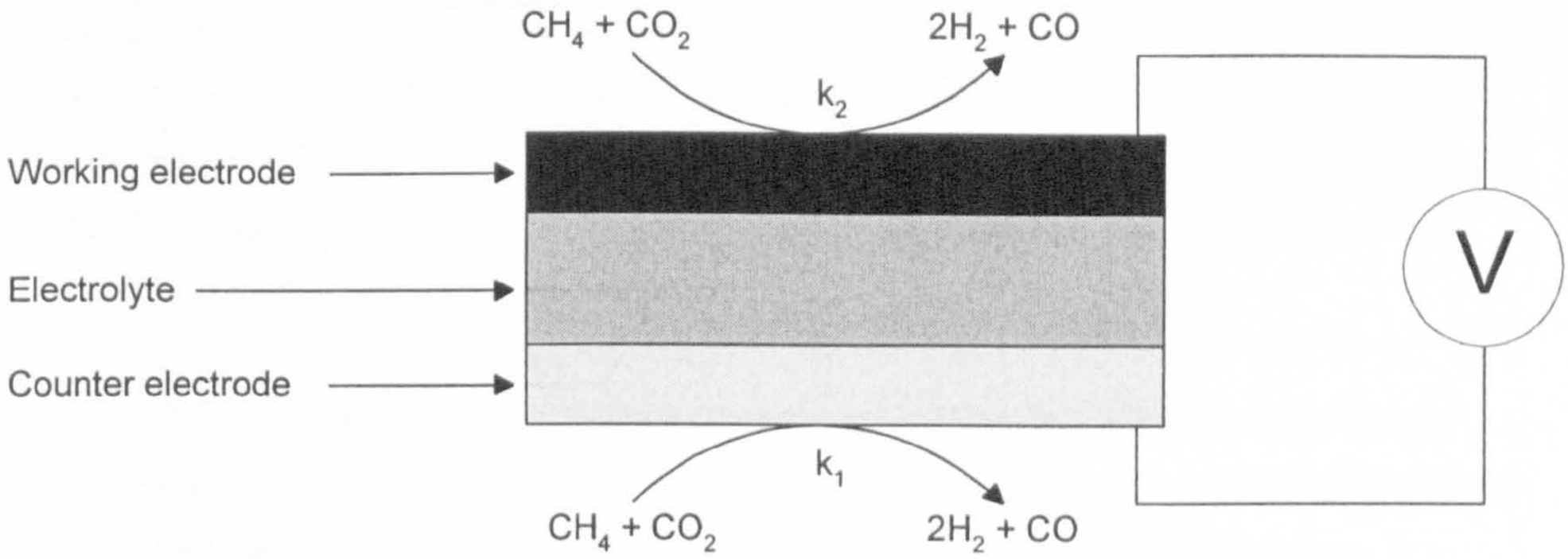

Figure 1.8: The schematic diagram of the sensing element in an electrochemical methane sensor. Note that $k_1 >> k_2$ give rise to the electrochemical potential difference generated across the proton-conducting solid electrolyte.

However, the power consumption of this sensor is relatively high because the operating temperature is between 600°C and 800°C in order to maintain the reactivity of the catalyst. Further investigation is required to determine the relationship between the sensitivity and environmental factors, such as humidity and catalyst poisoning.

1.1.5 Piezoelectric resonating sensor

When compressional waves are generated by a piezoelectric resonator, the ultrasonic longitudinal wave will propagate in the surrounding gas. If the target gas is induced to resonate at the same frequency, a large amount of vibration energy will be absorbed by the resonating gas [1.21]. As the ultrasonic velocities between various gases are significantly different, the target gas and its concentration can be identified by measuring the resulting ultrasonic velocity of the compressional wave (e.g. methane). This detection technique was first patented by Mecea and Bucur in 1978 [1.22].

However, as the piezoelectric material must be operated at low temperature, significantly below the Curie point, the selectivity and the sensitivity to the gas is affected. Although this gas resonating technique may not be appropriate in sensor applications, it can be used in gas chromatography.

1.2 Silicon-based micro-calorimetric gas sensor

The methane sensing techniques that have been described in the previous section possess distinctive characteristics, as given in table 1.1.

Table 1.1: Summary of the characteristics for different types of methane sensor.

Sensor category	Advantages	Disadvantages
1. Calorimetric gas sensor Sensitivity range: (0% - 90%) by volume	Simple construction, compact in size, well-established production and low – medium unit cost.	High power, medium production cost, catalyst poisoning and no failure detection.
2. Chemoresistive gas sensor Sensitivity range: (0% - 100%) by volume	Simple construction, compact in size, well-established production and high sensitivity.	High power, sensitivity affected by humidity and no failure detection.
3. IR spectroscopic gas sensor Sensitivity range: (0% - 100%) by volume	Allow failure detection, remote or long distance monitoring, suitable for large number of sensing points, power-free sensing point for extra safety and no poisoning.	Expensive, low-sensitivity, complex interface required. Sensitivity affected by temperature, aging component, dirty optics, pressure and humidity of gas sample.
4. Electrochemical gas sensor Sensitivity range: (0% - 90%) by volume	Simple construction, compact in size and low – medium unit cost.	High-power, sensitivity is temperature dependent and no failure detection.
5. Piezoelectric resonating gas sensor Sensitivity range: (0% - 100%) by volume	Allow failure detection and high sensitivity.	Sensitivity affected by humidity and low operating temperature.

It was found that considerable research efforts have been spent on the tin dioxide based chemoresistive and the IR spectroscopic gas sensors. The sensitivity and the selectivity of these gas sensors have been improving. The fundamental structure of a pellistor has not been advanced significantly since it was first commercialised in the 1970s, although porous alumina and Pd catalyst have been employed to improve sensitivity and poisoning resistance.

In order to satisfy modern sensing applications, the pellistor is now required to have lower unit cost, higher poison resistance and be more energy efficient. These requirements are not satisfied by the traditional pellistor bead construction. Alternative technologies and designs have to be identified to improve the cost effectiveness of the

sensors. Furthermore, as there is a growing demand for portable safety instruments, the power consumption has to be reduced for compatibility with battery-operated handheld gas monitors which are expected to operate continuously up to 10 hours before recharging. Therefore, the power budget of the sensor should be limited between 75 mW and 100 mW.

Planar technology is regarded as an appropriate technique to realise high volume batch production and hence improves upon existing labour-intensive pellistor production methods. The platinum wire coil in the pellistor can be made using planar technology. Although thick-film techniques that employ ceramic substrates (e.g. alumina tiles) can achieve batch production at relatively low cost, the power consumption required for 500°C operation is rather high (typically over 650 mW) compared to the pellistor bead (typically about 200 mW) [1.23]. Therefore, thin-film technology is the only realistic choice.

Recent advances in both silicon microtechnology and materials technology have resulted in the possibility of creating high-sensitivity, low-power high-temperature silicon planar micro-calorimeters. Several investigations have been carried out and these devices can be categorised into solid membrane and suspending beam structures. These structures reduce thermal losses and lead to lower power consumption.

Early work by Dibbern demonstrated that the platinum wire coil could be substituted by a planar meandering platinum film, sandwiched between two nitride membrane layers, as shown in figure 1.9 (a) [1.24]. The power consumption was only 75 mW at 300°C and the die size was about 3 mm × 3 mm. Further steps were taken by Gall to create a silicon planar micro-calorimeter with a thin layer of conventional porous catalyst [1.25]. Figure 1.9(b) shows the prototype of a micro-calorimeter pair, both sensor and compensator element. However, this prototype required 12 mW to 20 mW to produce a temperature of 100 °C. The power consumption would become considerably higher when operated at 500°C above room temperature.

Research on suspending beam structures was also carried out [1.26]. Instead of using a platinum micro-heater, the heating element was a phosphorous doped silicon wire that operates at 500°C, as shown in figure 1.10. A supporting column was included underneath the micro-heater to enhance mechanical stability, but additional power consumption of 20% was measured. Due to the relatively small device geometry (100 μm

× 100 μm), the power consumption of the device was between 15 mW and 25 mW at 500°C. This structure was subsequently used as a micro-calorimeter with a drop-coated catalyst, as shown in figure 1.11 [1.27]. However, the sensitivity of the sensor was affected by the small sensing area. The response time of the sensor is between 30 s and 120 s, due to the thick and non-uniform catalyst layer. The power consumption of the sensor was expected to increase accordingly. Hence, alternative catalyst or a different deposition method could be used to reduce the thickness of the catalyst film, in order to lower the thermal capacitance of the sensor. Therefore, the power consumption and the response time of the sensor can both be reduced for optimised performance.

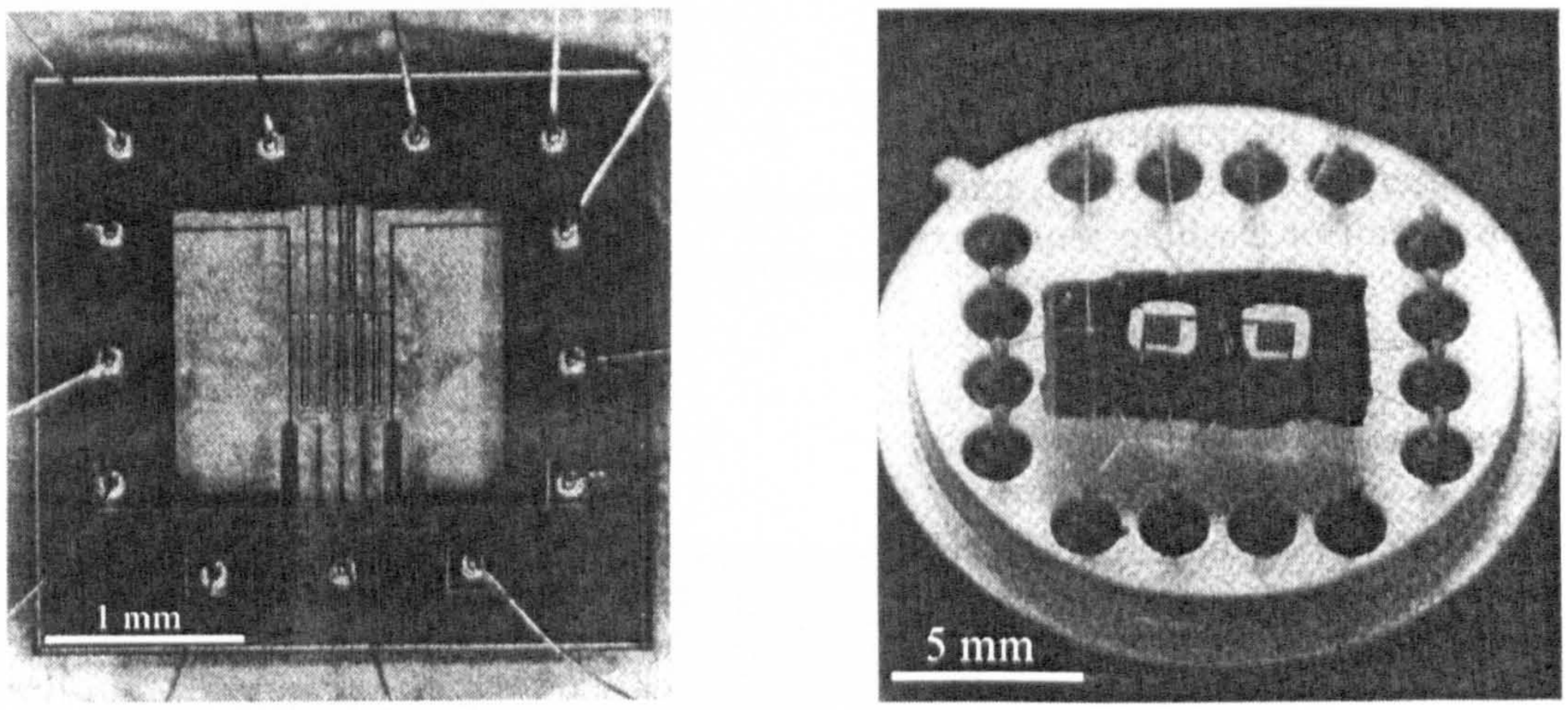

(a) (b)

Figure 1.9: Sensor prototypes from earlier work on micro-calorimeters based on membrane structures. (a) Micro-calorimeter showing the Pt micro-heater by Dibbern [1.24]. (b) Both sensor and compensator elements are on a same die by Gall [1.25].

Although improvements are required for the micro-calorimeter described above, these research efforts verified the feasibility of creating micro-calorimeters by silicon micro-machining technology. This technology should also offer some of the advantages of micro-fabrication, such as small size, lightweight and reproducibility. More importantly, it may realise batch production which allows sensors to be manufactured more cost effectively.

In addition, as low-power solid-state amplifiers and micro-controllers are commonly available, digital interface circuits can be adopted. Therefore, the compensator and the balancing resistors in the traditional Wheatstone bridge circuit could be removed.

This would reduce the overall power consumption without impairing the stability of the detection system.

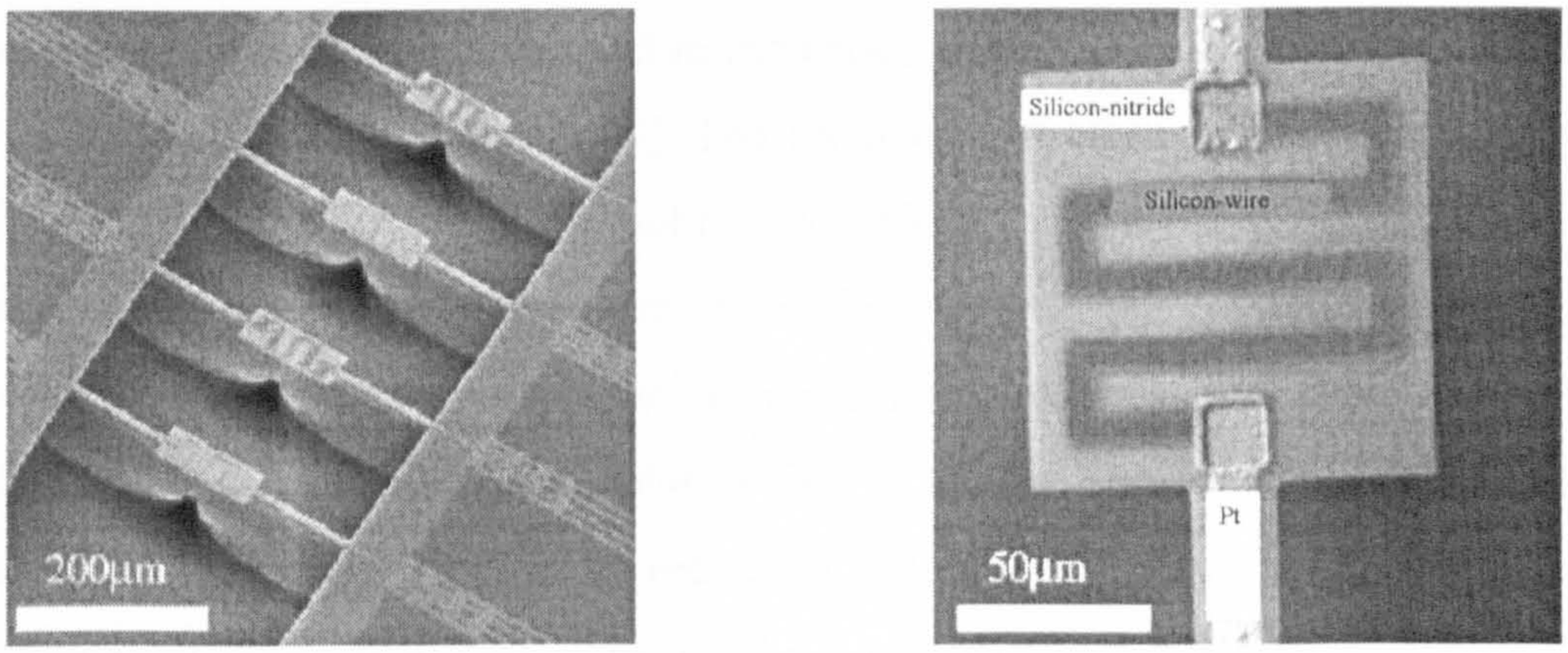

(a) (b)

Figure 1.10: Micro-filament based on suspending beams that can be applied as a micro-calorimeter. (a) Two pairs of suspending devices with a supporting column underneath. (a) A close-up view of the silicon micro-filament wire. [1.26]

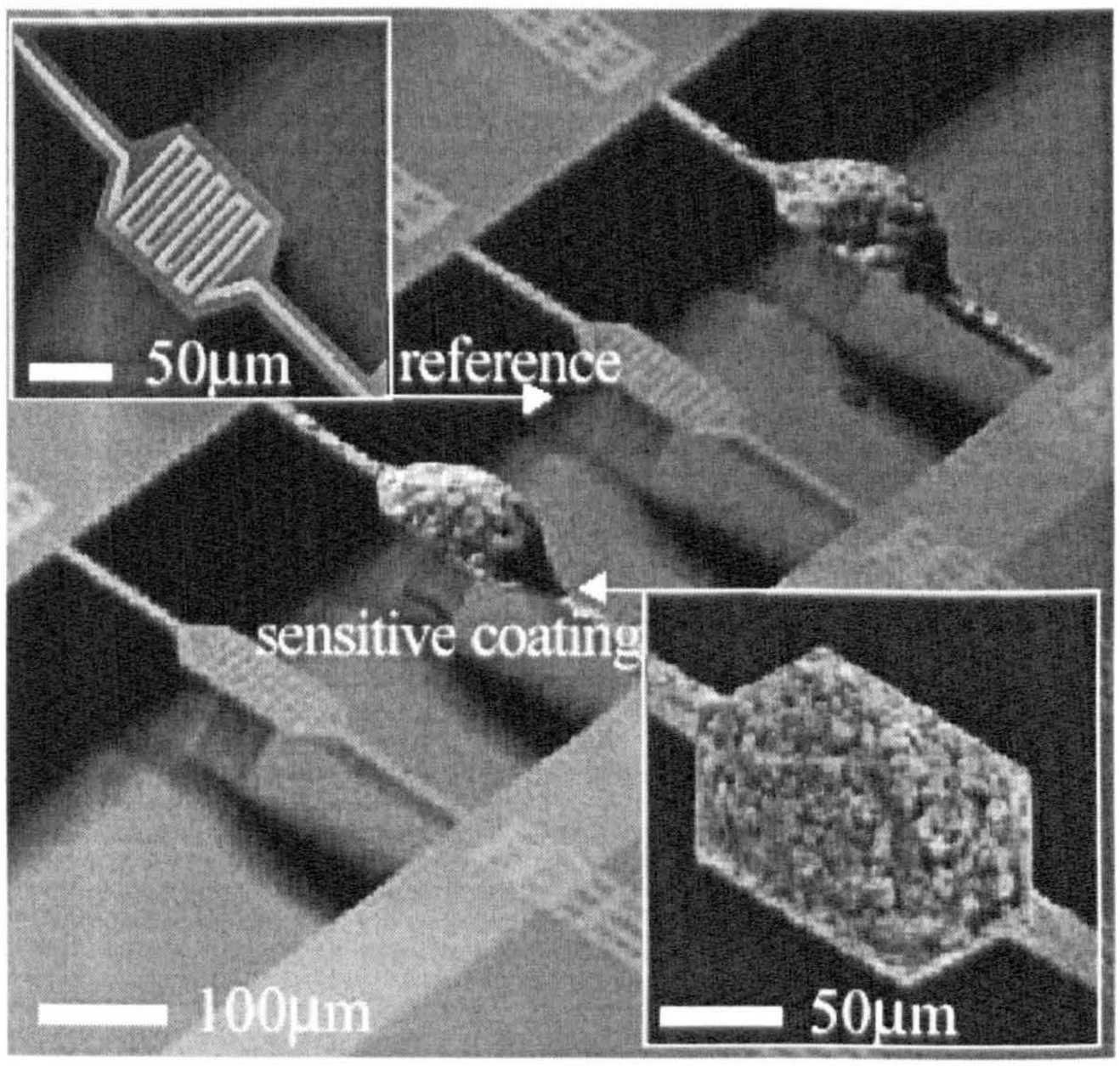

Figure 1.11: Prototype of micro-calorimeter with catalyst based on suspending beam and a supporting column underneath. The thick and non-uniform catalyst layer resulted in a very slow response time of over 2 minutes [1.27].

1.3 Nanoporous catalyst

A catalyst can be broadly defined as a substance that increases the rate of a chemical reaction without undergoing a net chemical change itself [1.28]. Palladium (Pd), as a heterogeneous catalyst, is widely used in industries and it is recognised as one of the best catalysts for methane oxidation [1.29]. The specific area where the catalyst is deposited and heated up during usual operation is referred to as the active area. With miniaturisation, the size of the sensor and surface area of the catalyst will be reduced. This will affect the sensitivity of the micro-calorimeter accordingly. Therefore, instead of a sintered catalyst, nanostructured catalyst film is used to provide a higher surface area and to compensate for the size reduction. Here, fundamental theory about the electrochemical deposition technique of the nanostructured catalyst film is described while the actual deposition procedures are provided in Chapter 3.

1.3.1 Electrochemical deposition technique

There are two types of liquid crystal categorised as either thermaltropic or lyotropic. The phase changes are caused by temperature alteration in thermaltropic liquid crystals. However, a phase change in lyotropic liquid crystals may depend on either temperature or composition. The deposition of the nanostructured catalyst film makes use of the special properties of lyotropic liquid crystal. A graphical representation of a C16EO8 lyotropic liquid crystal molecule is shown in figure 1.12. The molecule includes a hydrophilic head group (EO8) and the hydrophobic carbon tail (C). In the presence of water and an appropriate temperature, the molecules align themselves to form specific building blocks according to the concentration of the surfactant, as shown in figure 1.13 [1.30]. As the concentration of the surfactant increases, a larger self-assembled nanostructure is produced.

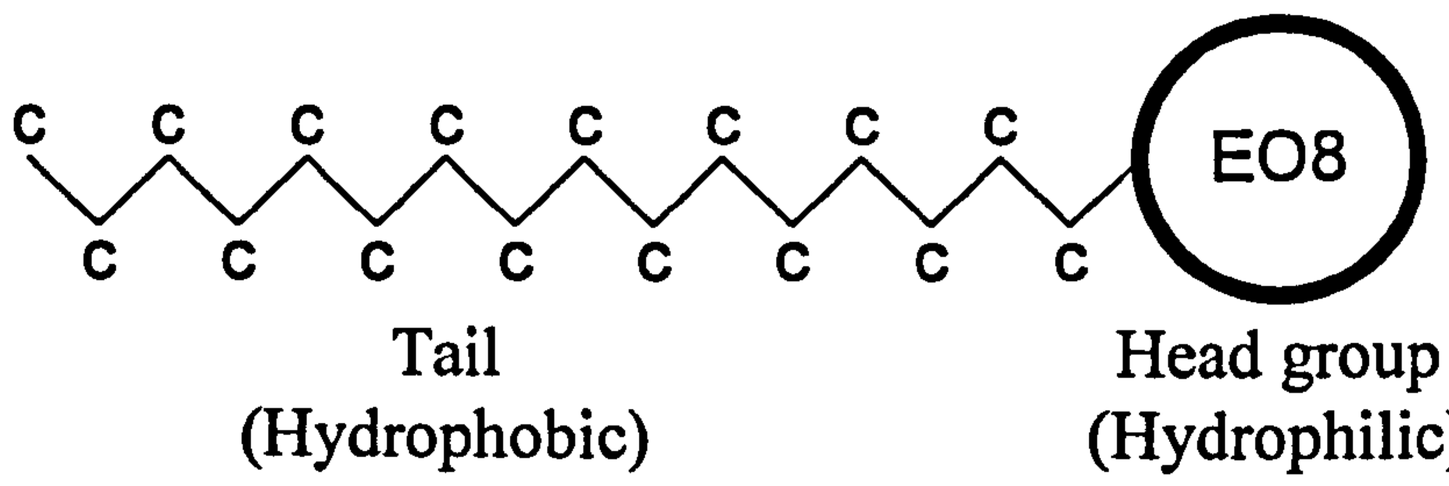

Figure 1.12: Graphical representation of a lyotropic liquid crystal molecule for C16EO8, indicating the head group and the carbon tail.

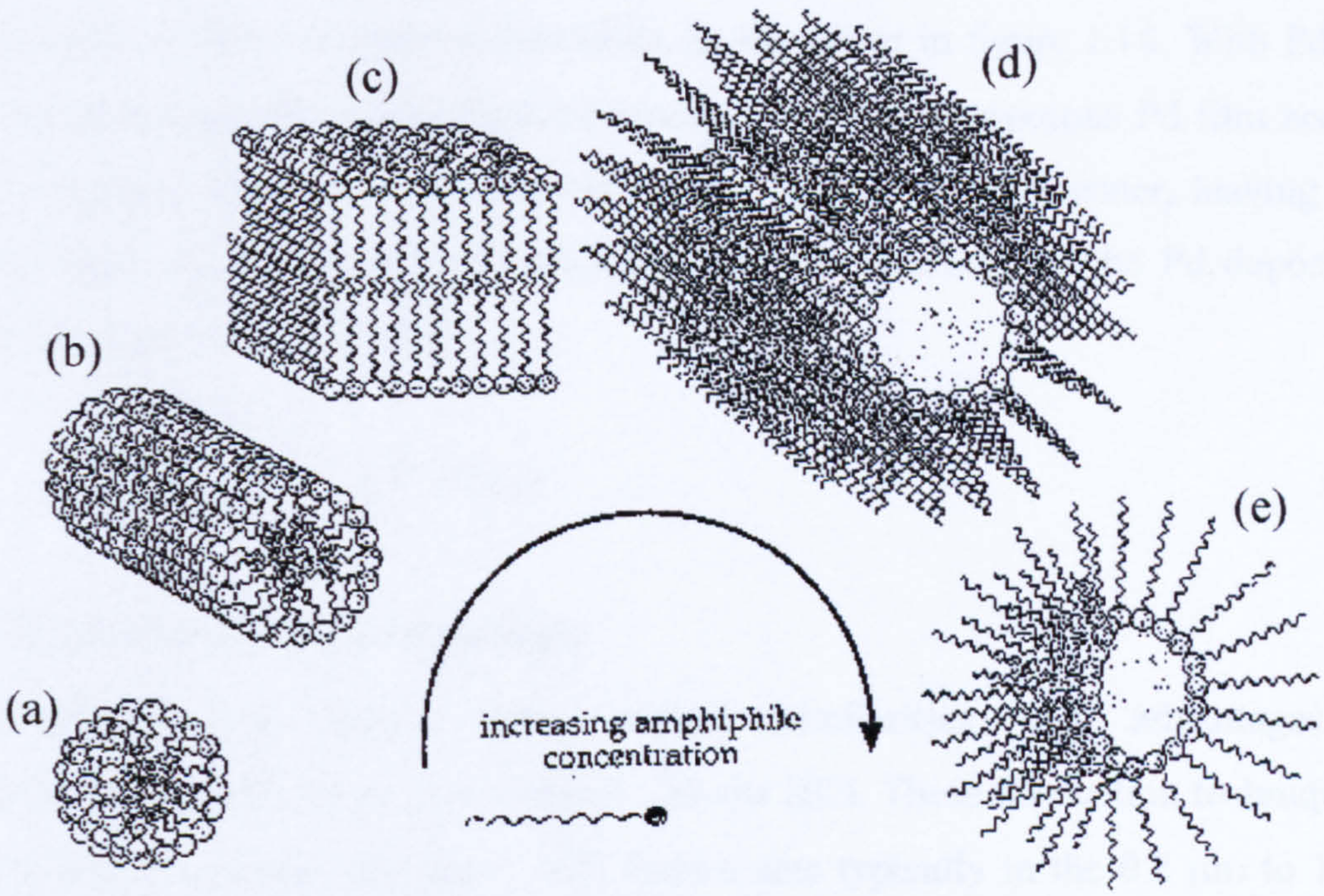

Figure 1.13: The various structures of lyotropic liquid crystal due to increasing concentration of surfactant in water [1.30]. The phases are (a) micellar, (b) hexagonal and cubic, (c) lamellar, (d) inverse hexagonal and inverse cubic, (e) inverse micellar.

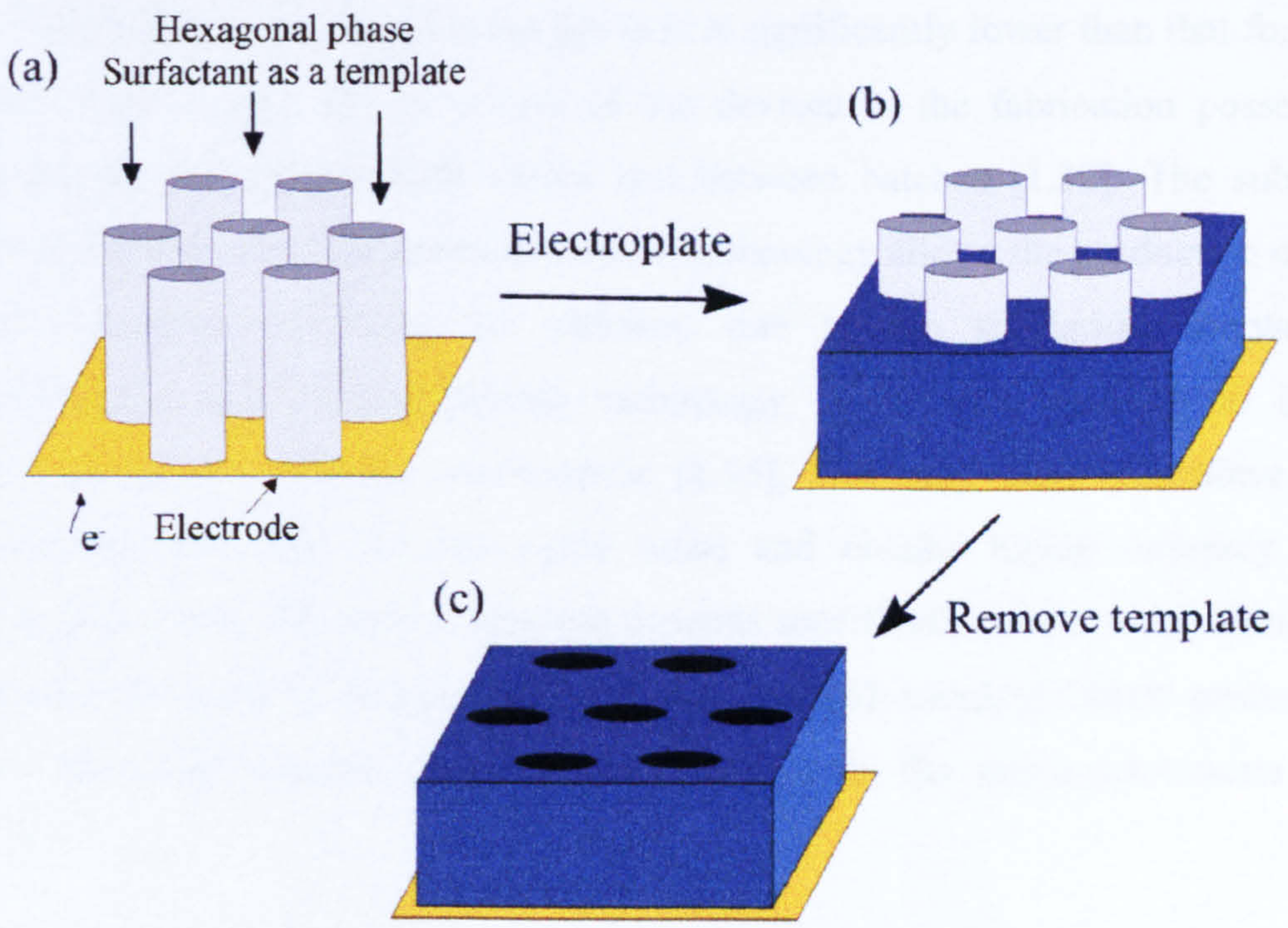

Figure 1.14: Graphical representation of the template-deposition of the nanostructured Pd catalyst (not to scale) [1.31]. (a) Hexagonal phase lyotropic liquid crystalline template placed on electrode. (b) Pd catalyst electrodeposited around surfactant. (c) The surfactant template is removed to create nanoporous Pd matrix.

When the hexagonal phase surfactant is applied onto an electrode, a template is formed by the self-assembled columns (molecules), as illustrates in figure 1.14. With Pd mixed with the surfactant, the electrochemical process creates a nanoporous Pd film according to the template. The aqueous surfactant is then washed away in water, leaving the Pd catalyst layer on the electrode. The electrochemical reduction for the Pd deposition is shown in equation (1.2) [1.32].

$$Pd^{2+}(aq) + 2e- \rightleftharpoons Pd(s) \qquad (1.2)$$

1.4 Micromachining technology

Micromachining techniques share several similarities and advantages with microelectronics fabrication of Integrated Circuits (IC). These fabrication techniques can produce highly complex structures with feature size typically in the 0.2 μm to 100 μm range with the advantages of batch production [1.33]. Similar or identical techniques can be used to fabricate transducers.

Micromachining technology usually uses a silicon wafer as a substrate and allows a large quantity of complicated structure or components to be fabricated simultaneously [1.32]. Therefore, the production cost per unit is significantly lower than that for current pellistors. Furthermore, the properties of the devices in the fabrication possess have remarkable reproducibility, both within and between batches [1.32]. The sub-micron resolution inherited from the microelectronics technology allows the production of highly precise ultra-small structures. In addition, due to the similarities between the microelectronics and micromachining technology, it is often possible to integrate interface electronics into the microsensor [1.35]. Not only does it achieve further miniaturisation, but also reduces signal noise and obtains higher accuracy for the measurements. However, such integration depends specifically on the fabrication process and material involved. As platinum is not compatible with standard CMOS processes, the interface electronic circuits cannot be embedded onto the micro-calorimeter in this research.

1.4.1 Micro-fabrication techniques

Numerous processes and materials have been established for micro-fabrication. This leads to a large number of alternative process options for any particular structure.

However, the various processes can be categorised into several repetitive operations, namely layering, patterning and etching.

The operation employed to add a layer to the wafer surface is known as layering. This layer can be an insulator, conductor or semiconductor, grown or deposited by different methods, as shown in figure 1.15.

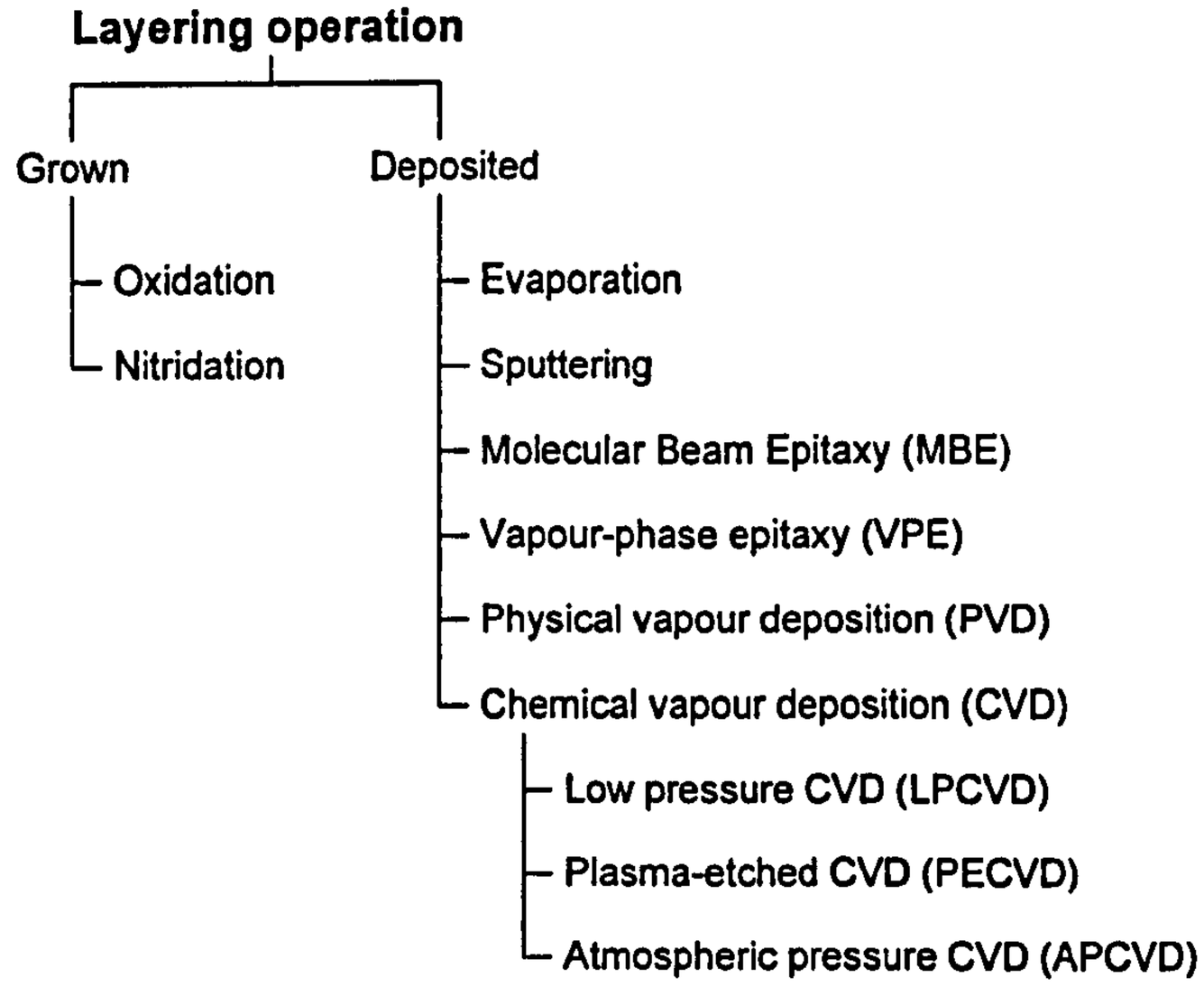

Figure 1.15: The different options for layering operation.

Growing a layer implies that some of the material at the wafer surface is consumed during the process. For example, up to 44% of total thickness of the silicon oxide that grows by oxidation is taken from the silicon wafer itself [1.32]. Therefore, growing technique only applies to the compounds that are within the material of the substrate. Metals and other materials are layered by deposition through Chemical Vapour Deposition (CVD), evaporation or sputtering. A high quality non-metal layer can be deposited by CVD, such as silicon nitride, epitaxial silicon and polysilicon. Evaporation is only applied to some low boiling point pure metals while sputtering technique can deposit additional higher melting point metals and alloys [1.32].

Selected portions of the added layer can be removed by a patterning process and etching. An optical mask carrying the designed pattern is used to replicate itself onto the wafer and the process is commonly known as photolithography. This is achieved via a layer of photoresist that is spun onto the wafer and exposed with Ultra-Violet (UV) through the optical mask. Under the exposing beam (e.g. UV), positive photoresist

becomes water-soluble but negative photoresist is polymerised. Depending on the polarity of the mask and the photoresist, the pattern transferred may be in a form of island or hole, as shown in figure 1.16. Then the photoresist layer itself becomes a mask, covering the appropriate regions of wafer. Finally, an etching process can be carried out to create the desired pattern on the substrate.

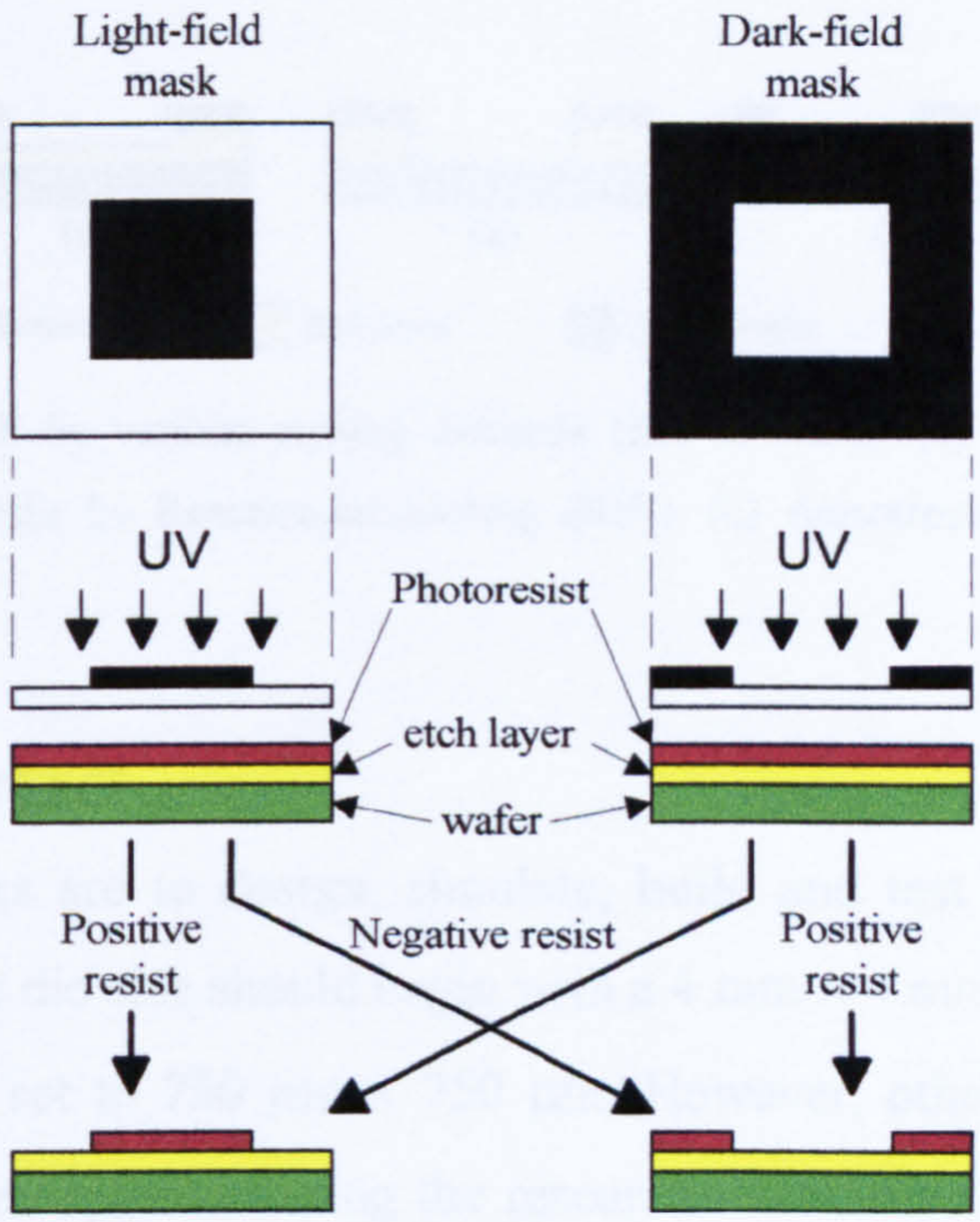

Figure 1.16: Illustration of the results obtains from the combinations between the mask field and the photoresist polarity (not to scale).

As the desired pattern is transferred from the optical mask to the photoresist, the structure can be realised by removing the exposed areas of the wafer. Unlike conventional engineering (e.g. cutting and grinding), chemical methods are used to etch the unwanted areas. Etching is generally classified into wet etching and dry etching. The wafer is immersed in a liquid that dissolves the exposed layer in wet etching. For a silicon wafer, this etching method is usually isotropic and undercuts the masking layer of photoresist, as shown in figure 1.17. However, anisotropic wet etching of silicon using potassium hydroxide (KOH) allows deep structures to be fabricated although the limited range of possible geometries are determined by the crystalline orientation of the wafer. Alternatively, Deep Reactive-Ion-Etching (DRIE) can be used when a deep trench with arbitrary shape is required. This dry etching method employs a gaseous etchant which

can be ionised and propelled towards the masked wafer surface [1.32]. The areas that are not protected by photoresist will be bombarded by the energised gaseous ions and gradually etched away. Other micromachining techniques for deep structures like *Lithographie, Galvanoformung, Abformung* (LIGA) and stereolithographic rapid prototyping have also been developed to create 3-D structures. However, these techniques are generally expensive and less common.

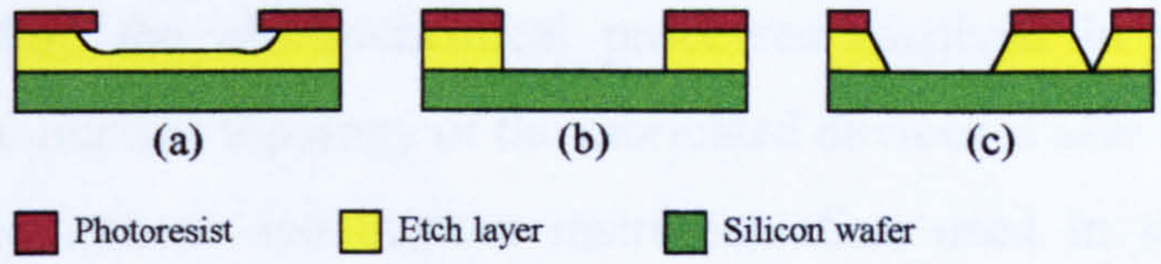

Figure 1.17: Etching result by various etching methods (not to scale). (a) Undercut by wet isotropic etching. (b) Straight sidewalls by Reactive-ion-etching (RIE). (c) Anisotropic wet etching by KOH on <100> wafer.

1.5 Research objectives

The research objectives are to design, simulate, build and test a novel silicon planar micro-calorimeter. The die size should begin with a 4 mm × 4 mm square and the micro-heater size is initially set to 750 μm × 750 μm. However, other sizes for the die and micro-heater should be explored during the research in order to further reduce the unit cost and improve sensitivity. The power consumption of the device should be 30% less than the existing product manufactured by City Technology Ltd. UK, i.e. 167 mW instead of 250 mW, while the operating temperature is maintained at about 500°C. The driving voltage should be below 5 V for compatibility of digital interface electronics. The response time towards methane should be in the order of milliseconds. The technology of electrochemically deposited nanostructured Pd catalyst film will be employed. The properties and characteristics of the device with nanostructured catalyst films on the devices will be investigated to develop a low-power micro-calorimeter with improved poison resistance. The lifetime of the sensor should be at least 5 years under normal operating condition.

1.6 Outline of thesis

This thesis describes two new generations of micro-calorimeters from design, simulation, and fabrication to testing. The first chapter provides an overview of the various methane

detection techniques, their characteristics and applications. The basic theory about the electrochemical deposition using lyotropic liquid crystals is also described. Several micro-machining techniques are given.

The progressive designs and simulations for the micro-heater to improve thermal homogeneity at the active area are explained in Chapter 2. The design strategies and detail dimensions are included.

The fabrication details for the micro-machined devices are documented in Chapter 3, including the electrochemical processes involved in the nanoporous Pd catalyst deposition. Surface topology of the fabricated devices is also investigated.

The test equipment and custom instrumentation used in the experiments are described in Chapter 4. It includes specifications about the gas test stations, data logging systems, driving and interface electronics.

Chapter 5 describes the steady-state characterisation of the micro-calorimeters. Various device properties have been investigated, such as temperature coefficient of resistivity, base-line resistance, power consumptions and temperature homogeneity using infrared thermography. As different modes of heat transfer have been studied, a power optimisation model which related the membrane-to-heater ratio (*MHR*), has also been suggested.

The chemical responses in both continuous power and pulse mode are discussed in Chapter 6. The sensitivity and catalyst efficiency of the micro-calorimeters under different conditions (e.g. temperature) have been investigated. Dynamic properties of several selected micro-calorimeter designs and their chemical responses have been characterised.

Finally, the conclusions toward the research objectives and further work are discussed in the Chapter 7.

References

[1.1] Anon, Monitoring the atmosphere in underground mines, *Mining Magazine*, December, 1988, pp 483-487.

[1.2] E. R. Steyn, The early detection of inflammable gas at the working face, *Journal of the Mine Ventilation Society of South Africa*, July, 1985, pp 81-82.

[1.3] *Combustible gas detector elements,* Product data handbook, EEV Ltd. 1977.

[1.4] K. Menzefricke, Introduction to the European Industrial Gas Sensors Market, *International Environmental Technology*, Vol. 10, Issue 3 May/ June 2000.

[1.5] D. Carrillo, Contact Sensors Losing the Battle against Non-contact Sensors, *The Automator online magazine*, article April 2002, web-site: http://www. automatedbuildings.com

[1.6] A. Baker, Improvements in Electrically heated filaments used in connection with the detection of combustible gases in air, UK patent application 892530A, 1959.

[1.7] J. W. Gardner, S. M. Lee, P. N. Bartlett, S. Guerin, D. Briand and N. F. de Rooij, Silicon Planar Microcalorimeter Employing Nanostructured Films, *Digest of technical papers vol 1*, Transducers '01 Eurosensors XV, 2001, pp. 820-823.

[1.8] *The 4-series Citicels® handbook*, City Technology Ltd. UK, p44, 1999.

[1.9] *EEV Gas sensor catalogue*, UK, 1999.

[1.10] P. T. Moseley, B. C. Tofield, *Solid State Gas Sensor*, Adam Hilger, pp 28-29, 1987

[1.11] H. Baltes, W. Göpel, J. Hesse, *Sensors Update*, Volume 2, Wiley-VCH, Weinheim, 1996.

[1.12] Instruments for the detection of combustible gases, *British Standard BS 6020*, British Standards Institution 1982.

[1.13] H. Meixner, U. Lampe, Metal oxide sensors, *Sensors and Actuators B*, 33, pp 198-202, 1996.

[1.14] F. Quaranta, R. rella, P. Siciliano, S. Capone, M. Epifani, L. Vasanelli, A. Licciulli, A. Zocco, A novel gas sensor based on SnO_2/Os thin film for the detection of methane at low temperature, *Sensors and Actuators B*, 58, pp 350-355, 1999.

[1.15] J. Orts, E. Lobet, X. Vilanova, J. Brezmes, X. Correig, Selective methane detecion under varying moisture conditions using static and dynamic sensor signals, *Sensors and Actuators B*, 60, 106-117, 1999.

[1.16] G. Williams, G. S. V. Coles, The semistor: a new concept in selective methane detection, *Sensors and Actuators B*, 57, pp 108-114, 1999.

[1.17] K. Komatsu, S. Akai, K. Fukui, Gas sensor, European patent EPA 0115953, 1984.

[1.18] B. Culshaw, G. Stewart, F. Dong, C. Tany, D. Moodie, Fibre optic techniques for remote spectroscopic methane detection – from concept to system realisation, *Sensors and Actuators B*, 51, pp 25-37, 1998.

[1.19] J. Jarivs, The chemical Engineers' resource, web site: http://www.cheresources.com/gasdetect.shtml

[1.20] L. N. Van Rij, J. Le, R. C. Van Landschoot, J. Schoonman, A novel Ni-CERMET electrode based on a proton conducting electrolyte, *Journal of Materials Science*, 36, pp 1069-1076, 2001.

[1.21] V.M. Mecea, Vibrating piezoelectric sensors, *Sensors and Actuators A*, 41-42, pp 630-637, 1994.

[1.22] V. M. Mecea, R. V. Bucur, A new method for the detection of a dangerous gas in the atmosphere, Rom. Patent No. 76 465, 1978.

[1.23] D. Lee, W. Chung, M. Choi, Jong Baek, Low-power micro gas sensor, *Sensors and Actuators B*, 33, pp 147-150, 1996.

[1.24] U. Dibbern, A substrate for thin-film gas sensors in Microelectronic Technology, *Sensors and Actuators B*, 2, 1990, pp. 63-70.

[1.25] M. Gall, The Si planar pellistor array, a detection unit for combustible gases, *Sensors and Actuators B*, 15-16, 1993, pp. 260-264.

[1.26] P. Fürjes, Zs. Vizváry, M. Ádám, A. Morrissey, Cs. Dücső, I. Bársony, Thermal investigation of micro-filament heaters, *Sensors and Actuators A*, 99, pp 98-103, 2002.

[1.27] Cs. Dücső, M. Ádám, P. Fürjes, M. Hirschfelder, S. Kulinyi, I. Bársony, Explosion-proof monitoring of hydrocarbons by micropellistor, EUROSENSORS XVI, *Proceedings of the 16th European Conference on Solid-state Transducers*, W1B4, Prague, Czech Republic, September 15-18, 2002.

[1.28] G. C. Bond, *Catalysis by Metal*, Academic Press, New York, pp 537, 1962.

[1.29] C. F. Cullis and B. M. Willatt, Journal of Catalyst, 83, pp 267, 1983.

[1.30] S. Guérin, Planar pellistors: An application of electrodeposited mesoporous palladium films for the detection of combustible gases, *PhD Thesis*, University of Southampton, 1999.

[1.31] S. A. A. Leclerc, M. J. Willett, S. M. Lee, J. W. Gardner, J. Marwan, P. N. Bartlett, Novel combustible gas sensors employing micromachined silicon substrates and nanostructured catalysts, submitted to *Sensors and Actuators B* in July.

[1.32] Y. M. Tan, Mesoporous materials, *PhD Thesis*, University of Southampton, 2001.

[1.33] E. Yeatman, Introduction to Microsystems, *Course note in microsystem technology*, Imperial College, UK, 1999.

[1.34] S. M. Sze, *VLSI Technology*, 2nd Edition, McGraw Hill, New York, 1988.

[1.35] J. W. Gardner, V. K. Varadan, O. O. Awadelkarim, *Microsensors MEMS and Smart Devices*, Chapter 1, pp. 3, John Wiley & Sons, Ltd. Chichester, 2001.

Chapter 2

Design and simulation of silicon planar micro-calorimeters

2.1 Introduction

This chapter describes the design of two generations of micro-calorimeter, including an overview of the characteristics for the original micro-hotplate design, the SRL 136. Here, the design work has been focused on optimising the power consumption, thermal homogeneity of the active area, and the voltage requirements. The basic device structure is identical for both design generations. Minor modifications were made to the first generation devices in order to allow direct comparisons with the original design. However, a total of 54 different designs and variants were created in the second generation to explore various design ideas for optimised performance and so enable other investigations.

Thermo-mechanical simulations have also been performed on selected designs to estimate the device performance. Geometrical models were created and a specific database of the material properties have been established through a continuous parameters update. Therefore, the simulation models could be used to improve the efficiency of future micro-calorimeter designs.

2.2 The original meander-type device

The structures of the new micro-calorimeters are based on the early design of a silicon micro-hotplate (SRL 136) from the Sensors Research Laboratory, University of Warwick by A. Pike [2.1], as shown in figure 2.1. However, this device suffered from several practical problems, such as a relatively high power consumption and non-uniform thermal distribution over the active area [2.2]. Compared with a standard commercial pellistor bead, although the SRL 136 reduces power consumption by a factor of two, typically 180 mW, its power requirements are still too high for battery powered operation

[2.3]. Further power reduction is necessary to prolong the lifetime of the battery in a portable safety instrument. Moreover, the operating voltage of the device was 7.5 V which is incompatible with modern low-voltage (3.3 V) digital interface electronics. For these reasons, the full potential of the device was not realised commercially.

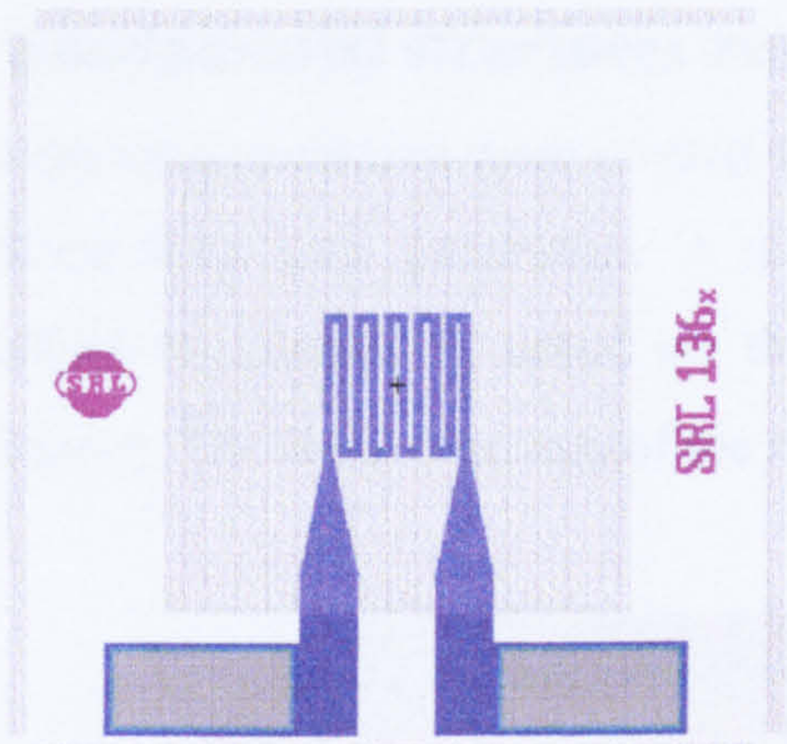

(a)

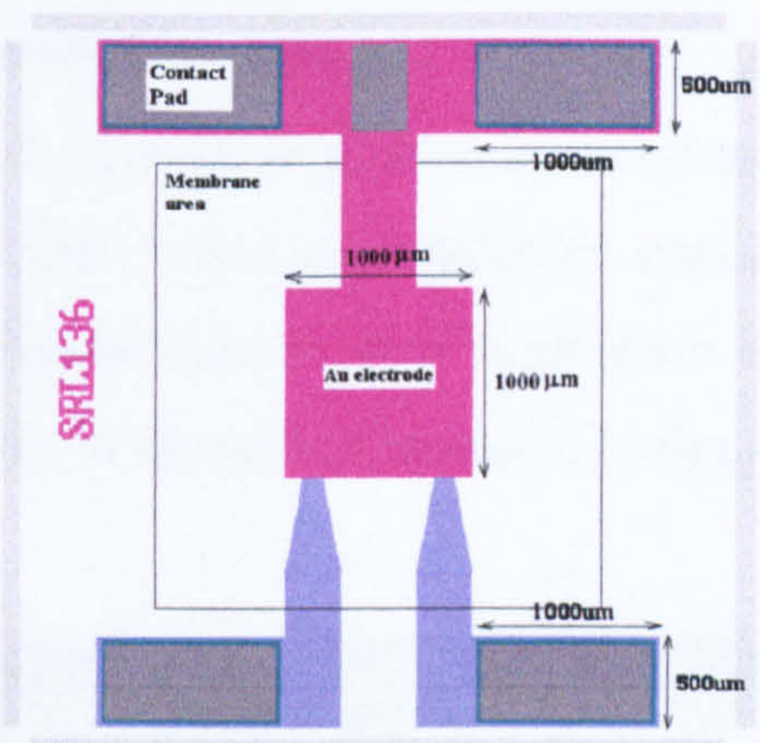

(b)

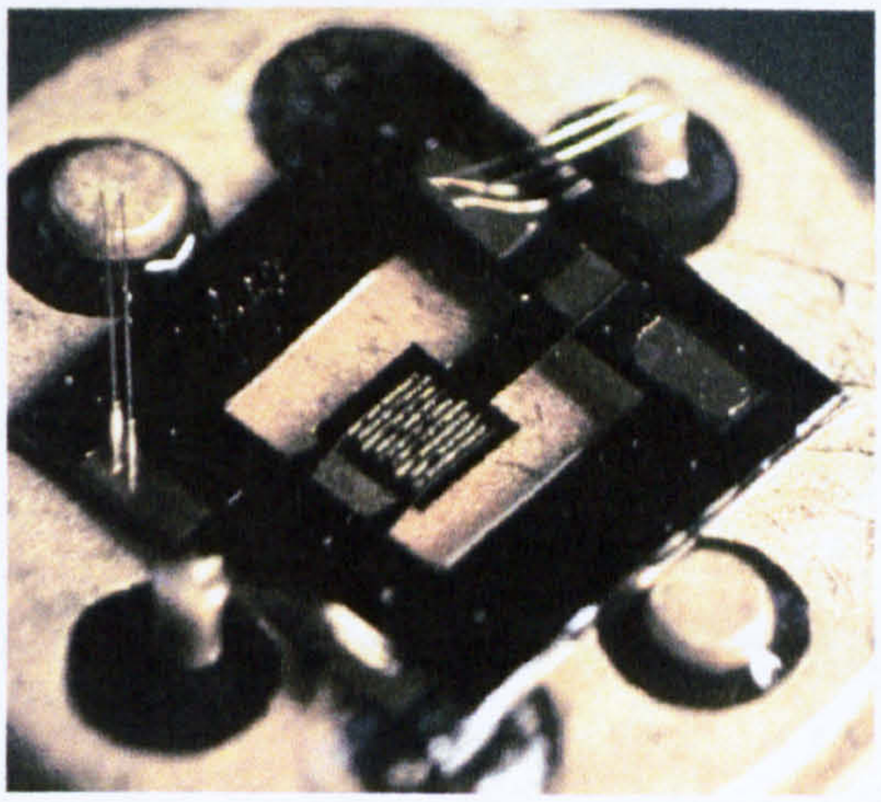

(c)

Figure 2.1: Former design of a silicon planar micro-calorimeter (SRL 136). (a) Schematic diagram of the device without the Au gate electrode, exposing the Pt micro-heater tracks. (b) Schematic diagram of the micro-calorimeter with Au gate electrode. (c) The initial fabrication of the device shows that the active area is slightly off-centre.

An additional limitation of the SRL 136 was the observation of a local hot spot in the active area. This causes uneven catalyst reaction to the target gas and reduces the device sensitivity. Furthermore, the potential of over-heating could damage the gold electrode and affect its long-term reliability. In addition, a misalignment of the back-etching resulted in an off-centred active area, as shown in figure 2.1(c). This caused an uneven

thermally induced stress on the membrane and further degraded the performance and reliability of the device. Micro-machining techniques have been advanced over the intervening years and devices can be manufactured to a higher accuracy. Therefore, a new generation of micro-hotplate was required to overcome the above limitations.

2.3 Fundamental structures and design considerations

Two device generations were created in this research and essential device properties were collected from each generation. A set of design-rules would eventually be created, as described in Chapter 7, based on the device characterisation data from each design generation. The basic structure of the micro-calorimeter design is illustrated in figure 2.2.

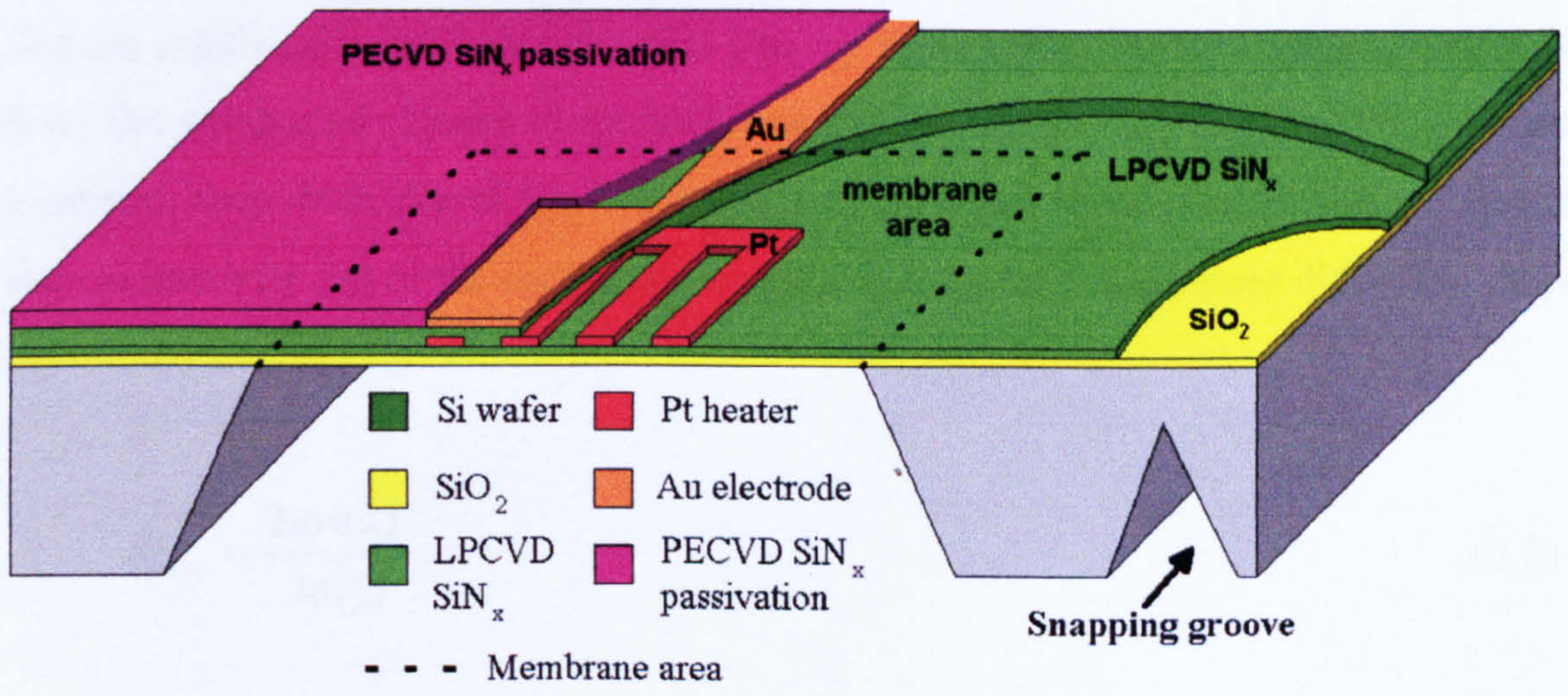

Figure 2.2: The basic structure of the micro-calorimeter substrate.

The micro-calorimeter substrate comprises a thin membrane structure and uses a <100> silicon wafer as the inert substrate. The membrane possesses a 250 nm thick platinum resistive heater whose resistance depends upon its size and supply voltage requirement. The micro-heater is sandwiched between two LPCVD silicon nitride layers, 500 nm and 250 nm thick above and below, respectively. A 150 nm layer of gold is then deposited on and patterned, using a lift-off technique, to form an electrode directly above the micro-heater. This creates a working electrode for the electrodeposition of the nanoporous catalyst. Anisotropic (KOH) back etching solution was used to create both the square membrane and snapping grooves that are used to define the die size in dicing process. A final passivation silicon nitride (PECVD) layer is optional for additional mechanical stability and chemical resistance.

2.3.1 Heat loss mechanisms

As all the micro-calorimeters were designed for low power operation, the thermal loss of the device was a major consideration. Heat loss can occur by three mechanisms as shown in equation (2.1), namely conduction, convection and radiation.

$$P_{tol} = P_{mem} + P_{air} + P_{rad} \tag{2.1}$$

where P_{tol} = total heat loss
P_{mem} = conduction through the membrane material
P_{air} = convection or conduction to the surrounding air
P_{rad} = radiation losses above and below membrane

Dibbern published models for the heat loss by these three different mechanisms [2.4]. Here, the conduction losses in the membrane material (P_{mem}), are given by geometric quantities, such as thickness (t), length (u), length of the active area (a) and the specific heat conductivity (σ) of the membrane material and by the temperature difference ΔT, as stated in equation (2.2).

$$P_{mem} = \frac{2\pi\sigma t\Delta T}{\ln\left(\frac{u}{a}\right)} \tag{2.2}$$

The heat loss by convection to air, P_{air}, is dependent on the size of the active area, as stated in equation (2.3). For ordinary silicon ICs with encapsulated packaging, the effect of convection is negligible. However, in sensor applications, the sensing element has to be exposed to react with the target gas. In addition, as the operating temperature of the device is 500°C, convection to the surrounding air becomes prominent. This dependence is complex and proportional to the length, a, of the active area. In the expression, the cooling effect by the gas flow has been assumed to be negligible due to the relatively enclosed sensor package.

$$P_{air} \approx (0.33\Delta T \ \text{mW/mm}^2) \times (a^2) \tag{2.3}$$

The approximation of the radiation loss P_{rad} is shown in equation (2.4).

$$P_{rad} \approx (10mW/mm^2) \times (a^2) \tag{2.4}$$

Although there were many assumptions made in Dibbern's model, it provides a simple parametric description of the power consumption for the devices at its early design stage. However, detailed investigations were conducted employing thermomechanical simulation software which are discussed in section 2.6.

2.3.2 Membrane-to-heater ratio (*MHR*)

Although both convection and radiation loss is surface area dependent, the radiation loss is inevitable once the micro-heater temperature has been elevated above 300 °C [2.5], according to the model suggested in the last section. Therefore, only conductive and convective loss can be tuned to optimise the power consumption [2.6].

The silicon nitride membrane is used to isolate the conductional loss from the micro-heater to the supporting frame. Ideally, the membrane area should be maximised while the die size remains small in order to achieve low convective loss and high packing density on a wafer. Therefore, the ratio between the membrane and the micro-heater is a critical parameter to manipulate the conductive loss of the device. The ratio of the length of membrane over the length of micro-heater is defined here as the Membrane-to-Heater Ratio (*MHR*). This important parameter had been used frequently throughout device optimisation and characterisations.

2.3.3 Span-to-width ratio (*SWR*)

The Span-to-Width Ratio (*SWR*) is the width of the membrane divided by its thickness. This is an important parameter because it defines the robustness of the new device. In general, the lower the *SWR*, the higher the mechanical stability and better yield during device fabrication. However, a higher value will result in a lower time constant and better thermal isolation of a device. Therefore, it has to be tuned cautiously with the *MHR* to achieve optimised performance.

2.3.4 The resistivity of the thin film

As the thickness of the heater and the membrane are relatively small compared to classical mechanical designing, conventional physical properties might not be valid. Sondheimer's thin film theory was considered in the micro-calorimeter design.

The electron mean-free-path is one of the important factors in terms of electrical conductivity. It can be affected due to scattering by phonons, impurities and deflections. When the thickness of the material is reduced to a certain level, the surface boundary will violate the condition of perfect periodicity. Therefore, although it was generally agreed that the interactions of electrons with the surface are mostly by diffusion, the effect of electron collision with a surface should be considered. Sondheimer developed a theory for this scattering by considering an electron at an arbitrary point in the film and by noting what would happen if its velocity were in a certain direction [2.7]. After integrating over all the positions in the film and over all the directions for the velocity, the resistivity as a function of thickness had been achieved, as shown in equation (2.5) [2.8].

$$\frac{\rho}{\rho_\infty} = \frac{1}{1 - \frac{3}{8x} + \frac{e^{-x}}{16x}\left(x^3 - x^2 - 10x + 6\right) - \frac{x}{16}\left(x^2 - 12\right)\int_x^\infty \frac{e^{-y}}{y}dy} \tag{2.5}$$

where $x = \frac{d}{\lambda_\infty}$; λ_∞ = mean free path for infinite thickness; and d = thickness

The Sondheimer relationship indicated that the thick and thin film approximation are equal when $x = 0.1$. The thick film approximation is shown in equation (2.6a) and the thin film approximation is shown in equation (2.6b).

$$\frac{\rho}{\rho_\infty} = 1 + \frac{3\lambda_\infty}{8d} \qquad \text{for } \frac{d}{\lambda_\infty} > 0.08 \tag{2.6a}$$

$$\frac{\rho}{\rho_\infty} = \frac{1}{3d\left(\ln\frac{\lambda_\infty}{d} + 0.4228\right)} \qquad \text{for } \frac{d}{\lambda_\infty} < 0.08 \tag{2.6b}$$

Based on the material thickness for the micro-calorimeter design, we have $\frac{d}{\lambda_\infty} = 22.73$, where $\lambda_\infty \approx 11$ nm at 0°C [2.9], and hence, the thick film approximation was applied.

Therefore,

$$\frac{\rho}{\rho_{\infty}} = 1 + \frac{3\times(11\times10^{-9})}{8\times(250\times10^{-9})} \approx 1.0165 \tag{2.7}$$

The result in equation (2.7) shows that there is a small increase of resistivity by thin film effects in the order of 1.65%. Therefore, the resistance of the platinum micro-heater was expected to increase accordingly. In addition, impurities in the material will also contribute additional resistance to the actual value.

2.4 First generation micro-calorimeter design

The first generation designs were similar to the former micro-calorimeter design. However, due to defects and non-matured micro-machining fabrication processes mentioned earlier, the properties of the new designs were difficult to predict. The main objective of the first generation design was to produce a functional device to evaluate the actual device properties and allow the electrochemical deposition process for the nanoporous catalyst to be established. Therefore, only one device was designed and the modifications were kept to a minimum to ensure the device functionality.

2.4.1 Design specifications for the first generation devices

The die size was set to 4 mm × 4 mm to allow convenient device handling with a membrane size of 2 mm × 2 mm. The micro-heater was of a meandering style to ensure predictable device behaviour but the size could be reduced for optimisation. The device comprised of three terminals, two terminals for the micro-heater contacts and one connected to the gold electrode. The material employed for the electrode was gold because of the electrochemical process required to deposit the nanoporous catalyst. The contact pad size was 1000 μm × 500 μm. The width of the snapping grooves was 150 μm since the wafer thickness was identical to the wafer that produced the former micro-hotplate. The different layer thicknesses of the materials are shown in table 2.1. A final passivation was included in the design although it was not present on all the wafers processed. Only one out of twelve wafers included this passivation for evaluation purposes.

Table 2.1: Various material thicknesses for the micro-calorimeter designs

Material	Layer thickness
Silicon wafer (Si)	280 μm
Silicon dioxide (SiO_2) as etch-stop layer	50 nm
LPCVD Silicon nitride (Si_3N_4)	250 nm
Tantalum (Ta) adhesion layer for micro-heater	20 nm
Platinum (Pt) micro-heater	220 nm
LPCVD Silicon nitride (Si_3N_4)	500 nm
Tantalum (Ta) adhesion layer for micro-heater	15 nm
Gold (Au) layer as the gate electrode	150 nm
PECVD Silicon nitride (Si_3N_4) *(optional)*	200 nm

2.4.2 Meander-type micro-heater design

The schematic diagram of the first generation micro-heater design is shown in figure 2.3. A new micro-heater design was created as shown in figure 2.3(a) with an overall micro-heater geometry of 570 μm × 570 μm. The track-width and the separation are equal at 30 μm. Comparing with the former micro-heater design, the connectors between the micro-heater track and the contact pads have been modified to taper on one side due to the reduced micro-heater area.

The micro-heater resistance is highly dependent on a number of factors, such as impurity level, the fabrication process and the thickness of the material as mentioned in section 2.3.3. Therefore, the resistance of the design was approximated by the sheet resistance based on the bulk material properties, about 0.55 Ω per square [2.10] and the aspect ratio of the micro-heater track, as shown in equation (2.8) and (2.9).

$$R_H = \text{aspect ratio} \times R_{sheet} \tag{2.8}$$

$$\text{aspect ratio} = \frac{L}{W} \tag{2.9}$$

where R_H is the resistance of the micro-heater; R_{sheet} is the sheet resistance
L is the length of the micro-heater track; W is the width of the micro-heater track

With the length of the meander track (L) of 5970 μm and width (W) of 30 μm, the aspect ratio of the design was 199. The resistance of the micro-heater was estimated to be 109 Ω.

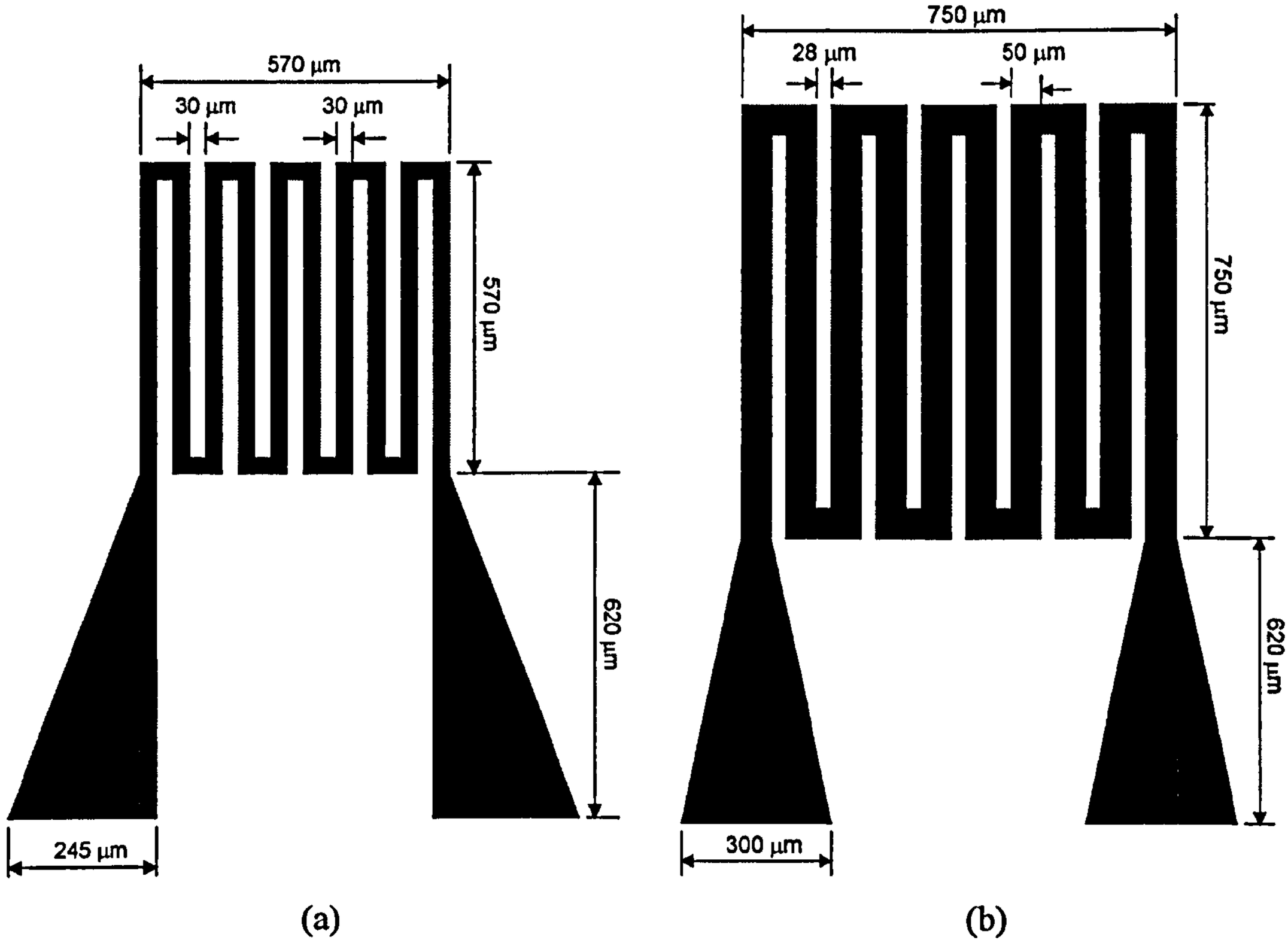

Figure 2.3: The schematic diagram of the micro-heater designs (not to scale). (a) The first generation of new micro-heater design with even track spacing. (b) The former micro-heater design.

As it was important to reproduce the former micro-calorimeter design for evaluation, it was also included in this design generation. The overall micro-heater size is 750 μm × 750 μm with a track width (W) of 50 μm and separation of 28 μm. The track length (L) is 4340 μm and the aspect ratio was 155. Therefore, the micro-heater resistance, R_H, was estimated to be 85.3 Ω.

2.4.3 Design families and optimisations

The completed first generation micro-calorimeter design is shown in figure 2.4. A device reference was assigned to the new design which employed the smaller micro-heater as SRL 162g, in accordance with the order of the design library at the Sensors Research

Laboratory, University of Warwick. Although the former design was referenced as SRL 136, the design was numbered as SRL 136a to distinguish the different fabrication run.

The micro-heater area of the SRL 162g had been decreased by 42% in order to reduce the power loss by convection. As the size of the silicon nitride membrane remained as 2 mm × 2 mm, the *MHR* was increased to 3.5 to minimise the power consumption. The micro-heater track separation was increased to lower the track coverage to about 57%. Therefore, the local hot spot could be reduced so improving the reliability of the device. Moreover, the width of the track connecting the Au gate electrode and the contact pad was reduced to further minimise thermal losses.

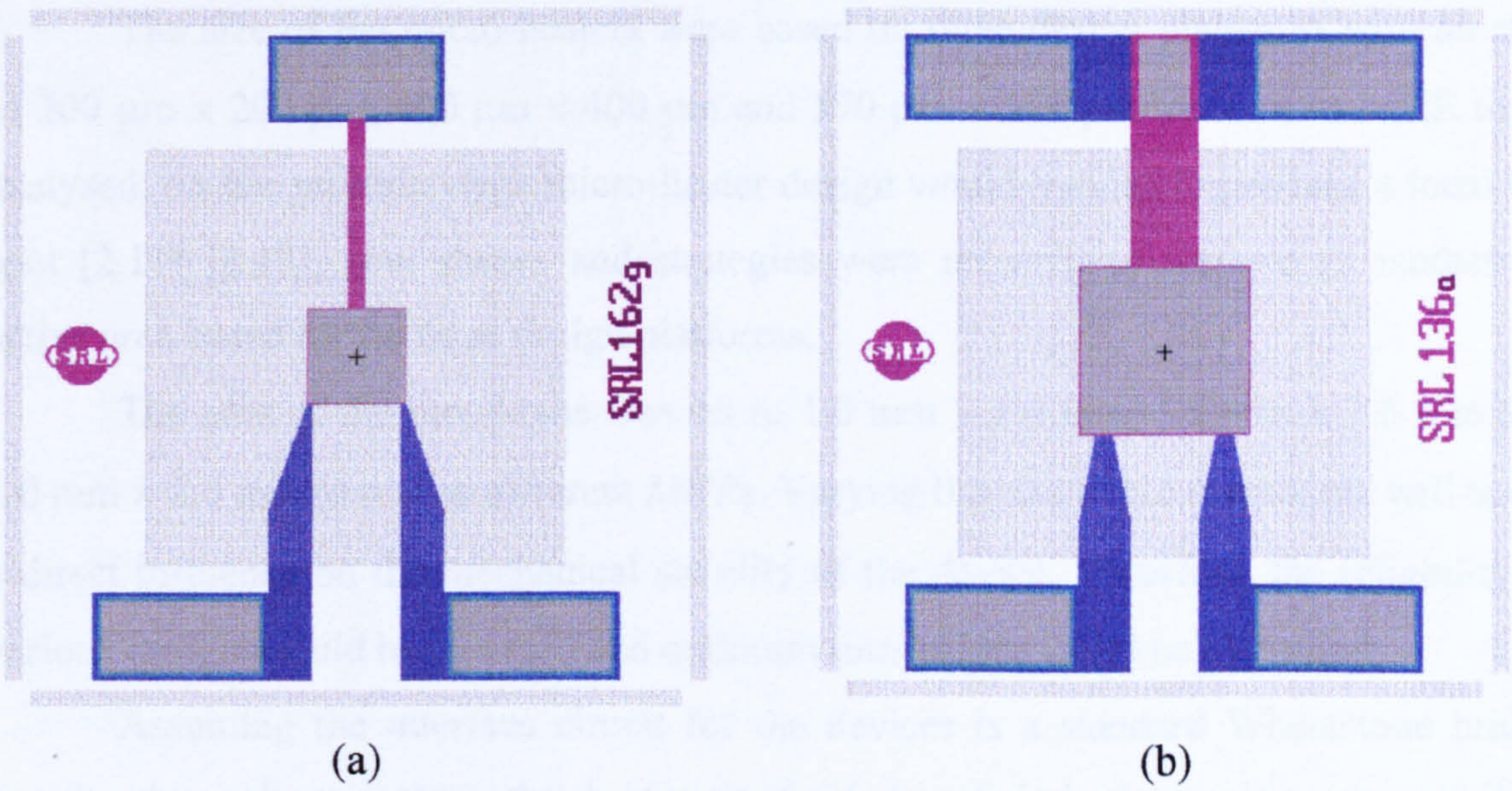

Figure 2.4: The completed design of new first generation micro-calorimeter design. (a) The SRL 162g with higher MHR. (b) The re-organised former design as SRL 136a.

Although the design layout for SRL 136a was identical to the former design, the device properties would be different due to a modified fabrication process, e.g. different material impurity and thicknesses. Therefore, it was essential to retain this design for reference purposes.

2.5 Second generation micro-calorimeter design

The second generation of devices was designed based on the characterisation results, from the previous generation, discussed in chapter 5. Improved understanding of the device properties allowed greater flexibility for innovation without affecting the

functionality. Therefore, 54 different design variants were created to explore various ideas.

2.5.1 Design specifications for the second generation devices

Apart from the 4 mm × 4 mm cells, the second-generation designs included some 2 mm × 2 mm cells for evaluation. A reduction of the die size might cause additional difficulties in device handling, especially in the dicing process. However, not only does the smaller chip size provide higher packing density that leads to lower production cost, but also reduces heat loss via convection. Therefore, it was essential to investigate if smaller devices could retain sufficient mechanical stability.

The size of the micro-heaters were based on three design platforms with an area of 200 μm × 200 μm, 400 μm × 400 μm and 570 μm × 570 μm for various MHR to be analysed. As the meander-type micro-heater design would inevitably produce a local hot spot [2.11] [2.12], new shapes and strategies were required to achieve an isothermal active area based on the three design platforms.

The area of the membrane was set to 1.0 mm × 1.0 mm, 1.5 mm × 1.5 mm and 2.0 mm × 2.0 mm to realise different *MHR*s. Varying the size of the membrane will cause a direct influence on the mechanical stability of the device. Therefore, the reliability of various designs could be assessed and optimum dimensions could be identified.

Assuming the interface circuit for the devices is a standard Wheatstone bridge circuit, the voltage across the bridge is 5 V for digital electronics compatibility. Therefore, the voltage requirement across each device should be 2.5 V in order to reach the operating temperature of 500°C. For the SRL 162g, the resistance of the second generation devices were derived from equation (2.10).

$$\text{Power consumption} = \frac{V_{162g}^{\ 2}}{R_{162g}} = \frac{V_{new}^{\ 2}}{R_{new}} \tag{2.10}$$

where V_{162g} and R_{162g} are the voltage and resistance required for SRL 162g to reach operating temperature, respectively.

V_{new} and R_{new} are the voltage and resistance required for the new designs to reach operating temperature, respectively.

With the characterisation result for SRL 162g documented in Chapter 5, the required resistance of the micro-heater was 35 Ω. The actual required resistance for a 2.5 V supply voltage would also depend on the heating efficiency which might be varied with different micro-heater designs. Nevertheless, equation (2.10) provided a valuable reference when the new micro-heaters were designed.

A final passivation layer was included only on two wafers so that its influence on the new designs could be investigated. All the layer thicknesses were identical to the first-generation design, as given in table 2.1.

2.5.2 Ultra-low resistance micro-heater design

The Ultra-low resistance micro-heater design is shown in figure 2.5 with the dimensions given in table 2.2. Although the calculated micro-heater resistance was 35 Ω, as suggested in the design specifications, it was useful to explore the device behaviour with a low resistance micro-heater. Therefore, the performance between a micro-machined device and a commercial calorimeter with comparable resistance could be evaluated.

The design employs a unique shape to re-distribute the thermal energy. The micro-heater track separation increases towards the centre of the design in order to allocate more power to the edge. These are the measures employed in attempting to eliminate the centre hot spot. Furthermore, the semi-circle replaces the rectangular edges which should reduce mechanical stress within the membrane.

The track resistances were calculated by using equations (2.8) and (2.9) with the sheet-resistance of the platinum obtained from the characterisation result of the first generation devices, as mentioned later in Chapter 5. The micro-heater tracks arrangement is equivalent to six resistors in parallel as shown in figure 2.5. Therefore, the overall resistance is very low, between 4 Ω and 6 Ω depending on the overall micro-heater sizes.

In addition, the parallel arrangement provides extra reliability to the designs as the functionality of the micro-heater will not be affected if one or two tracks are defective.

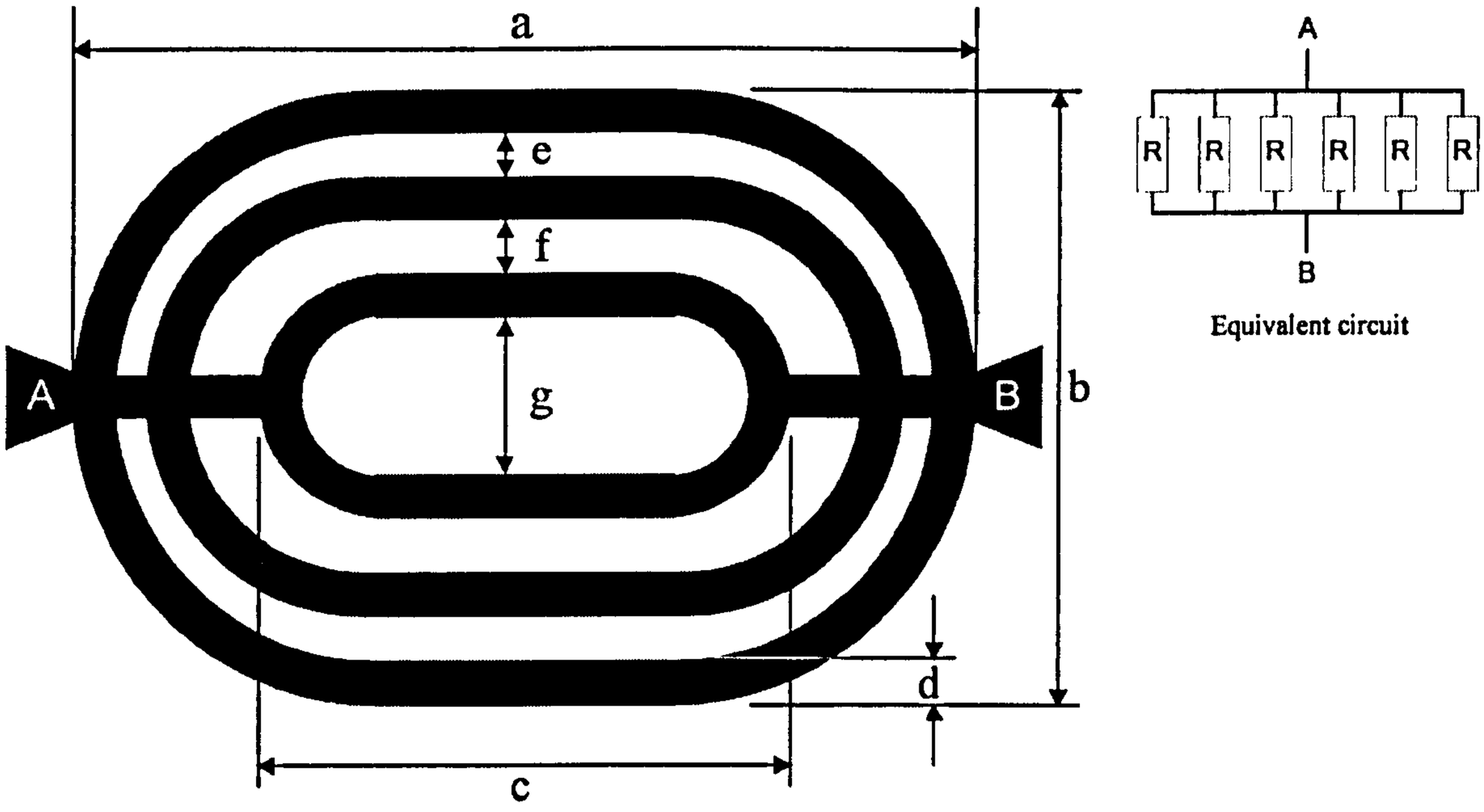

Figure 2.5: The Ultra-low resistance micro-heater design (not to scale) and the equivalent circuit. The labelled dimensions are tabulated in table 2.2.

Table 2.2: Dimensions and resistances of the Ultra-low resistance micro-heater design

	Micro-heater design platform		
Dimension label (μm)	**(570 × 570) μm²**	**(400 × 400) μm²**	**(200 × 200) μm²**
a	855	600	300
b	570	400	200
c	570	400	200
d	40	30	10
e	30	20	10
f	40	30	20
g	190	120	80
Estimated micro-heater resistance (Ω)	3.6	4.0	6.0

2.5.3 Honeycomb micro-heater design

The Honeycomb micro-heater design is shown in figure 2.6. These designs were based on the three sizes suggested from the specifications presented in section 2.5.1. Dimensions for each of the design platforms are given in table 2.3.

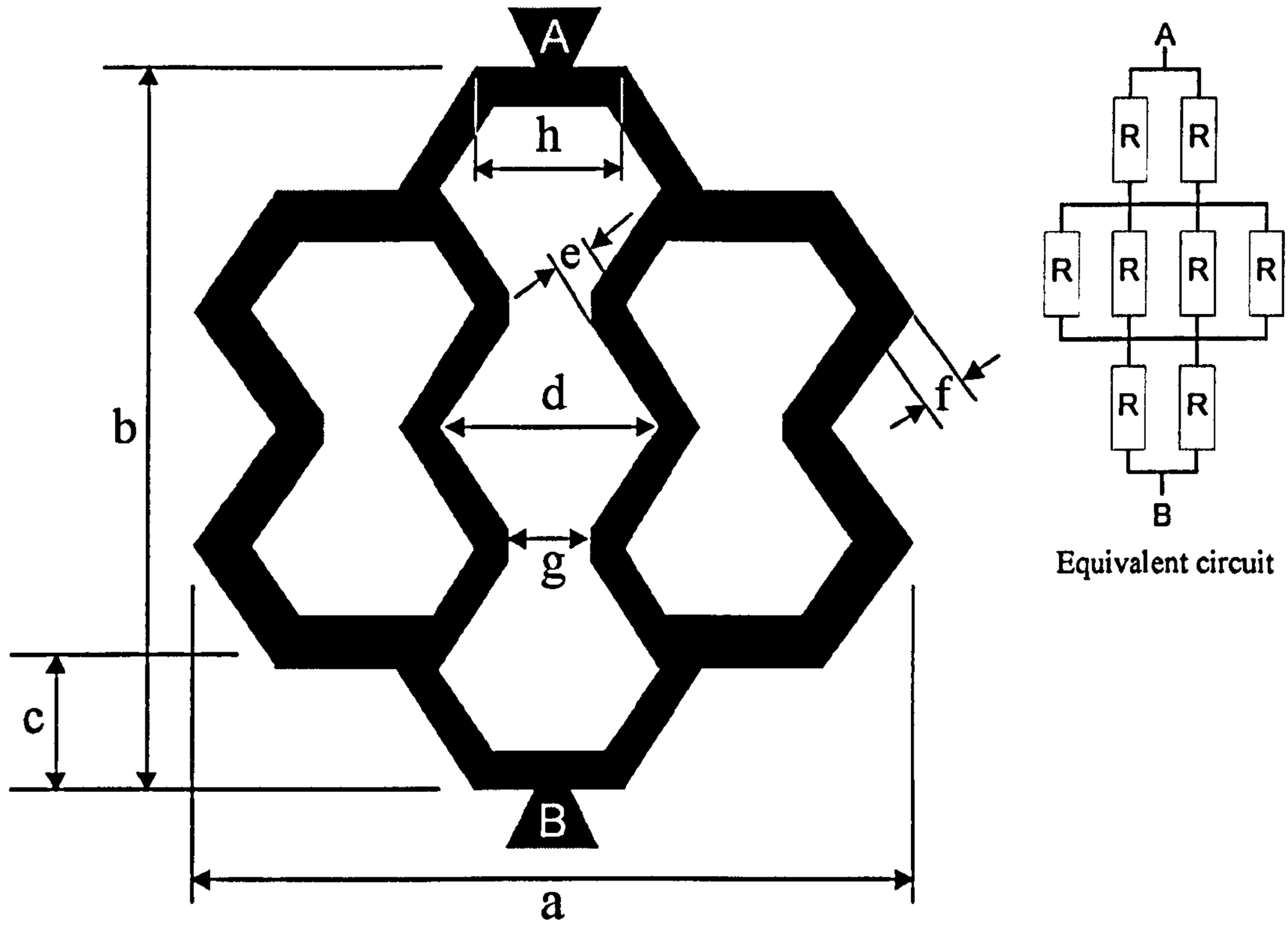

Figure 2.6: The Honeycomb micro-heater design (not to scale) and the equivalent circuit. The labelled dimensions are tabulated in table 2.3.

Table 2.3: Dimensions and resistances of the Honeycomb micro-heater design

	Micro-heater design platform		
Dimension label (μm)	**(570 × 570) μm²**	**(400 × 400) μm²**	**(200 × 200) μm²**
a	570	400	200
b	570	400	200
c	90	65	33
d	169	119	60
e	30	20	10
f	40	25	15
g	65	45	23
h	114	80	40
Estimated micro-heater resistance (Ω)	9	12.6	12.6

The design concept is to arrange a set of hexagons to avoid any micro-heater tracks at the centre of the membrane and so evenly distribute thermal energy across the active area. The area within each hexagon is identical but the micro-heater tracks are thicker at the two sides, allowing more current to flow at a constant applied voltage. Moreover, the resistance is higher at the top and bottom of the micro-heater which leads to higher power dissipation. Therefore, more thermal energy will be dissipated at the fringe of the micro-heater to achieve a more isothermal active area.

The series-parallel resistive equivalent circuit is shown in figure 2.6. The micro-heater track resistances of the micro-heater were estimated by the aspect ratio and the sheet-resistance of the platinum. Applying the equivalent circuit with the corresponding track resistances, the overall micro-heater resistances for various sizes were calculated, as shown in table 2.3. Although the resistances are below the recommended value stated in the specifications, lower micro-heater resistance should reduce the supply voltage requirements. Therefore, the performance of a set of micro-calorimeter devices with a wide range of voltage requirements could be determined.

2.5.4 Drive-wheel micro-heater design

The Drive-wheel micro-heater design is shown in figure 2.7 and the labelled dimensions are given in table 2.4. The micro-heater sizes follow the design specifications in section 2.5.1.

The unique micro-heater shape avoids thermal energy dissipation at the centre of the active area. The tracks separation increases towards the centre where the entire area is void to eliminate a hot spot. The higher track density at the fringe of the design results in higher power dissipation in order to compensate for the void centre. Therefore, an isothermal active area could be achieved.

The micro-heater tracks are uniform in the design to provide identical thermal profiles at both constant current and voltage. In order to maintain the overall resistance, the micro-heater structure is equivalent to a pair of resistors in parallel, as shown in figure 2.7. The resistances were obtained by applying equations (2.8) and (2.9) with the specific aspect ratio and material properties, as performed for the other two designs. In addition, a circular design reduces the thermally induced stress in the silicon nitride membrane and enhances the reliability of the device.

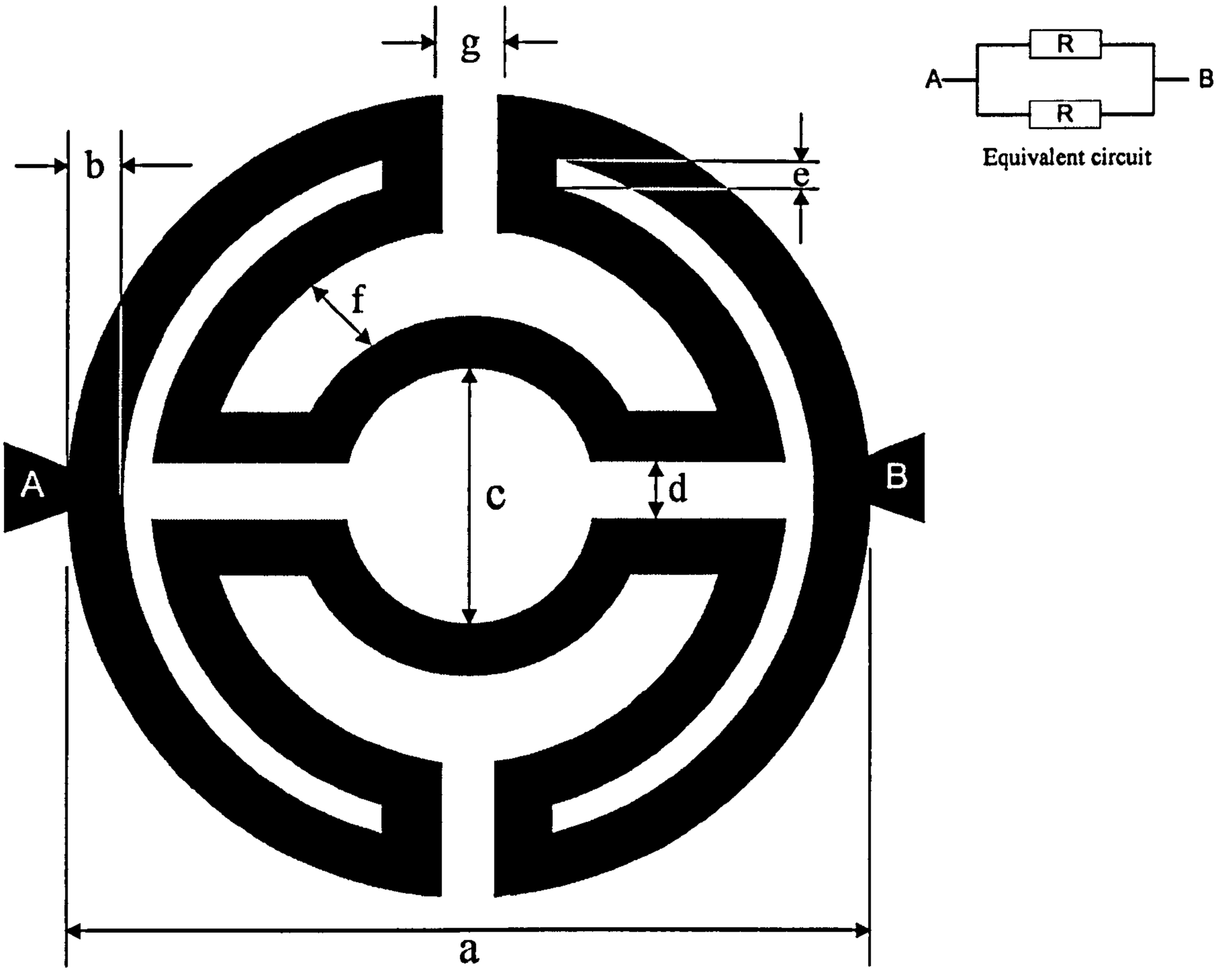

Figure 2.7: The Drive-wheel micro-heater design (not to scale) and the equivalent circuit. The labelled dimensions are tabulated in table 2.4.

Table 2.4: Dimensions and resistances of the Drive-wheel micro-heater design

	Micro-heater design platform		
Dimension label (μm)	**(570 × 570) μm²**	**(400 × 400) μm²**	**(200 × 200) μm²**
a	570	400	200
b	40	30	10
c	190	120	80
d	35	25	15
e	30	20	10
f	40	30	20
g	35	20	15
Estimated micro-heater resistance (Ω)	27.0	24.0	40.0

2.5.5 Device families of the second-generation device

Once the micro-heater design had been completed, a variety of micro-calorimeter designs could be generated with different combinations of membrane size. The major differences compared to the previous device generation were the micro-heater design and the MHR while the material thicknesses remain unchanged, as illustrated in figure 2.8.

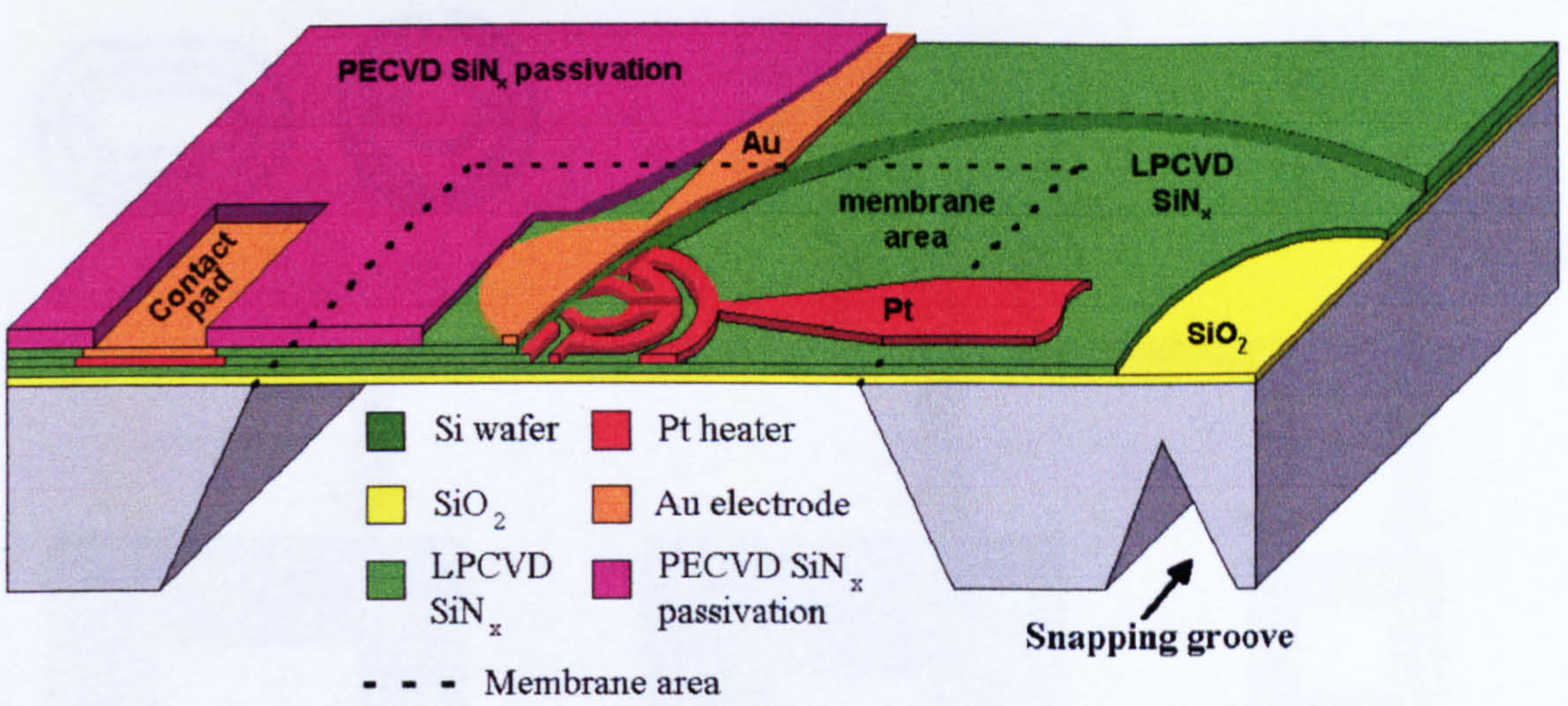

Figure 2.8: The schematic diagram illustrating the general structure of the second generation device with Drive-wheel micro-heater design (not to scale).

With the new micro-heater designs and different *MHR* requirements as stated in the specification, it was possible to categorise the designs into six device families. The classification of the families is based on the estimated power consumption, mechanical robustness and die size. The organisation of the design concept is illustrated in figure 2.9.

The micro-heater designs are initially sorted according to the size of the design platforms. The micro-heaters were assembled with the various membrane sizes as shown in figure 2.9 to create different device families with different *MHR*. Therefore, each device family includes three design variants with the same *MHR*.

The Standard family (SRL 176) uses an identical *MHR* to the previous generation designs. The *MHR* for the Low-power family (SRL 177) had been increased so the power consumption was expected to be lower than other families. With reduced *MHR*, the power consumption of the device from the Small-mem/ robust family (SRL 178) should increase. However, the mechanical robustness of such devices is increased with a smaller membrane and thicker supporting frame. Therefore, devices with different levels of mechanical stability could be investigated in relation to their electrical properties.

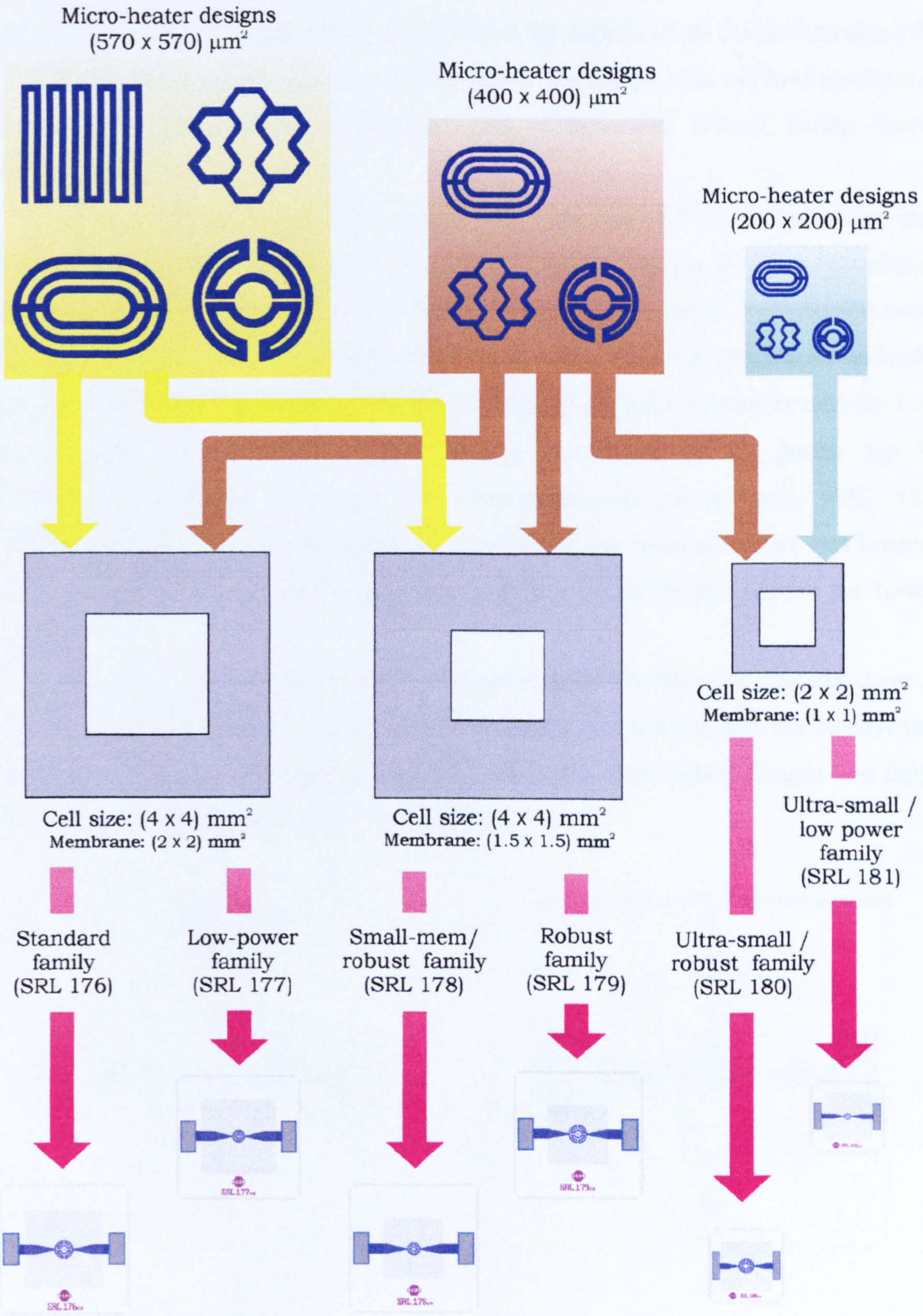

Figure 2.9: An illustration of the design concept and the various design families of the 2nd generation micro-calorimeter designs.

The Robust family (SRL 179) employs a smaller membrane and a standard size micro-heater. The power consumption is expected to be the highest of all the designs since the lowest *MHR* has been used. However, this family should provide the best mechanical stability and highest commercial yield. This is especially critical during device fabrication and the dicing process.

Ultra-miniature devices were created with a die size of 2 mm × 2 mm. Not only does this increase the packing density on a wafer, but also reduces the convectional heat loss due to smaller surface area of the device. Therefore, the power consumption could be further reduced. The Ultra-small/ robust family (SRL 180) employs the micro-heater from the 400 μm × 400 μm design platform. Although the *MHR* is smaller than the Low power family, lower convectional loss should compensate for the power loss by conduction through the membrane. The Ultra-small/ low power family (SRL 181) employs the same *MHR* as the Low-power family and the convection loss was lowered by the miniature die size. Hence, devices from this family should require the lowest power.

The Au gate electrode for all the designs is generally the same size and shape as the micro-heater, as shown in figure 2.10(a). However, the devices with the Honeycomb micro-heater employed an identical gate electrode as the Drive-wheel designs (see figure 2.10(b)), due to the irregular edges of this design.

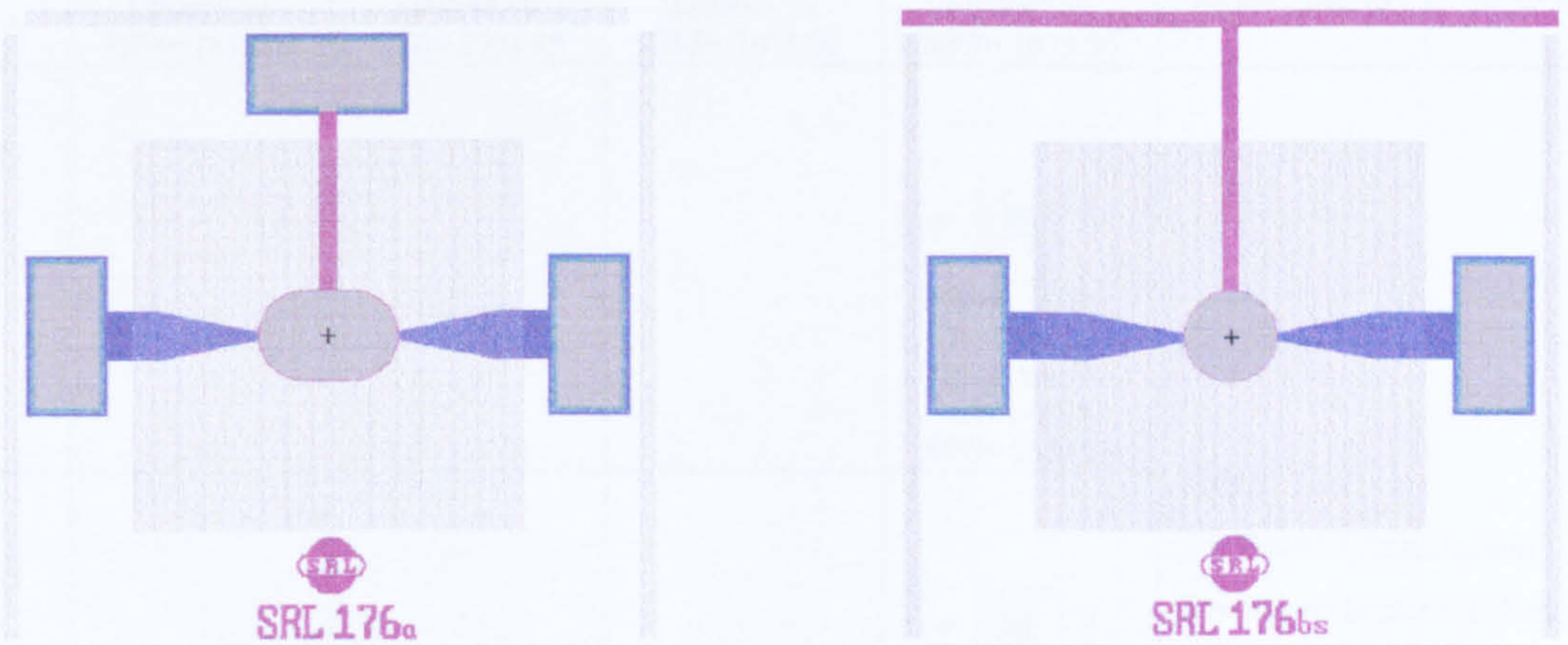

(a) (b)

Figure 2.10: Example of the second-generation micro-calorimeter designs. (a) The Standard family with Ultra-low resistance micro-heater (SRL 176a) and individual gate. (b) The Standard family with Honeycomb micro-heater (SRL 176bs) and common gate connection. Note that the heater structure is hidden below the solid gate.

	SRL 176 The standard Family *Membrane size:* *2mm x 2mm* *Heater size:* *570μm x570μm*	**SRL 177** The low Power Family *Membrane size:* *2mm x 2mm* *Heater size:* *400μm x400μm*	**SRL 178** The small-mem/robust Family *Membrane size:* *1.5mm x 1.5mm* *Heater size:* *400μm x400μm*	**SRL 179** The robust Family *Membrane size:* *1.5mm x 1.5mm* *Heater size:* *570μm x570μm*	**SRL 180** The ultra small/robust Family *Membrane size:* *1mm x 1mm* *Heater size:* *400μm x400μm*	**SRL 181** The ultra small/low power Family *Membrane size:* *1mm x 1mm* *Heater size:* *200μm x200μm*
a	 P=106mW R=3.60Ω *MHR*=3.51 *SWR*= 2551.25	 P=44mW R=3.70Ω *MHR*=5.00 *SWR*= 2551.25	 P=88mW R=3.7Ω *MHR*=3.75 *SWR*= 1875.00	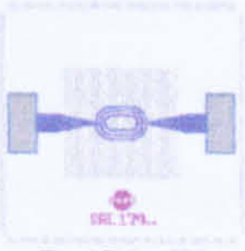 P=176mW R=3.6Ω *MHR*=2.63 *SWR*= 1875.00	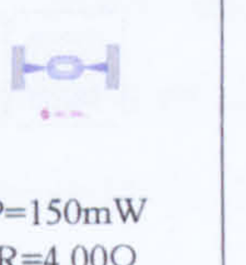 P=150mW R=4.00Ω *MHR*=2.37 *SWR*=1182.50	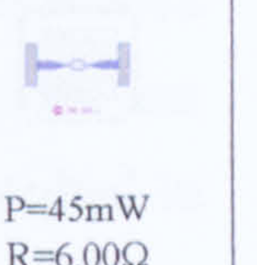 P=45mW R=6.00Ω *MHR*=4.73 *SWR*= 1182.50
b	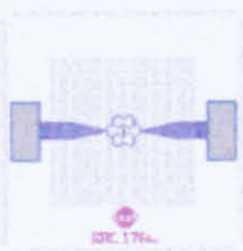 P=106mW R=9.00Ω *MHR*=3.51 *SWR*= 2551.25	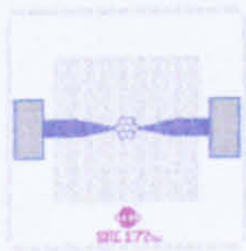 P=44mW R=12.60Ω *MHR*=5.00 *SWR*= 2551.25	 P=88mW R=12.60Ω *MHR*=3.75 *SWR*= 1875.00	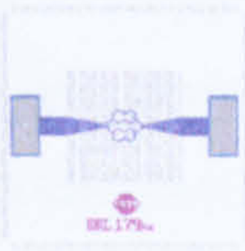 P=176mW R=9.00Ω *MHR*=2.63 *SWR*= 1875.00	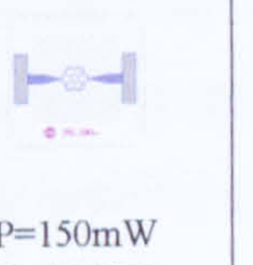 P=150mW R=12.60Ω *MHR*=2.37 *SWR*= 1182.50	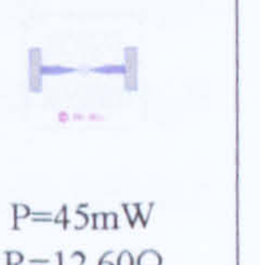 P=45mW R=12.60Ω *MHR*=4.73 *SWR*= 1182.50
c	 P=106mW R=26.58Ω *MHR*=3.51 *SWR*= 2551.25	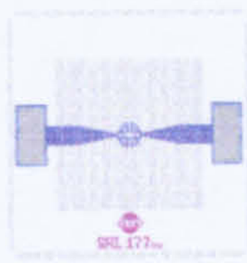 P=44mW R=24.00Ω *MHR*=5.00 *SWR*= 2551.25	 P=88mW R=24.00Ω *MHR*=3.75 *SWR*= 1875.00	 P=176mW R=26.58Ω *MHR*=2.63 *SWR*= 1875.00	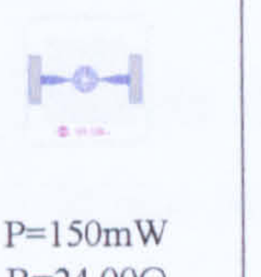 P=150mW R=24.00Ω *MHR*=2.37 *SWR*= 1182.50	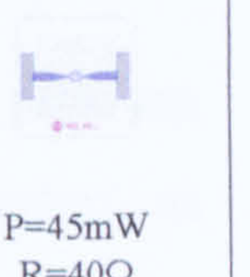 P=45mW R=40Ω *MHR*=4.73 *SWR*= 1182.50
d				 P=176mW R=235.00Ω *MHR*=2.63 *SWR*= 2551.25	Key: P = Power Consumption R = Micro-heater resistance *MHR* = Membrane-to-Heater Ratio *SWR* = Span-to-Width Ratio	
e				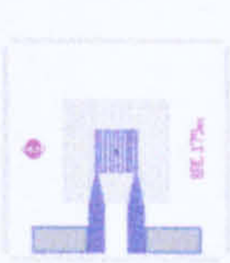 P=220mW R=183.00Ω *MHR*=2.00 *SWR*= 1875.00		

Figure 2.11: A summary of specifications for the 2nd generation micro-calorimeter designs. The gate electrodes (individual or common) are omitted for clarity.

Apart from the devices with a conventional individual gate contact, several selected devices included the special common gate contact for wafer-level nanoporous catalyst deposition, as shown in figure 2.10(b). Details of the layout strategy used with device quantities on each wafer for this design variant are documented in Chapter 3.

A summary of the devices is shown in figure 2.11 [2.13] but the gate electrodes are excluded for the sake of clarity. The figure also specifies the SRL code corresponding to the device type and other essential parameters, such as *MHR*, *SWR* and estimated resistance. However, the devices shown do not include all of the variants of devices, due to the number of different designs involved. The full range of devices is described in detail in Appendix 2a. Furthermore, the power consumption for each of the devices is approximated solely by the MHR and the power requirement from the first generation device (SRL 162g). The percentage increase in the *MHR* based on the SRL 162g design was expected to cause a power reduction by the same percentage. However, this rough estimation had not taken into account the change of convection loss and the micro-heater efficiency.

2.5.6 Test structures

A number of test structures were also created for direct comparison with the previous generation devices and to facilitate further investigation into the device properties, as shown in figure 2.12 [2.13].

SRL 136o Former Micro-pellistor design *Membrane size:* *2 mm x 2 mm* *Heater size:* *750 μm x 750 μm*	**SRL 136em** Emulated device *Membrane size:* *2 mm x 2 mm* *Heater size:* *750 μm x 750μm*	**SRL 136sg** Stress measurement device *Membrane size:* *2 mm x 2 mm* *Heater size:* *750 μm x 750 μm*	**SRL 162o** Former Micro-pellistor design *Membrane size:* *2 mm x 2 mm* *Heater size:* *570 μm x 570 μm*	**SRL 176us** Limit-checking device *Membrane size:* *2 mm x 2 mm* *Heater size:* *200 μm x 200 μm*
		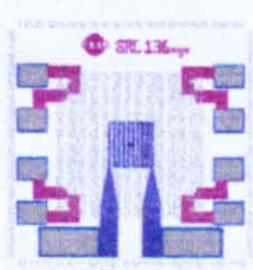	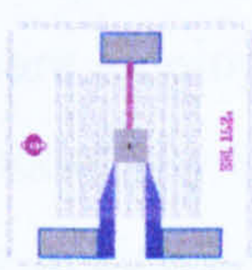	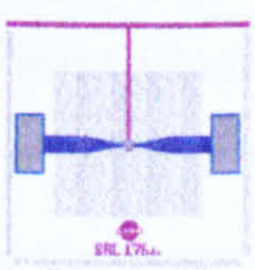
P=176mW R=183Ω *MHR*=2.67 *SWR*= 2551.25	P=176mW R=183Ω *MHR*=2.67 *SWR*= 2551.25	P=176mW R=183Ω *MHR*=2.67 *SWR*= 2551.25	P=106mW R=235Ω *MHR*=3.51 *SWR*= 2551.25	P=106mW R=40.00Ω *MHR*=3.51 *SWR*= 2551.25

P = Power Consumption; R = Micro-heater resistance; *MHR* = Membrane-to-Heater Ratio;
SWR = Span-to-Width Ratio

Figure 2.12: The various test structure specifications included in the 2nd generation design.

SRL 136o is the most primitive model and it is included purely for comparison purposes. This was treated as a test device to check against the previous wafer run for any process variations. All parameters were essentially identical to the SRL 136a.

SRL 136em is a device based on the former SRL 136a. The emulator is another meander track made of gold and placed on top of the micro-heater. However, the two layers avoided direct overlapping in order to reduce parasitic capacitance. Not only does the emulator mimic the exothermic reaction of the catalyst, but also acts as a temperature-sensing element.

SRL 136sg is an experimental device also is based on the SRL 136a design. This device has strain gauges at the corners of the membrane to investigate the stress on the membrane. The four stain gauges, each with a resistance of about 10 Ω, had been designed to be connected in a full Wheatstone bridge detection interface. Therefore, the measurement can be temperature compensated.

SRL 162o is identical to the SRL 162g that was fabricated in the first generation. In order to avoid confusion, it was renamed as SRL 162o. These devices had been included to provide additional information on any process variation from the wafer run.

SRL 176us is a special test device that is dedicated to investigate the effect of the MHR. It comprises the largest membrane 2 mm × 2 mm and the smallest micro-heater 200 μm × 200 μm from this design generation. Hence, the MHR for this device is 10. This device will allow the evaluation of the manufacturability and any improvement in the power consumption.

2.6 Thermo-mechanical simulations by SOLIDIS 3D

To improve the design effectiveness, 3-D thermo-mechanical simulations have been carried out before each fabrication. The SOLIDIS 3D program, version 6, by Integrated System Engineering (ISE) Ltd. has been used to investigate the performance of the designs as described in the previous sections. The software employs the Finite Element Method (FEM) with a set of difference equations that model physical laws. With a 3-D geometric model defined by the user, the software is able to simulate the performance of a design. Modern computers have sufficient capacity and speed to perform such simulations with reasonable accuracy. Moreover, the material properties of the device and the related physical conditions had been refined progressively after each fabrication run as they are critical to the accuracy of the simulation results.

Simulation helps to prevent the device from possessing fundamental design flaws which could ruin the results of an expensive silicon fabrication run. A single 12 wafer micro-calorimeter fabrication run in this research required about £ 30 000 including a set of optical masks. Furthermore, it has been recognised that it is difficult to measure the actual temperature and thermal profile for membrane-structured micro-calorimeters [2.14]. Common laboratory instruments, such as micro-thermopile, are inadequate for such measurements due to the tiny contact area and the relatively fragile membrane. Therefore, thermo-mechanical simulation will allow further development of a device with any micro-heater geometry and *MHR* to be evaluated effectively when a customised simulation model had been established.

2.6.1 Equations and models in SOLIDIS 3D

The simulation results are governed by a set of equations and models for the thermal and mechanical effects. Based on these equations and by employing FEM as the core of the simulation engine, complex geometries can be computed.

The heat transfer equation in solids and stationary fluids is defined by the flux continuity equation, as shown in equation (2.11) [2.15]. The thermal conductivity of the material is denoted as κ (W $m^{-1}K^{-1}$) and T is the temperature in Kelvin (K). The general heat generation or heat source is specified as H (W m^{-3}).

$$\vec{\nabla} \cdot \left(\kappa \vec{\nabla} T\right) - H = 0 \tag{2.11}$$

For the situation in non-stationary fluids, the effect of forced convection has to be considered. Hence, the heat transfer equation is then complemented by a convection term, as shown in equation (2.12) [2.15]. It includes the fluid density, ρ (kg m^{-3}), the specific heat capacity (J kg^{-1} K^{-1}) and $\vec{v}$ is the local fluid flow velocity vector.

$$\vec{\nabla} \cdot \left(\kappa \vec{\nabla} T\right) - H = \rho c \vec{v} \vec{\nabla} T \tag{2.12}$$

The steady-state mechanical effects are described by the equilibrium between external forces on a body and the internally generated reaction forces, as shown in equation (2.13) [2.16]. The second rank stress tensor or stress is denoted as σ (Pa) and the local body

force density vector is $\vec{F}$. However, the body forces are typically gravitational forces as shown in equation (2.14) [2.16].

$$\frac{\partial \sigma_{ij}}{\partial x_j} + \vec{F}_i = 0 \tag{2.13}$$

$$\vec{F} = \rho \vec{a} \tag{2.14}$$

where ρ is the density and $\vec{a}$ denotes the acceleration vector.

The state of deformation of a body is described by the small strain tensor which relates the strains to the displacements, as shown in equation (2.15). The small strain tensor is generally a good approximation within the elastic limit.

$$\varepsilon_{ij} = \frac{1}{2}\left(\frac{\partial u_i}{\partial x_j} + \frac{\partial u_j}{\partial x_i}\right) \tag{2.15}$$

Therefore, the displacements are the unknown variables for which the mechanical equation system is solved. The constitutive equation relating the stresses and strains is defined by Hooke's law within the elastic range, as shown in equation (2.16).

$$\sigma_{ij} = C_{ijkl}\varepsilon_{kl} \tag{2.16}$$

The C_{ijkl} term is a symmetric fourth rank tensor containing 81 elastic stiffness coefficients.

2.6.2 Boundary conditions

Boundary conditions are the limits of the variables in the equations described in the previous section. They are particularly essential when performing iterative computation, such as the simulation for the micro-calorimeter designs. Several boundary conditions were specified and applied to all the simulations performed.

Ambient temperature is defined as room temperature, here set to 300 K. A constant heat source is used to provide uniform heating covering the micro-heater tracks. The power input was 100 mW for the device with die size of 4 mm × 4 mm and 50 mW for the device with 2 mm × 2 mm die size. However, due to the variations of the micro-heater size for the different families, the power input per unit volume had been modified accordingly, as shown in table 2.5.

Moreover, heat flux was set to flow from a constant heat source to the membrane and thermal dissipation into the atmosphere occurred from both sides of the membrane by convection. In addition, the perimeter of the geometrical model was fixed while the silicon nitride membrane was allowed to deflect. Therefore, the thermally induced stress and the displacement of the membrane could be simulated.

Table 2.5: The specific heat source for various device families

	Die size = 4 mm × 4 mm			Die size = 2 mm × 2 mm	
	Micro-heater design platform			Micro-heater design platform	
	750 μm × 750 μm	570 μm × 570 μm	400 μm × 400 μm	400 μm × 400 μm	200 μm × 200 μm
Power (mW)	100	100	100	50	50
Heat source ($W\ m^{-3}$)	7.11×10^{11}	1.23×10^{12}	2.50×10^{12}	1.25×10^{12}	5.00×10^{13}

2.6.3 Material properties

The material properties required by the simulation software were not readily available as conventional bulk material properties might not be appropriate with dimensions in the nano-range. However, the layer thickness is not sufficiently thin to require thin film theory, i.e. Sondheimer theory, as described in section 2.3.3.

A customised simulation parameter database was established, as shown in table 2.6 [2.17], to enhance the accuracy of the simulation. The parameters had been accumulated progressively by device characterisation from each design generation and from published literature [2.18] [2.19].

Table 2.6: Material properties employed in the thermo-mechanical simulation in SOLIDIS

Property	Unit	Pt	Au	Si_3N_4	SiO_2	Si
Thermal Conductivity (κ)	W/m* K	73	315	22	1.4	157
Elasticity Modulus (Young's Modulus)	GPa	170	80	290	73	190
Poisson's Ratio	Unity	0.39	0.42	0.24	0.20	0.17
Thermal Expansion (β)	1/K	8.9×10^{-6}	14.3×10^{-6}	2.33×10^{-6}	0.55×10^{-6}	2.33×10^{-6}
Density (ρ)	kg/m^3	2.145×10^4	1.932×10^4	3.1×10^3	2.2×10^3	2.32×10^3
Specific heat capacity (C_p)	J/kg°C	130	130	600-800	730	700

2.6.4 Geometrical models of the micro-heater elements

Due to rectilinear meshing, SOLIDIS only accepts a rectangular geometrical model. Therefore, apart from the meander-type micro-heater, all the second-generation designs were approximated by rectangular edges, as shown in figure 2.13.

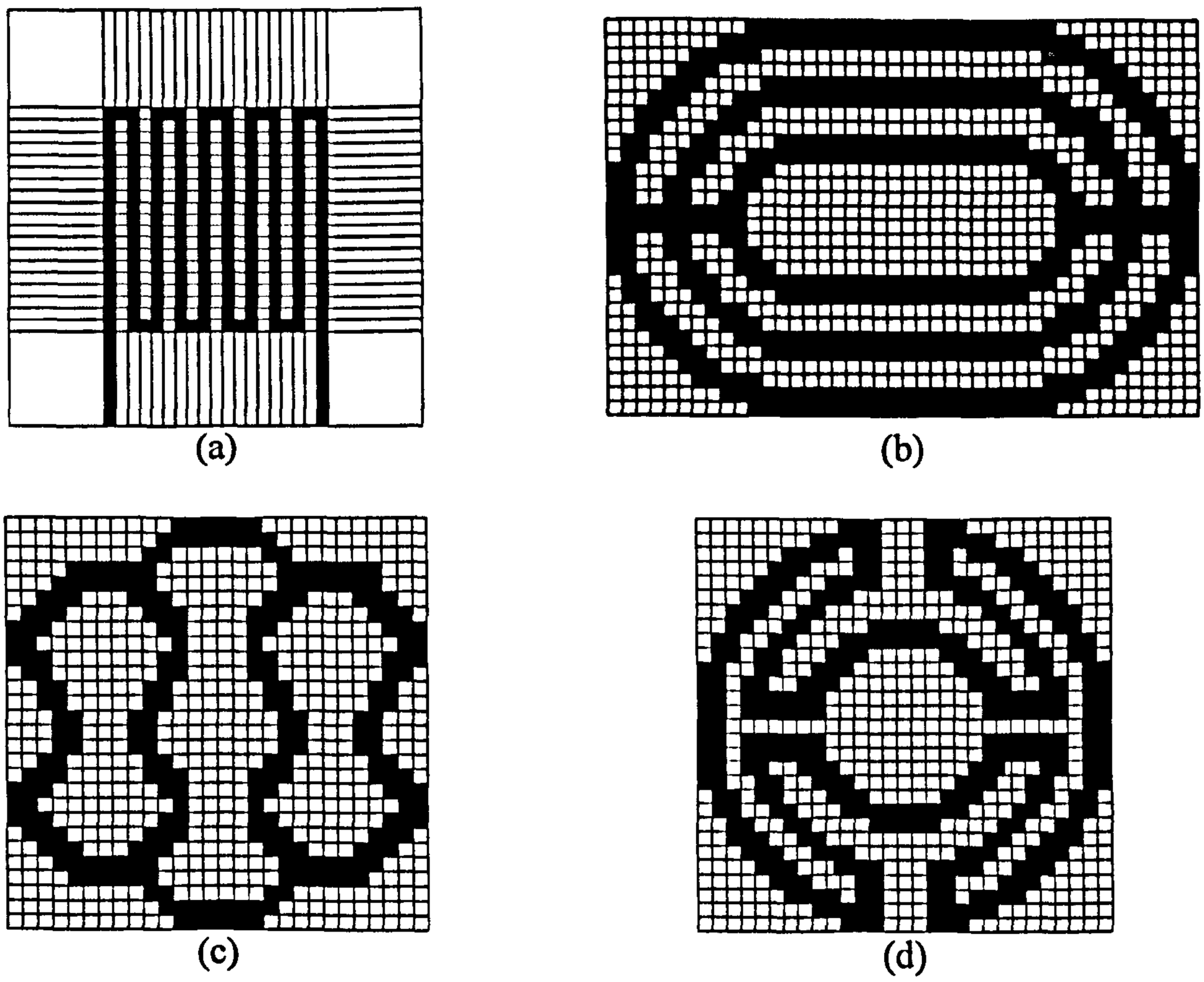

Figure 2.13: The modified rectilinear micro-heater geometrical model for thermo-mechanical simulation.

The hardware resources limited the number of mesh-lines which define the geometrical model. Therefore, the resolution of the micro-heater model was fixed by the number of pixels available. Although, the micro-heater geometries were only approximated by a limited number of pixels, the result was not affected substantially, as proven in Chapter 5.

2.6.5 Simulation of the micro-calorimeters

Initially, a geometrical model with a simple square heat source for a complete 4 mm × 4 mm cell was generated, as shown in figure 2.14.

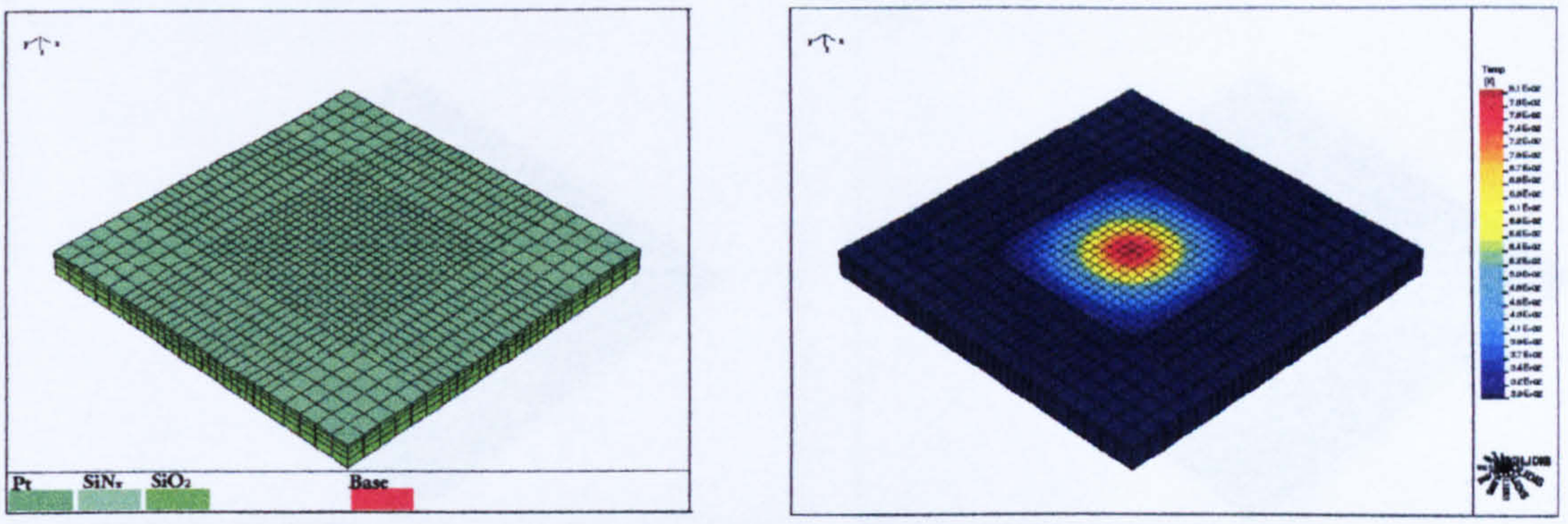

Figure 2.14: The simulation of the 1st generation meander-type micro-calorimeter (SRL 162g) based on a complete die. (a) The geometrical model, (b) the simulated result (refer 2.14(c) for the temperature scale). (c) The cross-section view of the simulated result showing the membrane and the supporting frame.

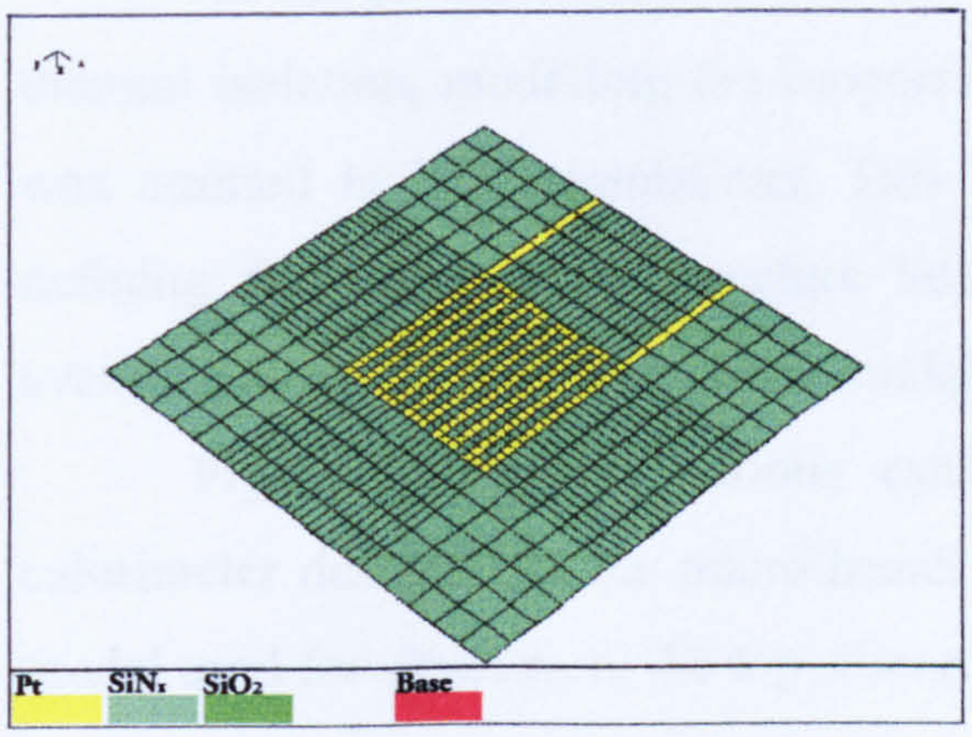

(a)

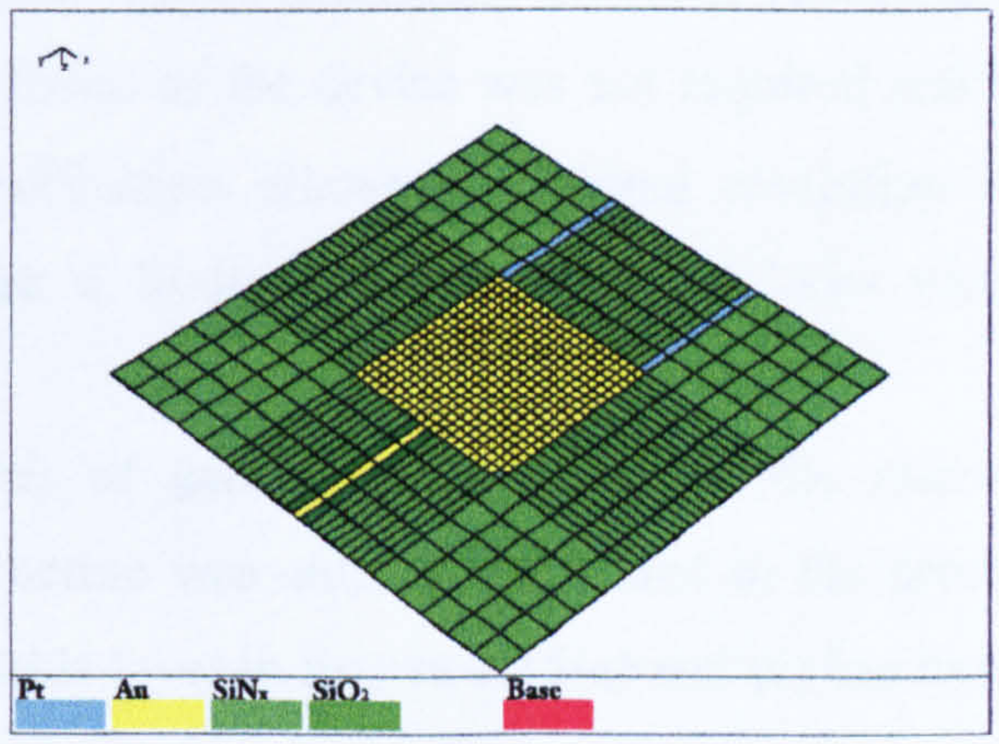

(b)

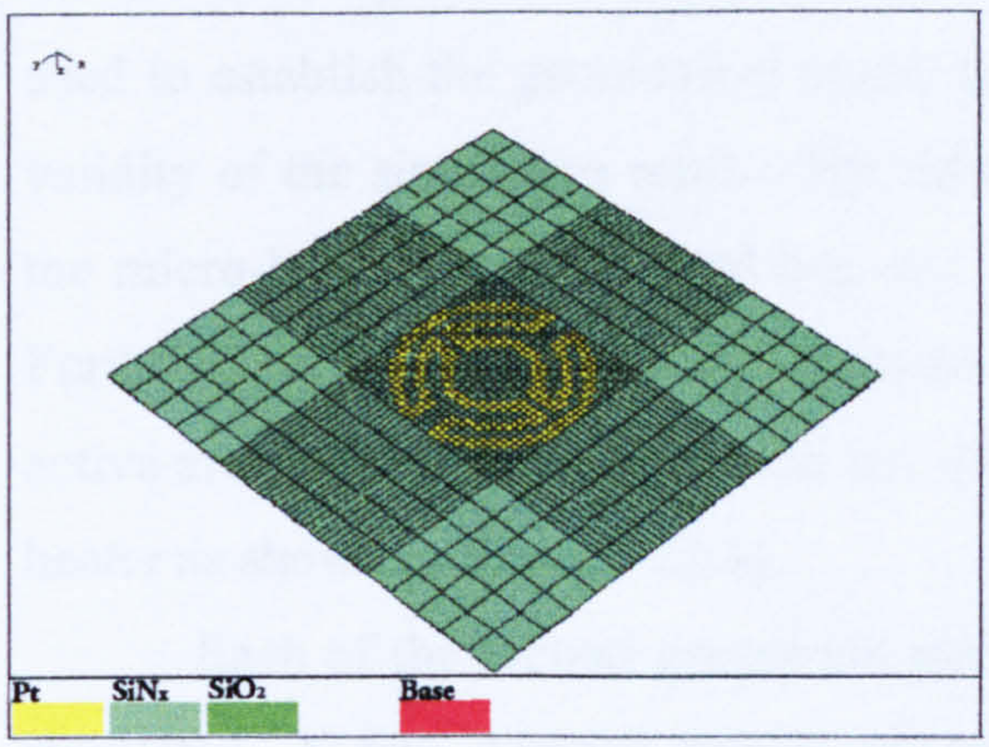

(c)

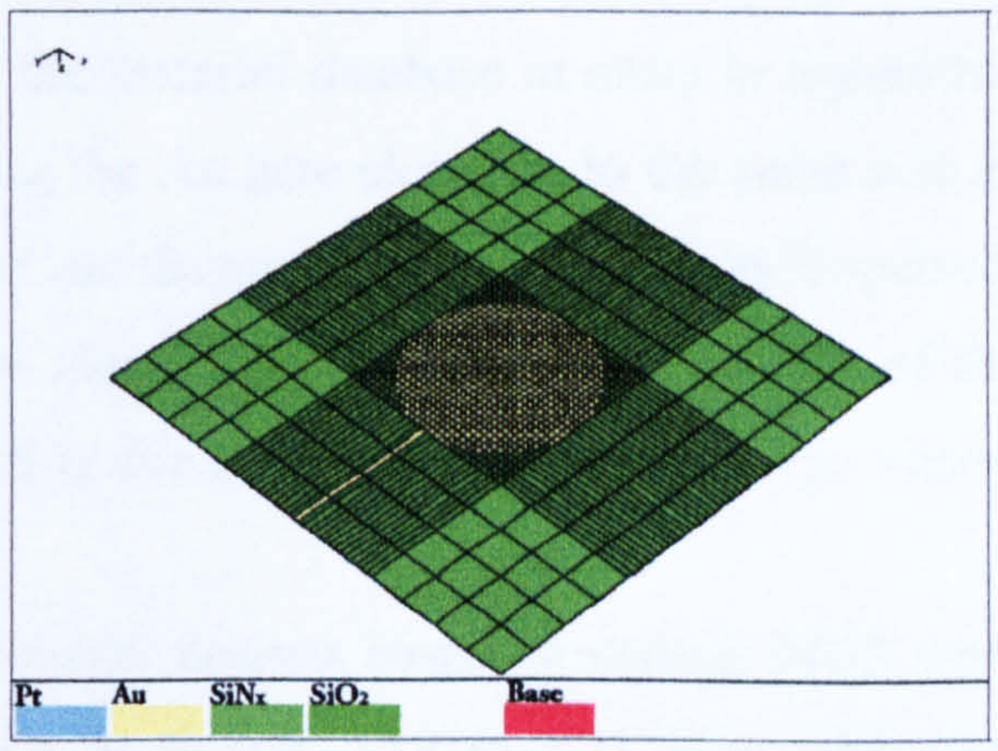

(d)

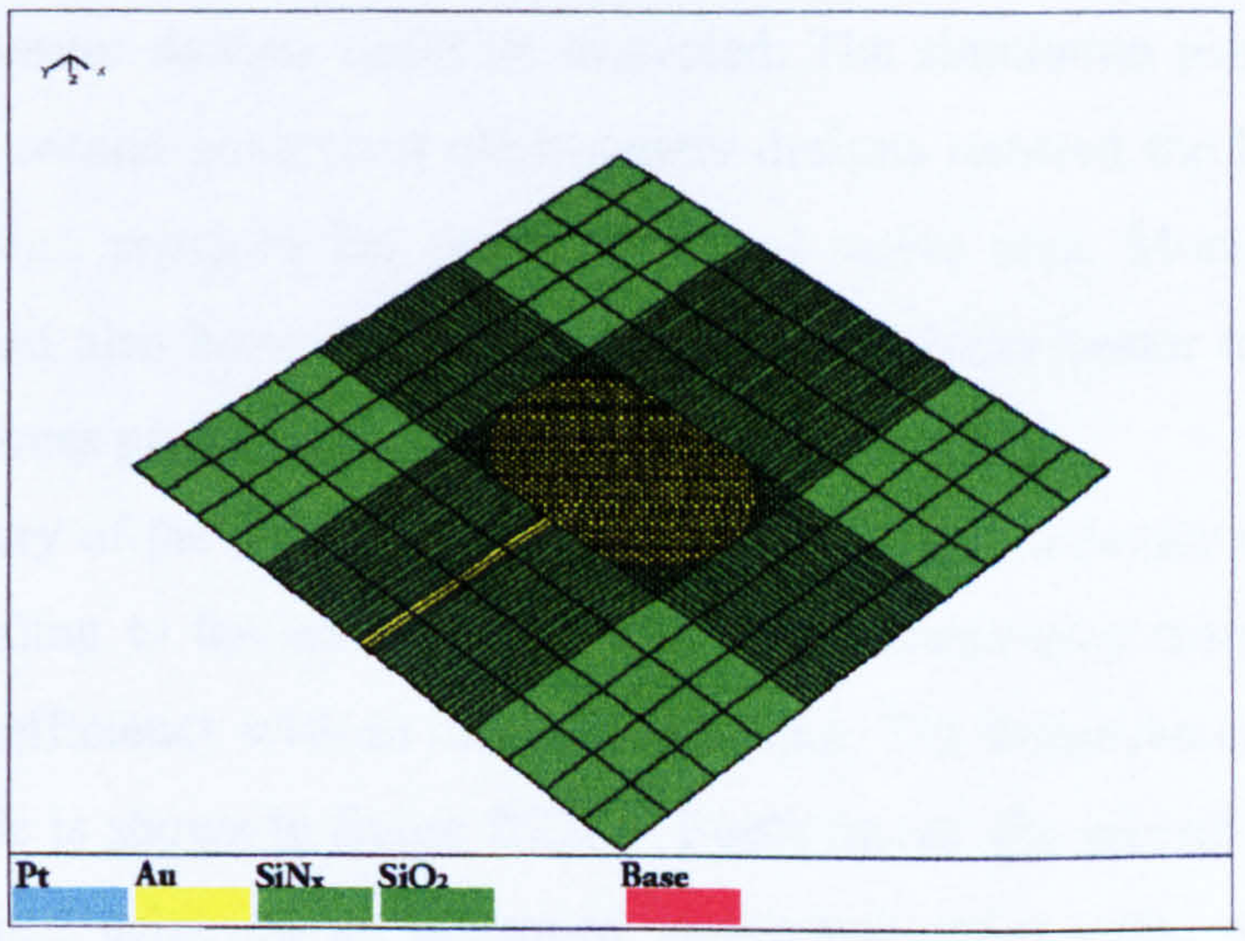

(e)

Figure 2.15: The geometrical models for SOLIDIS 3D. (a) The model for SRL 162g with the meander-type micro-heater exposed. (b) The geometrical model for SRL 162g employed for simulation. (c) The model for SRL 176c with the Drive-wheel micro-heater exposed. (d) The geometrical model for SRL 179c employed for simulation. (e) The geometrical model for SRL 176a for simulation.

As the results indicated that the silicon nitride membrane provided remarkable thermal isolation, modelling the supporting frame of the device was not required and it was omitted in later simulations. This modification allowed additional resolution in defining the micro-heater structure because a limited number of mesh lines were available to specify the geometrical model.

Figure 2.15 shows various examples of geometrical models for the micro-calorimeter designs. As the micro-heater structure was entirely embedded in the actual model used for simulation, the top silicon nitride layer in figures 2.15(a) and (c) has been excluded to reveal the micro-heater. The simulation results for SRL 136a and SRL 162g are shown in figures 2.16 and 2.17, respectively. Simulations for these two designs were used to establish the geometrical model and the material database in order to ensure the validity of the simulation results. By reducing the Au gate electrode to the same size as the micro-heater, both the local hot spot and the thermal induced stress was dispersed. Furthermore, the gate electrode increases the thermal conductivity at the surface of the active area. This disperses the local hot spot that was created by the meander-type micro-heater as shown in figure 2.22(a).

Each of the second generation micro-heater designs based on various *MHR* were simulated. A few selected results are shown in figures 2.18 to 2.21 with additional simulation results included in Appendix 2b. Using these results, the thermal profile of different micro-heater designs could be evaluated. The simulation results indicated that although all the second generation micro-heater designs reduced the local hot spot, the Drive-wheel design provides the most isothermal active area. Moreover, the thermal induced stress had also been evenly distributed as the micro-heater tracks were almost invisible in the stress plots.

A summary of the active area temperature for different device models is given in table 2.7. According to the simulation results, the meander-type micro-heater provides the best heating efficiency with an inevitable hot spot. The improvement provided by the Au gate electrode is shown in figure 2.22(a). Furthermore, the second generation micro-heater designs had achieved an improved isothermal active area, with higher power consumption, as shown in figure 2.22(b). However, the power consumption could be reduced by adjusting the *MHR* to create an isothermal active area. The simulation results were verified with the experimental results for actual devices as discussed in Chapter 5.

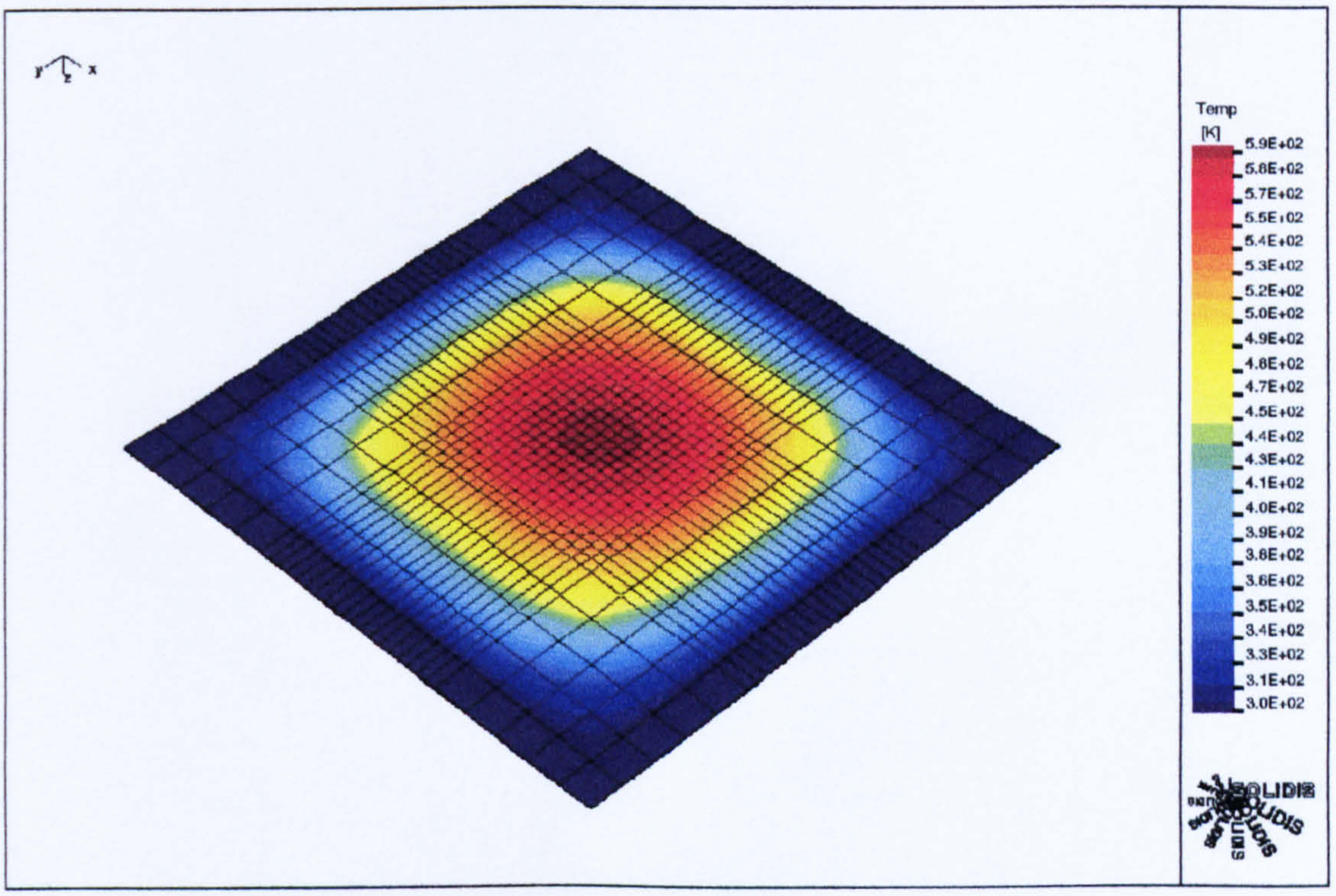

(a)

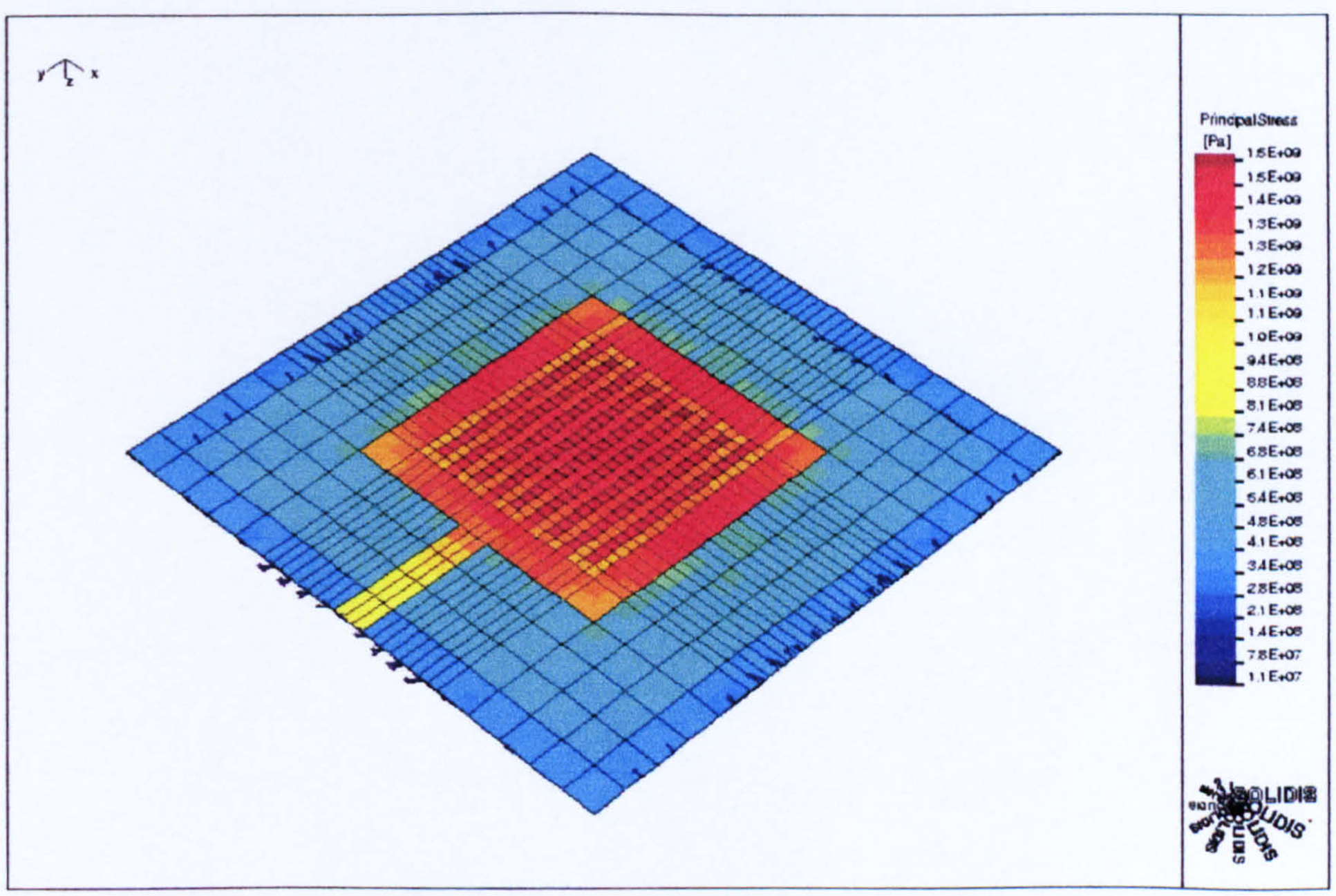

(b)

Figure 2.16: Thermo-mechanical simulation result for SRL 136a. (a) The simulated temperature profile at 100 mW, indicating the hot spot and (b) the thermal induced stress.

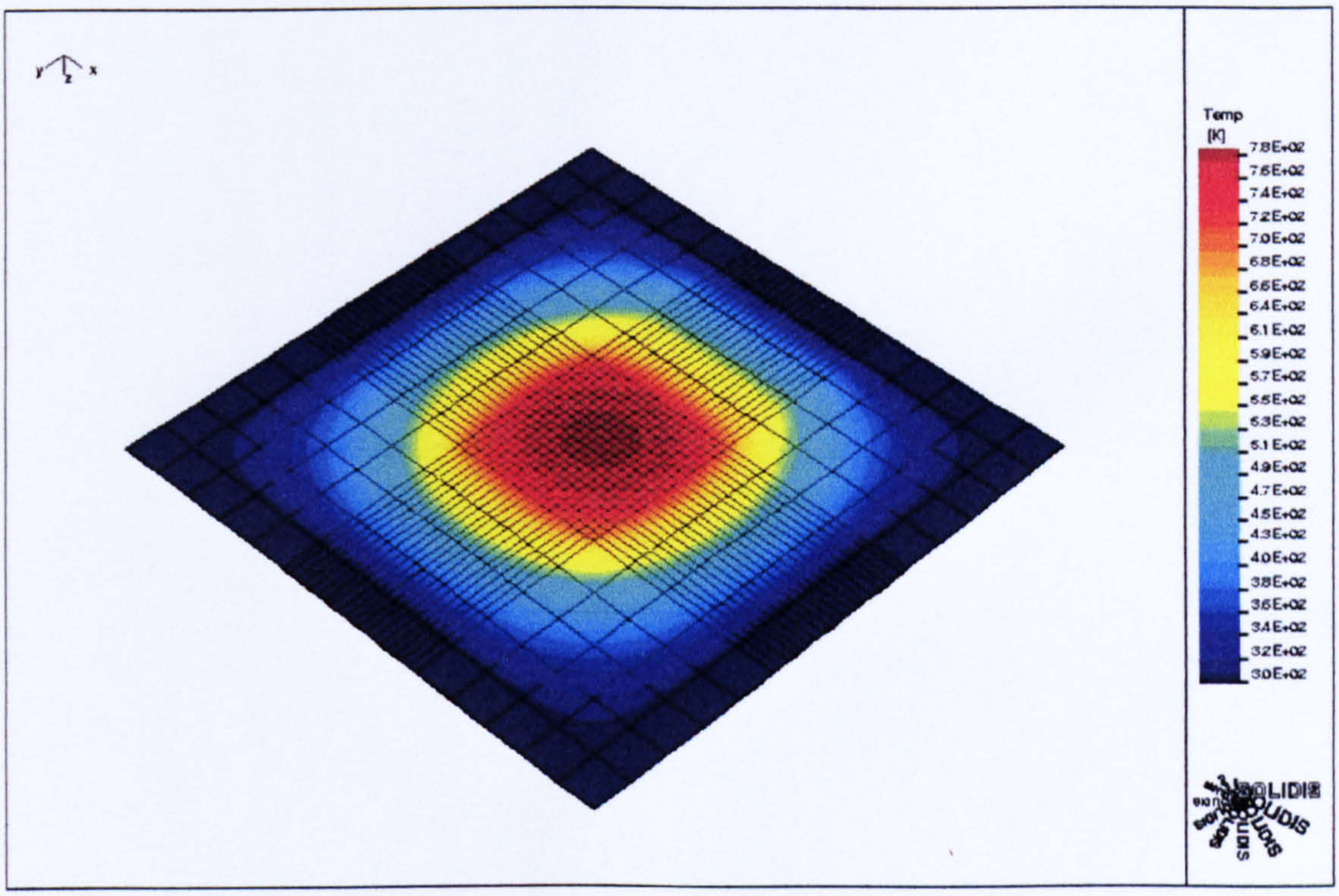

(a)

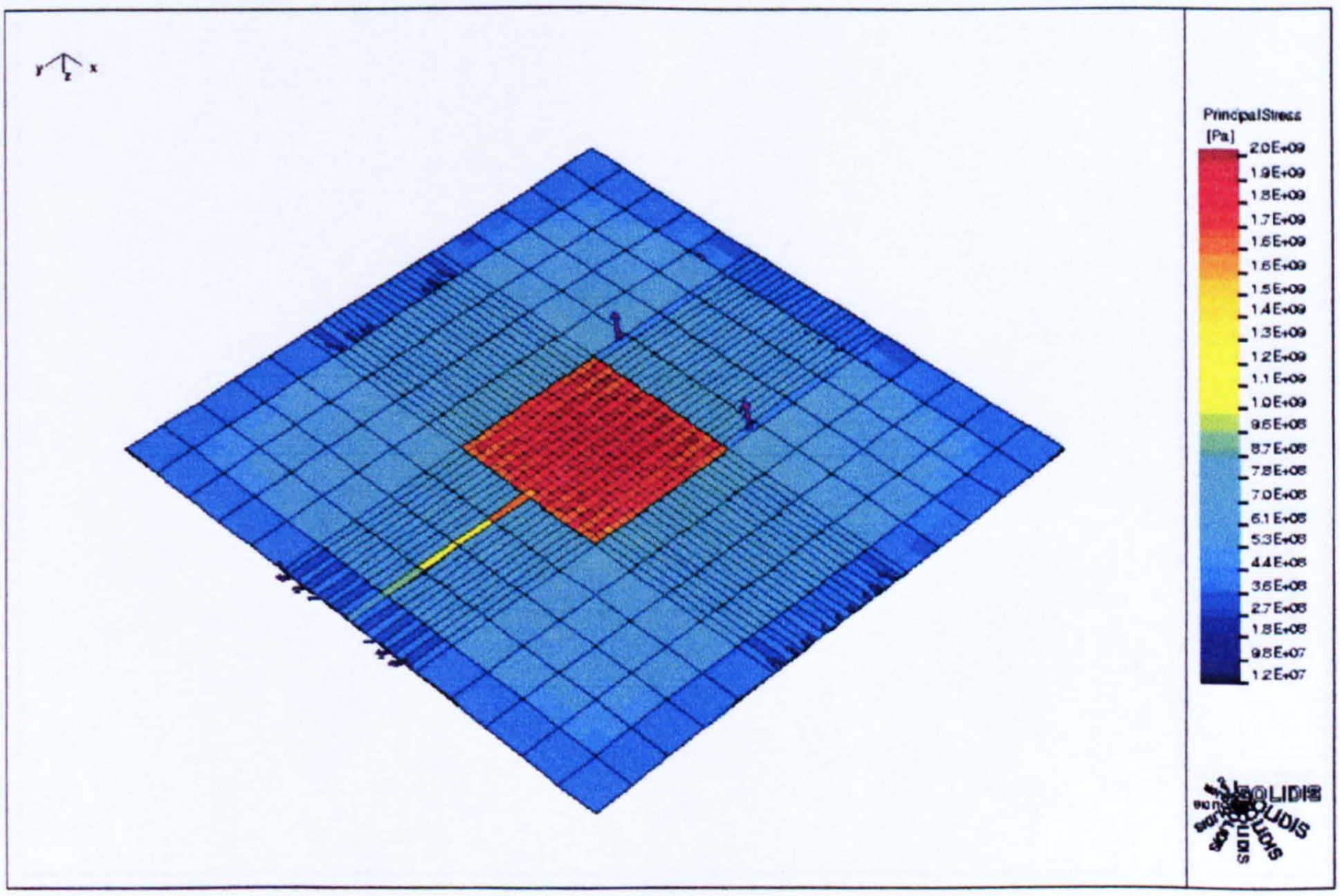

(b)

Figure 2.17: Thermo-mechanical simulation result for SRL 162g. (a) The simulated temperature profile at 100 mW, indicating the hot spot and (b) the thermal induced stress.

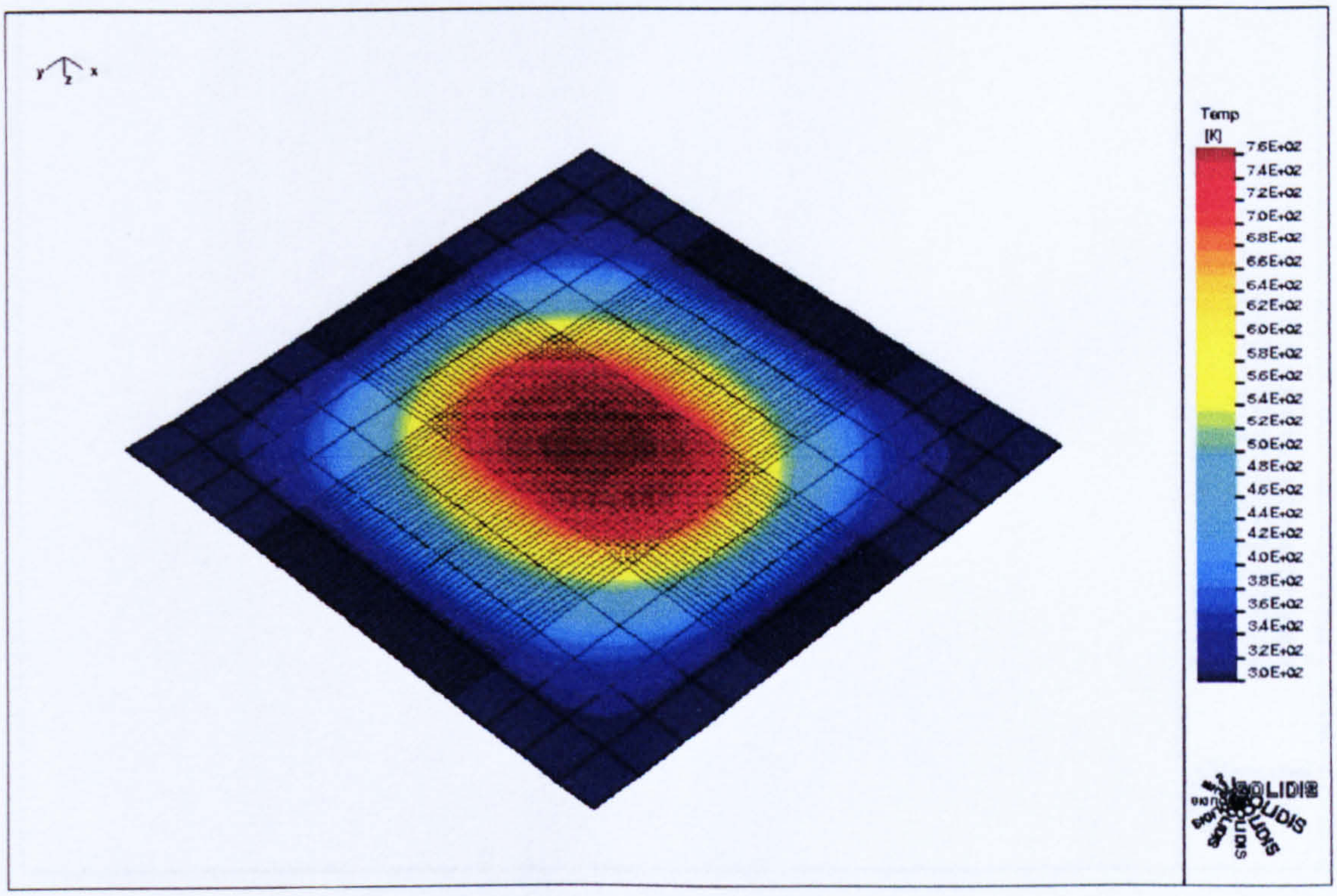

(a)

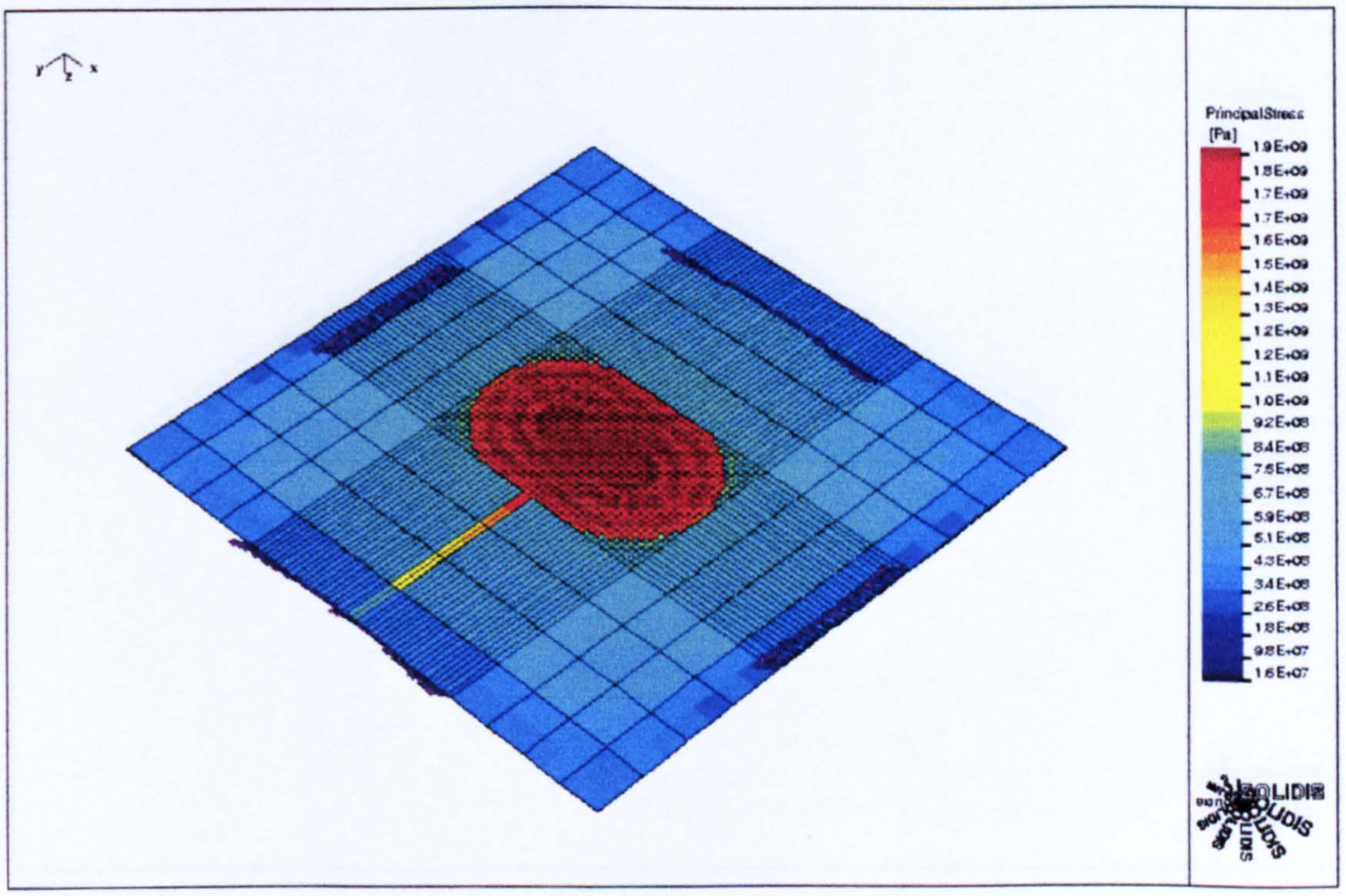

(b)

Figure 2.18: Thermo-mechanical simulation result for SRL 176a. (a) The simulated temperature profile at 100 mW with improved homogeneity at the active area. (b) The thermal induced stress and the micro-heater structure can be observed.

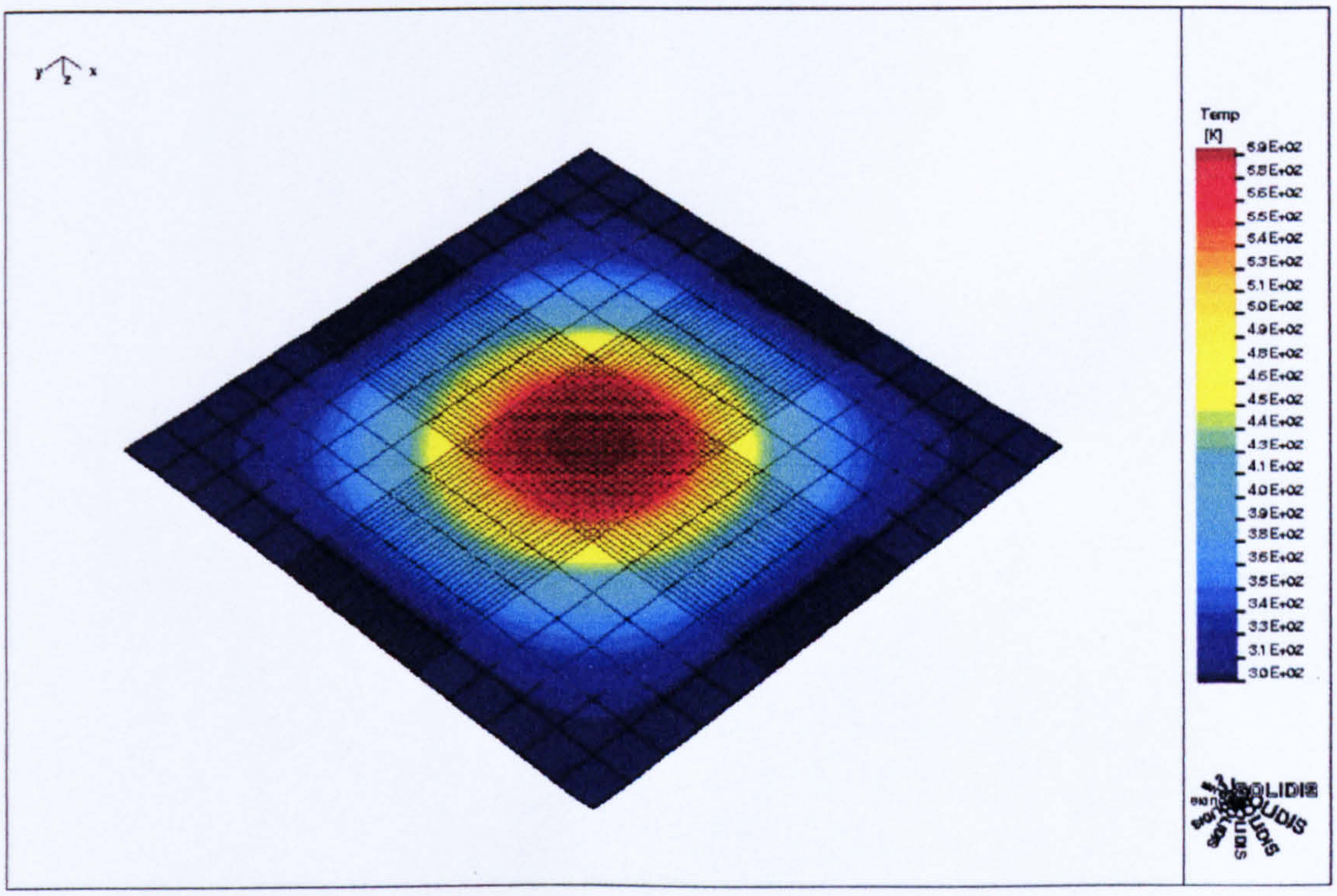

(a)

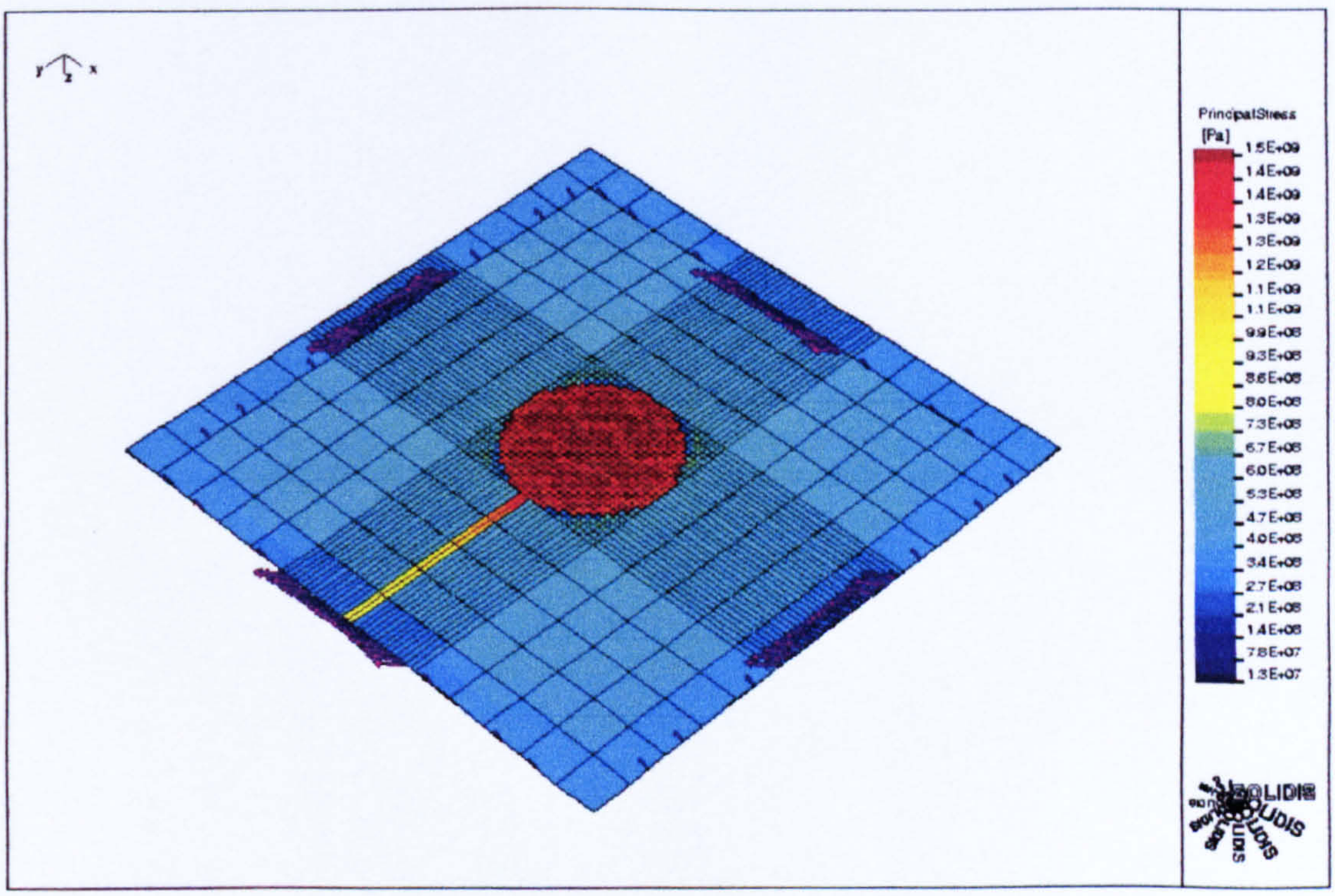

(b)

Figure 2.19: Thermo-mechanical simulation result for SRL 176b. (a) The simulated temperature profile at 100 mW with improved homogeneity at the active area. (b) The thermal induced stress and the micro-heater structure can be observed.

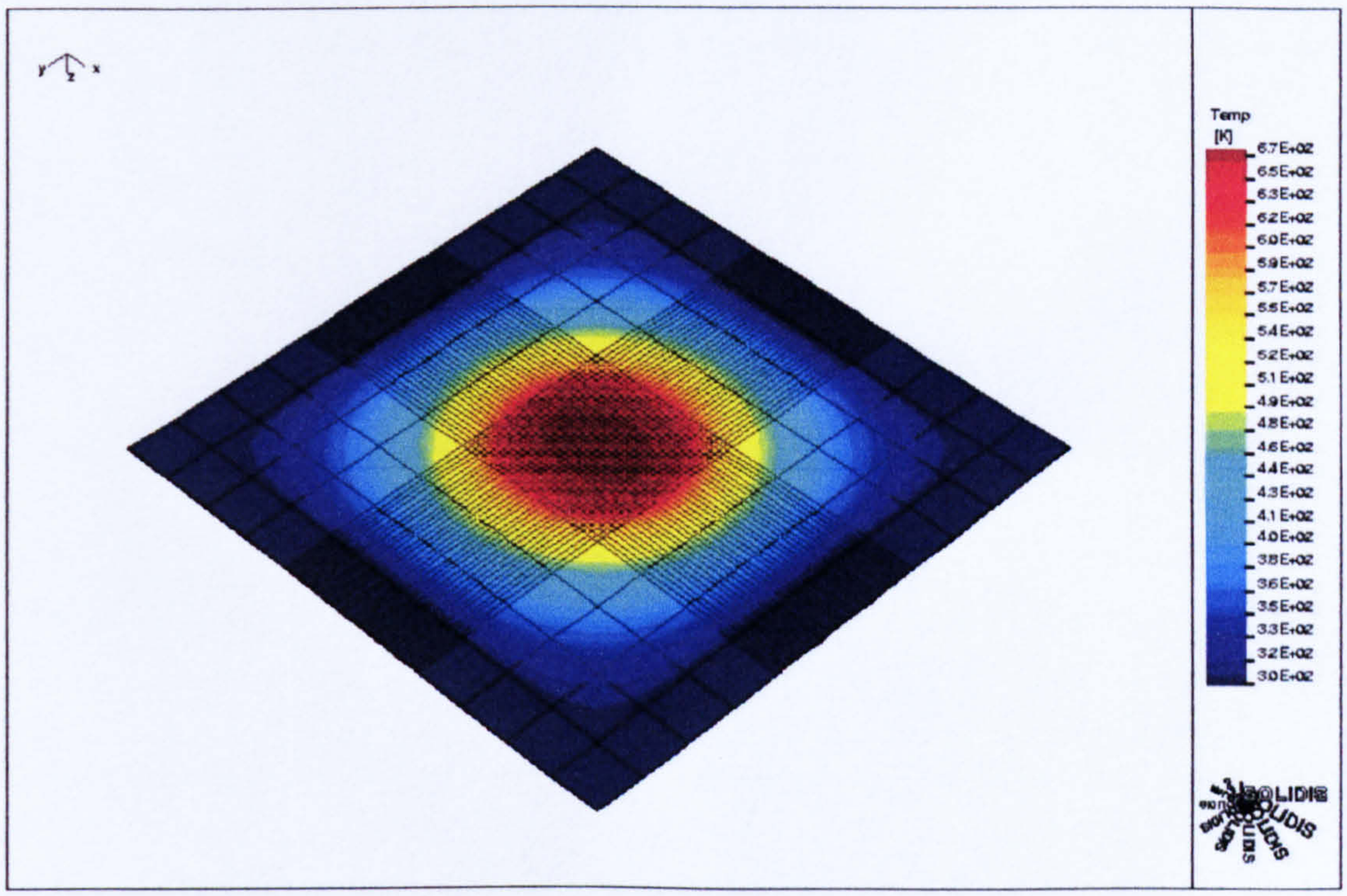

(a)

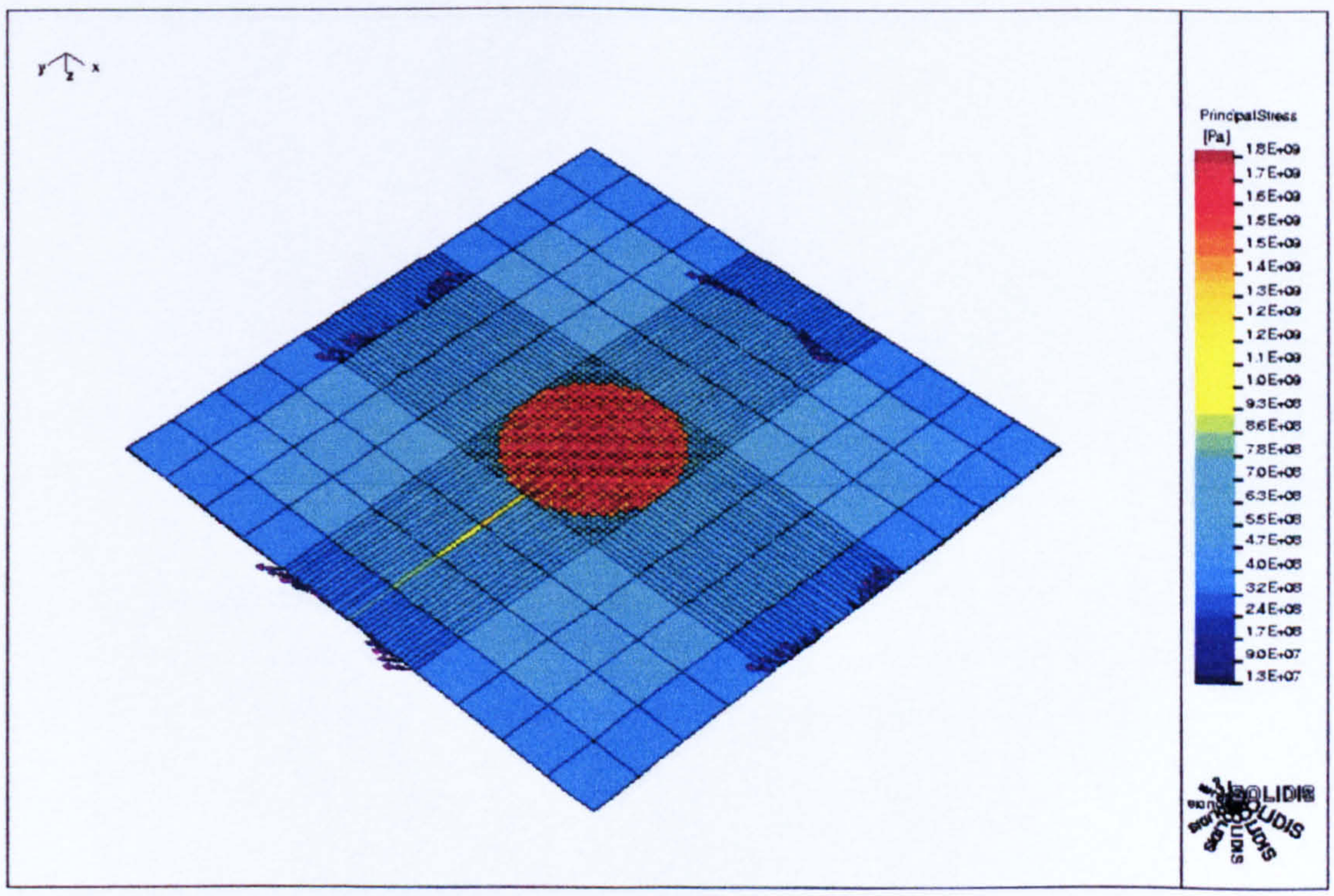

(b)

Figure 2.20: Thermo-mechanical simulation result for SRL 176c. (a) The simulated temperature profile at 100 mW with improved homogeneity at the active area. (b) The thermal induced stress is spread out because the micro-heater tracks are no longer obvious.

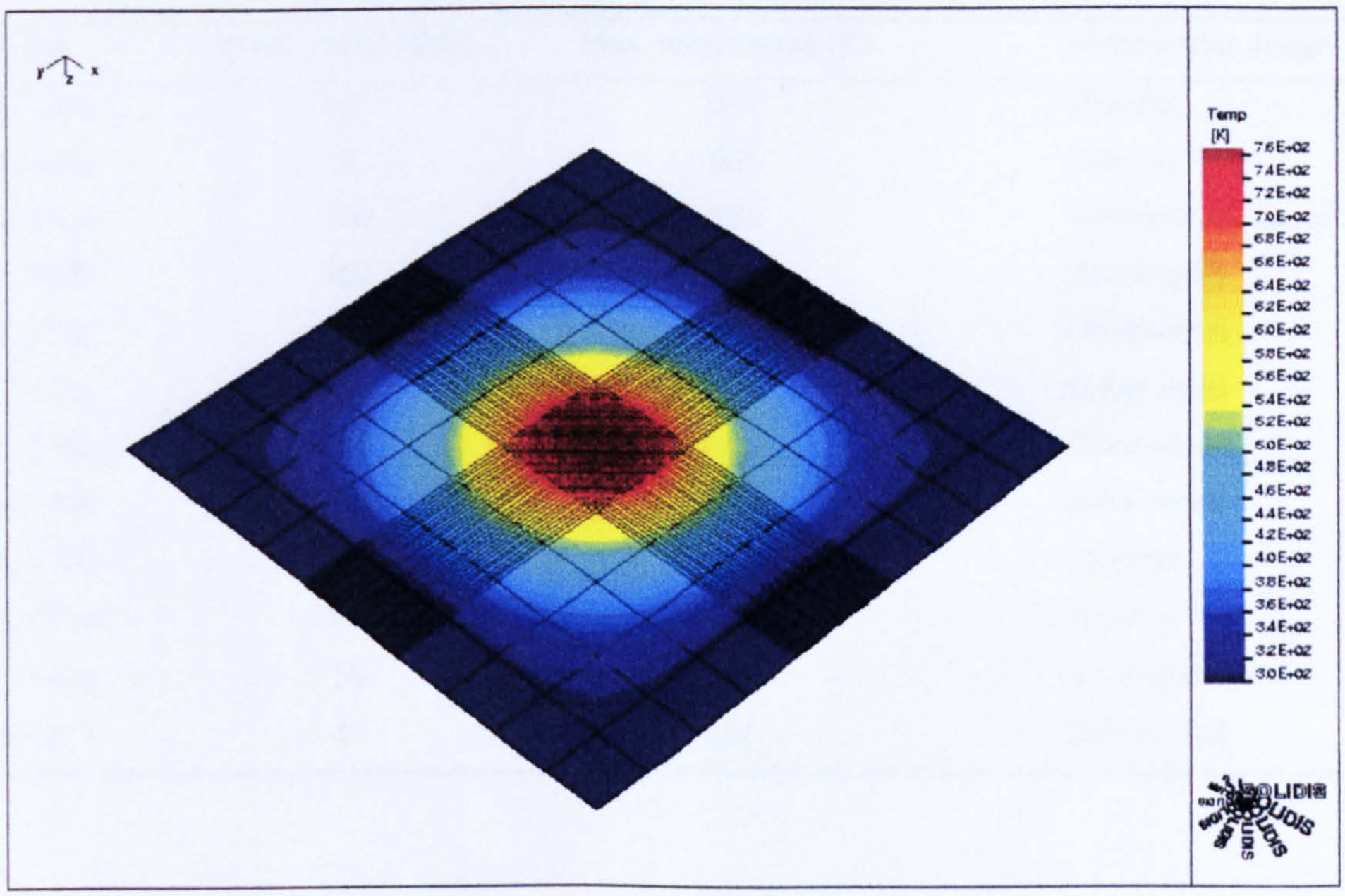

(a)

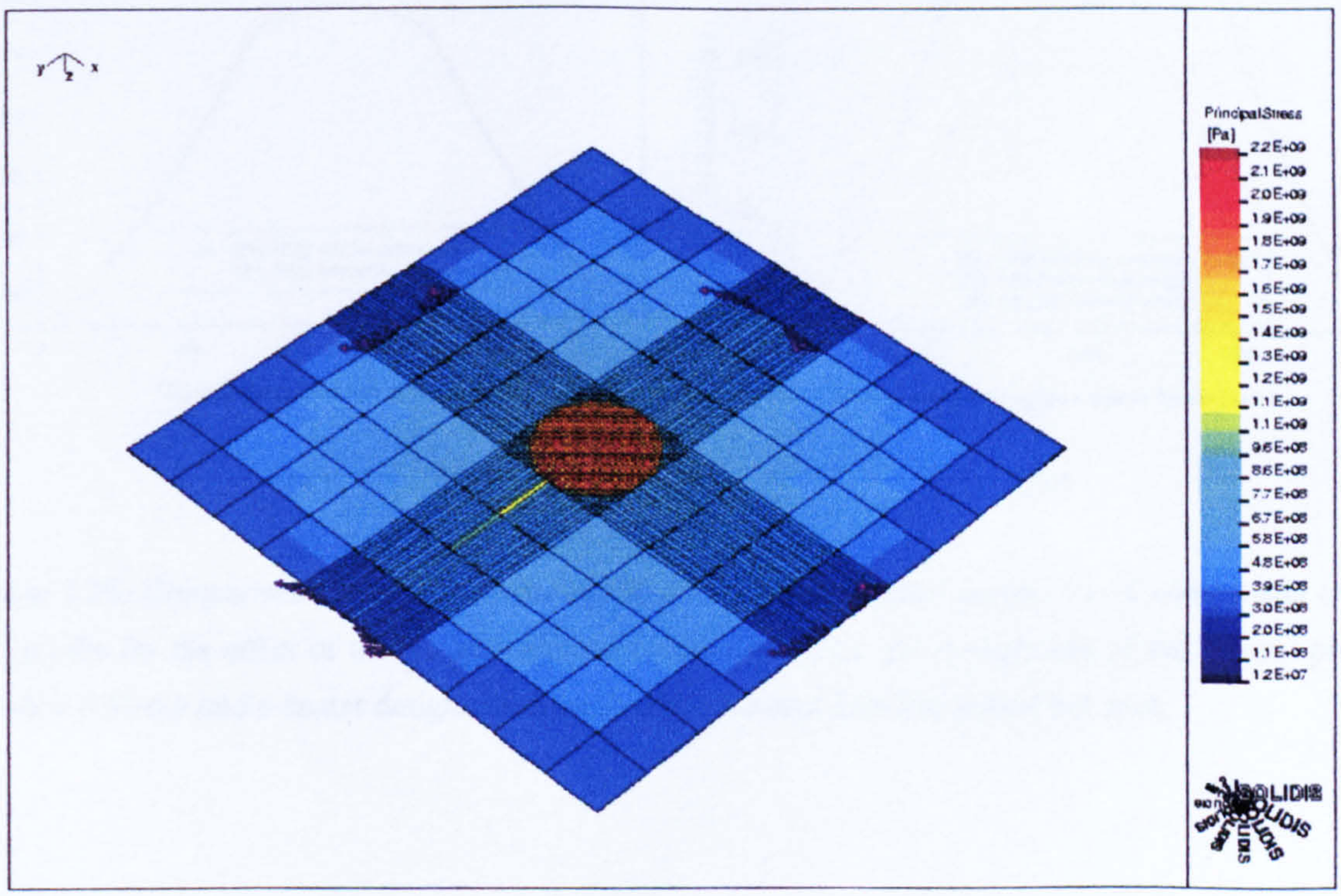

(b)

Figure 2.21: Thermo-mechanical simulation result for SRL 177c. (a) The simulated temperature profile at 100 mW with improved homogeneity at the active area. (b) The thermal induced stress is spread out because the micro-heater tracks are no longer obvious.

Table 2.7: The simulated relationship between power and temperature for various designs

SRL No.	Power input (mW)	Max. temperature (K)	Micro-heater design
SRL 136a	100	590	Meander
SRL 162g	100	780	Meander
SRL 176a	100	760	Ultra-low resistance
SRL 176b	100	590	Honeycomb
SRL 176c	100	670	Drive-wheel
SRL 177c	100	760	Drive-wheel
SRL 178c	100	680	Drive-wheel
SRL 179c	100	590	Drive-wheel
SRL 179d	100	660	Meander
SRL 179e	100	460	Meander
SRL 180c	50	440	Drive-wheel
SRL 181c	50	540	Drive-wheel

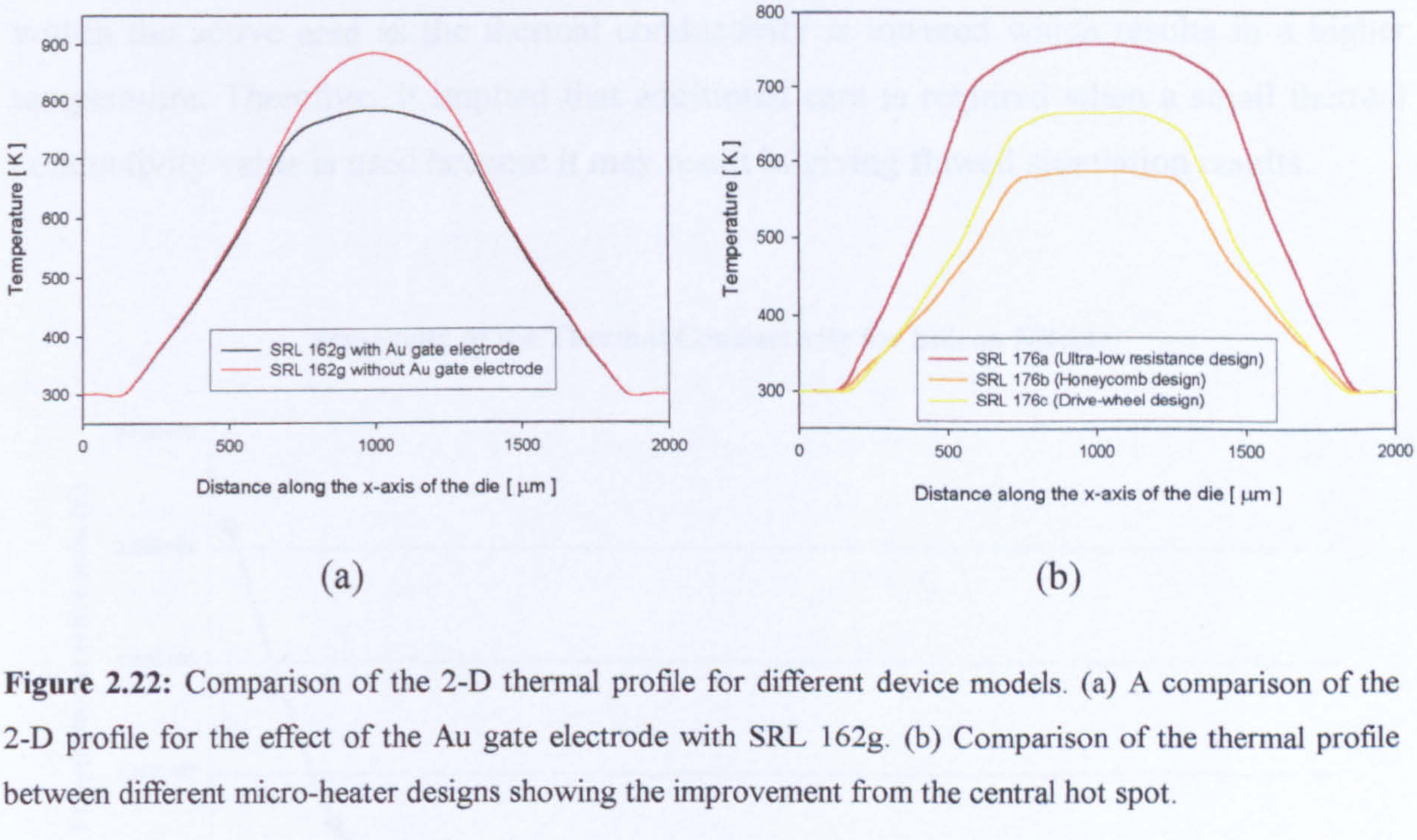

Figure 2.22: Comparison of the 2-D thermal profile for different device models. (a) A comparison of the 2-D profile for the effect of the Au gate electrode with SRL 162g. (b) Comparison of the thermal profile between different micro-heater designs showing the improvement from the central hot spot.

2.6.6 Parametric sensitivity investigation

As mentioned in section 2.6.1, the simulation software requires a set of special material properties. These values become the ultimate factor that governs the accuracy of the simulation results. However, material properties may vary under different conditions and a range of values can be found for a material from different sources in the literature. Therefore, it is essential to investigate the sensitivity of the simulated results to the material properties applied.

As an identical set of material properties was applied to all the simulations, only the geometrical model for SRL 162g was selected for investigation. The density and the thermal conductivity of various materials were simulated up to 50% below and 200% above the nominal value. Significant temperature changes were only identified with a fluctuation of the thermal conductivity of silicon nitride. The result of this experiment is shown in figure 2.23 [2.20]. It shows that the maximum temperature at the centre of the active area is highly depended on thermal conductivity. The thermal energy is confined within the active area as the thermal conductivity is lowered which results in a higher temperature. Therefore, it implied that additional care is required when a small thermal conductivity value is used because it may result in giving flawed simulation results.

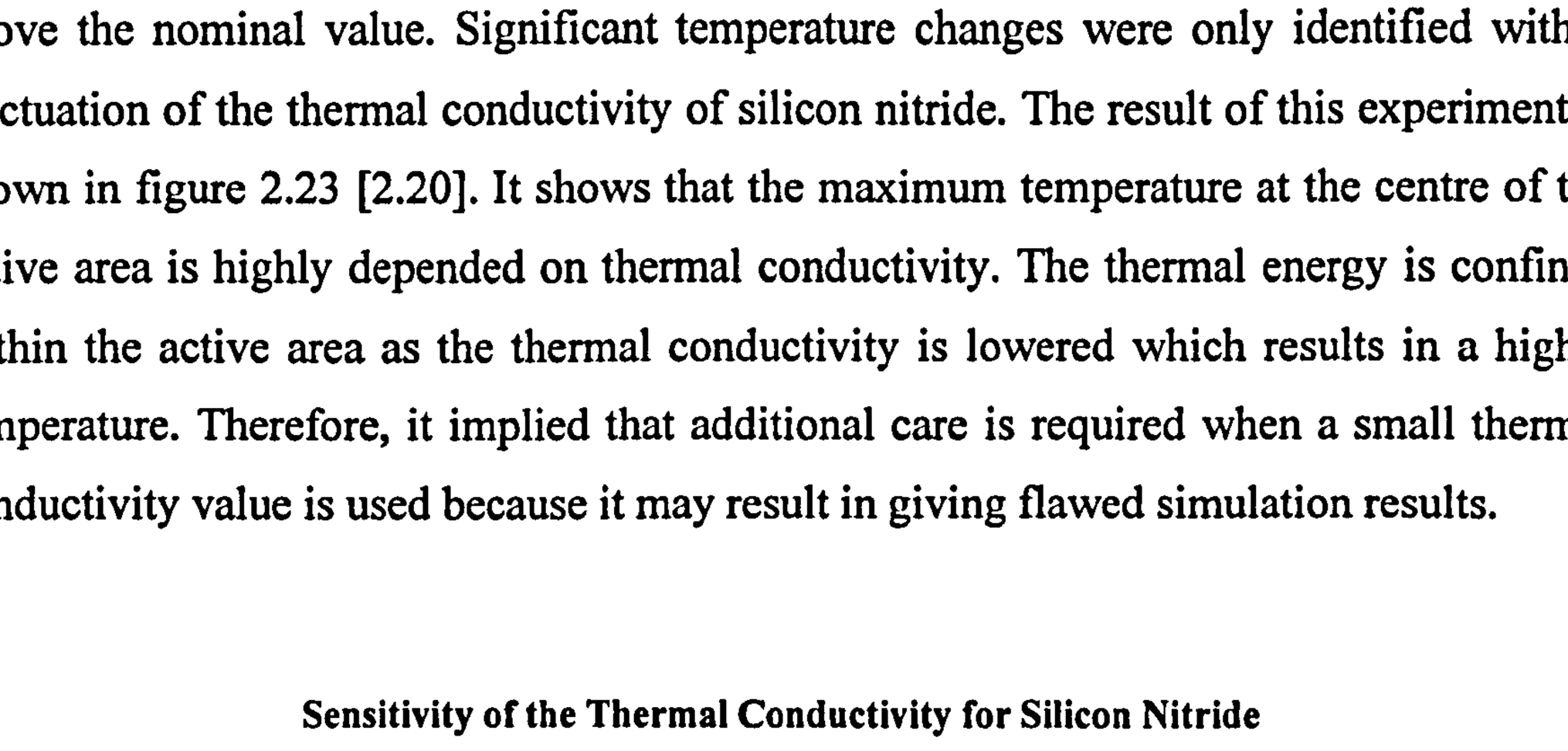

Figure 2.23: The parametric sensitivity of the thermal conductivity for the silicon nitride [2.20].

2.7 Conclusions

This chapter reports on two generations of micro-calorimeter design and the associated design considerations, such as the heat loss mechanisms. It has been shown that the convection and radiation loss are geometrically dependent in the heat transfer mechanism and conductive loss is the only controllable parameter in the design. *MHR* is the key parameter towards the thermal isolation and this concept was applied to the micro-calorimeter design.

The two families in the first generation devices used the meander-type micro-heater design. Therefore, only minimum modifications were introduced for direct comparison with the original micro-hotplate design. Enhanced understanding of the device properties enabled greater freedom to the design without impairing functionality. Six design families and fifty-four designs and variants were created with different optimisation strategies. Test structures were also included for other investigations, such as an emulator to mimic the catalyst effect.

Thermo-mechanical simulations were performed to evaluate the device performance. Geometrical models and a database of material properties had been established. Not only did it allow the assessment of the designed micro-calorimeters, but also created a tool for future device development.

The simulation results indicated that all the second generation micro-heater designs reduced the magnitude of the central hot spot. However, the meander-type micro-heater had provided the best heating efficiency while the Drive-wheel design achieved the most isothermal active area, up to ± 20°C at 500°C. The results also agreed with the *MHR* optimisation concept for power consumption so the device with the largest *MHR* required the lowest power. The simulation results and the device performances were verified and are reported in Chapter 5 and 6.

References

[2.1] A. Pike, J. W. Gardner; Thermal modelling and characterisation of micropower chemoresistive silicon sensors, *Sensors and Actuators B*, Vol 45 (1997) p19-26.

[2.2] J. W. Gardner, S. M. Lee, P. N. Bartlett, S. Guerin, D. Briand and N.F. de Rooij, Silicon Planar Microcalorimeter Employing Nanostructured Films, *Digest of technical papers vol 1*, Transducers '01 Eurosensors XV, 2001, pp. 820-823.

[2.3] S. M. Lee, J. W. Gardner, D. C. Dyer; *City Technology Ltd. Low power micropellistor project quarterly report (University of Warwick)*, No. 1, 1999.

[2.4] U. Dibbern, A substrate for thin-film gas sensors in Microelectronic Technology, *Sensors and Actuators B*, 2, 1990, pp. 63-70.

[2.5] F. P. Incropera, D. P. De Witt, *Fundamentals of heat and mass transfer*, Third edition, Chapter 12, p696, John Wiley & Son, Ltd, 1990.

[2.6] S. M. Lee, D. C. dyer and J. W. Gardner, Design and optimisation of a high-temperature silicon micro-hotplate for nanoporous palladium pellistors, *Microelecronics Journal*, 34, pp 115-126, 2003.

[2.7] K. L. Chopra, *Thin Film Phenomena*, McGraw-Hill Book Company, 1969.

[2.8] R. W. Berry, P. M. Hall, M. T. Harris, *Thin film technology*, Chapter 6, p310, D. Van Norstrand Company Inc.,1968.

[2.9] L. I. Maissel and R. Glang, *Handbook of thin film technology*, McGraw-Hill, New York, 1970.

[2.10] D. A. Pucknell and K. Eshraghian, *Basic VLSI Design*, 3rd Edition, Chapter 4, p95, Prentice Hall, Australia, 1994.

[2.11] S. Astié, A. M. Gué, E. Scheid, L. Lescouzéres, A. Cassagnes, Optimisation of an integrated SnO_2 gas sensor using a FEM simulator, *Sensors and Actuators A*, Vol 69, p 205-221, 1998.

[2.12] D. Lee, W. Chung, M. Choi, J. Baek, Low power micro gas sensor, *Sensors and Actuators B*, Vol 33, p147-150, 1996.

[2.13] S. M. Lee, J. W. Gardner; *City Technology Ltd. Low power micropellistor project quarterly report (University of Warwick)*, No. 5, 2000.

[2.14] Z. Vizvary, P. Furjes, I. Barsony, Thermomechanical analysis of hotplates by FEM, Microelectronics Journal 32, p833-837, 2001.

[2.15] *ISE TCAD user manual*, Release 6, Volume 6, Thermal Effects, Part 25, p25.28, 1999.

[2.16] *ISE TCAD user manual*, Release 6, Volume 6, Mechanical effects, Part 25, p25.21, 1999.

[2.17] S. M. Lee, J. W. Gardner; *City Technology Ltd. Low power micropellistor project quarterly report (University of Warwick)*, No. 6, 2001.

[2.18] A. M. James and M. P. Lord, *Macmillan's Chemical and Physical Data*, The Macmillan Press Ltd., London, 1992.

[2.19] G. C. M. Meijer, A. W. Herwaarden, *Thermal Sensors*, Institue of Physics Publishing, Appendix A, p290, 1994.

[2.20] S. M. Lee, J. W. Gardner; *City Technology Ltd. Low power micropellistor project quarterly report (University of Warwick)*, No. 7, 2001.

Chapter 3

Fabrication of silicon planar micro-calorimeter

3.1 Introduction

This chapter provides full details of the fabrication processes of the micro-calorimeter designs discussed previously. The two main processes involved in the sensor fabrication are the micro-machining of the silicon substrate and the electrochemical deposition of the nanostructured Pd catalyst film. The wafer layout strategies, mask details and silicon runs are explained for the two device generations. Evaluations of the fabrication process like the overall yield, defects and surface topology were undertaken to ensure optimal manufacturability of future runs. The nanoporous catalyst was then deposited onto the micro-machined substrate to complete the silicon micro-calorimeter. The composition of the surfactant and the catalyst deposition procedure with the droplet coating system is also described, although this work has been carried out by University of Southampton.

3.2 Fabrication of silicon planar micro-hotplate

The micro-hotplate serves as a heating element to elevate the temperature of the nanoporous catalyst to its operating temperature. Once the individual cell designs were completed, they were placed on a 4″ wafer according to the number desired. Since numerous device families and test structures had to be accommodated on a wafer, device mapping strategies were implemented to satisfy a number of specific requirements for each fabrication run. Incorporating a set of alignment marks and reference objects, a series of optical masks were manufactured at Compugraphics Ltd, UK. Two wafer fabrication runs have been carried out and a set of wafers from each run has undergone an additional passivation process. After fabrication, individual devices were diced out and packaged onto TO5 headers using ultra-sonic wire bonding, ready for nanoporous catalyst deposition.

3.2.1 Wafer layout for first wafer run

The first batch of devices were designed to obtain a relatively large quantity of functioning devices where only minor design modifications were made from the early micro-hotplate design [3.1]. Each wafer contained roughly 50% of the original micro-hotplate design, (SRL 136a) used in Sam Guerin's project [3.2]. There were several variations of the two micro-hotplate designs acting as test structures. These had either no membrane or an Au gate electrode. The quantity of each device type and quantities on each wafer is tabulated in table 3.1.

Table 3.1: Device types and quantity on a wafer in first silicon wafer fabrication run

Cell	*Membrane*	*electrode*	*No. off*	*Remarks*
A			18	Modified design (SRL 162g)
B		✓	18	Modified design (SRL 162g)
C	✓		12	Modified design (SRL 162g)
D	✓	✓	212	Former design (SRL 136a)
E	✓	✓	150	Modified design (SRL 162g)
F			4	Alignment Cell
		Total	414	

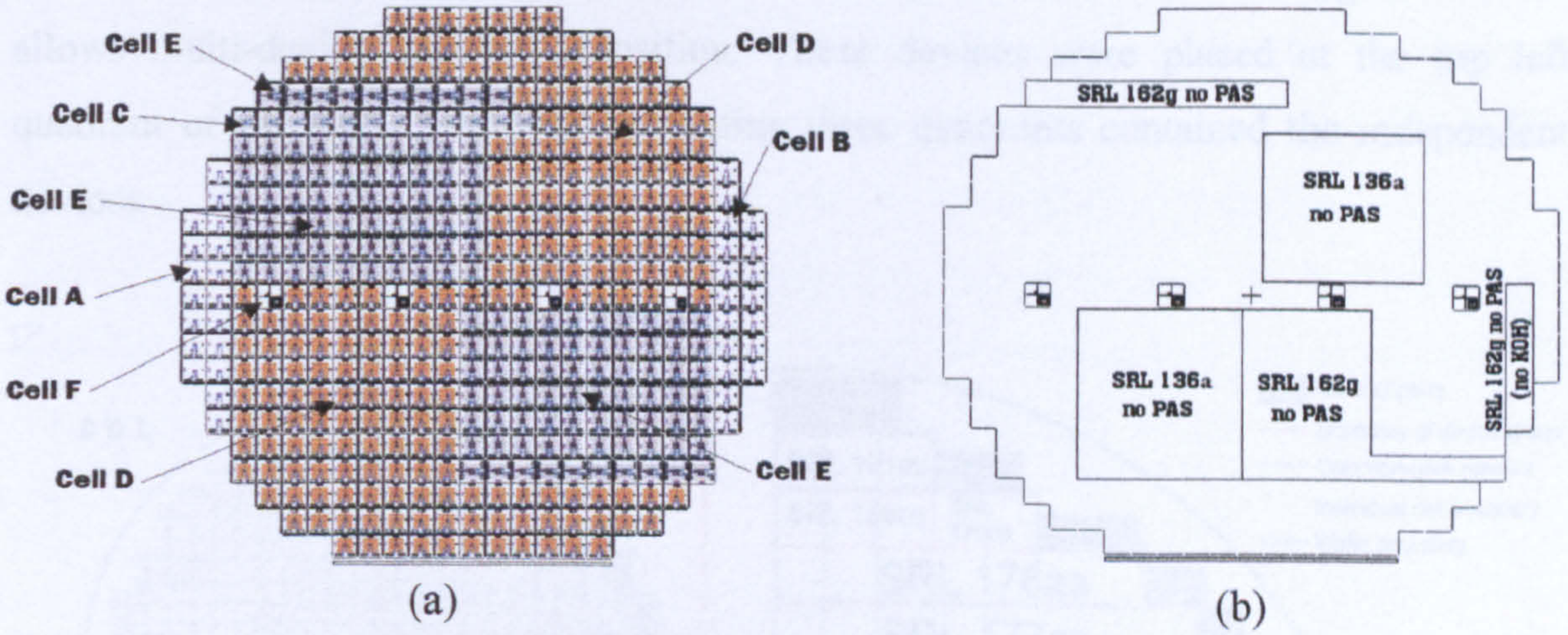

Figure 3.1: (a) Device mapping on the wafer. (b) Location of device without passivation.

According to the layout strategy employed, the test structures without a membrane were placed at the edge of the wafer and this provided additional mechanical strength for wafer handling. The two types of devices, SRL 136a and SRL 162g, were mapped in four groups and same device groups were placed diagonally as illustrated in figure 3.1(a). Hence, the effect of the local process variation can be ameliorated.

According to the micro-hotplate design described in Chapter 2, there is a layer of low-stress silicon nitride for the final passivation to provide additional mechanical stability to the devices. However, the effect of the passivation layer was initially uncertain because it increases the thickness of the membrane and so increases somewhat the lateral thermal loss. Consequently, it may alter the thermal time constant of the device. Therefore, without compromising the fundamental objectives, only two out of twelve wafers had a final passivation layer. In addition, the passivation layer did not cover the entire wafer, as shown in figure 3.1(b), where approximately 50% of the devices remained unpassivated.

3.2.2 Wafer layout for second wafer run

The second wafer run processed the improved designs which were discussed in chapter 2. As there were 54 different design variants, the quantity available for each device on a wafer was limited. Each design was allocated conscientiously in order to yield maximum process-related information. The placement strategy was based upon dividing a wafer into two areas as shown in figure 3.2(a). This included a reserved common-gate area that allows multi-device catalyst deposition. These devices were placed at the top left quadrant of the wafer while the remaining three quadrants contained the independent devices.

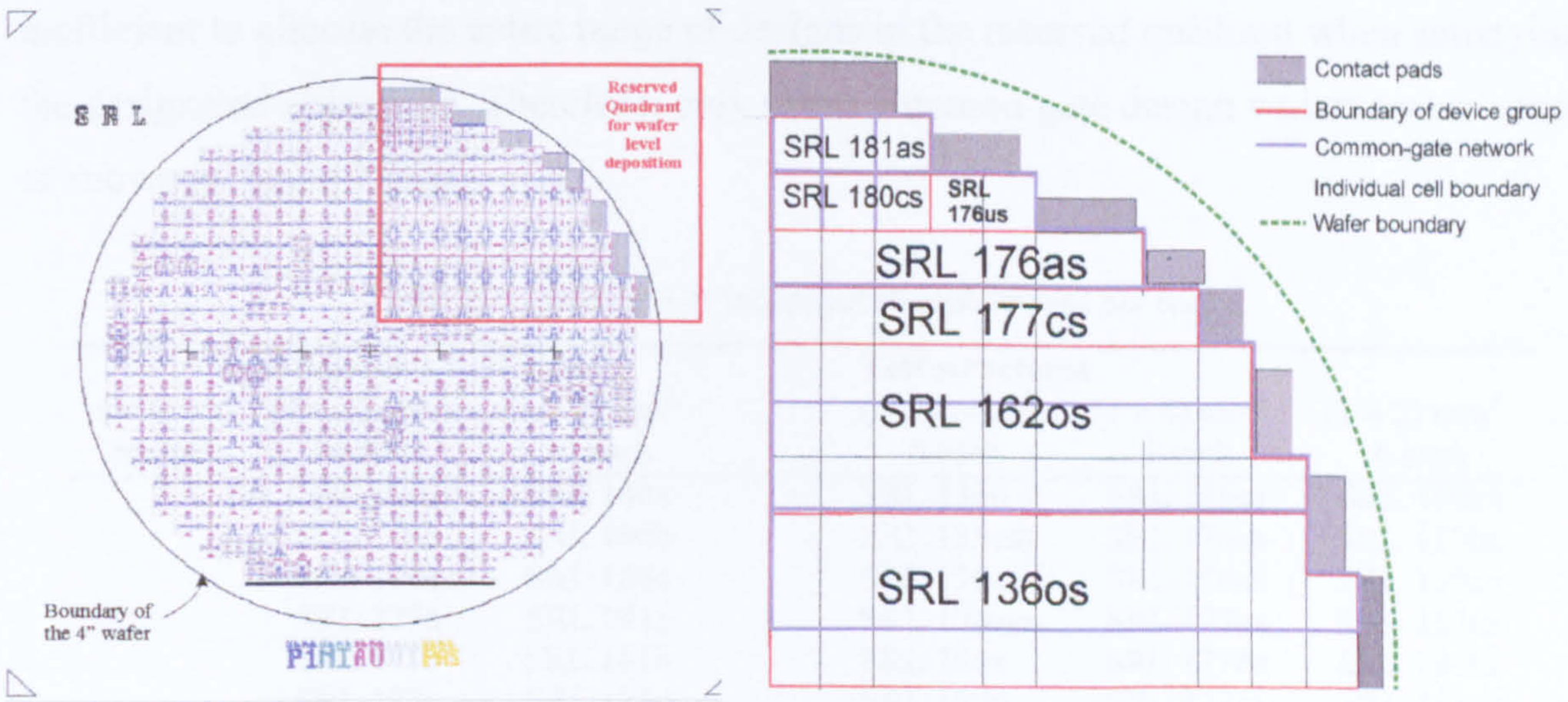

Figure 3.2: (a) Wafer layout of the 2nd wafer run with reserved quadrant. (b) The schematic of the reserved quadrant indicating the common-gate network.

Each quadrant of the independent-gate device contains the same mix of designs. However, the designs were not allocated at identical positions between each quadrant. Furthermore, each device has an individual device locator number so once the wafer is diced, the exact position of a device on the wafer is known. This allows intra-wafer variations in terms of the performance of the devices to be monitored. In addition, it helps to identify neighbouring devices that could be matched within a Wheatstone bridge interface to investigate the performance of dual-devices. A wafer map of device locators is included in Appendix 3a.

Assuming an identical fabrication process to the previous run, the process yield indicated that the top left quadrant would be the most robust section on the wafer (see section 3.3.1). It is important that the common-gate quadrant remains intact to allow the nanoporous catalyst to be electroplated on an array of devices in a single deposition. The quadrant consists of common-gate network connections that are linked to various common contact pads. Hence, in case of unexpected breakages, the device array can be accessed by other common contact pads. Therefore, the quadrant can be sectioned into various shapes and sizes for common-gate deposition.

The devices in the reserved quadrant are used to investigate the feasibility of wafer-level nanoporous catalyst deposition. It not only allows the investigation of film thickness uniformity for the catalyst, but also the behaviour of electrodes with various patterns and sizes in large scale electroplating. Nevertheless, it is impractical and inefficient to allocate the entire range of designs in the reserved quadrant when satisfying the designated objectives. Therefore, only seven common-gate design variants were used, as shown in figure 3.2(b).

Table 3.2: Quantities of independent-gate devices per wafer

	Main stream designs		**Test structures**		
Cell size	$(4 \times 4)\ mm^2$	$(2 \times 2)\ mm^2$	$(4 \times 4)\ mm^2$	$(4 \times 4)\ mm^2$	$(2 \times 2)\ mm^2$
No. off	16 each	10 each	6 each	4 each	4 each
	SRL 176a	SRL 180a	SRL 136o	SRL 176ax	SRL 180ax
	SRL 176b	SRL 180b	SRL 136em	SRL 176bx	SRL 180bx
	SRL 176c	SRL 180c	SRL 136sg	SRL 176cx	SRL 180cx
	SRL 177a	SRL 181a	SRL 136sgx	SRL 177ax	SRL 181ax
	SRL 177b	SRL 181b	SRL 136x	SRL 177bx	SRL 181bx
	SRL 177c	SRL 181c	SRL 162o	SRL 177cx	SRL 181cx
	SRL 178a		SRL 162x	SRL 178ax	
	SRL 178b		SRL 179d	SRL 178bx	
	SRL 178c		SRL 179dx	SRL 178cx	
	SRL 179a		SRL 179e	SRL 179ax	
	SRL 179b		SRL 179ex	SRL 179bx	
	SRL 179c			SRL 179cx	

The range of second generation designs included several test structures that do not require the same quantity as the standard micro-hotplate designs. However, the sample should be sufficient to facilitate the required characterisation and other experiments. The quantities of each independent-gate device on a wafer are tabulated in table 3.2 and a detailed account of the devices on a wafer is provided in Appendix 3b.

3.2.3 Mask Fabrication

When the micro-hotplate designs and wafer layouts were finalised, a set of optical masks were made. These are for the photolithography processes in the fabrication of the devices, specific to the requirements of the foundry. A mask is basically a patterned layer created by a thin chrome film deposited on a quartz or anti-reflective flat glass plate. A mask which carries the layer information for one single cell or device is known as a reticle, while a mask usually refers to the chrome-patterned glass plate that is applied to the entire wafer. In some mask printing processes, a reticle is used to copy the required pattern onto a mask by replicating itself across the mask plate. Through a set of mask plates, the design engineer conveys the information to the foundry about the device or structure that is required to be manufactured.

The artwork design of the masks was produced on the PC based layout editor package, L-Edit™ version 8.22 from Tanner Tools Ltd. Details of all the individual masks is attached in Appendix 8. The design software package exports the layer information into GDSII format which is a generic data format widely used in industry. The digitised data of the designed patterns is then fed into a computer that drives the e-beam mask generator.

The five masks required for each of the micro-hotplate fabrication processes were manufactured by Compugraphics International Ltd, UK. As the device fabrication was based on a circular 4″ wafer, a set of 5″ square mask plates was required. The mask plates were plotted in A1 size to be inspected for defects and errors before fabrication. The mask printing employed an electron-beam process with a resolution of 0.5 μm. Another important quality factor is the registration error which refers to the situation when two masks used to image the level pattern do not overlay perfectly. It might be caused by several contributions [3.3]. The mask stacking, alignment and fabrication processes are the three main areas that contribute to registration error and the fabricated masks obtained registration tolerance of ± 1.0 μm.

3.2.4 Wafer processing and bulk silicon micromachining

The two batches of wafers were processed by the Institute of Microtechnology (IMT), University of Neuchâtel, Switzerland. The fabrication processes involved the combination of microelectronic processes, such as layering and patterning, as well as the bulk anisotropic wet etching of silicon wafers. The process is shown in figure 3.3.

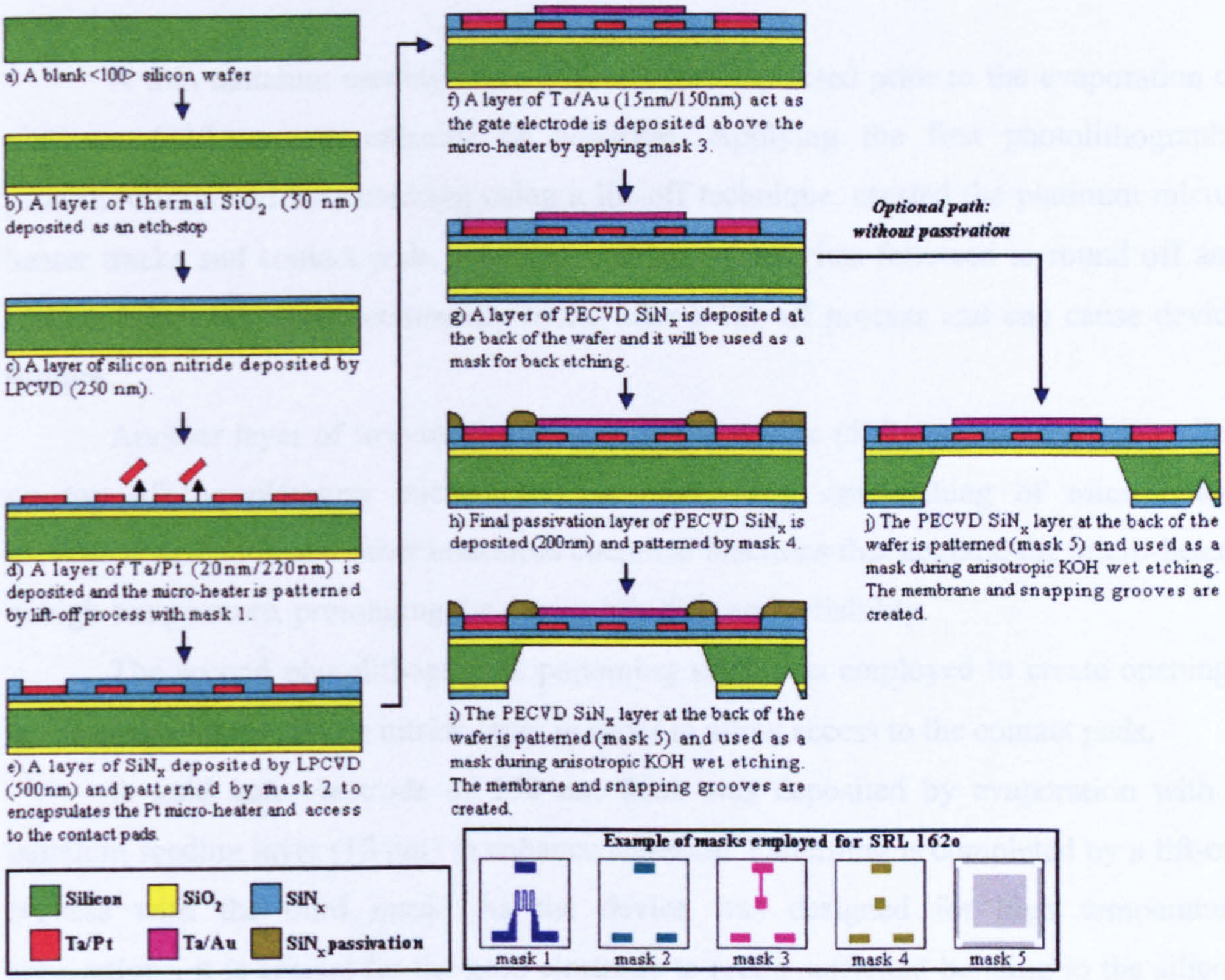

Figure 3.3: An illustration of the fabrication process used to fabricate the silicon micro-machined micro-hotplate with a set of masks (example for SRL 162o (not to scale)).

The starting wafers are a batch of double polished 4", <100> orientated, n-type wafers. A standard cleaning process was conducted for degreasing and removing of contaminants. Photolithography, as defined in Chapter 1, was employed repeatedly for all the patterning processes. The dark-field contact masks were used in conjunction with a spin-coated negative photoresist.

The first step was to thermally grow a layer of silicon oxide to a thickness of 50 nm at 1100°C. This layer is used as an etch-stop and will be discussed later to accurately

control the thickness of the silicon nitride membrane. The intrinsic stress of this layer has been removed [3.4, 3.5] to ensure the quality of the membrane.

The 250 nm low-stress silicon nitride layer was deposited as the lower half of the membrane by low-pressure chemical vapour deposition (LPCVD). A silicon-rich nitride reduces the residual stress and this property is essential to realising the ultra thin membrane. It improves the reliability and durability of the device for high temperature operation.

A thin tantalum seeding layer (20 nm) was deposited prior to the evaporation of platinum (220 nm) to enhance its adhesion. Applying the first photolithography procedure followed by patterning using a lift-off technique, created the platinum micro-heater tracks and contact pads. An extra etching process has followed to round off any spiking edges which are commonly found after a lift-off process and can cause device rupture.

Another layer of low-stress LPCVD silicon nitride (500 nm) was then deposited on top of the platinum micro-heater structure. The sandwiching of micro-heater prevented oxidation and other undesired chemical reactions that degrade the micro-heater at high-temperature, prolonging the device life-time and reliability.

The second photolithographic patterning stage was employed to create openings in the encapsulated silicon nitride layer in order to allow access to the contact pads.

A gold gate electrode of 150 nm thick was deposited by evaporation with a tantalum seeding layer (15 nm) to enhance adhesion. Patterning is completed by a lift-off process with the third mask. As the device was designed for high temperature applications, it is critical for the gold electrode to retain sufficient bonding to the silicon membrane during operation.

At this point, two wafers from each fabrication run underwent an additional passivation process before bulk micro-machining. The top layer structure was passivated by a PECVD layer to provide additional mechanical and chemical stability for the device. PECVD was used to avoid damage to the gold layer as LPCVD processes involve high temperatures. Openings on the layer were created with the fourth mask in order to expose the contact pads and the gold gate electrode.

As the etchant employed in the bulk silicon micro-machining process reacts only with silicon, sealing the top-side is unnecessary. A layer of PECVD silicon nitride was deposited on the back of the wafer to form a back-etching protective layer. It was

patterned with the fifth mask and a Reactive Ion Etching (RIE) process. The thermal silicon oxide was then removed from the back of the wafer by buffered hydrofluoric acid (HF). The silicon membrane and the snapping grooves were created by anisotropic wet KOH etching at 60°C until the etch-stop layer was reached. A photograph of a completed wafer is shown in figure 3.4.

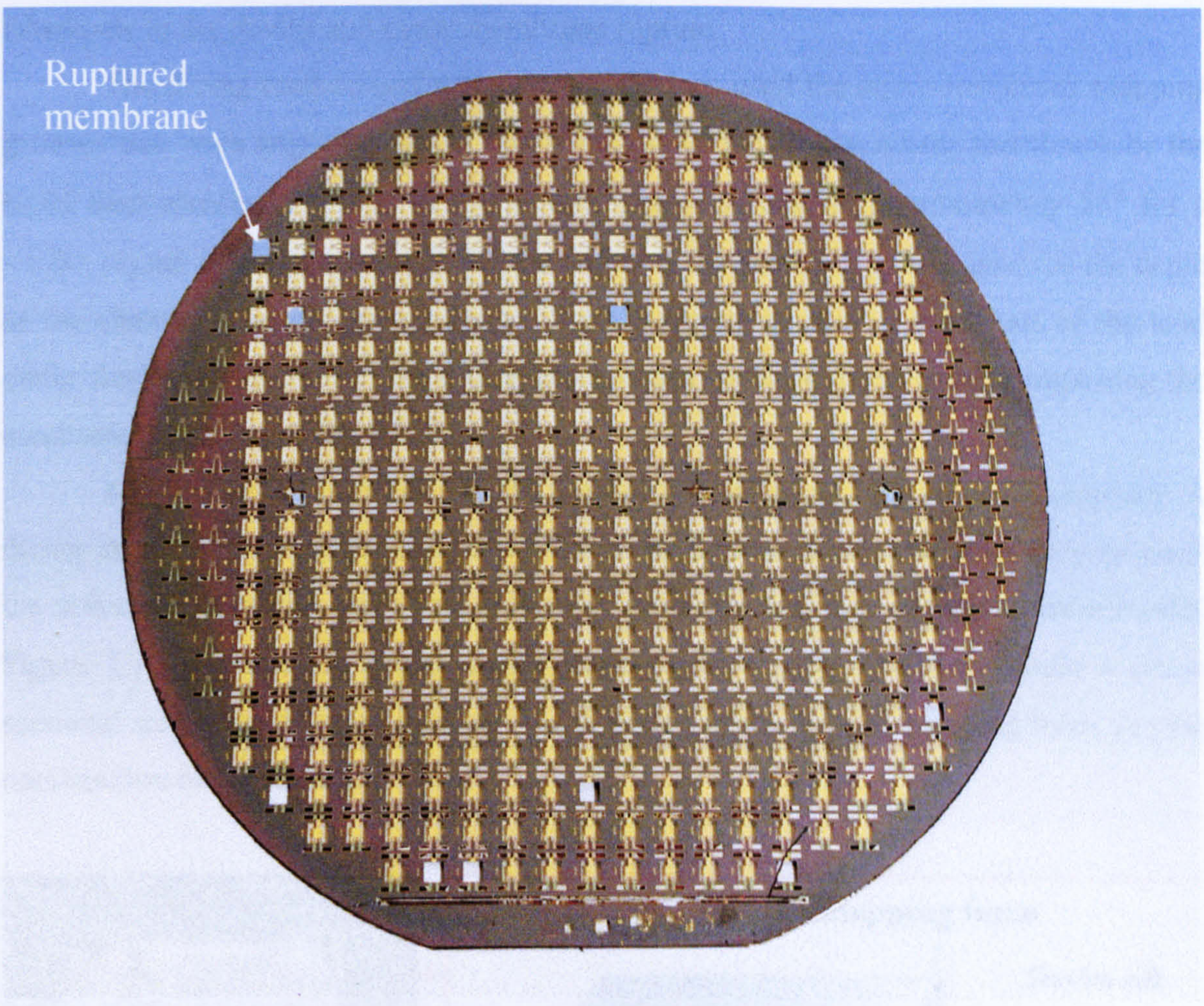

Figure 3.4: A completed wafer from first fabrication run. Several devices with damaged membranes can be observed.

3.2.5 Wafer dicing and packaging

The dicing and packaging of the devices were performed at the University of Warwick, UK. Dicing separates the cells from the wafer to become a die, either (4×4) mm^2 or (2×2) mm^2. There are numerous established dicing methods in the semiconductor industry and the most common processes are diamond scribing, laser scribing and diamond wheel sawing. However, these methods are either expensive or would induce intolerable vibrations to the device and cause membrane rupture.

The dicing method performed on the devices used the micro-machined snapping grooves that were engraved during the formation of the silicon nitride membrane by the KOH back-etching process. As the etching angle is fixed at approximately 55° for a <100> crystal orientated wafer [3.6], the width of the snapping groove governs the depth of the channel. The designated depth of the snapping groove is about half of the total wafer thickness. Therefore, the dicing process can be carried out without impairing the mechanical stability of the wafer.

A common failure mode for this method is membrane rupture while snapping. A dicing station was designed and fabricated in the Sensors Research Laboratory to assist the process. The wafers were first separated into strips and then individual device cells. Figure 3.5 illustrates the actual dicing station with a strip of devices while a cross-sectional schematic diagram indicates the direction of the applied snapping force and the construction of the station.

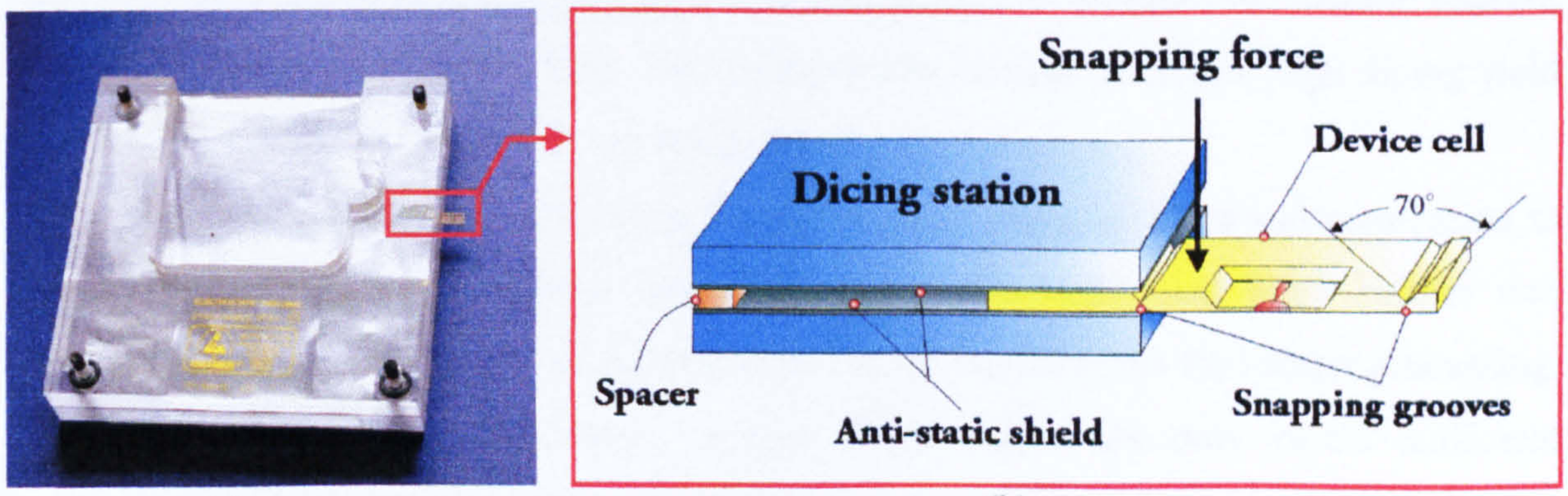

Figure 3.5: (a) The dicing station and a strip of wafer (marked in red) ready to be diced. (b) The cross-section schematic diagram of the dicing station that corresponds to the red rectangle area in (a), indicating the construction of the dicing station and the strip of wafer to be diced (not to scale).

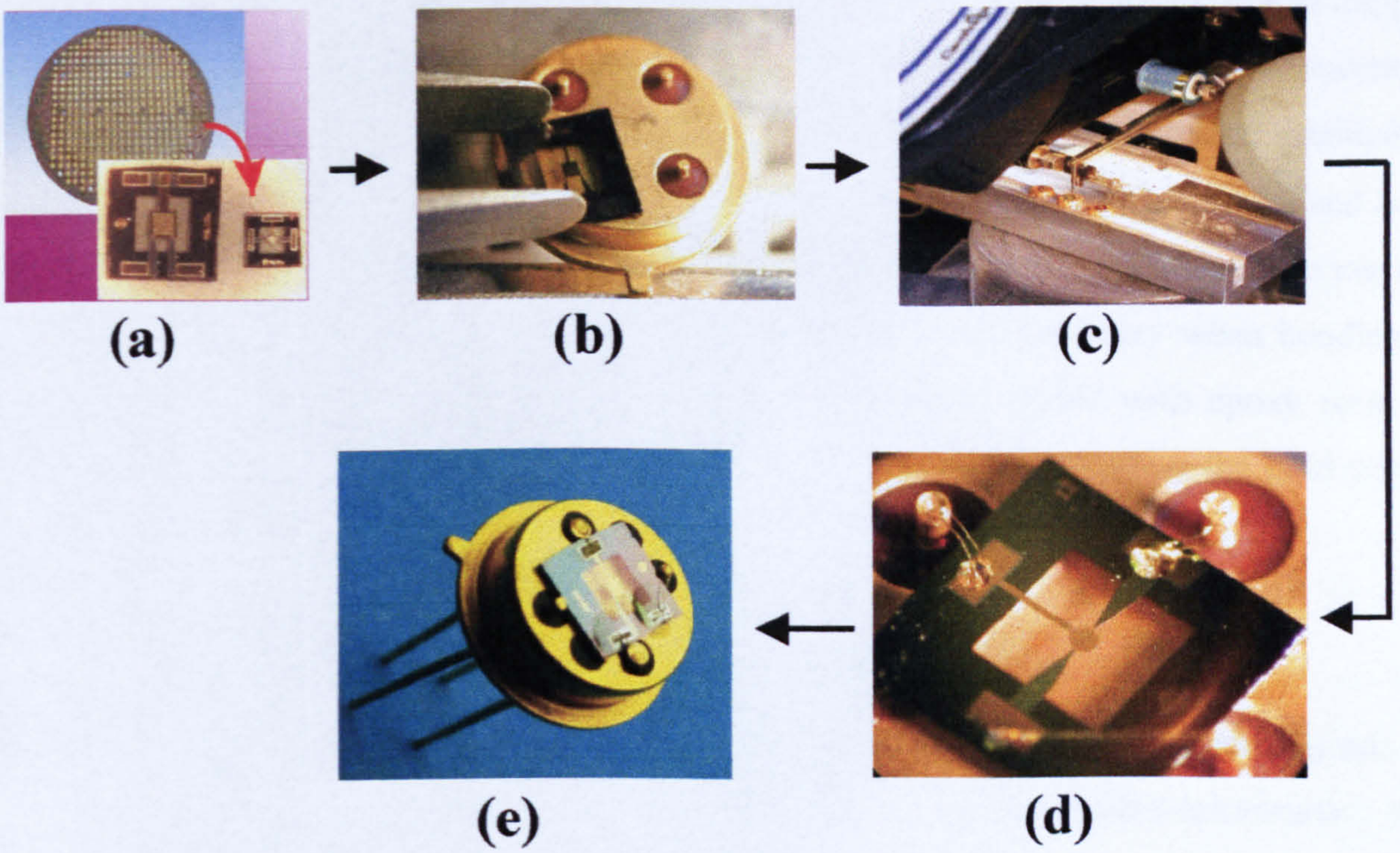

Figure 3.6: The post-fabrication process conducted in the Sensors Research Laboratory, University of Warwick. (a) Dicing process, (b) mounting devices onto TO5 header, (c) ultrasonic wire bonding, (d) wire bond passivation on SRL 177c, and (e) sample of a packaged micro-hotplate, SRL 162g.

A disadvantage of this dicing method is that a 100 % process yield is not achievable, as some devices would be inevitably damaged during the process. The failure rate depends largely on the experience and skills of the operator. As an additional precaution, an anti-static shield was laminated on the acrylic dicing station to prevent electrostatic charges from accumulating on the surface. This is especially critical to sustain high dicing yield when a large quantity of devices are being diced.

The individual dies are fragile and difficult to make an electrical connection to before packaging. A chemically inert gold-plated standard 4-pin TO-5 header was selected as the package on which to mount the micro-calorimeters for further processing. The industrial standard Transistor Outline (TO) header not only offers sufficient terminals, remarkable electrical conductivity and connectivity, but it is also compatible with other commercial calorimeter packages allowing better adaptability for existing test equipment.

Figure 3.6 illustrates the stages involved in the post-fabrication process for the micro-calorimeter substrate pictorially. The dies were mounted on the TO5 header with Loctite epoxy resin that hardens at room temperature in about 10 minutes. It is critical to

include a clearance between the silicon die and the header to allow the air that is trapped underneath the membrane to be expelled at high temperatures. Electrical connections between the contact pads on the device and the terminals of the header were established by ultra-thin gold wire (25 μm) that was ultrasonically bonded using a Kulicke and Sofa inc., 4126 ultra-sonic bonder. Double bonding was performed in order to reduce current flow per bond and enhance reliability. However, this is not necessary when bonding is performed to a commercial standard. All the joints were coated with epoxy resin to provide extra mechanical strength and stop catalyst being deposited on the gold wires/ pads.

3.3 Manufacturability of micro-calorimeter substrates

Apart from the possible ultra-low power budget, batch fabrication is regarded as one of the major driving forces behind the need for a silicon micro-calorimeter, the manufacturability is, therefore, a critical factor to be evaluated. It had been assessed in three aspects, namely fabrication yield, process-related defects and surface topology.

3.3.1 Fabrication yield

The yield is the percentage of intact devices over the total devices at the beginning of the process. An intact device is referred to as one without irreparable damage observed visually, including membrane rupture and incomplete layer structures. Due to the relatively low functional failure rate from similar device structures fabricated previously [3.7], only the physical integrity of the device has been considered in the yield statistics. The yield statistics were computed for both fabrication runs and the failure mode has been assessed.

The overall yield is defined in equation (3.2) where the front-end yield is the yield after the fabrication run in the foundry; dicing yield is the percentage after dicing process and assembly yield is the survival rate after the devices were packaged.

$$\textit{Overall yield (\%)} = \textit{front-end yield (\%)} \times \textit{dicing yield (\%)} \times \textit{assembly yield (\%)} \quad (3.2)$$

The first wafer fabrication run aimed to establish an effective fabrication process and to supply actual devices for characterisation and simulation purposes. When the wafers were dispatched from the foundry, a relatively large number of devices were sacrificed

for various experiments. Alternative dicing tools and mounting methods were explored to determine appropriate techniques in order to achieve maximum process yield. Hence, obtaining an overall yield was trivial and only the front-end yield was considered.

Of the twelve wafers processed, ten wafers survived the fabrication run, including one of the wafers with an additional passivation layer. All the wafers delivered from the foundry by post were intact and achieved 96% front-end yield on average. However, it was found that the mechanical strength of the wafer was not evenly distributed as the alignment cells and other reference marks became very fragile after back etching. The top left quarter of a wafer was furthest from such features and an experiment was conducted on four wafers, attempting to preserve the quadrant during the dicing process. All the reserved quadrants managed to remain intact when other parts of the wafer had been diced. Therefore, the first quadrant of the wafer could provide maximum mechanical stability.

For the second wafer run, detailed yield statistics were acquired as the post-fabrication process had already been established previously. Ten wafers were sent for fabrication, of which eight wafers had completed the fabrication run, including one wafer with the additional passivation layer. Apart from the special reserved common-gate quadrant, dicing of individual devices from all the eight wafers was completed.

Although the overall yield is defined in equation (3.2), a nearly perfect assembly yield was proven empirically. Therefore, it was excluded from the computation of the yield statistics in order to enhance the efficiency and cost effectiveness of the accounting procedures. In addition, the overall yield was determined at various scales, as tabulated in Table 3.3.

According to Table 3.3 [3.8], the four families with (4 × 4) mm^2 cell sizes achieved an overall fabrication yield of over 82% which implied at least 90% yield or higher at each post-fabrication stage. Due to the relatively small sample size for the ultra-small families, the yield statistics fluctuated with a greater range but the average yield is still over 62%.

The majority of the ultra-small devices failure is in the dicing process related to the uneven shearing force developed by the surrounding standard-size devices. Therefore, the failure mode could be minimised by grouping similar size devices in the same area on a wafer and by increasing the width of the frame.

Table 3.3: Overall yield statistics for individual gate devices in 2nd fabrication run at various levels.

		Percentages of the yield from different wafers, (%)									
	SRL model	*wafer 9*	*wafer 5*	*wafer 1*	*wafer 8*	*wafer 4*	*wafer 3*	*wafer 7*	*wafer 10*	mean	
Test structures	136em	66.67	83.33	66.67	50	100	66.67	83.33	100	77.08	mean: 83.63%
	136sg	66.67	100	83.33	100	66.67	100	100	66.67	85.42	
	136sgx	100	100	100	100	100	100	100	100	100.00	
	136o	66.67	100	66.67	100	50	66.67	83.33	50	72.92	
	136x	100	50	100	100	50	83.33	66.67	100	81.25	
	162o	50	100	100	50	100	100	100	100	87.50	
	162x	83.33	66.67	66.67	83.33	66.67	83.33	100	100	81.25	
Standard family	176a	75	66.67	58.33	91.67	75	83.33	83.33	83.33	77.08	mean: 82.19%
	176ax	75	100	75	75	100	75	100	100	87.50	
	176b	85.71	78.57	42.86	100	78.57	64.29	100	100	81.25	
	176bx	100	75	100	75	75	100	75	100	87.50	
	176c	85.71	78.57	92.86	92.86	92.86	57.14	100	78.57	84.82	
	176cx	66.67	100	33.33	66.67	66.67	66.67	100	100	75.00	
Low power family	177a	78.57	85.71	78.57	71.43	92.86	71.43	85.71	85.71	81.25	mean: 82.14%
	177ax	50	75	100	100	100	100	75	100	87.50	
	177b	78.57	85.71	100	100	107.14	85.71	85.71	100	92.86	
	177bx	50	100	75	50	100	75	75	75	75.00	
	177c	90.91	81.82	63.64	72.73	54.55	63.64	90.91	81.82	75.00	
	177cx	100	75	50	100	75	50	100	100	81.25	
Small-mem /robust family	178a	66.67	83.33	75	83.33	83.33	100	100	75	83.33	mean: 85.67%
	178ax	75	100	100	100	100	100	75	75	90.63	
	178b	88.89	66.67	100	88.89	77.78	100	88.89	77.78	86.11	
	178bx	100	100	75	100	100	75	50	75	84.38	
	178c	73.33	93.33	73.33	86.67	93.33	93.33	100	93.33	88.33	
	178cx	50	75	100	75	100	100	75	75	81.25	
Robust family	179a	60	90	80	90	90	70	90	100	83.75	mean:89.25%
	179ax	66.67	100	66.67	100	100	100	100	66.67	87.50	
	179b	90.91	90.91	81.82	90.91	90.91	81.82	100	90.91	89.77	
	179bx	75	100	100	100	100	100	75	100	93.75	
	179c	75	100	68.75	81.25	100	87.5	93.75	87.5	86.72	
	179cx	100	100	100	100	66.67	66.67	66.67	100	87.50	
	179d	100	100	100	75	100	100	100	100	96.88	
	179dx	100	83.33	83.33	66.67	100	66.67	100	100	87.50	
	179e	83.33	100	100	83.33	100	100	100	100	95.83	
	179ex	83.33	83.33	83.33	100	100	66.67	66.67	83.33	83.33	
Ultra-small / robust family	180a	100	25	100	75	100	100	50	100	81.25	mean: 63.54%
	180ax	25	75	100	75	100	0	75	50	62.50	
	180b	83.33	50	83.33	66.67	66.67	83.33	66.67	33.33	66.67	
	180bx	100	25	25	50	25	25	75	75	50.00	
	180c	50	100	50	50	33.33	50	50	33.33	52.08	
	180cx	75	75	50	75	25	100	50	100	68.75	
Ultra-small / low power family	181a	33.33	83.33	50	83.33	50	33.33	66.67	16.67	52.08	mean: 62.07%
	181ax	75	50	75	75	100	75	50	100	75.00	
	181b	37.5	62.5	87.5	87.5	87.5	75	75	75	73.44	
	181bx	75	25	50	25	25	50	75	100	53.13	
	181c	37.5	87.5	37.5	50	75	75	12.5	75	56.25	
	181cx	100	0	50	100	50	25	100	75	62.50	
Overall yield		75.56	80.63	75.56	82.86	82.22	76.83	84.13	84.13	80.24	

Although the robust families achieved the highest mechanical stability, there was only between 4 % and 7 % improvement from the low power families on average. This implies that the devices with larger membranes had not significantly influenced the yield.

Hence, it is a feasible strategy to reduce the power budget with larger MHR while maintaining reasonable fabrication yield.

In addition, there were a considerable number of device types that managed to achieve 100% yield and only two instances where a total loss had occurred. Compared to some of the fabrication yields in similar processes which could fall below 40% [3.9], a reasonable fabrication yield had been achieved, especially when one considers this is a research programme.

3.3.2 Analysis of process-related defects

Inspections performed on the wafers received from both fabrication runs showed several types of process-related defects. Some of these were inevitable from the batch fabrication while others might be the result of mishandling. Depending on the type of defects, they will directly or indirectly be related to the overall process yield. Therefore, it is essential to understand their origins and affects. It is interesting to note that the type of defects between the two silicon runs were unique to the specific wafer run and the defects were not repeated.

In the first wafer fabrication run, adhesion failures were found on a number of devices. Through a general inspection across the wafer, the gold layer at the contact pads had adhered poorly and appeared to be black in colour (see figure 3.7(a)). It is important to scratch off this loosely attached layer otherwise it will cause insecure connection during wire bonding (see figure 3.7(b)). As the tantalum adhesion layer is designed for the gold gate electrode to adhere onto the silicon nitride directly above the micro-heater, the bonding of the gold layer onto the platinum layer might be as efficient.

A small number of samples were selected randomly and inspected under a Prior optical microscope. It was found that there was some non-uniformity and poor adhesion within the active area, as shown in figure 3.7(c) and (d). This fault might be caused by the inadequate material step coverage, by either the silicon nitride or the gold, in the deposition processes. The quality of the deposited film is controlled by various factors including pressure, temperature and impurities. The devices with smaller gate area appeared to be less susceptible to this problem as shown in the figure 3.7(d).

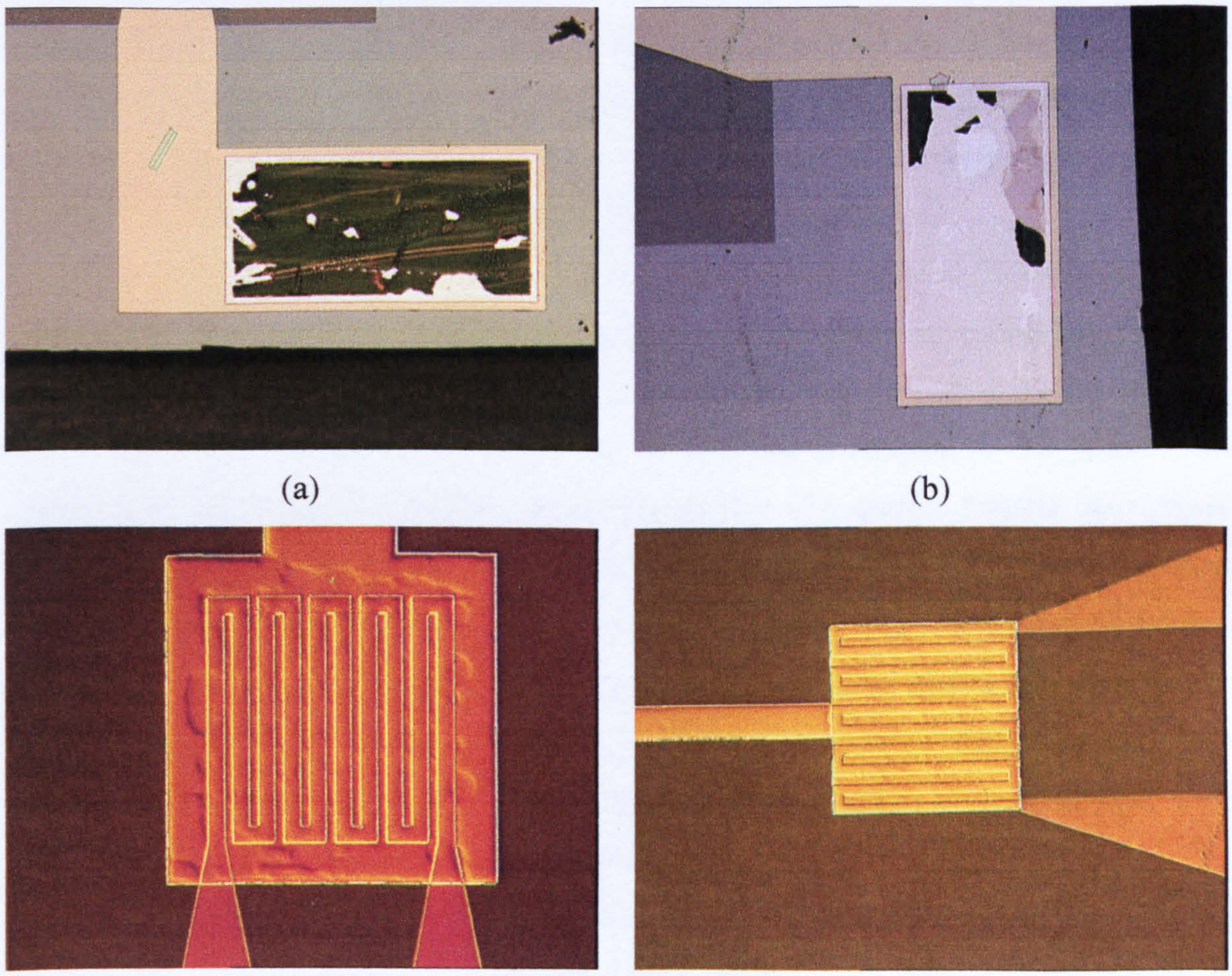

Figure 3.7: Adhesion defects identified from the first wafer run. (a) Adhesion problem of the gold layer on platinum at the contact pad. (b) The gold layer had been stripped off before wire bonding. (c) Non-uniform active area (SRL 136a). (d) The active area of SRL 162g.

For certain samples, the resistance of the platinum micro-heater had been reported by Southampton to be unstable. It could change from 230 Ω to as low as 23 Ω after the mesoporous catalyst deposition process. In an investigation elaborated on in chapter 5, this is unlikely to be the result of the failure of the silicon nitride as breakdown field strengths of 36 MV/m had been measured during device characterisation [3.10]. However, spikes along the fringes of the metal features had been noticed in surface topography studies (see section 3.3.3). The failure mechanism could be the result of spikes formed by the lift-off process. When the height of the protruding spike is over the encapsulating silicon nitride, an electrical short between the platinum and gold layer will be created. This defect is entirely process-related and two wafers, wafer 3 and 4, from this fabrication run were discovered with such defects.

For the second wafer fabrication run, more defects were identified as there were more features involved. Moreover, the foundry (IMT) reported that different equipment had been utilised due to an equipment up-grade. This resulted in minor modifications to the wafer layout where a group of devices were sacrificed but all the design types were retained. The details of the affected devices is shown in Appendix 3c.

Residues of gold were found to remain on the device after the lift-off process, see figure 3.8(a). In some situations, this created a short between terminals, parasitic capacitance which increases the response time constant, non-uniform thermal expansion on the membrane, or simply a veiling of the device locator number. In this process, the wafers were placed into a container filled with acetone after pattern transfer onto photo-resist and layering process. Unwanted areas were virtually "shaken off" by the vibration generated by an ultra-sonic vibrator underneath the container. Apart from various process parameters including vibration time, strength, layer thickness and temperature which might cause the defect, contamination by the lifted gold fragments might also contribute to the defects. However, statistics showed that the percentage of such defects were limited to only 2 % of the total device population.

A number of devices were found to have an incomplete or missing heating element printed onto the cell, see figure 3.8(b) and (c). This type of defect results in functional failure due to the open-circuit micro-heater. Various mechanisms could lead to such a defect. For instant, contamination or scratches from wafer handling could cause poor adhesion of the photoresist and resulting improper layer deposition. However, this defect is not commonly found and it is within a tolerable level.

Over-etching could be identified in many locations, such as the snapping grooves, the fringes of the membrane and the device frame as shown in figure 3.9. It enlarged the designated etching area and impaired the device framework. This created a local weak-point that might shatter itself and the surrounding structures due to uneven shearing forces along the snapping grooves in the dicing process. Nearly all the devices that inherited this defect could not sustain the mechanical stress induced by the snapping force. The dicing failure rate was elevated when the defective section was surrounded by the ultra-small devices. As one of the characteristics of anisotropic wet etching on a <100> wafer, any pattern after over etching will become a square shape and the enlarged pattern leads to breakage. Over etching could be the consequence of inaccurate pattern transfer, contamination or scratched photo-resist during photolithography. However,

KOH back etching is generally regarded as the most complicated process in the micro-hotplate fabrication and the defect rate was maintained at an acceptable level of about 2% of the eight wafers received. Although over-etching also occurred on the alignment cells, their integrity after dicing proved that sufficient mechanical strength was maintained for the process, as shown in figure 3.10(a).

Roughly, 7 % of the devices contained membrane rupture from the eight wafers received. The ultra-thin membrane is obviously the weakest part of the device and so breakage is unavoidable during handling. All the damaged devices were marked with a red ink dot to calculate the pre-dicing yield as shown in figure 3.10(b).

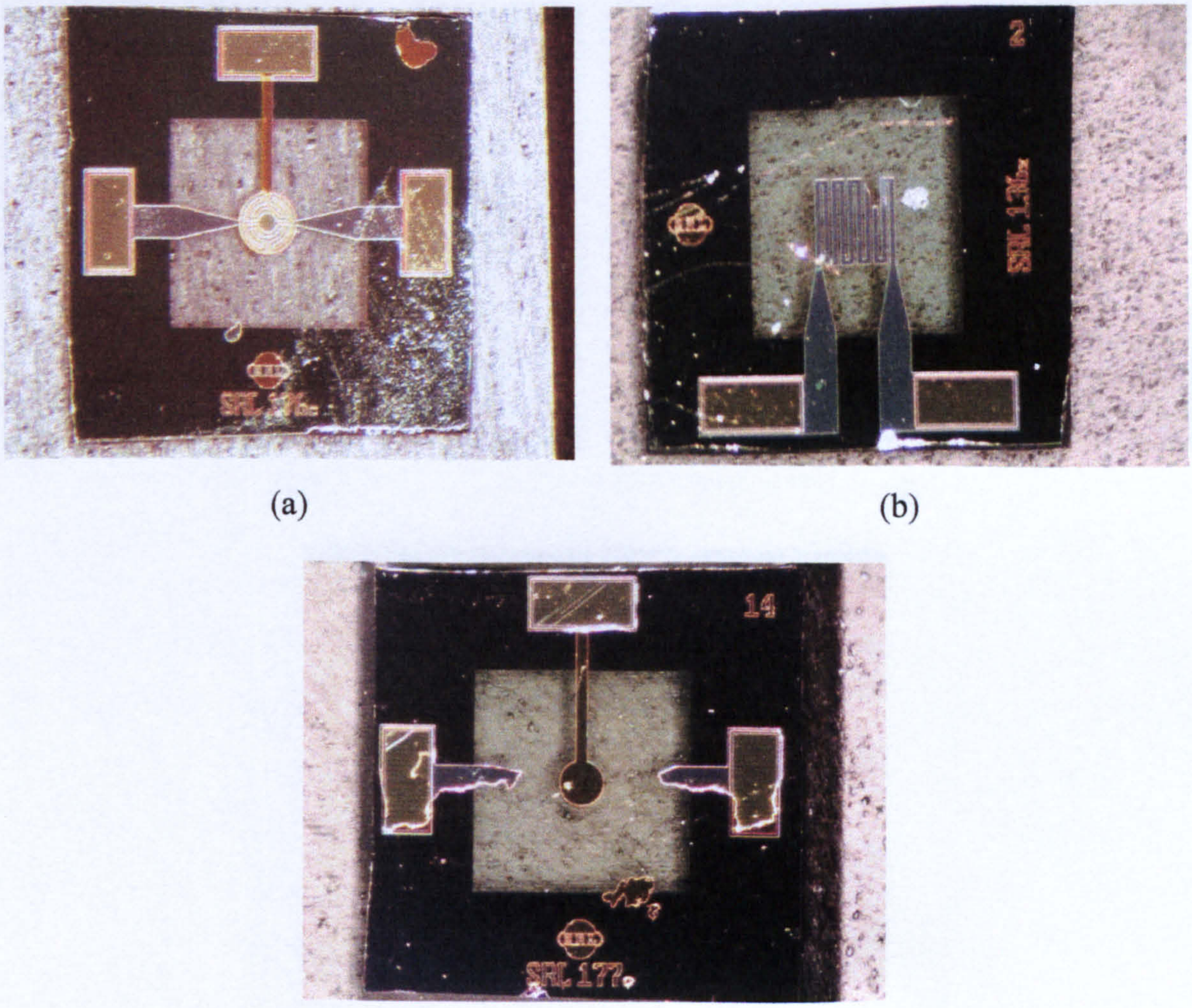

(a) (b)

(c)

Figure 3.8: Layer defects identified in 2nd fabrication run. (a) Residues of lift-off process veiled the device locator. (b) Incomplete micro-heater track. (c) Incomplete layering (Au and Pt).

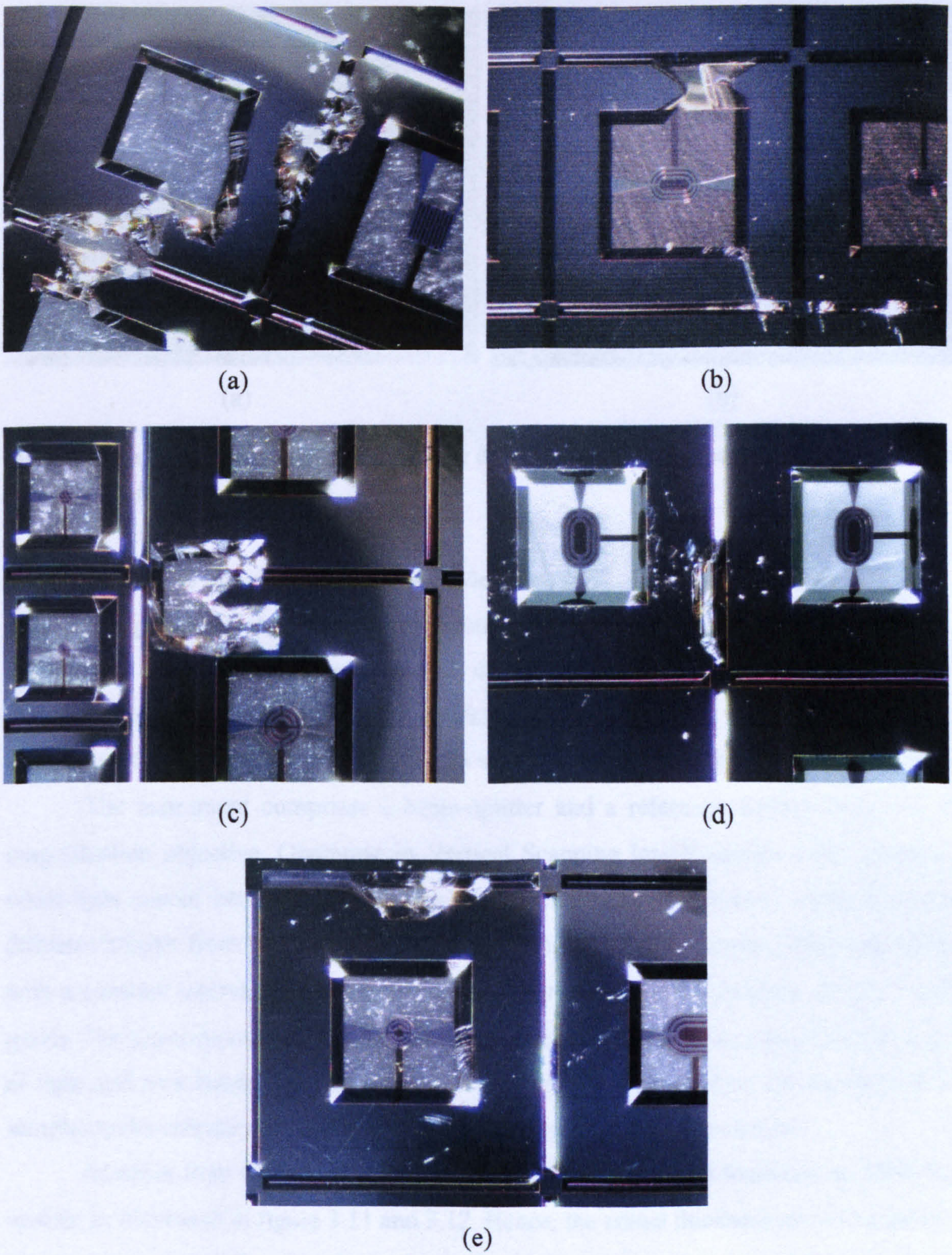

(a) (b)

(c) (d)

(e)

Figure 3.9: Over-etchings identified in the 2nd fabrication run. (a) Over-etching spreads across device. (b) Over etching resulted in broken frame. (c) Over-etched groove spread onto the frame. (d) Over-etching at the snapping groove. (e) Over-etching on snapping groove and membrane area.

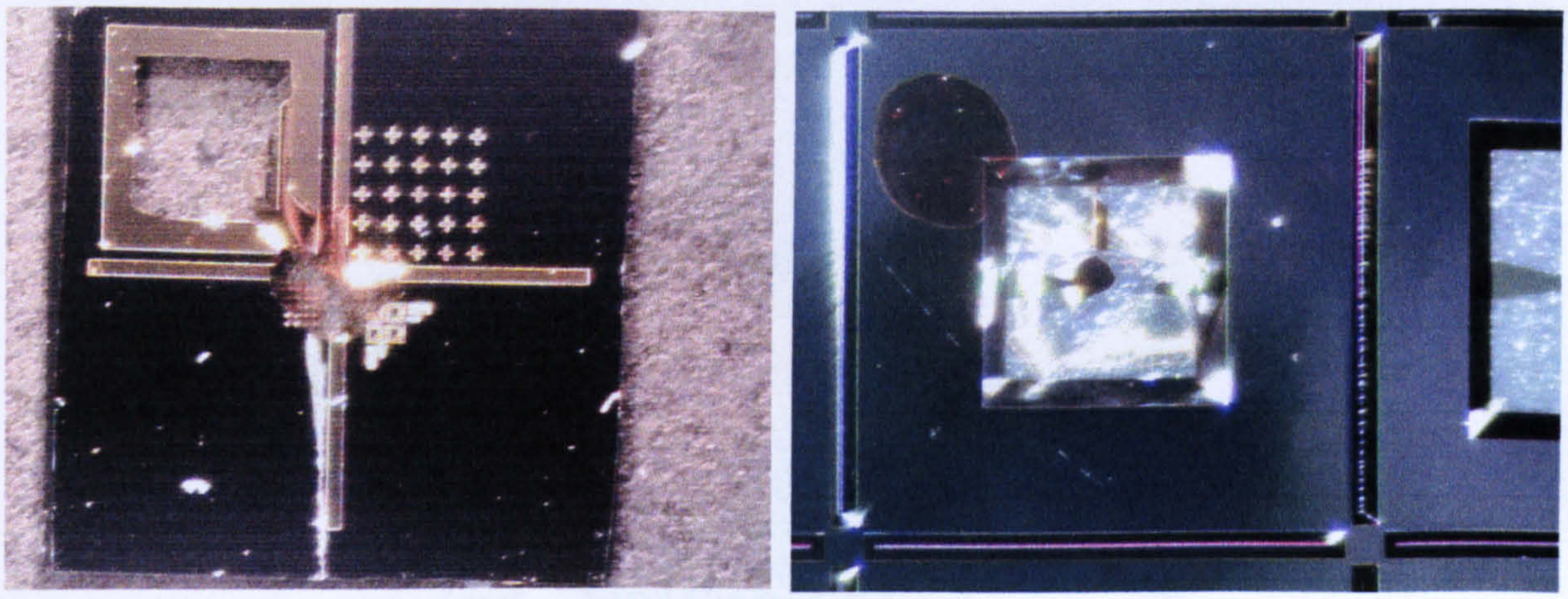

(a) (b)

Figure 3.10: (a) Alignment cell remained intact after dicing process. (b) Damaged device marked with a red ink dot, (top-left).

3.3.3 Topology of the micro-machined devices

The topology of the micro-machined devices provides essential information on the fabrication quality and parameters for thermomechanical simulations. A WYKO interferometer which provides non-contact measurement has been employed to investigate the surface profile of the devices with a vertical resolution of 0.1 nm [3.11].

The instrument comprises a beam-splitter and a reference surface built into a magnification objective. Operating in Vertical Scanning Interferometry (VSI) mode, a white-light source beam is divided into a number of scanning beams which focus at different heights from the reference plane. Scanning across the sample surface vertically with a constant interval, each image frame is recorded by a detector array of 368 × 240 pixels. The superimposed image frames will then create interference regions in a pattern of light and dark bands, known as the interference fringes. Therefore, the topology of a sample can be calculated according to the fringe contrast across the surface.

Samples from both fabrication runs were taken at identical locations on different wafers, as illustrated in figure 3.11 and 3.12. Hence, the actual thickness of various layers can be assessed in order to evaluate the inter-wafer process variations and the deviations between each batch of devices.

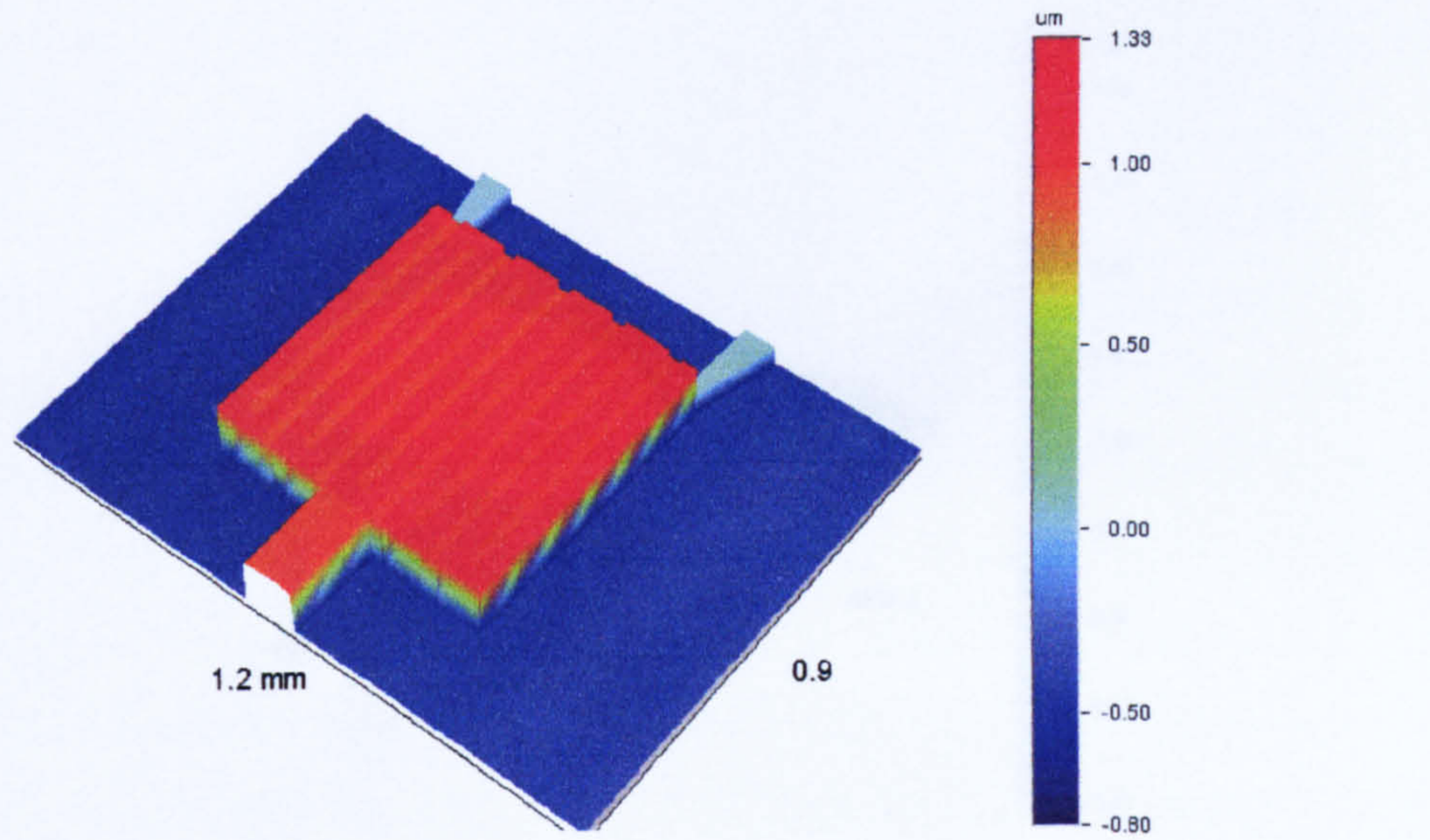

(a)

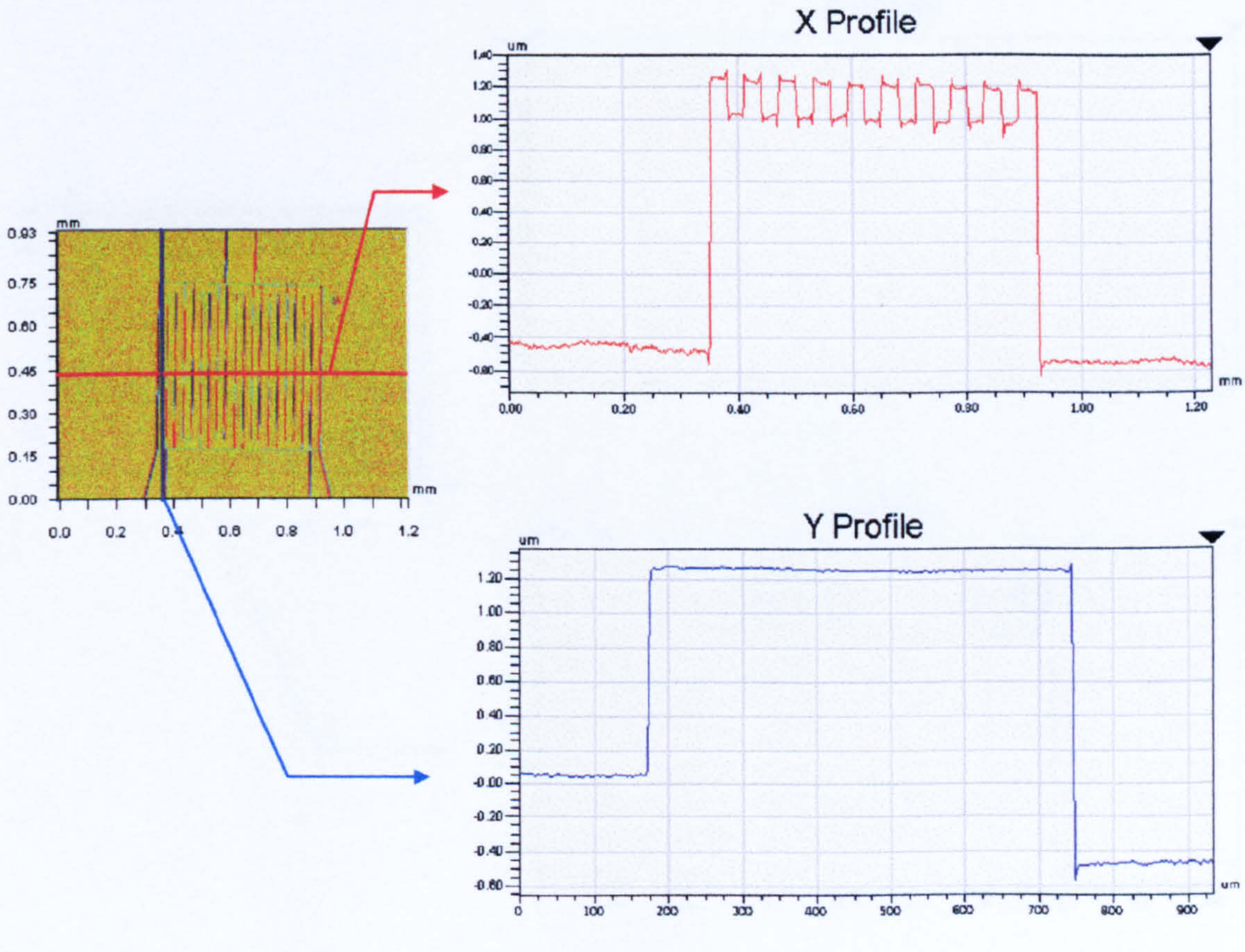

(b)

Figure 3.11: Surface topology of SRL 162g (without membrane) on wafer 3 from the first fabrication run. (a) 3-D image captured by the WYKO interferometer in VSI mode. (b) 2-D profile along specific location illustrating the various heights of the gold and platinum layer from the silicon substrate. The smallest diagram indicates the red and blue cut-line that correspond to the X Profile and Y Profile, respectively.

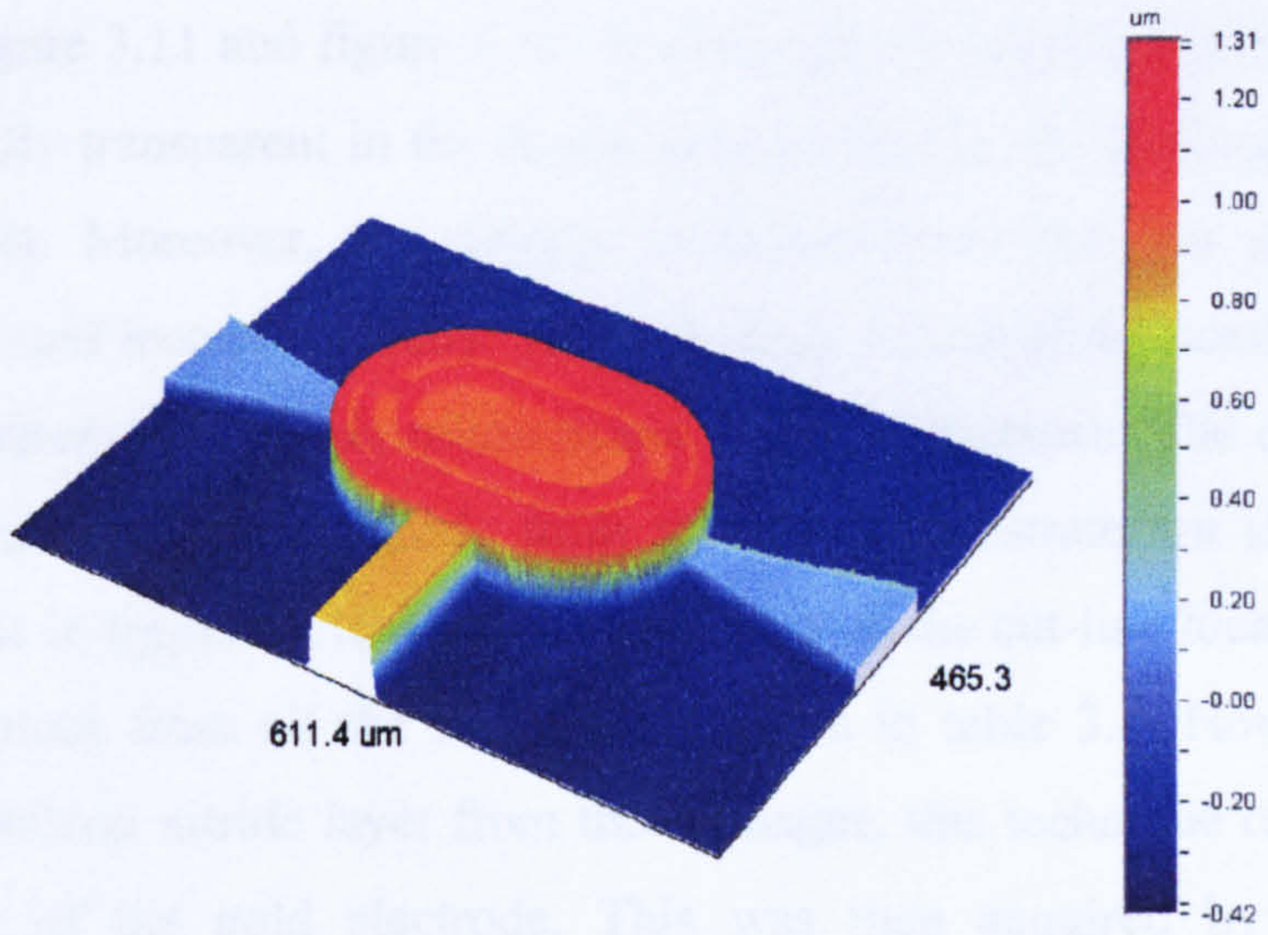

(a)

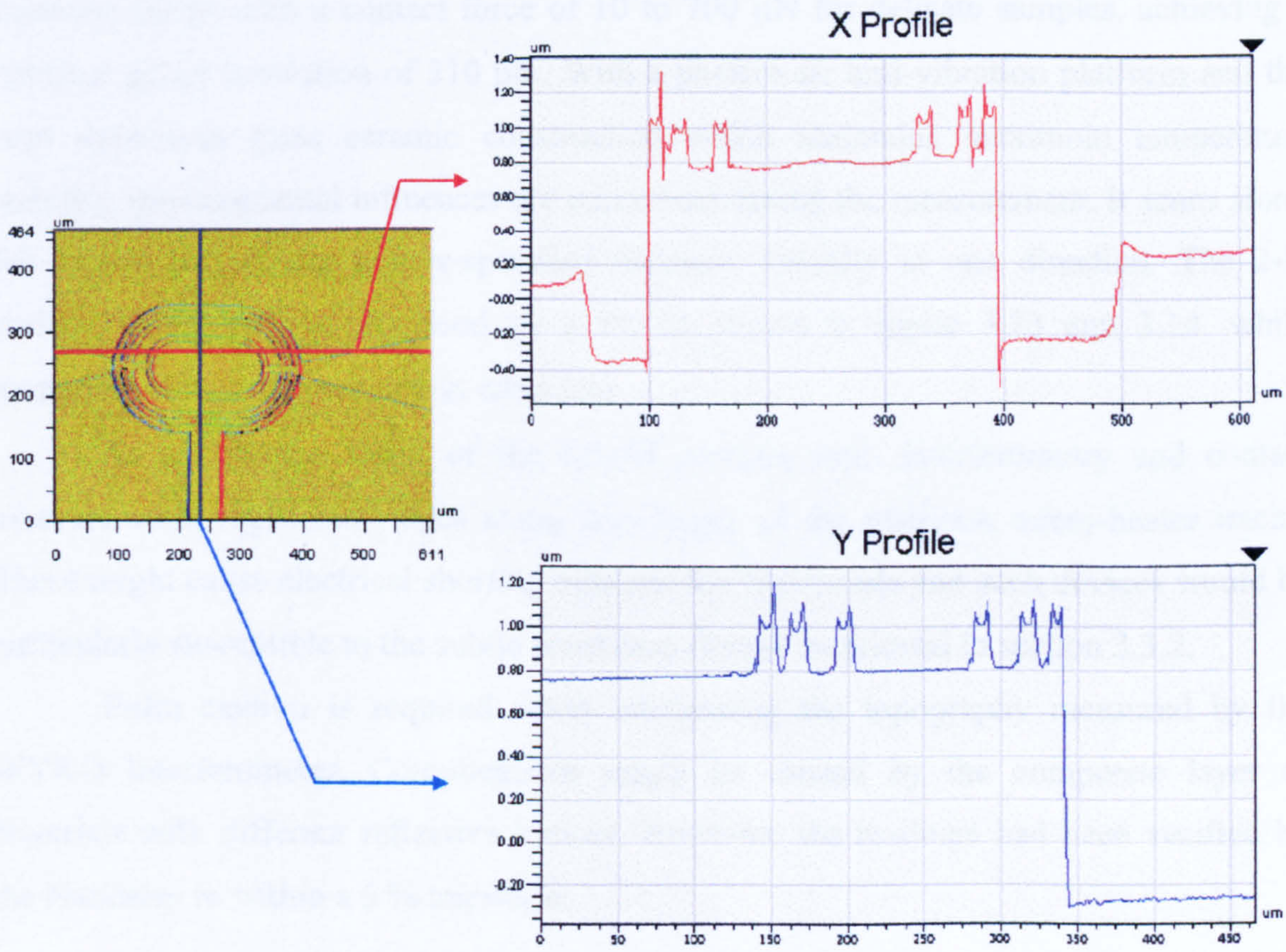

(b)

Figure 3.12: Surface topology of SRL 180as (without membrane) on wafer 9 from the second fabrication run. (a) 3-D image captured by the WYKO interferometer in VSI mode. (b) 2-D profile along specific location illustrating the various heights of the gold and platinum layer from the silicon substrate. The smallest diagram indicates the red and blue cut-line that correspond to the X Profile and Y Profile, respectively.

Examples of 2-D and 3-D profiles from the first and second wafer fabrication run are shown in figure 3.11 and figure 3.12, respectively. As the silicon nitride layer on the device is optically transparent in the interferometry profile, the platinum layer is visible for measurement. Moreover, the devices evaluated were the test structures without membranes to avoid incorrect results. The 3-D images showed the uneven gold layer that reflected the pattern of platinum micro-heater tracks underneath. The distances between the platinum and the gold electrode from the silicon substrate are shown in the 2-D topology profiles in figure 3.11(b) and figure 3.12(b) at the cut-line location. The average material thicknesses from all the samples are given in table 3.4. However, due to the absence of the silicon nitride layer from these images, this technique cannot provide the exact thickness of the gold electrode. This was then acquired by using a contact measurement, the Nanostep (Taylor Hobson Ltd). The instrument is equipped with a diamond stylus with a contact force of 10 to 700 μN for delicate samples, achieving a nominal gauge resolution of 310 pm. With a passive air anti-vibration platform and the zero expansion glass ceramic construction which maintains maximum temperature stability, environmental influences are minimised during the measurement. It scans along the device surface for a user-specified distance, laterally in one direction. The 2-D surface topography is processed by a PC as shown in figure 3.13 and 3.14, while numerical values are included in table 3.4.

As a common result of the lift-off process, both interferometry and contact measurements registered ridges along the fringes of the platinum micro-heater tracks. These might cause electrical shorting between the two metals and such devices would be particularly susceptible to the subtle resistance change mentioned in section 3.3.2.

Extra caution is required when interpreting the topography measured by the WYKO interferometer. Complications might be caused by the composite layer of materials with different reflective indices. However, the readings had been verified by the Nanostep to within a 5 % tolerance.

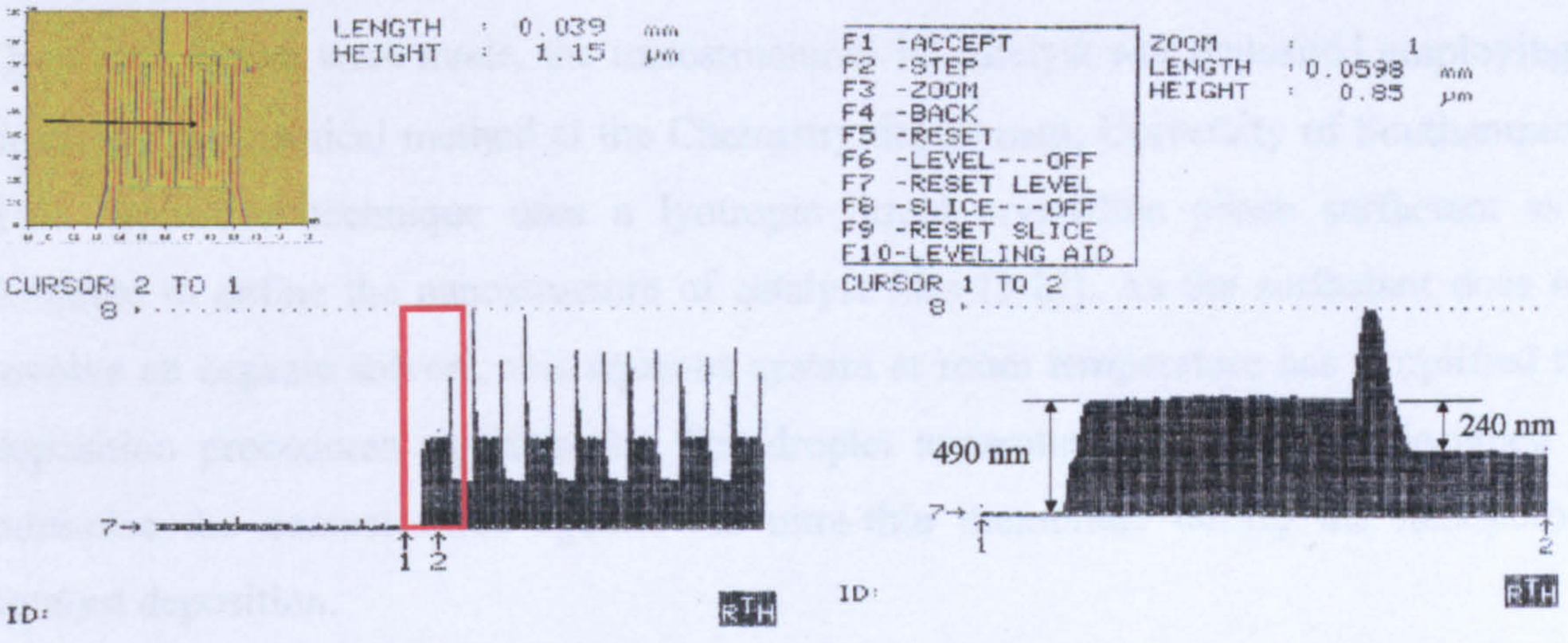

(a) (b)

Figure 3.13: 2-D surface topology using Nanostep for SRL 162g on wafer 3 from first silicon fabrication run. (a) Surface profile across half of the active area. (b) Magnified view of the red-boxed region in (a), indicating the actual height of the gold electrode and the spike as a common artefact of lift-off process.

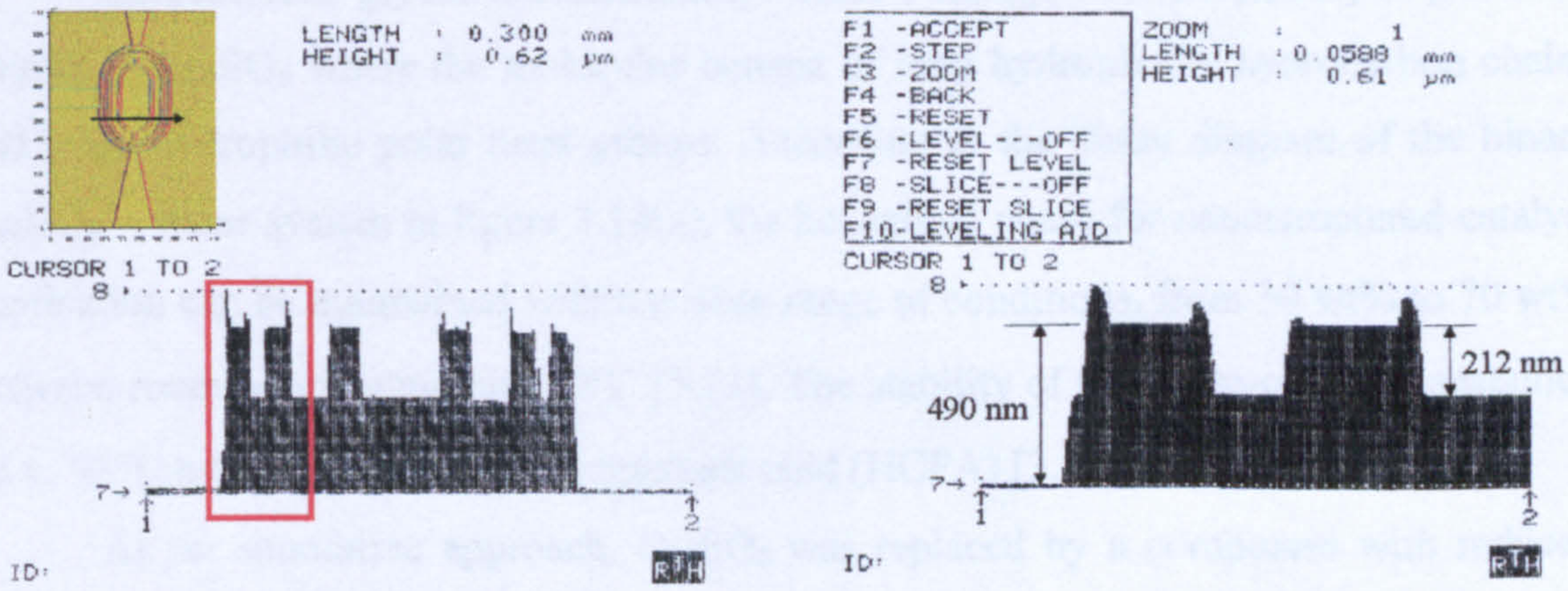

(a) (b)

Figure 3.13: 2-D surface topology using Nanostep for SRL 180as on wafer 9 from second silicon fabrication run. (a) Surface profile across the active area. (b) Magnified view of the red-boxed region in (a), indicating the actual height of the gold electrode and the spike as a common artefact of lift-off process.

Table 3.4: Summary of the average material thickness for the two fabrication runs

Material	**Nominal designed value**	**Wafer fabrication run**		**Measuring method**	
		Run 1	Run 2	WYKO	Nanostep
Au* (nm)	165	250	280		✓
Pt* (nm)	240	231	219	✓	✓
SiN_x + SiO_2 (nm) (membrane)	800	993	857	✓	✓

* Material included adhesion layer

3.4 Nanoporous catalyst deposition

Once the devices were made, the nanostructured Pd catalyst was deposited employing a novel electrochemical method at the Chemistry department, University of Southampton. This deposition technique uses a lyotropic liquid crystalline phase surfactant as a template to define the nanostructure of catalyst film [3.12]. As the surfactant does not involve an organic solvent, this aqueous system at room temperature has simplified the deposition procedures significantly. The droplet apparatus is specifically designed to minimise the contact force against the ultra-thin membrane during the nanoporous catalyst deposition.

3.4.1 Plating mixture and surfactants

The dark brown viscous plating mixture comprises ammonium tetrachloropalladate ($(NH_4)_2PdCl_4$), the surfactant, de-ionised water and heptane. The two appropriate non-ionic commercial surfactants are $C_{16}EO_8$ and Brij® 56.

Octaethylene glycol monohexadecyl ether [$C_{16}H_{33}(OCH_2CH_2)_8OH$] is generally known as $C_{16}EO_8$ where the molecules consist of long hydrophobic hydrocarbon chains and large hydrophilic polar head groups. According to the phase diagram of the binary $C_{16}EO_8$ – water system in figure 3.14(a), the hexagonal phase for nanostructured catalyst application can be maintained within a wide range of conditions, from 30 wt% to 70 wt% between room temperature and 60°C [3.13]. The stability of the phase could be sustained up to 95°C by including hexachloroplatinic acid (HCPA) [3.14].

As an alternative approach, $C_{16}EO_8$ was replaced by a compound with reduced purity, Polyoxyethylene(10) cetyl ether [$C_{16}H_{33}(OCH_2CH_2)_{10}OH$], commercially known as Brij® 56. It contains a mixture of head groups and chain lengths centred on $C_{16}EO_{10}$ and a phase diagram is shown in figure 3.14(b).

Besides the reduction of purity, Brij® 56 has the advantages of low cost and availability over $C_{16}EO_8$ which is about £20 per gram as opposed to 7p per gram for Brij® 56, at 2002 prices. Regardless which of the two non-ionic surfactants had been utilised as the template, it appeared that the performance of the micro-calorimeter was not affected [3.15]. Therefore, the general plating mixture employed 60 wt% (hexagonal phase) Brij® 56 and 40 wt% of 1.06 M $(NH_4)_2PdCl_4$/ heptane (4/1) mol at 25 °C, although other compositions might be used for experimental purposes [3.14].

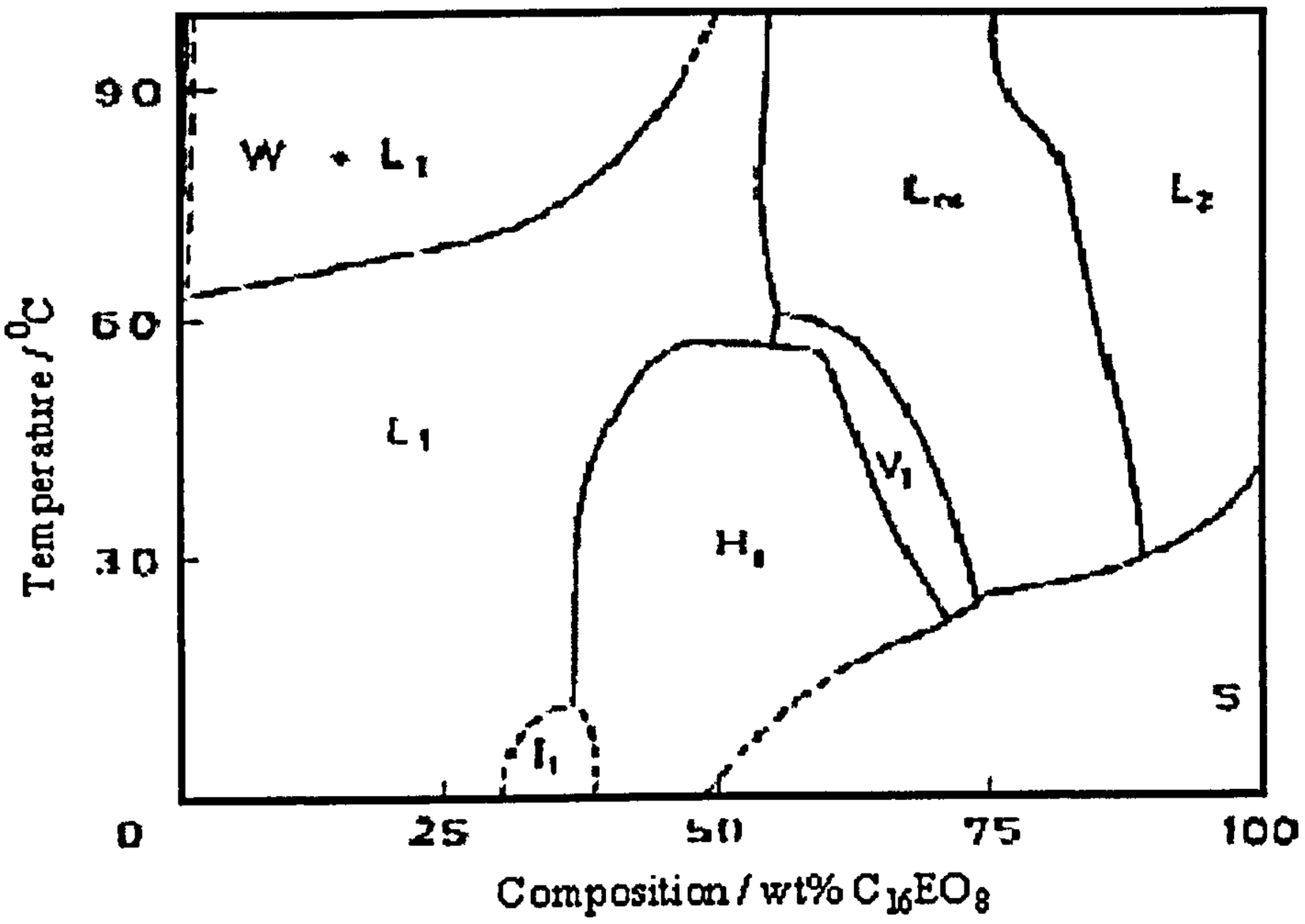

(a)

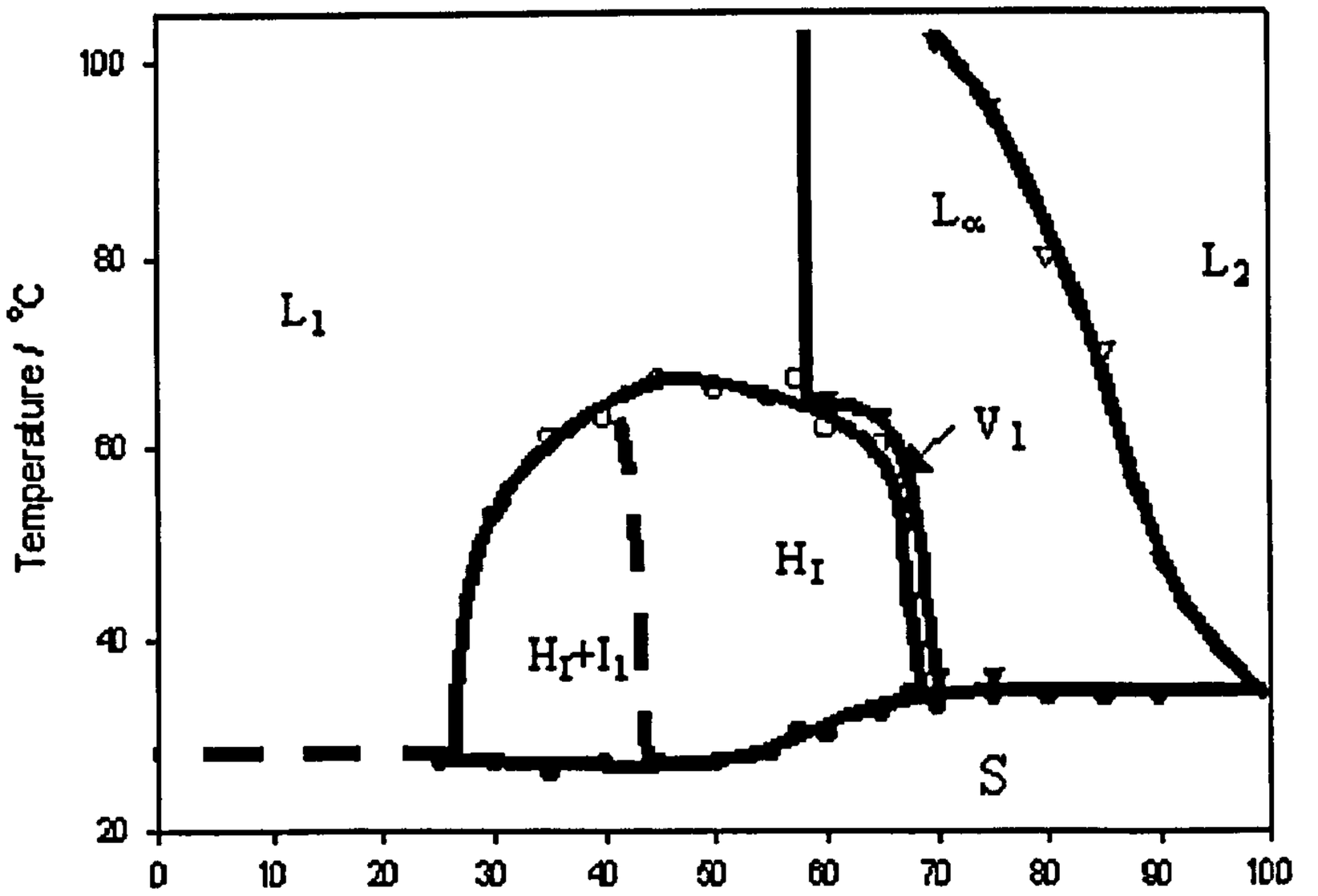

(b)

L_1: Micellar phase; L_2: Liquid surfactant phase containing dissolved water;

L_α: Lamellar phase; H_I: Hexagonal phase; V_1: bicontinuous cubic phase; I_1: close-packed spherical micellar cubic phase, S: Solid surfactant; W: water.

Figure 3.14: The phase diagram for the non-ionic surfactant [3.14]. (a) Phase diagram of binary surfactant-water system of $C_{16}EO_8$. (b) Phase diagram for Brij® 56.

3.4.2 Electrochemical deposition of Pd catalyst

The deposition was carried out with a droplet coating system, developed and patented by Gardner and Bartlett [3.16], that localises the Pd electrochemical deposition to a single drop of plating mixture on the designated location. Figure 3.15 illustrates the actual apparatus and schematic diagram of the coating system. The reference electrode, Saturated Calomel Electrode (SCE) is used as a benchmark for all other potentials during the deposition processes and it is stored delicately in saturated potassium chloride solution. The counter electrode is made of platinum gauze which was cleaned thoroughly before each deposition process. The working electrode is the gold electrode layer (i.e. gate electrode) at the centre of the micro-machined devices.

The reference electrode is clamped firmly on a stand while the working electrode is mounted on a microstage where the device can be moved in any X-Y-Z directions. As the plating mixture had been applied onto the counter and working electrodes, the device is slowly raised by the microstage, making electrical contact only via the Pd based plating mixture between the two electrodes. Therefore, the contact force is minimised, allowing deposition onto a membrane structure.

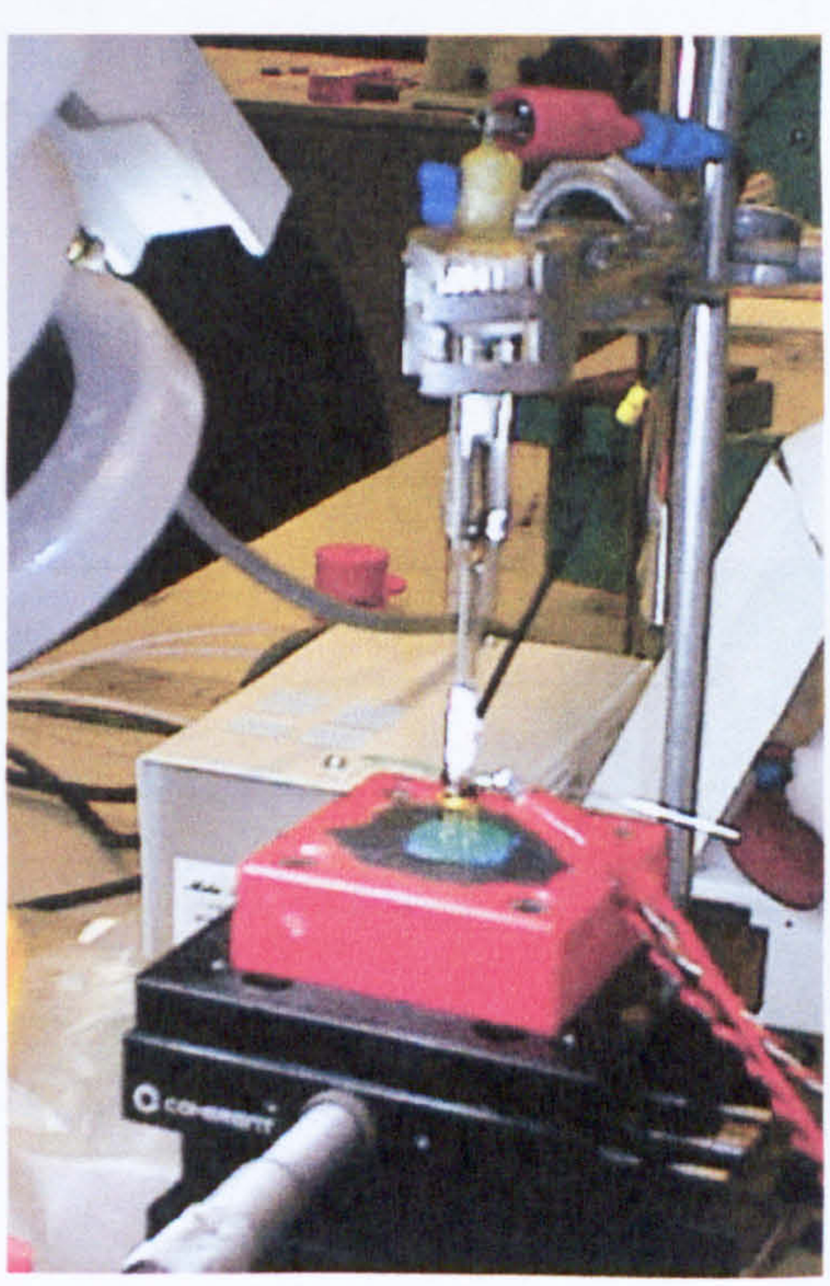

(a)

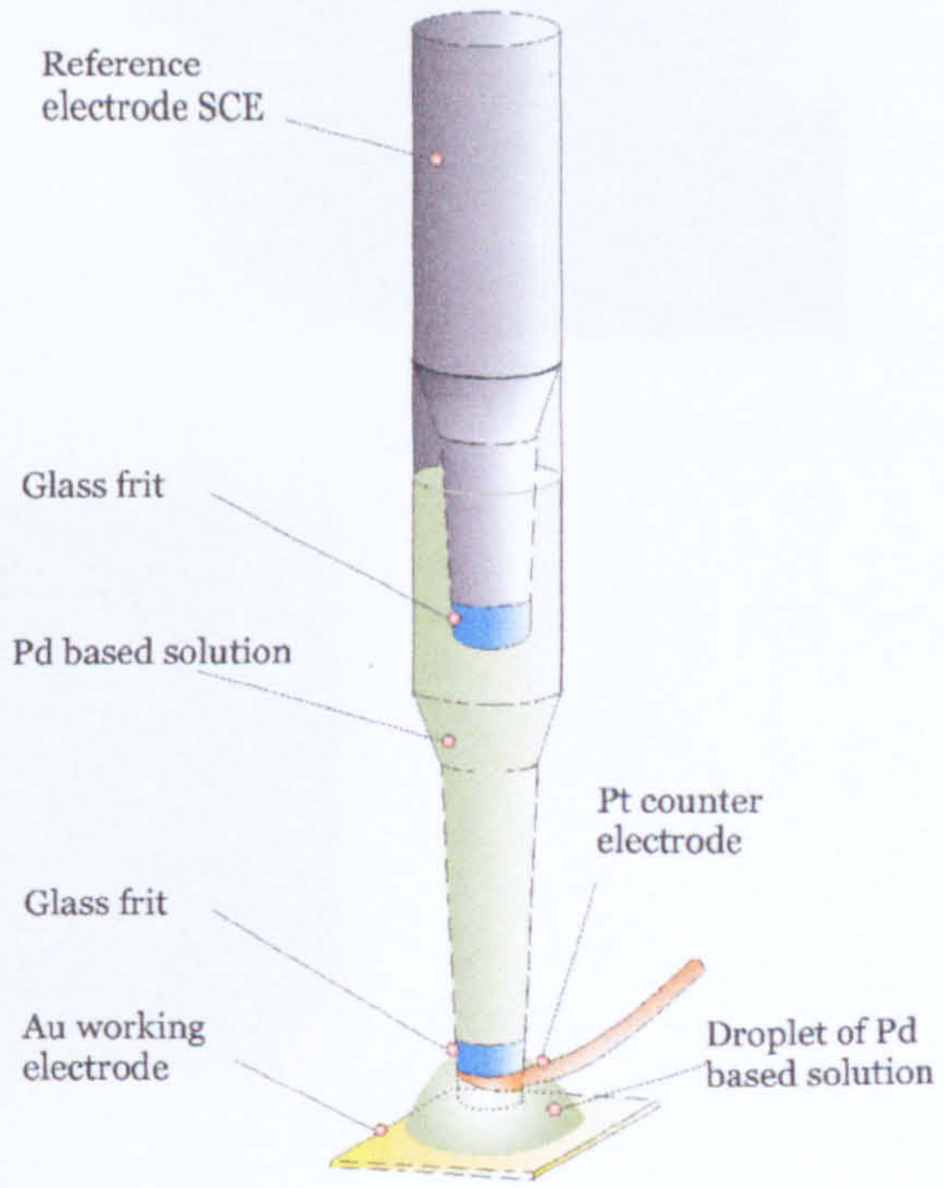

(b)

Figure 3.15: Droplet coating system for nanostructured catalyst deposition at City Technology Ltd. (a) The actual set-up on a microstage. (b) The schematic diagram of the droplet coating system.

Prior to the electrodeposition, the gold working electrode was cleaned electrochemically by cycling between the limits of –0.2 V and 1.8 V at 200mVs^{-1} in 1M sulphuric acid. Such pre-treatment is a critical step to ensure the performance and the adhesion of the catalyst. Other polishing and cleaning techniques are not applicable in this case due to the ultra-thin membrane.

The computer-controlled electroplating process was conducted by the potential step method. The potential of the Au working electrode was stepped from an upper limit of 0.4 V where no reaction occurred, to a lower limit of 0.12 V at which Pd is deposited as shown in figure 3.16(a). The charge density was maintained at 2.55 C cm^{-2} on the working electrode [3.17]. A silvery grey nanostructured film was deposited on the working electrode. Figure 3.16(b) illustrates a Transmission Electron Microscope (TEM) image of the nanoporous Pd film that indicates the hexagonal phase close packed pores [3.18], according to the chemical compositions and procedures mentioned earlier. A deposited micro-calorimeter (SRL 179c) is shown in figure 3.16(c).

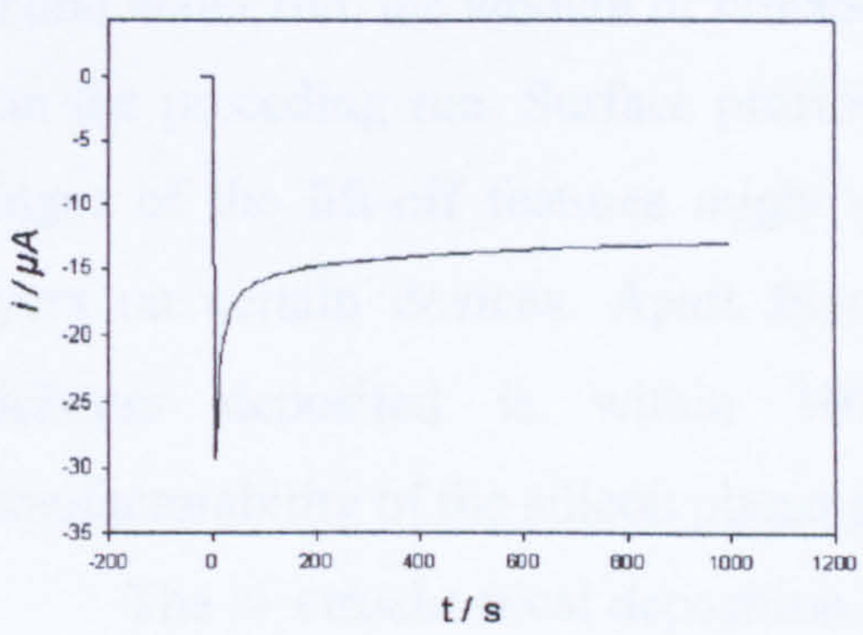

(a)

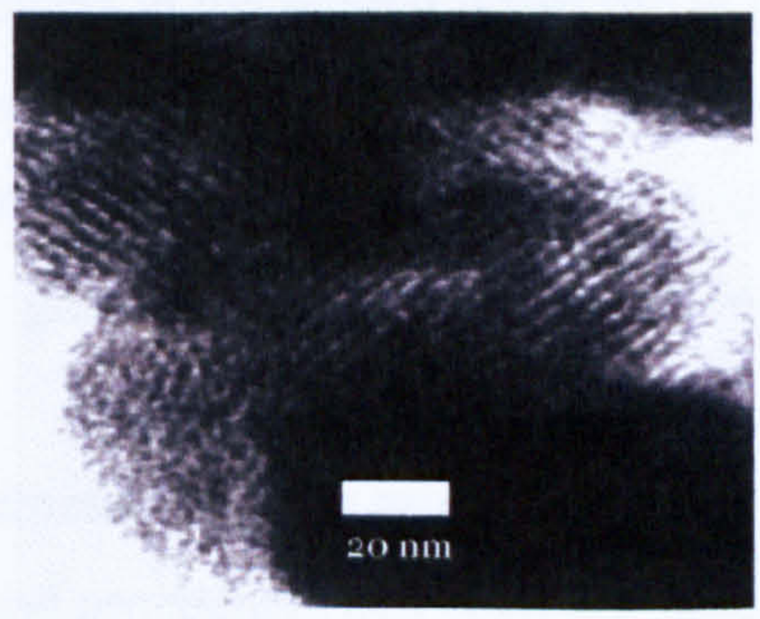

(b)

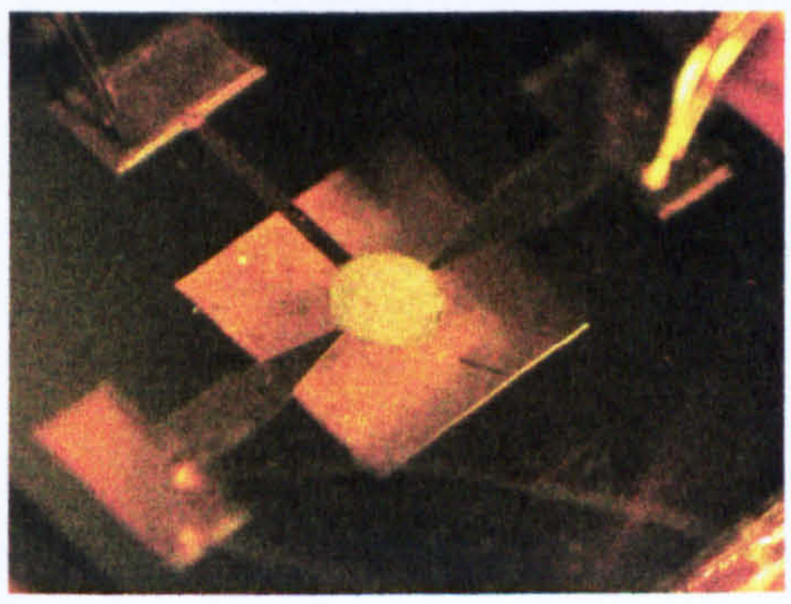

(c)

Figure 3.16: (a)The current-time transient at the working electrode during Pd electrochemical deposition [3.17]. (b) A sample of nanostructured Pd film employing the droplet coating system with Brij® 56 at the suggested composition [3.18]. The hexagonal closed packed phase is clearly visible. (c) A deposited micro-calorimeter (SRL 179c).

3.5 Conclusions

This chapter described the full fabrication details for the two silicon runs used to fabricate the silicon planar micro-calorimeters. The objectives and strategies involved in the device mapping for each of the fabrication runs have been detailed and the associated sets of 5″ masks were manufactured. The 5-mask wafer processing and the bulk silicon micro-machining on the 4″ wafers were successfully completed. The devices were diced and packaged onto commercial TO-5 headers while the required techniques and experiences had been established from the first fabrication batch.

The fabrication quality of the micro-hotplate had been inspected optically to extract the fabrication yield, process-related defects and the surface topology of the devices. Although the overall yield had not been accounted for during the first wafer run due to the intensity of the experiments performed in post-fabrication processes, the yield in the second wafer run reached 82% on average. Passivated devices had not presented significant advantages in the dicing process. As there are additional features in the second wafer run, the amount of process-related defects in the second wafer run is greater than the preceding run. Surface profiling indicated that the ridge-like artefact along the fringes of the lift-off features might cause electrical shorting between the Pt and Au layers on certain devices. Apart from the gold gate electrode, the average material thickness deposited is within 10% of the designed values. Therefore, the manufacturability of the silicon planar micro-calorimeter has been proven.

The electrochemical deposition apparatus and procedures had been outlined. Brij® 56 is the selected surfactant for the majority of Pd nanostructured catalyst deposition throughout this research due to the low-cost and abundant supply.

In conclusion, the yield of 82% on a research project is very good and higher yield should be achievable when wafers are processed on a commercial basis.

References

[3.1] A. Pike, J. W. Gardner, Thermal modelling and characterisation of micropower chemoresistive silicon sensors, *Sensors and Actuators B*, Vol 45 (1997) p19-26.

[3.2] S. Guérin, Planar pellistors: An application of electrodeposited mesoporous palladium films for the detection of combustible gases, *PhD Thesis*, University of Southampton, 1999.

[3.3] S. M. Sze, *VLSI Technology*, 2nd Edition, McGraw Hill, 1988.

[3.4] L. M. Mack, A. Reisman and P. K. Bhattacharya, Stress measurement of thermally grown thin oxides on (100) Si Substrates, *Journal of Electrochemistry Society*, 136, No. 11, 3433-3437, 1989.

[3.5] D. Kouvatsos, J. G. Huang, V. Saikumar, P. J. Macfarlane and R. J. Jaccodine, SiO_2 Film stress, thickness dependence, non-planar oxidation and fluorine-related effects, *Journal of Electrochemistry Society*, 139, No. 8, 2322-2326, 1992.

[3.6] J. W. Gardner, V. K. Varadan, O. O. Awadelkarim, *Microsensors MEMS and Smart Devices*, Chapter 5, p119, John Wiley & Son, Ltd, 2001.

[3.7] A. Pike, Design of chemoresistive silicon sensors for application in gas monitoring, *PhD Thesis*, University of Warwick, 1996.

[3.8] S. M. Lee, J. W. Gardner, *City Technology Ltd. Project quarterly report (University of Warwick)*, No. 9, 2001.

[3.9] S. Astié, A. M. Gué, E. Scheid, L. Lescouzéres, A. Cassagnes, Optimisation of an integrated SnO_2 gas sensor using a FEM simulator, *Sensors and Actuators A*, 69, p 205-221, 1998.

[3.10] S. M. Lee, J. W. Gardner, *City Technology Ltd. Project quarterly report (University of Warwick)*, No. 8, 2001.

[3.11] *WYKO manual*, WYKO Instrument Ltd. UK, 1996

[3.12] G. S. Attard, P. N Bartlett, N. R. B Coleman, J. M Elliott, J. R Owen and J. H Wang, Mesoporous platinum films from lyotropic liquid crystalline phases, *Science*, 1997, 278, p.838

[3.13] D. J. Mitchell, G. J. Tiddy, L. Waring, T. Bostock and M. P. J. McDonald, *Journal of Chemical Society*; Faraday Trans. 1, 1983, 79(1), p. 975.

[3.14] Y. M. Tan, Mesoporous materials, *PhD Thesis*, University of Southampton, 2001.

[3.15] Y. M. Tan, P. N. Barttlett, *City Technology Ltd. Project quarterly report (University of Southampton)*, No. 2, 2001.

[3.16] J. W. Gardner and P. N. Bartlett, Microsensor deposition device, British patent application no. 9400855.4.

[3.17] Y. M. Tan, P. N. Barttlett; *City Technology Ltd. Project quarterly report (University of Southampton)*, No. 3, 2000.

[3.18] P. N. Bartlett and S. Guerin, A micromachined calorimetric gas sensor: an application of electrodeposited nanostructured palladium for the detection of combustible gases, *Journal of Analytical Chemistry*, (in press).

Chapter 4

Test equipment and custom instrumentations for micro-calorimeters

4.1 Introduction

This chapter describes the various test equipment and custom instrumentation which have been designed and fabricated to investigate the characteristics of the micro-calorimeters. Two gas-test systems are described, namely the main gas-test system in the SRL, University of Warwick, UK and the industrial system in City Technology Ltd., UK, covering their operating principles, chamber design and interface electronics. In order to evaluate the life expectancy of the device, a life-time testing system has been constructed. It has been designed to automatically record the number of operating hours for a device under test before failure. In addition, an A.C. power driver and measuring system has also been produced to enable the micro-calorimeters to operate in pulse mode. It can be used in conjunction with other testing systems, such as the gas-test systems.

4.2 Main gas-test system

A gas-test system has been developed at the Sensor Research Laboratory (SRL), University of Warwick, UK, as shown in figure 4.1. The system uses a controlling computer for the gas rig and a separate computer for data logging.

The gas rig, as shown in figure 4.2(a), comprises a group of valves, filters, test chamber and signal conditioning electronics. The test chamber accommodates the devices under a controlled environment to ensure the repeatability of the test results. The signal conditioning electronics provides A/D conversions and power regulations for the control signals between the test chamber and the controlling computer. The flow rate within the system is controlled by four mass flow controllers [4.1]. Dry air and the blended gas from compressed cylinders (supplied by BOC) are fed into the sensor chamber and exhaust via a flow sensor to monitor the leakage within the system.

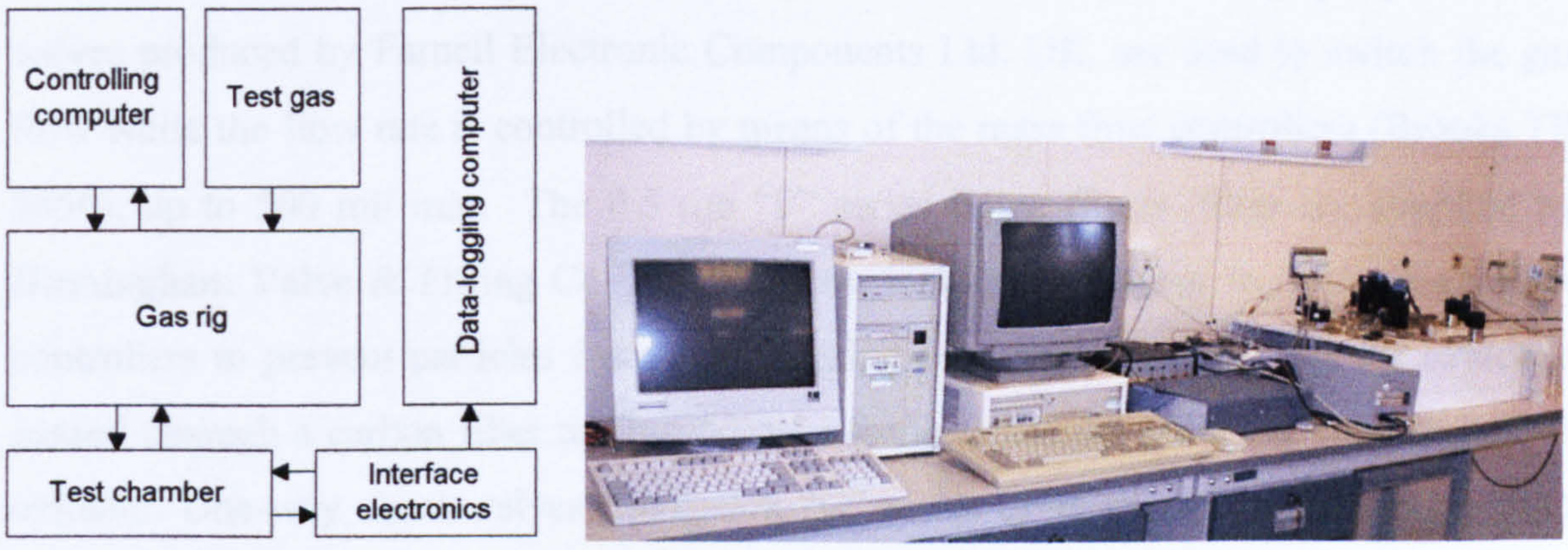

(a) (b)

Figure 4.1: The main gas-test system. (a) Block diagram of the system indicating the signal flows. (b) Photograph of test equipment.

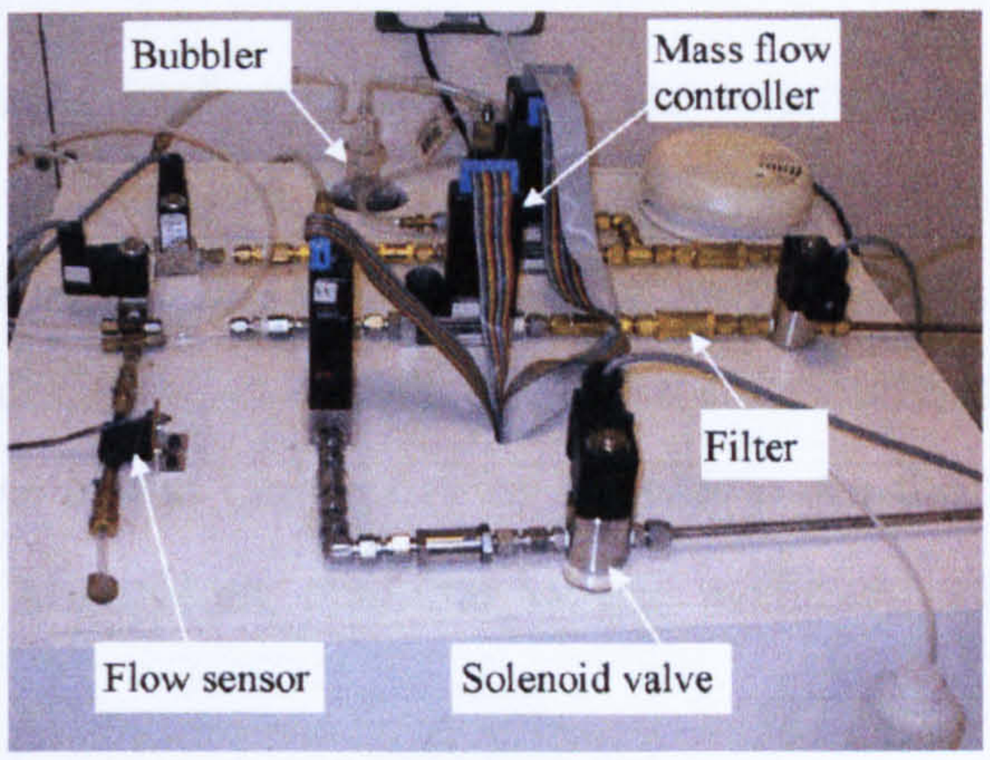

(a)

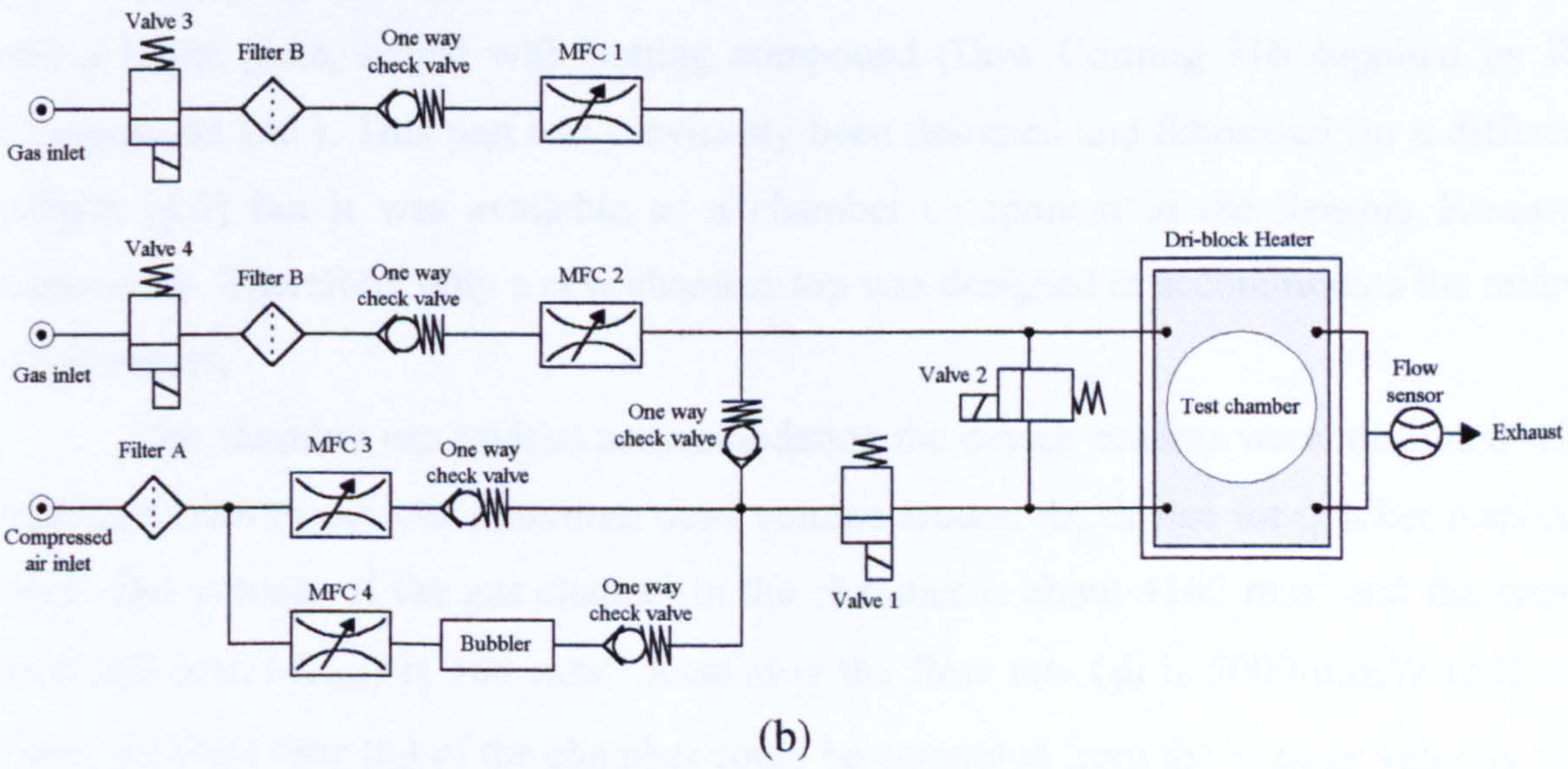

(b)

Figure 4.2: (a) A photograph of the gas rig. (b) The schematic diagram of the gas rig [4.1].

A schematic diagram of the gas rig is shown in figure 4.2(b) [4.1]. Solenoid valves produced by Farnell Electronic Components Ltd. UK, are used to switch the gas flow while the flow rate is controlled by means of the mass flow controllers (Brooks TR 5850), up to 500 ml/ min. The 0.5 μm "F" series inline filters (filter B), supplied by Birmingham Valve & Fitting Co. Ltd., UK, are included upstream from the mass flow controllers to prevent particles from accumulating in the aperture. The dry air source is passed through a carbon filter to absorb any organic molecules from the compressed air cylinder. One-way check valves (Swagelok "C" series by Birmingham Valve & Fitting Co. Ltd, UK) are placed at various points in the system to prevent backpressure from damaging any sensitive components. The time constant of the gas flow is about 6 s to 10 s, for the mass flow controller to switch from 0 ml/min to 250 ml/min.

4.2.1 Test chamber

The purpose of the test chamber is to expose the sensors to the gas flow. Here, the sensors are exposed to a known humidity, gas concentration and temperature. The chamber is comprised of a gas heat exchanger and a customised chamber top that accommodates four pairs of TO-5 headers for batch characterisation. The entire chamber was fabricated in-house at the University of Warwick. As the test gas is a mixture of methane and air, an aluminium chamber offers sufficient chemical resistance at a relatively low cost.

Figure 4.3 illustrates the assembly of the test chamber which is comprised of a chamber top and a lower chamber [4.2]. The lower chamber is assembled from a central and a lower plate, sealed with potting compound (Dow Corning 316 supplied by RS Components Ltd.). This part had previously been designed and fabricated for a different project [4.2] but it was available as a chamber component in the Sensors Research Laboratory. Therefore, only a new chamber top was designed to accommodate the micro-calorimeters.

The chamber top cavities accommodating the device headers were machined with high precision to achieve minimum dead volume around the device for quicker response time. The volume of the gas channel in the chamber is about 4160 mm^3 and the cross-sectional area (A_{cross}) is 104 mm^2. Assuming the flow rate (ϕ) is 5000 mm^3/s (300 ml/ min), the dead time (t_d) of the chamber could be computed from the average velocity (υ_a) and the length of the gas channel, as shown in equations (4.1) and (4.2).

$$\upsilon_a = \frac{\phi}{A_{cross}} = \frac{5000\text{mm}^2/\text{s}}{104\text{mm}^2} = 48.1 \text{ mm/s} \tag{4.1}$$

$$t_d = \frac{\ell}{\upsilon_a} = \frac{40\text{mm}}{48.07\text{mm/s}} = 0.832 \text{ s} \tag{4.2}$$

Therefore, the dead time of the chamber was minimised approximately to less than 1 s, in order to reduce the overall time constant of the gas flow in the rig.

A schematic diagram of the chamber top is shown in figure 4.4. The devices were placed at the middle of the gas channel between the gas inlet and the exhaust. In this way, not only does it avoid direct gas injection from the inlet which could causes additional cooling, but also the axisymmetric design prevents any effect of gas depletion.

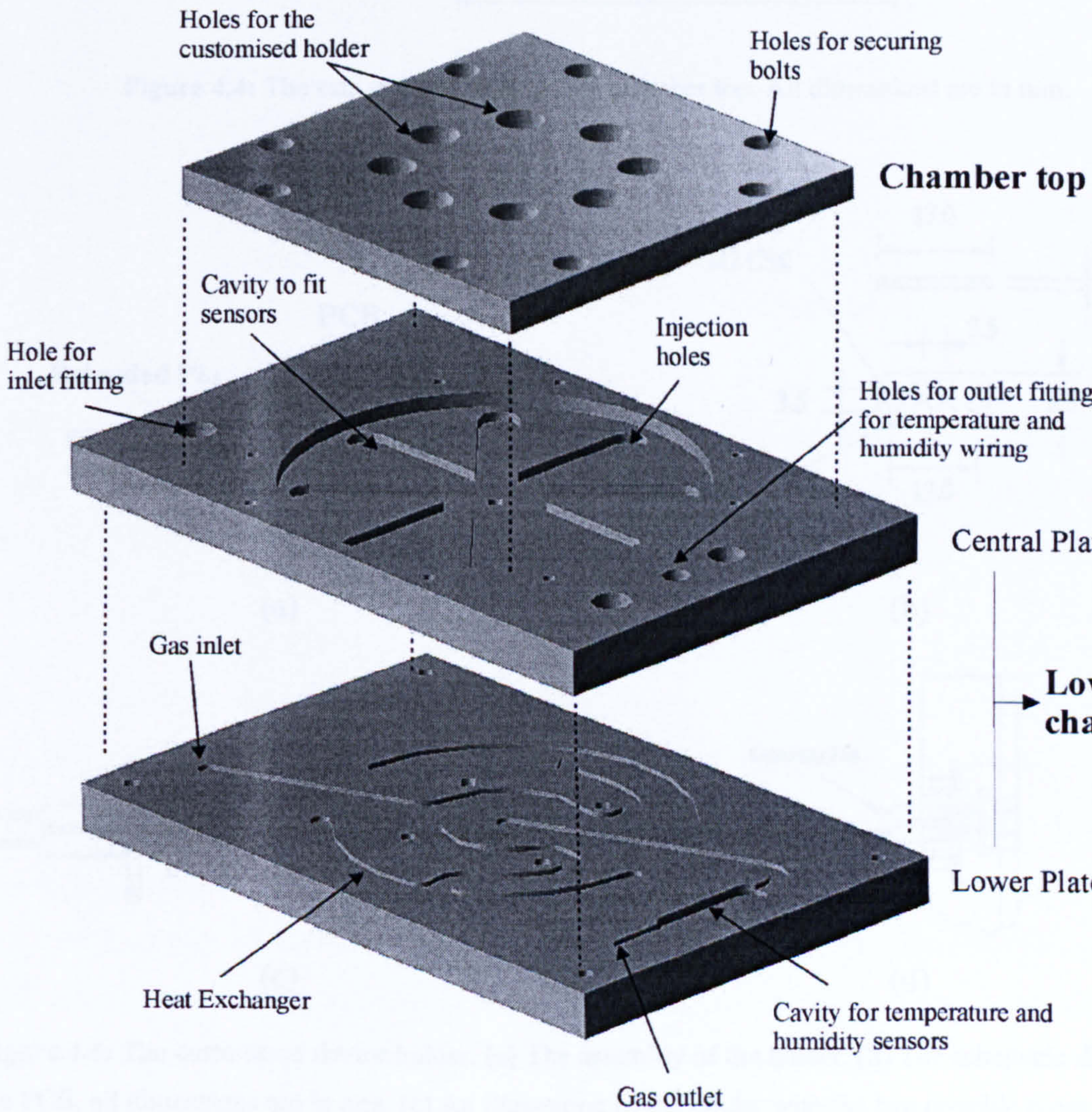

Figure 4.3: The assembly of the gas test chamber.

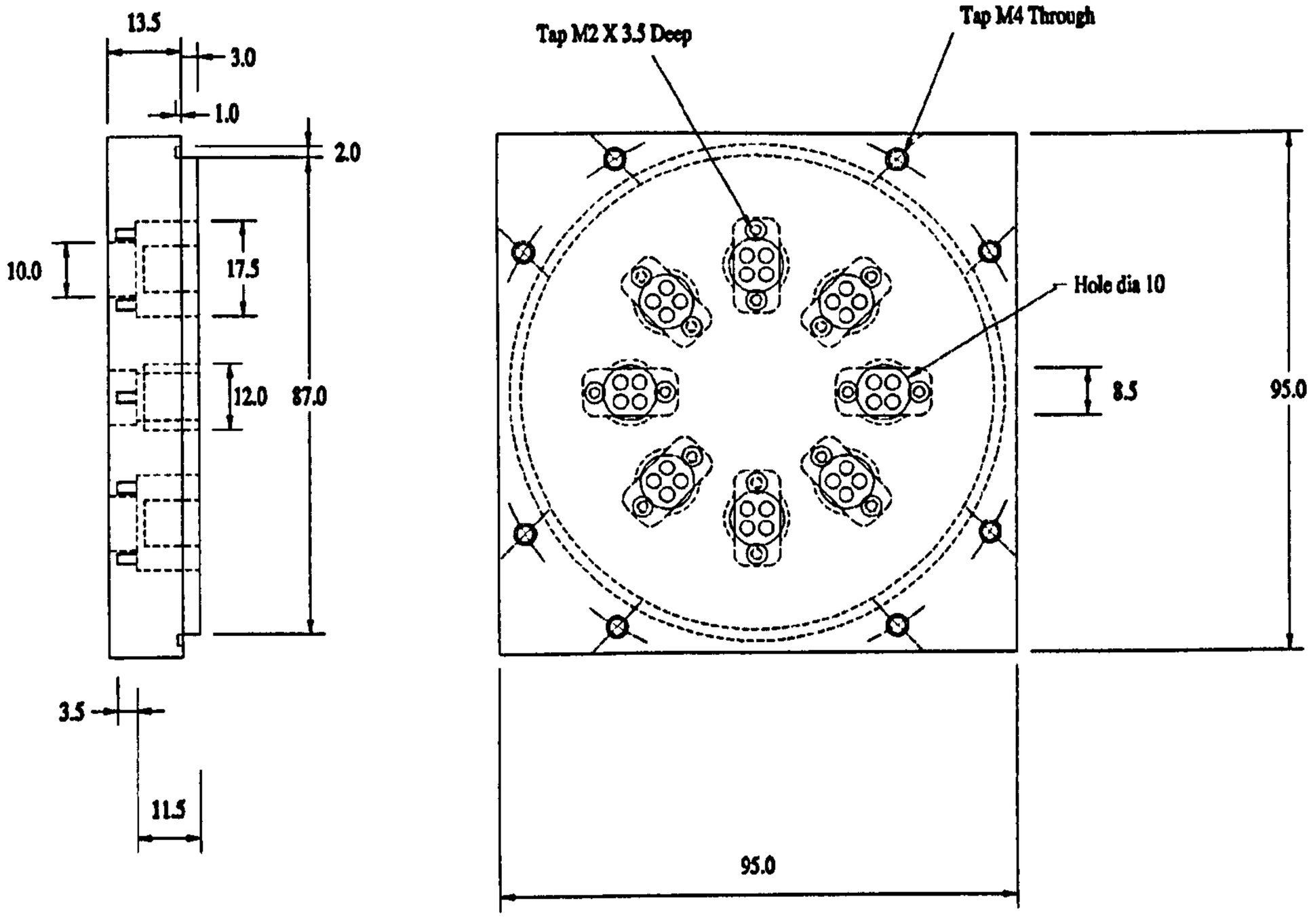

Figure 4.4: The side and plan view of the chamber top. All dimensions are in mm.

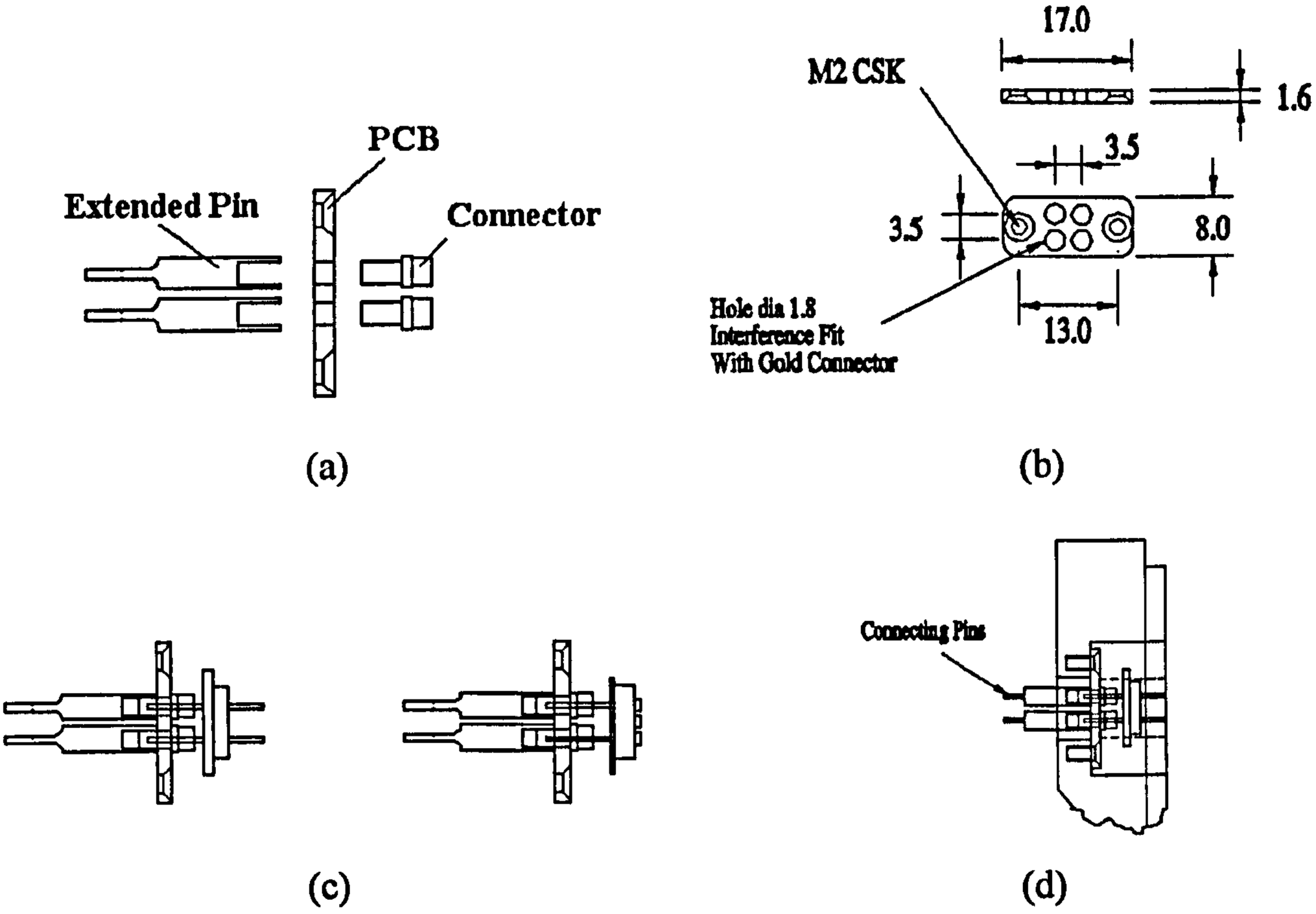

Figure 4.5: The customised device holder. (a) The assembly of the holder. (b) The schematic diagram for the PCB, all dimensions are in mm. (c) An illustration of the holder with the two possible types of header. (d) An illustration of the holder mounted onto the chamber top.

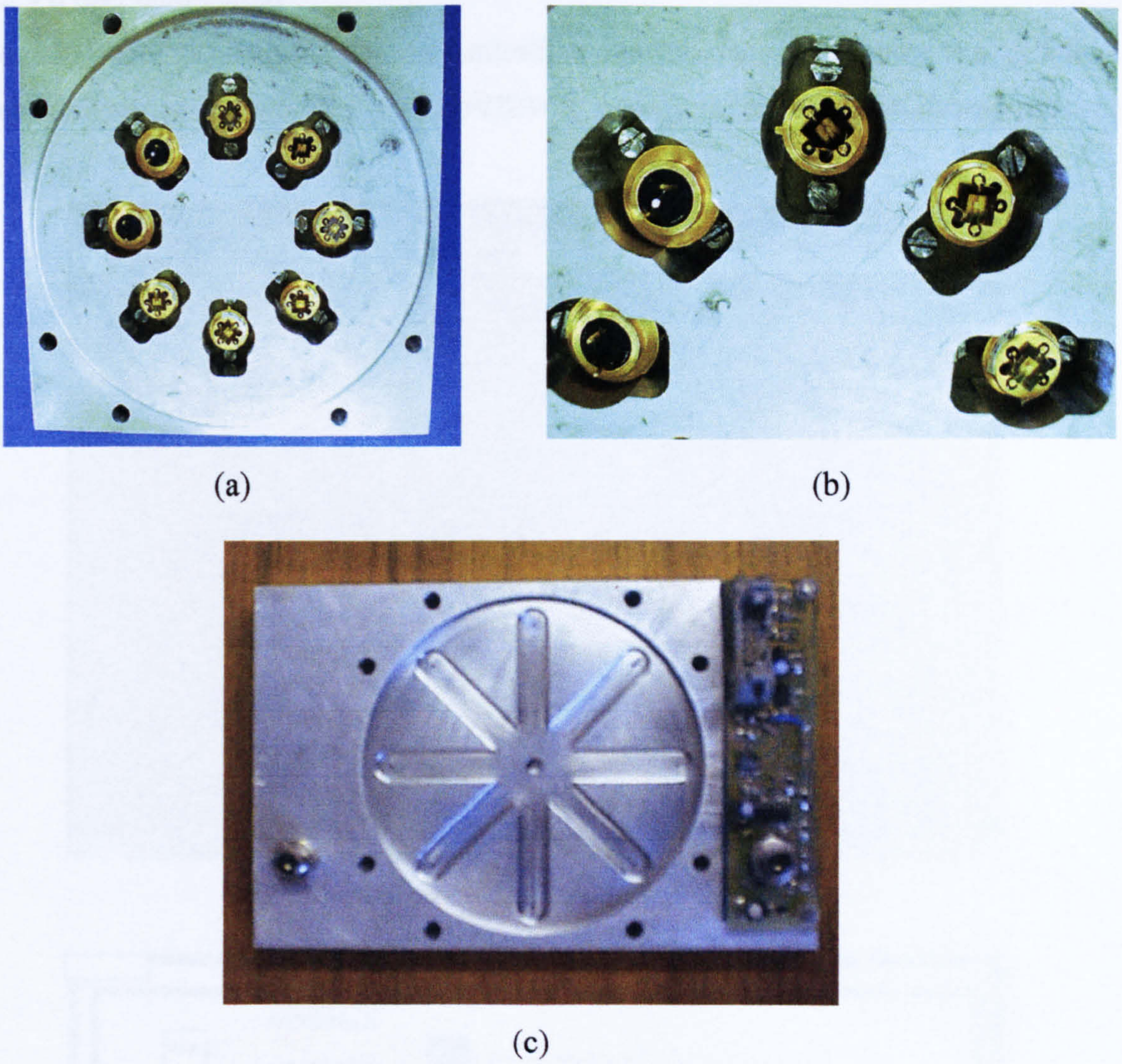

(a) (b)

(c)

Figure 4.6: The test chamber components. (a) The chamber top with mounted devices. (b) A close-up view of the cavities at the top chamber, showing two different type of package header accommodated. (c) The existing lower chamber component which is the assembled central plate and the lower plate.

A customised, slim and low profile sensor holder was designed and fabricated for the top chamber because an ordinary commercial TO-5 holder did not satisfy the specifications, as shown in figure 4.5. This consists of custom-made aluminium extended pins and a PCB support (fabricated in house) and gold plated connectors (H8505-05) supplied by Harwin components plc. The customised device holder is compact in size, chemically inert and has a low contact resistance. As the device characterisation would involve comparisons to commercial pellistors, the holder was also made compatible with the commercial package, as shown in figures 4.5 and 4.6(b). The completed chamber is shown in figure 4.6.

4.2.2 Virtual instrument

Automated data collection software controlling the interface electronics was designed using commercial software called LabVIEW®, version 5, by National Instrument Inc.

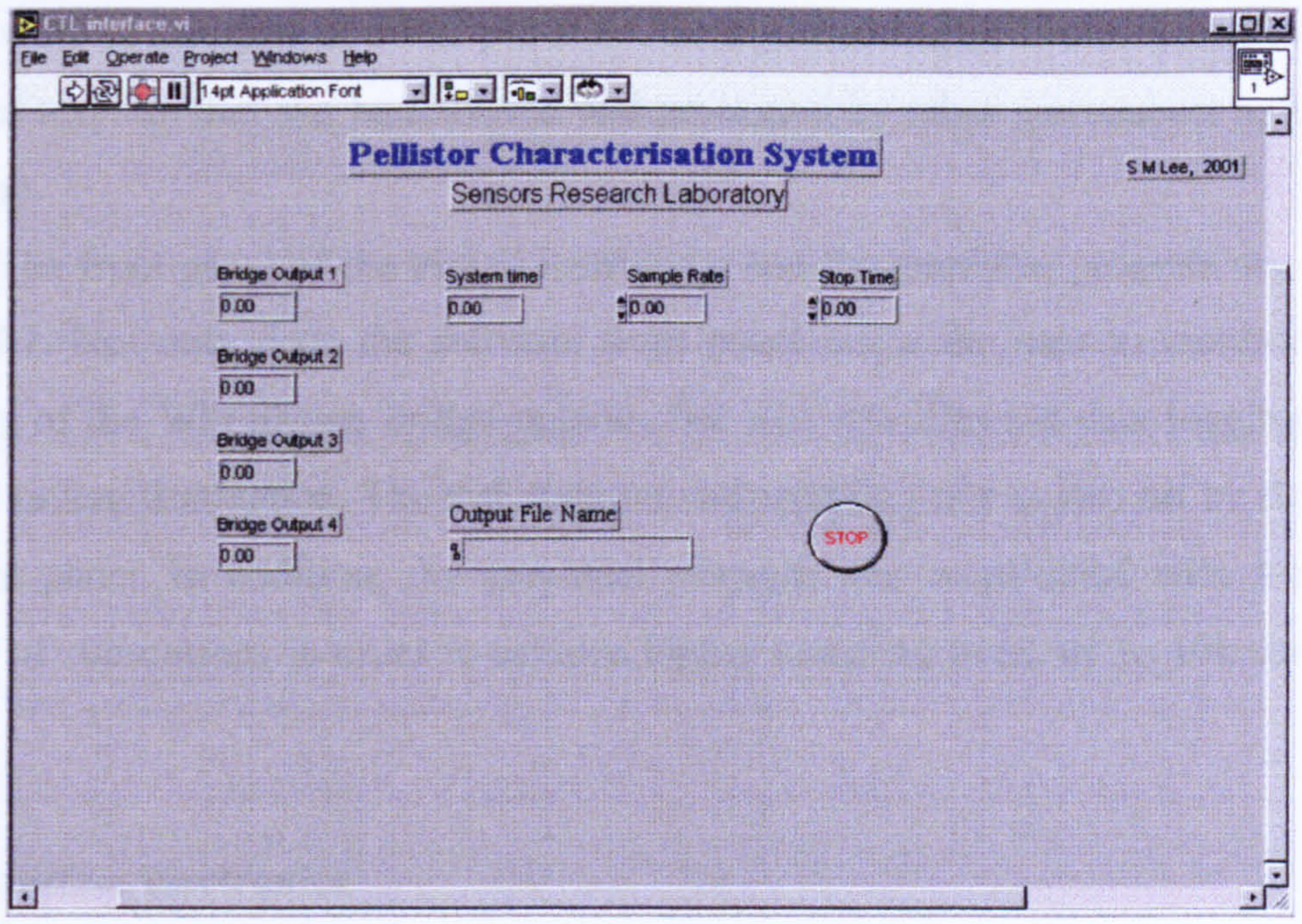

(a)

(b)

Figure 4.7: The virtual instrument created by LabVIEW®, version 5. (a) The front panel of the virtual instrument. (b) The graphical program of the virtual instrument.

This graphical programming software established a PC based control to capture the analogue output signals from the interface circuit via a data acquisition card, AT-MIO-16-XE50 (National Instrument Inc.). It converts the analogue output signal of the interface circuit into a digital signal by the on-board 16-bit Analogue-to-Digital converter (ADC) with an accuracy of 3 bits per mV. The digitised output is then saved into a user-specified text file that can be retrieved and processed by other spreadsheet software at a later time.

The front panel of the virtual instrument and the graphical program are shown in figure 4.7. Not only does the software front panel allow the user to monitor the four channels of the Wheatstone bridge outputs, but also specifies the data logging duration and file saving destination. The test duration and sampling rate is also set by the user via the front panel. In addition, the graphical program was constructed with a minimum number of subroutines in order to achieve higher sampling rates, up to 10k samples per second.

4.2.3 Interface electronics

The function of the interface electronics is to set initial signal conditions and to measure the response of the micro-calorimeter when it is exposed to a target gas. As the measurement electronics are also required to monitor the change of the device resistance during operation, two circuits were designed, as shown in figure 4.8.

The device response detection circuit, as shown in figure 4.8(a), is based on the standard Wheatstone bridge circuit which has been employed for commercial pellistors [4.3]. However, the value of the balance resistors, R_b, was increased from 27 Ω to 400 Ω for compatibility between the new micro-machined devices (10 Ω to 230 Ω) and existing commercial pellistors. In addition, the potentiometer value was changed from 1 kΩ to 20 kΩ to maintain a ratio of 50 with the balancing resistor, in order to achieve good thermal stability. This is further explained in Appendix 4a.

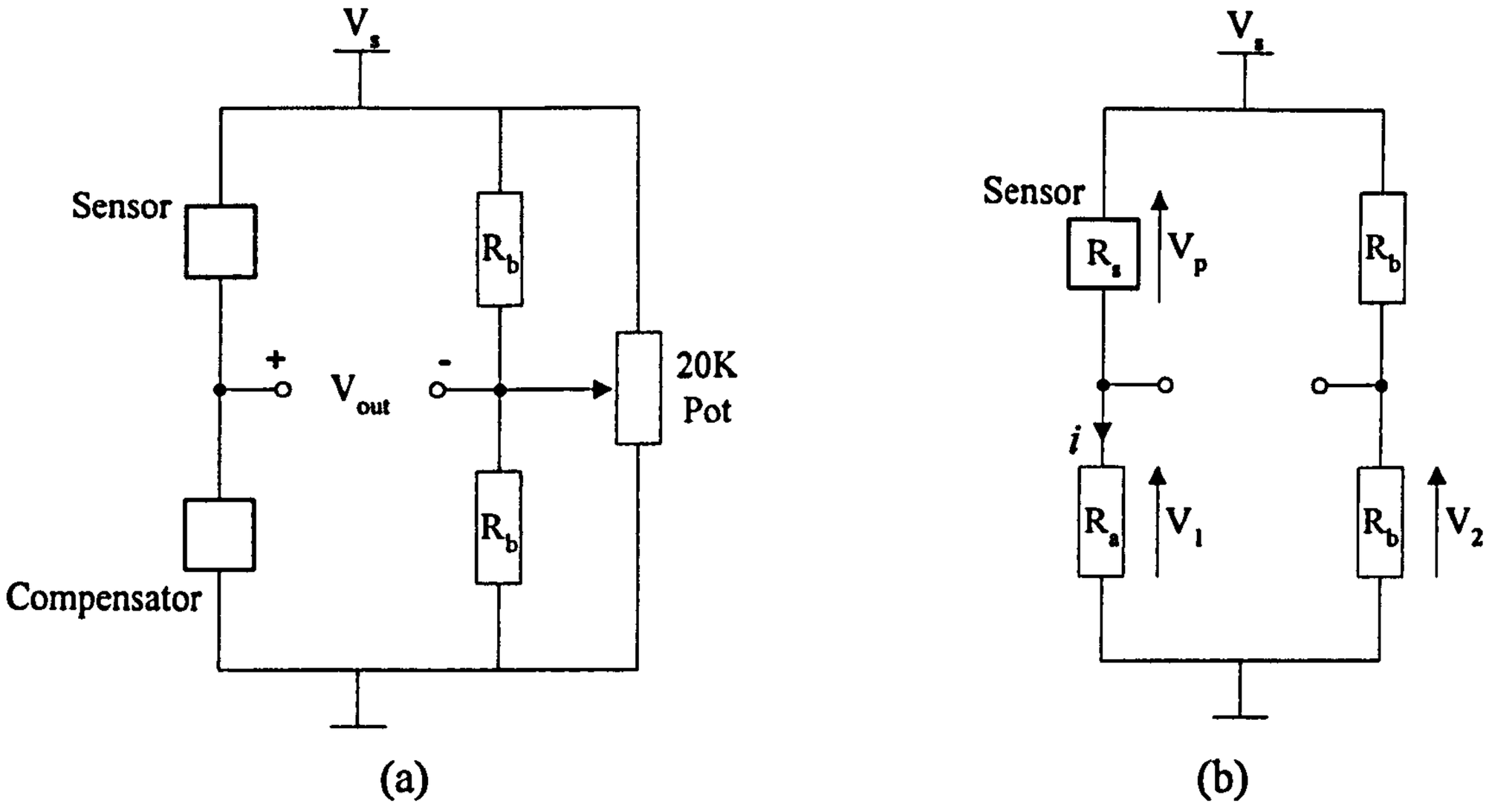

Figure 4.8: Interface circuits. (a) Wheatstone bridge circuit with compensator for commercial pellistors [4.3]. (b) Wheatstone bridge circuit for resistance measurement.

The resistance measurement bridge circuit is shown in figure 4.8(b). The measurement is based on the voltage drop across the sensor, the current sensing resistor (3 Ω), R_a and the balancing resistor, R_b. The resistance of the sensor is expressed in equations (4.3) to (4.6).

$$V_s = 2V_2 \tag{4.3}$$

$$V_p = (V_s - V_1) = (2V_2 - V_1) \tag{4.4}$$

$$i = \frac{V_1}{R_a} \tag{4.5}$$

$$R_s = \frac{V_p}{i} = \frac{V_p \times R_a}{V_1} = \frac{(2V_2 - V_1)R_a}{V_1} \tag{4.6}$$

where R_s is the resistance of the sensor; V_p is the voltage across the sensor;
R_a is the current sensing resistor; V_2 is the voltage across the balancing resistor;
V_1 is the voltage across the current sensing resistor.

Therefore, the resistance of the micro-calorimeter is obtained by taking a measurement at each bridge output node with respect to ground, instead of a differential bridge output. Moreover, the circuit removes the effect of any possible fluctuations in the supply voltage (V_s) since V_1 and V_2 scale in proportion to V_s.

A power circuit had been designed to provide a constant voltage supply to the interface bridge circuits, as shown in figure 4.9. The required voltage for the interface circuit is used as the source voltage (V_{ss}). The source follower circuit which employs a high precision op-amp (OPA 251PA), supplies a constant voltage to the bridge interface circuit, at (V_s). The enhancement mode power MOSFET (IRL 2703) provides the high current to the Wheatstone bridge which is needed to heat up the micro-calorimeters. Furthermore, the low-pass filter prevents any high frequency power surges from V_{ss} to the bridge circuit. It protects the high precision op-amp and enhances the reliability of the power supply. The switch, S1, is used as the main switch to the circuit.

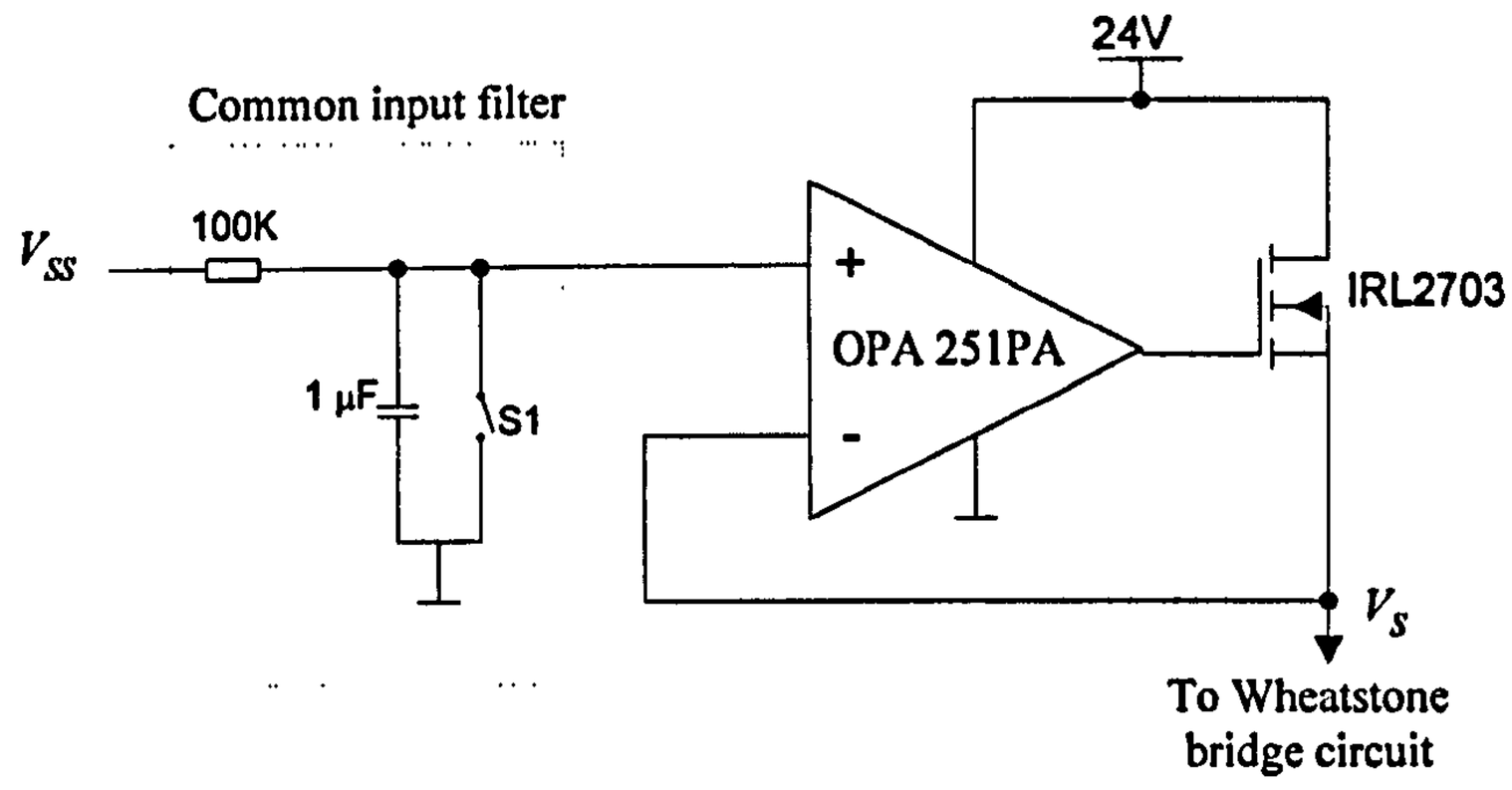

Figure 4.9: Input buffering circuit, showing a low-pass filter and a source follower circuit.

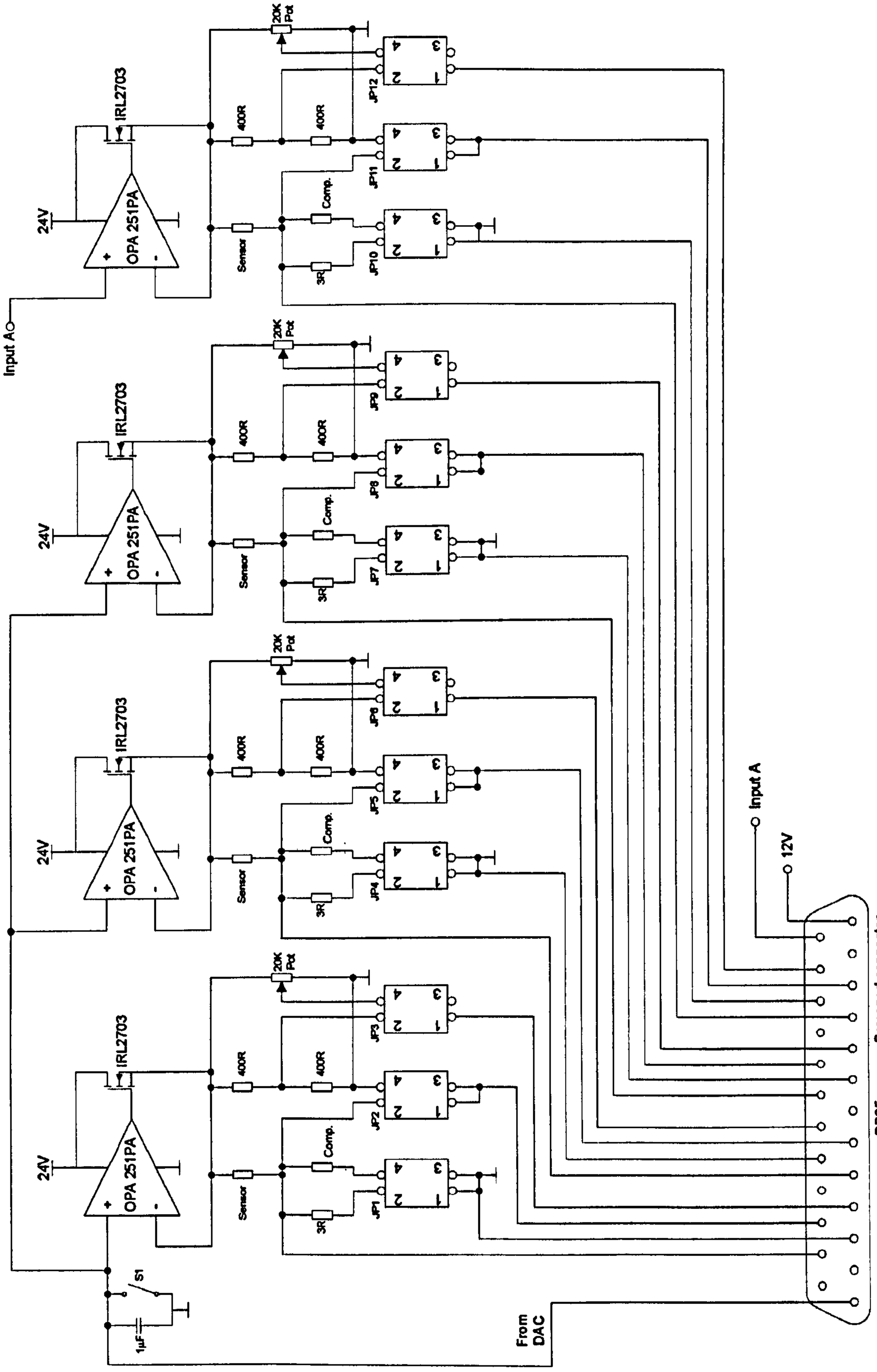

Figure 4.10: The micro-calorimeter interface circuit.

A complete circuit diagram for the interface electronics is shown in figure 4.10. The two bridge circuits were merged with their functionality switched by on-board jumpers. Therefore, a dual function electronic interface circuit was created in a compact manner. It could improve the efficiency of device characterisation since resistance measurement and device response tests could be performed consecutively by switching the functionality of the interface circuit board.

To ensure sufficient current drive up to 1 A, individual packaged op-amps were used to power each of the four Wheatstone bridge circuits. In addition, to accommodate the different voltage requirements between the commercial and micro-machined devices, three Wheatstone bridge circuits were connected to the common voltage supply and one was connected to a separate voltage supply. The maximum source voltage (V_{ss}) for the interface circuit is 24 ± 0.5 V. However, the maximum voltage delivered to the Wheatstone bridge (V_s) is about 22 V because of the voltage drop across the MOSFET transistor, therefore max. (V_s) = (V_{ss} – 2 V).

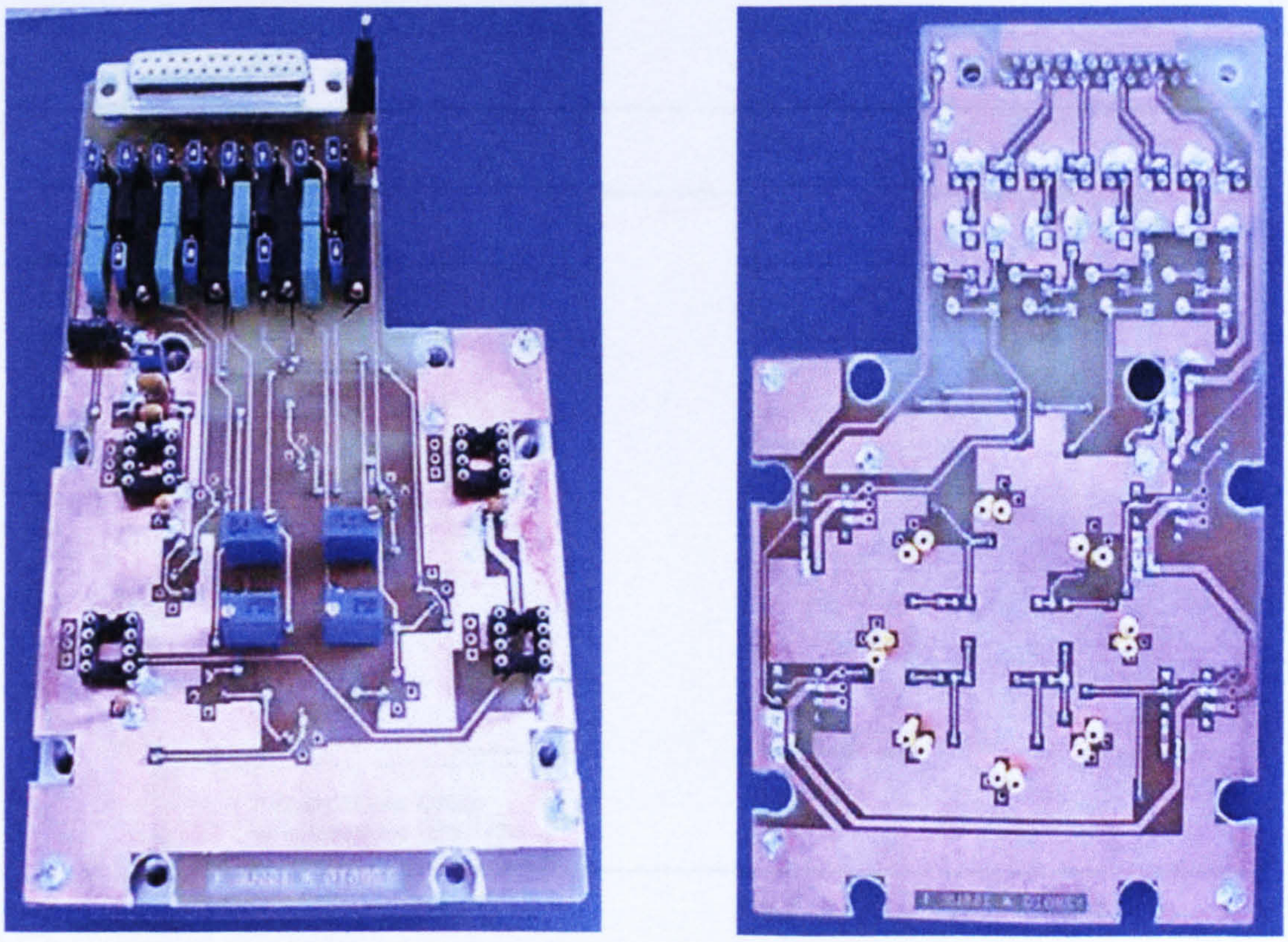

(a) (b)

Figure 4.11: The fabricated micro-calorimeter interface circuit board. (a) Top view of the PCB with all the components. (b) Bottom view of the circuit board with the connectors to the device in the test chamber.

Once the interface circuit design was completed, a double-sided printed circuit board (PCB) was fabricated, as shown in figure 4.11. Details of the PCB artwork are included in Appendix 4b. In order to minimise the parasitic resistance arising due to wiring and contact resistances, the circuit board was designed to be placed above the chamber top. The interface circuit board employed high precision resistors with tolerances of 0.01% and the TCR is 0.5 ppm/°C. The layout included a ground plane to reduce signal noise.

Therefore, high precision measurements could be achieved with a signal-to-noise ratio at full scale of only 0.008%. A comparison of the Wheatstone bridge output between an ordinary metal film resistor (±0.1%) and a micro-calorimeter is shown in figure 4.12. The micro-calorimeter clearly exhibits a transient as the power supply is switched between 2 V and 6 V at 10 Hz. Unlike the resistor, the transient is mainly caused by the thermal time constant of the silicon nitride membrane as the device was heated up to 500°C. Such a delay became the limitation of the maximum operating frequency for the device. Further analysis of this phenomenon had been studied with relation to the power consumption and is discussed in Chapter 6.

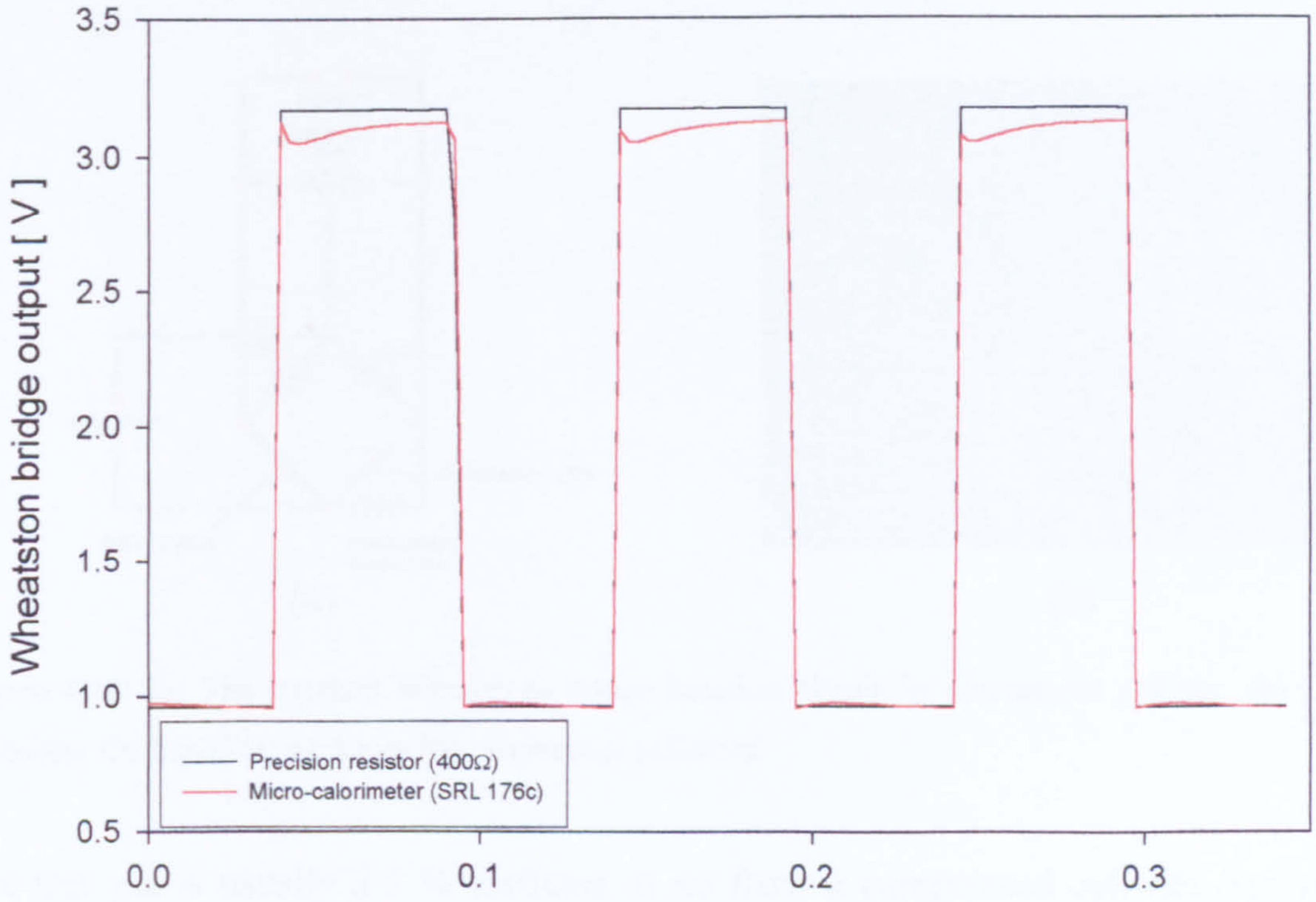

Figure 4.12: Comparison of the Wheatstone bridge output between ordinary resistor and micro-calorimeter (SRL 176c) at 10 Hz with a supply voltage switching between 2 V and 6 V.

4.3 Industrial gas-test system

An industrial characterisation system was also used to test devices. This system gives the most direct method to compare the performance of the micro-calorimeters against previous commercial data on standard pellistors. Permission was granted by City Technology Ltd. to test the micro-machined devices using their pellistor characterisation system. A simplified block diagram of the system is shown in figure 4.13.

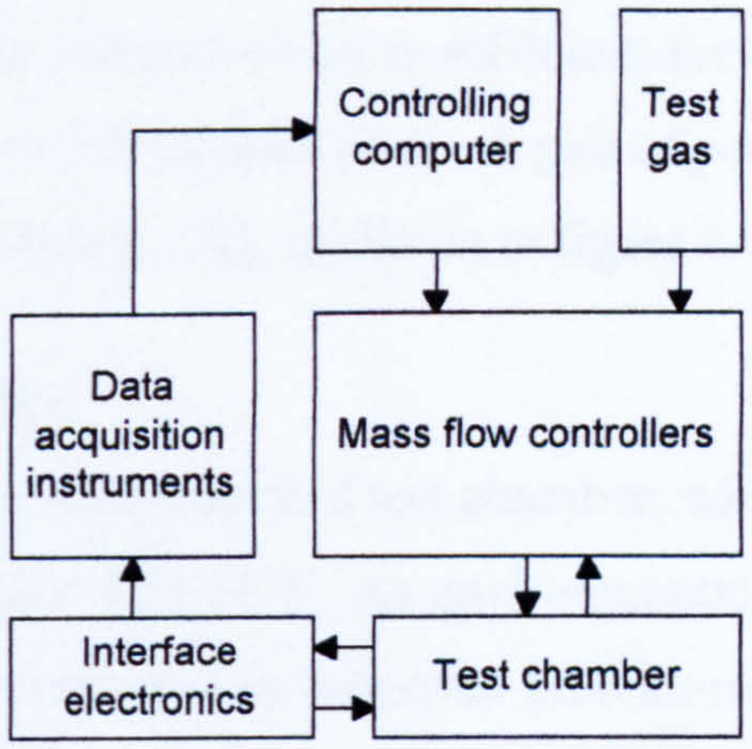

Figure 4.13: Block diagram of the characterisation system at City Technology Ltd.

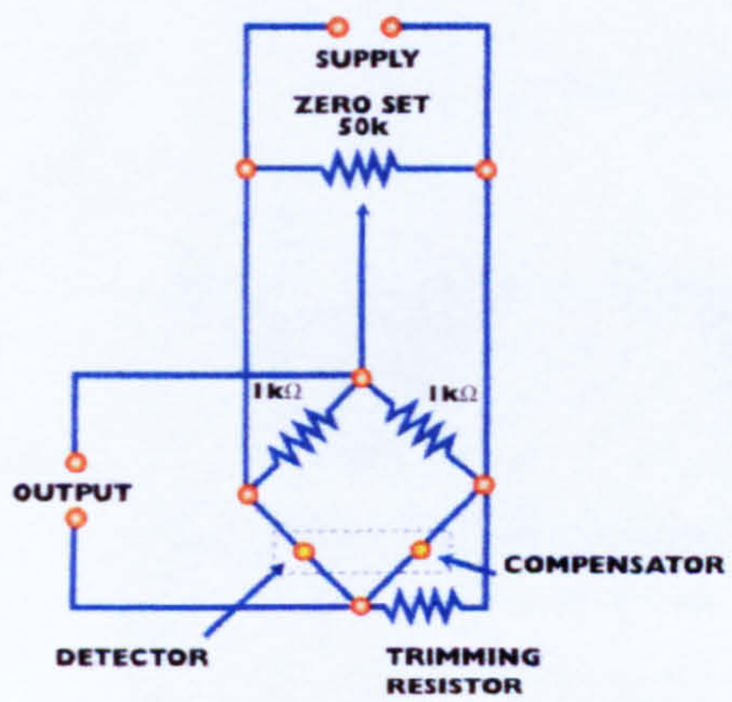

(a)

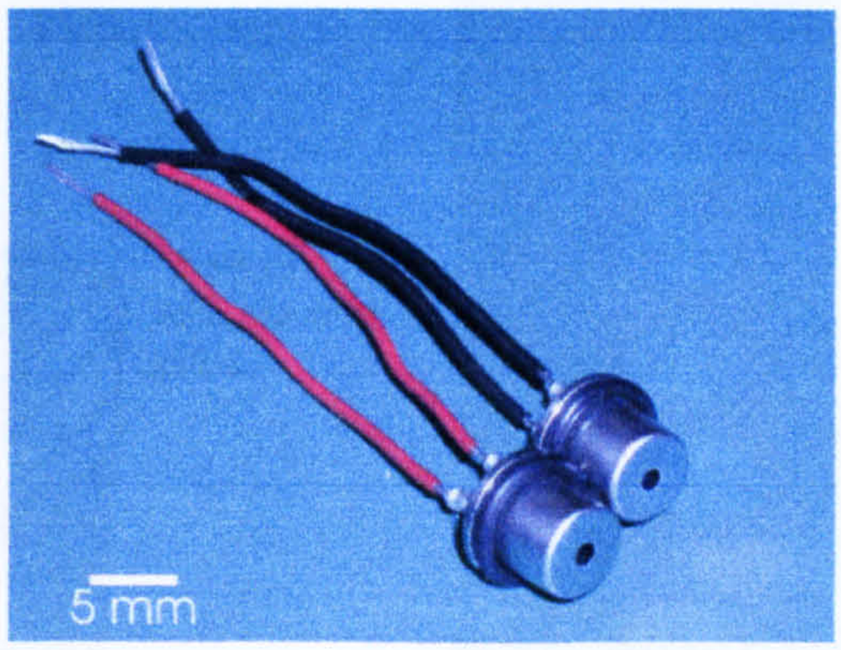

(b)

Figure 4.14: (a) The standard Wheatstone bridge interface circuit for commercial pellistor. (b) Common Transistor Outline (TO) packages for commercial pellistors.

The test gas is usually 2.5 % methane in air from a compressed cylinder (supplied by BOC special gases Ltd.), regulated by mass flow controllers (UFC-1000 produced by Unit Instruments Ltd. UK) with a maximum flow rate up to 600 ml/min. The controlling computer feeds the signals to the mass flow controllers to allow a specific volume of the test gas to reach the test chamber. The interface electronics is a standard quarter

Wheatstone bridge, with a maximum supply voltage of 30 V, as shown in figure 4.14(a) [4.3]. However, the compensator element was replaced with a resistor block, manufactured by TIME electronics Ltd. The test chamber is capable of accommodating up to ten devices. The data acquisition is performed by a high precision voltmeter (Keithley 2000), and the ten channels are multiplexed by a Keithley 7001 switching system. The digitised response signals are then collected by the controlling computer and the data can be retrieved by additional spreadsheet software. The data-logging rate is typically 2 seconds per data sample which is sufficient for commercial pellistors which have a response time of about 15 seconds [4.4]. A pair of packaged commercial pellistor, manufactured by City Technology Ltd., is shown in figure 4.14(b).

4.3.1 Industrial test chamber

The construction of the industrial standard test chamber, which accommodates five pairs of devices, is shown in figure 4.15 [4.5]. As environmental chambers and temperature-controlled workstations are common in industrial laboratories, a built-in thermal control facility such as a heat exchanger is not necessary. This leads to a simpler chamber design.

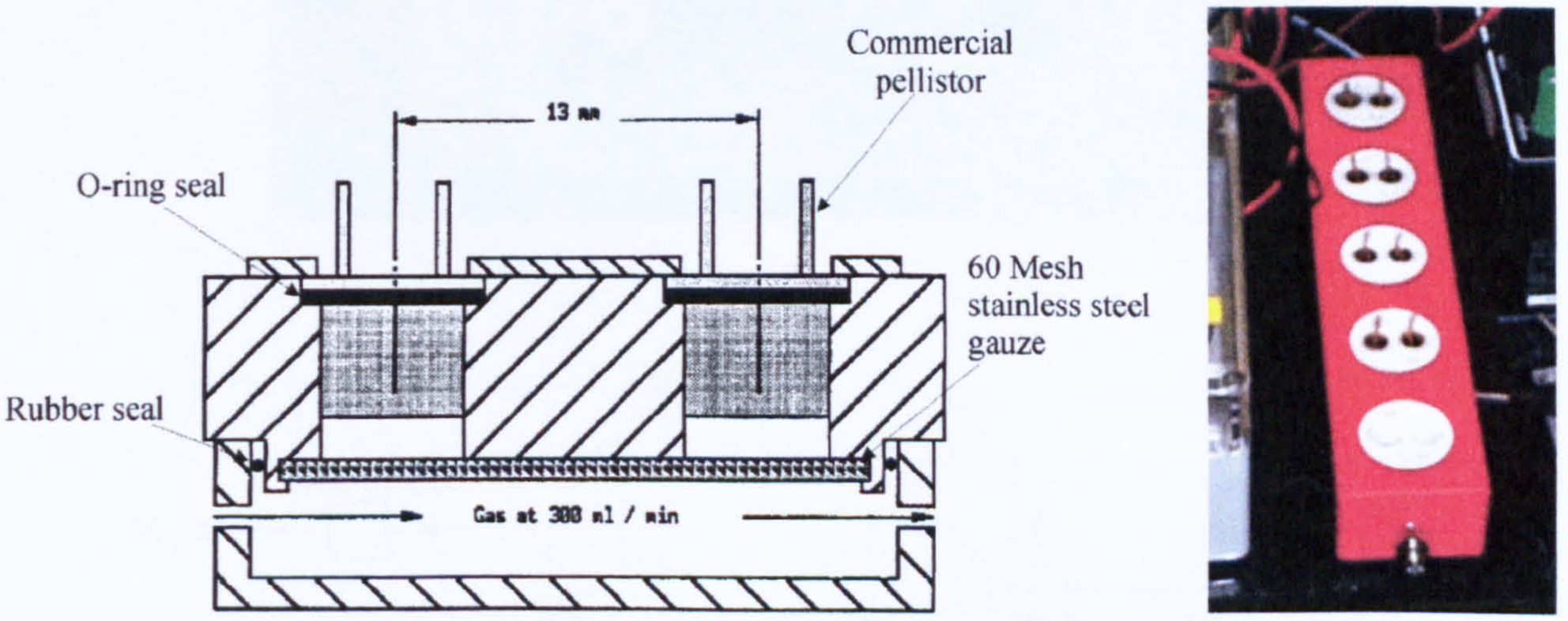

Figure 4.15: The industrial standard test chamber. (a) The cross-section schematic diagram of the test chamber [4.5]. (b) The actual test chamber at City Technology Ltd. UK.

4.4 Life-time testing system

The life expectancy of the micro-calorimeter is an important parameter to be established before commercialisation. As the experiment will be over an extended period of time, a long-term test station was designed and fabricated to minimise the effort of monitoring the devices under test. The station accommodates up to two devices with the two TO-5 sockets on the front panel, as shown in figure 4.16(a). The devices are enclosed by a TO-5 can mounted with a heat sink to minimise environmental interference. The devices can be operated at either D.C. or pulse modulated mode, at the typical operating temperature of 500°C. The failure detection electronics was designed to achieve automatic monitoring of the devices and the circuit involved is shown in figure 4.16(b).

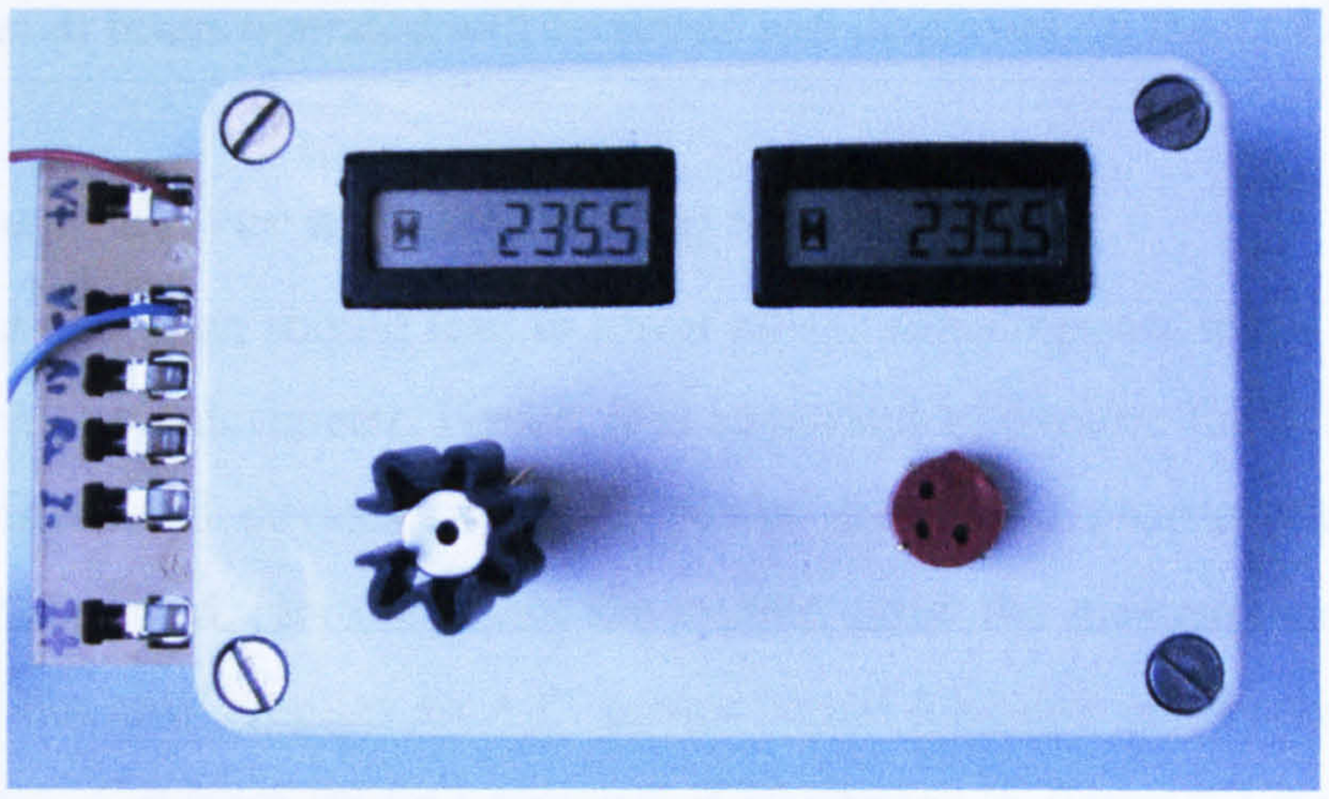

(a)

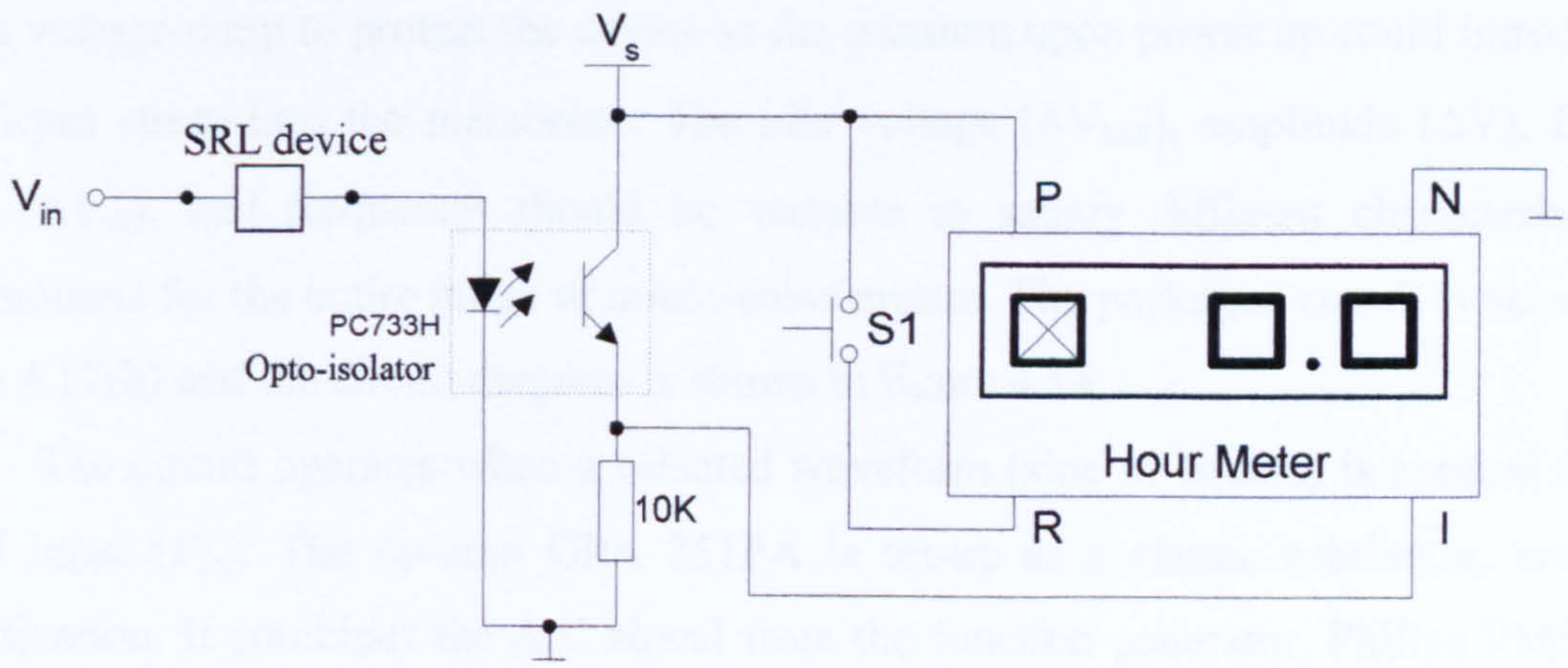

(b)

Figure 4.16: Determining device life-time. (a) The life-expectancy test station with two TO-5 sockets on the front panel with a device mounted with a heat sink. (b) The circuit design of the failure detection module.

The circuit employs a digital LCD display hour-meter, model 703 (Curtis Instrument Ltd., UK) that counts up to 99999 hours with a decimal place to indicate 1/10 of an hour, with a tolerance of ± 30 s per 8 hours. The meter can be reset by closing switch S1. The counting is enabled when a supply voltage (V_s) is applied to pin I. When a voltage (V_{in}) is applied to the sensor, the opto-isolator is forward-biased and the counting commences. When a constant voltage supply (V_{in}) is used (max. 15V), it should be adjusted accordingly to compensate for the 2 V drop across the opto-isolator. The buffered output signal is then amplified to the supply voltage (V_s) to activate the counter. This arrangement allows the circuit to adapt different power supply requirements for various micro-calorimeter designs. As soon as the device fails resulting in an open circuit, the opto-isolator is turned off and the potential at pin I falls to 0 V. The counting is disabled and the number of hours operated will be stored and displayed on the LCD.

4.5 A.C. power driver and measuring system

As pulse-mode operation should lead to lower power consumption, it is a major potential benefit of the micro-calorimeter. Hence, it is important to explore the dynamic response of the micro-machined devices. An A.C. power driver and measurement system was designed and fabricated. Not only does the system assist the measurement of the device time constant, but also supplies an A.C. power signal for other test systems, such as the gas-test systems. A typical driving protocol is illustrated in figure 4.17(a) with a square wave output, although a sine wave could also be required. The waveform shown begins with a voltage ramp to protect the device as the transient upon power up could introduces significant stress into the membrane. The idle voltage (ΔV_{idle}), amplitude (ΔV), Duty-cycle (ΔT_{on}), and frequency should be variable to satisfy different characterisation requirements for the entire range of micro-calorimeters. The packaged circuit is shown in figure 4.17(b) and the circuit diagram is shown in figure 4.18.

The circuit operates when a selected waveform (sine or square) is applied at the signal input (V_{in}). The op-amp OPA 251PA is set-up as a classic subtractor, without amplification. It combines the A.C signal from the function generator, Philips PM5168, and an adjustable D.C. offset voltage (via a 100k Pot) to create the desired waveform. The maximum voltage output is equal to the supply voltage (V_s), 24 V. The waveform is then fed into the source-follower buffer which includes a power op-amp (TCA0372) and a MOSFET (IRL 2703) to enhance the current drive up to 1 A. At this point, an optional

output (V_{in}') can be tapped to power the micro-calorimeters for other experiments. However, the maximum output is reduced to about 22 V due to the voltage drop across the MOSFET transistor.

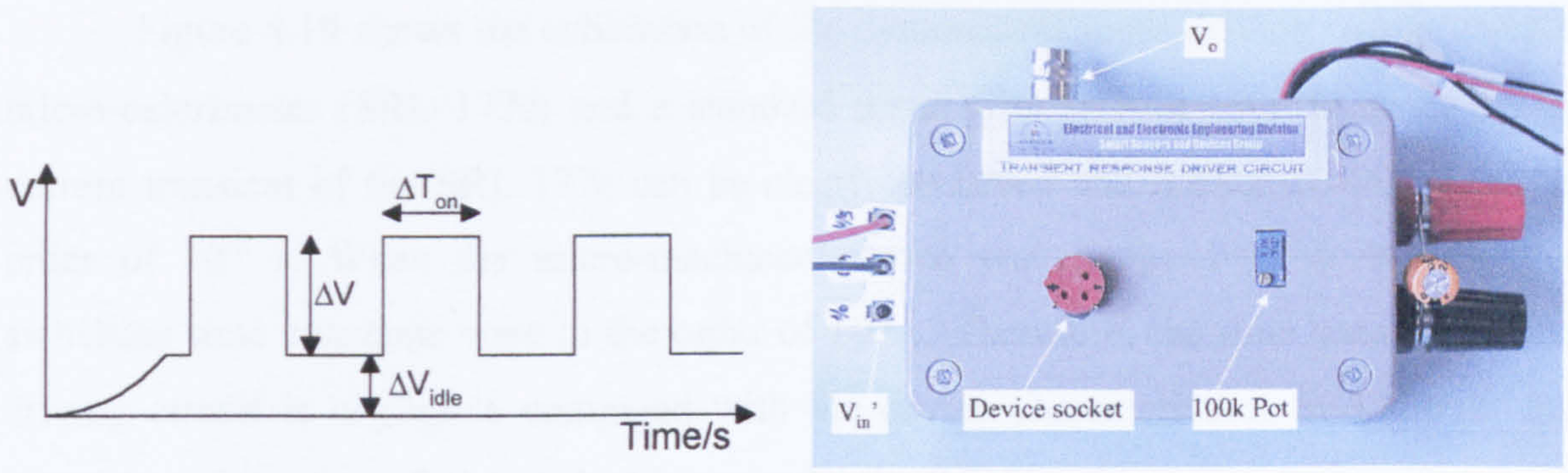

(a) (b)

Figure 4.17: The dynamic driving protocol and the driving circuitry. (a) The fundamental driving protocol. (b) The packaged AC driving circuit.

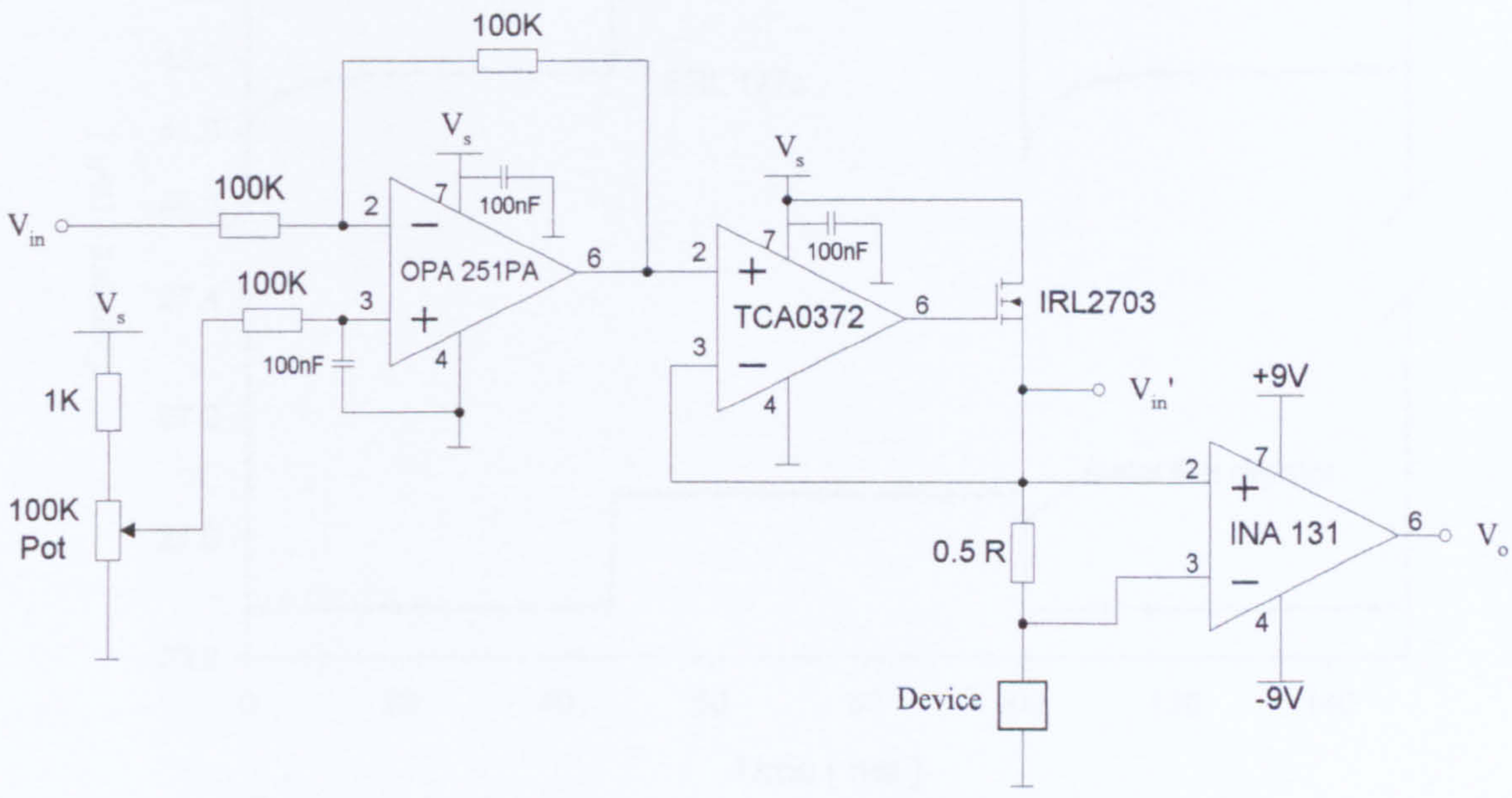

Figure 4.18: Circuit diagram of the driving circuit for the pulse-mode operation employing the micro-machined devices.

As this arrangement creates a constant voltage-driving source, the information about the voltage transient is excluded. Therefore, a current sensing resistor (0.5 Ω), which causes negligible voltage drop across the device, and an instrumentation amplifier (INA 131), with a fixed gain of 100, had been included to detect the current transient induced by the

device. The output signal (V_o) of the difference amplifier, is monitored by a digital storage oscilloscope, Tektronics TDS 210. The corresponding current can then be computed by Ohm's law from the readings that are obtained from the digital oscilloscope.

Figure 4.19 shows the calibration of the dynamic response driving circuit using a micro-calorimeter (SRL 177c) and a standard metal film resistor (100 Ω ± 1%). The current transient of the SRL 177c can be clearly observed and measured, and is in the order of 10^{-3} s. When the micro-machined device was replaced by a resistor, the switching time constants were in the order of 10^{-6} s. Therefore, the time constant of the driving circuit is negligible compared with the device characteristics. In addition, the signal-to-noise ratio at full scale had improved up to 0.01%.

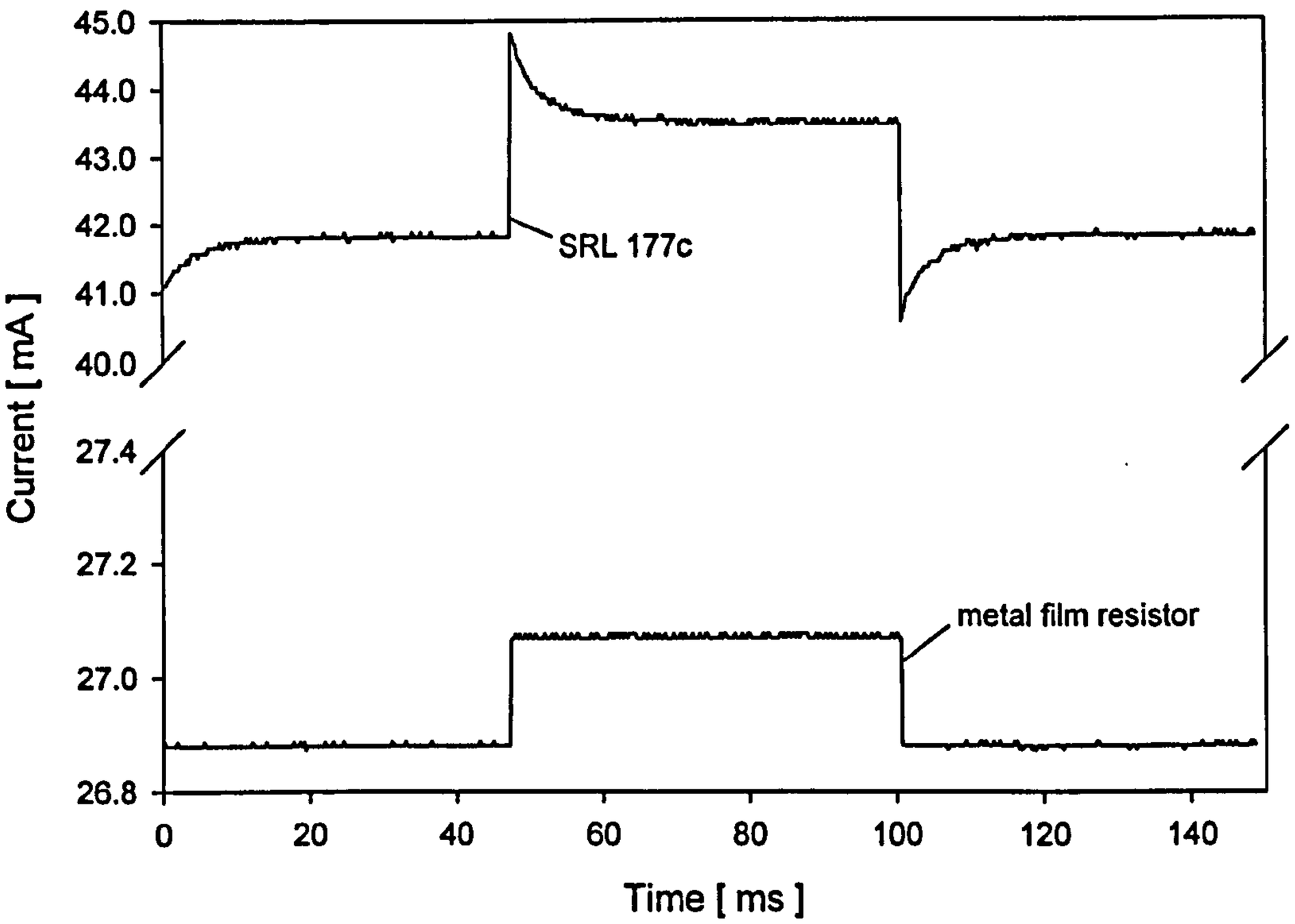

Figure 4.19: Calibration of the dynamic response driving circuit with micro-calorimeter and a standard metal film resistor, showing finite switching time constants of the micro-machined device.

4.6 Conclusions

This chapter described the different test equipment used to characterise the micro-calorimeters. A summary of the specifications of the gas-test systems and custom instrumentations is shown in table 4.1. The basic structure of the main gas-test system

and part of the sensor chamber is based upon an existing design. This system allows four pairs of sensors to be characterised simultaneously.

An overview of an industrial gas-test system for commercial pellistors at City Technology Ltd. UK has been provided. This system was used to compare the response of micro-machined devices with commercial pellistors. By using such a system, the improvements of the micro-machined devices can be verified.

Table 4.1: Specifications of the micro-calorimeter characterisation systems and customised electronics.

Specifications	Values
1. Main gas-test system	
Maximum flow rate	500 ml/ min
Time constant of the gas flow	6s – 10s
Data logging rate	10 k Hz
Maximum current drive	1 A
Maximum supply voltage	24 V
Maximum input voltage to the Wheatstone bridge interface	22 V
Detection range	± 10 V
Signal-to-noise ratio at full scale	0.007 %
2. Industrial gas-test system	
Maximum flow rate	600 ml/ min
Data logging rate	0.5 Hz
Maximum supply voltage	30 V
Maximum input voltage to the Wheatstone bridge interface	30 V
3. Life-time testing system	
Maximum input voltage	15 V
Maximum input current	150 mA
Accuracy of the hour-meter	± 30 s per 8 hours
4. A.C. power driver and measuring system	
Rang of the output voltage	0 V – 12 V
Maximum current drive	1 A
Maximum frequency	1 M Hz
Signal-to-noise ratio at full scale	0.01 %

A life-time test system has also been developed. It allows two devices to be tested simultaneously for an extended period of time. An automated failure detection circuit was designed to sense the breakdown of the device and to record the length of operation.

An A.C. power driver and measuring system was also developed to facilitate the investigation of the dynamic response for the micro-calorimeters. This allows amplitude, frequency and the idle voltage of the driving waveform to be varied. Therefore, various driving strategies can be generated in order to evaluate a variety of micro-calorimeter designs. The system can either be operated alone for time constant measurement, or used in conjunction with other test equipment, such as the gas-test systems.

References

[4.1] A. Pike, Design of chemoresistive silicon sensors for application in gas monitoring, *PhD Thesis*, University of Warwick, Chapter 7, p162, 1996.

[4.2] J. A. Covington, CMOS and SOI CMOS FET-based Gas sensors, *PhD Thesis*, University of Warwick, 2001.

[4.3] *The 4-series Citicels® handbook*, City Technology Ltd., Operating instructions, PEL –5, 1999.

[4.4] *The 4-series Citicels® handbook*, City Technology Ltd., p44, 1999.

[4.5] *Product data handbook*, City Technology Ltd., p61, 1992.

Chapter 5

Steady-state device characterisation for micro-calorimeters

5.1 Introduction

The objective of this chapter is to provide the steady-state device characteristics of both generations of the micro-calorimeter designs. The Voltage – Current (V-I) characteristic of the micro-calorimeters has been investigated for all the micro-calorimeter designs. The temperature coefficient of resistivity (α) and the base-line resistance (R_o) were obtained by steady-state thermal characterisation of the resistive micro-heater. From these measurements and additional thermal calibration, it was concluded that the platinum micro-heater could then be used as a resistive thermometer.

As the various device parameters were obtained from the different characterisations, the relationship between the steady-state power consumption and the micro-heater temperature was established. The results were sorted according to their design families to investigate the relationship between power consumption and *MHR*. A power optimisation model based upon the *MHR* is then proposed.

Distribution of the heat loss by different mechanisms is also evaluated to improve understanding necessary for device optimisation. Thermal images were acquired by infrared microscopy for surface temperature profile analysis. Therefore, the thermal distribution of the active area can be assessed to verify the performance of the micro-heater designs. Finally, the breakdown field strength of the silicon nitride was investigated to ensure that the electrical isolation would not be affected during measurements.

5.2 Voltage – Current (V-I) characteristics

This characterisation provided the voltage and current relationship and allowed the corresponding device resistance to be calculated. These are critical device parameters for performance evaluation, and are used for the analysis of the power consumption as discussed in section 5.4. The characterisation set up consisted of a constant source (Knick DC Calibrator J 152), digital multimeter (1503 HA by Thurlby) and a customised device holder, as shown in figure 5.1.

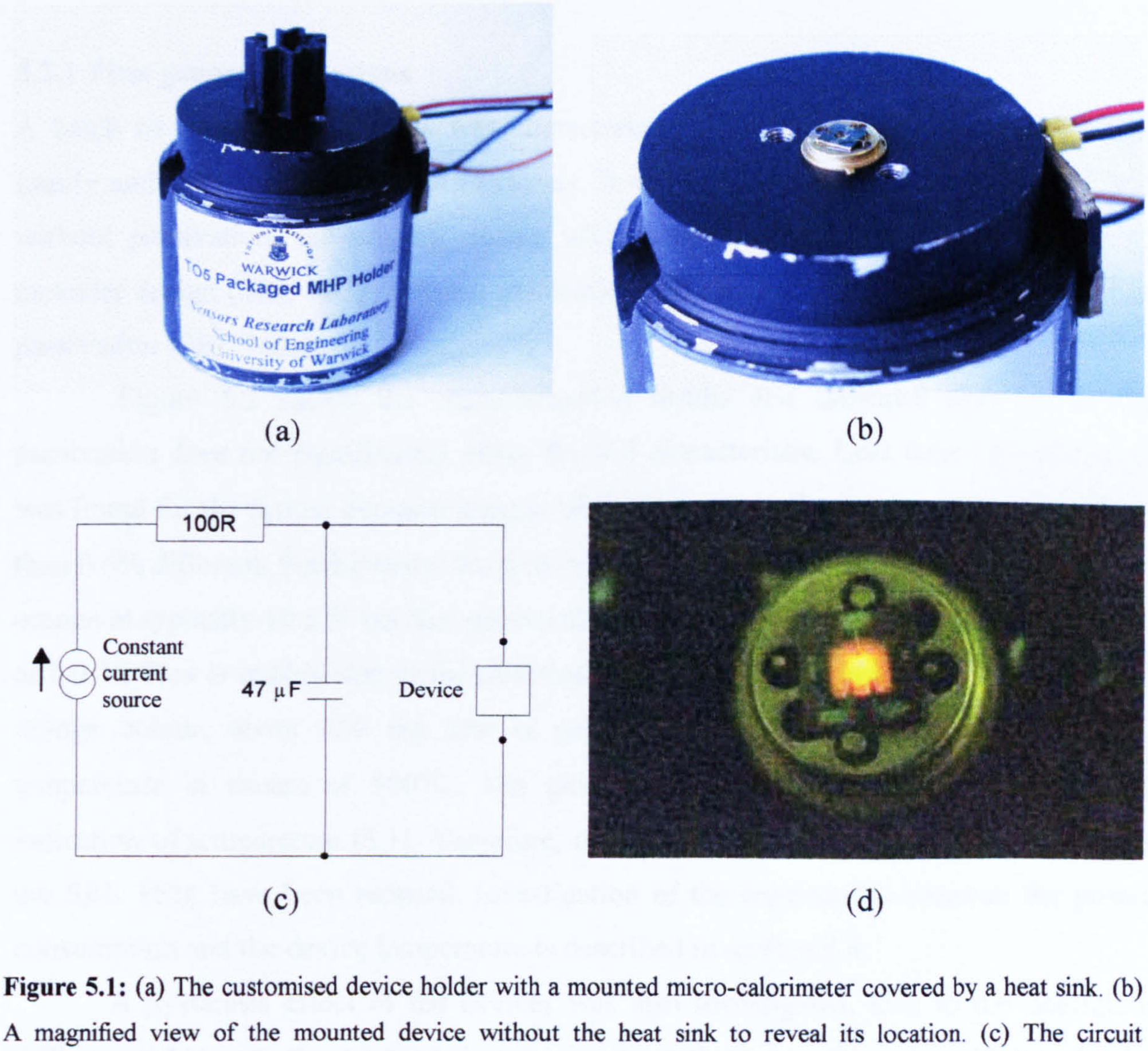

Figure 5.1: (a) The customised device holder with a mounted micro-calorimeter covered by a heat sink. (b) A magnified view of the mounted device without the heat sink to reveal its location. (c) The circuit diagram of the built-in low-pass filter. (d) A micro-calorimeter (SRL 162g) glowing red hot with a power consumption of about 100 mW.

The aluminium device holder allowed the device under test to be harnessed securely and handled conveniently. The holder and the heat sink act as a thermal grounding for the TO-5 package. This is an essential measure to minimise thermal noise during

characterisation. Moreover, the entire holder was painted matt black in colour to reduce the emissivity when imaging, using an IR microscope system.

A built-in RC filter was included with the holder (see figure 5.1(c)) because the input transient upon power up could cause membrane rupture. All characterisations were performed in a temperature-controlled laboratory, regulated to 22°C. The devices were powered up at a range of current values until the temperature of the micro-heater was sufficiently high to glow orange, as shown in figure 5.1(d). All the numerical results are tabulated in Appendix 5a.

5.2.1 First generation designs

A batch of twenty-four devices was characterised with six devices from each design family and their variants selected randomly. It included the original design (SRL 136a) without passivation, the original design with passivation (SRL 136p), the optimised meander design (SRL 162g) without passivation and the optimised meander design with passivation (SRL 162p).

Figure 5.2 shows the characterisation results and indicates that the device passivation does not significantly affect the V-I characteristic. Less than 1% difference was found for the former meander design, while the optimised meander designs were less than 0.6% different. Furthermore, the former design (SRL 136a) would only start to glow orange at typically 10.5 V but the optimised meander design (SRL 162g) begins to glow at 8.0 V. This is mainly due to the different micro-heater resistance. The wavelength of orange colour, about 650 nm and is generated when the micro-heater reaches a temperature in excess of 500°C. The glowing of the micro-heater is a reasonable indication of temperature [5.1]. Therefore, this implied that the voltage requirements of the SRL 162g have been reduced. Investigation of the relationship between the power consumption and the device temperature is described in section 5.4.

A hysteresis effect of the devices was also investigated. Due to the negligible differences between the passivated and unpassivated devices (less than 1%), only the standard unpassivated devices are shown in figure 5.2. The graphs prove that the voltage hysteresis of the devices was minimal. Furthermore, figure 5.2 records the devices being powered up for the first time. It would be expected that any hysteresis effect would decrease as the membrane becomes annealed after being powered up repeatedly.

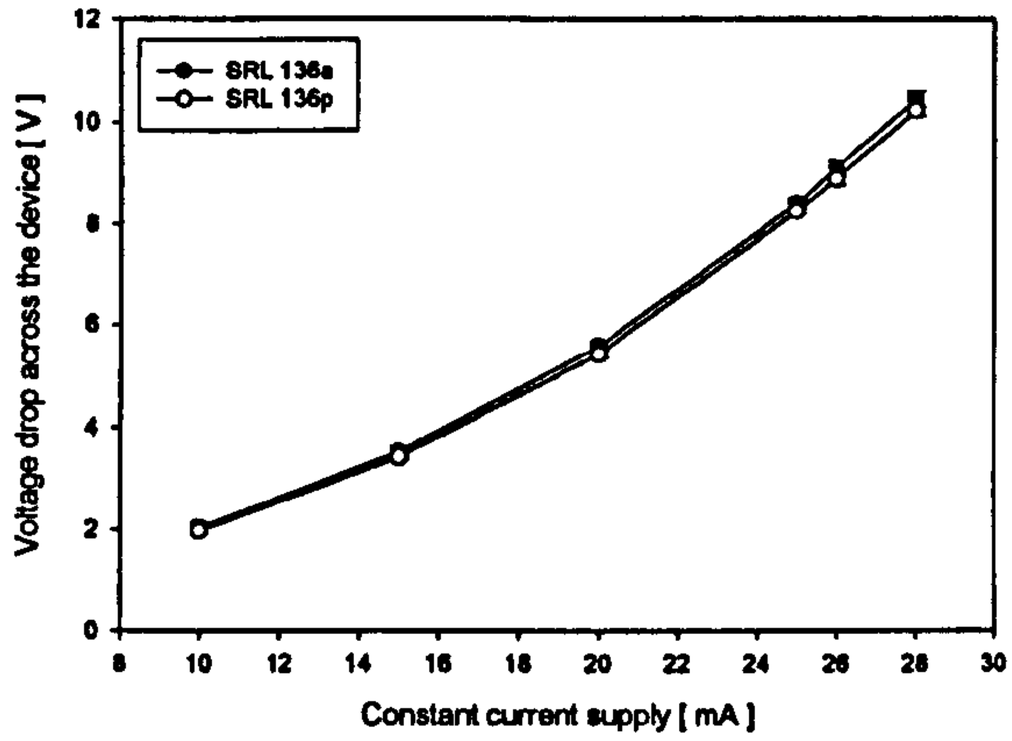

(a)

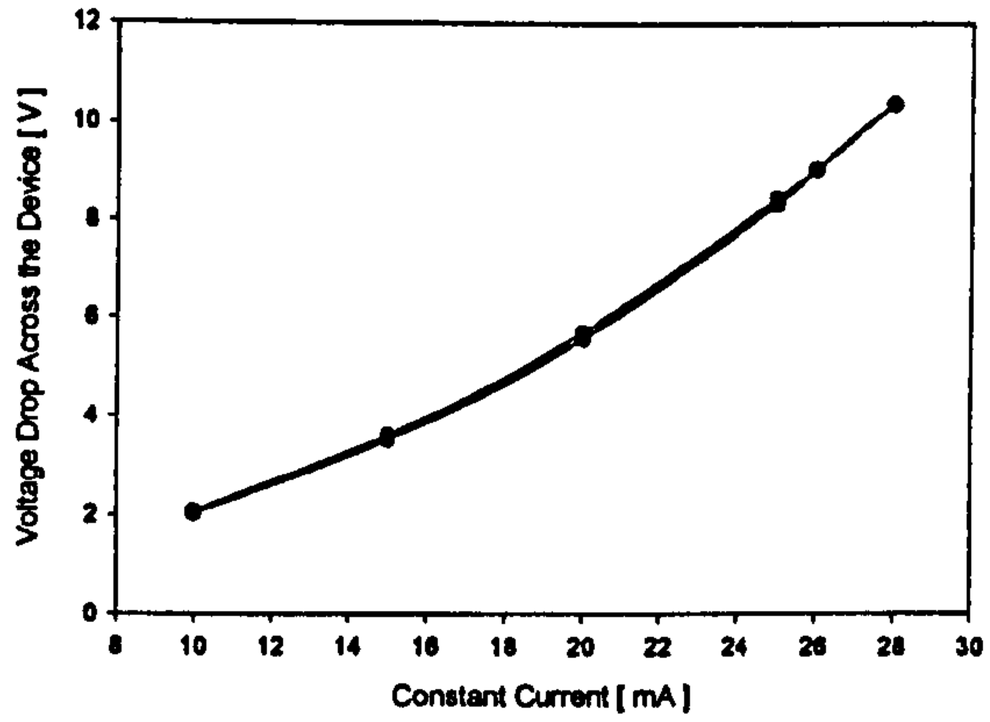

(b)

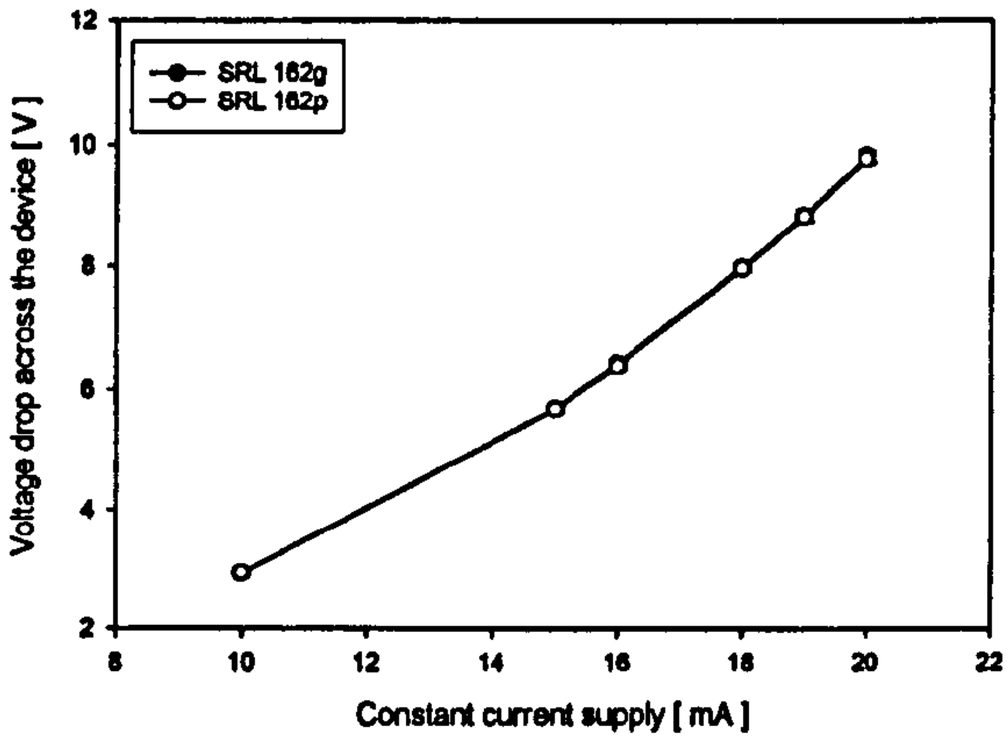

(c)

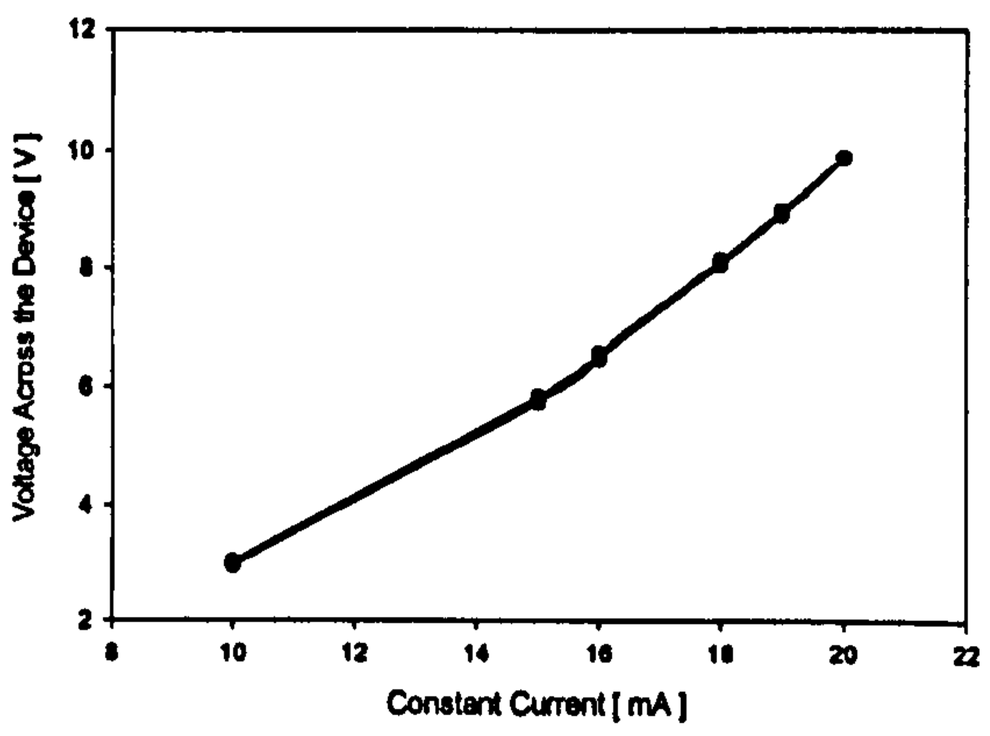

(d)

Figure 5.2: The average V-I characteristics (6 samples from each design) for the first generation devices with error bars. (a) The average V-I characteristics for the former meander designs (SRL 136a and SRL 136p). (b) Typical voltage hysteresis of SRL 136a. (c) The average V-I characteristics for the optimised meander designs (SRL 162g and SRL 162p). Here the two plots are almost the same. (d) Typical voltage hysteresis of SRL 162g.

5.2.2 Second generation designs

Due to the number of design families and variants in the second generation, there are potentials for a very large number of designs to be characterised. A limited number of device samples were strategically selected to obtain the most information. The sample set should reflect the regional inter-wafer process variations and the average power consumption of the devices.

Wafers 7, 8, and 10 were chosen to supply the devices required for the characterisation. Wafers 8 and 10 were unpassivated while wafer 7 was the only passivated wafer and previous results proved that they deliver improved performance for

both electrical and mechanical stability. All samples are single gate devices as the common gate variants were reserved to test wafer-level catalyst deposition.

One device was taken from each quadrant of wafer 7 and one device from the first quadrant of wafers 8 and 10 so that the performance across the entire wafer could be obtained. Devices were chosen from similar or the same location on different wafers in order to make direct comparisons for process variations. However, due to the smaller population of ultra-small families, two samples were taken from wafer 7 and one each from wafers 8 and 10. As SRL 136o, 162o and SRL 179d, 179e acted as reference devices, the number of samples taken was identical to the ultra-small families. Therefore, over one hundred device samples were selected for characterisation. Details of the number of samples, the location of the devices on the wafer and the numerical results are included in Appendix 5b.

Figures 5.3 to 5.8 show the V-I characteristics and the hysteresis of the main families in the second generation designs, namely the Standard family, Low power family, Small-mem/ robust family, Robust family, Ultra-small/ robust family and Ultra-small/ low power family. The voltage requirements of the devices had clearly been reduced as expected from the design specifications to below 5V. The fluctuations of the V-I characteristics were well below 2% for each type of device. No obvious differences were identified from the passivated devices. Furthermore, the hysteresis of the devices was minimal.

The V-I characteristics of the second generation of devices proved to be stable and reproducible. The device resistance corresponding to the voltage and power has been obtained. The parameters were employed to derive a relationship between the power and micro-heater temperature, as described in section 5.4.

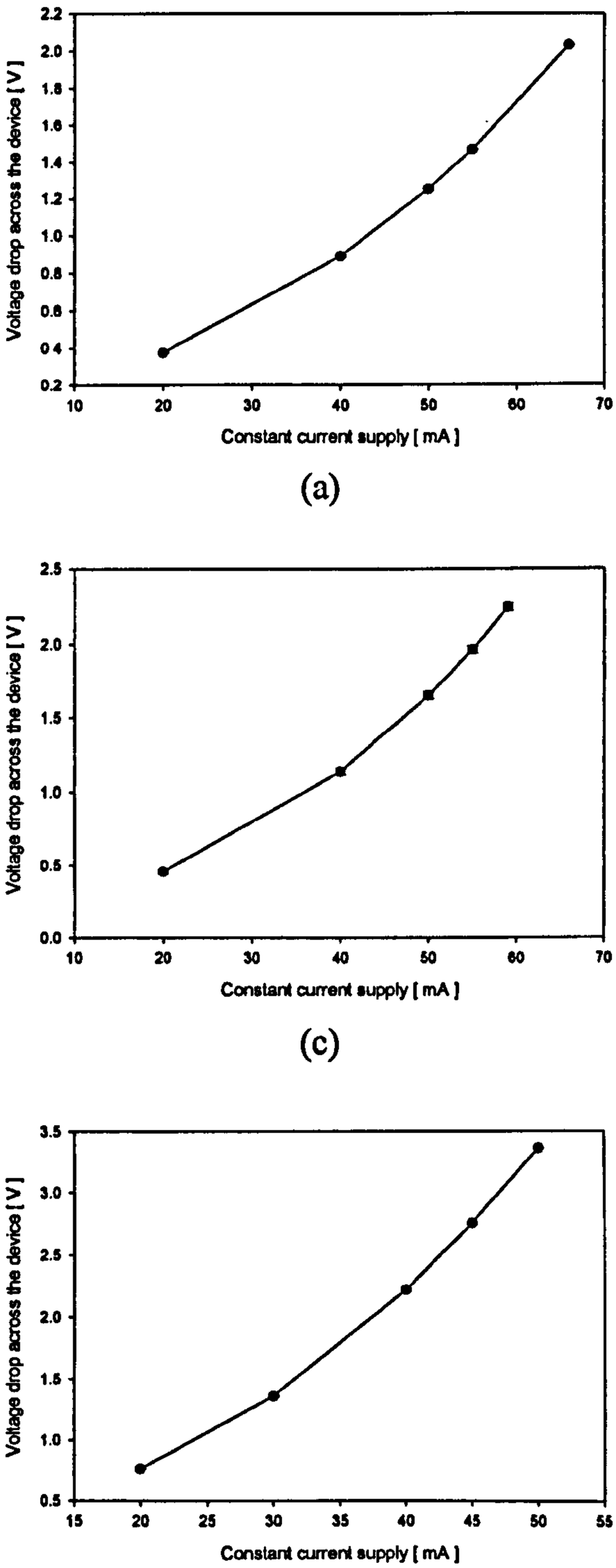

Figure 5.3: The V-I characteristic of the Standard family in second-generation devices with error bars. For the Ultra-low resistance design, SRL 176a, (a) the average V-I characteristic and (b) typical voltage hysteresis. For the Honeycomb design, SRL 176b, (c) the average V-I characteristic and (d) typical voltage hysteresis. For the Drive-wheel design, SRL 176c, (e) the average V-I characteristic and (f) typical voltage hysteresis.

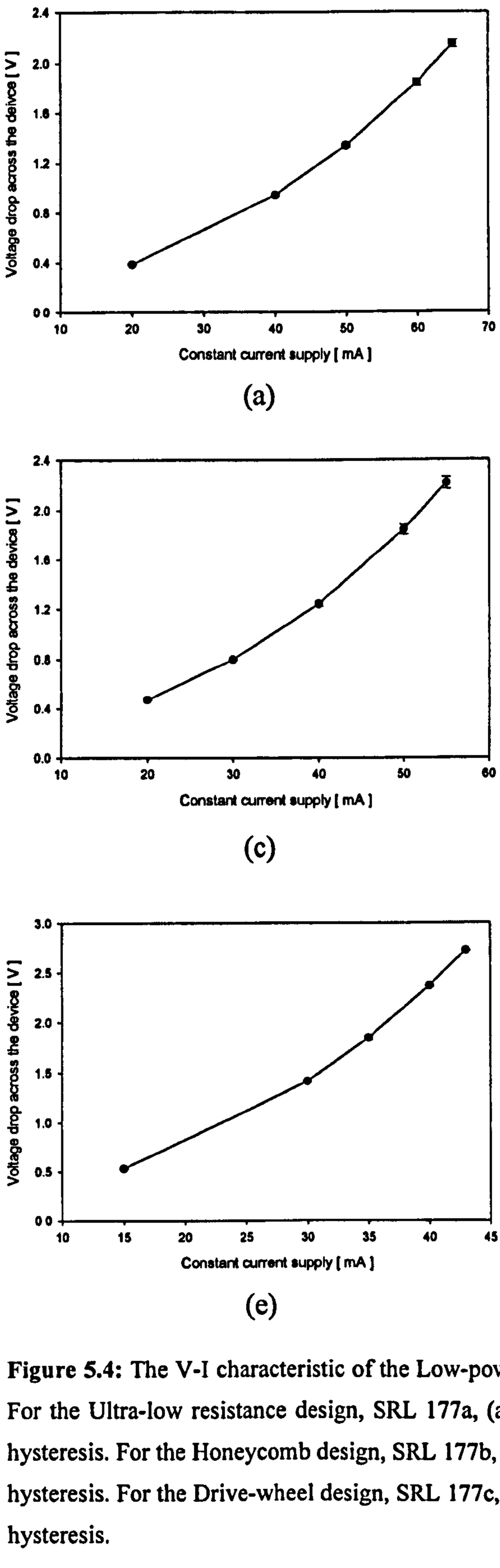

Figure 5.4: The V-I characteristic of the Low-power family in second-generation devices with error bars. For the Ultra-low resistance design, SRL 177a, (a) the average V-I characteristic and (b) typical voltage hysteresis. For the Honeycomb design, SRL 177b, (c) the average V-I characteristic and (d) typical voltage hysteresis. For the Drive-wheel design, SRL 177c, (e) the average V-I characteristic and (f) typical voltage hysteresis.

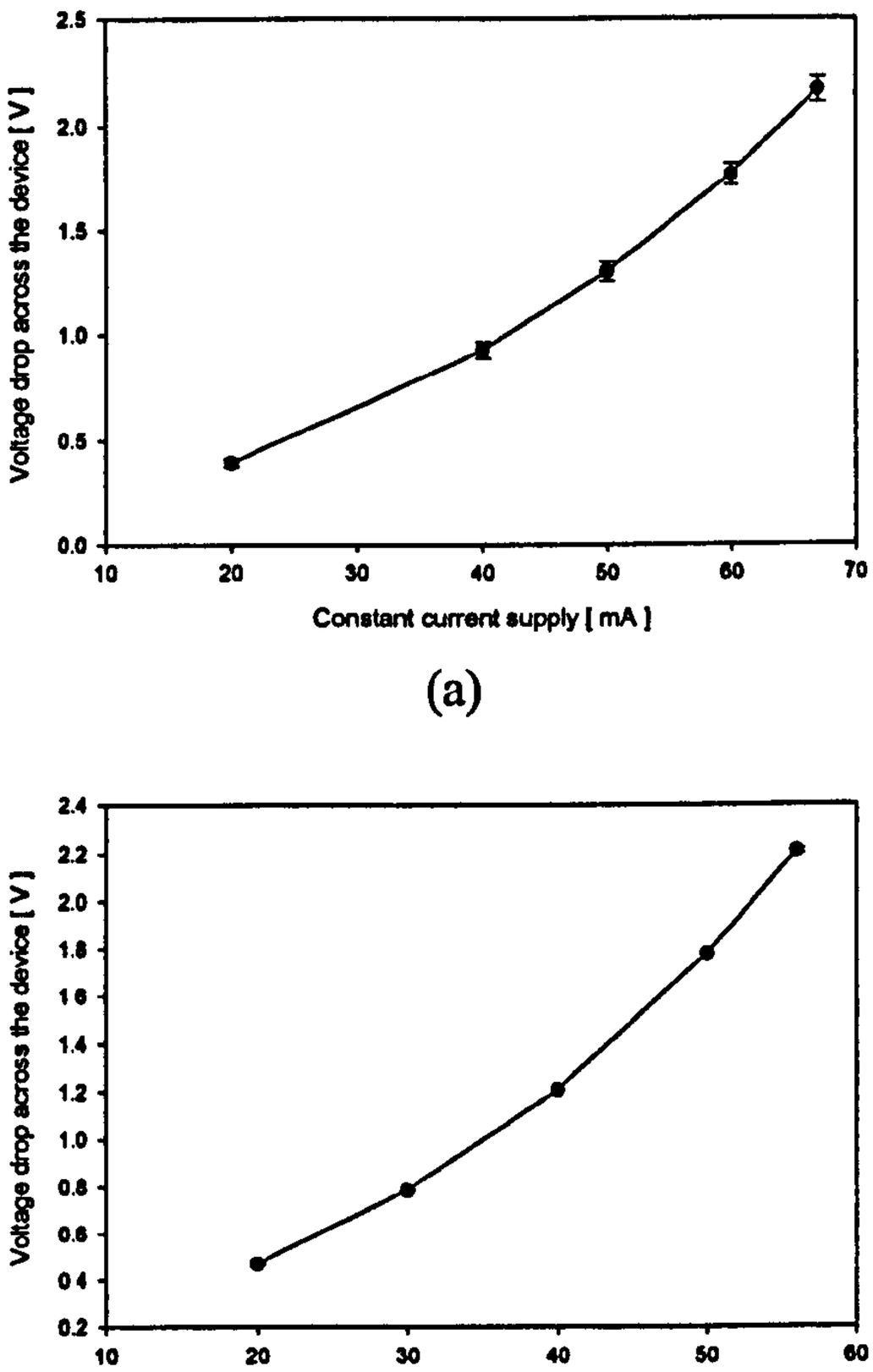

Figure 5.5: The V-I characteristic of the Small-mem/ robust family in second-generation devices with error bars. For the Ultra-low resistance design, SRL 178a, (a) the average V-I characteristic and (b) typical voltage hysteresis. For the Honeycomb design, SRL 178b, (c) the average V-I characteristic and (d) typical voltage hysteresis. For the Drive-wheel design, SRL 178c, (e) the average V-I characteristic and (f) typical voltage hysteresis.

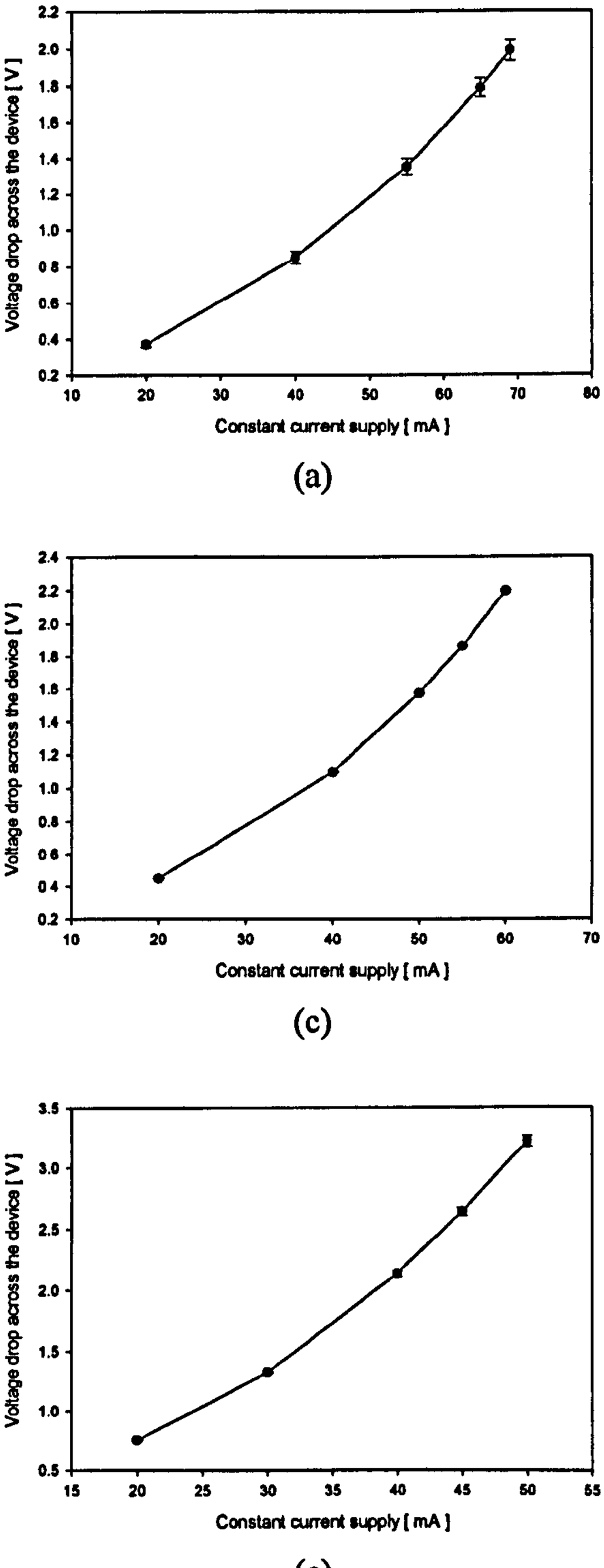

Figure 5.6: The V-I characteristic of the Robust family in second-generation devices with error bars. For the Ultra-low resistance design, SRL 179a, (a) the average V-I characteristic and (b) typical voltage hysteresis. For the Honeycomb design, SRL 179b, (c) the average V-I characteristic and (d) typical voltage hysteresis. For the Drive-wheel design, SRL 179c, (e) the average V-I characteristic and (f) typical voltage hysteresis.

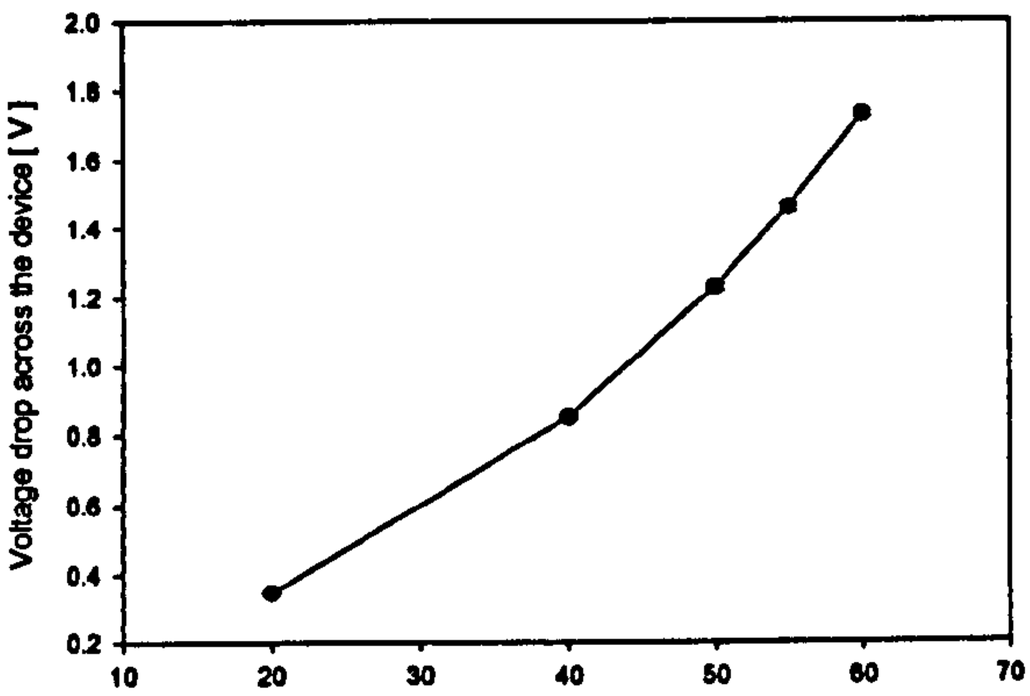

(a)

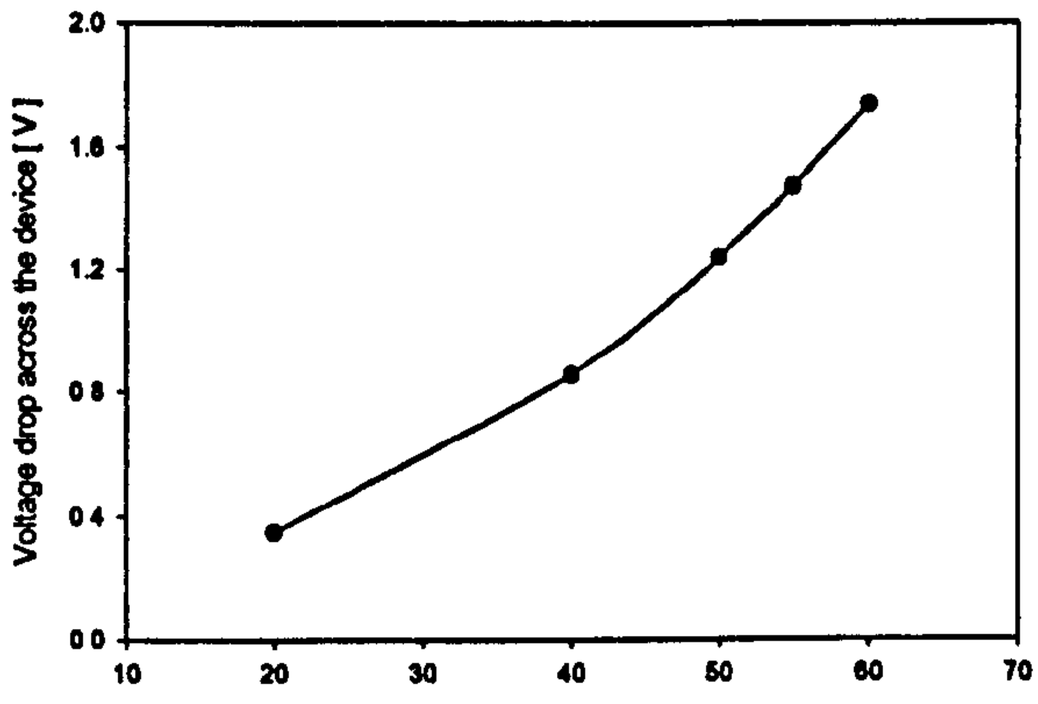

(b)

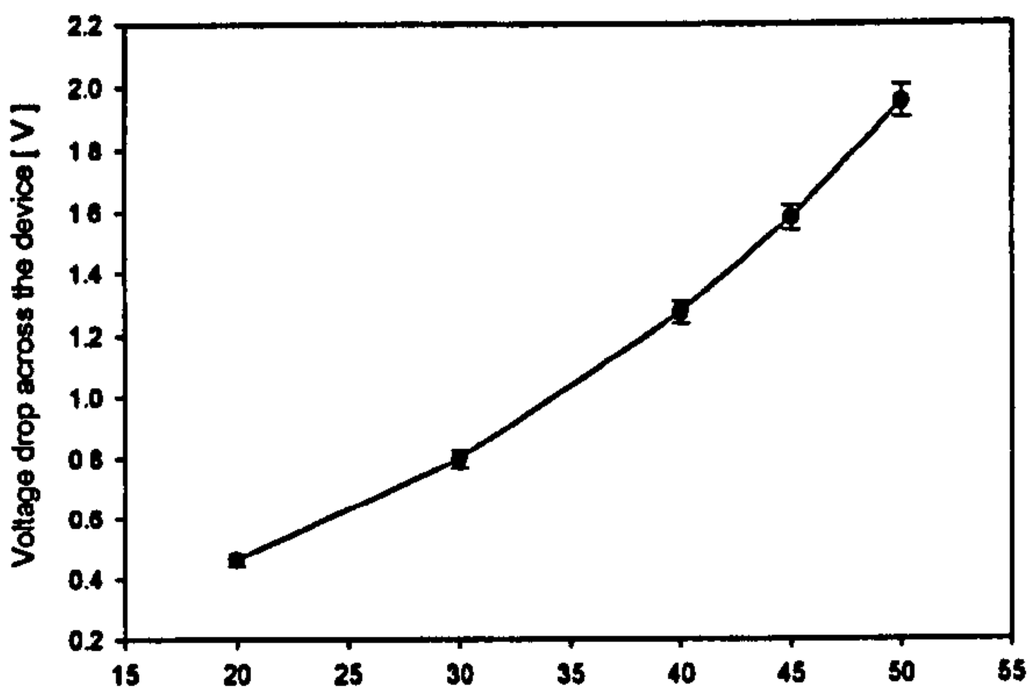

(c)

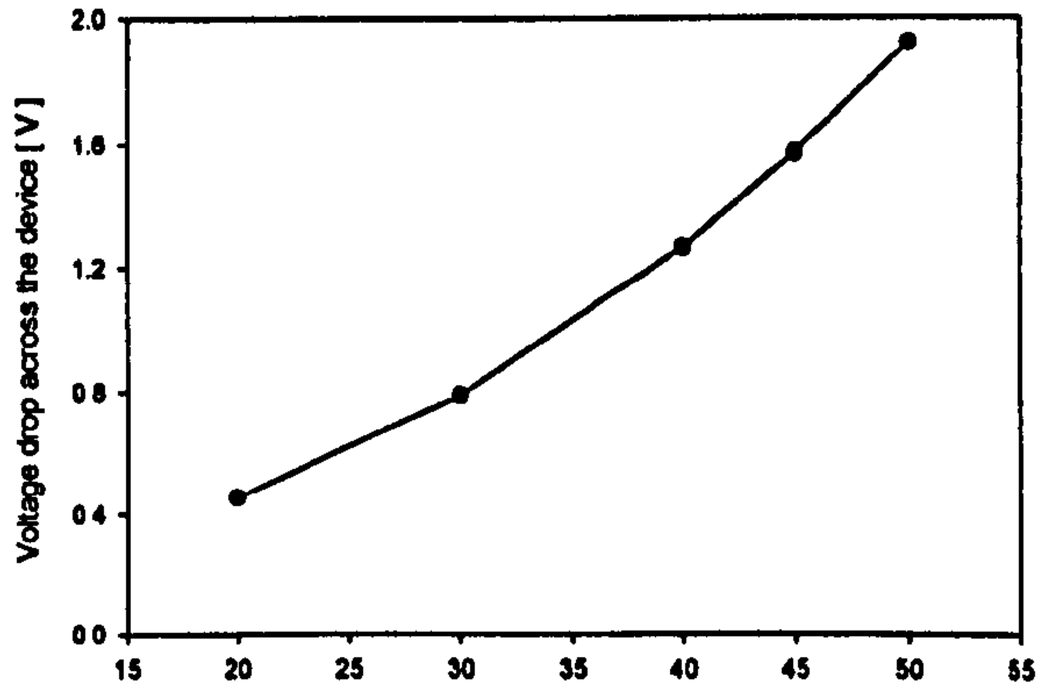

(d)

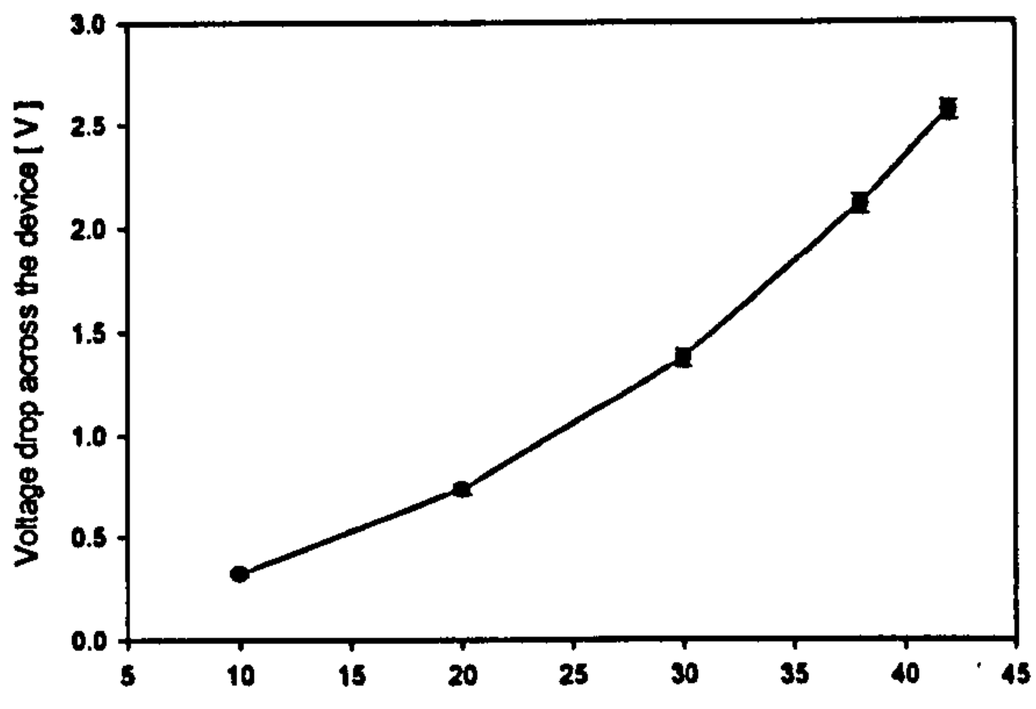

(e)

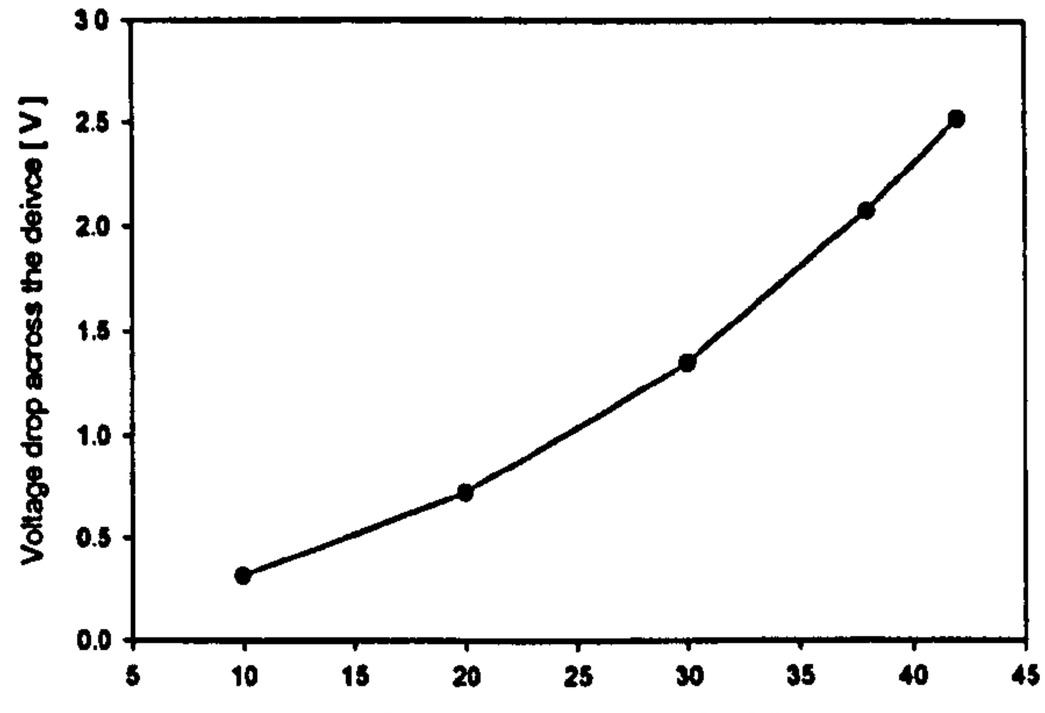

(f)

Figure 5.7: The V-I characteristic of the Ultra-small/ robust family in second-generation devices with error bars. For the Ultra-low resistance design, SRL 180a, (a) the average V-I characteristic and (b) typical voltage hysteresis. For the Honeycomb design, SRL 180b, (c) the average V-I characteristic and (d) typical voltage hysteresis. For the Drive-wheel design, SRL 180c, (e) the average V-I characteristic and (f) typical voltage hysteresis.

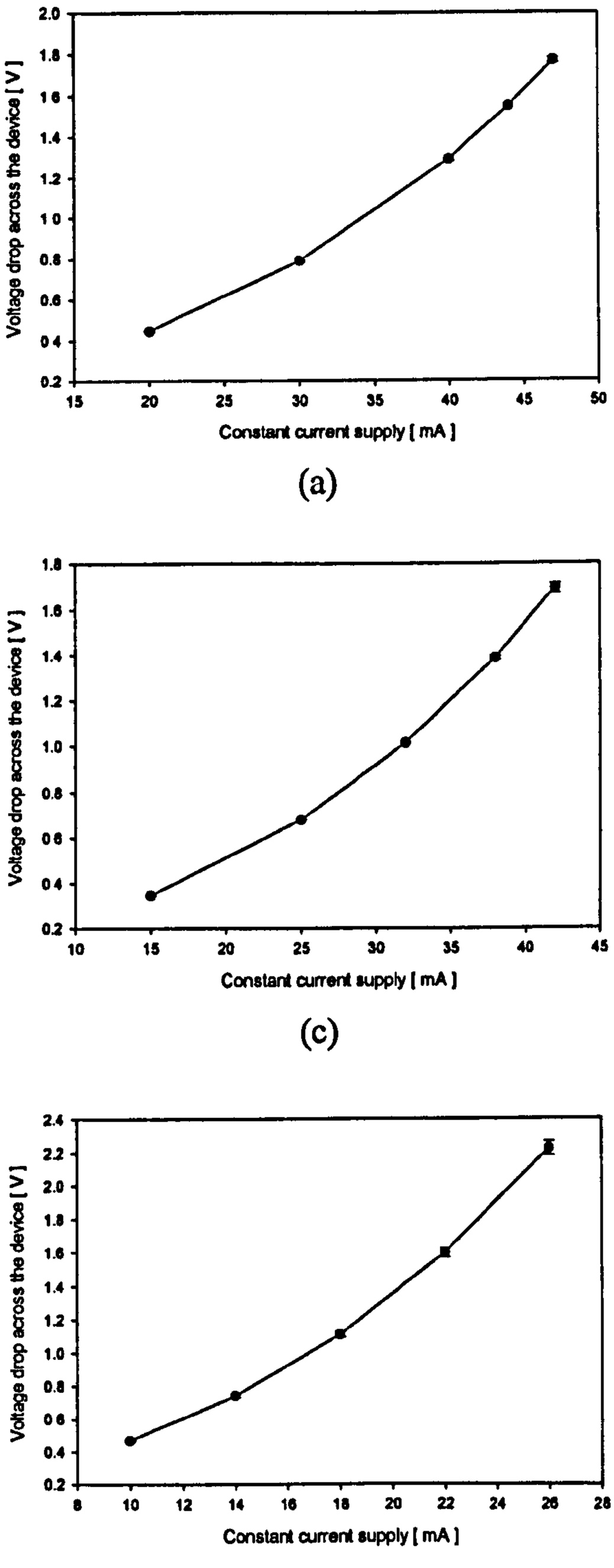

Figure 5.8: The V-I characteristic of the Ultra-small/ low-power family in second-generation devices with error bars. For the Ultra-low resistance design, SRL 181a, (a) the average V-I characteristic and (b) typical voltage hysteresis. For the Honeycomb design, SRL 181b, (c) the average V-I characteristic and (d) typical voltage hysteresis. For the Drive-wheel design, SRL 181c, (e) the average V-I characteristic and (f) typical voltage hysteresis.

5.3 Steady-state thermal characterisation

In order to obtain the base-line resistance, R_o, and the linear temperature coefficient of the micro-heater, α, a steady-state thermal characterisation has been performed on both device generations. The characterisation calibrated the micro-heater resistance against several known temperatures, without self-heating effects. These are also crucial parameters in assessing the material properties, such as sheet resistance, and the device performance. Furthermore, the platinum micro-heater itself could be calibrated and eventually be used as a thermometer to obtain its own temperature. All numerical results are tabulated in Appendices 5a and 5b.

5.3.1 Low temperature characterisation

As the devices required to be characterised against some fixed temperature, a laboratory convectional oven, Model-F manufactured by LabPak Ltd. UK, was used to set the temperature externally and so elevate the relative resistance change of the devices, as shown in figure 5.9(a). Due to the large number of device samples, a customised device probe was constructed to accommodate up to six devices in the oven. Therefore, an array of devices could be characterised simultaneously. As ordinary wire insulation cannot withstand a temperature above 120°C, glass capillary tubes were employed as insulation. The tubes were moulded into a circular grout head and the gold connectors were soldered to the end of the wire, as shown in figure 5.9(c). The devices were inserted into the oven, as shown in figure 5.9(d), and the resistances were measured remotely with a digital multimeter, 1503HA manufactured by Thurlby, to minimise temperature fluctuations

Due to the remarkable linearity of the temperature coefficient for platinum up to 800°C [5.2], the devices were only characterised between 20°C and 180°C and results were extrapolated up to 700°C. The device samples from both device generations were identical to those used for the V-I characterisation. The statistics of the characterisation results for the first and second generation designs are given in tables 5.1 and 5.2, respectively.

The temperature coefficient of resistivity (TCR) of the platinum (α) is independent from the micro-heater geometry but largely process related. The average TCR is 1.66×10^{-3} /°C for the first generation devices, with a standard deviation of only 2.5%. The base-line resistance, R_o for each device type was remarkably consistent, within 2% tolerance. The R_o for devices with additional passivation are nearly identical to the

unpassivated device, especially for the optimised meander devices with a typical deviation of 3% for the former meander designs.

(a)

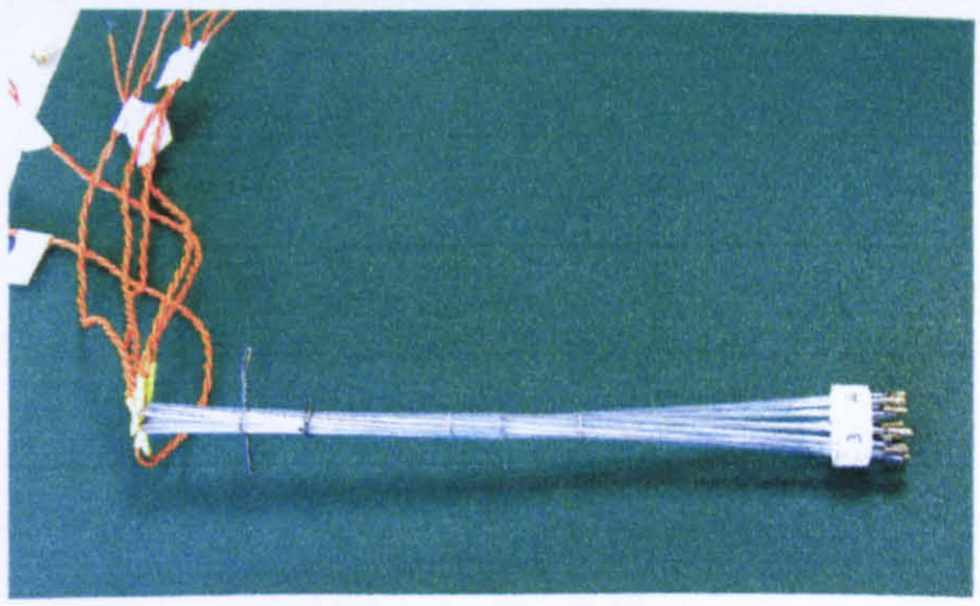

(b)

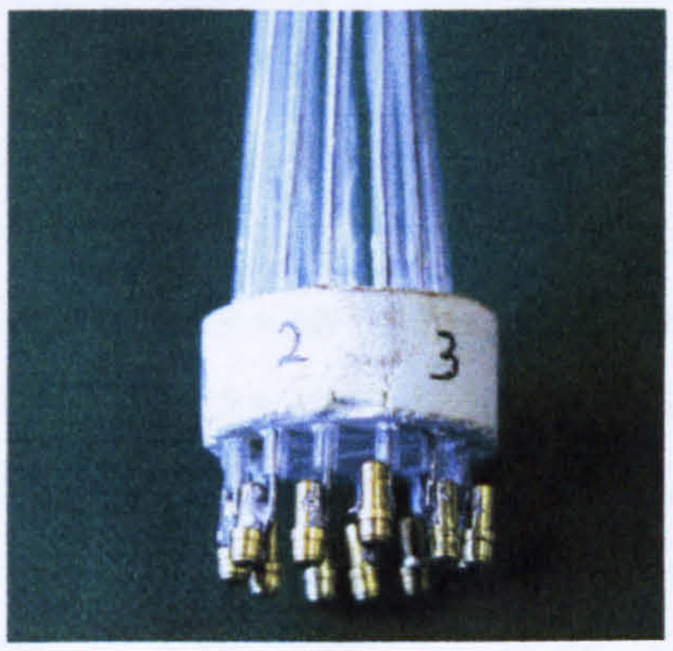

(c)

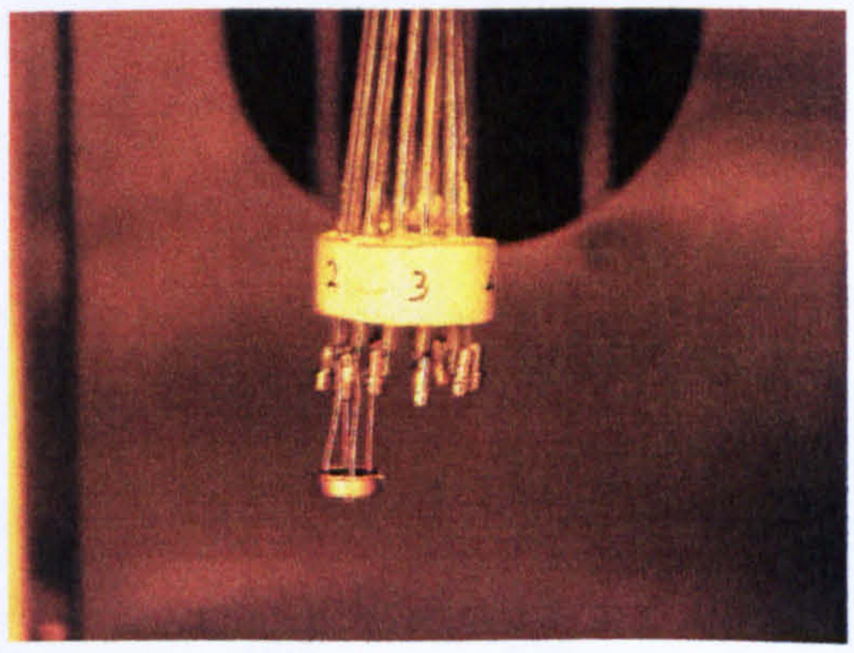

(d)

Figure 5.9: (a) The laboratory convectional oven (Model-F manufactured by LabPak Ltd. UK) and (b) the customised device probe. (c) The close-up view of the probe head, showing the gold connectors and the glass capillary tubes cast into the grout head. (d) The probe placed in the oven holding a device.

Table 5.1: Statistics of the platinum micro-heater properties from the low-temperature steady-state thermal characterisation for first-generation devices.

	Temperature coefficient of Resistance, α (/ °C)		Base-line resistance, R_o (Ω)	
	Mean	Standard deviation	Mean	Standard deviation
SRL 136a	1.67×10^{-3}	7.48×10^{-5}	173.7	4.28
SRL 136p	1.74×10^{-3}	1.21×10^{-4}	167.3	4.11
SRL 162g	1.66×10^{-3}	4.80×10^{-5}	220.5	2.67
SRL 162p	1.66×10^{-3}	3.93×10^{-5}	220.9	2.53

Table 5.2: Statistics of the platinum micro-heater properties from the low-temperature steady-state thermal characterisation for second-generation devices.

	Temperature coefficient of Resistance, α (/ °C)		Base-line resistance, R_o (Ω)	
	Mean	Standard deviation	Mean	Standard deviation
SRL 136o	2.12×10^{-3}	2.73×10^{-5}	147.1	1.64
SRL 162o	2.12×10^{-3}	3.79×10^{-4}	192.2	1.27
SRL 176a	2.16×10^{-3}	6.76×10^{-5}	17.0	0.18
SRL 176b	2.16×10^{-3}	6.72×10^{-5}	20.1	0.38
SRL 176c	2.18×10^{-3}	8.04×10^{-5}	31.8	1.22
SRL 177a	2.14×10^{-3}	3.28×10^{-5}	17.3	0.10
SRL 177b	2.13×10^{-3}	5.36×10^{-5}	20.7	0.12
SRL 177c	2.13×10^{-3}	5.41×10^{-5}	31.1	1.37
SRL 178a	2.15×10^{-3}	4.45×10^{-5}	17.9	0.69
SRL 178b	2.22×10^{-3}	2.98×10^{-5}	20.4	0.18
SRL 178c	2.18×10^{-3}	4.80×10^{-5}	30.4	0.59
SRL 179a	2.12×10^{-3}	2.30×10^{-5}	17.2	0.47
SRL 179b	2.20×10^{-3}	1.44×10^{-5}	20.0	0.13
SRL 179c	2.19×10^{-3}	3.18×10^{-5}	31.3	0.21
SRL 179d	2.15×10^{-3}	2.24×10^{-5}	189.3	0.89
SRL 179e	2.16×10^{-3}	3.50×10^{-5}	146.7	1.51
SRL 180a	2.18×10^{-3}	3.77×10^{-5}	15.5	0.13
SRL 180b	2.18×10^{-3}	3.56×10^{-5}	19.8	0.66
SRL 180c	2.19×10^{-3}	5.04×10^{-5}	29.2	0.91
SRL 181a	2.21×10^{-3}	5.53×10^{-5}	18.6	0.18
SRL 181b	2.17×10^{-3}	5.64×10^{-5}	20.1	0.10
SRL 181c	2.17×10^{-3}	2.19×10^{-5}	39.4	0.34

The second silicon fabrication run had further improved the consistency of the material properties, as shown in table 5.2. The TCR is about 2.15×10^{-3} /°C with a tolerance of 2% for all the other devices. Furthermore, R_o was also improved with a tolerance of only about 1% for each of the device types.

As each of the devices had a locator code, it was found that the device resistance of the forth quadrant on the wafer tested was higher than the rest. This could be caused by a non-uniformity of the layer thickness or impurities on the wafer. Nevertheless, the devices exhibited remarkable consistency of the material properties and the manufacturability of the micro-calorimeter has been proven.

The sheet resistances, R_{sheet}, of the platinum micro-heater from each of the device generations were computed, as shown in equation (5.1).

$$R_{sheet} = \frac{R_H}{A.R.} \tag{5.1}$$

The measured micro-heater resistance is denoted by R_H and the $A.R.$ is the aspect ratio of the micro-heater. Therefore, based on the geometry of the optimised meander micro-heater design, the measured sheet resistance for the first and second generation devices were 1.16 Ω/sq and 1.01 Ω/sq, respectively.

5.3.2 High temperature characterisation

Although the low temperature characterisation provided an efficient way to obtain the essential parameters, it was equally important to demonstrate the superior linearity of the platinum micro-heater. Therefore, the accuracy of the parameters from the low temperature characterisation could be verified. As the epoxy resin used for the device bonding does not withstand temperatures in excess of 200°C, an alternative bonding technique was employed on a different set of samples. However, this did not require the full range of devices and a pair was selected from the device types that had undergone characterisation, namely the SRL 162g, SRL 177c, SRL 180c and SRL 181c.

Allicin compound was used to temporally glue the device onto the TO-5 header before it was wire-bonded. The silicon die was then released by dissolving the organic enzyme in water for 30 minutes. The compound is quick-to-dry, provides good adhesiveness, it is non-toxic and completely soluble in water. Furthermore, it is extremely low cost since it can be readily extracted from garlic.

The bonded devices were placed into a furnace (TF75 manufactured by Severn Furnaces Ltd.) and the temperature was regulated by a Eurotherm 818P digital controller and a thermocouple, as shown in figure 5.10(a). The characterisation performed ranged from 22°C to 600°C and the results are shown in figure 5.10(b).

The characterisation results indicated remarkable linearity of the micro-heater resistance up to 600°C. Moreover, the R_o and the TCR were within 2% of the average values compared to the low temperature calibration. Therefore, the validity of the low temperature steady-state characterisation has been shown.

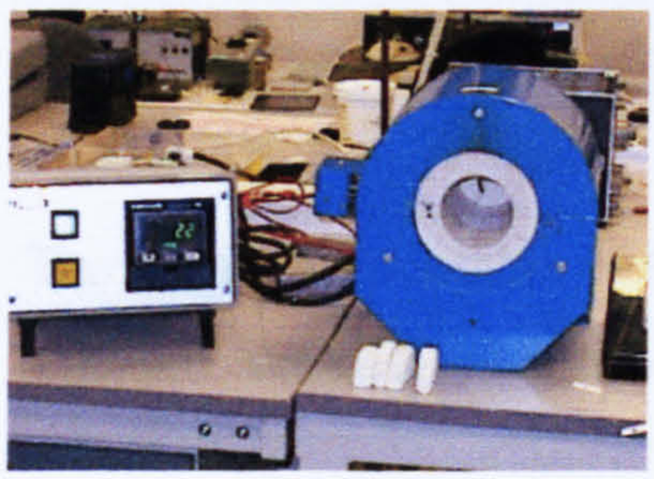

(a)

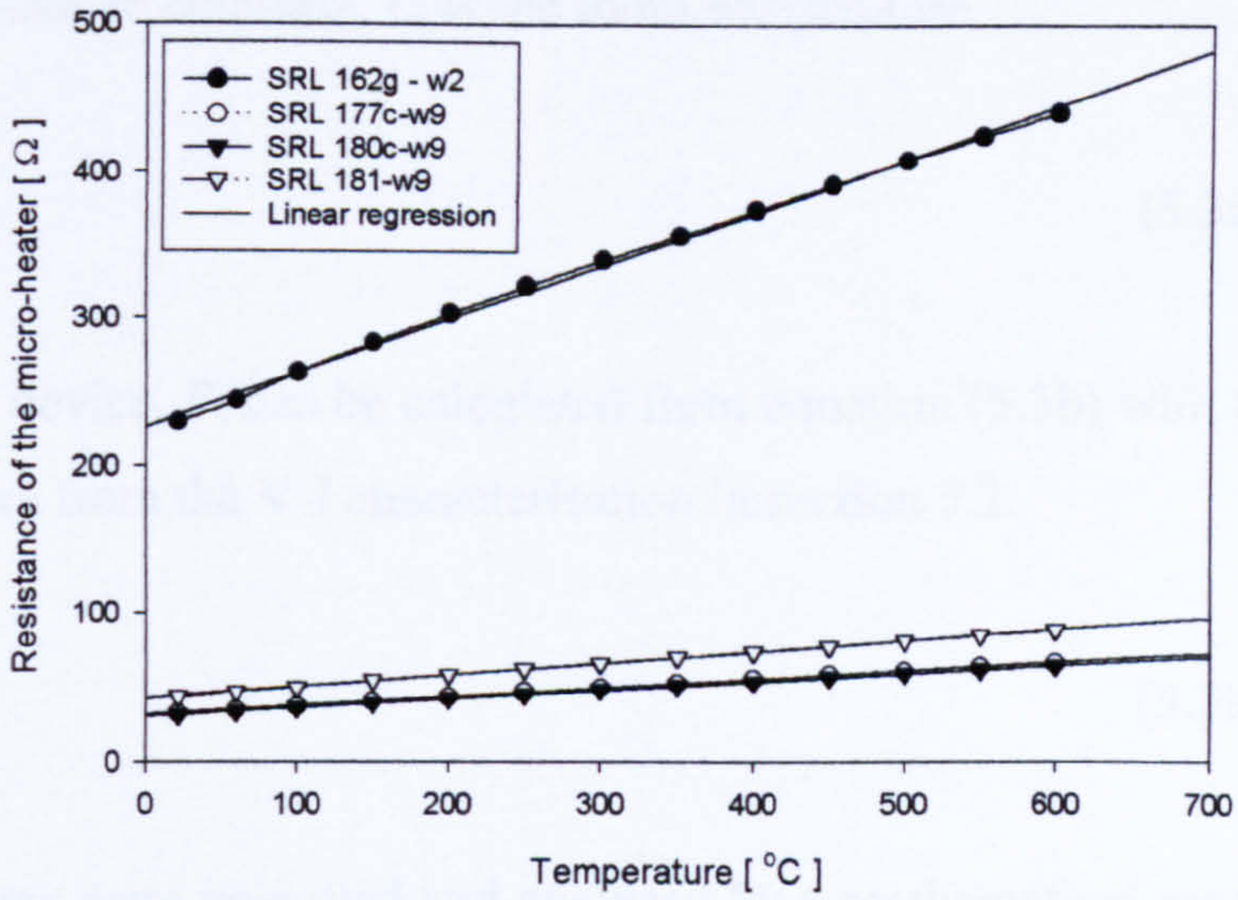

(b)

Figure 5.10: High temperature characterisation. (a) The electrical furnace and the temperature control unit. (b) The characterisation result, showing the linearity of the temperature coefficient of resistance for the selected devices.

5.4 Power consumption of the micro-calorimeters

The power consumption of the micro-calorimeter depends on a range of factors that are inter-related, as expressed in equation 5.2. Here the thickness of the membrane is assumed constant. These factors are responsible for the different thermal transfer mechanisms described in equation (5.4a).

$$P = f(MHR, R_o, \alpha, A_{heater}, \varphi, A_{chip}) \tag{5.2}$$

where MHR is the Membrane-to-heater ratio; R_o is the base-line resistance; α is the temperature coefficient of resistivity; A_{heater} is the area of the micro-heater; φ is the percentage of the micro-heater coverage and A_{chip} is the area of the chip.

The temperature dependence of the micro-calorimeter is expressed by the temperature coefficient of resistivity, α, of the platinum resistor and the base-line resistance, R_o, as shown in equation (5.3a) [5.3]. These two essential parameters are provided from the

characterisations described earlier, so the micro-heater resistance (R_T) at different temperatures (T) in Kelvin (K) can be obtained. T_o is the room temperature.

$$R_T = R_o\left(1+\alpha(T-T_o)\right) \tag{5.3a}$$

The power consumption of the device, P, can be calculated from equation (5.3b) with the constant current (I) measurement from the V-I characterisation in section 5.2.

$$P = I^2 R_T \tag{5.3b}$$

The data for various device types were compiled and analysed by a mathematical model for the total power loss (P) through various mechanisms, as given in equation (5.4a) [5.4]. The model consists of conduction loss via the membrane, P_c, convection loss to air, P_v and radiation loss, P_r.

$$P = P_c + P_v + P_r \tag{5.4a}$$

The individual terms can be related to temperature by an empirical model as shown in equation (5.4b) [5.5], where P (mW) is the power, T (K) is the micro-heater temperature and T_o (K) is the room temperature.

$$P = a(T-T_o) + b(T-T_o)^2 + c(T^4 - T_o^4) \tag{5.4b}$$

This model had been used to analyse the power consumption of all the devices from both the first and second generations, from 0°C to 700°C above ambient temperature. However, it is essential to note that the modelled micro-heater temperatures were the average temperature across the active area and the peak temperatures were higher. The mathematical proof of the model is included in Appendix 5c and further analysis is provided by the infrared thermography (section 5.6).

5.4.1 Power consumption of the first generation devices

The average power consumption of the first generation meander type micro-calorimeter design is shown in figure 5.11. The coefficients of the power curves are included in Appendix 5d. The standard deviation of each curve was less than 3% from the mean values. The *MHR* of the SRL 162g was optimised with a 31.6% increase from the former design, from 2.67 to 3.51. It proved that the power budget of the optimised meander device (SRL 162g) was reduced by 37% from the original design (SRL 136a), i.e. from 175 mW to 110 mW at 500°C. The performance of the devices was sustained regardless of the presence of the additional passivation layer.

Moreover, the local hot spot for the SRL 162g was reduced in size. General observation indicated that the SRL 162g could reach a higher average temperature than the former meander design (SRL 136a), up to 870°C without failure. This implied that the temperature gradient of the SRL 162g at the active area was reduced as predicted in the thermo-mechanical simulation, as discussed in Chapter 2. Therefore, the reliability of the device was improved due to this low stress. Further details about the thermal profiles of the devices are included in the infrared thermography section 5.6.

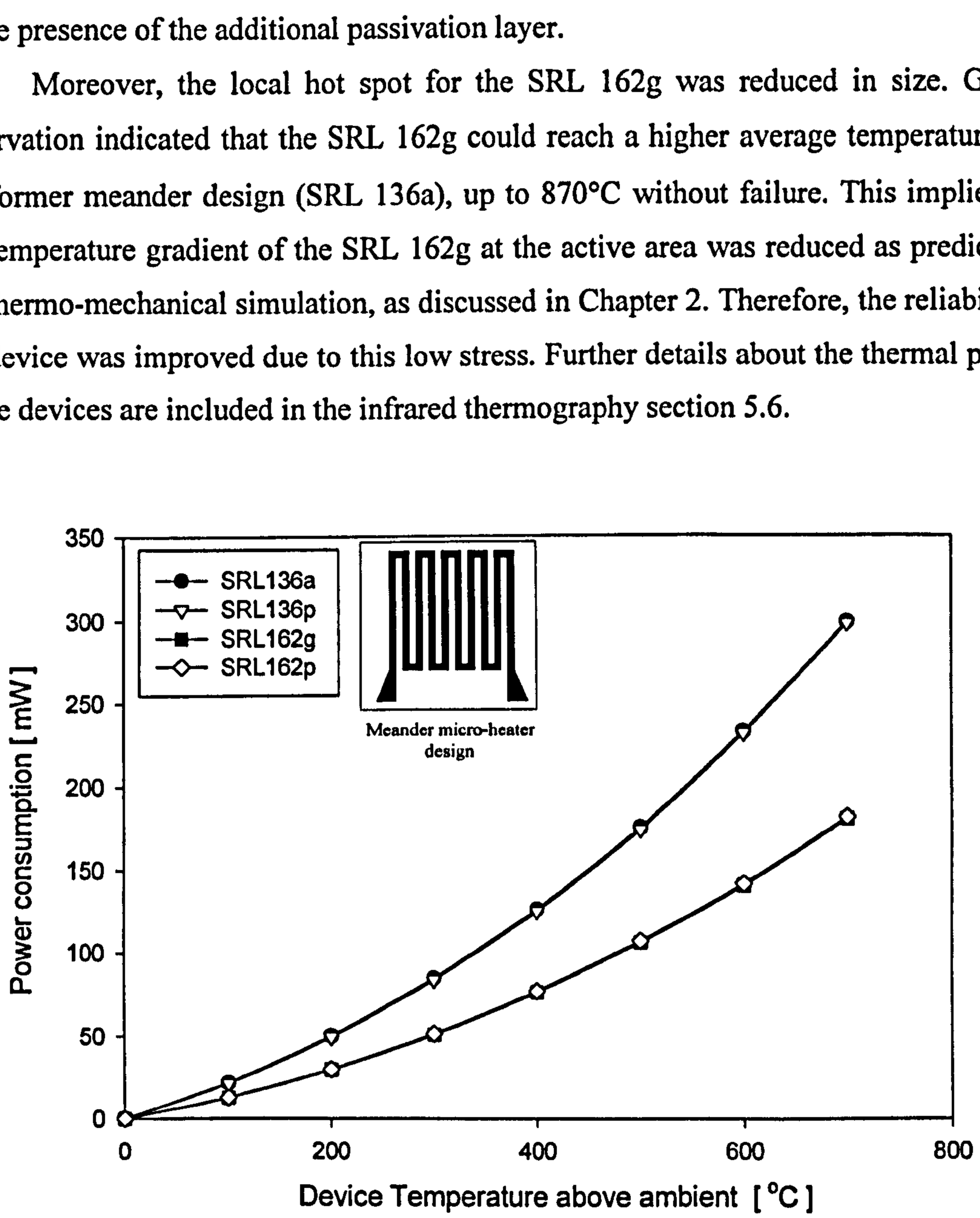

Figure 5.11: The power consumption of the first generation meander type micro-calorimeters, indicating identical power budget between the passivated and un-passivated devices. The ambient temperature is 25°C.

5.4.2 Power consumption of the second generation devices

Due to the number of the devices in the second generation design, the average power consumption for each device has been plotted according to the type of micro-heater design. Therefore, a direct comparison between the power budget and the *MHR* was provided, as shown in figures 5.12 and 5.13. The standard deviation of each curve was within 3% from the mean values. The coefficients of the power curves are included in Appendix 5d.

The graphs show that all the device power consumptions varied according to the order of their *MHR*. However, the reduction of power might not be proportional to an increase of *MHR* since there are other factors involved in the total power loss, as explained by equations (5.2) and (5.4a). Therefore, although the *MHR* for devices employing Honeycomb and Drive-wheel designs was identical, different power inputs were required.

An average power consumption at the nominal operating temperature, 500°C, of the entire design range is plotted in figure 5.14. The graph is sorted in descending order to illustrate the relativity of the power budgets between the different designs. The Ultra-small/ low power family achieved the best power saving where the one with drive-wheel micro-heater design requires only 51 mW.

However, the actual power consumption deviated from the initial estimations suggested in Chapter 2. This was mainly because of the track coverage, φ, that influences the heating efficiency. Moreover, the estimations were solely based on the *MHR* and neglecting the other essential factors for simplicity.

The differences between the thermo-mechanical simulation results and the actual device performances were calculated, as shown in table 5.3. The simulations had achieved a standard deviation of 4.5% for the devices employing the Drive-wheel micro-heater design. However, when the heating efficiency of the device becomes very different from meander type, such as the Ultra-low resistance design, the tolerance could reach 31%. Furthermore, as the overall device geometry was reduced for the Ultra-small families, then the convection loss was significantly reduced and the devices in these families consume much lower power. The thermal coefficients in the simulation model could be modified to compensate for this deviation. In addition, an improved optimisation model had been developed which is described in the next section, based on the actual characterisation results, *MHR* and convectional loss.

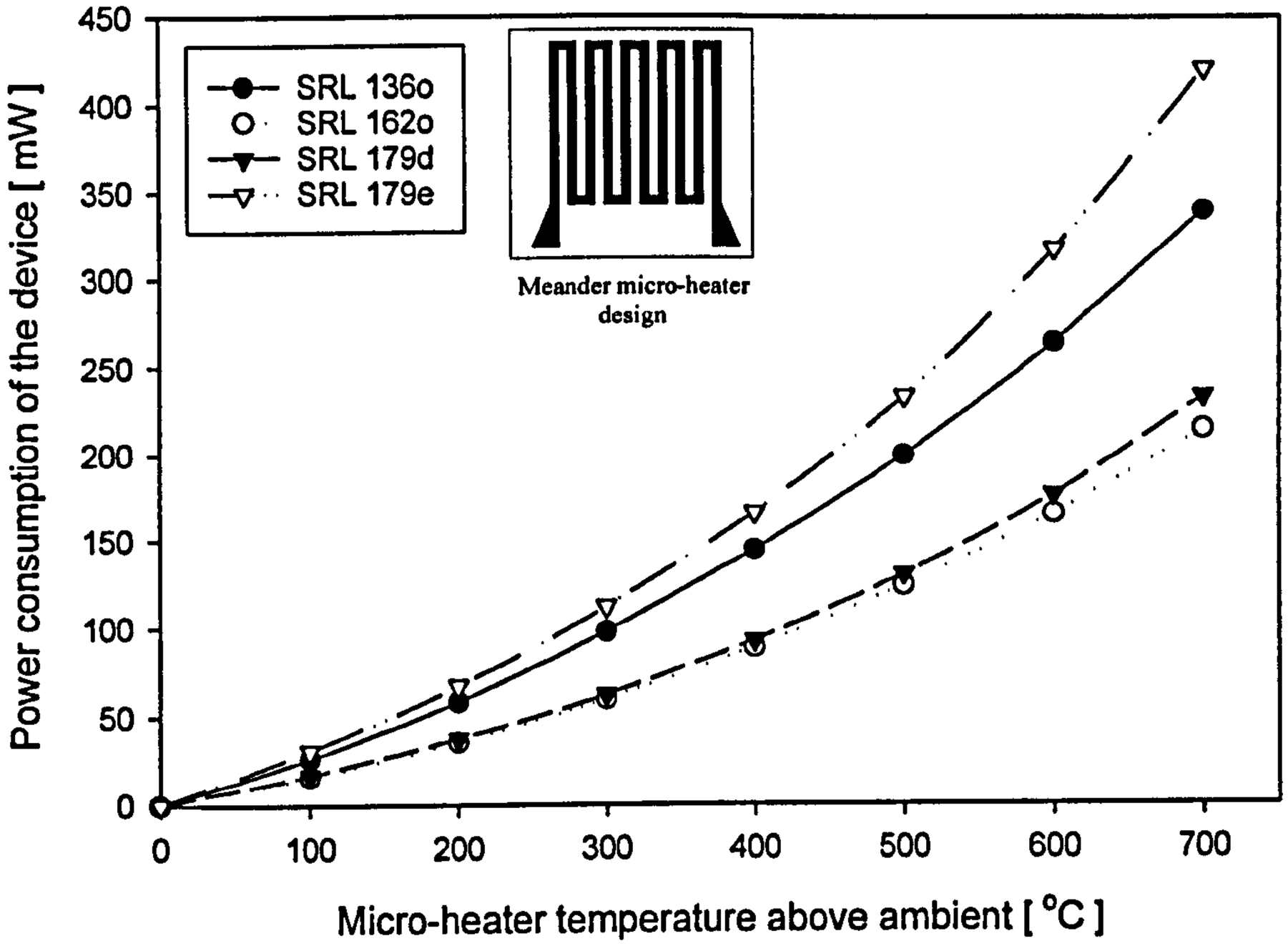

(a)

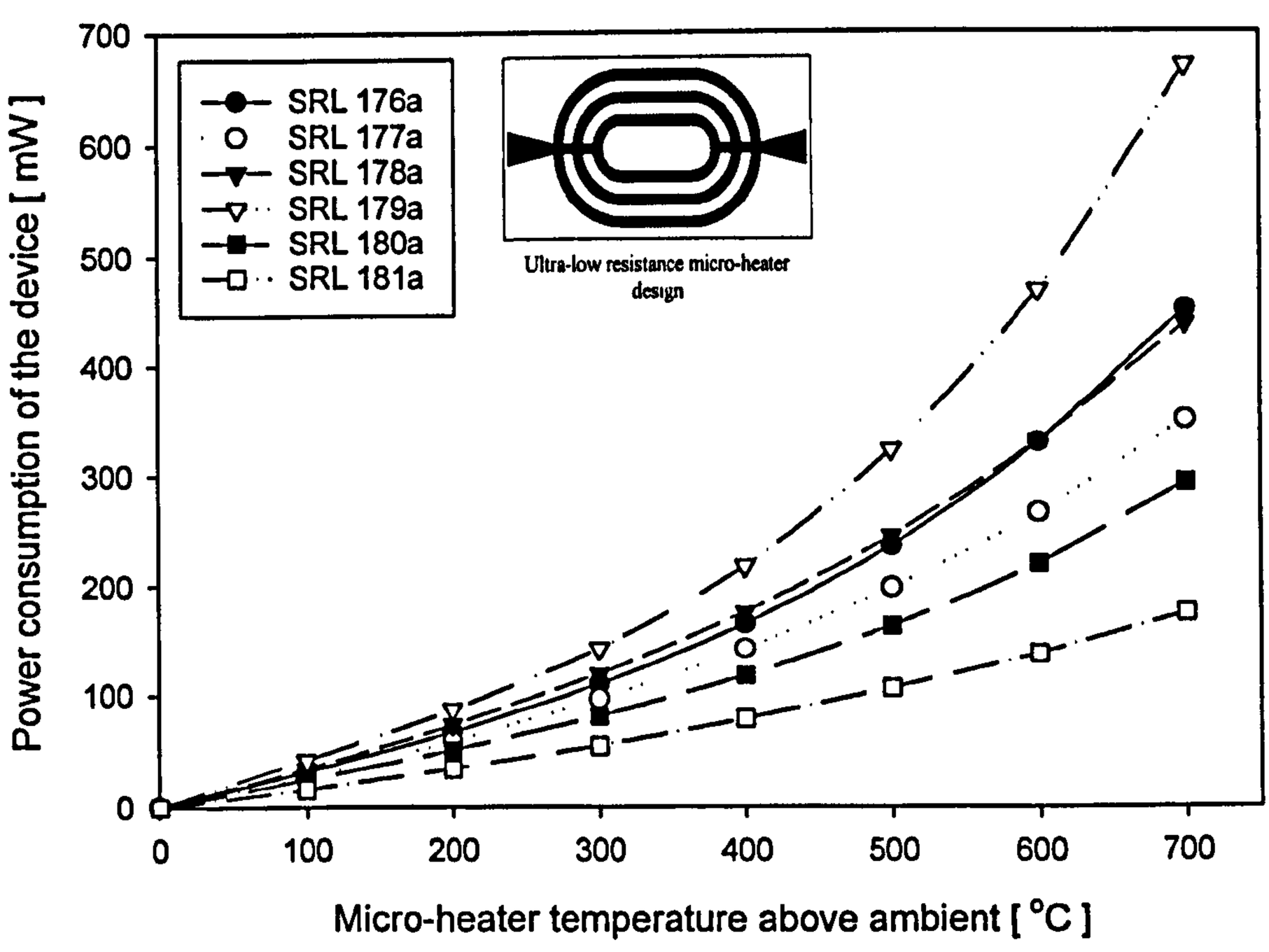

(b)

Figure 5.12: Average power consumption (5 samples from each design) of the 2nd generation micro-calorimeter designs, with ambient temperature at 25°C. (a) Devices employing the Meander type micro-heater design. (b) Devices employing the Ultra-low resistance micro-heater designs.

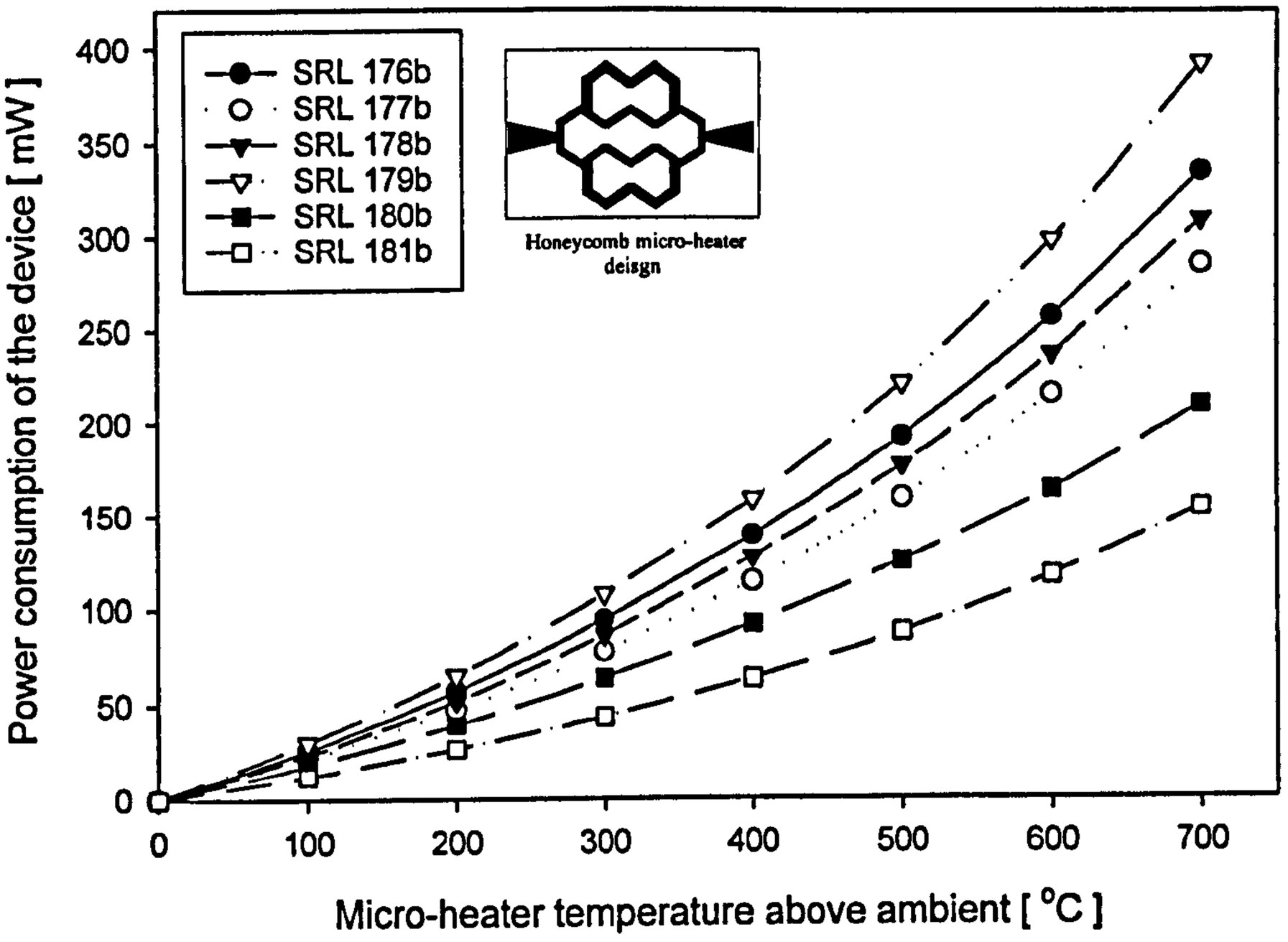

(a)

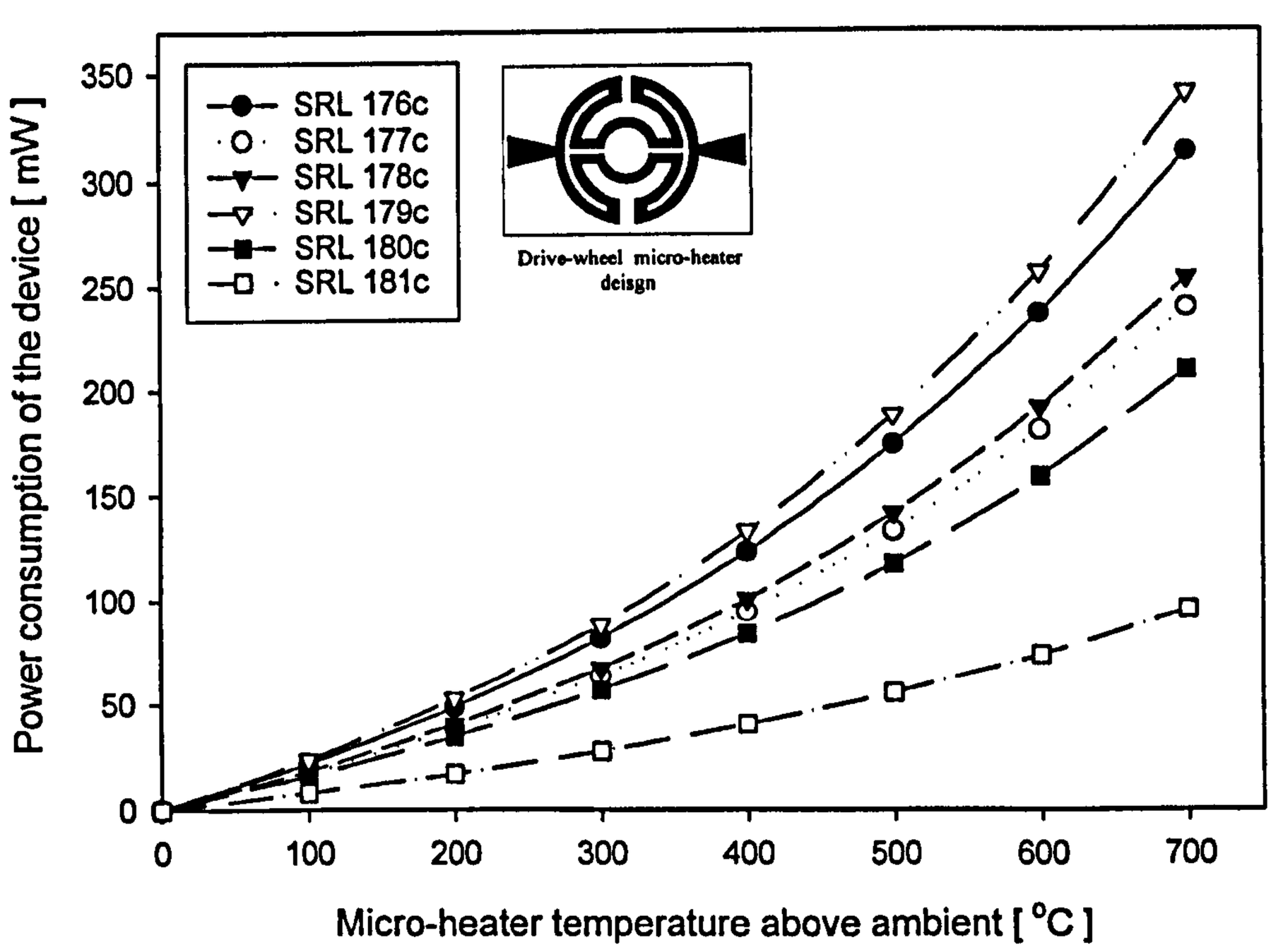

(b)

Figure 5.13: Average power consumption (5 samples from each design) of the 2nd generation micro-calorimeter designs, with ambient temperature at 25°C. (a) Devices employing the Honeycomb micro-heater design. (b) Devices employing Drive-wheel micro-heater design.

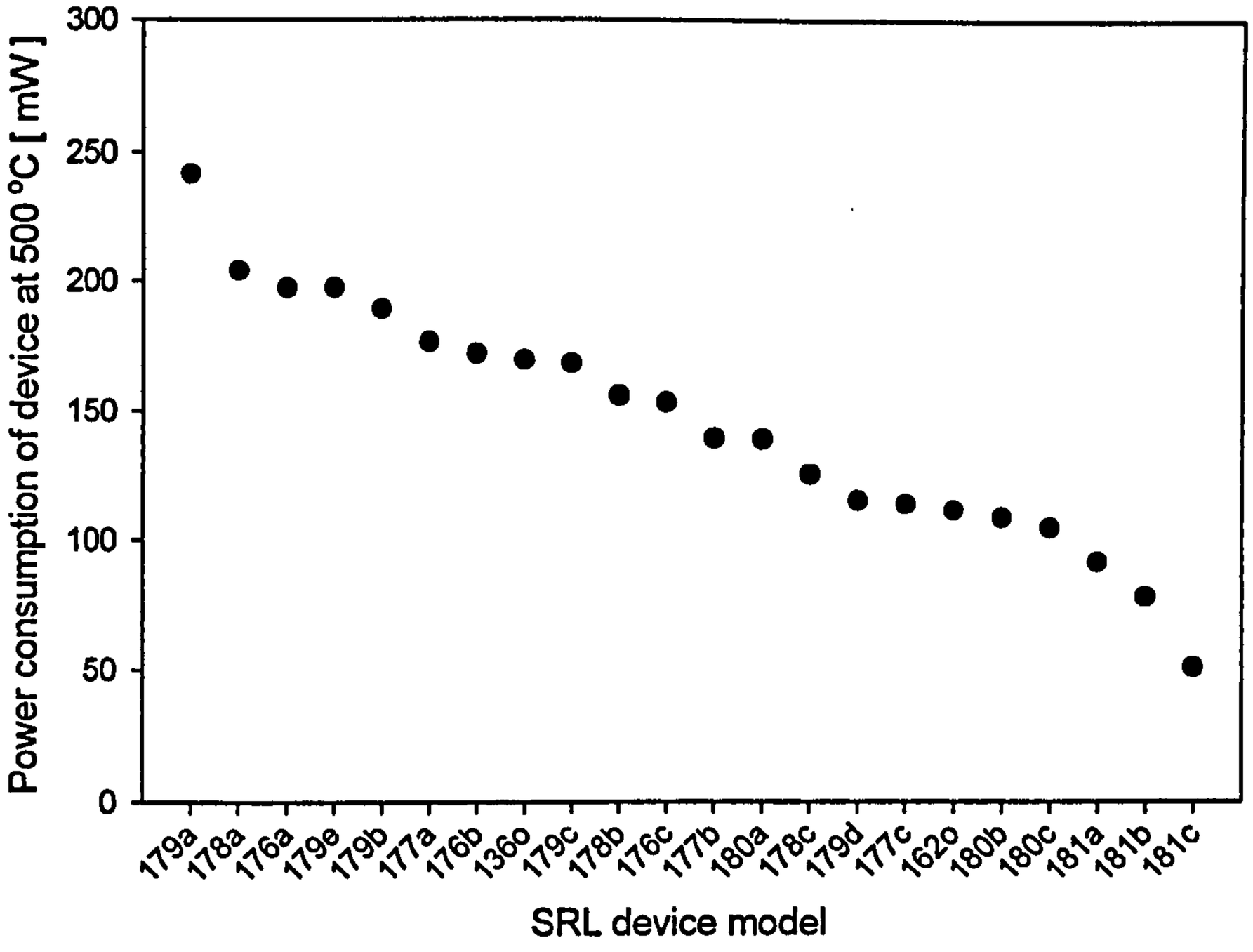

Figure 5.14: Average power consumption (5 samples from each designs) of the 2nd generation micro-calorimeter design at 500°C.

Table 5.3: The comparison between the simulation and the actual measurement of the device performance.

SRL No.	Power input (mW)	Simulated temperature (K)	Measured temperature (K)	Tolerance (%)
SRL 136a	100	590	630	-6.3
SRL 162g	100	780	760	2.6
SRL 176a	100	760	580	31.0
SRL 176b	100	590	615	-4.1
SRL 176c	100	670	665	0.8
SRL 177c	100	760	735	3.4
SRL 178c	100	680	705	-3.5
SRL 179c	100	590	635	-7.1
SRL 179d	100	660	730	-9.6
SRL 179e	100	460	585	-21.4
SRL 180c	50	440	580	-24.1
SRL 181c	50	540	773	-30.1

According to figure 5.14, not only does the drive-wheel micro-heater design provide the best heating efficiency and the maximum power reduction among the second generation devices, but also delivers the most isothermal active area, as shown in section 5.6.

Therefore, further analysis had been concentrated on the devices employing the Drive-wheel micro-heater.

5.4.3 Power optimisation model with *MHR*

Obtaining the various device parameters to calculate power consumption of the micro-calorimeters is tedious and impractical in the early design stage, as shown in equations (5.2) to (5.4). A simplified power optimisation model was desirable to assist the designing of micro-calorimeter. Early work on the micro-calorimeter indicated that over 70% of the power loss was due to convection [5.6]. Therefore, the model considered the die size which contributes to the convectional power loss, apart from the *MHR*.

Based on the Drive-wheel micro-heater design with a die size of 4 mm × 4 mm, the relationship between the power consumption (P) in mW and the *MHR* is expressed in equation (5.5). The logarithmic relationship agreed with early work on micro-hotplates by Dibbern [5.7]. However, in order to accommodate the different die sizes, a scaling factor should be included.

$$P = (262.54 - 89.83 \ln MHR) \text{ mW} \tag{5.5}$$

The die size influences the convectional loss of the device but surface heat transfer is established by a complicated physical process [5.8]. Hence, the Nusselt number (Nu) is commonly employed to obtain the convectional heat transfer coefficient. This dimensionless analysis simplified the computation into a few variables, such as the material properties and the length of the device, as shown in equation (5.6a) [5.8].

$$Nu = G'' \frac{\ell}{\kappa} \tag{5.6a}$$

As the heat-transfer coefficient (G'') and the thermal conductivity (κ) are constant for identical micro-calorimeter structures, the remaining factor that governs the convection is the length of the device (ℓ). Therefore, with the original 4 mm × 4 mm die, the scaling factor is expressed as (5.6b).

$$\frac{Nu}{Nu_o} = \frac{\ell}{\ell_o} = \frac{\ell}{4} \tag{5.6b}$$

where Nu_o and ℓ_o denote the original Nusselt number and length of the die in mm, respectively.

With these equations, a final *MHR* optimisation model was established, as expressed in (5.7) [5.9]. As the model considered the convectional heat loss, it also applies to the other micro-heater design with different heating efficiencies. Therefore, the *MHR* can be optimised to minimise the power consumption of future micro-calorimeter designs which employ similar structure and fabrication processes.

$$P = \ell(65.6 - 22.5 \ln MHR) \text{ mW} \tag{5.7}$$

5.5 Heat transfer mechanisms

An investigation was performed to enhance the understanding of the heat transfer mechanisms in order to achieve an optimum power budget and mechanical stability. Since the previous investigations showed that the deviation of the device parameters was insignificant, one device from each of the selected device types was used for this investigation. R_o and α of the devices were obtained through steady-state thermal characterisation. The power consumption was calculated when the devices were operated in air and in a vacuum. The difference of the two results eliminated the convective heat loss, leaving only the conductive and radiative effect. The radiation term, P_{rad}, was then computed using the Stefan-Boltzmann law of black body radiation as shown in equation (5.8) [5.10]. The micro-heater temperature above ambient, T, is in Kelvin, A is the area of the micro-heater, σ is the Stefan-Boltzmann constant and an emissivity (ε) of 0.35 was used. As radiation loss occurs on both side of the active area, the values of equation (5.8) should be doubled. The characterisation distinguishes each mode of thermal transfer which assists in defining the design boundaries and constraints.

$$P_{rad}(T) = \varepsilon \sigma A T^4 \tag{5.8}$$

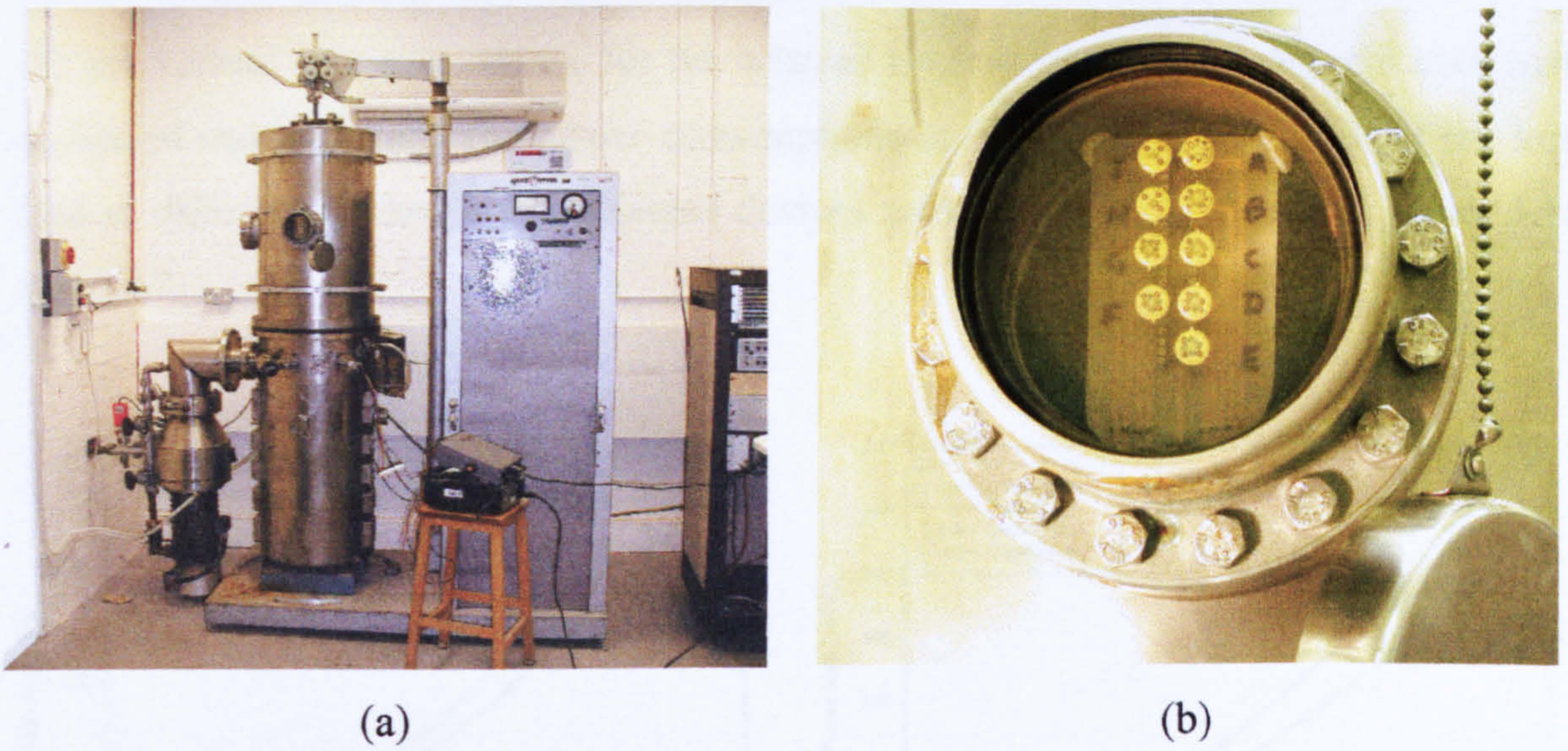

(a) (b)

Figure 5.15: (a) The vacuum system for V-I characterisation. (b) The micro-calorimeter under test mounted on the custom-made device holder.

In order to calculate the power consumption without the effect of convection, V-I characterisation was performed in a vacuum chamber (Variant Ltd. UK) at a pressure of 3×10^{-5} mbar, as shown in figure 5.15. A customised device holder was constructed to harness a batch of devices and establish electrical connection to the measuring instruments outside the chamber. Pumping was carried out in two stages. The rotary pump (T80 Edwards Ltd. UK) took one hour to reach low vacuum (3×10^{-2} mbar) before the diffusion pump (Edwards High Vacuum Ltd., UK) started and achieved high vacuum at 3×10^{-5} mbar in another three hours. Then the V-I characterisation was carried out in air, as described in section 5.2.

In order to provide a direct comparison between the commercial devices and the micro-machined devices, two commercial devices were supplied by City Technology Ltd. UK. The two device models had undergone identical characterisations as the micro-calorimeters. A summary of the characterisation results for various devices at the normal operating temperature is shown in table 5.4.

5.5.1 Thermal transfer in different modes

As the various characterisations for the selected devices were completed, the data were compiled and analysed. The power consumptions in air and the distribution of the heat loss in different modes for the selected devices were obtained, as shown in figure 5.16 and 5.17.

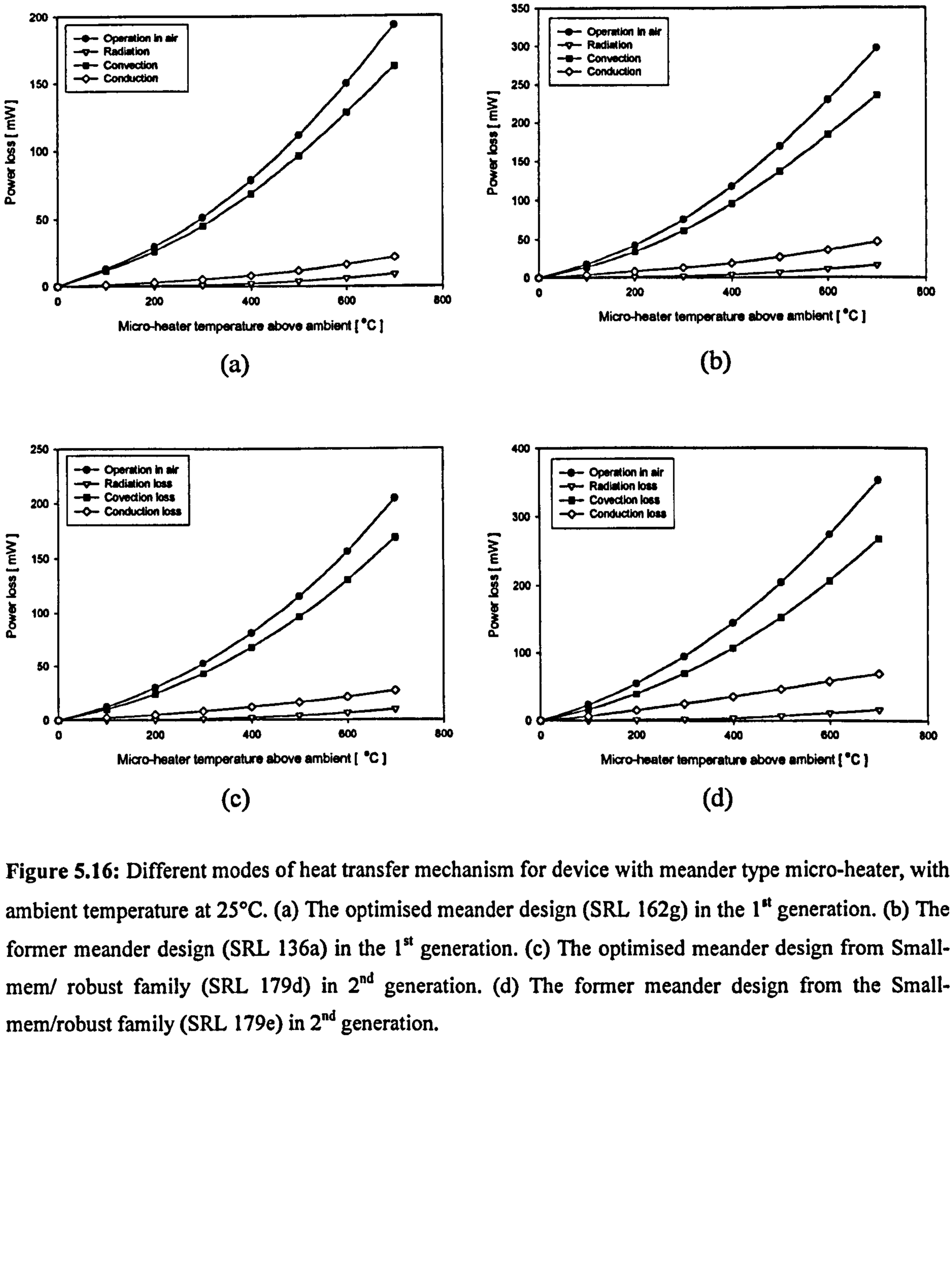

Figure 5.16: Different modes of heat transfer mechanism for device with meander type micro-heater, with ambient temperature at 25°C. (a) The optimised meander design (SRL 162g) in the 1st generation. (b) The former meander design (SRL 136a) in the 1st generation. (c) The optimised meander design from Small-mem/ robust family (SRL 179d) in 2nd generation. (d) The former meander design from the Small-mem/robust family (SRL 179e) in 2nd generation.

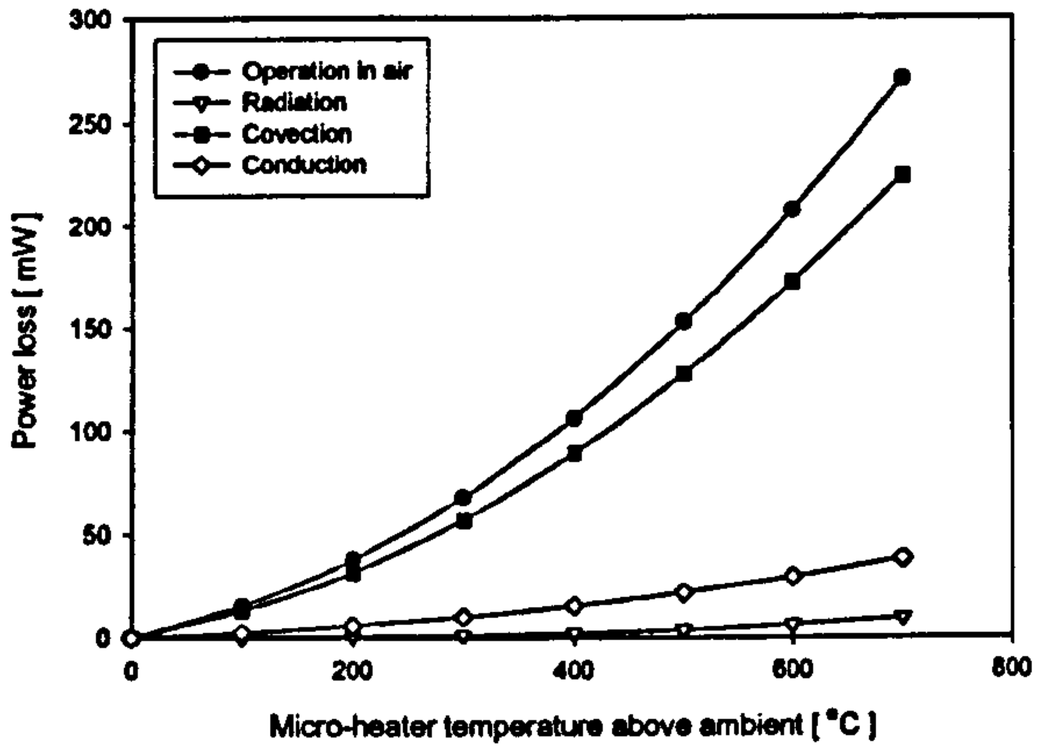

(a)

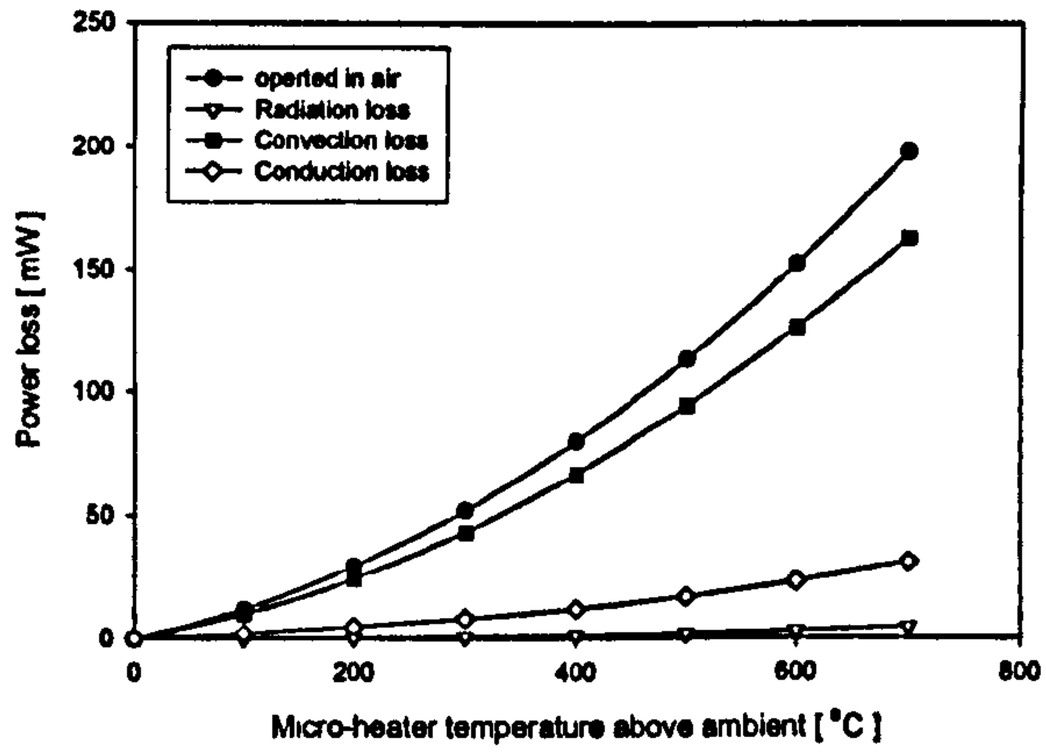

(b)

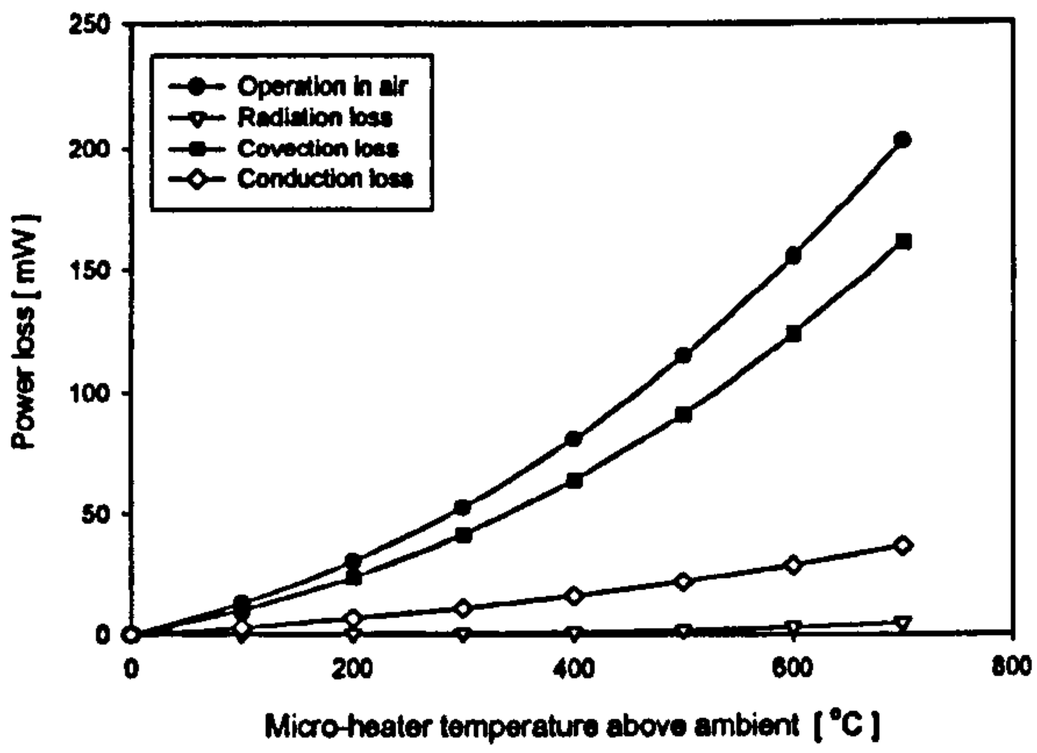

(c)

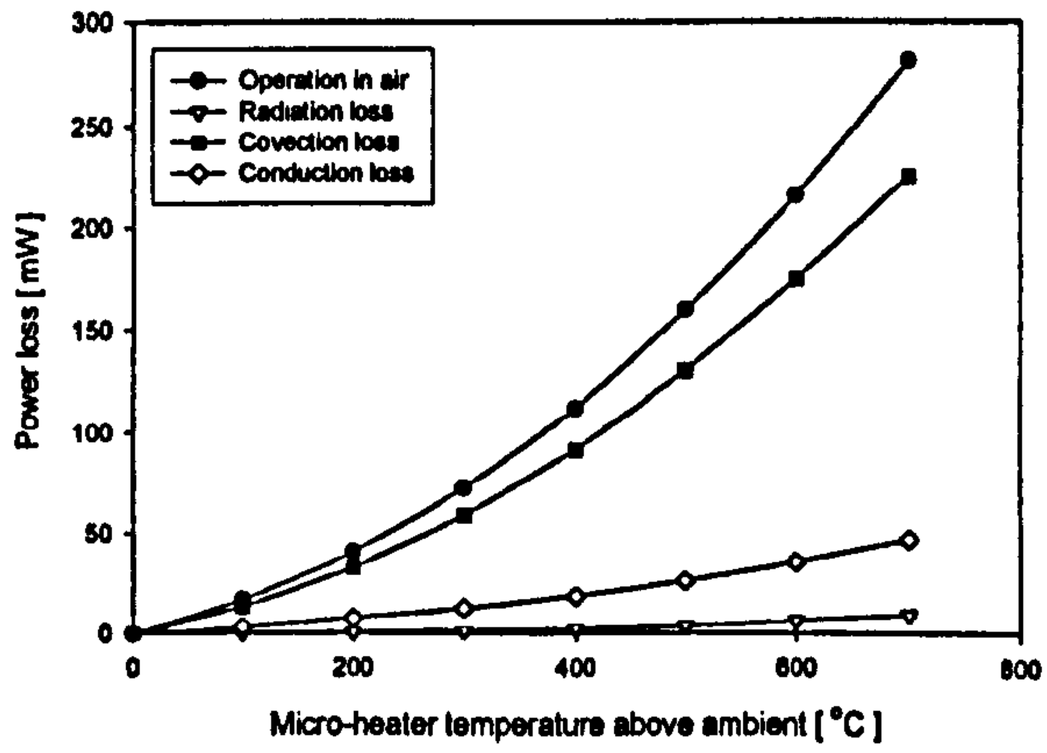

(d)

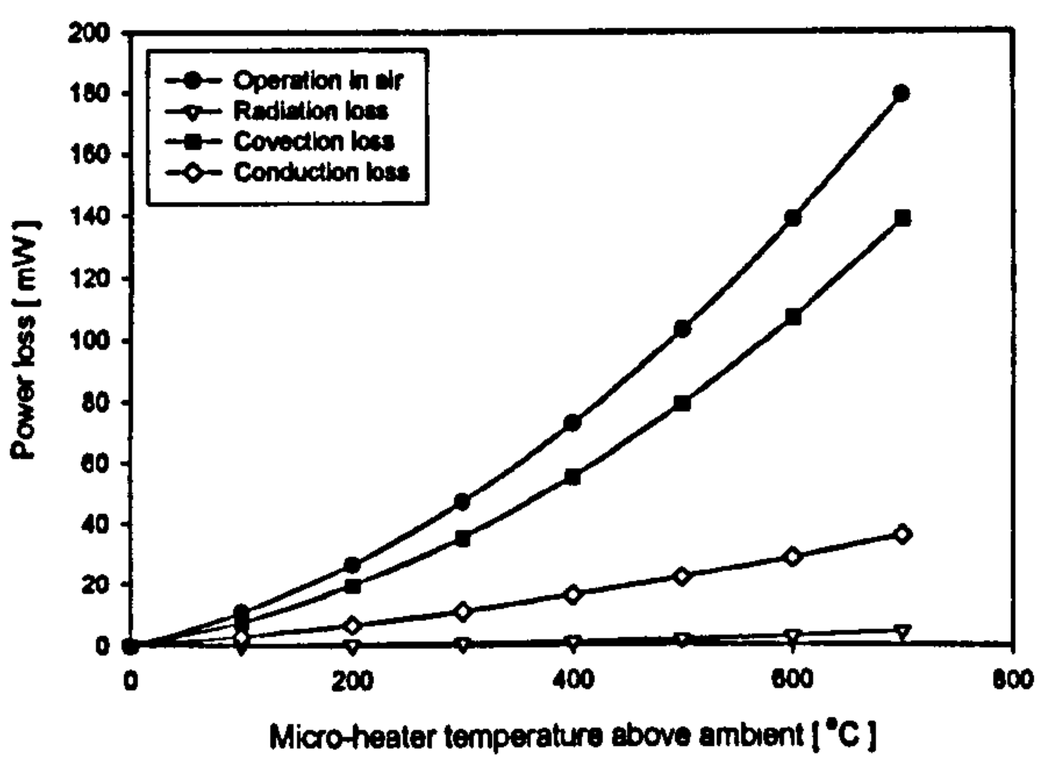

(e)

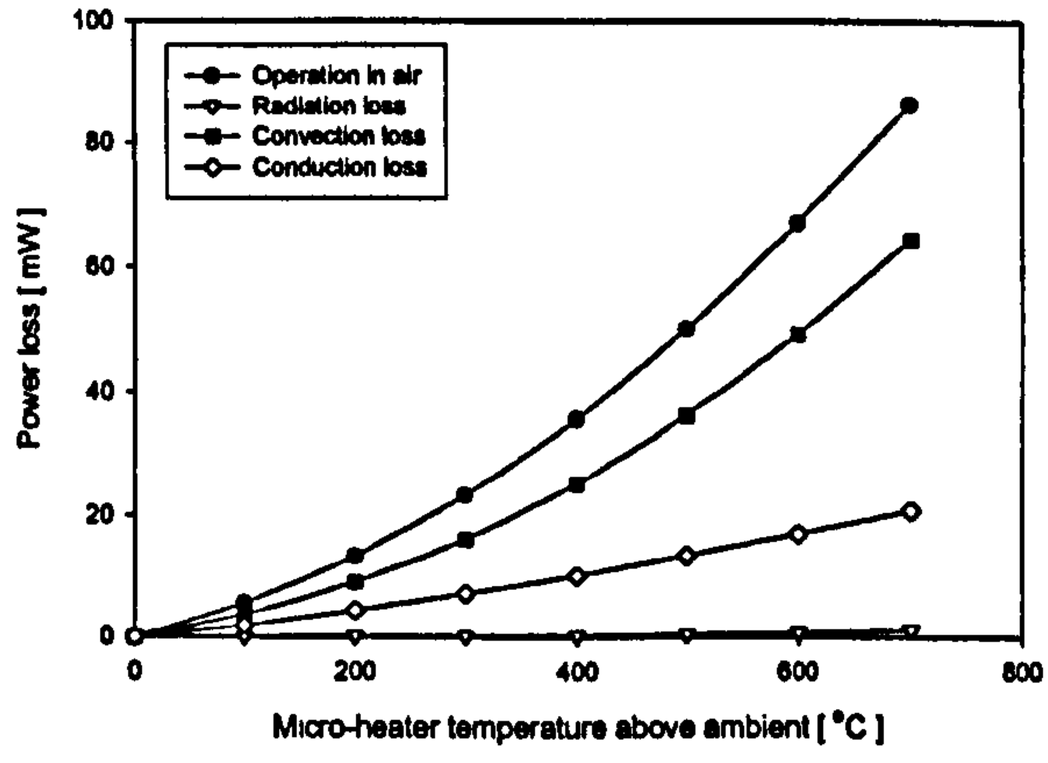

(f)

Figure 5.17: Different modes of heat transfer mechanism for device with Drive-wheel micro-heater design, with ambient temperature at 25°C. (a) The Standard family (SRL 176c), (b) the Low-power family (SRL 177c), (c) the Small-mem/ robust family (SRL 178c), (d) the Robust family (SRL 179c), (e) The Ultra-small/ robust family (SRL 180c) and (f) the Ultra-small/ low power family (SRL 181c).

Table 5.4: Summary of various modes of heat transfer at 500°C

μ-heater design	Device No.	MHR	Cell size (mm sq.)	Typical power consumption @500°C (mW)	Percentage of different mechanism at 500°C (%)		
					Convection	Conduction	Radiation
Meander	136o	2.0	4	169.00	80.9	15.4	3.7
	162o	3.6	4	111.36	86.5	10.2	3.2
	179d	2.6	4	114.86	83.2	13.6	3.1
	179e	1.5	4	204.78	74.8	22.2	3.1
Drive-wheel	176c	3.5	4	152.52	83.5	14.2	2.4
	177c	5.0	4	113.24	83.3	15.1	1.6
	178c	3.8	4	115.16	79.5	18.9	1.6
	179c	2.6	4	159.45	81.5	16.3	2.3
	180c	2.5	2	102.82	76.8	21.5	1.7
	181c	5.0	2	50.18	72.2	26.9	0.9
Commercial	50P	N/A	N/A	135.99	78.6	21.4	0.01
(CTL)	300P	N/A	N/A	173.96	52.6	47.3	0.1

The results indicate that the convective loss for the micro-calorimeters could reach 87% of the total heat loss (SRL 162o) while all other devices were over 72%. Therefore, this is the major heat loss mechanism for the devices during operation, which can only be reduced by minimising the surface area of the devices. This percentage is inversely proportional to the micro-heater temperature elevated from the ambient. Radiative losses increase significantly when the device begins to glow above 500°C.

However, when the heater size decreased from 4 mm × 4 mm to 2 mm × 2 mm, reduction of surface area results in a smaller proportion of convection loss and leads to a lower power consumption. Radiative loss is negligible since the devices only begin to glow orange in colour over 500°C, which does not exceed 2% of the total energy loss.

A relationship was observed between the *MHR* and the conduction loss. When the absolute power loss due to conduction was compared based on the micro-heater design, the conduction loss increased as the *MHR* decreased.

As for the commercial devices manufactured by City Technology Ltd. (CTL), the results indicated a similar trend as for the micro-calorimeters. The larger the bead, the higher percentage of convective loss due to increased surface area. Furthermore, the percentage of conduction loss is generally higher than the micro-machined devices, due to the absence of the thermal isolation for the platinum heater coil.

5.6 Infrared thermography

Infrared thermography was performed to investigate the surface thermal profile of the devices. Therefore, the temperature homogeneity of the active area can be assessed to enhance the understanding of the micro-heater efficiency. A thermal microscope system was borrowed from the EPSRC funded Rutherford Appleton Laboratory, UK. This system is superior to ordinary thermal imaging systems as they usually suffer from insufficient spatial resolution. The system included an Agema Thermovision 800 infrared camera attached to a microscope and a controlling computer, TIC-8000, as shown in figure 5.18. A personal computer with thermal analysis software was also provided for post-processing of the captured images. The CCD camera was attached to the microscope for view finding and focusing. The viewing of the system can be switched between the infrared camera and the CCD camera by a prism. In addition, in order to improve the accuracy of the measurement, the imaging process was conducted in a dark room which eliminated all possible reflections in the visible light band. Furthermore, all essential equipment involved in the imaging was painted black in colour to minimise interference.

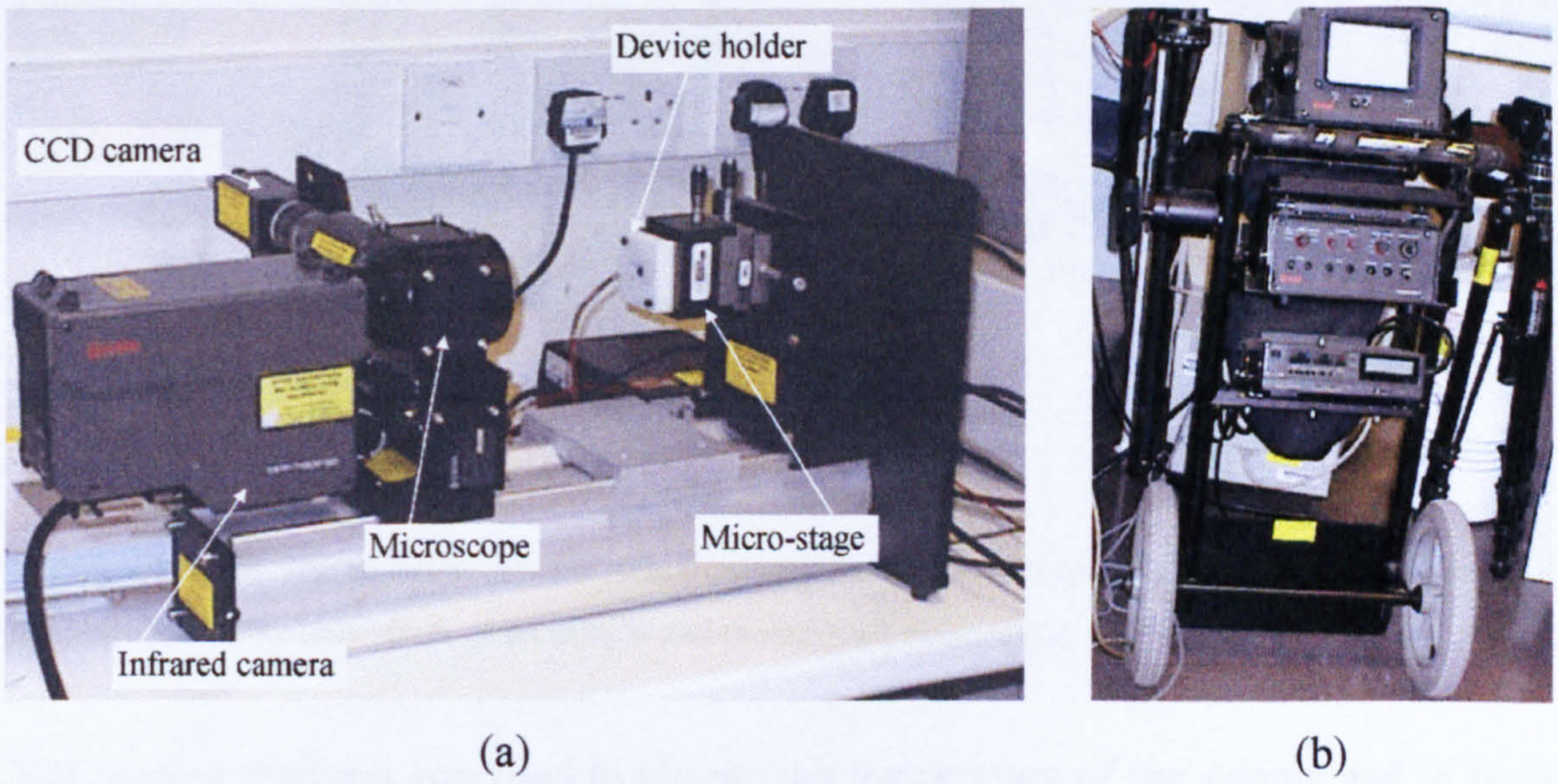

Figure 5.18: (a) The infrared microscope system. (b) The control unit of the system.

5.6.1 Emissivity calibration

Emissivity, ε, is a radiative property of the material surface. This value is in the range of $0 \leq \varepsilon \leq 1$ and indicates the efficiency of the surface radiation compared to an ideal black body radiator [5.10]. However, this property varies greatly with material and surface roughness. Therefore, emissivity calibration of the materials involved was critical. Otherwise, the absolute temperature from the thermal images could not be considered as accurate.

The calibration of the emissivity was performed with a sample of nanoporous Pd catalyst deposited on gold with a glass substrate, supplied by Southampton University. The sample was heated on an aluminium heating platform with a blowtorch and the actual temperature on the surface was measured with a Digitron type-K thermocouple. The arrangement of the apparatus is shown in figure 5.19.

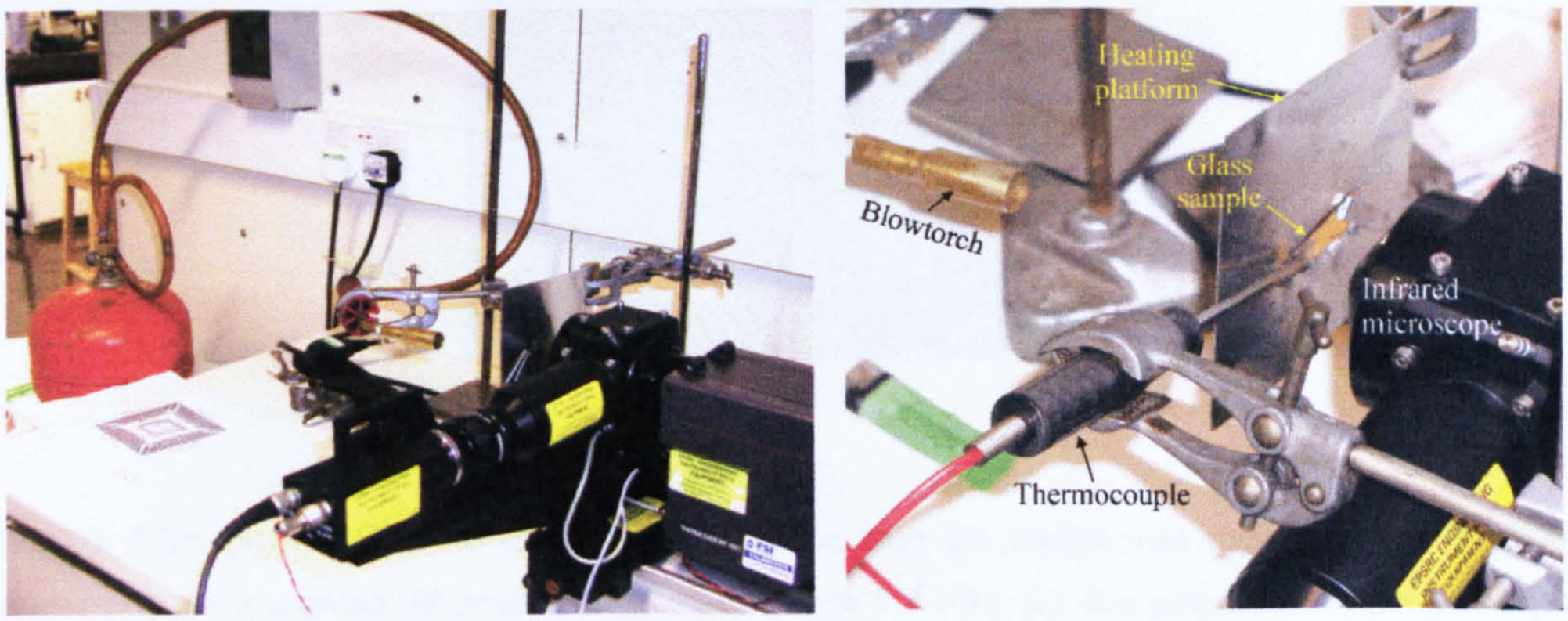

(a) (b)

Figure 5.19: (a) The apparatus for the emissivity calibration. (b) The close-up view of the setting showing the positions of the blowtorch, glass sample and the infrared microscope.

The heating platform was used to elevate the temperature of the sample and to prevent turbulence which could affect the calibration results. An ordinary laboratory hotplate was not appropriate for this application because glass is an insulator and it would take a long time to heat up to between 200°C and 300°C. The blowtorch allows the heating platform to reach about 350°C within minutes and the temperature measured on the glass sample was about 250°C.

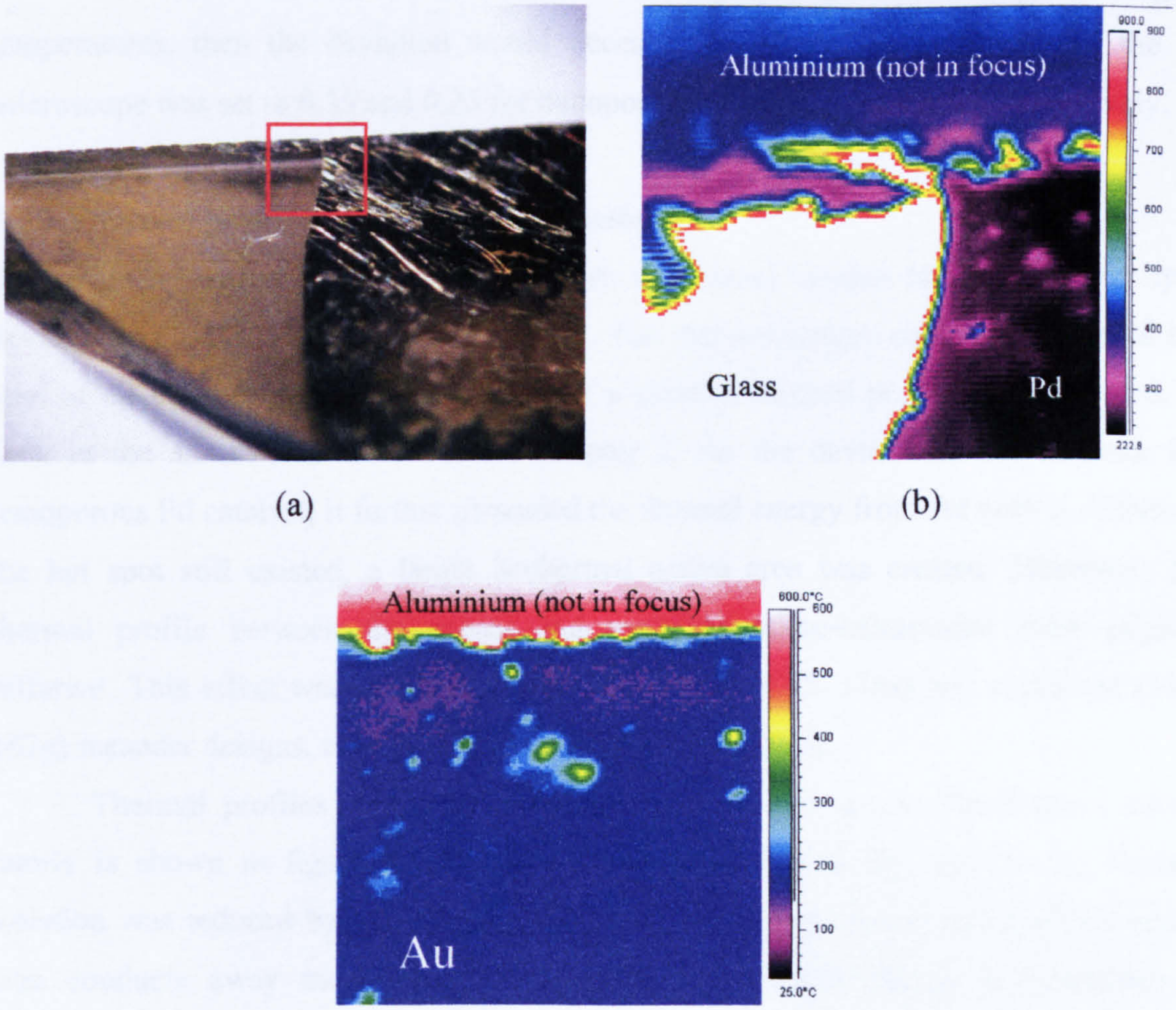

Figure 5.20: (a) The glass sample for the calibration with the studied area marked in red. (b) The calibration result showing different material regions, with $\varepsilon = 0.35$. (c) The calibration for the gold layer with $\varepsilon = 0.25$.

Figure 5.20(a) shows the area used for calibration and the IR image of the Pd sample indicates the different temperatures for different material regions shown in figure 5.20(b). Although the temperature of the glass sample was the same, materials with different emissivities give out different levels of radiation. The emissivity of the IR detector was set to 0.35 to measure the surface temperature of the Pd layer. As the emissivity of glass is typically above 0.8, the temperature of the bare glass area appeared to be much higher than the nanoporous Pd region. The measurement showed that there was only a 15°C deviation from the infrared image. Calibration for gold was also performed as shown in figure 5.20(c). With the emissivity set to 0.25, the IR image indicated about 20°C difference compared to the measurement from the thermocouple.

As the emissivity of the material is expected to be different at higher temperatures, then the deviation would decease. Therefore, the emissivity of the IR microscope was set to 0.35 and 0.25 for nanoporous Pd catalyst and gold, respectively.

5.6.2 Thermal profile of the micro-calorimeters

Based on the calibrated emissivity, a series of thermal images for the meander type devices were taken, as shown in figure 5.21. The thermal images confirmed the local hot spot of all the meander type devices. Here a circular thermal profile was observed, as seen in the simulations described in Chapter 2. As the device was coated with the nanoporous Pd catalyst, it further dispersed the thermal energy from the centre. Although the hot spot still existed, a larger isothermal active area was created. Moreover, the thermal profile between the coated and uncoated micro-calorimeter were slightly different. This effect was demonstrated by the former (SRL 136a) and optimised (SRL 162g) meander designs, as shown in figures 5.21(a) to 5.21(d).

Thermal profiles of the optimised meander designs in the Small-mem/ robust family is shown in figure 5.21(e). It indicates a prominent hot spot as the thermal isolation was reduced by the smaller *MHR*. Thermal energy at the fringe of the active area conducts away more rapidly. Therefore, the thermal energy (temperature) is concentrated at the centre of the active area.

The Standard meander design (SRL 162g) without the Au gate electrode was also tested, as shown in figure 5.21(f). Due to the absence of the gold layer, the temperature generated by the micro-heater was not dispersed resulting in an obvious hot spot. However, the absolute temperature cannot be deduced from this thermal image because the emissivity of silicon nitride was not calibrated and a value of 0.25 was employed.

Thermal images for the second generation micro-heater designs are shown in figure 5.22. The Drive-wheel micro-heater design demonstrated remarkable temperature homogeneity with a standard deviation of about 10°C across the active area [5.9]. The Ultra-low resistance and Honeycomb designs indicated two small hot spots at the contacts, as shown in figures 5.22(e) and 5.22(f), which was not foreseen by the thermo-mechanical simulation. In addition, the thermal image is distorted by the surface roughness of the Pd catalyst layer when the coated devices were tested, as shown in figures 5.22(b) and 5.22(d).

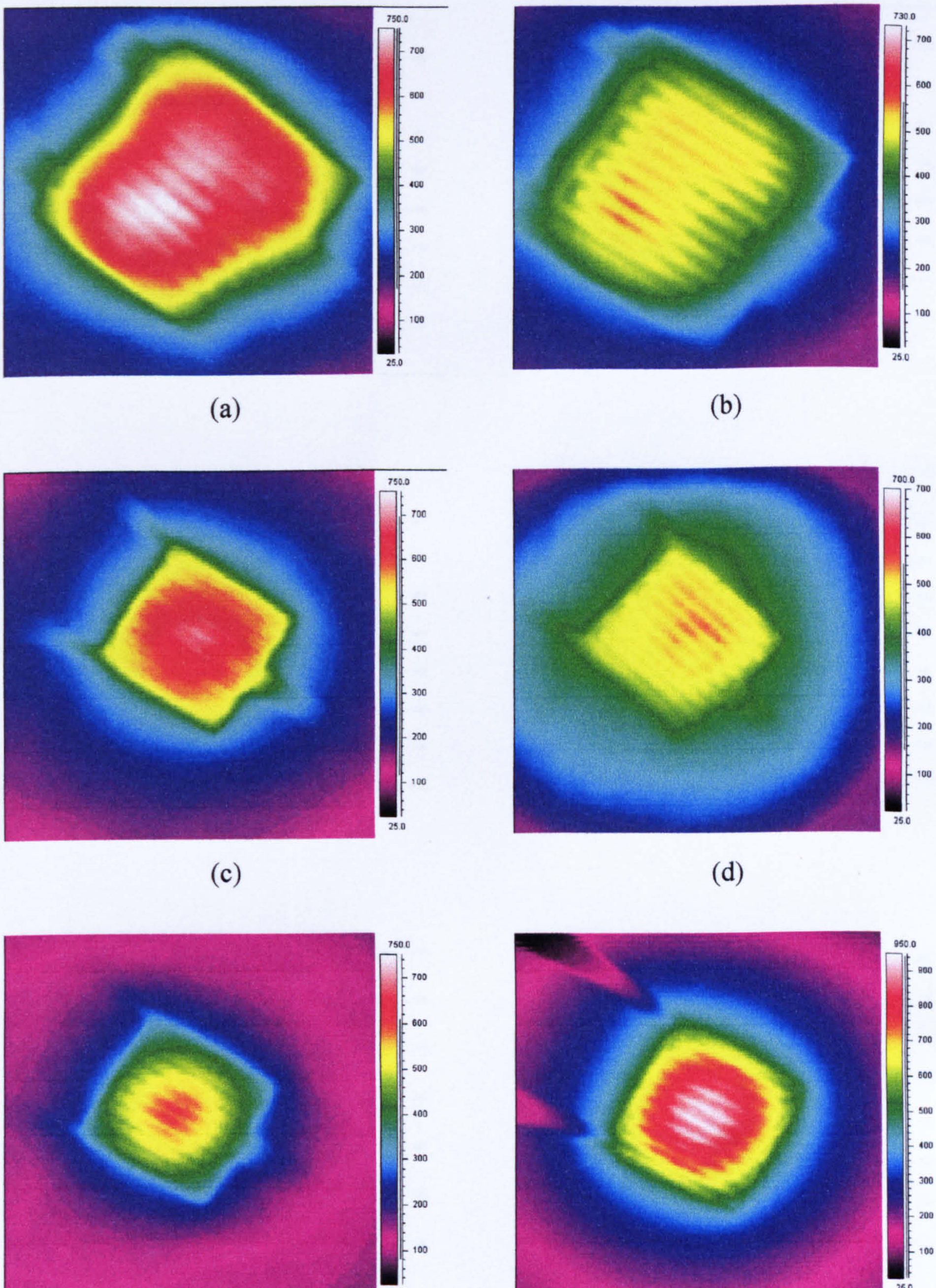

Figure 5.21: Thermal images of the devices employing meander type micro-heater design. The emissivity setting was 0.25 for uncoated devices and 0.35 for coated devices. (a) Uncoated and (b) coated 136a. (c) Uncoated and (d) coated 162g. (e) Uncoated 179d. (f) SRL 162g without Au gate electrode ($\varepsilon = 0.25$).

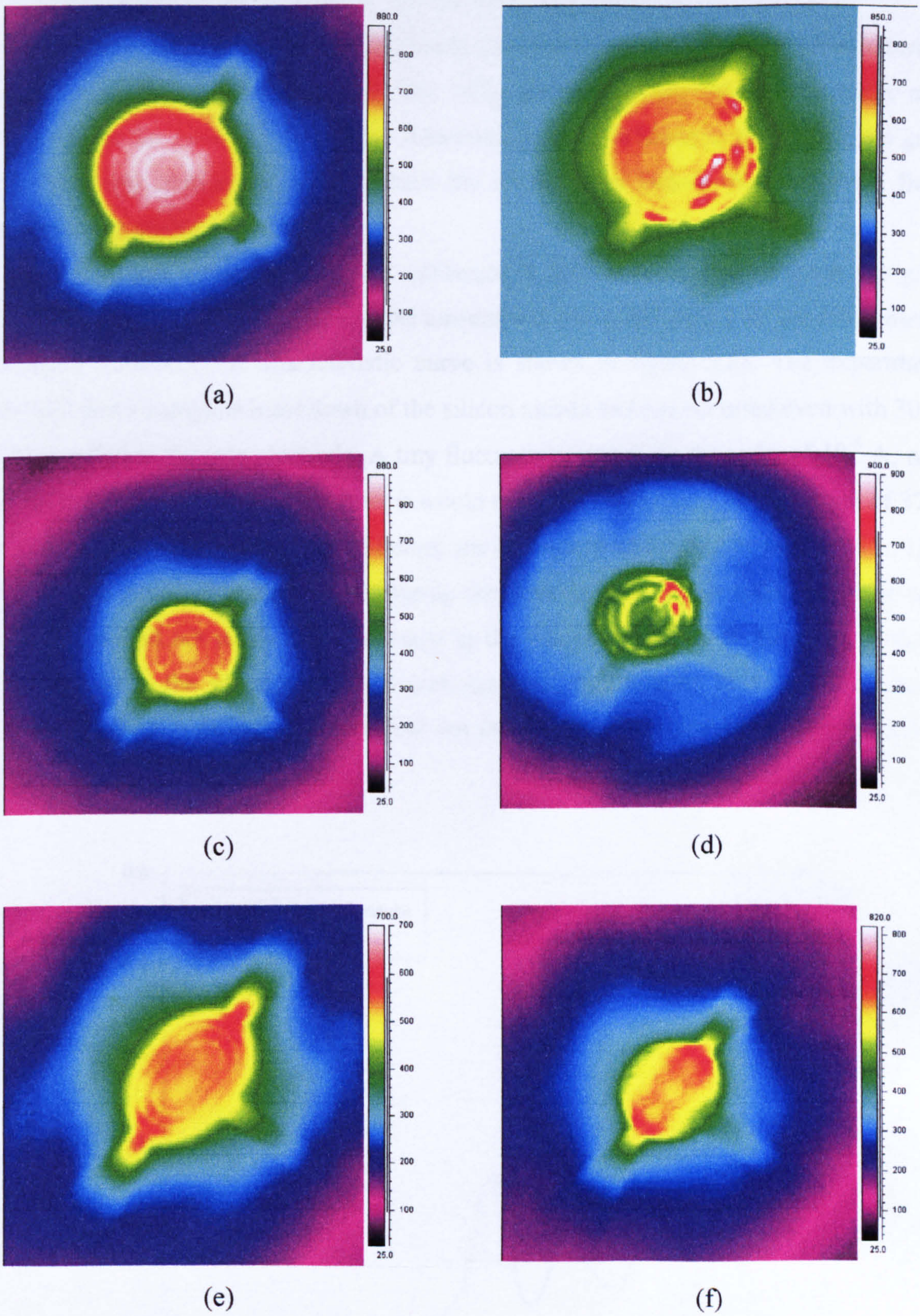

Figure 5.22: Thermal profile for 2nd generation devices. The emissivity was 0.25 for uncoated devices and 0.35 for coated devices. (a) Uncoated and (b) coated SRL 176c. (c) Uncoated and (d) coated SRL 177c. (e) Uncoated Ultra-low resistance design SRL 177a. (f) Uncoated Honeycomb design SRL 177b.

5.7 Breakdown field strength of the silicon nitride

An experiment was conducted to investigate the breakdown voltage of the silicon nitride sandwiching the micro-heater. Two SRL 162g specimens were selected randomly and mounted on the usual TO-5 headers. Additional tests were made to ensure that the gate electrode was completely isolated from the micro-heater before the breakdown field strength was measured.

Constant voltage (Knick DC calibrator S 252) was applied between the gate electrode and the micro-heater, and the current was measured with a digital multi-meter (Thurlby 1503 HA). A characteristic curve is shown in figure 5.23. The experiment showed that a complete breakdown of the silicon nitride had not occurred even with 30 V D.C. applied at the gate electrode. A tiny fluctuating current, in the order of 10^{-6} A, was measured after 12 V D.C. Therefore, it would require a breakdown field strength of 37.5 MV/m applied to the gate electrode before any leakage current could be detected [5.11].

The result indicated that operating the devices with higher voltages or for test purposes would not result in any damage to the silicon nitride layer. However, defects inherited from the process, such as pinholes, will significantly reduce the electrical insulation. Such a defective device had not been found from previous characterisation test.

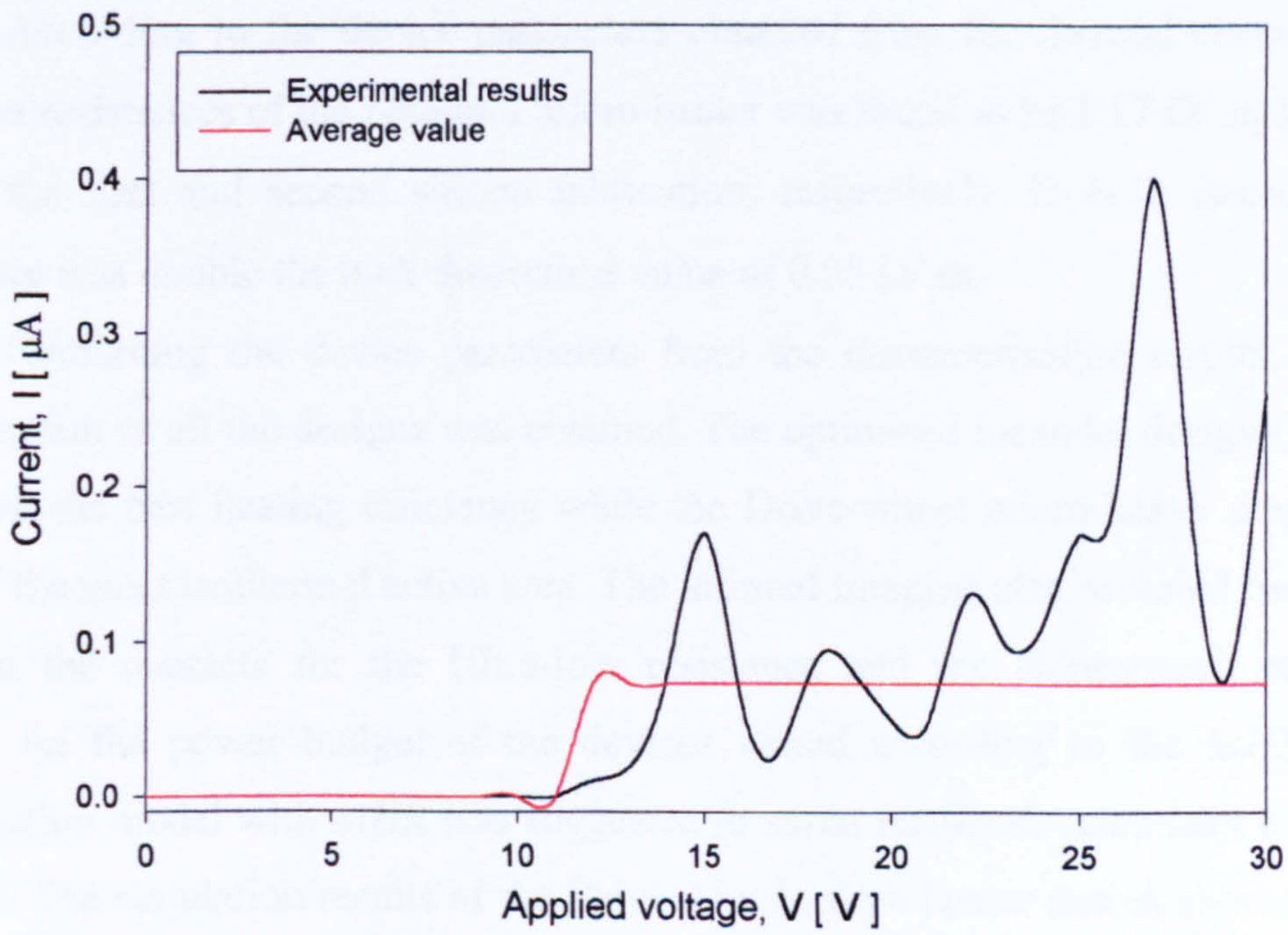

Figure 5.23: The I-V characteristic of the silicon nitride layer with constant voltage applied between the gate and the platinum micro-heater.

5.9 Conclusions

In this chapter, the device steady-state characteristic have been reported. The characterisation initially used a qualitative approach where over one hundred fifty devices were tested from the first and second generations. After the Drive-wheel micro-heater design was identified as the best design, further characterisations, such as heat transfer mechanisms and thermal imaging, focused on this micro-heater design.

The V-I characterisation showed that the voltage requirement for digital interface compatibility had been achieved. The voltage requirement to reach the operating temperature had dropped from the original 7.5 V for SRL 136a to 2.0 V for SRL 181c. Furthermore, the entire design range from the second generation required a voltage supply of only 2.0 V to 3.8 V.

The temperature coefficient of resistance, α, and the base-line resistance, R_o, for the platinum micro-heaters were obtained from the steady-state thermal characterisation. In general, low temperature characterisation between room temperature and 180 °C was applied to the devices. Due to the superior linearity of the thermal resistivity, characterisation of the entire design range could be efficiently performed. Moreover, high temperature characterisation from room temperature to 600°C was also conducted on selected devices. The results proved that the standard deviation between the two characterisation methods was less than 3%.

According to the device parameters obtained from the thermal characterisation, the sheet resistances of the platinum micro-heater was found to be 1.17 Ω/ sq and 1.00 Ω/ sq for the first and second silicon fabrication, respectively. In both cases, the sheet resistance was double the bulk theoretical value of 0.55 Ω/ sq.

Combining the device parameters from the characterisation results, the power consumption of all the designs was obtained. The optimised meander design (SRL 162g) delivered the best heating efficiency while the Drive-wheel micro-heater design proved to have the most isothermal active area. The infrared imaging also revealed two small hot spots at the contacts for the Ultra-low resistance and the Honeycomb micro-heater design. As the power budget of the devices varied according to the *MHR*, a power optimisation model with *MHR* was suggested to assist further development of additional devices. The simulation results of the Drive-wheel micro-heater design showed that only a 4.5% standard deviation from the actual measured values could be achieved. Although

the tolerance for other designs was higher, the thermal coefficients in the simulation models could be modified accordingly to improve the accuracy.

The thermal transfer mechanisms were identified through the vacuum characterisation. Depending on the device type, between 72% and 85% of the power loss was caused by convection, at the operating temperature of 500°C. Therefore, it implied that the overall geometry of the device should be minimised to effectively reduce the convectional loss. It also proved that the conduction loss was controlled by the optimisation of the *MHR*.

Lastly, the breakdown field strength of the silicon nitride was measured to be 37.5 MV/m. Therefore, the device will not be damaged accidentally during measurement.

References

[5.1] M. Nelkon, P. Parker, *Advanced level Physics*, Chapter 14, p302, Fourth edition, Heinemann, London, 1980.

[5.2] B. E. Noltingk, *Instrumentation reference book*, Part 2, p21, Butterworths & Co. Ltd., New York, 1990.

[5.3] W. Bolton, *Measurement and instrumentation systems*, Chapter 5, p100, Butterworth- Heinemann, London, 1996.

[5.4] S. M. Lee, J. W. Gardner, D. C. Dyer, P. N. Bartlett, Y. M. Tan, Silicon planar pellistor employing nanostructured films and a micro-hotplate, *Euspen nanotechnology workshop and Joint Warwick-Tokyo Nanotechnology Symposium*, University of Warwick, UK, 2000.

[5.5] J. W. Gardner, S. M. Lee, P. N. Bartlett, S. Guerin, D. Briand and N. F. de Rooij, Silicon Planar Microcalorimeter Employing Nanostructured Films, *Digest of technical papers vol 1*, Transducers '01 Eurosensors XV, Munich, Germany, 2001, pp. 820-823.

[5.6] A. Pike, J. W. Gardner; Thermal modelling and characterisation of micropower chemoresistive silicon sensors, *Sensors and Actuators B*, Vol 45 (1997) p19-26.

[5.7] U. Dibbern, A substrate for thin-film gas sensors in Microelectronic Technology, *Sensors and Actuators B*, 2, 1990, pp. 63-70.

[5.8] G. C. M. Meijer, A. W. Herwaarden, *Thermal Sensors*, Institue of Physics Publishing, Appendix A, p290, 1994.

[5.9] S. M. Lee, D. C. Dyer and J. W. Gardner, Design and optimisation of a high-temperature silicon micro-hotplate for nanoporous palladium pellistors. *Microelecronics Journal,* 34, pp 115-126, 2003.

[5.10] F. P. Incropera, D. P. De Witt, *Fundamentals of heat and mass transfer*, Third edition, Chapter 12, p696, John Wiley & Son, Ltd, 1990.

[5.11] S. M. Lee, J. W. Gardner; City Technology Ltd. Low power micropellistor project quarterly report (University of Warwick), No. 8, 2001.

Chapter 6

Chemical characterisation of the micro-calorimeters

6.1 Introduction

Previously the fundamental electro-thermal characteristics of the micro-calorimeter have been investigated. This has included the power-temperature behaviour of these devices. Here the chemical response of the micro-calorimeters is investigated. The test conditions, including both the test gas concentration and flow-rate, were in accordance with the industrial safety standards. Therefore, the experimental results could be compared with commercially tested calorimeters.

In a continuous powering mode, the magnitude of the output voltage was measured for various micro-calorimeter designs. The changes in resistance and temperature of the calibrated micro-heater element due to the catalytic reaction were calculated. Hence, the efficiency of the nanoporous Pd catalyst was assessed in terms of its output voltage and other aspects, such as *MHR* and size of the electrode were considered. Moreover, the voltage sensitivity of the micro-machined devices had been calibrated at different temperatures. Therefore, the relationship between the sensitivity and operating temperature can be evaluated and so in the future, the sensor power characteristics could be predicted for various applications.

In a pulse operation mode, the time constants (rise time (τ_{rise}) and fall time (τ_{fall})) of the sensors were characterised for both a small-signal mode and a power modulation mode in air. The maximum operating frequency of the sensors could be determined for each pulsing regime. The chemical dynamic response of the sensor under the two pulsing modes was also analysed. Furthermore, the power consumption of the micro-calorimeters at different frequencies was determined. Finally, the reliability of the devices have been analysed based on the life expectancy and the poisoning resistance using a standard poisoning test gas.

6.2 Methane response in continuous powering mode

The devices response to methane in continuous powering mode was characterised with the gas test station at City Technology Ltd. described in Chapter 4. The test conditions were in accordance with the industrial safety standard, BS EN 50014: 1993 and BS EN 50018: 1995. The concentration of the methane employed was 50% of the Lower Explosive Limit (LEL), corresponding to 2.5% (25000 ppm) methane in air, with an ambient temperature of (20 ± 5)°C. A volumetric gas flow rate of 300 ml/min was used. All the experiments were conducted without a micro-machined compensator; the compensator element in the Wheatstone bridge circuit was replaced by a resistor block as discussed in Chapter 4, section 4.3.

6.2.1 Output response for various micro-calorimeter designs

Initially, to understand the performance of the various micro-calorimeter designs, the output magnitude of the devices had to be measured for both design generations. The conventional meander type designs and the Drive-wheel designs, which deliver superior performance among the second generation design, were selected for the investigation.

A batch of twenty-four sensors coated with nanoporous Pd catalyst, three from each of the selected design families, was evaluated by a commercial pellistor characterisation system (City Technology Ltd. UK). The devices were run first in clean dry air to create a baseline signal before the test gas was introduced to the chamber for a minimum of 60 seconds. Then dry air was switched back to check for a genuine response to the test gas [6.1]. Typical sensor responses are shown in figures 6.1 and 6.2. The standard deviation of the sensor responses was well within 3% of the values shown in the figures. The voltage supply for both of the devices was 7.5 V, for direct comparison.

Figure 6.1 indicates that the output magnitudes are 38 mV and 45 mV for the devices SRL 136a and SRL 162g, respectively. The optimised meander design produced a higher response despite using a smaller amount of nanoporous Pd catalyst at identical supply voltages. This showed that the catalyst reaction had been improved by approximately 10.5%. However, it is important to note that the rise time of the device cannot be measured from this data. The rise-time and the fall-time in the figures illustrate the combination of the time taken for either the air or the test gas to be purged from the test chamber and the actual time constant of the devices. The analysis of the catalyst

efficiency is included in section 6.2.3 and the dynamic properties of the sensors were investigated by other methods, as described in section 6.3.

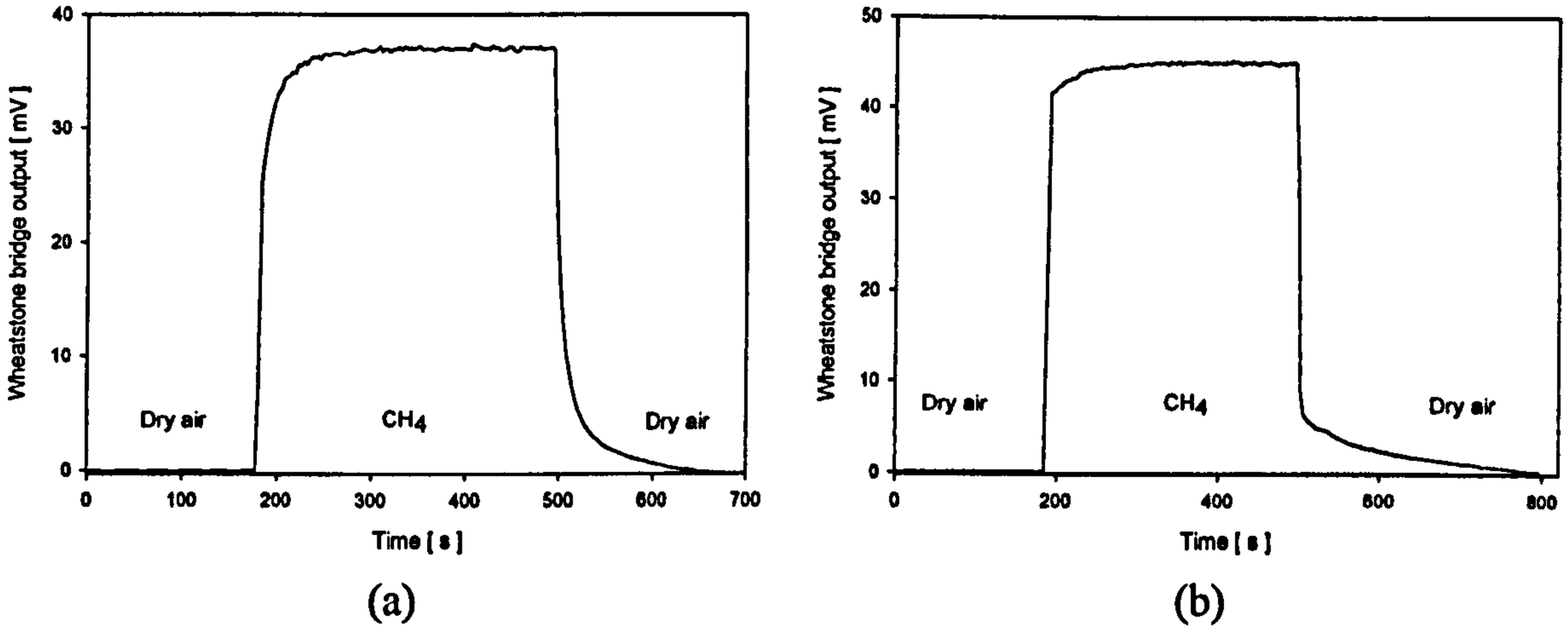

Figure 6.1: Typical responses of the nanoporous Pd coated micro-calorimeters to CH_4 at 50% LEL for the 1st generation devices with a supply voltage of 7.5 V. (a) The former meander design (SRL 136a) and (b) the optimised meander design (SRL 162g).

The responses of the second generation micro-calorimeters using the Drive-wheel micro-heater design were investigated [6.2], as shown in figure 6.2. It includes the designs from the Standard family (SRL 176c), Low power family (SRL 177c), Small-mem/robust family (SRL 178c), Robust family (SRL 179c), Ultra-small/robust family (SRL 180c) and the Ultra-small/low power family (SRL 181c). The test conditions and equipment were identical to the experiments for the first generation devices but were operated at their nominal operating temperature of 500°C above ambient. However, as the voltage requirements of the devices were reduced (as discussed in Chapter 5), the sensor responses fell between 5 mV and 19 mV, depending on the device model. The standard deviation of the Wheatstone bridge output for each of the device models was within 4%.

An offset voltage from the Wheatstone bridge output was observed for some sensors when the methane-filled test chamber was purged by dry clean air. This could be caused by the metal-based TO-5 headers acting as highly efficient heat sinks for the devices. Although the header itself required a much longer time to cool down, the curve would eventually return to zero. Therefore, a glass insulated TO-5 header was used to reduce the thermal time constant of the package.

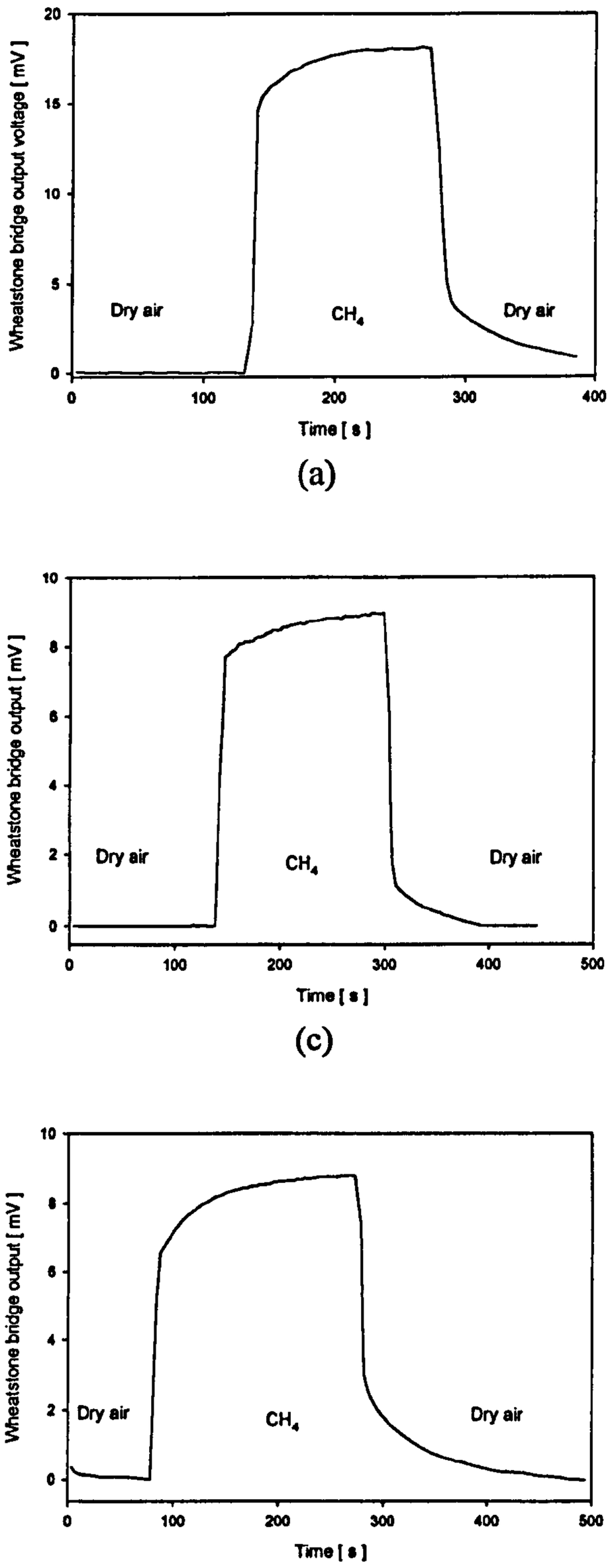

(a)

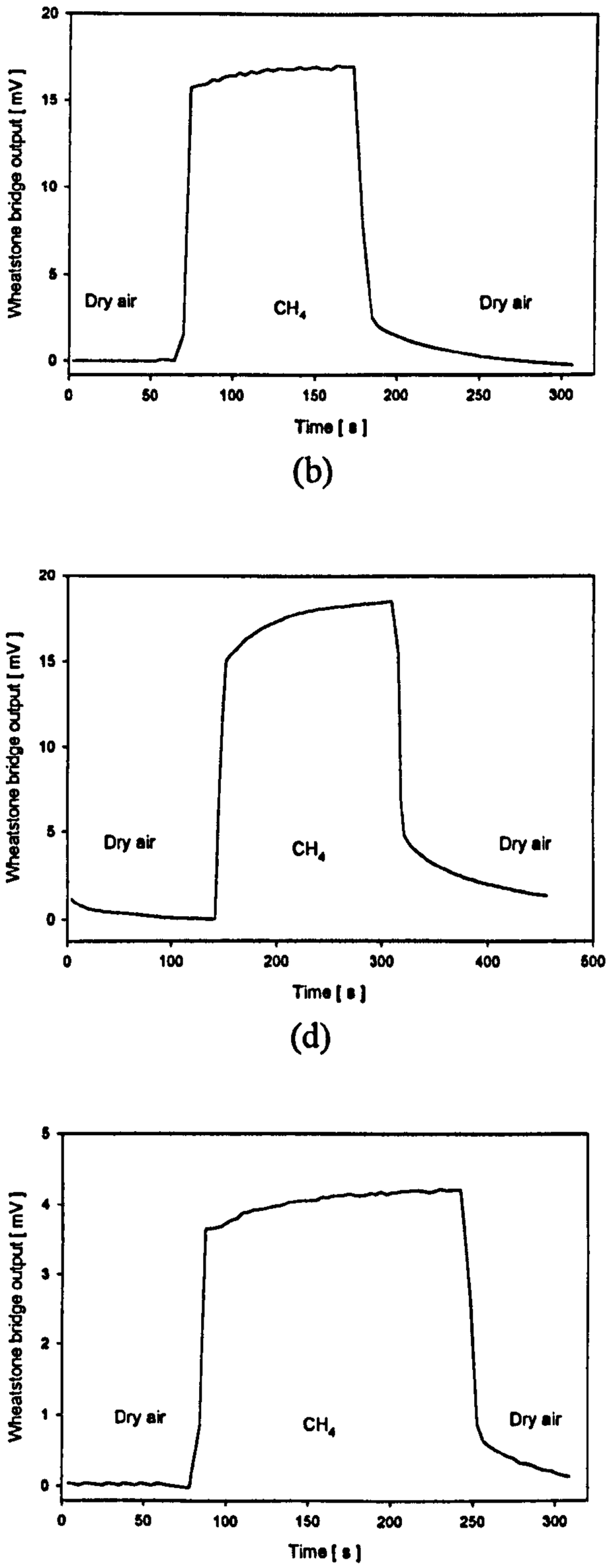

(b)

(c)

(d)

(e)

(f)

Figure 6.2: Typical responses of the micro-calorimeters to CH_4 at 50% LEL for the 2nd generation devices at the nominal operating voltages. (a) The Standard family (SRL 176c) at 3.1 V; (b) the Low power family (SRL 177c) at 2.7 V; (c) the Small-mem/robust family (SRL 178c) at 2.8 V; (d) the Robust family (SRL 179c) 3.2 V; (e) the Ultra-small/robust family (SRL 180c) at 2.5 V; Ultra-small/low power family (SRL 181c) at 2.0V.

6.2.2 Sensor responses at various operating temperatures

The sensitivity of the sensors was calibrated against a range of micro-heater temperatures by varying the input voltage. Sensors from several design families were selected based either on their outstanding sensitivity or on specific reference purposes. These included the former (SRL 136a) and optimised meander (SRL 162g) from the first generation as well as the Drive-wheel design in the Standard family (SRL 176c), the low power family (SRL 177c) and the Ultra-small/low power family (SRL 181c).

The test gas and dry clean air were cycled in the chamber at each different operating temperature. As the catalytic effect begins at a temperature of about 400°C, non-uniform thermal profile at the active area resulted in different level of the catalytic activity. Therefore, the higher the operating temperature, the more catalyst is involved in the reaction. Typical responses of the sensors at various operating temperatures are shown in figures 6.3 to 6.5 [6.2]. As the maximum operating temperature of the sensors ranges from 700°C to 900°C, the sensors were tested up to 650°C to avoid membrane rupture. The micro-calorimeter outputs were directly proportional to the operating temperature without saturating until device failure, as shown in figure 6.6, unlike the commercial pellistors which saturate at about 600°C.

Due to a small difference in the voltage requirements between the former (SRL 136a) and optimised (SRL 162g) meander micro-calorimeters, the same input voltages were used during the experiments (6.0 V, 7.5 V and 8.5 V). The sensors were checked for functionality after the experiments. The responses of the first generation sensors are shown in figure 6.3. The results showed that the sensitivity of the device increases with the operating temperature but there is still a considerable response to the standard test gas, about 12 mV per % CH_4, at 400°C. Furthermore, the second generation sensors also demonstrated that there could be a detectable output for a temperature as low as 280°C, as shown in figure 6.4. For example, the power consumption for the SRL 176c could be reduced by 47% if a particular application could tolerate an output voltage of 4.0 mV per % CH_4 instead of 6.8 mV.

In addition, a device without the nanoporous Pd catalyst also indicated a response to the test gas, as shown in figure 6.5 [6.1]. Hence, an uncoated device is not entirely inert to the target gas but can act as conductivity sensor and so cannot be employed as a compensator element in the Wheatstone interface circuit. Nevertheless, this experiment showed that the catalyst boosted the sensitivity of the sensor by approximately 35% on

average, for different operating temperatures. It reduces the power budget of the micro-calorimeter by lowering the operating temperature but retaining an identical output.

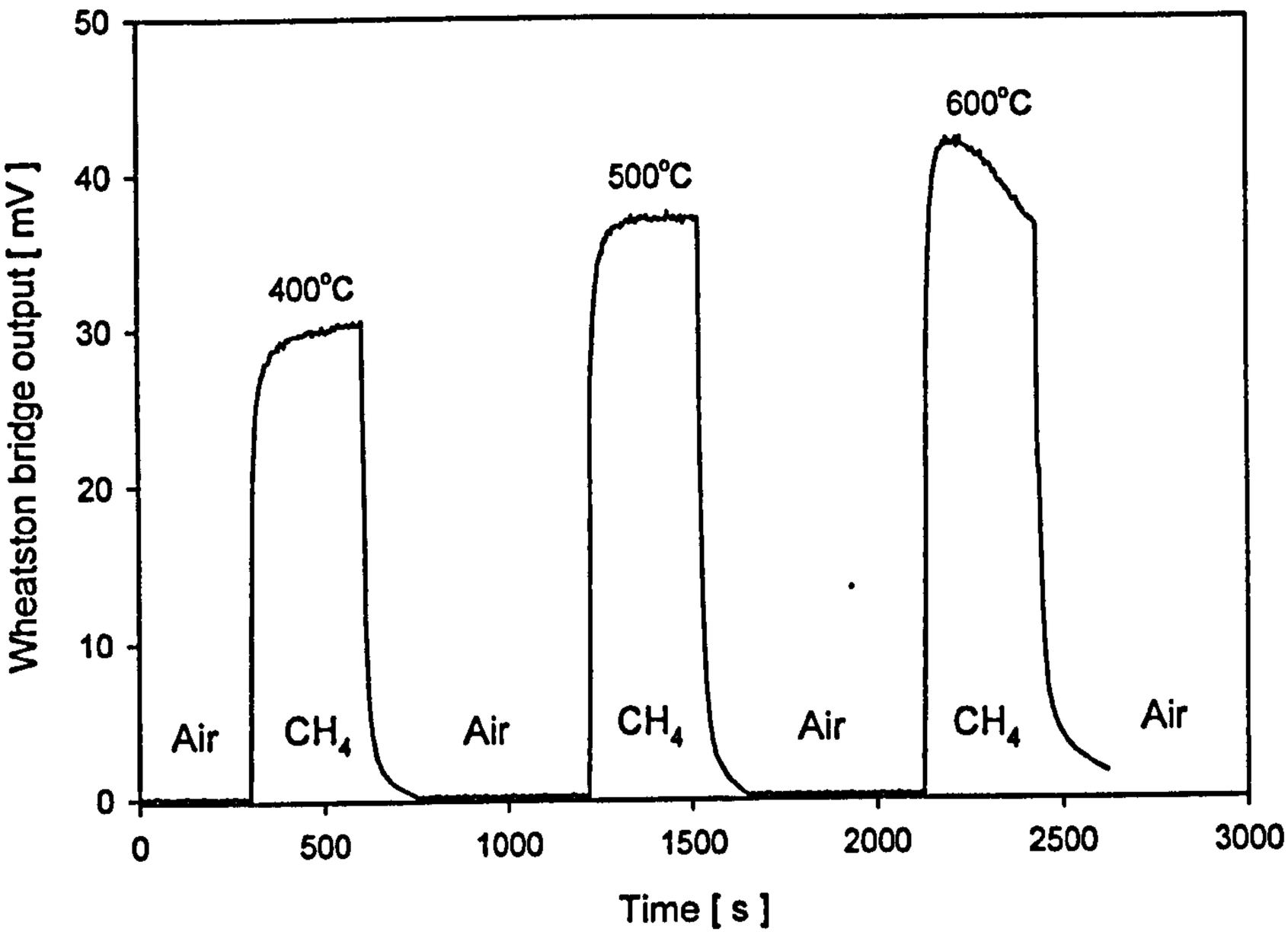

(a)

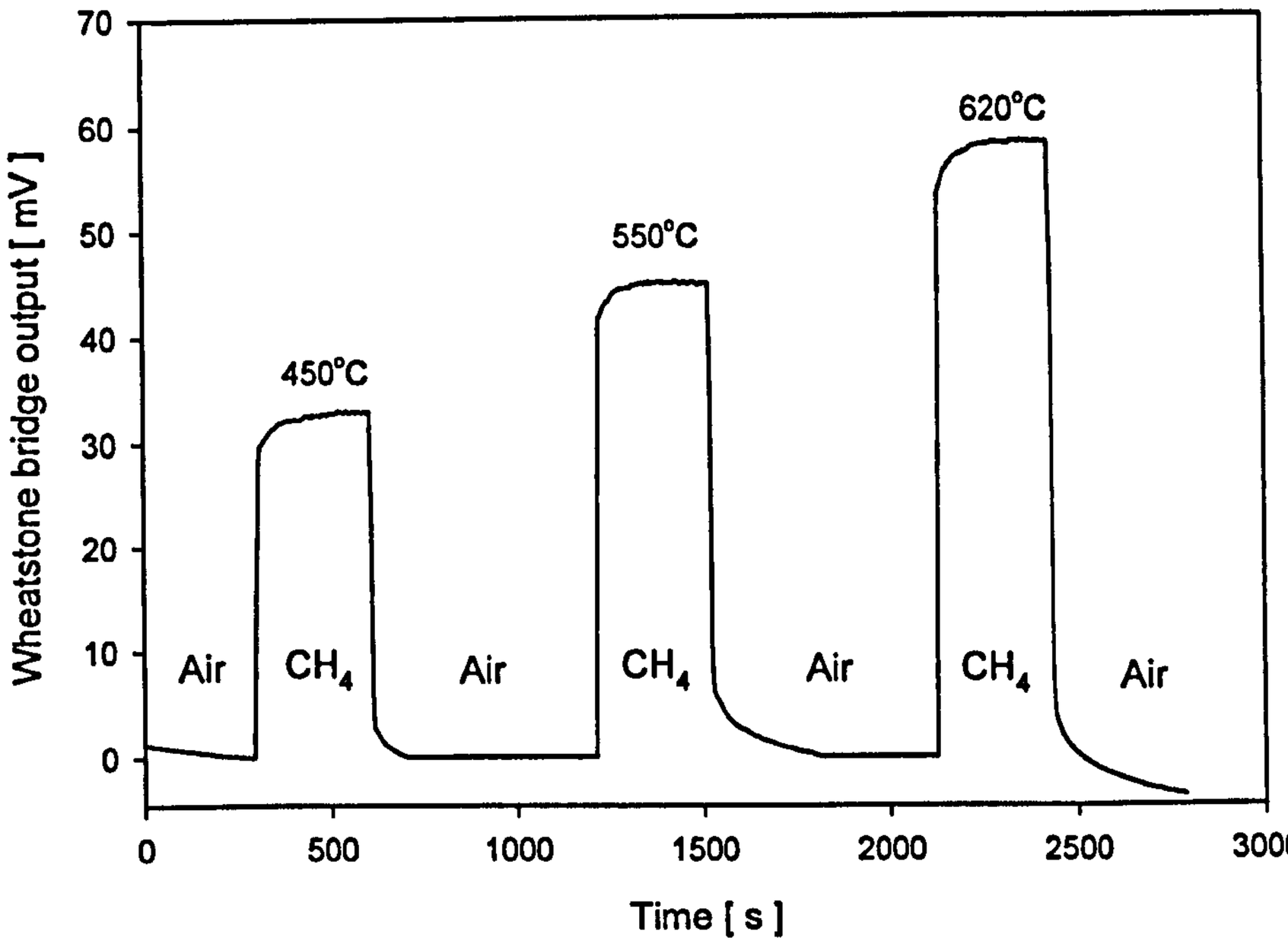

(b)

Figure 6.3: Output magnitude at various operating temperatures. The input voltages were 6.0 V, 7.5 V and 8.5 V. (a) The former meander design (SRL 136a) and (b) the optimised meander design (SRL 162g).

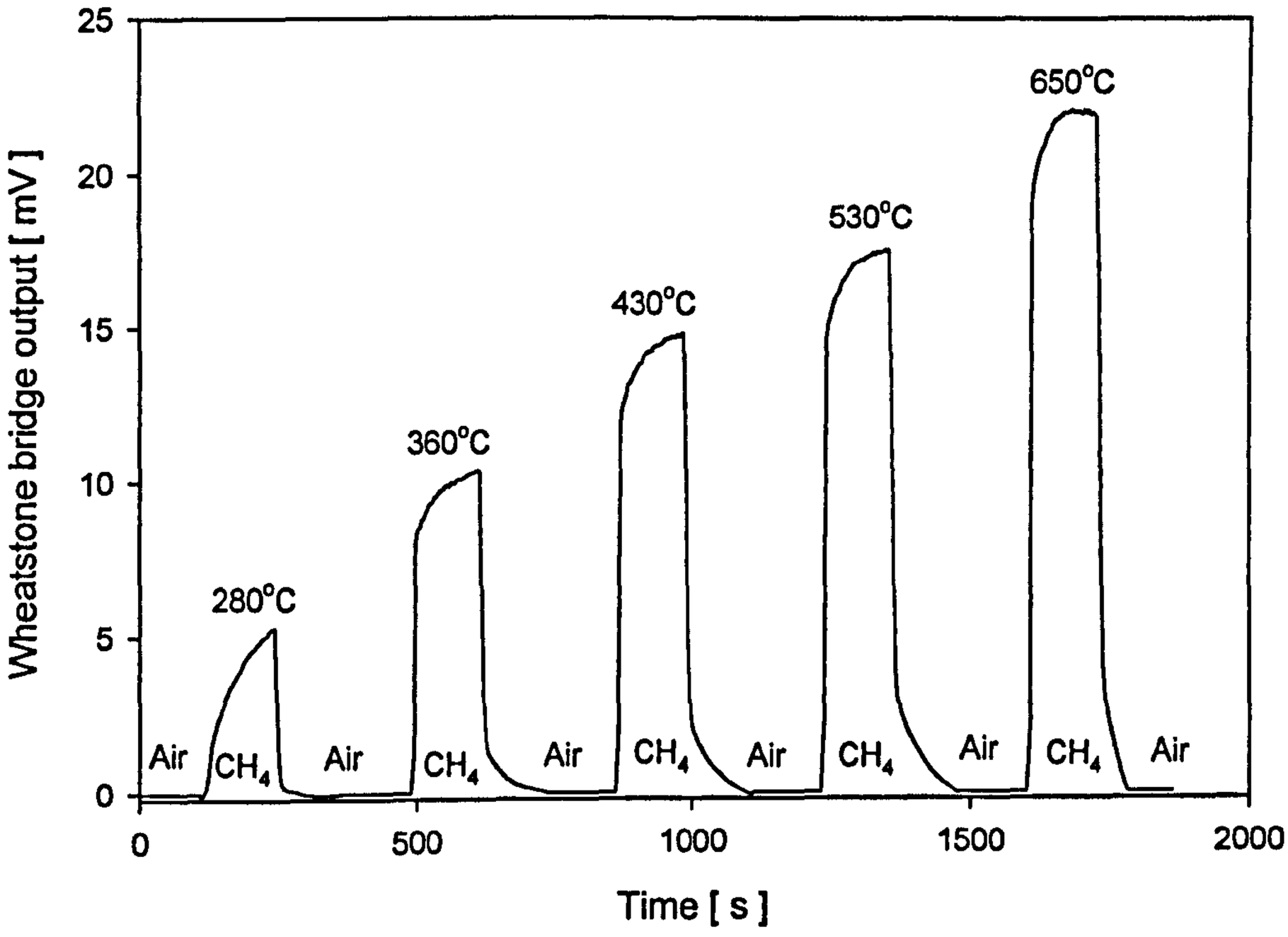

(a)

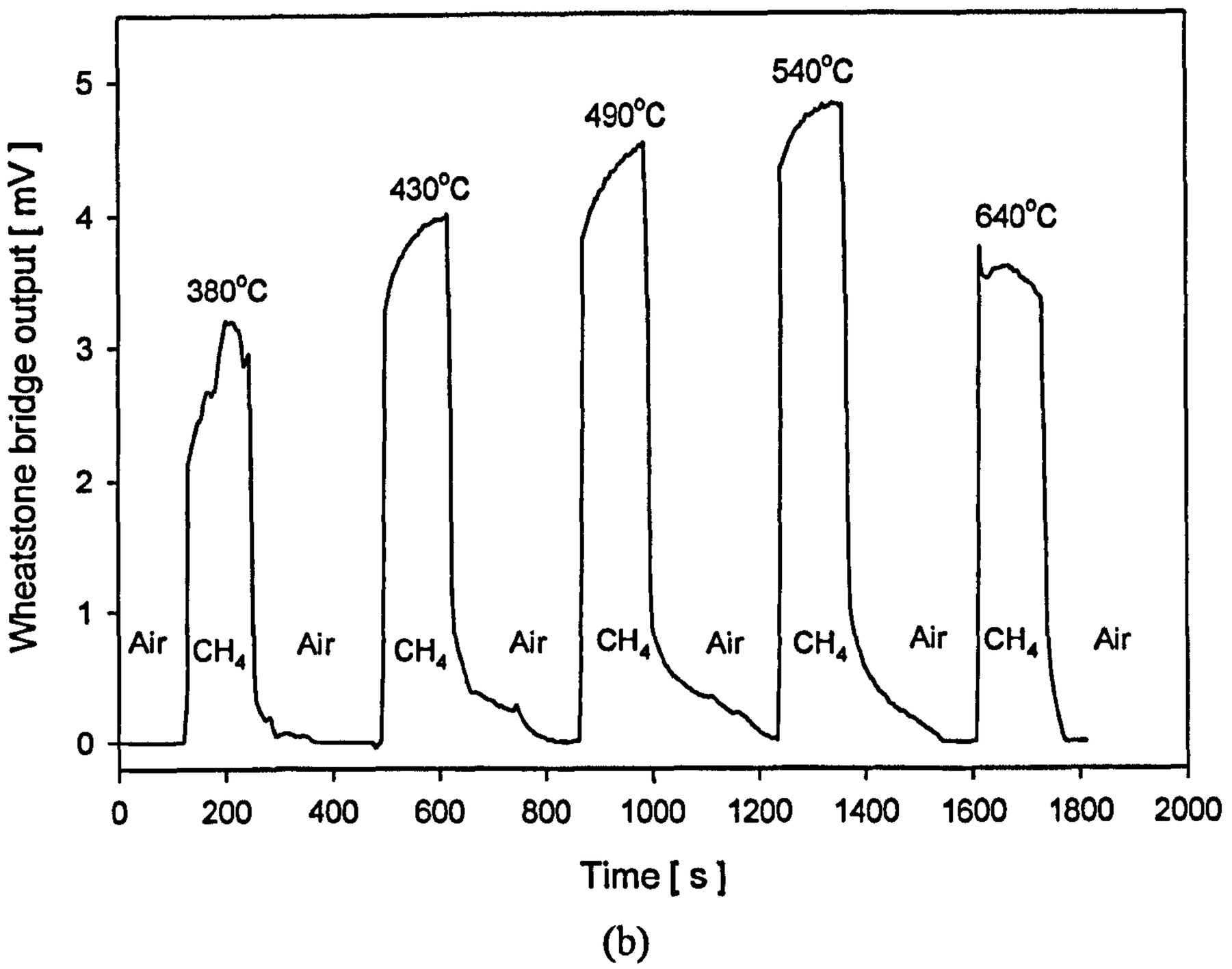

(b)

Figure 6.4: Output magnitude at various operating temperatures. (a) The SRL 176c with supply voltage varied from 1.7 V to 3.2V in 0.5 V steps. (b) The SRL 181c with supply voltage from 1.5 V to 2.3 V in 0.2 V steps.

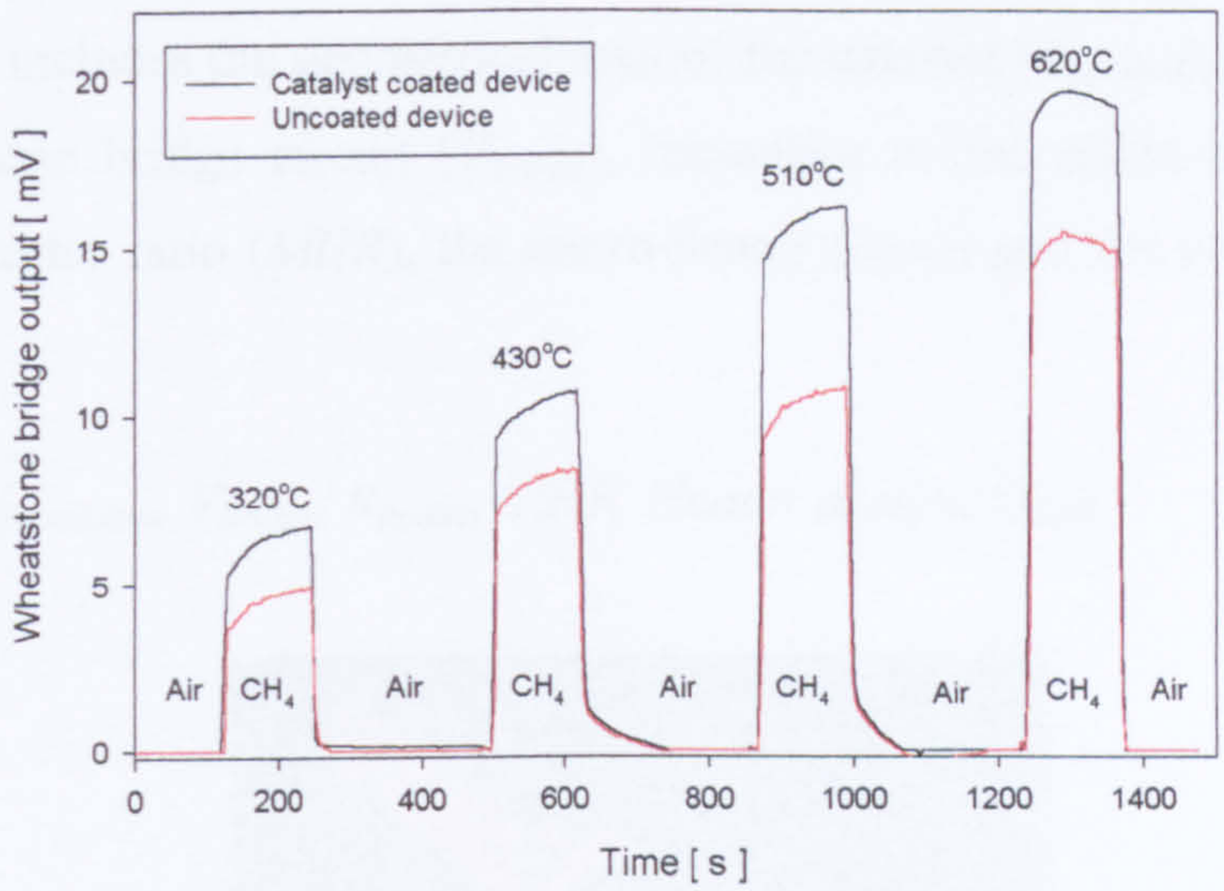

Figure 6.5: Comparison of the responses showing the effect of the nanoporous catalyst to 2.5% methane in air for SRL 177c with supply voltage varied from 1.7 V to 3.2 V in 0.5V steps.

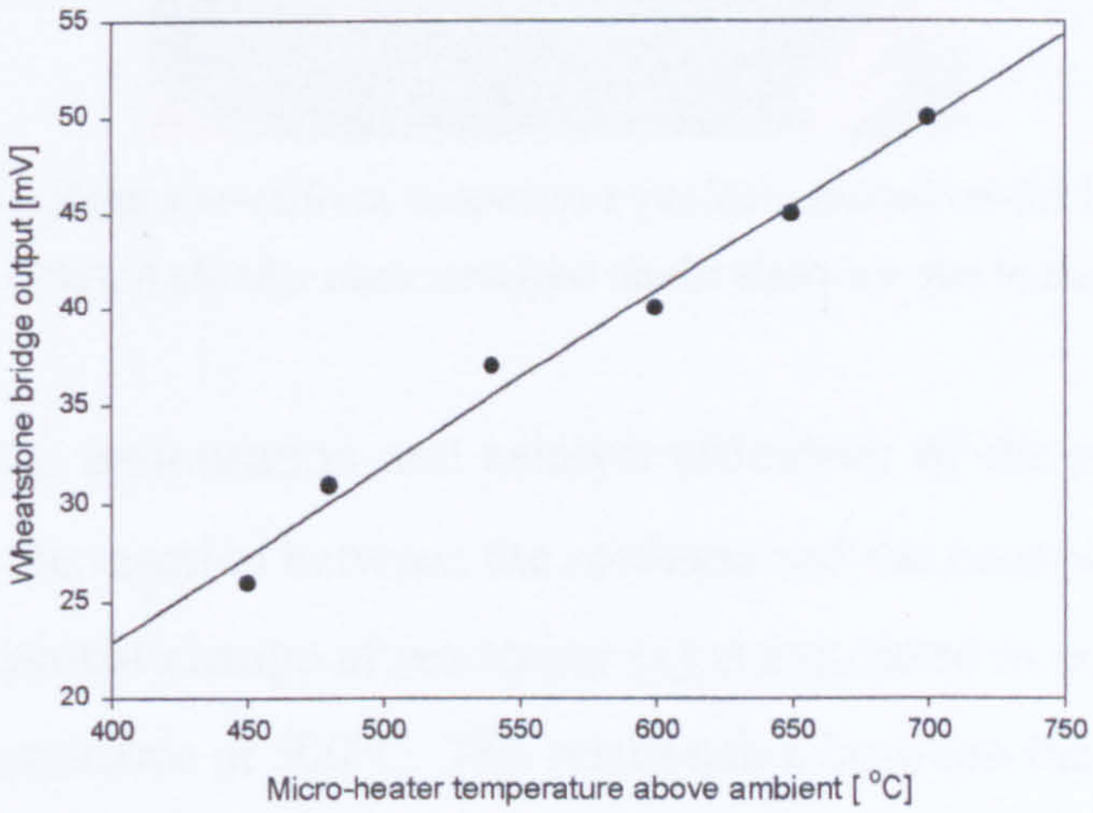

Figure 6.6: A typical response of the micro-calorimeter (SRL 136a) that increases linearly with temperature until device failure.

6.2.3 Analysis of the sensor optimisation and catalyst efficiency

Various sensors optimisations were evaluated after the power and active area optimisations had already been analysed as described Chapter 5. A non-uniform temperature profile within the active area could cause uneven catalyst reaction and affect performance, as shown in figure 6.7. According to the device response under various conditions, described in the last two sections, further analysis of the optimisation and catalyst efficiency for the devices was required.

Although, the output magnitude, V_{out}, of the bridge interface circuit is the most crucial parameter in terms of methane detection, it does not necessarily measure the

reaction efficiency of the catalyst. It can be influenced by several factors as expressed in equation 6.1. It includes the geometrical area of the catalyst ($A_{catalyst}$), the supply voltage of the Wheatstone bridge circuit (V_{bridge}), resistance of the micro-heater (R_{heater}), the Membrane-to-heater ratio (MHR), the micro-heater design and the concentration of the test gas (G_{con}).

$$V_{out} = f\,(A_{catalyst},\ V_{bridge},\ R_{heater},\ MHR,\ Heater\ design,\ G_{con}) \tag{6.1}$$

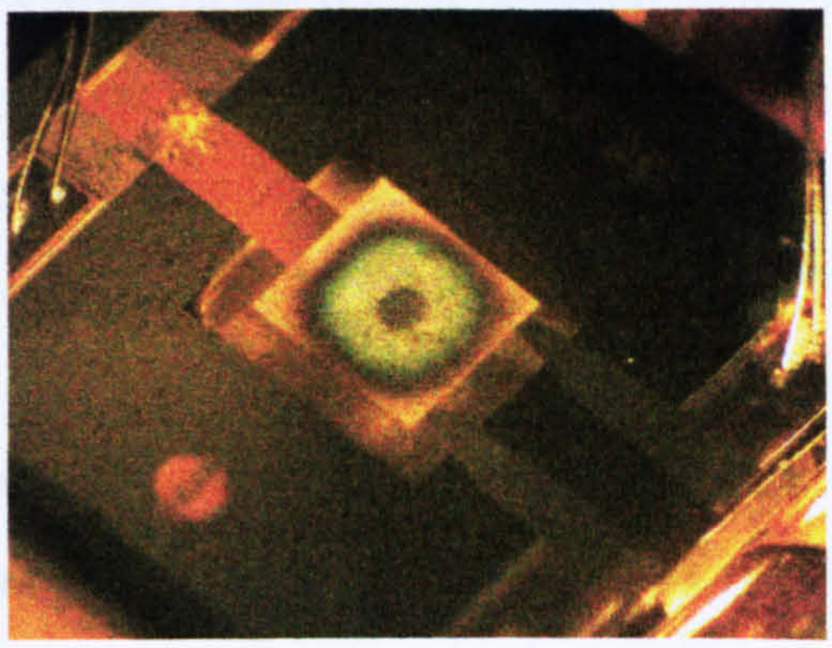

Figure 6.7: An example of the non-uniform temperature profile occurred on the former meander design in the robust family (SRL 179e). A circular mark remained on the electrode due to the central hot spot.

In order to verify the optimisation and catalyst efficiency of the sensor, the resistance change, ΔR, due to the reaction between the methane and the nanoporous Pd catalyst was calculated. The fractional change of resistance (x) is expressed in equation (6.2a), where R_{500} is the device resistance at 500°C. The relationship between the fractional resistance (x) and the voltage output of a Wheatstone bridge circuit is expressed in equation (6.2b). Therefore, the change of sensor resistance due to a catalyst reaction can be obtained from equation (6.2c). Derivations of these equations are given in Appendix 6a.

$$\frac{\Delta R}{R_{500}} = x \tag{6.2a}$$

$$\frac{V_{out}}{V_i} = \frac{x}{2(2+x)} \tag{6.2b}$$

Therefore,

$$\frac{\Delta R}{R_{500}} = \frac{4V_{out}}{V_i - 2V_{out}} \tag{6.2c}$$

Hence, the actual temperature generated, ΔT, can be obtained by relating the change of resistance with the temperature coefficient of resistivity, α, of the platinum micro-heater. However, the ΔT is related to V_{out} which is highly dependent on the different functions described in equation (6.1). As the factors are co-related to each other, it is necessary to isolate and evaluate them individually.

Analysis indicated that the SRL 162g provided the highest output voltage per percent methane in air at the nominal operating voltage, as shown in figure 6.8(a). However, the standard deviation of the output between different samples is higher for the SRL 136a and SRL 162g. The influence of the *MHR* was also reflected in the results. Although the micro-heater sizes for SRL 177c, SRL 178c and SRL 180c are identical, the SRL 177c provided twice the output of the others. As the *MHR* is similar between the SRL 178c and SRL 180c, their output responses are almost identical.

The distribution of the temperature change, ΔT, by the nanoporous Pd catalyst for various devices at nominal supply voltages has also been investigated, as shown in figure 6.8(b). The highest temperature change per percent methane in air was achieved by the SRL 177c. This analysis allows different device types to be selected for specific applications which require different thermal characteristics. For instance, a high methane concentration environment might require a device with a lower ΔT to prevent over-heating and impairing reliability.

After the output voltages and the temperature changes had been normalised according to area of the electrode (i.e. output voltage per unit area), the efficiency of the catalyst could be evaluated, as shown in figure 6.9. The Wheatstone bridge output per percent methane in air indicates that the SRL 177c and the SRL 181c provided the highest efficiency per unit area. It was found that all the optimised designs had improved sensitivity from the original micro-calorimeter designs. In addition, the normalised temperature increase also showed similar results. The improved thermal profile of the active area enhanced the reactivity of the catalyst which led to a higher output magnitude.

The sensitivity of the devices was evaluated to improve the understanding of the catalyst efficiency as shown in figure 6.10. Here, the voltage sensitivity, S_V, and the thermal sensitivity, S_T, at the nominal operating voltages were calculated from equations (6.3) and (6.4) respectively [6.3].

The voltage and thermal sensitivity of the sensors per percent methane in air indicated that the SRL 177c delivered the highest sensitivity which was higher than the

meander micro-heater designs. This showed that the Drive-wheel design created an improved isothermal active area and allowed higher catalyst reactivity.

$$S_V = \frac{d(V_{out}/V_{in})}{dG_{con}} \times 100\% \text{ per } \% \tag{6.3}$$

$$S_T = \frac{d(\Delta T/500^{o}C)}{dG_{con}} \times 100\% \text{ per } \% \tag{6.4}$$

where V_{out} is the Wheatstone bridge output; V_{in} is the voltage supply to the bridge circuit; ΔT is the temperature elevated by the catalyst; G_{con} is the gas concentration.

The sensitivity of the sensors was normalised according to the area of the electrode (i.e. sensitivity in % per unit area) to evaluate the effectiveness of the optimisations, as shown in figure 6.11. The results showed that the Ultra-small device (SRL 181c) achieved the highest sensitivity and the lowest power consumption. The Low power, Drive-wheel design (SRL 177c) also delivered outstanding performance. Both of the designs employed the largest *MHR* which provided sufficient thermal isolation to boost the performance towards methane detection.

The relationship between the *MHR* and the normalised sensitivities of the sensors is illustrated in figure 6.12. Once again, the sensitivity was proportional to the *MHR*. However, the other factors mentioned in equation (6.1) could affect the linearity of the graphs. Therefore, although the SRL 177c and SRL 181c have identical *MHR*s, the device sensitivities are different.

The relationship between the geometrical area of the Au gate electrode and the normalised sensitivities per percent methane in air was established, as shown in figure 6.13. The inversely proportional relationship demonstrated that smaller electrodes reduce the thermal loss by convection and enhance the device sensitivity. In addition, the output magnitude and the sensitivities of the devices were linear with gas concentrations, between 0.25% and 2.5% methane in air [6.4].

Therefore, the results proved that all the optimised designs had improved the original device. Although the optimised meander design (SRL 162g) provided the highest absolute output magnitude, the Drive-wheel designs had delivered the most isothermal active area and enhanced catalyst efficiency.

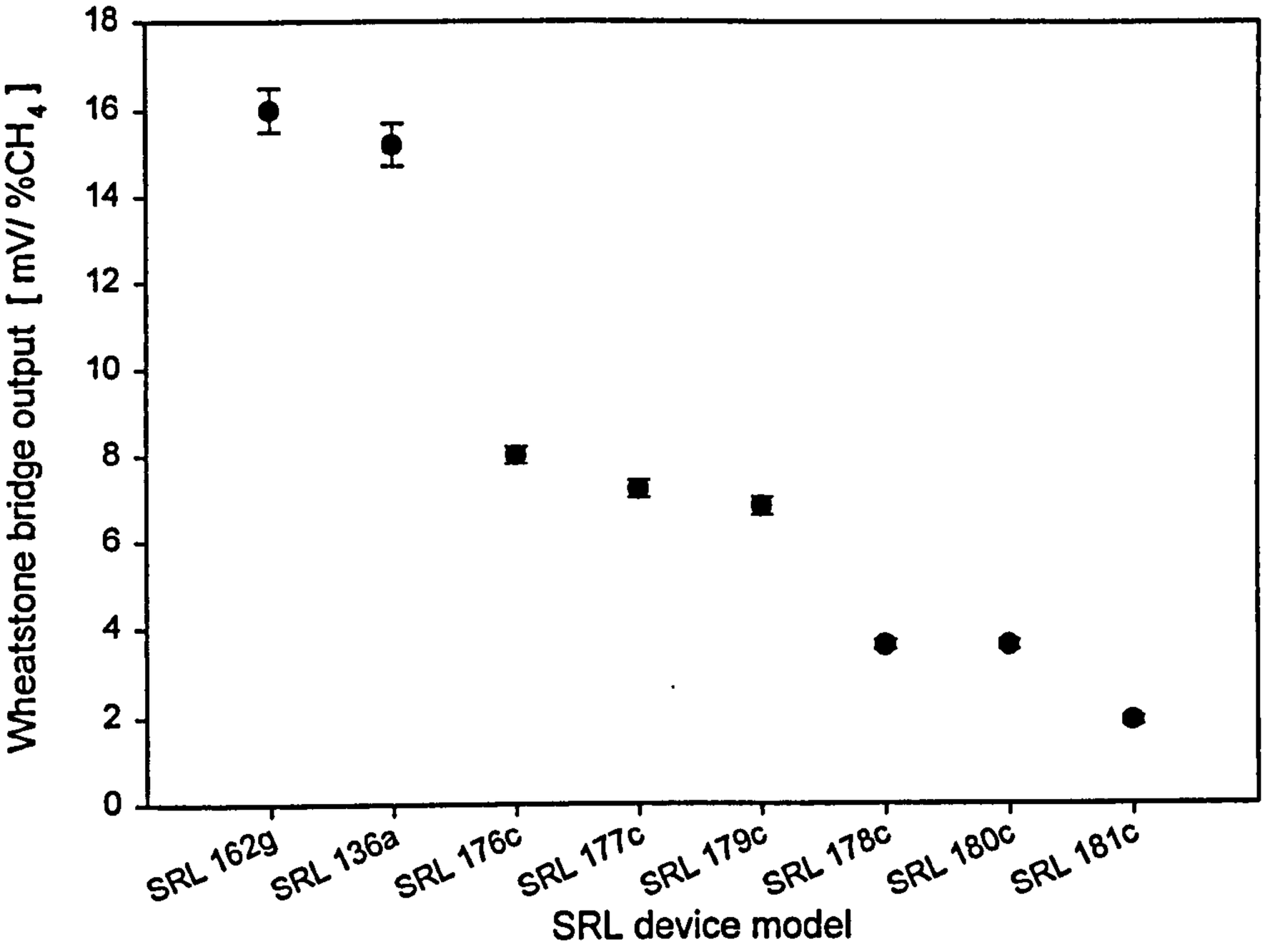

(a)

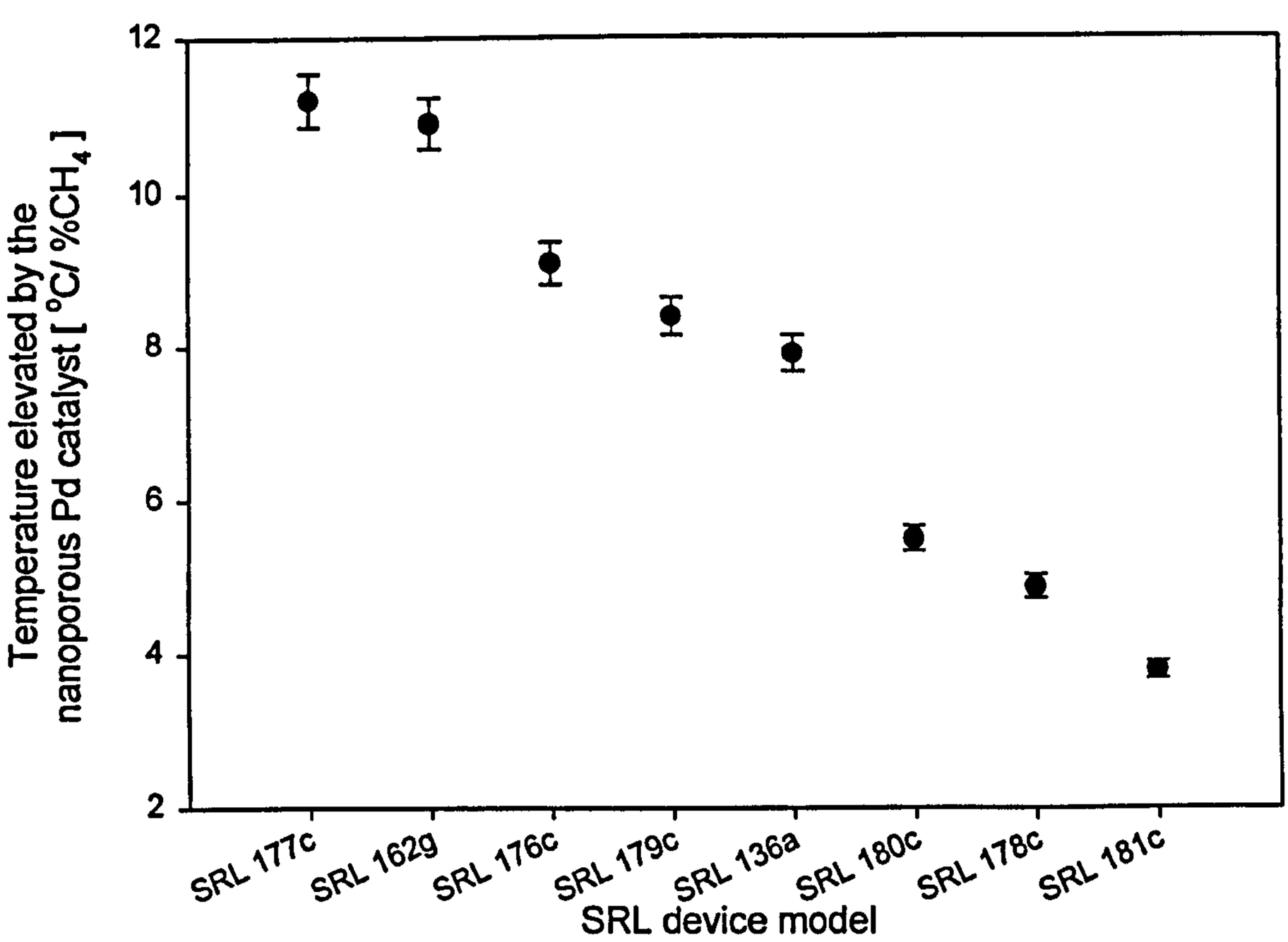

(b)

Figure 6.8: Evaluation of the device optimisation per % methane in air at nominal operating voltage for various devices based on (a) the differential output voltage from the Wheatstone bridge circuit and (b) the temperature changes.

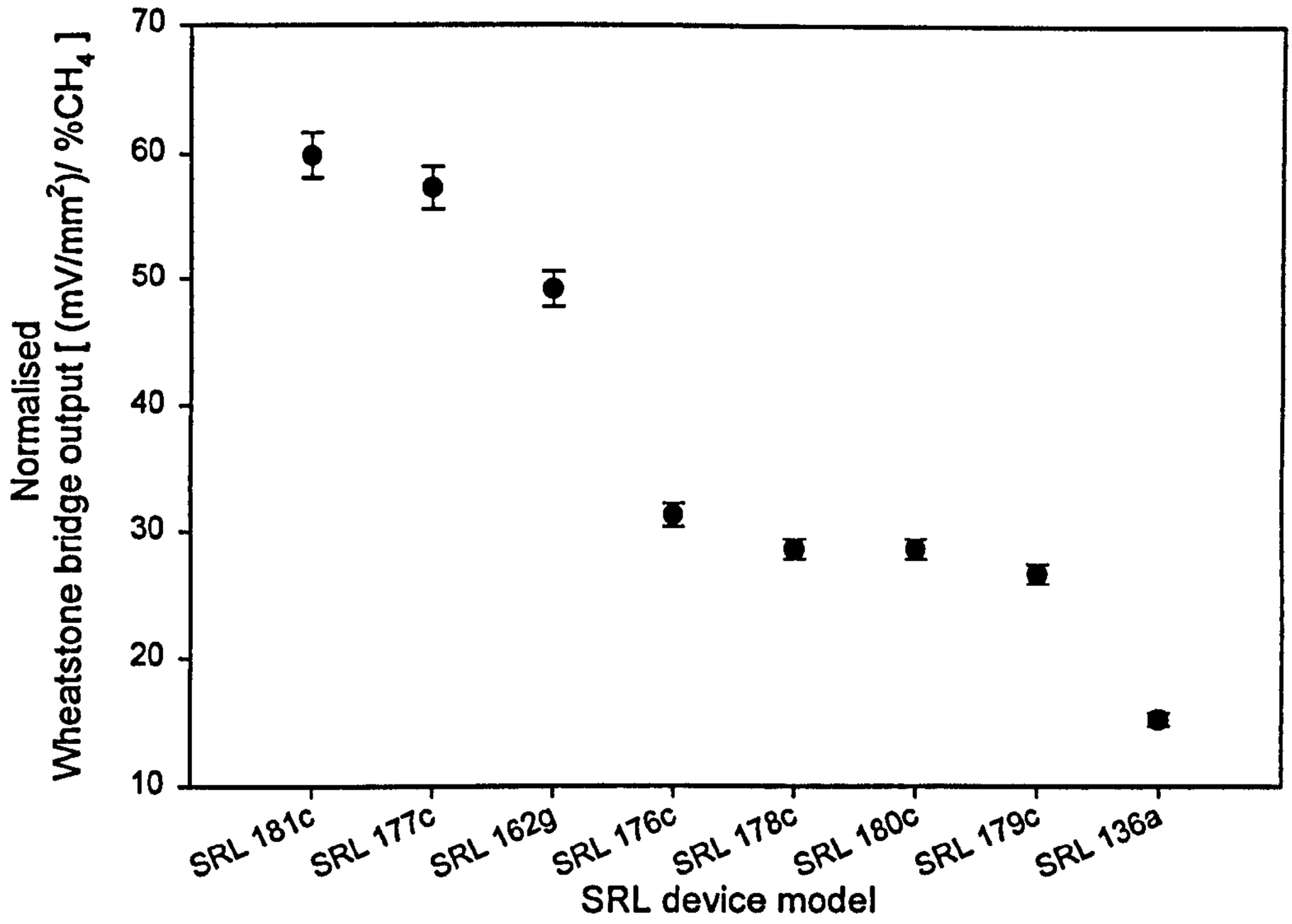

Figure 6.9: Evaluation of the device optimisation per % methane in air at nominal operating voltages for various SRL micro-calorimeters based on (a) the normalised output voltage and (b) the normalised temperature change.

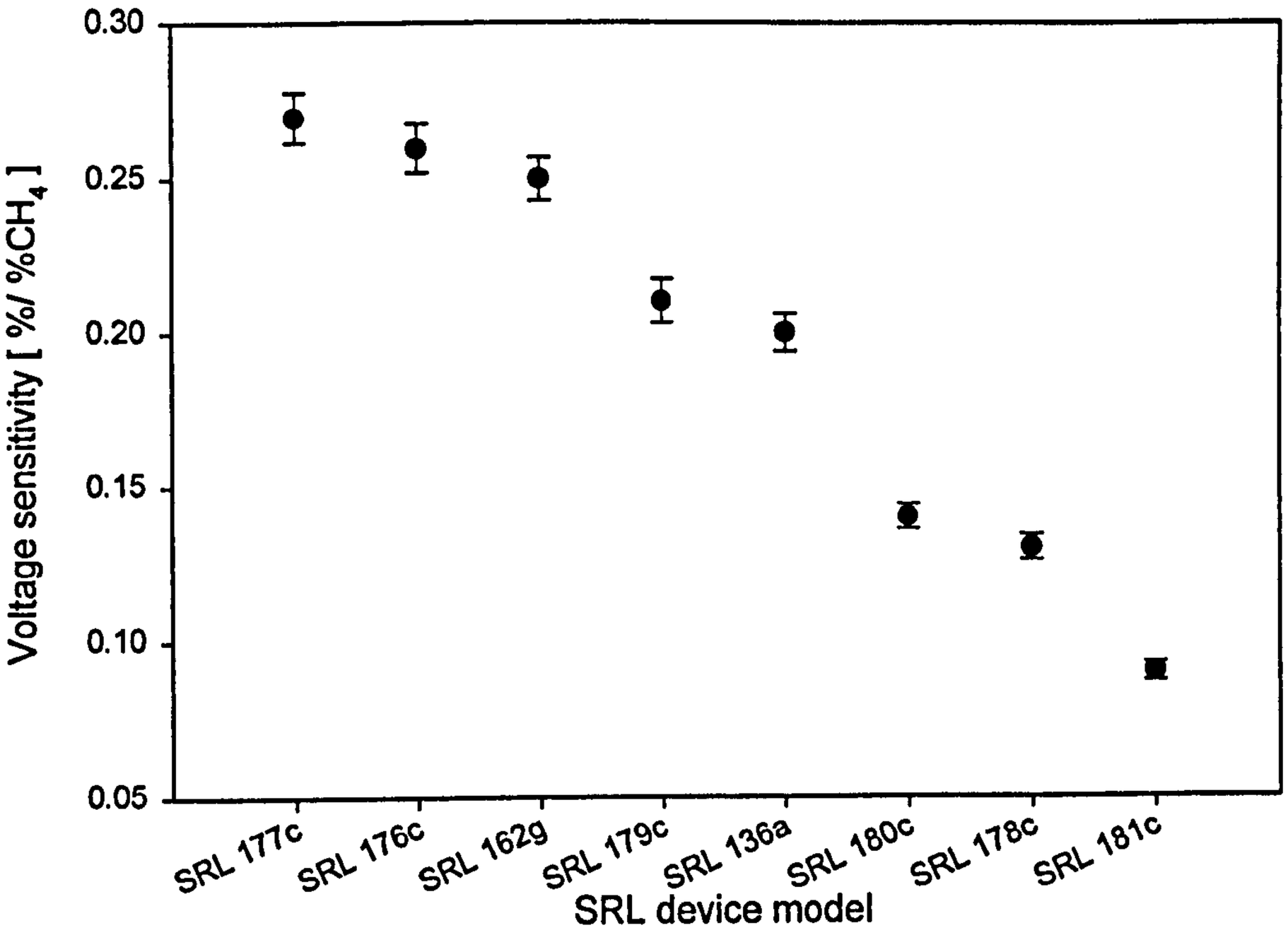

(a)

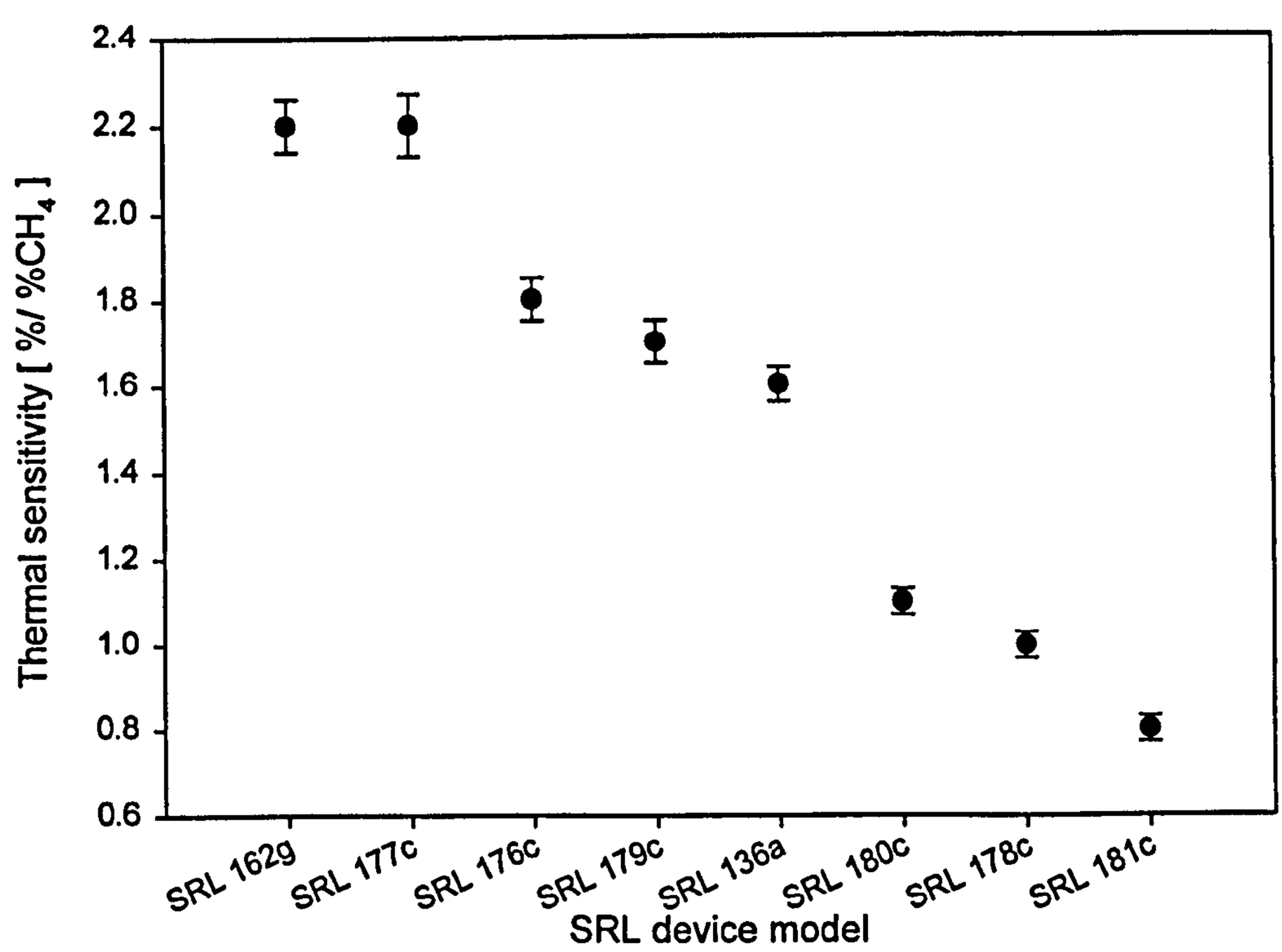

(b)

Figure 6.10: Evaluation of the device optimisation per % methane in air at nominal operating voltages for various SRL micro-calorimeters based on (a) the voltage sensitivity (S_V) and (b) the thermal sensitivity (S_T).

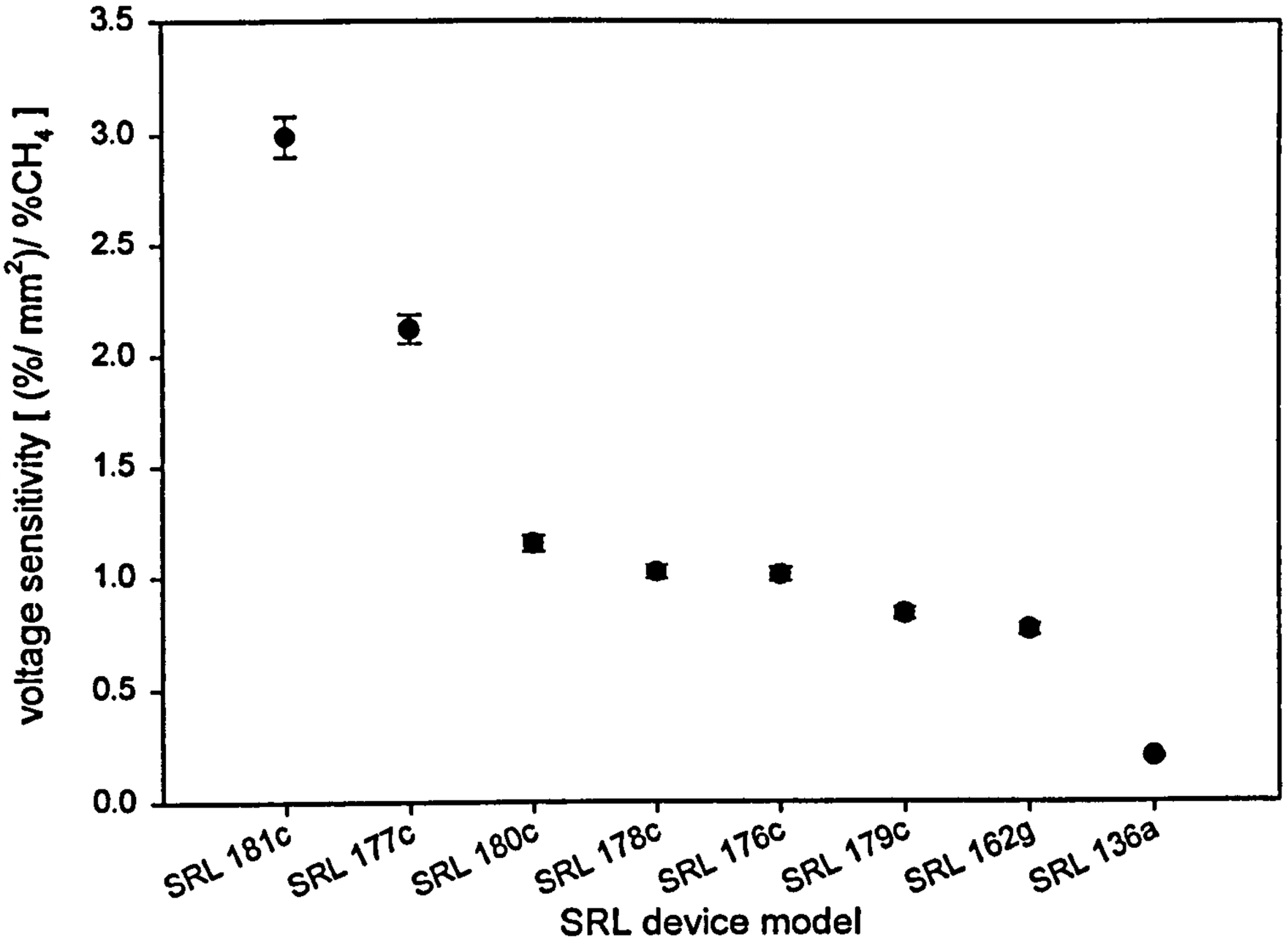

(a)

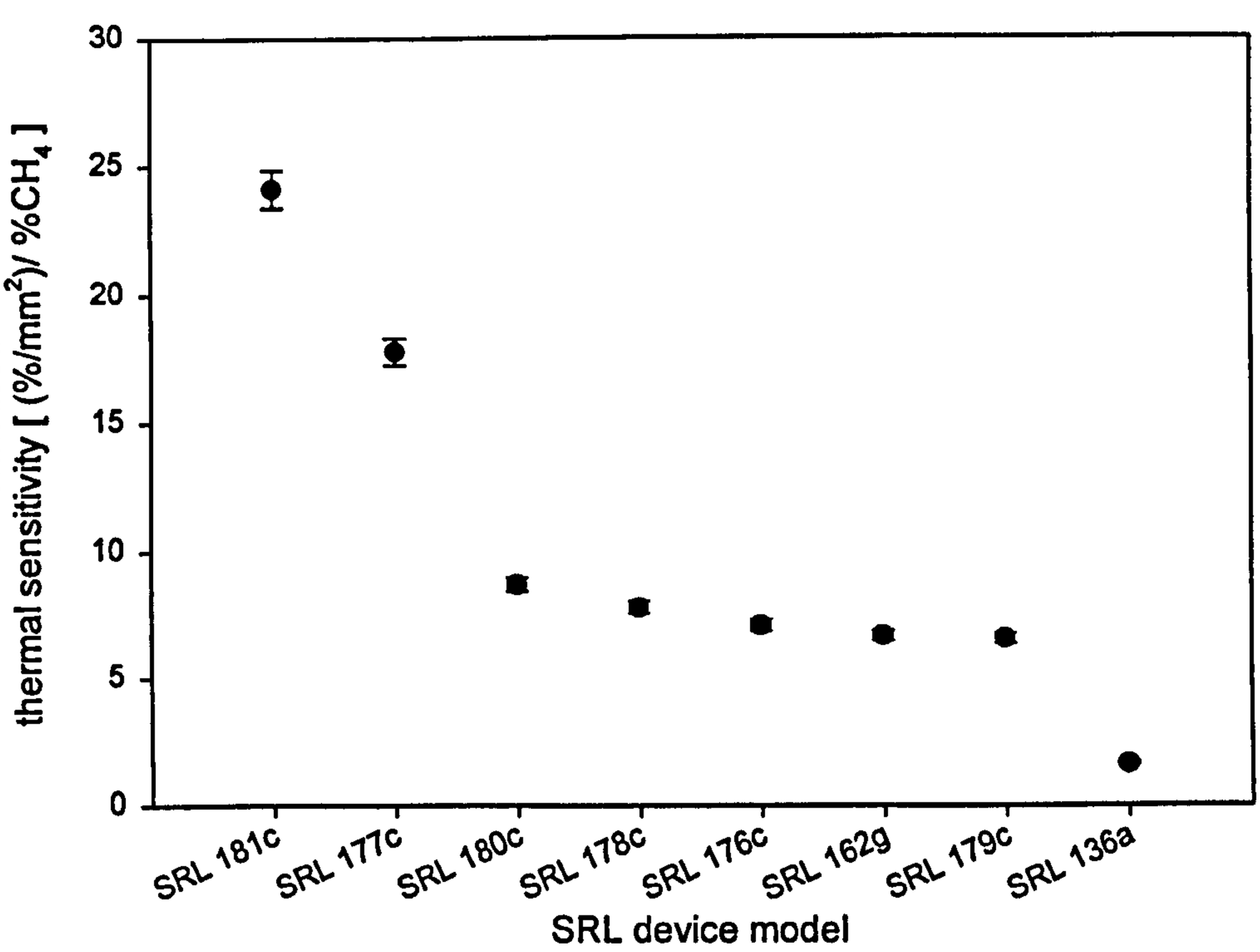

(b)

Figure 6.11: Evaluation of the device optimisation per % methane in air at nominal operating voltages for various SRL micro-calorimeters based on (a) the normalised voltage sensitivity (S_V) and (b) the normalised thermal sensitivity (S_T).

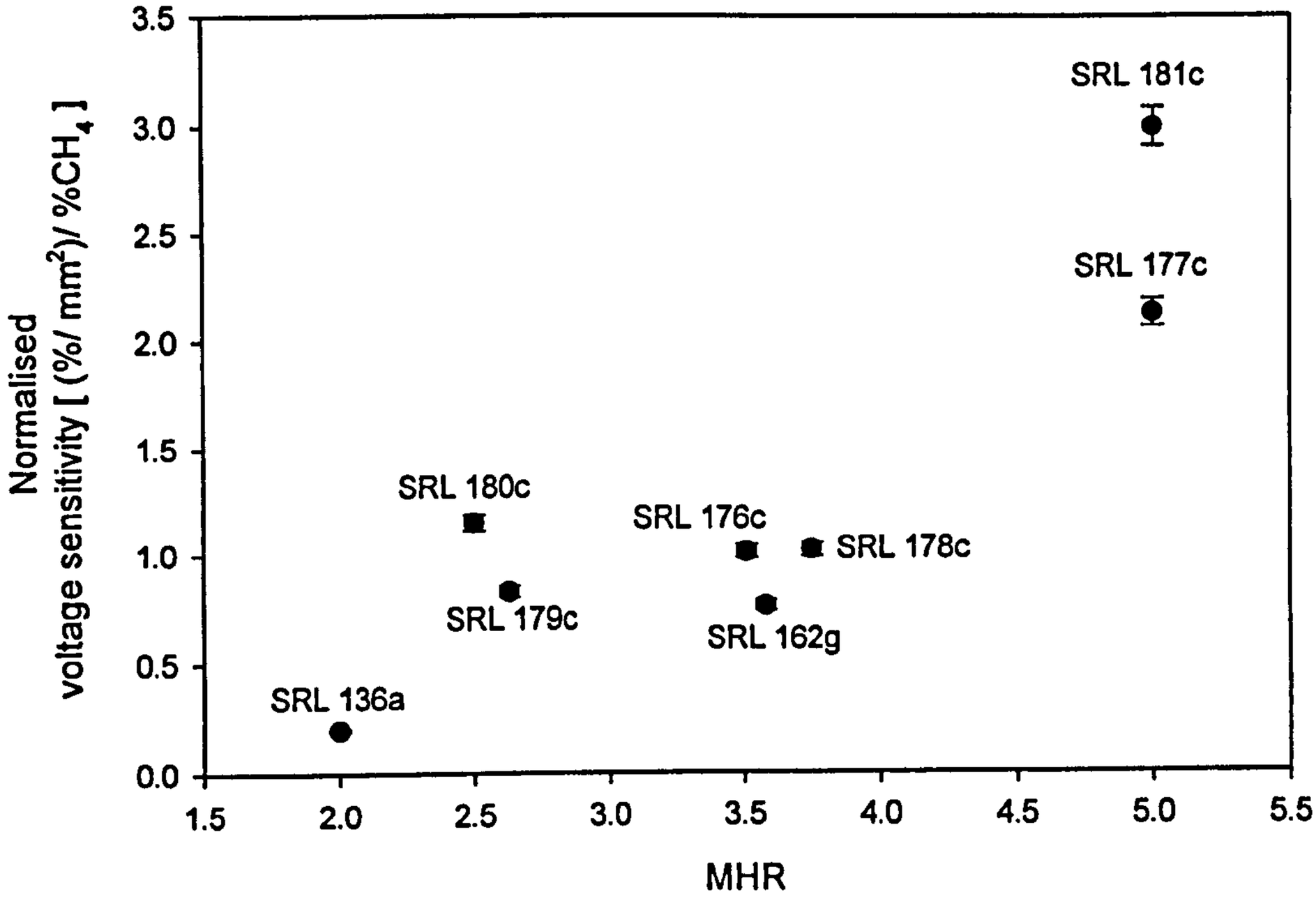

(a)

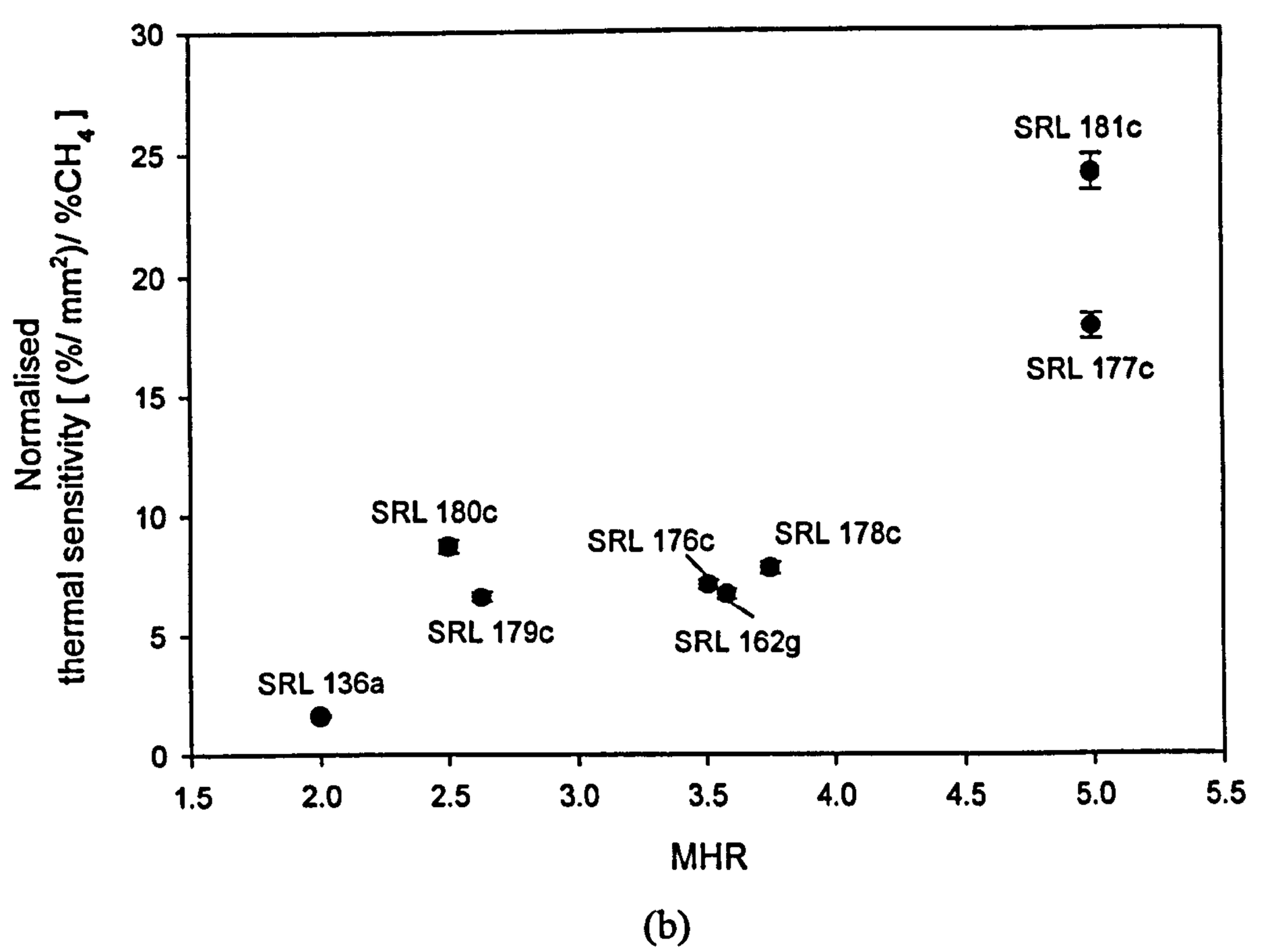

(b)

Figure 6.12: The catalyst efficiency per % CH_4 in air at nominal operating voltage for various SRL micro-calorimeters based on the relationship between the MHR and (a) the normalised voltage sensitivity (S_V); (b) the normalised thermal sensitivity (S_T).

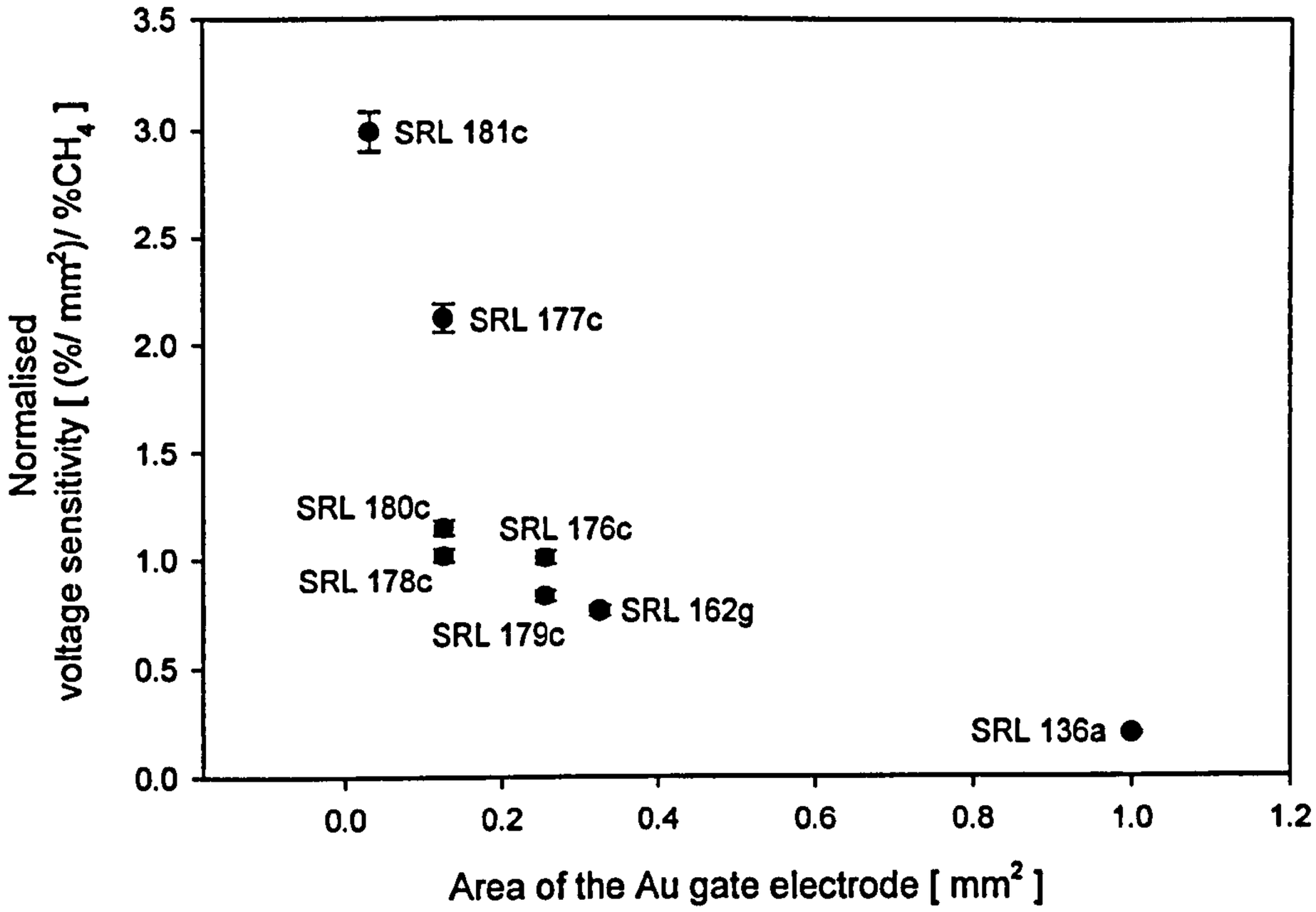

(a)

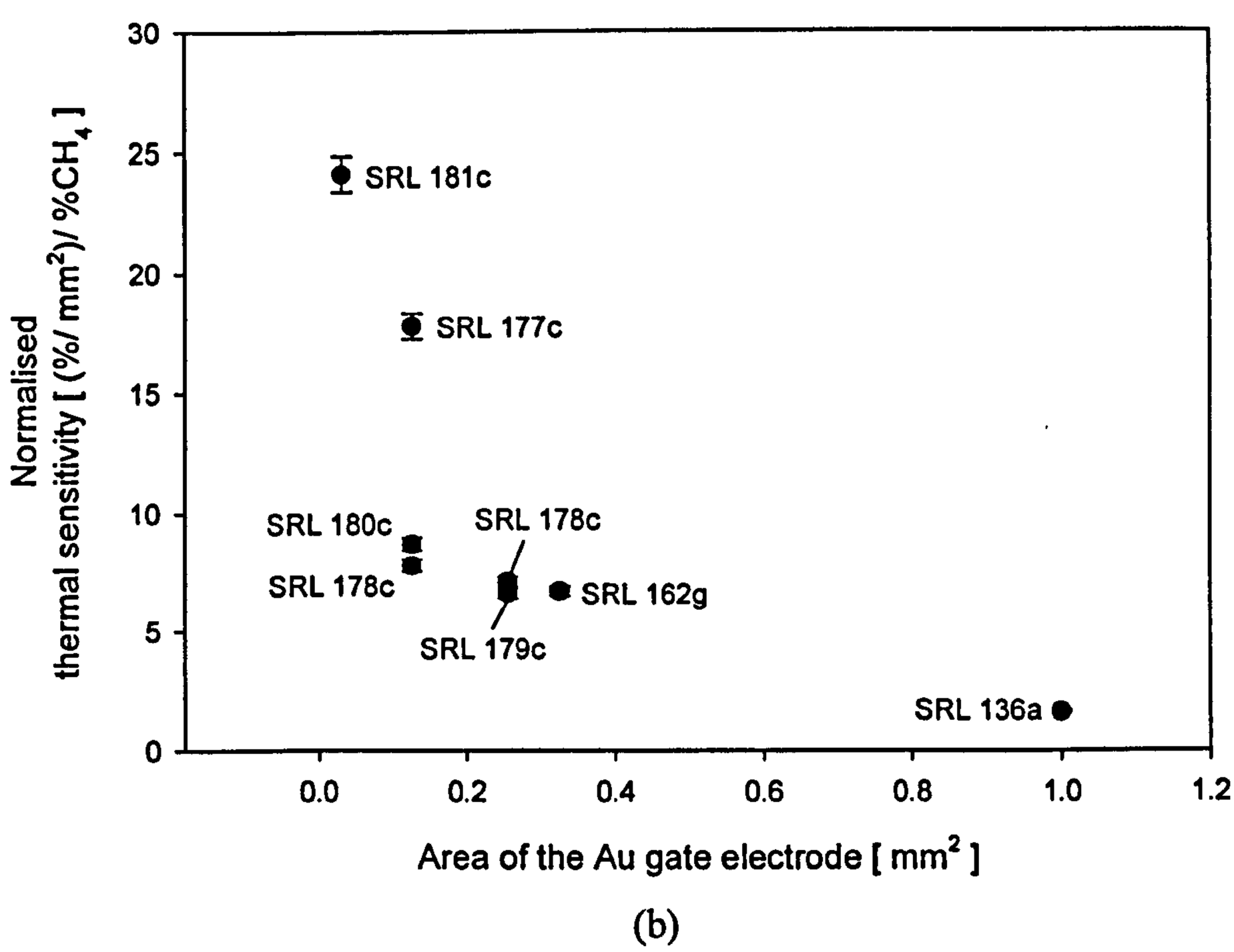

(b)

Figure 6.13: The catalyst efficiency per % CH_4 in air at nominal operating voltage for various SRL micro-calorimeters based on the relationship between the area of the electrode and (a) the normalised voltage sensitivity (S_V); (b) the normalised thermal sensitivity (S_T).

6.3 Dynamical properties of the micro-calorimeters in air

Another major advantage of the micro-machined sensor over the conventional bead-type sensor is the smaller time-constant. It was essential to investigate the dynamic behaviour of the sensors at different temperatures. Various powering regimes and waveforms were established in order to identify an optimised driving signal for the micro-calorimeter. The total time constant of the device operating in air consists of the electrical ($\tau_{electric}$) and thermal ($\tau_{thermal}$) time constant, as shown in equation (6.5). They are related to the parasitic capacitance of the micro-heater and the thermal capacity of the membrane, assuming a multi-exponential model.

$$\tau_{rise/fall} = \tau_{electric} + \tau_{thermal} \tag{6.5}$$

A time constant is defined as the time taken for the output voltage to rise up to 63.2% of its final value (τ_{rise}) and an output to fall to 36.8% of its final value (τ_{fall}). The output voltage is considered to be at steady-steady after 5 time constants. The time constant of present commercial sensors is up to 10 seconds and so cannot be operated in pulse mode [6.5]. A pair of sensor samples from each of the meander and Drive-wheel design families was selected to perform these investigations. The dynamic driving circuit described in Chapter 4 was used to generate the required signals for the experiments involved.

6.3.1 Small signal time constant

The dynamic response of the micro-calorimeter was a fundamental property to be investigated since it governs the maximum operating frequency of the sensor. The small-signal dynamic responses were measured at different temperatures. The results could illustrate the relationship between the response time required in the presence of methane and the sensor operating temperature.

This small-signal experiment was performed to determine the thermal time constant of the sensor, assuming negligible chemical reaction kinetics for the catalyst. The sensor was supplied a constant voltage, ΔV_{idle}, to reach a pre-defined temperature (500°C) and a square wave ripple was superimposed onto the input voltage at 1 Hz, as shown in figure 6.14. The magnitude of the ripple, ΔV, was adjusted to oscillate about

the operating temperature (V_{T500}) and mimic the catalyst reaction to 2.5% methane in air. As a square wave was used, the rise time and fall time of the sensors could be measured directly from a digital storage oscilloscope, Tektronics TDS 210. Furthermore, a voltage ramp upon power up was included to avoid thermal shock and induced stresses that could lead to membrane rupture. The specifications of the driving signals and the numerical results are given in Appendix 6b.

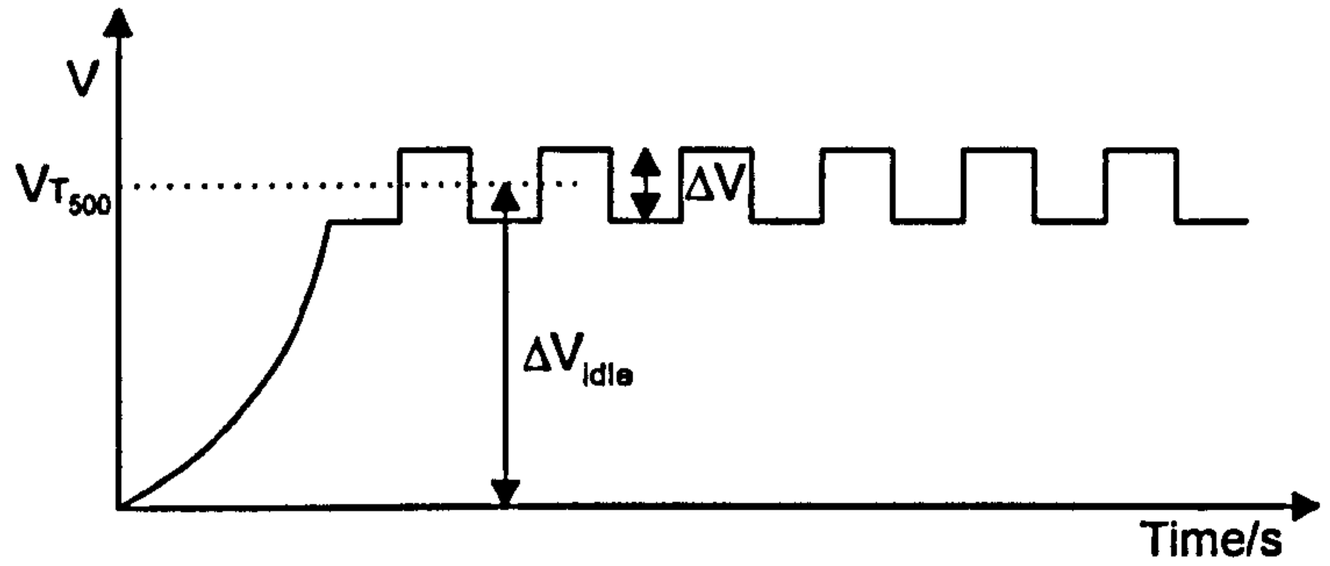

Figure 6.14: An illustration of the waveform employed to mimic the catalyst effect in dynamic response investigations, including a ramp at the beginning for device protection.

The typical small signal response of the SRL 177c micro-calorimeter is shown in figure 6.15(a). A comparison between the micro-machined device, SRL 177c, and the conventional sensor 50P supplied by City Technology Ltd. is shown in figure 6.15(b). The time constant for the micro-calorimeter is generally about 200 times smaller than that for the commercial sensors. In addition, as the power requirement of the SRL 177c is similar to the commercial bead-type device, it increased the potential to directly replace the existing pellistor products.

The time constants at the rising edge and the falling edge of the selected micro-calorimeters are shown in figure 6.16. This shows that the optimised devices from both design generations had improved from the original micro-calorimeter design. Moreover, the time constant of the devices from the Ultra-small/low power family (SRL 181c) achieved a sub-millisecond response. It allows the operating frequency for the device to reach about 160 Hz without any attenuation of temperature. In general, the results indicated that the higher the operating temperature, the smaller the time constant. The thermal rise time (τ_{rise}) for the devices was between 0.5 ms and 3.6 ms, depending on the operating temperature. The falling time constant (τ_{fall}) entirely depends on natural cooling to return to the idle voltage and it was found that this was at least twice as slow as the rising edge, ranging from 1.2 ms to 7 ms.

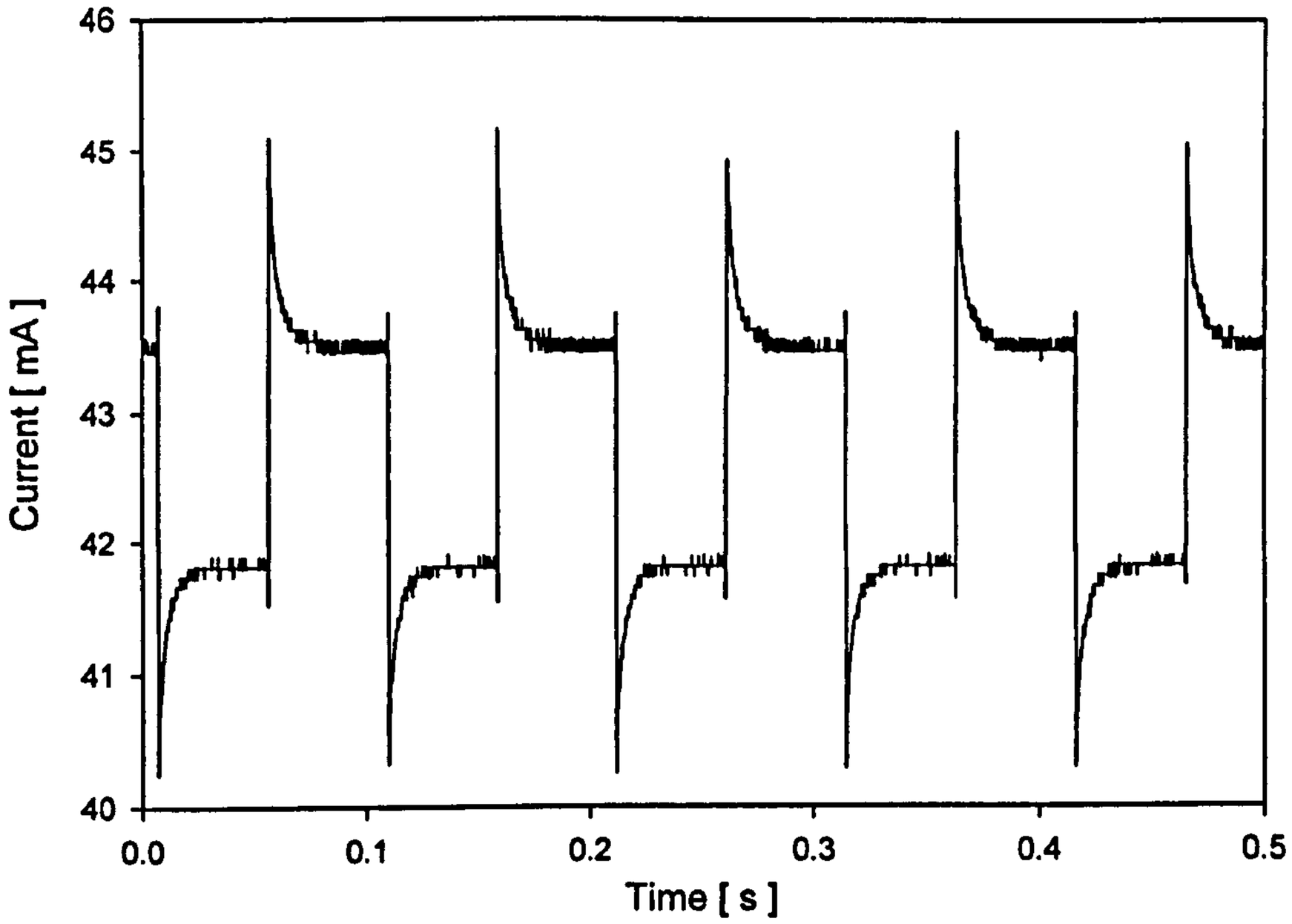

(a)

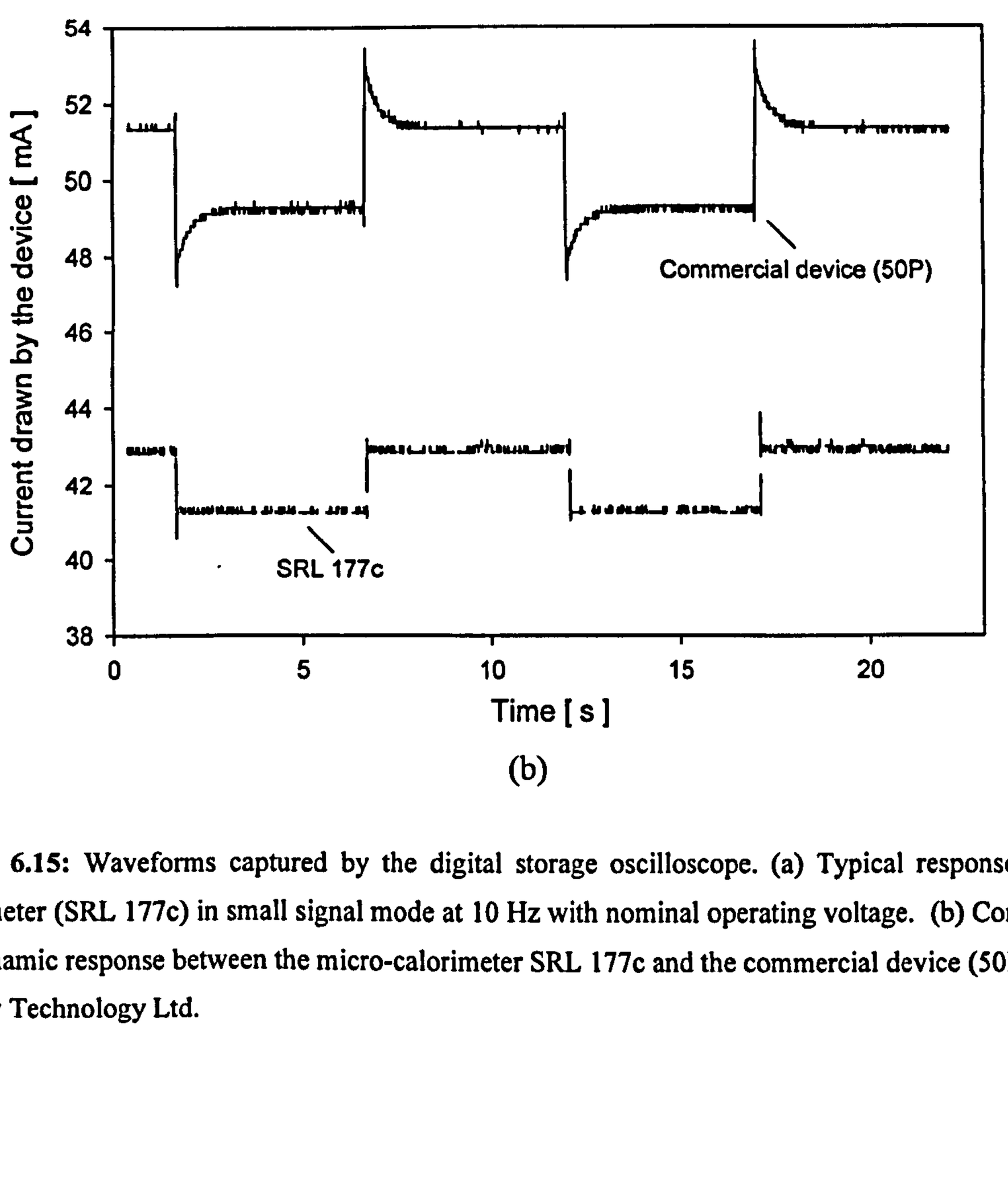

(b)

Figure 6.15: Waveforms captured by the digital storage oscilloscope. (a) Typical response of micro-calorimeter (SRL 177c) in small signal mode at 10 Hz with nominal operating voltage. (b) Comparison of the dynamic response between the micro-calorimeter SRL 177c and the commercial device (50P), supplied by City Technology Ltd.

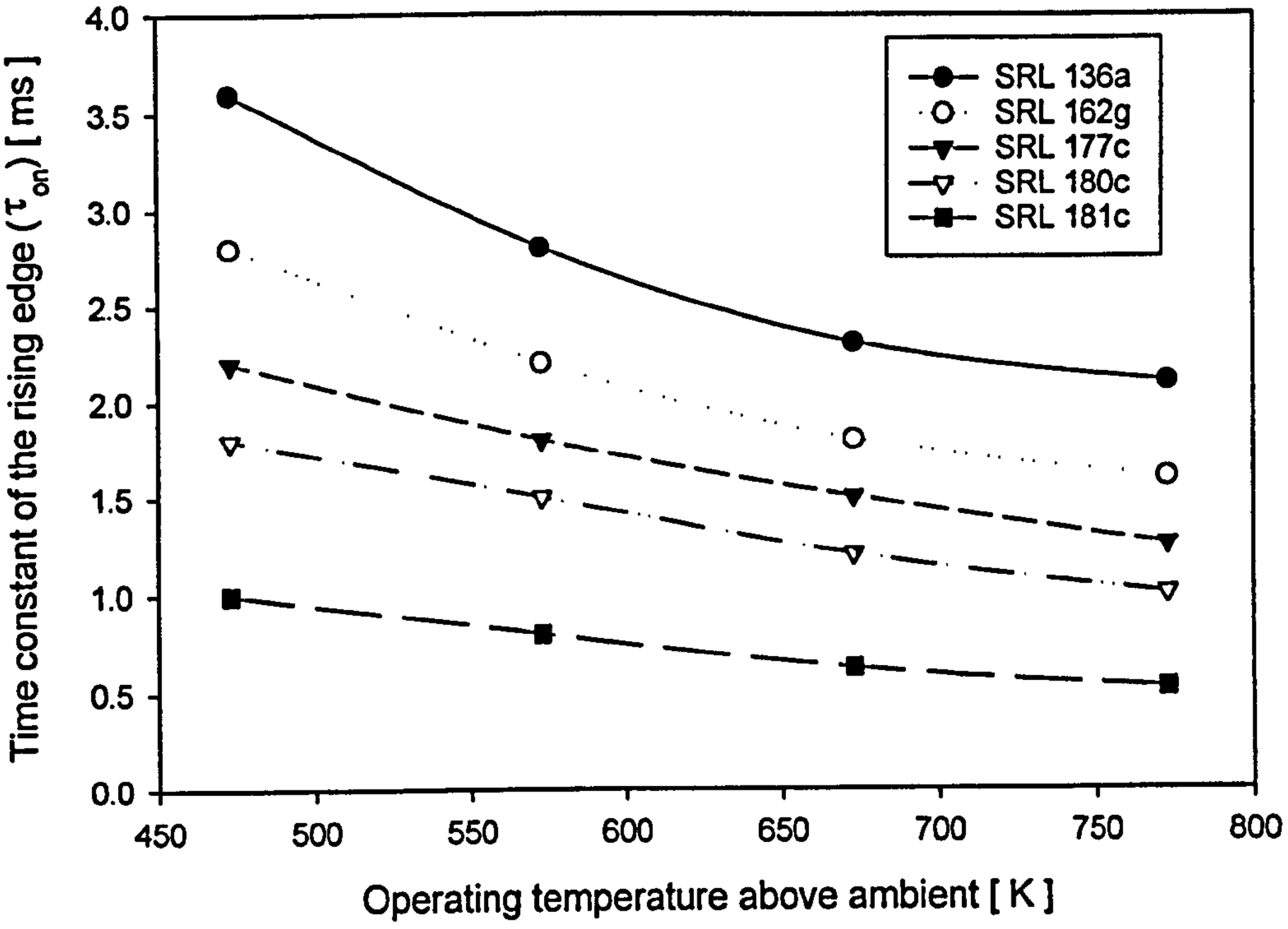

(a)

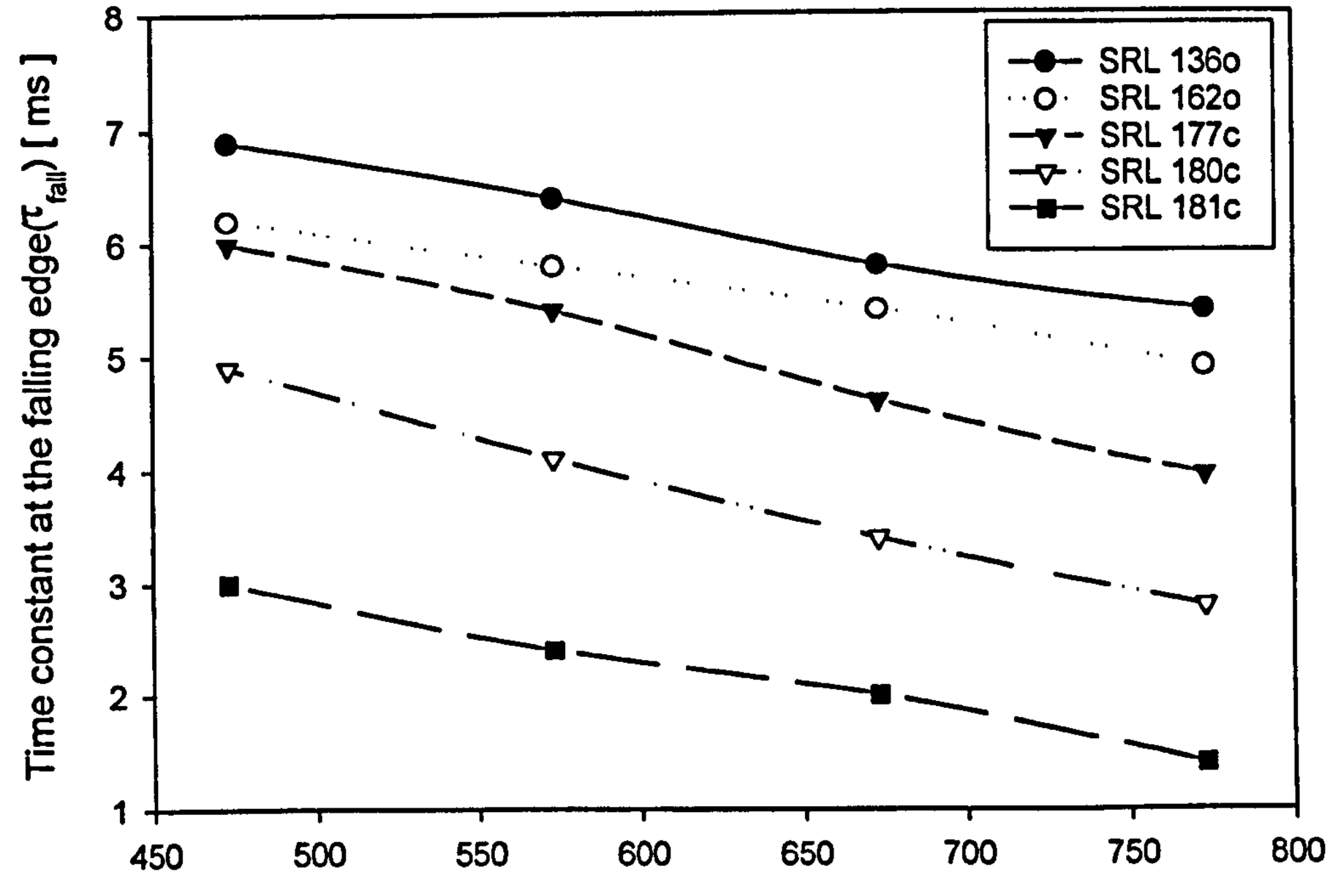

(b)

Figure 6.16: Thermal time constants of the micro-calorimeters in small signal dynamic response at various operating temperature for the various design families at (a) rising edge (τ_{rise}) and (b) falling edge (τ_{fall}).

The sensor thermal time constant is the product of the thermal resistance (R_{th}) and the thermal capacitance (C_{th}). They consist of several temperature dependent parameters, such as the specific heat capacity (c_p) and thermal conductivity (κ), as shown in equations (6.5a-c) [6.6]. It is difficult to quantify the contribution of a particular property but certain properties could be dominant. For example, the thermal conductivity of silicon nitride decreases by about 20% in the temperature range 0°C to 300°C.

$$\text{Thermal time constant} = R_{th} \times C_{th} \tag{6.5a}$$

$$R_{th} = \int_{r1}^{r2} \frac{1}{\kappa A(x)} dx \tag{6.5b}$$

$$C_{th} = c_p \times m \tag{6.5c}$$

As the micro-heater was circular, the thermal resistance (R_{th}) is evaluated for the material between the radius of the heated part (*r1*) and the radius of the entire object (*r2*). The (*A)* is denoted as the area of the object and (*m*) is the mass of the material. The theoretical time constants of various devices are shown in table 6.1.

6.3.2 Power modulation

An optimum-powering regime for the micro-calorimeter was designed in order to measure the minimum switching time for the sensors, as shown in figure 6.17. The sensor was turned-on to an idle voltage (V_{idle}), of about 150°C above ambient. Then an oscillation with a magnitude that reaches the operating temperature of about 500°C above ambient was superimposed. The switching time constant for the sensor was measured with a digital storage oscilloscope, Tektronics TDS 210. Therefore, by varying these parameters, the minimum pulse width, the maximum operating frequency and the minimum duty-cycle for methane detection could be identified. This power modulation method was used instead of a 0°C to 500°C cycling regime because it reduces the stress in the membrane and the interference of humidity with the target gas. The specifications of the waveforms are included in Appendix 6c.

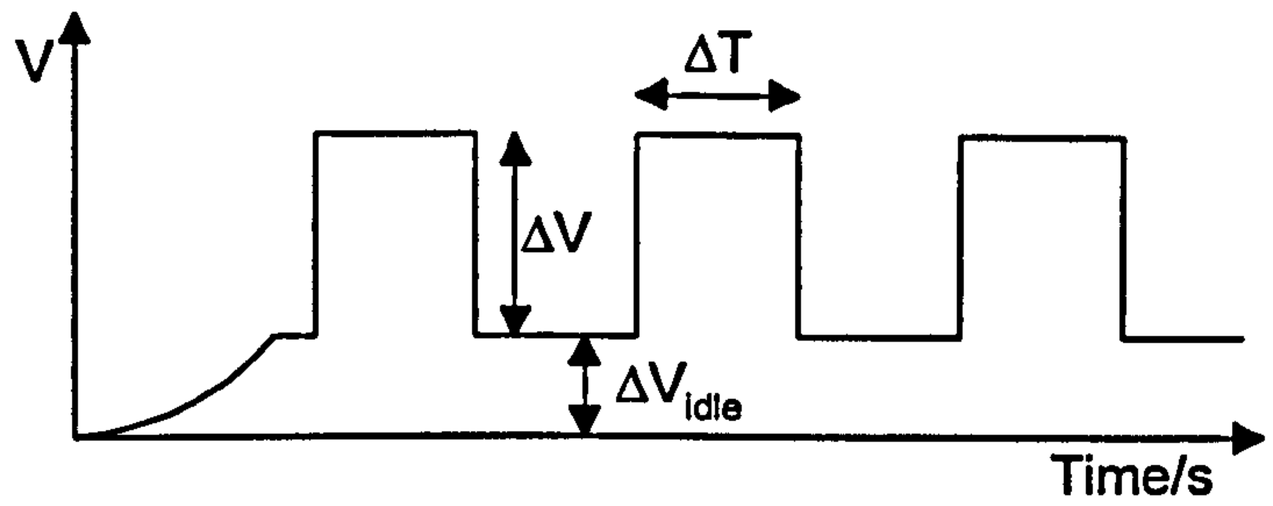

Figure 6.17: The optimised driving pulse train for the power modulation experiments.

Table 6.1: Comparisons between the experimental and theoretical time constant for the micro-calorimeters.

SRL code	Experimental τ_{rise} (ms)	Experimental τ_{fall} (ms)	Theoretical time constant (ms)
SRL 136a	1.1 ± 0.2	13.2 ± 0.2	9.9
SRL 162g	1.2 ± 0.2	11.7 ± 0.1	5.8
SRL 176c	0.9 ± 0.1	13.7 ± 0.1	5.8
SRL 177c	0.7 ± 0.1	15.0 ± 0.1	3.7
SRL 178c	0.8 ± 0.1	9.0 ± 0.2	3.0
SRL 179c	1.0 ± 0.1	10.6 ± 0.3	4.5
SRL 180c	0.7 ± 0.1	9.6 ± 0.2	2.1
SRL 181c	0.4 ± 0.1	4.8 ± 0.2	0.9

The experiments indicated that the time constants of the sensors in the power modulation mode are much higher than in the small signal mode, as shown in table 6.1. As the temperature of the devices had to drop about 400°C and relied only on the natural cooling, the time constant on the falling edge is generally slower by a factor of 10 compared to the rising edge.

The relationship between the power consumption and the time constant of the devices is shown in figure 6.18. As the devices that employ identical micro-heater design were compared, it was interesting to observe the time constant of the device was increasing with the *MHR*. Moreover, the increase of the time constant is approximately linear with the power consumption of the devices. However, it was not possible to relate the original design to the other optimised designs due to the different micro-heaters and associated heating efficiency. In addition, similar experiments were performed with commercial pellistor beads for comparison, as shown in figure 6.18. As the time constant of these sensors is so much larger, these devices are not appropriate for this power modulation regime.

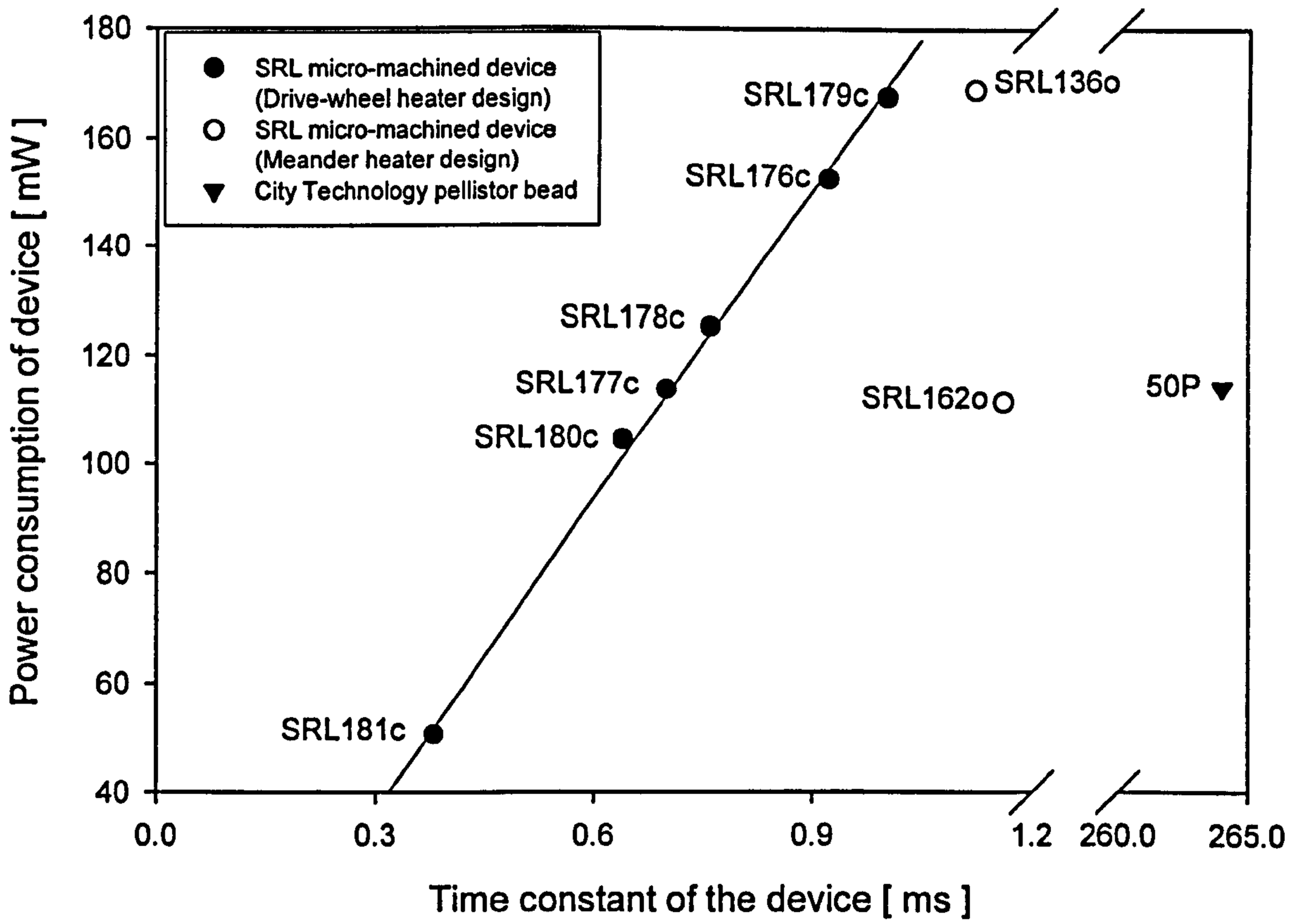

Figure 6.18: The relationship between the power consumption and the time constant (τ_{rise}) for various SRL micro-calorimeter designs. One commercial pellistor (50P) is included, supplied by City Technology Ltd.

6.3.3 Power consumption in power modulation mode

The typical power consumption (P_{tol}) in the pulse-operating mode is estimated by the idle power (P_{idle}), the power during the oscillation (P_{osc}) and the additional power consumption at the current transient (P_{tran}), as shown in equation (6.6a). The idle power maintains the sensor at 150°C and this term was obtained from the device characterisation presented in Chapter 5. The power of the oscillation (P_{osc}) is the product of the voltage and current input to the sensor required to reach an operating temperature of 500°C. Moreover, it is a function of the duty-cycle, as shown in equation (6.6b).

A constant voltage supply in the form of a square-wave had been used for pulse mode operation where only the current transients were considered. However, due to the asymmetrical rise and fall time, the current transient is modelled by the magnitude of the current transient (I_{tran}), and the rise and fall time constants (τ_{rise} and τ_{fall}), as shown in equation (6.6d) and (6.6e). The equations were solved to obtain the current transient, as

shown in equation (6.6c). The voltage at the rising edge is the total voltage (V) for the sensor to reach operating temperature and the voltage at the falling edge is the voltage at idle temperature (V_{idle}). Finally, the transient power for each cycle is multiplied by the operating frequency, as shown in equation (6.6c). The estimated power consumption for the devices is shown in table 6.2. It indicated that the power consumption of the micro-calorimeter varied when it is operated in pulse mode.

$$P_{tol} = P_{idle} + P_{osc} + P_{tran} \tag{6.6a}$$

$$P_{osc} = V_{osc} \times I_{osc} \times Duty\text{-}cycle \tag{6.6b}$$

$$P_{tran} = [V I_{tran} (\tau_{rise} (1 - e^{-5})) + V_{idle} I_{tran} (\tau_{fall} (4 + e^{-5}))] \times frequency \tag{6.6c}$$

$$i_{rise} = I_{tran} \int_{0}^{5\tau} \exp(-\frac{t}{\tau_{rise}}) dt \tag{6.6d}$$

$$i_{fall} = I_{tran} \int_{0}^{5\tau} \left(1 - \exp(\frac{t}{\tau_{fall}})\right) dt \tag{6.6e}$$

Table 6.2: Power consumption of the micro-calorimeters in power modulation mode.

SRL No.	P_{idle} (mW)	P_{osc} (mW)	P_{tran} per cycle (mW)	P_{tol} at 10Hz (mW)	P_{tol} at 100 Hz (mW)
SRL 176c	35	40.5	0.255	78.1	101.0
SRL 177c	22	28.5	0.199	58.5	74.0
SRL 181c	10	15.8	0.082	26.62	34.0

The power consumption in pulse mode is linearly related to the operating frequency. The semi-log graphs in figure 6.19 shows that the power consumption increases significantly beyond 100 Hz and the power budget nearly equals the continuous powering mode at 500 Hz. Therefore, the higher the frequency, the more power is dissipated into the micro-calorimeter which it is related to the sensor sensitivity as discussed in the next section.

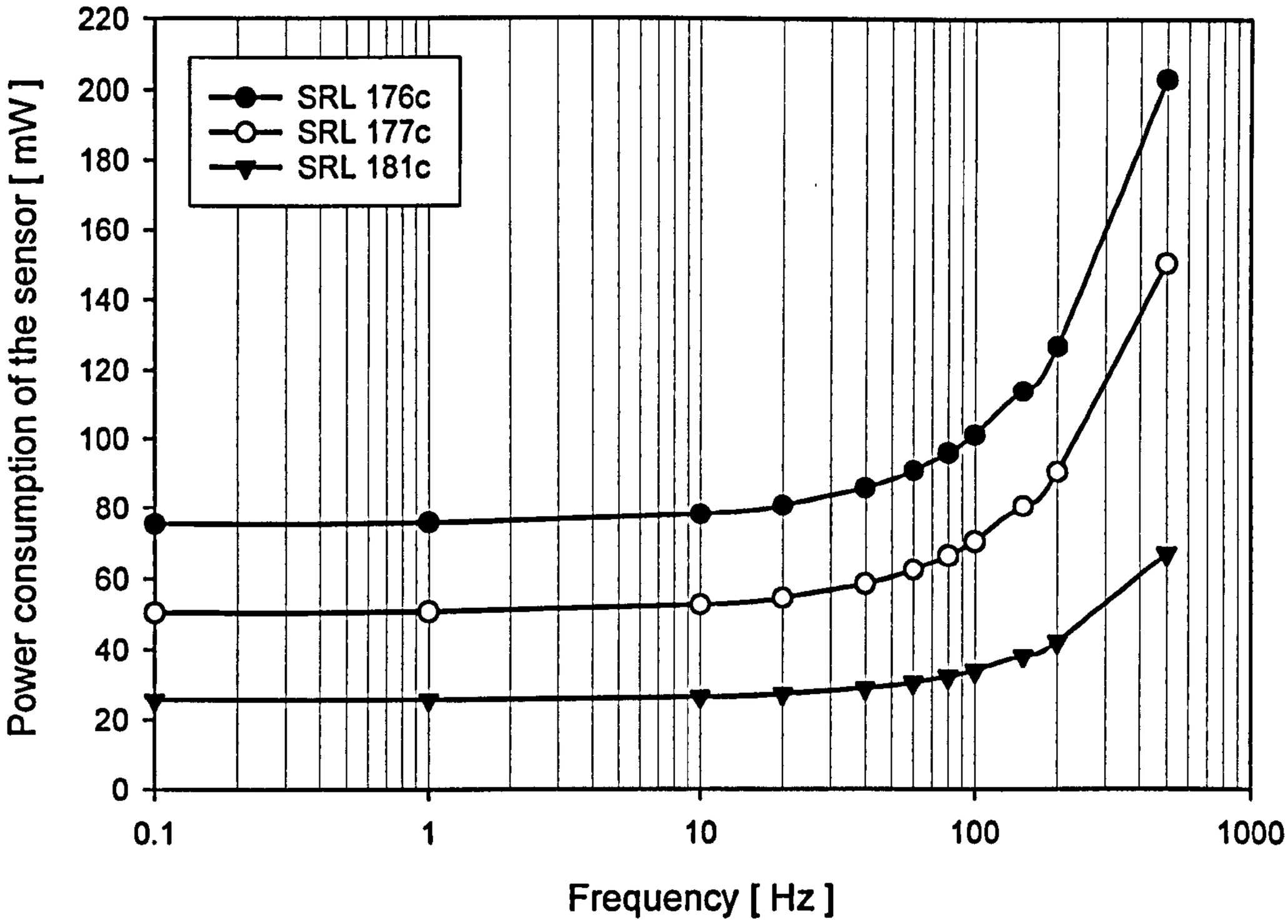

Figure 6.19: Power consumption of three micro-calorimeters at different operating frequencies.

6.4 Chemical dynamic response

The chemical dynamic responses of the micro-calorimeters were evaluated by driving the devices in pulse-mode with the standard test gas, 2.5% methane in air. The fast data-logging characterisation system in the Sensors Research Laboratory (University of Warwick) had been used to perform these experiments. The sensors were interfaced via the Wheatstone bridge circuit and the dynamic driving circuit, as described in Chapter 4. Three device types with the Drive-wheel design were selected for these experiments, namely the Standard family (SRL 176c), the Low-power family (SRL 177c) and the Ultra-small low-power family (SRL 181c). The micro-calorimeters were deposited with the nanoporous Pd catalyst but the SRL 177c was left uncoated for comparisons.

6.4.1 Sine-wave analysis

The devices were investigated under both power modulation and small signal mode with their nominal supply voltages. A sinusoidal waveform was used for the chemical dynamic response to avoid spikes that might be induced by the square wave. However,

the amplitudes and the idle voltages were identical to the driving waveform illustrated in figures 6.14 and 6.17.

The responses of the sensors at various frequencies were obtained by computing the difference between the Wheatstone bridge output of the sensor in air and in the test gas. However, the two waveforms should not be subtracted directly to obtain the sensor output due to a phase shift in the output signal or an RC phase lag, as shown in figure 6.20. This might be caused by a time delay when the catalyst reacts with the test gas. Although a fast Fourier transform could be applied to the experimental results to remove the frequency component of the signal, it is complicated and requires long wave trains. Therefore, the amplitudes of the output waveforms were compared manually to extract the actual sensor response.

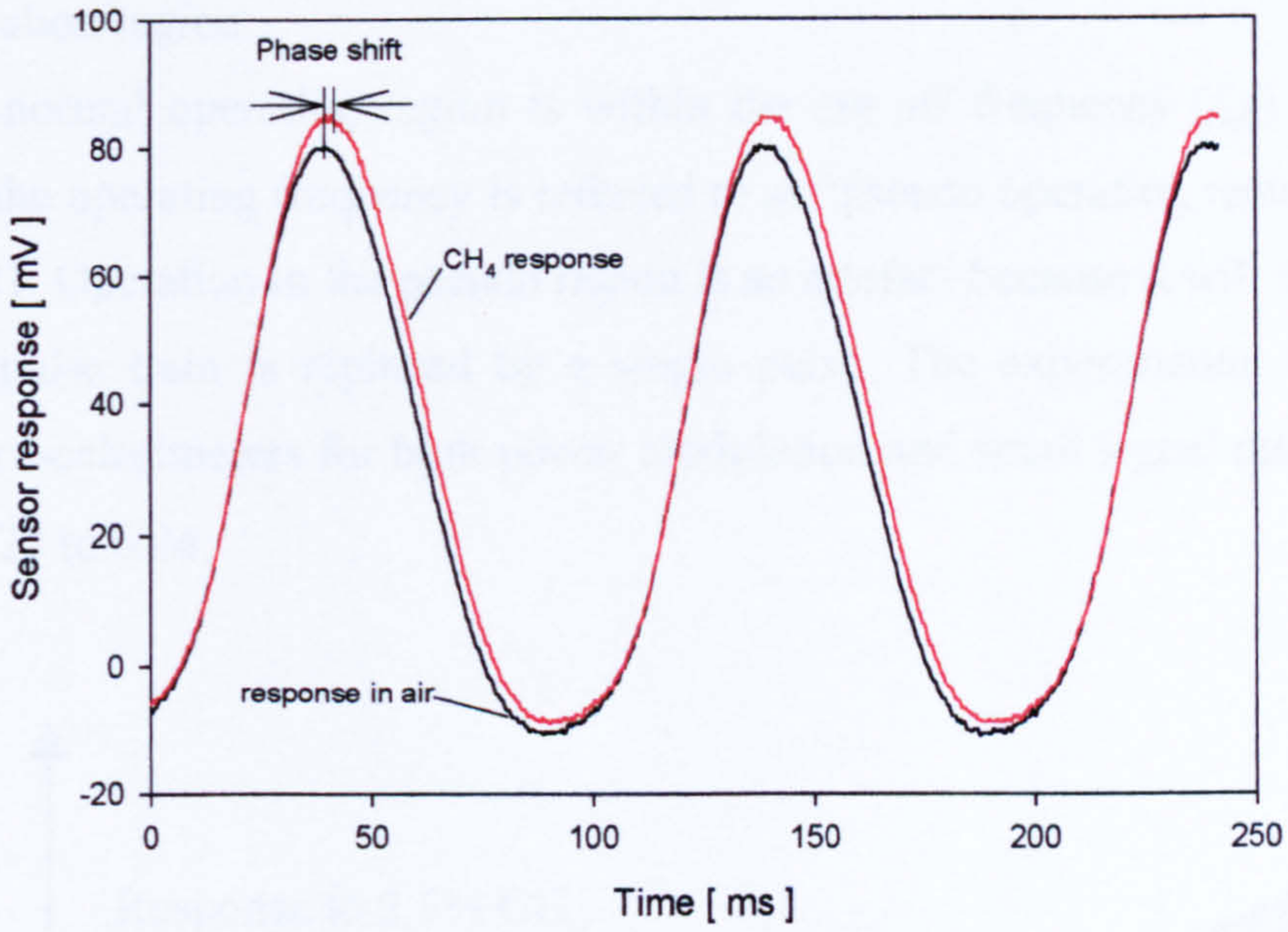

Figure 6.20: Comparison of the Wheatstone bridge output between air and 2.5% CH_4 in air for the micro-calorimeter (SRL 176c) at 10 Hz with nominal* supply voltage. It shows the phase shift and CH_4 response of the sensor.

A schematic diagram of the chemical dynamic response of the devices is shown in figure 6.21. It summarises the general behaviour of the devices in the sinusoidal operation mode. The sensor sensitivity is relatively constant before it reaches the corner frequency (f_c) or the -3 dB point, due to the thermal time constant of the silicon nitride membrane.

---

* Nominal supply voltage refers to the voltage required for the device to reach the nominal operating temperature of 500°C.

As the average temperature of the micro-calorimeter continued to decline with increasing frequency, the sensor response was diminished accordingly. It was eventually extinguished at the cut-off frequency (f_{off}). However, the sensitivity had been regenerated due to the increase of average device temperature. The devices can be heated very quickly (0.5 ms to 3 ms) because of the small thermal time constant, as shown in table 6.1. The cooling time is rather slow in comparison with the rise time, up to a factor of 10, since it relies solely on the natural cooling mechanism, i.e. convection. The average temperature of the device was increased again when there is insufficient cooling time at a frequency beyond the cut-off frequency (f_{off}). The device behaved as if it was operated in continuous powering mode. Furthermore, the power consumption of the micro-pellistor increased significantly when operated in the pseudo region, as shown in figure 6.25. The device consumed 30% additional power at 100 Hz when the sensor response entered the pseudo operation region.

The normal operating region is within the cut-off frequency (f_{off}) while further increase of the operating frequency is referred to as "pseudo operating region", as shown in figure 6.21. Operation in the pseudo region is an artefact because it will not exist if the continuous pulse train is replaced by a single pulse. The experimental results of the various micro-calorimeters for both power modulation and small signal mode are shown in figures 6.22 to 6.24.

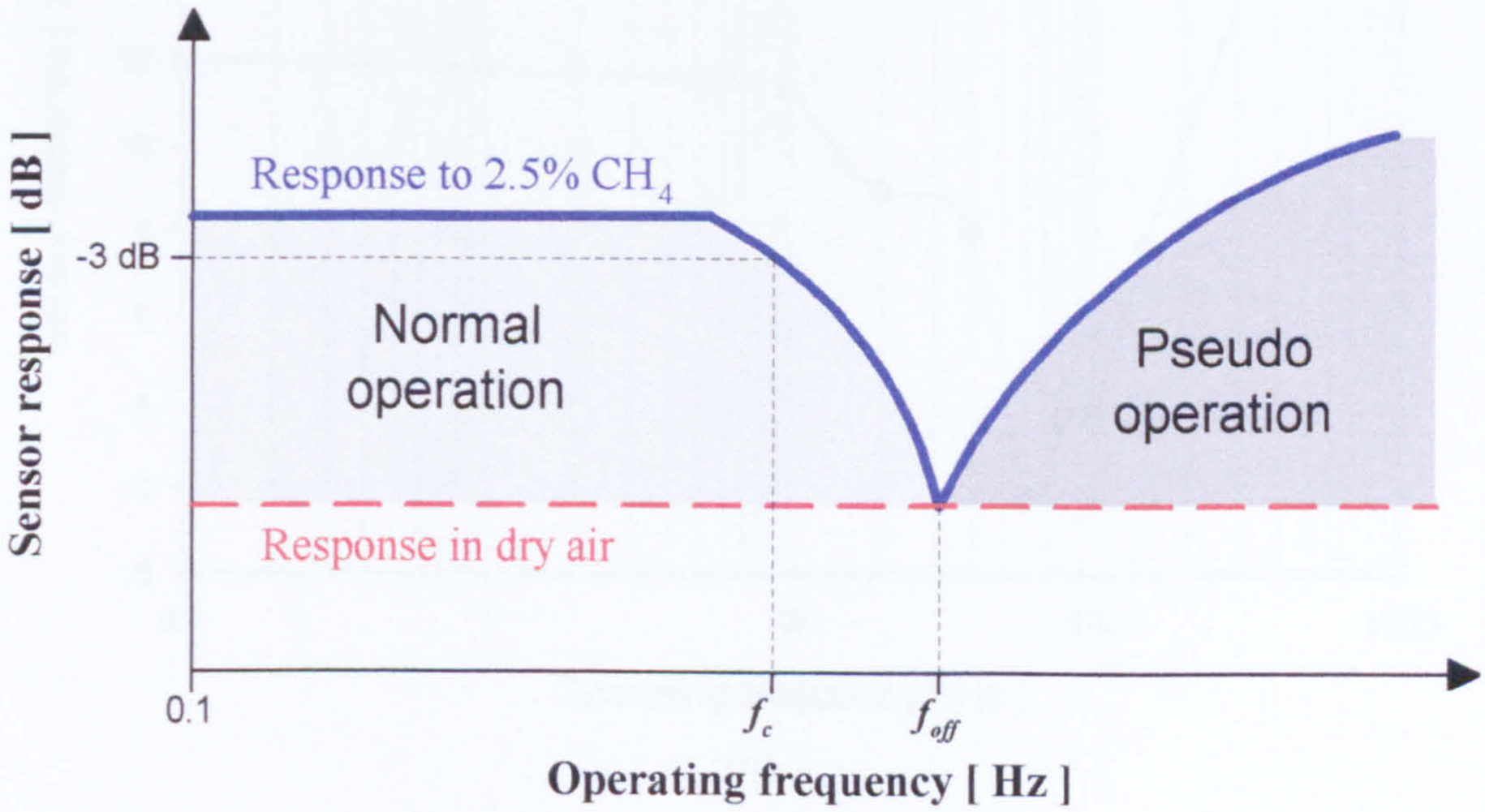

Figure 6.21: Schematic diagram of the characteristic chemical dynamic response of the micro-calorimeters (not to scale).

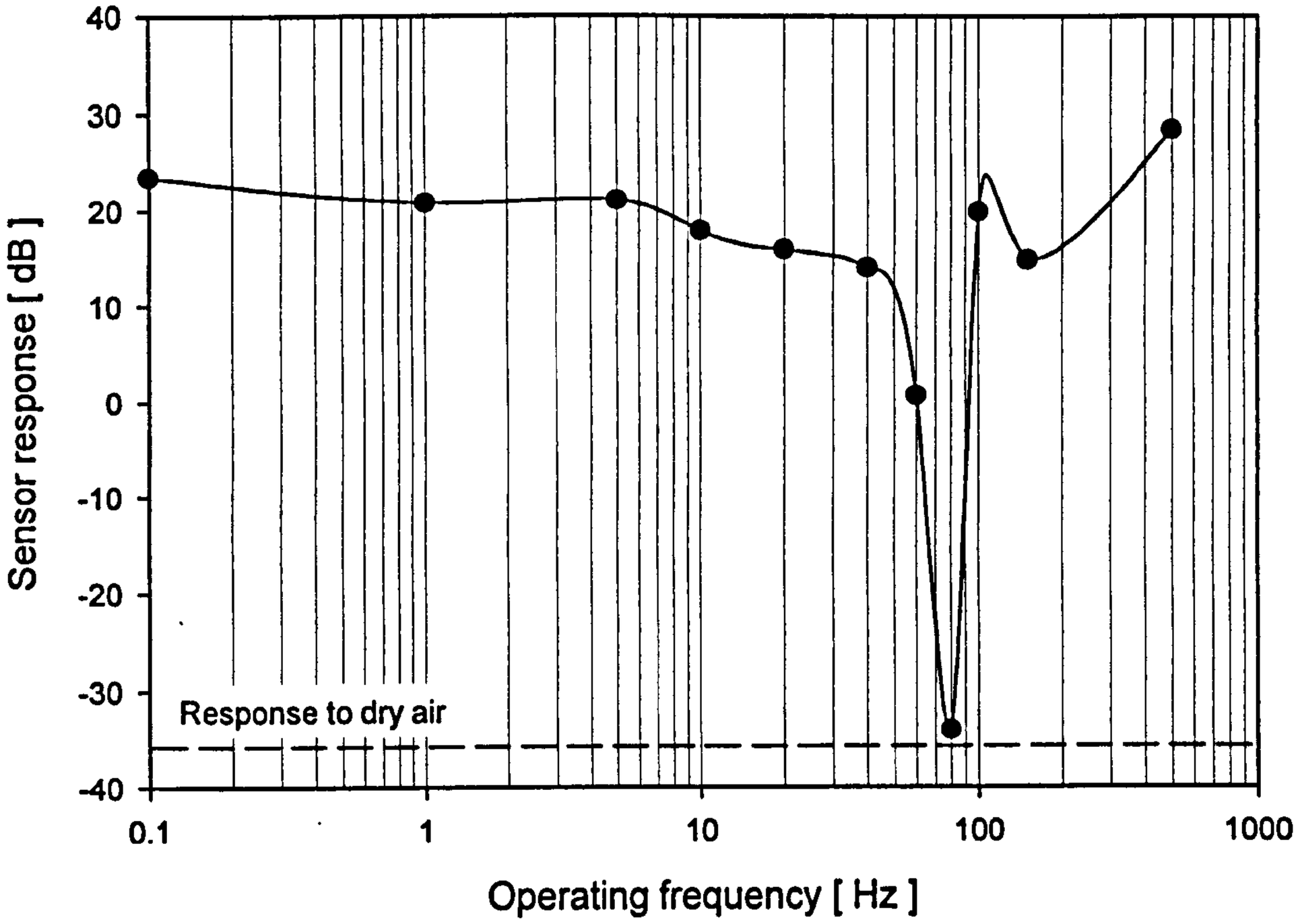

(a)

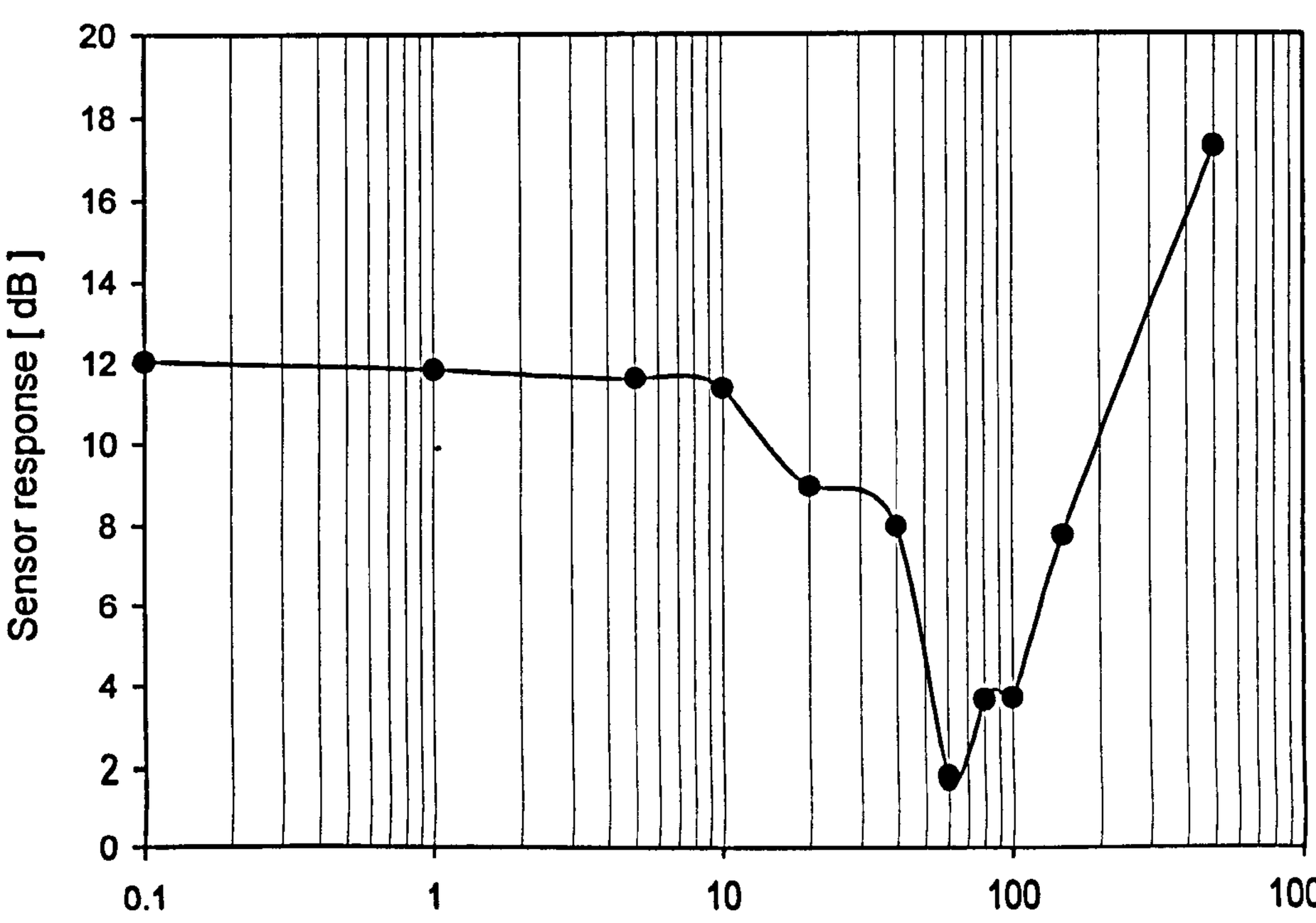

(b)

Figure 6.22: Chemical dynamic response for micro-pellistor (SRL 176c) with sinusoidal wave and nominal supply voltage in (a) power modulation mode and (b) small signal mode.

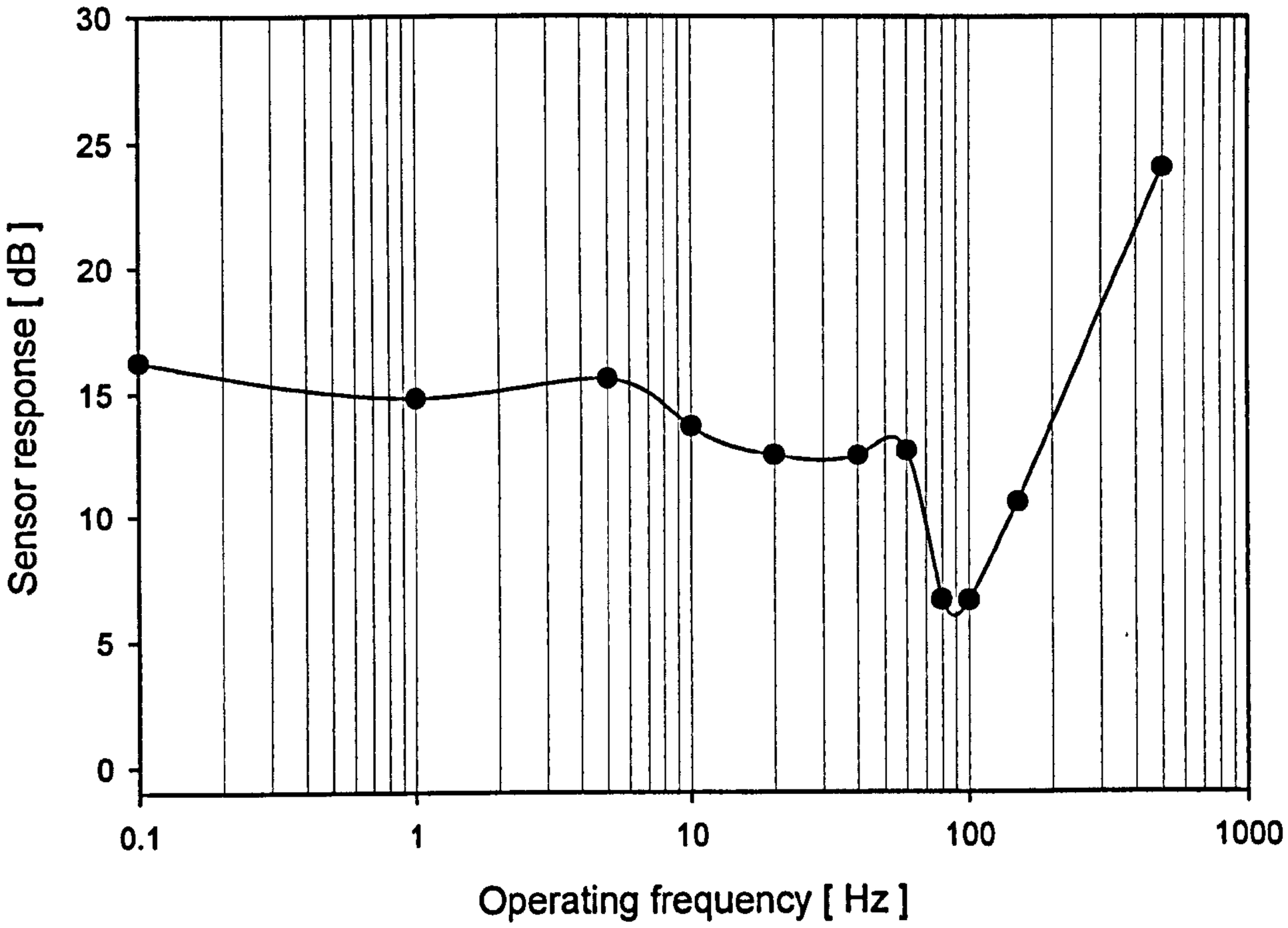

(a)

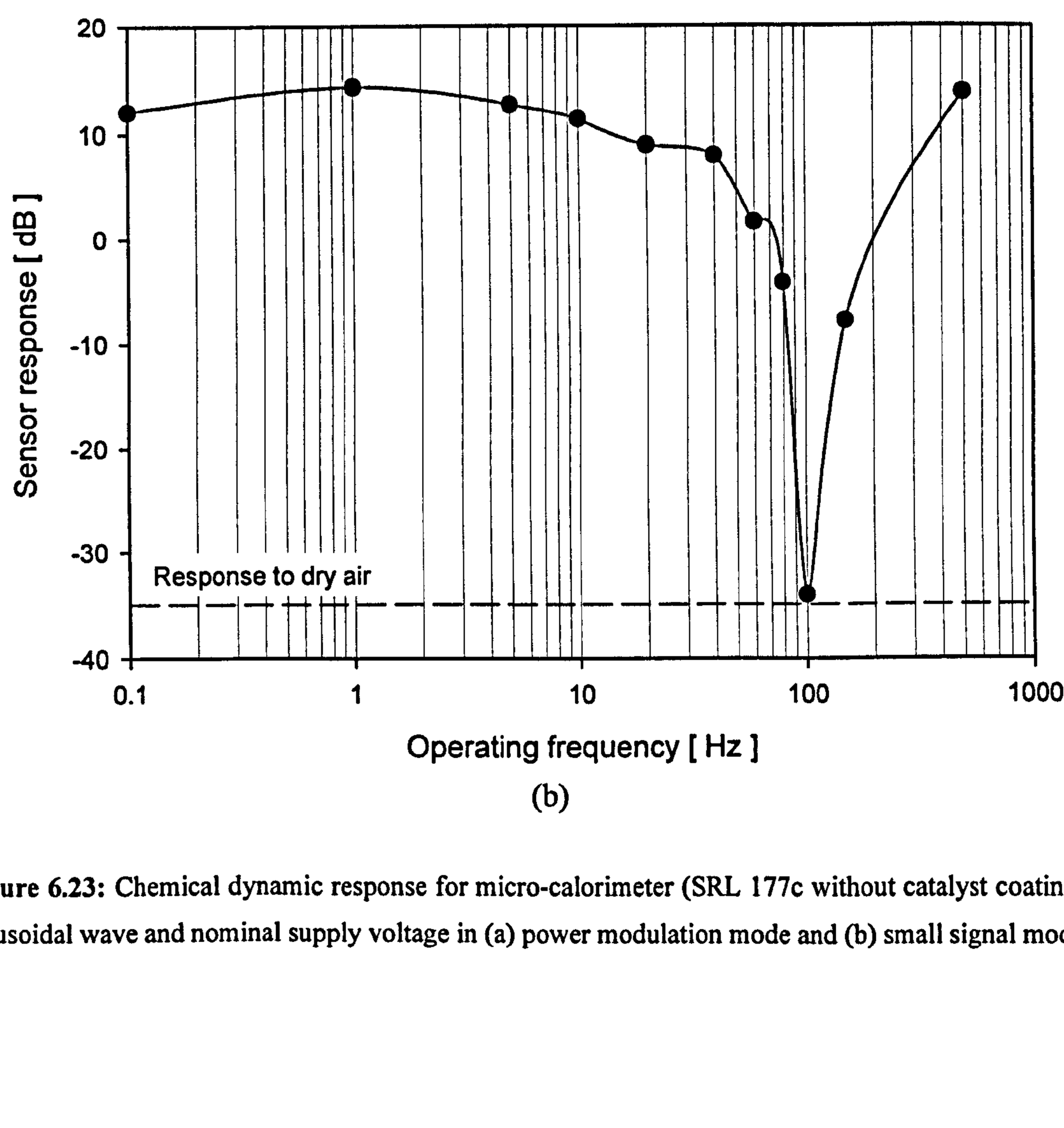

(b)

Figure 6.23: Chemical dynamic response for micro-calorimeter (SRL 177c without catalyst coating) with sinusoidal wave and nominal supply voltage in (a) power modulation mode and (b) small signal mode.

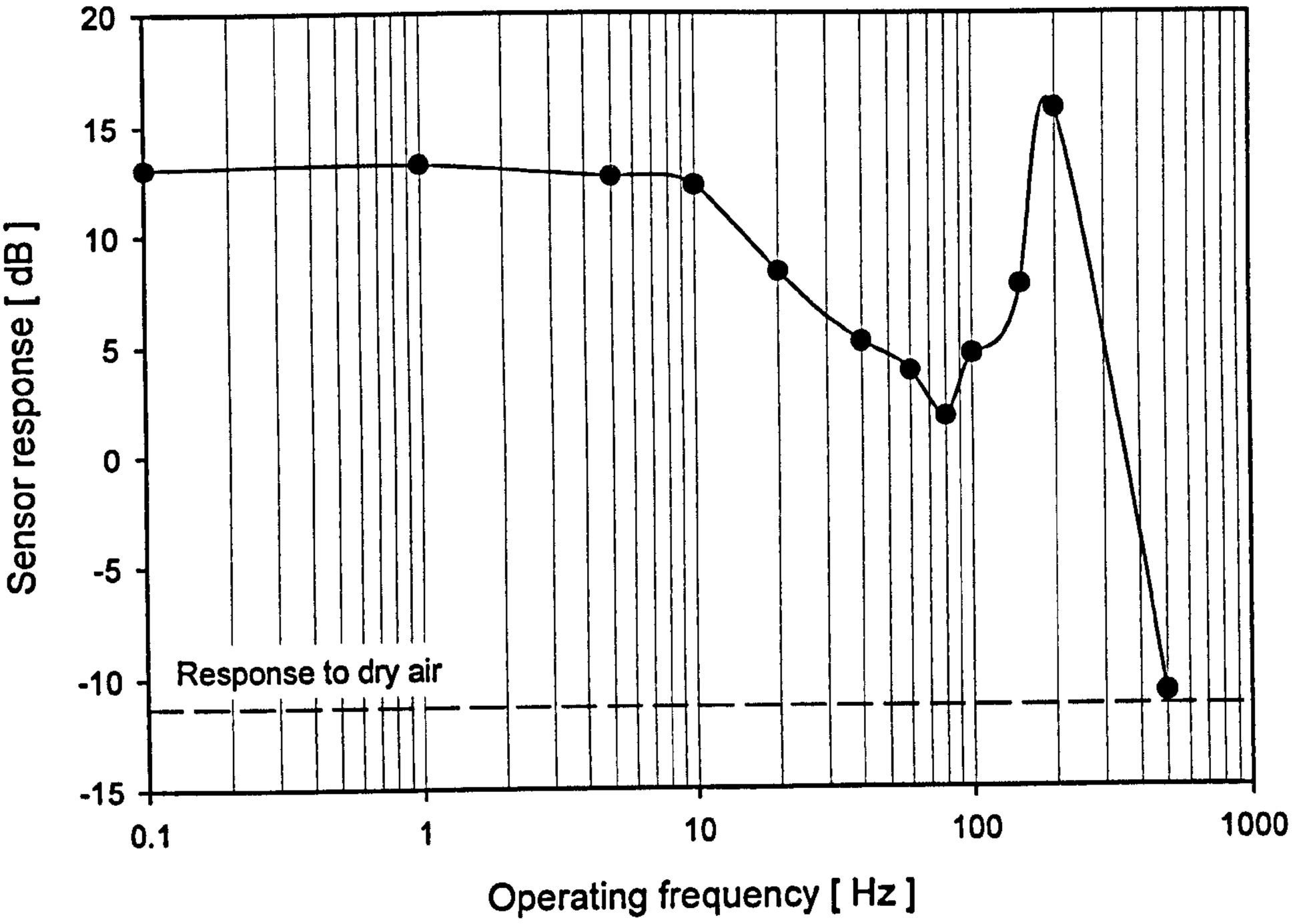

(a)

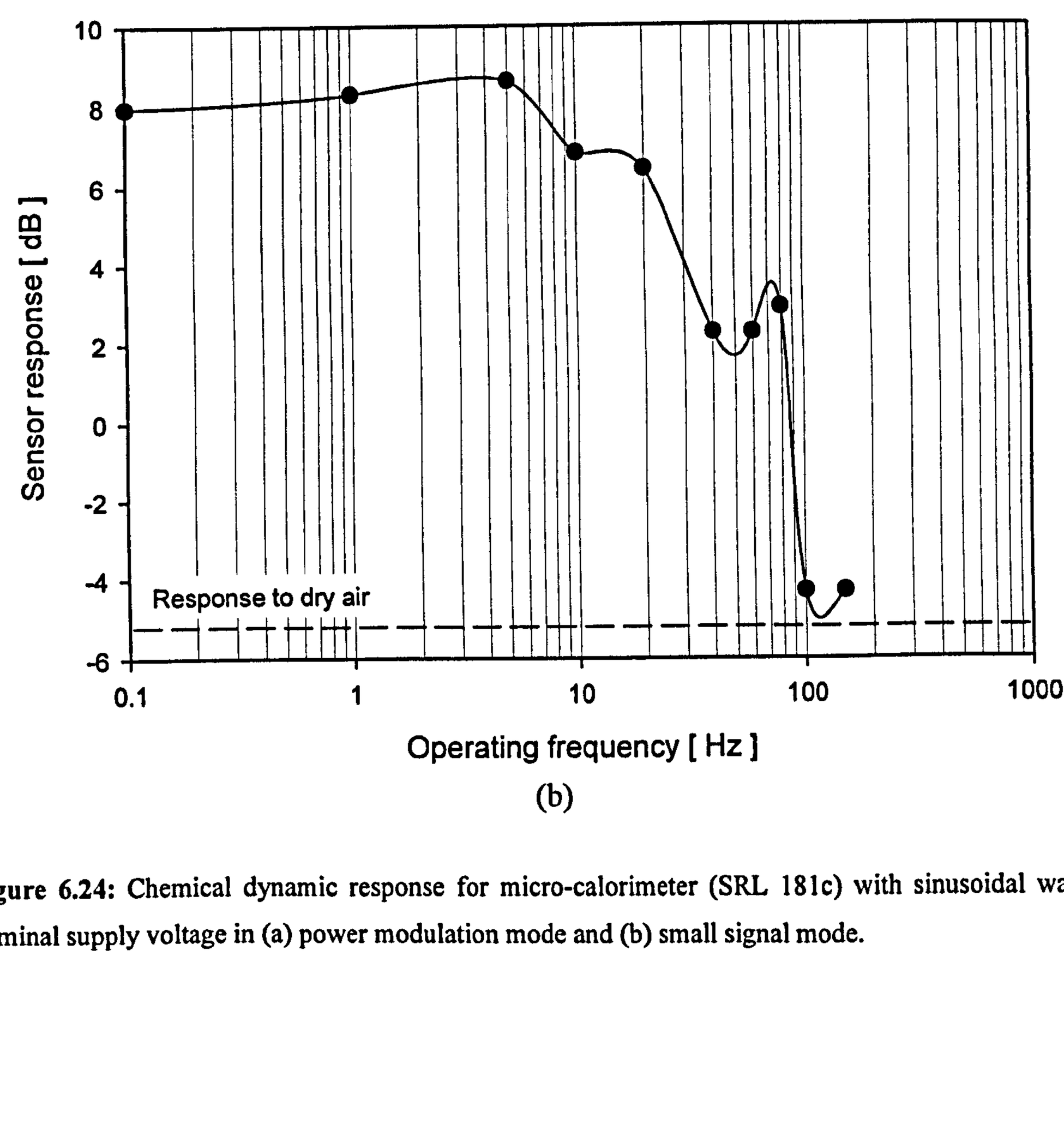

(b)

Figure 6.24: Chemical dynamic response for micro-calorimeter (SRL 181c) with sinusoidal wave and nominal supply voltage in (a) power modulation mode and (b) small signal mode.

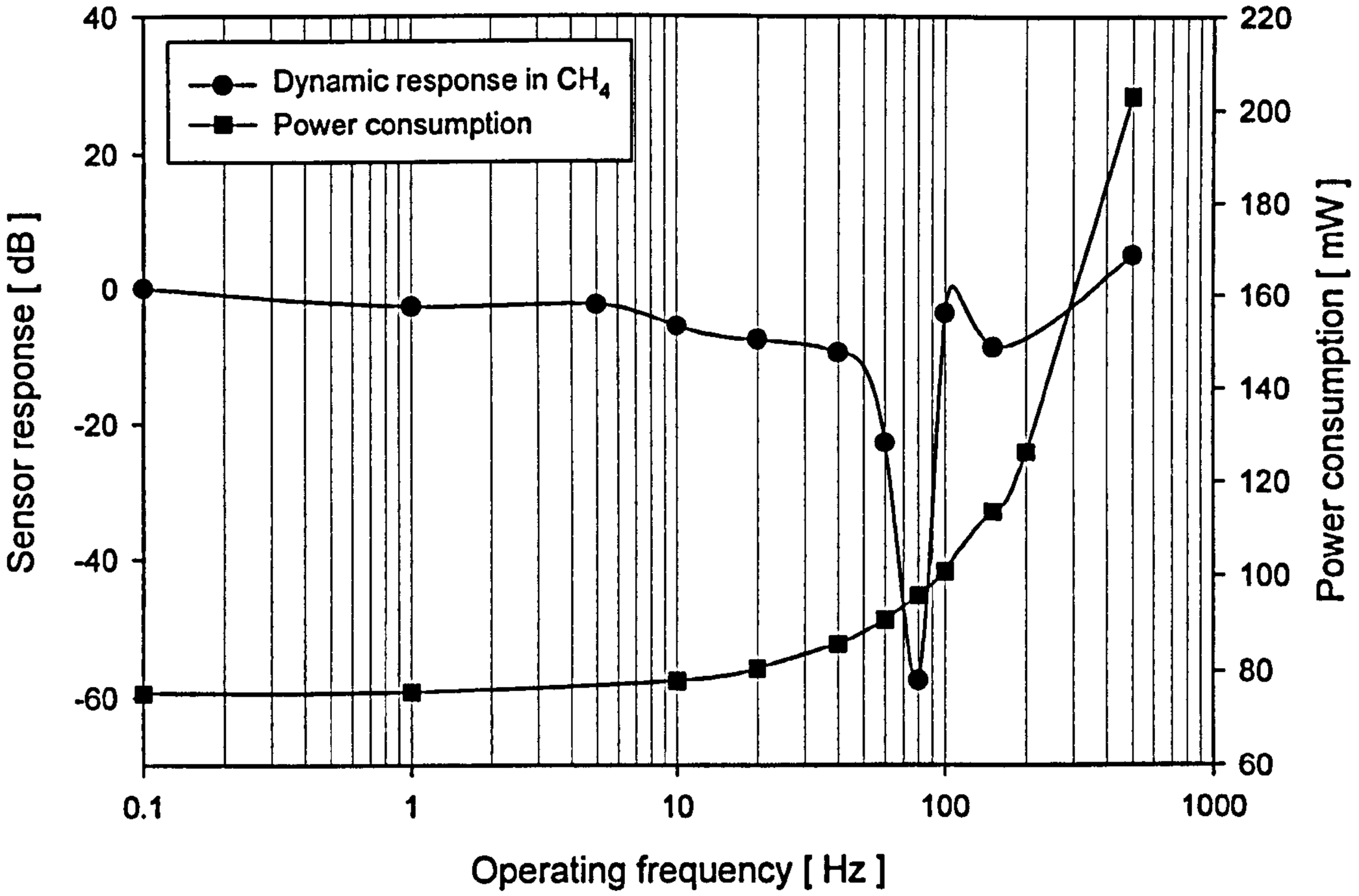

Figure 6.25: The relationship between the power consumption and the dynamic response of the SRL 176c at the nominal supply voltage.

The dynamic response of the SRL 176c micro-calorimeter is shown in figure 6.22. The sensor response was obtained by taking the difference between the Wheatstone bridge output in the test gas (V_{gas}) and in air (V_{air}). The responses were converted to decibels (dB), as shown in equation (6.7).

$$\text{Sensor response in dB} = 20 \times \log (V_{gas} - V_{air}) \qquad (6.7)$$

The operating temperature could influence the output response of the sensor, as discussed in section 6.2.2. The Bode-plot in figure 6.25 indicates that the response of the sensor started to decrease at 10 Hz with nominal supply voltage when exposed to the test gas. A minimum output signal occurred at 80 Hz because there was still sufficient cooling time (12.5 ms) for the devices. As mentioned in the earlier section, the thermal time constant at the rising edge (τ_{rise}) differs from the falling edge (τ_{fall}) and it resulted in an asymmetry waveform. When the operating frequency increased beyond 100 Hz, the "OFF" period of a cycle was inadequate for the sensor to cool down completely. It caused the average

temperature of the sensor to rise and consumed higher power, as shown in figure 6.25. Therefore, the sensor output had been regenerated. Similar phenomenons have been observed for the SRL 177c and SRL 181c in both power modulation and small signal mode, as shown in figures 6.23 and 6.24, respectively.

As for the uncoated SRL 177c micro-calorimeter, a relatively small response was measured due to the absence of the nanoporous Pd catalyst, as shown in figure 6.23. However, it still performed in a similar manner to the coated devices. Therefore, the micro-calorimeter could react with a single pulse up to the corner frequency between 10 Hz and 30 Hz, depending on the design. The corner frequency (f_c) for various designs according to the thermal time constant (τ_{th}) of the silicon membrane was computed from equation 6.8. The results in table 6.3 agreed with the experimental observations. This indicated that the corner frequency of the micro-calorimeter was determined by a thermal effect. However, as the response of the sensor could be regenerated above 100 Hz, a pulse train with a duration of 100 ms could be used to elevate the device temperature to the required operating condition.

$$f_c = \frac{1}{2\pi\tau_{th}} \tag{6.8}$$

In addition, a square wave was also used in the power modulation mode where similar results were observed. The methane response of the sensor pulsed with a square wave in power modulation mode is attached in Appendix 6d.

Table 6.3: The theoretical corner frequency for various micro-calorimeter designs

SRL code	Experimental time constant (ms)	Theoretical corner frequency f_c (Hz)
SRL 136a	13.2	12.1
SRL 162g	11.7	13.6
SRL 176c	13.7	11.6
SRL 177c	15.0	10.6
SRL 178c	9.0	17.7
SRL 179c	10.6	15.0
SRL 180c	9.6	16.6
SRL 181c	4.8	33.2

6.4.2 Thermal conductivity analysis of the test gas

The influence of the thermal conductivity of the test gas was also investigated to ensure genuine catalytic reaction had occurred. The electrical power and the practical heat loss can be modelled approximately as shown in equation (6.9a), (the radiative term has been neglected).

$$\frac{V_h^{\,2}}{R_h} \approx a(T - T_o) + b(T - T_o)^2 \qquad (6.9a)$$

The constant voltage supply is denoted as V_h and the resistance of the micro-heater is R_h. Coefficients a and b are the conductive and convective loss terms, respectively. The convective coefficient b is related to the conductivity of the test gas (λ_{gas}). As the resistance of the micro-heater R_h, is temperature dependent, it can be expressed with the base-line resistance and the temperature coefficient of resistivity, as shown in equation (6.9b).

$$R_h = R_o(1 + \alpha\Delta T) \qquad (6.9b)$$

Therefore, substituting equation (6.9b) into the (6.9a), it can be expanded to equation (6.9c).

$$\frac{V_h^{\,2}}{R_o} \approx (1 + \alpha\Delta T)\,(a\Delta T + b\Delta T^2) \qquad \text{where } \Delta T = (T - T_o) \qquad (6.9c)$$

Applying to total differentiation theorem with variables ΔT and b, and re-arranging gives equation (6.10).

$$\frac{d(\Delta T)}{\Delta T} = d\frac{T}{\Delta T} = -\frac{(\Delta T + \alpha\Delta T^2)b}{a + 2(a\alpha + b) + 3\alpha b\Delta T^2}\left(\frac{db}{b}\right) \qquad (6.10)$$

Finally, it is assumed that fractional change of the conductive loss ($\Delta b/b$) is equal to the fractional change of the thermal conductivity of the test gas ($\Delta\lambda/\lambda$). The thermal

conductivity of air and methane is 2.41×10^{-2} $Wm^{-1}K^{-1}$ and 3.02×10^{-2} $Wm^{-1}K^{-1}$ respectively [6.6]. Hence, the difference of thermal conductivity between 2.5% methane and air is about 0.63%. This results in about a 1°C decrease at 500°C and should be negligible when compared to the effect of the catalyst reaction. Therefore, it shows, as expected, that the reduction of the thermal conductivity due to the test gas is unlikely to interfere with sensor operation.

6.5 Reliability of the micro-calorimeter

After the performance of the micro-calorimeters was evaluated, the reliability of the sensors was investigated. The study focused on the mechanical stability and the poisoning resistance of the sensors. Therefore, the robustness of the micro-calorimeter and the chemical stability of the micro-calorimeter could be specified, before commercial exploitation.

6.5.1 Long-term stability

Four pairs of micro-calorimeters were tested in the customised long-term test station, as described in Chapter 4. The optimised meander (SRL 162g) and the Low-power Drive-wheel micro-calorimeter designs were selected for these experiments. Both continuous powering and power modulation modes (at 1 Hz) with nominal supply voltages were performed for each selected sensor model. All the devices maintained their functionality after 1000 hours (42 days) of operation and the mechanical stability in both operating modes were ensured.

In addition, it was speculated that an aging effect, due to the diffusion of the gold electrode into the silicon nitride membrane, could lead to a reduction of the micro-heater resistance. With a silicon nitride layer of 500 nm and a diffusion coefficient of gold into silicon nitride of 1.0×10^{-18} cm^2s^{-1}, it would require 20 years of continuous operation for the gold to reach the platinum micro-heater [6.7]. Therefore, this is not a problem.

6.5.2 Poisoning resistance

As mentioned in Chapter 1, certain chemical compounds reduce the response of commercial calorimeters and this is referred to as poisoning. A pair of devices from the two micro-calorimeter models, namely SRL 177c and SRL 181c, were tested with the industrial standard poisoning gas, hexamethyldisiloxane (HMDS) [6.8]. The experiments

were carried out at City Technology Ltd (UK), with identical Wheatstone bridge interface circuits. The technical specifications of the gas test station are described in Chapter 4.

In general, the concentration of HMDS is between 5 ppm and 20 ppm and the sensitivity of the commercial device would be affected almost instantaneously, as shown in figure 6.26. However, the micro-calorimeters exhibited a remarkable poisoning resistance and sustained its sensitivity even with an increased poison concentration up to 100 ppm, as shown in figure 6.27. These encouraging results significantly enhance the potential of commercialisation of these micro-machined devices.

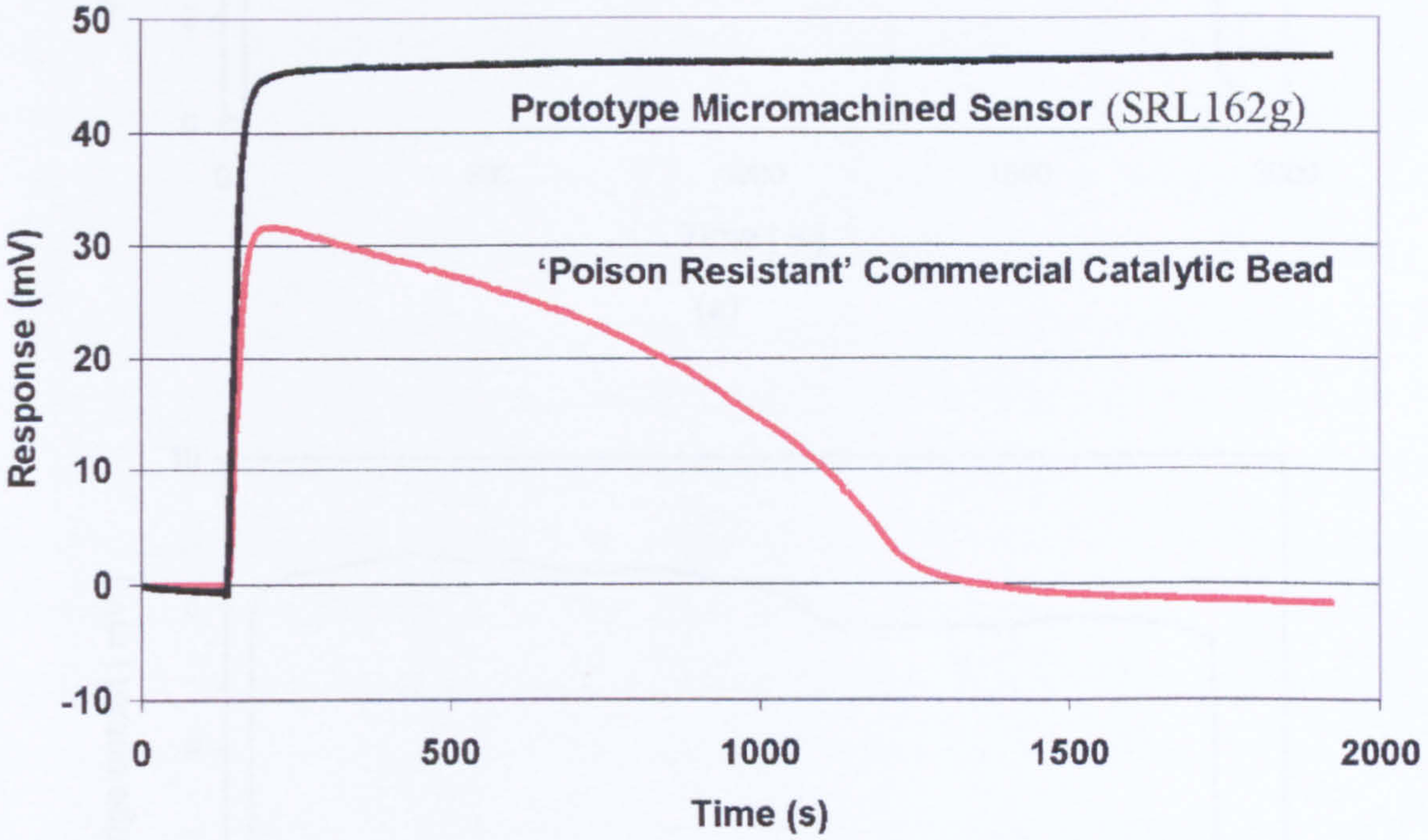

Figure 6.26: Comparison of the poisoning effect for the commercial pellistor and the micro-calorimeter (SRL 162g) [6.4].

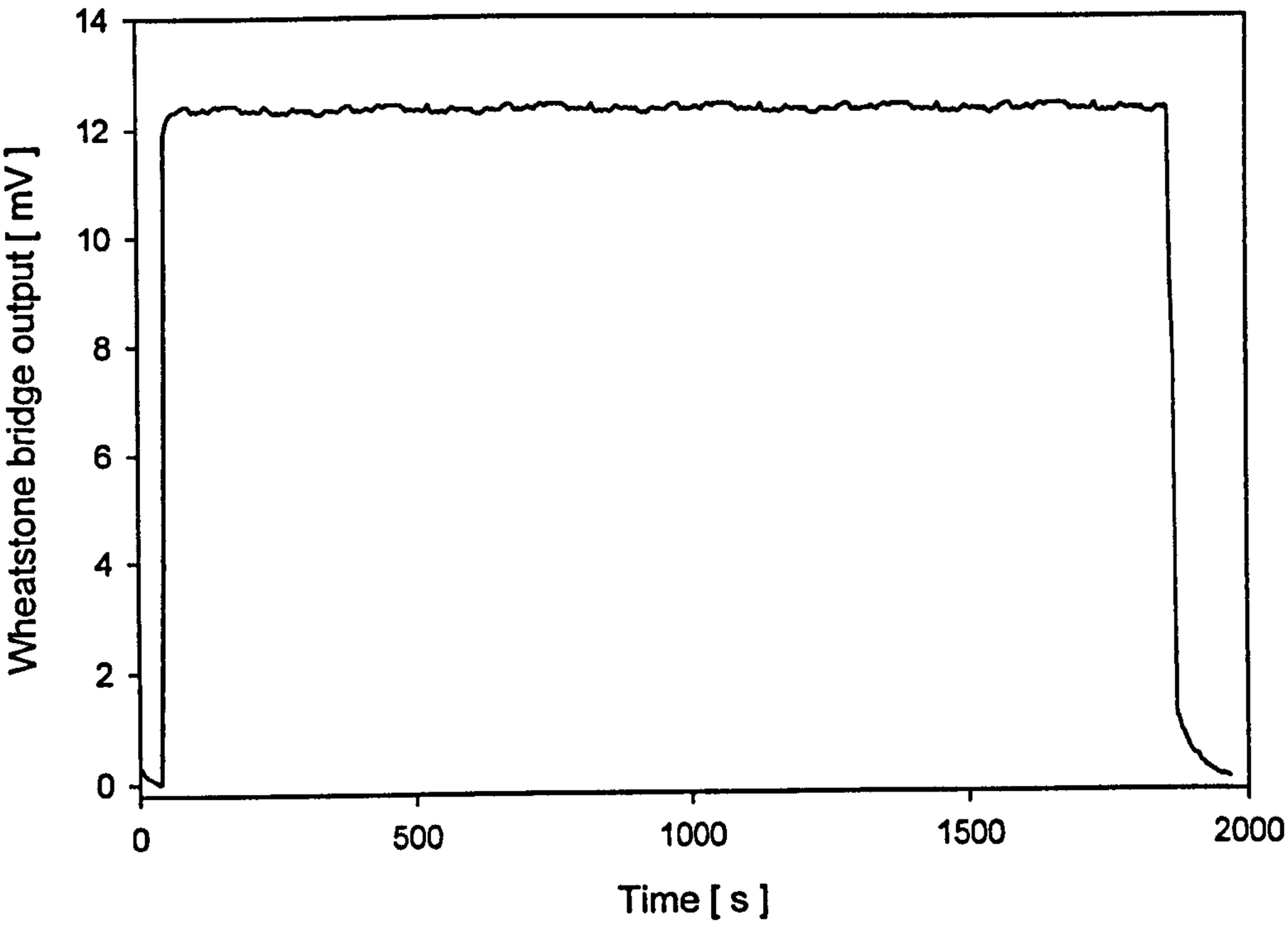

(a)

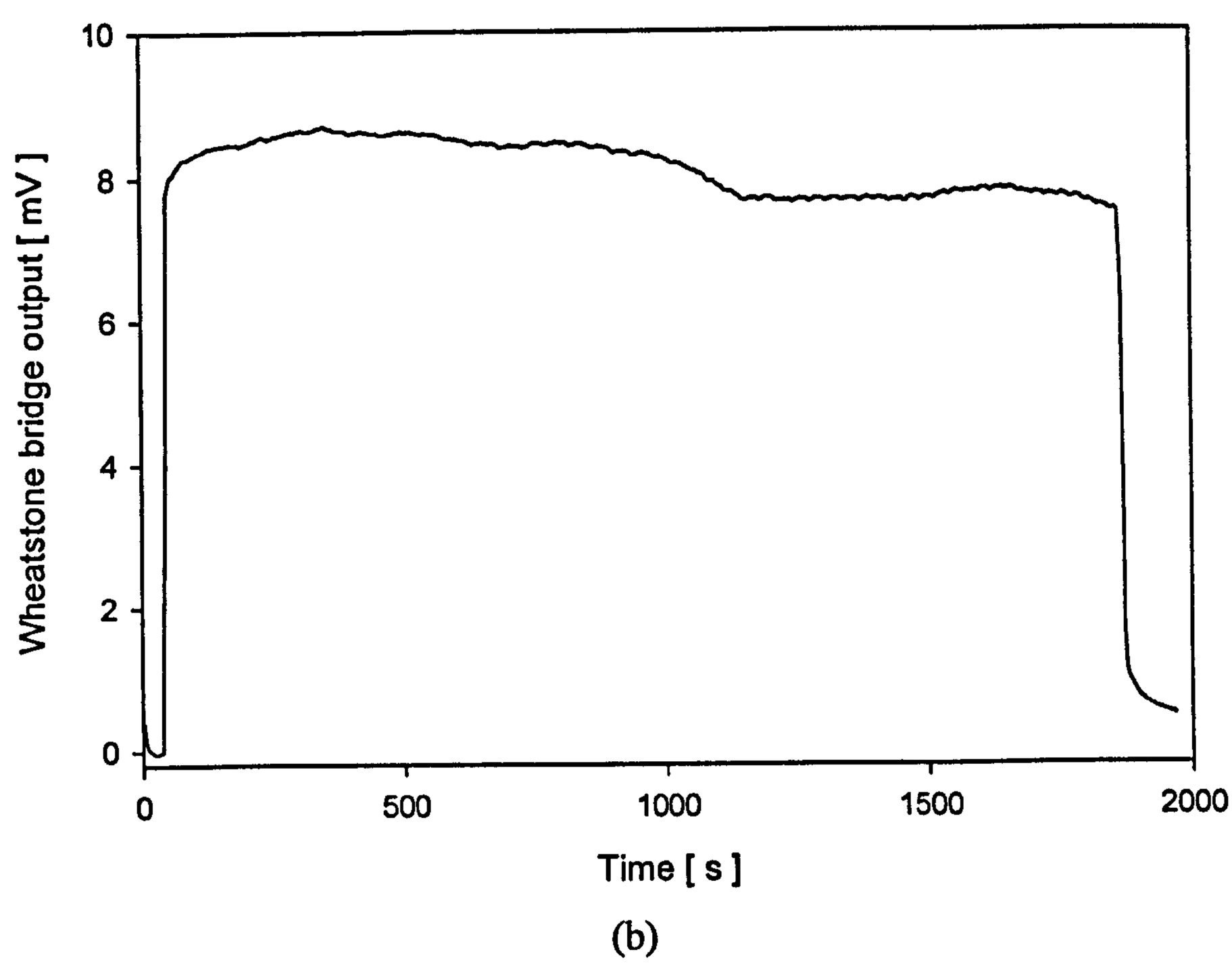

(b)

Figure 6.27: Typical poisoning resistance of micro-calorimeters with 100 ppm HMDS and 2.5% CH_4 in air at nominal supply voltages for Drive-wheel design in (a) Low-power family (SRL 177c) and (b) Ultra-small/low-power family (SRL 181c).

6.6 Conclusions

This chapter reported on the chemical characteristics of the micro-calorimeters in both continuous and pulse modes of operation. The output response for the Drive-wheel and the meander design from different families were investigated with a continuous powering mode. The sensor responses to the standard test gas (2.5% CH_4 in air) ranged from 5 mV to 40 mV, depending on the device type. However, this absolute output magnitude is not a unique measure of the nanoporous Pd catalyst efficiency. It also relates to a number of factors, such as MHR, geometrical area of the Au electrode, the supply voltage to the bridge and other factors as mentioned in the expression (6.1). The temperature increase per unit area per percent methane in air for the sensors was found to vary with design from 8 °C to 120 °C. Analysis indicated that the optimised meander design (SRL 162g) delivered the best heating efficiency and a high response. The Drive-wheel design in the Low-power family (SRL 177c) and the Ultra-small low-power family (SRL 181c) achieved the most isothermal active area, best catalyst efficiency and highest sensitivity.

The dynamic properties of the micro-calorimeters have been evaluated in small-signal and power modulation operating modes. These proved that the response time for the micro-machined sensors had been reduced significantly to about ~ 4 ms as compared to the commercial pellistors which are in the order of 100 ms. This enables the micro-machined devices to be operated in a pulse mode. Furthermore, as the cooling at the active area relies only on natural heat loss mechanisms, it leads to asymmetrical time constants at the rising (τ_{rise}) and falling edge (τ_{fall}). The power consumption of the device is directly proportional to the time constant as well as the operating frequency.

The chemical dynamic response to methane with an applied sinusoidal waveform could be categorised into Normal and Pseudo operation mode. The sensors behaviour in the Normal mode was stable and reproducible. It became unstable and required significantly higher power consumption when it was operated in the Pseudo operation mode. The experiments indicated that the corner frequency for various micro-calorimeter designs were between 10 Hz and 30 Hz. The output magnitude of the sensor would continue to decline until the cut-off frequency, up to 100 Hz (boundary of Normal operation mode). The sensitivity was regenerated beyond the cut-off frequency and entered into the pseudo operation mode. Therefore, the minimum pulse width should be at least 50 ms with a space of 950 ms, for a sampling rate of 1 Hz. Clearly, the dynamic response of the device was limited by the thermal time constant of the membrane. It

could only be concluded that the reaction kinetics of the catalyst were faster than 100 Hz. The power saving for the micro-calorimeter operated in pulse mode could typically reach up to 50% at 10 Hz, when compared with the continuous powering mode.

Finally, The reliability of the devices had been evaluated by the life-expectancy experiments on the long-term test station. It proved that the devices could be operated for at least 1000 hours continuously without failure in both D.C. and A.C. modes. In addition, the poisoning test in 100 ppm HMDS proved that the micro-calorimeter possesses a remarkable poisoning resistance over the conventional pellistor bead.

In conclusion, the silicon planar micro-calorimeter has significant potential for applications in low-power methane gas detectors.

References

[6.1] S. S. Leclerc, M. Willett, *City Technology Ltd. Project quarterly report (City Technology Ltd.)*, December 2001.

[6.2] S. M. Lee, J. W. Gardner, *City Technology Ltd. Project quarterly report (University of Warwick)*, No. 10, 2002.

[6.3] S. M. Lee, J. W. Gardner, City Technology Ltd. Project quarterly report (University of Warwick), No. 11, 2002.

[6.4] S. A. A. Leclerc, M. J. Willett, S. M. Lee, J. W. Gardner, J. Marwan, P. N. Bartlett, Novel combustible gas sensors employing micromachined silicon substrates and nanostructured catalysts, submitted to *Sensors and Actuators B* in July 2002.

[6.5] *The 4-series Citicels® handbook*, City Technology Ltd., p50, 1999.

[6.6] A. M. James and M. P. Lord, *Macmillan's Chemical and Physical Data*, The Macmillan Press Ltd., London, 1992.

[6.7] S. M. Lee, D. C. Dyer and J. W. Gardner, Design and optimisation of a high-temperature silicon micro-hotplate for nanoporous palladium pellistors. Submitted to *Microelecronics Journal*, 34, pp115-126, 2003.

[6.8] P. T. Moseley, B.C. Tofield, *Solid State Gas Sensor*, Adam Hilger, Bristol, 1987

Chapter 7

Conclusions and further work

7.1 Overview

This research has been motivated by a commercial need to develop a new micro-calorimetric gas sensor to replace an existing commercial pellistor. All the principal objectives have been achieved. The manufacturability and reproducibility have been proven by the two generations of micro-calorimeters. Their performances, in terms of power consumption, sensitivity, reproducibility, production cost and voltage requirement, have exceeded all previous efforts. The power consumption of the SRL 181c is even lower than the initial specification by a factor of three. A power optimisation model and a simulation database have been developed to assist the design of future micro-calorimeters. Possible further works has also been suggested.

7.2 The design and fabrication of new micro-calorimeters

Two generations of silicon micro-calorimeters have been designed in this research period. The first generation included only meander style micro-heater designs. These provided a reasonably large quantity of functional devices to facilitate various essential experiments, such as establishing appropriate electrochemical deposition procedures. As the optimised meander design (SRL 162g) was based on the original meander design (SRL 136), similar but improved device characteristics resulted, as described in Chapter 5. Moreover, it allowed the development of the silicon fabrication process and the post-fabrication steps, such as dicing and bonding. Furthermore, the appropriate composition of the surfactant for the electro-chemical catalyst deposition could be established.

The second generation of micro-calorimeter designs explored numerous design concepts and strategies for improving heater performance. Fifty-four different designs and variants were created and categorised into six families, namely the Standard family (SRL 176), the Low-power family (SRL 177c), the Small-mem/ robust family (SRL

178), the Robust family (SRL 179), the Ultra-small/ robust family (SRL 180) and the Ultra-small/ Low-power family (SRL 181). Furthermore, test structures were also included to allow specific investigations, such as the thermally induced stress in the membrane. The major differences between the first and second wafer fabrication run are listed in table 7.1. Improvements in performance of the second generation designs have been identified. In particular the Drive-wheel design showed a superior thermal profile and became the focus of subsequent research. The supply voltage, temperature homogeneity at the active area, catalyst efficiency and sensitivity had been optimised in this design generation. Therefore, the voltage compatibility to the digital interface and the enhanced sensitivity had exceeded previous research efforts [7.1] [7.2].

Table 7.1: The major differences between the first and second fabrication run for the micro-calorimeter.

Key feature	***Run 2***	***Run 1***	***Remarks***
Wafer size	4"	4"	No changes made.
Au gate electrode	Yes	Yes	No changes made.
Wafer Thickness	300 μm	280 μm	390 μm suggested by the foundry (IMT) after the mask fabrication. Settled for 300 μm to avoid major modifications.
Passivation layer	1 out of 8	1 out of 10	Requested for 2 passivated wafers out of 10 at Run 2. Only 1 out of 8 received.
Die size	$(4 \times 4)mm^2$ $(2 \times 2)mm^2$	$(4 \times 4)mm^2$	(2×2) mm^2 devices were included as a test vehicle to reduce production cost.
Size of membrane	$(2 \times 2)mm^2$ $(1.5 \times 1.5)mm^2$ $(1 \times 1)mm^2$	$(2 \times 2)mm^2$	A mixture of Membrane-to-Heater Ratio (*MHR*) to be investigated in Run 2.
Alignment marks	For 5-masks	For 5-masks	Identical for both Run 1 and Run 2.
Reserved quadrant	¼ each wafer	No	It allows experiments for wafer-level deposition.
Common gate device	Yes	No	It allows wafer-level deposition.
Device locator	Yes	No	A facility to obtain the location of a device on a wafer.
7.5 mm clearance around the wafer border	Yes	No	Required by the IMT for compatibility to the mask aligner. 5 mm clearance was required in Run 1.
12 mm × 50 mm clearance adjacent to the primary flat	Yes	No	Required by the IMT for compatibility to the mask aligner.

Electro-thermo-mechanical simulation models have been established through continuous device-property updates, extracted from device characterisations from both design generations. As a high level of accuracy has been achieved (down to a standard deviation of 4.6%), further design concepts could be evaluated by computer simulations. This can lead to improvements in design efficiency for the micro-calorimeter.

The high cost and labour intensive production process could be transformed into a batch fabrication route by using the planar micromachined devices. The manufacturability of the devices has been proved by the high front-end, dicing and assembly yield. Over 82% yield on average was recorded in the second silicon run. The high quality silicon nitride layer provided excellent insulation between the Au gate electrode and the platinum micro-heater element. The measured breakdown field strength of the silicon nitride layer reached 37.5 MV/m [7.3], which is similar to the theoretical value of 20 MV/m.

7.3 General design rules for micro-calorimeters

From the experimental work on many different micro-heater designs, it is possible to create a set of general design rules, as described below.

- The overall geometry of the device should be minimised to reduce convection because this is responsible for almost 80% of the thermal energy loss. However, it must be sufficiently large to be handled and hence show a practical dicing yield. The dimensions should not be below 2 mm × 2 mm square.
- The supply voltage of the device is obviously directly proportional to the Wheatstone bridge output. The same is true for a current-driven bridge or half-bridge. It is also highly dependent on the application and the interfacing electronics. When a standard Wheatstone bridge interface circuit is used, the supply voltage should be at least 2 V to ensure a detectable output without amplification. However, modern solid-state amplifiers like op-amps are low-cost and commonly available. It can be included in the interface circuit to increase the signal output. Hence, the supply voltage can be further reduced.
- Membrane-to-heater ratio (*MHR*) is an important tuning parameter in designing a micro-calorimeter. Typically, a large value is desirable. It reduces the lateral conduction that not only allows a higher temperature increase by the catalyst, but

also decreases power consumption. The power consumption of a design can be estimated by the model in equation (7.1) [7.4].

$$\text{Power consumption} = \ell(65.6 - 22.5\ln MHR) \tag{7.1}$$

where ℓ is the length of the device in units of mm

- The shape of the micro-heater is critical to the thermal distribution within the active area. Although a central hot spot cannot be completely eliminated, it can be optimised as shown by infrared thermography for SRL 162g. Moreover, this device provides the best heating efficiency over any other designs in this research. Nevertheless, the size of the micro-heater is limited whilst the catalyst area at operating temperature should be maximised. The Drive-wheel micro-heater design is able to disperse the hot spot and prevent over-heating at the active area. Therefore, it creates an isothermal active area and enhances the sensitivity.
- The size of the active area should be reduced in line with the optimised *MHR* in order to minimise the convectional loss. The electrode should be the same size as the micro-heater to ensure thermal homogeneity of the active area. In addition, the device resistance should remain at about 40 Ω to maintain the voltage requirement between 2 V and 3 V for compatibility with digital interfacing.
- The minimum size of the micro-calorimeter depends on a number of factors some of which depend on the fabrication process. In the situation where the fabrication process and quality remained unchanged, the minimum overall geometry of the device is about 2 mm × 2 mm. This can accommodate a maximum membrane area of 1 mm × 1 mm. The limit of the micro-heater comes from the size and the track-width. As the size becomes comparable to the membrane thickness, lateral thermal isolation cannot be maintained and the power consumption will increase. However, the main restriction arises from the track-width which directly affects the reliability of the device due to the relatively high current density (e.g. 3.8 A/mm^2 for SRL 181c) and high operating temperature (about 500°C). Although the micro-heater element can be scaled down whilst maintaining the aspect ratio and resistance, the minimum suggested track-width was estimated to be about 5 μm to prevent electromigration. The minimum area of the micro-heater should then be about 100 μm × 100 μm and the maximum allowable *MHR* is 10. The

power consumption for such a device is estimated to be about 27.6 mW, based on the power consumption model in equation (7.1). However, these restrictions are not necessarily applicable when a different silicon processing technique is employed. For example, the die size can be further reduced if the membrane structure is created by isotropic Deep Reactive-Ion-Etching (DRIE) instead of the anisotropic KOH wet etching. Therefore, the restriction of the minimum device size is process dependent and can be adjusted for a specific application.

7.4 Characteristics and performance of the micro-calorimeters

The voltage requirement of the micro-calorimeters has been reduced from 7.5 V for the original design (SRL 136a) to under 5 V in the second generation. In addition, the micro-heater resistance has been reduced by a factor of 4. The purpose of these changes is to produce sensors that could adopt digital interface electronics directly without additional voltage regulations. The power consumption of the devices has been reduced from 195 mV to as low as 52 mW. A pair of SRL 181c micro-calorimeters could be operated for 8.5 days approximately, in continuous powering mode by three AA size alkaline batteries (2.85 Ah) in a Wheatstone bridge interface circuit. When compared with a certain commercial product where the battery could only sustain for about 10 hours in a sensor pair (PGM-6010 by Drae), the continuity and the portability of the micro-calorimeter has been significantly improved. A summary of the properties for the most representative models from this research is shown in table 7.2.

The thermal distribution at the active area has been optimised in the Drive-wheel micro-heater design. Infrared thermal imaging revealed that the standard deviation of the active area temperature during operation (550°C) could be as low as 10 K. Therefore, an isothermal active area at a fixed operating temperature could maximise the catalyst efficiency. This leads to enhanced output voltage per unit area and the sensitivity (normalised) per percent methane in air.

Two pulsing regimes were designed to investigate the sensors' transient behaviour, namely the small-signal mode and the power modulation mode. The switching time constants of the micro-calorimeters are in the order of milliseconds. As the cooling of the devices relies solely on the natural heat loss mechanisms, the time constants of the rising and falling edges are asymmetrical. Furthermore, the difference between the two time constants could be a factor of 10, in the power modulation mode. Therefore, it leads

to higher power consumption across the sensors with an operating frequency over 100 Hz where this increase is linearly related to the frequency (see table 7.2 for time constant values).

Table 7.2: Properties for the various models of micro-calorimeters to operate at 550°C.

Properties	SRL 136a	SRL 162g	SRL 176c	SRL 177c	SRL 181c
Continuous mode					
Nominal operating voltage [V]	7.5	6.5	3.1	2.7	2.0
Nominal operating current [mA]	26	17	50	43	26
Power consumption [mW]	195	111	155	116	52
Micro-heater type*	M	M	D-W	D-W	D-W
Base-line resistance, R_o, of the micro-heater [Ω]	147.0 ± 3.0%	230.0 ± 3%	31.8 ± 3.0%	31.1 ± 3.0%	39.4 ± 3.0%
Voltage output [mV/%CH_4]	15.2 ± 3.0%	16.0 ± 3.0%	8.0 ± 3.0%	7.2 ± 3.0%	1.9 ± 3.0%
Normalised voltage output [(mV/mm^2)/%CH_4]	15.2 ± 3.0%	49.2 ± 3.0%	31.3 ± 3.0%	57.3 ± 3.0%	59.9 ± 3.0%
Pulse mode operation					
Small-signal mode					
Rising edge, τ_{rise} [ms]	2.1 ± 0.2	1.6 ± 0.1	2.0 ± 0.4	1.3 ± 0.3	0.5 ± 0.1
Falling edge, τ_{fall} [ms]	5.4 ± 0.3	4.9 ± 0.3	4.4 ± 0.4	4.0 ± 0.2	1.4 ± 0.2
Power modulation mode					
Rising edge, τ_{rise} [ms]	1.1 ± 0.2	1.2 ± 0.2	0.9 ± 0.1	0.7 ± 0.1	0.4 ± 0.1
Falling edge, τ_{fall} [ms]	13.2 ± 0.2	11.7 ± 0.1	13.7 ± 0.1	15.0 ± 0.1	4.8 ± 0.2

*M = Meander type design; D-W = Drive-Wheel design.

Methane detection with the sensors operating in the pulse modes was evaluated. Here test ranges between 0.1 Hz and 500 Hz were used. Due to the asymmetrical rise and fall time, there is still sufficient time for the sensor to cool down at the falling edge when the operating frequency was below 80Hz. The average temperature of the sensor was inversely proportional to the operating frequency. Hence, the sensor sensitivity decreased above 10 Hz. However, without sufficient cooling time, the temperature and the power dissipation across the micro-calorimeter above 80 Hz increased. The sensor started to behave as if it was being operated in continuous powering mode and the sensitivity increased by up to 8 dB.

Finally, excellent poisoning resistance was exhibited by the micro-calorimeters. Experiments indicated that the sensitivity was maintained even when exposed to 100 ppm HMDS which is four times stronger than the usual concentration used for testing commercial devices. Together with the positive long-term life expectancy test (1000 hours), the reliability has been proven for the silicon micro-machined micro-calorimeter with nanoporous Pd catalyst.

7.5 Further work

Although this research has exceeded the initial research objectives, several other properties may also be investigated. Some further work is suggested below to improve the understanding of the micro-calorimeter.

1. As individual cells had been used throughout the research, it would be interesting to characterise device pairs which remain physically joined. Several such device pairs were reserved in the dicing process to allow such investigation.
2. For commercialisation, wafer level deposition of the nanoporous catalyst is required using common-gate devices. Devices in the reserved quadrants (2^{nd} fabrication run) can be characterised in order to evaluate the practicality of the catalyst deposition in production.
3. Theoretically, the micro-calorimeter with the nanoporous Pd catalyst can be applied to other combustible and toxic gases, such as carbon monoxide. The micro-calorimeters can be calibrated for multiple gas detection.
4. This research proved that the sensors could be operated in a pulsed mode. Various pulsing regimes could be considered to optimise the sensitivity with minimum power consumption. In addition, the phase shift in the sensor response for different types of combustible gas could be investigated for a revolutionary detection method, apart from the voltage output magnitude.
5. Finally, instead of employing the classical Wheatstone bridge interface circuit, modern electronic devices, such as op-amp chips and microcontrollers with thermal cycles, can be considered to eliminate the need for a compensator. Therefore, fabrication would become more cost effective. Further power reduction can be achieved whilst maintaining stability from device aging and fluctuations in ambient conditions.

References

[7.1] M. Gall, The Si planar pellistor array, a detection unit for combustible gases, *Sensors and Actuators B*, 15-16, 1993, pp. 260-264.

[7.2] R. Aigner, M. Dietl, R. Katterloher, V. Klee, Si-planar-pellistor: designs for temperature modulated operation, *Sensors and Actuators B*, 33, 1996, pp 151-155.

[7.3] S. M. Lee, J. W. Gardner, *City Technology Ltd. Project quarterly report (University of Warwick)*, No. 8, 2001.

[7.4] S. M. Lee, D. C. Dyer and J. W. Gardner, Design and optimisation of a high-temperature silicon micro-hotplate for nanoporous palladium pellistors. *Microelecronics Journal* (in press).

Appendix 1

Market maturity of the pellistor

Market Maturity of the pellistor

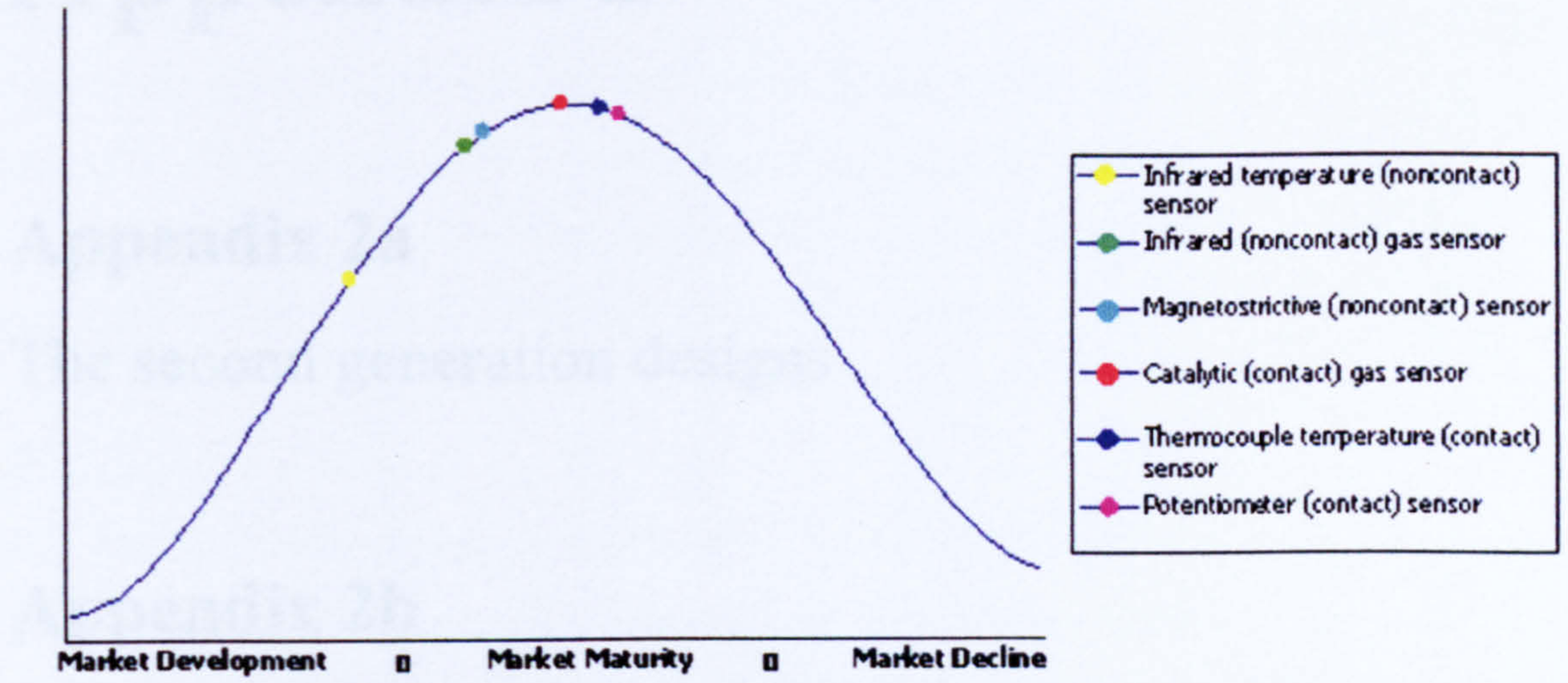

Figure A1.1: A comparison of the market maturity between pellistor and various sensor techniques.

A study has been conducted by Carrillo, Frost & Sullivan, in April 2002 at the North America region to investigate the market maturity of various sensing techniques, shown in figure A1.1. Here, the catalytic gas sensor refers mainly to pellistors. The results indicate that the pellistor market has already reached a maturity level. While Infrared (IR) gas sensor is in a growing market with a potential in some emerging end-user markets like automotive industry. Although an IR gas sensing module is significantly more expensive than a pellistor, an improvement on the pellistor performance is necessary to maintain its market share before it is substituted by other innovative technology.

Appendix 2

Appendix 2a

The second generation designs

Appendix 2b

The SOLIDIS 3D simulation results

Appendix 2a

The second generation designs

SRL 136o

This is the most primitive model and it is included purely due to the need of comparison. This is treated as a test device to check against the previous wafer run for any process variations. All parameters are essentially identical to the previous design.

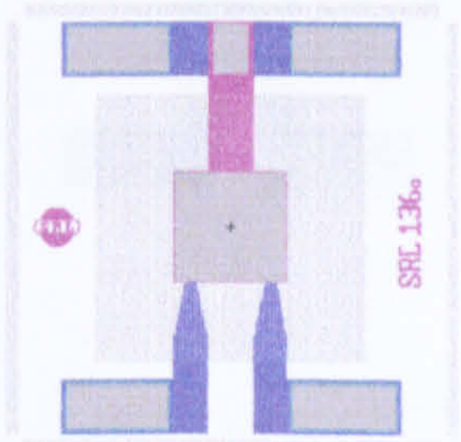

SRL 136em

The emulated device based on the former micro-calorimeter design SRL 136a. The emulator tracks avoided direct overlapping of the platinum heater tracks, in order to prevent a large parasitic capacitance. The emulator is made of gold and not only does it mimic the exothermic reaction power of the catalyst, but also acts as a temperature-sensing element from resistance.

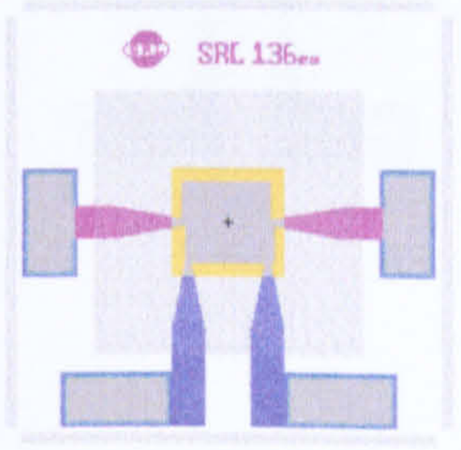

SRL 136sg

This is another test device with 4 strain gauges to investigate the stress on the membrane. The four stain gauges of about 10 Ω each, can form two half-bridge arrangement for temperature compensated measurement. The SRL 136a structure was chosen to include the strain gauges because it already has both calibration and simulation data collected previously. Therefore, the thermal properties of the device is known.

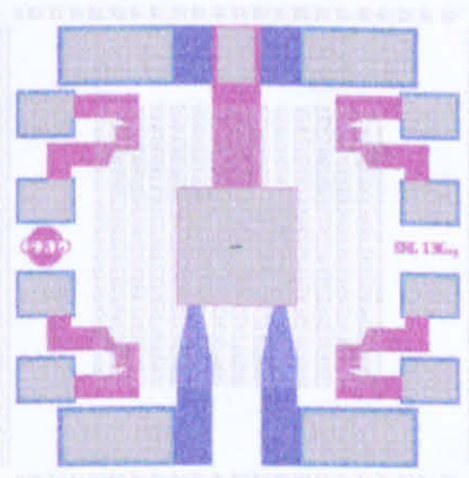

SRL 136sgx

This type of device is similar to SRL 136sg apart from the exclusion of the gate electrode. It assists the investigation about the effect of the gate electrode on the stress/temp distribution of a device.

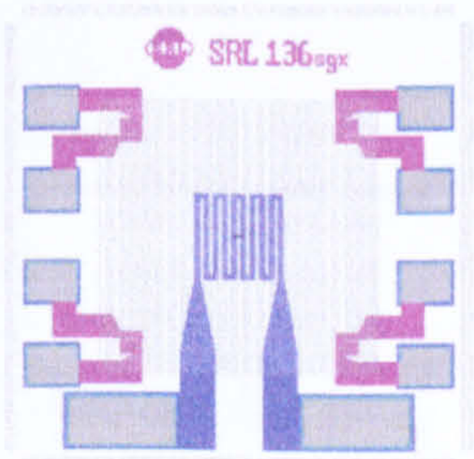

SRL 136os

This is the common gate variant of the SRL 136o. It is allocated in the reserved quadrant on the wafer for common gate deposition. Hence, the potential of the wafer level deposition can be explored.

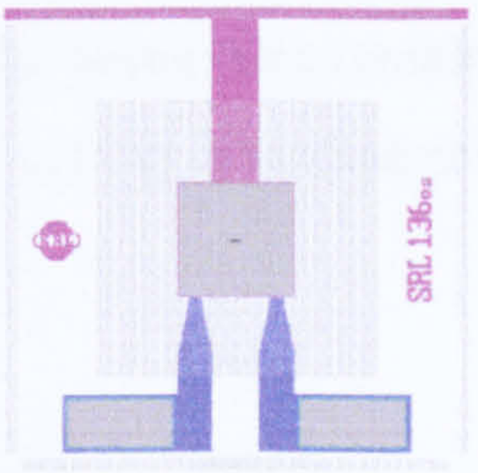

SRL 136x

This test device allows a comparison between the micro-hotplate with or without gate. At the same time, this would be used to investigate the process variation compared to the previous wafer run, if any.

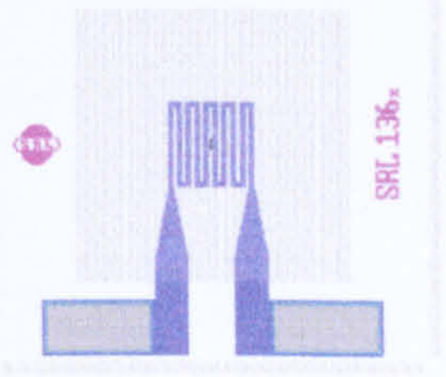

SRL 162o & SRL 162x

This is the same design as the SRL 162g that was fabricated in the previous wafer run. In order to avoid confusion, it was renamed as SRL 162a while SRL 162x excluded the gold gate pad. These devices will provide additional information and further confirmation when there is any doubt on process variation from the wafer run.

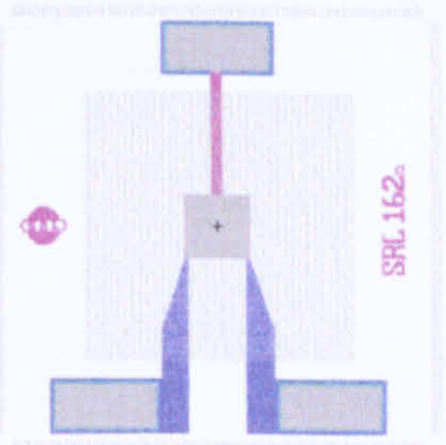

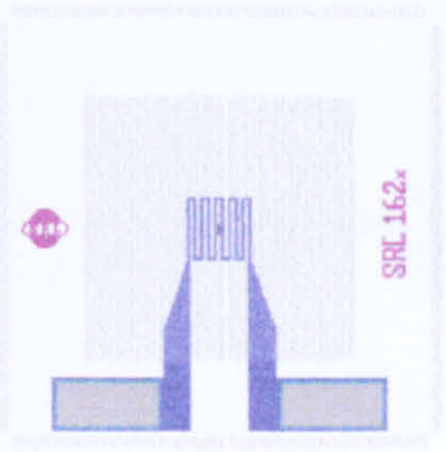

SRL 162os

This is the common gate version of the SRL 162o design and it allows the wafer level deposition to be performed on this device. It can be used to check for any performance drift from the previous fabrication.

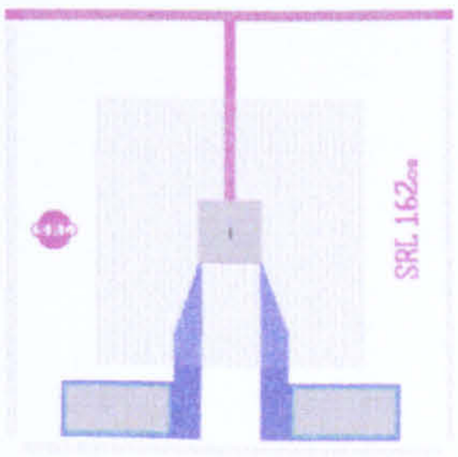

SRL 176 – The standard family

The attribute of this family is that the size of the membrane and the heater area remain the same as SRL 162g. Therefore, the Membrane to Heater Ratio (*MHR*) is unchanged which leads to similar power consumption.

SRL 176a

The heater for this device has a very low resistance. So it is expected to have a supply voltage lower than the specification. The information is useful to prove the *MHR* theory and to understand the performance of ultra-low resistance devices.

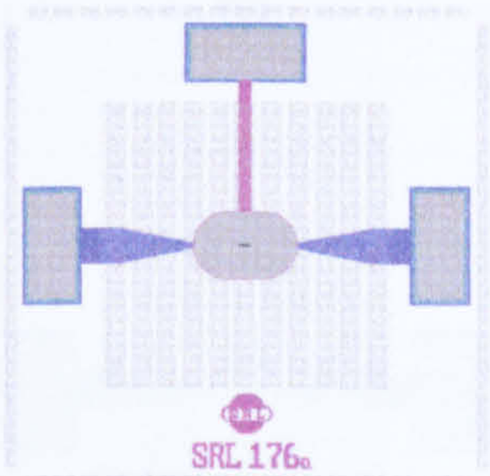

A variant of this type is SRL 176as. It is the common gate device and the gate pad was replaced by a common connector which connects the other common gate design to a contact pad.

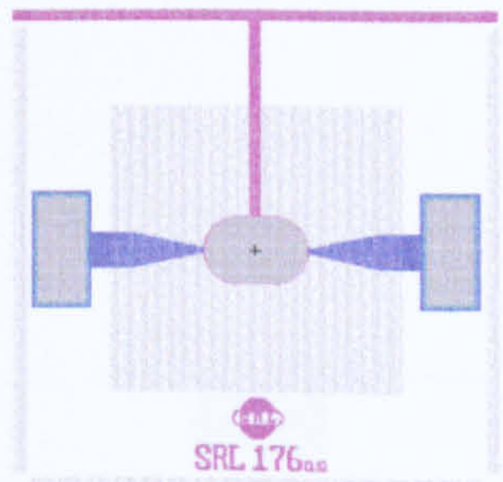

Another variant is SRL 176ax and the only different is that the gate area was excluded for investigation of the heat distribution without the gate electrode.

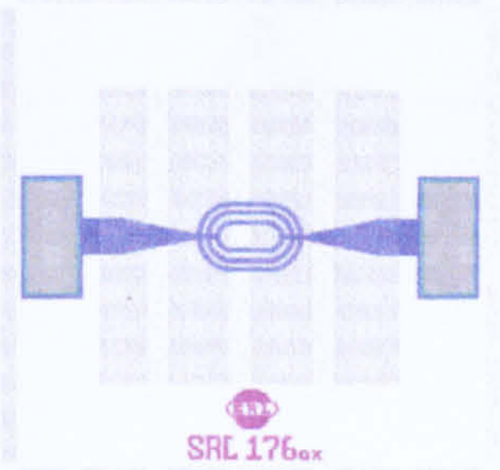

SRL 176b

The heater for this device employed the honey-comb design and the main purpose was to evaluate the performance of such a heater design. More importantly, this device can be used to develop alternative micro-heater designs for more evenly thermal distribution.

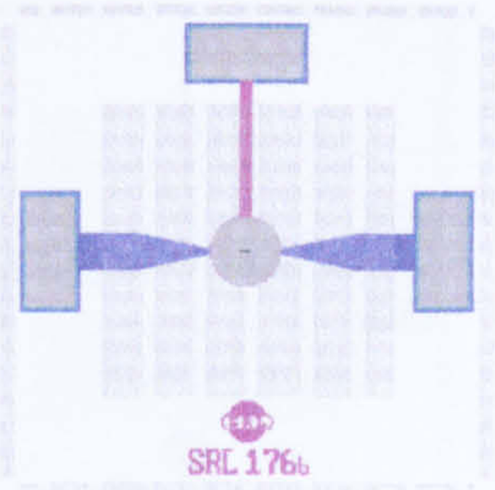

SRL 176bx is the design without the gold gate electrode in order to investigate the heat distribution and the stress profile. Therefore, additional information such as robustness of the device can be investigated.

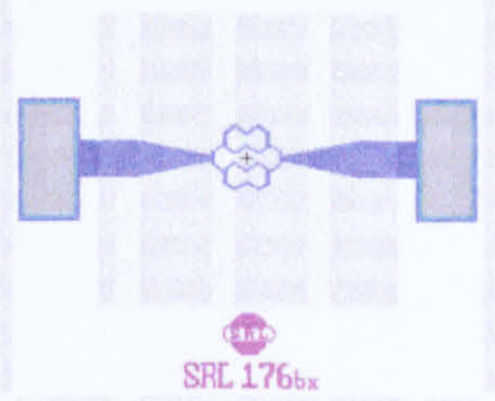

SRL 176c

The attribute of this design is the circular micro-heater design. This design will be used to prove that the micro-heater design can effectively reduce the stress on the membrane and improve the thermal profile of the active area. Furthermore, it can also be used to investigate the circular micro-heater which has not been done before.

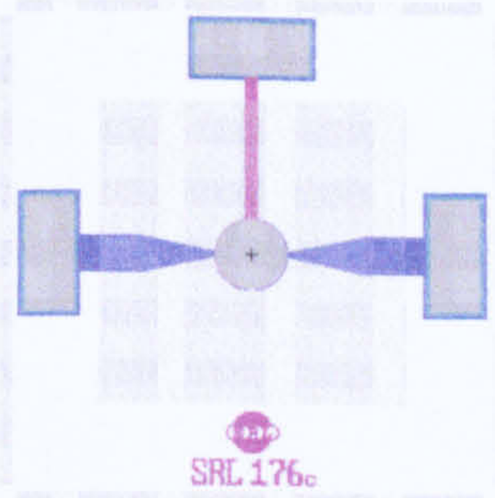

SRL 176cx was the gate-less version. It allows the actual thermal profile of the circular micro-heater design to be studied. This will provide essential information since the circular micro-heater design is novel. Once the performance of circular design has been proven, SRL 176cx will demonstrate the even thermal distribution without the gold electrode.

SRL 176us

This is a special additional device. It provides the two extreme cases of maximum size of membrane and minimum size of micro-heater. This will serve as a back-up investigation device. This design will supply additional information about the *MHR*, the stress on the membrane and the robustness of the device in this extreme situation.

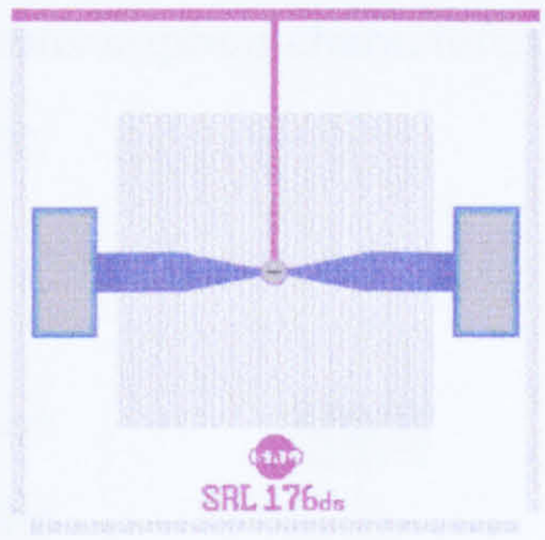

SRL 177 – The low power family

This family of devices was designed to deliver the low power consumption characteristic. The *MHR* was widened by reducing the area of the micro-heater.

SRL 177a

This device employed the reduced size ultra-low resistance micro-heater. The applied voltage is likely to be lower than the specifications. However, it is useful to obtain information in the situation when both heater size and the *MHR* have been altered.

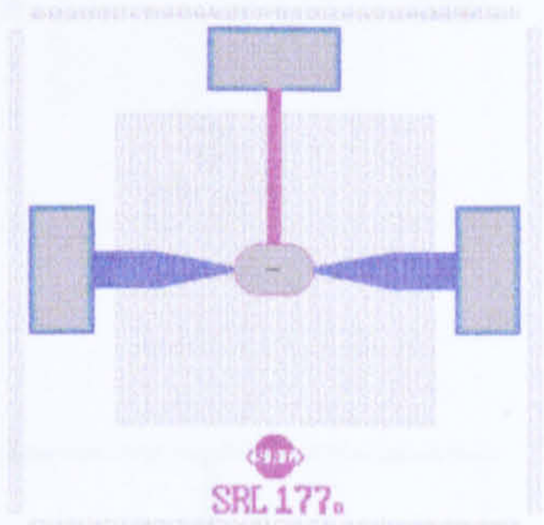

A variant is the SRL 177ax. This device excluded the gate electrode in order to allow investigation on the heater itself. The thermal profile and the stress on the membrane caused solely by the micro-heater can be studied.

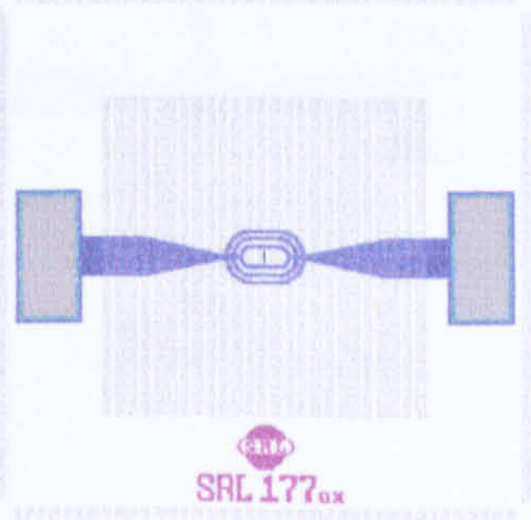

SRL 177b

The device employs the reduced size honey-comb micro-heater design. However, as the *MHR* of the device is larger, the estimated power consumption would be lower than the former SRL 162g.

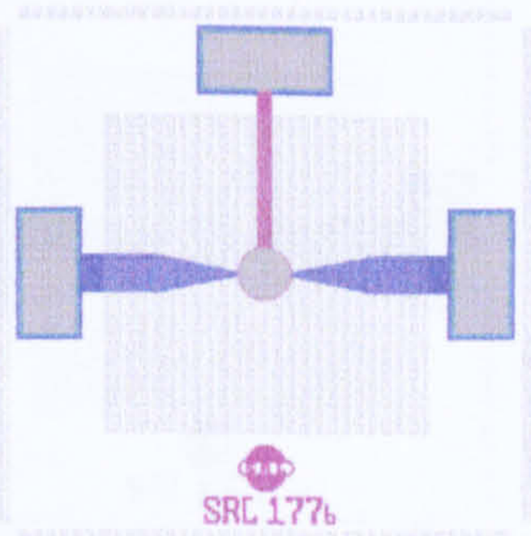

SRL 177bx is a test device which excludes the gate electrode in order to provide an opportunity to study the performance of the micro-hotplate. Information like thermal profile, thermal induced stress on the membrane can be collected. This valuable data can be used to verify the simulation results.

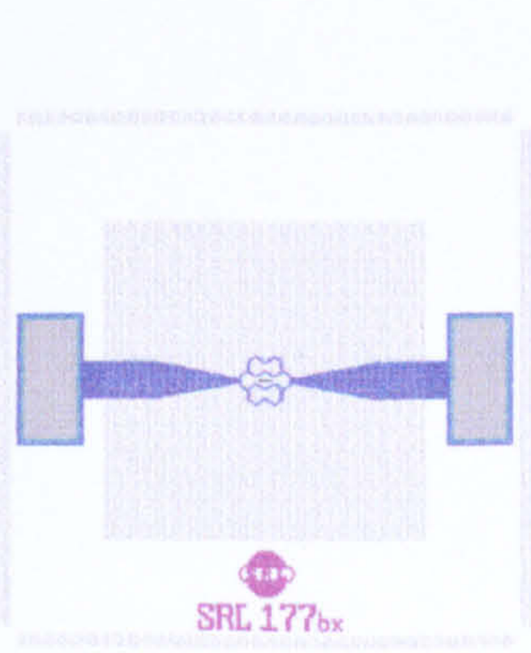

SRL 177c

The attribute for this type of design was the reduced size drive-wheel micro-heater was used. The effect of the reduced heater size can be compared with the standard device to increase our understanding of micro-heaters.

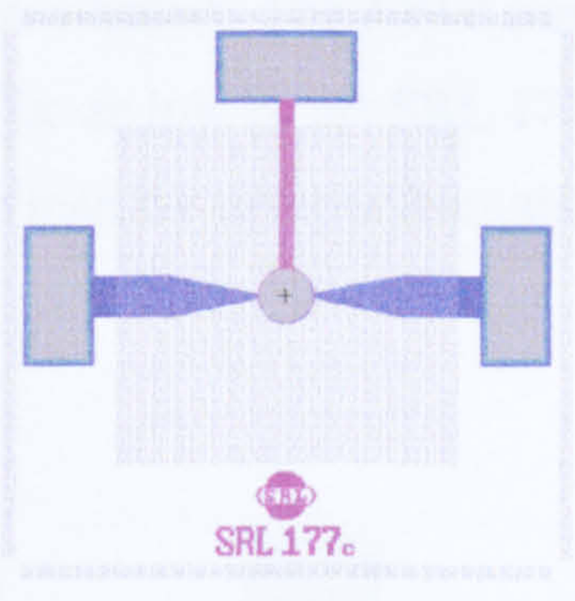

SRL 177cs is the common gate variant and the gate contact pad was replaced by the common gate connector. It links the gate electrode to all other common gate devices and is fed into the common contact pad.

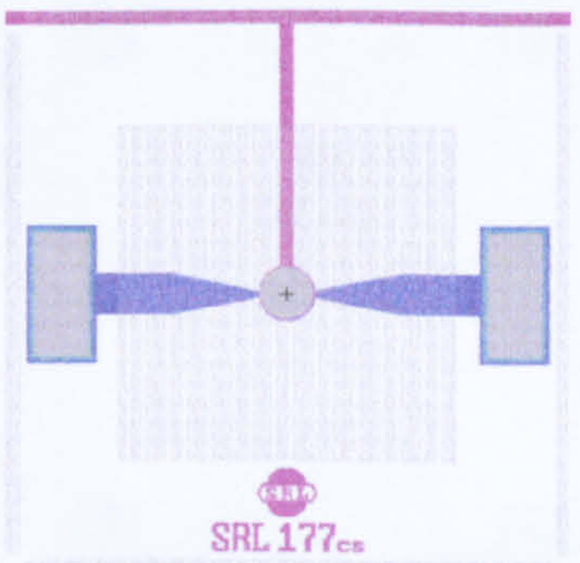

SRL 177cx is the test structure of this design. The gate electrode was removed to expose the bare micro-heater. It allows the actual thermal and stress profile of the micro-heater to be studied.

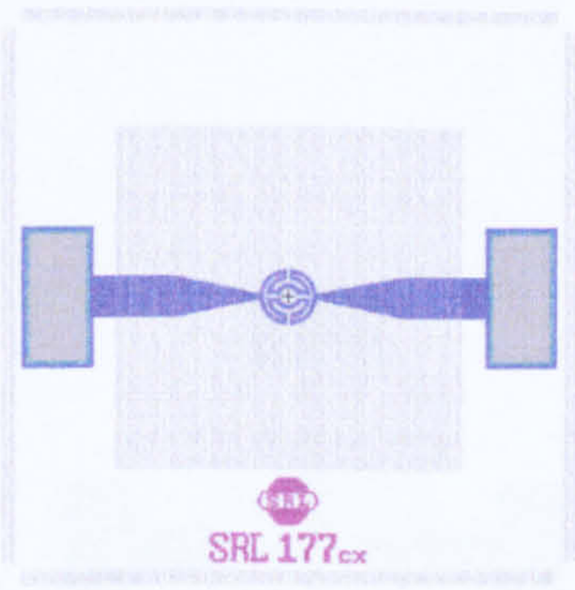

SRL 178 – The small-membrane & robust family

This family employs both the reduced size membrane and micro-heater. The *MHR* was reduced, hence, the power consumption of this family will not be as low as the SRL 177 family but the estimated power consumption would still be less than the devices from the standard family.

SRL 178a

This device employs the reduced size ultra-low resistance micro-heater; the area of the membrane was also reduced. This provides an opportunity to investigate the feasibility of further reducing the area membrane. The information will be collected and can be made use of for further development of micro-calorimeter.

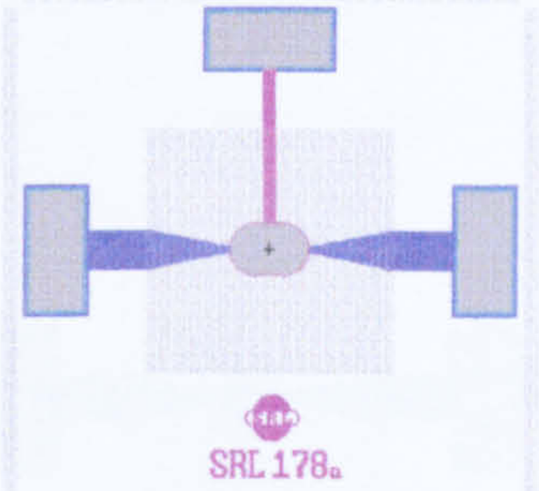

A variant of the design is the SRL 178ax. The gate electrode was removed so that the characteristic of the micro-heater can be studied.

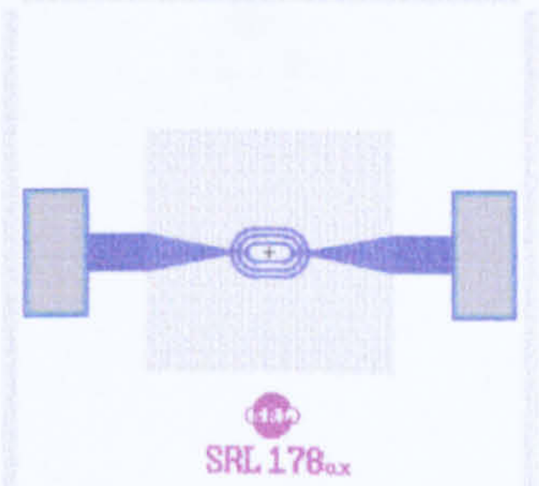

SRL 178b

This design involves the reduced size honey-comb micro-heater and the performance of the reduced size membrane and heater will be an essential information to develop further micro- calorimeter.

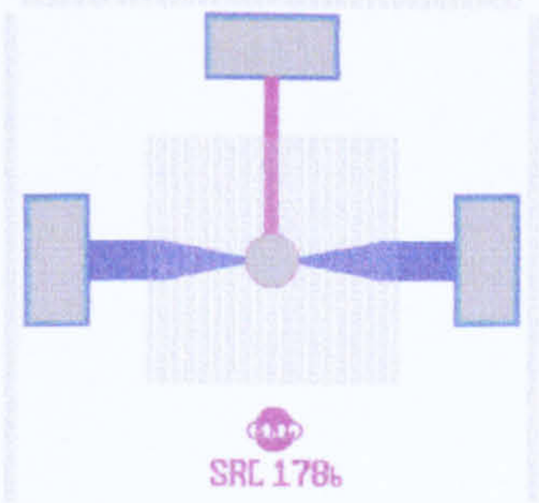

A variant of this design is the SRL 178bx. The gate electrode was excluded for the investigation of the thermal and stress profile of the device.

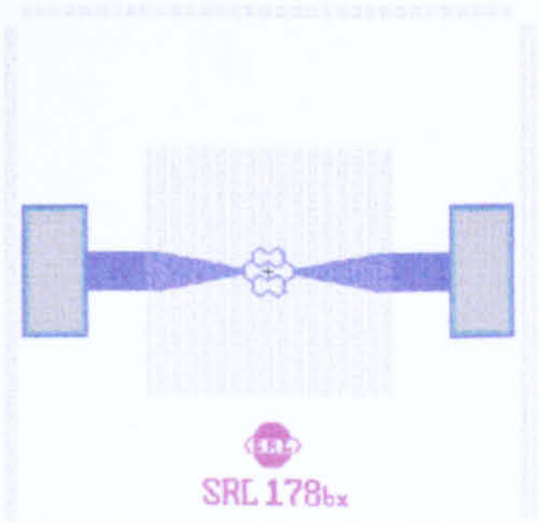

SRL 178c

This device possesses the reduced size drive-wheel micro-heater design. It is essential to understand the changes of the performance with this micro-heater design in relation with the size of the membrane.

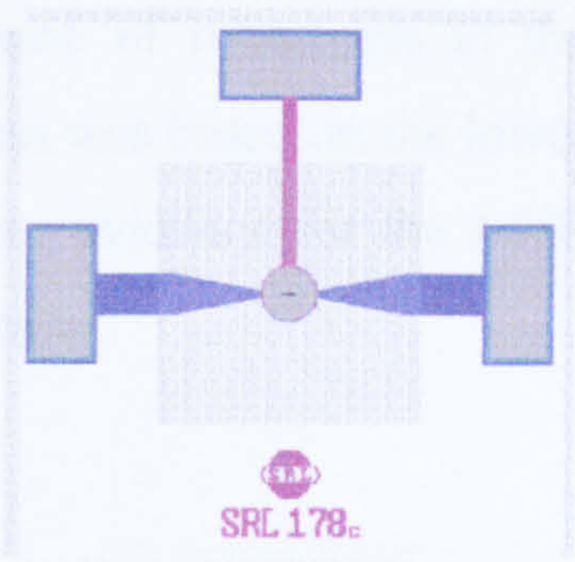

SRL 178cx is the gate-less device. It is essential to obtain the information on the thermal profile and responses of the membrane with a bare micro-heater. Such information will be valuable for future development of micro- calorimeter.

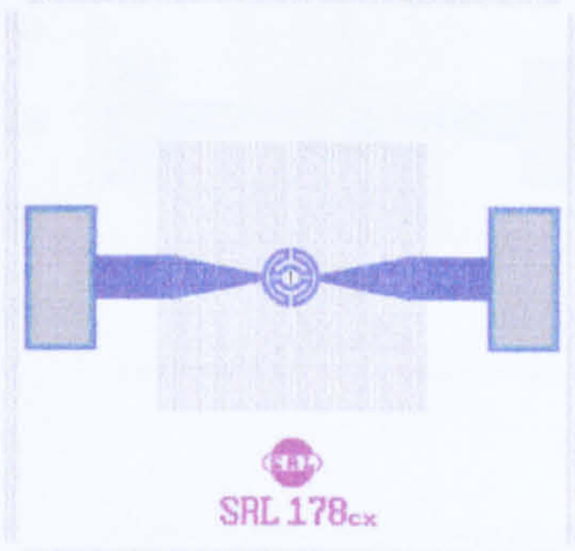

SRL 179 – The robust Family

Devices from this family should have the better characteristic of robustness at the expense of higher estimated power consumption. The robustness was based on the lower Span-to-width Ratio (*SWR*). These devices will provide further evidence for the *MHR* theory and it is critical for future development of micro-calorimeter.

SRL 179a

This device uses the standard size ultra-low resistance micro-heater but the size of the membrane was reduced in order to increase the *SWR*. As the robustness of the micro-calorimeter is an important issue for a commercial device, the device will be used to evaluate the performance apart from higher power consumption.

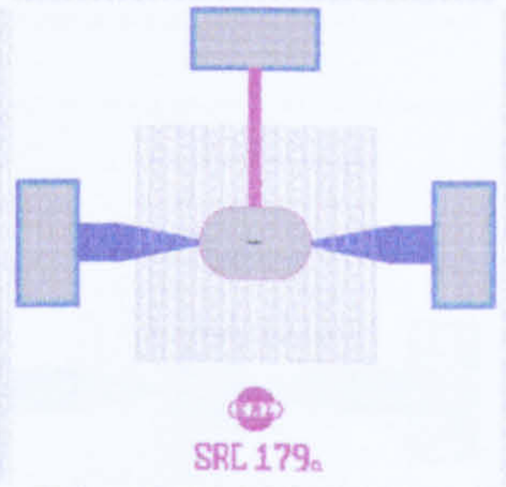

A variant of the design is the SRL 179ax and the gate electrode of the device was removed to enable the investigation on the micro-heater itself. It is an important test device to understand the characteristics of the micro-heater without the interference of the gate electrode.

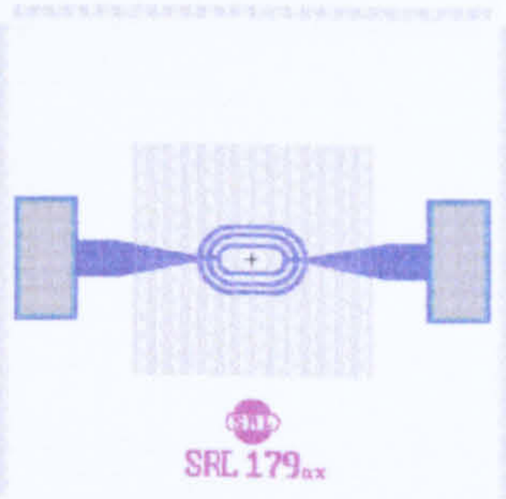

SRL 179b

This device employs the standard size honeycomb micro-heater design with the reduction of membrane in size. This device is essential to understand the characteristics of lower *SWR*. This helps to achieve the compromise with the mechanical strength and the power consumption of the device.

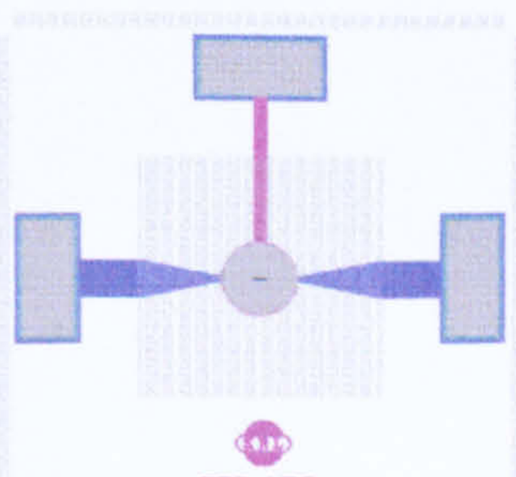

The gate exclusion variant of the design is SRL 179bx. This allows the performance of the micro-heater to be studied. This is a piece of important information as the effect of the catalyst can be isolated and investigate separately.

SRL 179c

This device employs the standard size drive-wheel micro-heater and it is important to understand the characteristics of this combination of membrane size and this type of micro-heater. Such data are essential to achieve the compromise between the robustness and the performance of the device.

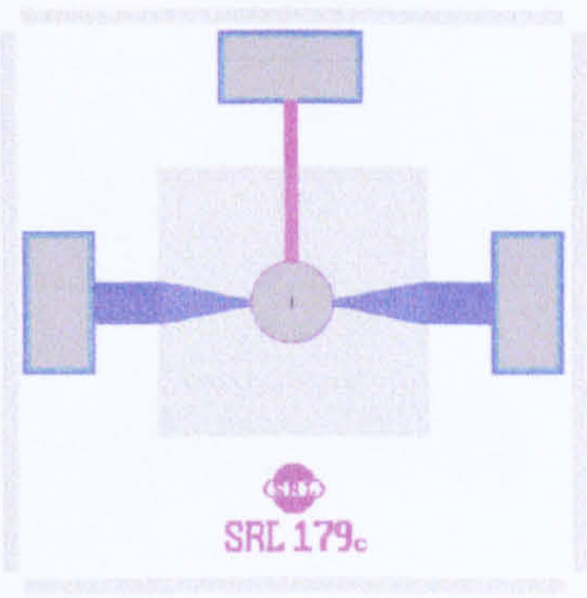

A variant of this design is the SRL 179cx which is the gate-less version. The gate electrode was removed and allows the bare micro-heater to be examined for the thermal and stress profile.

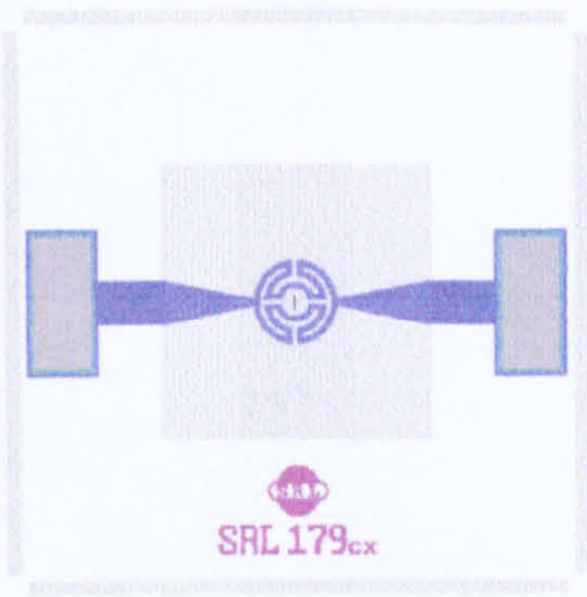

SRL 179d

This is a test device which employs the same micro-heater as in SRL 162a with the size of the membrane reduced. It provides a direct comparison for the changes that had been made in the new designs of micro-calorimeter. The device will prove the theory about the *MHR* and assist in the development of future development of micro-calorimeters.

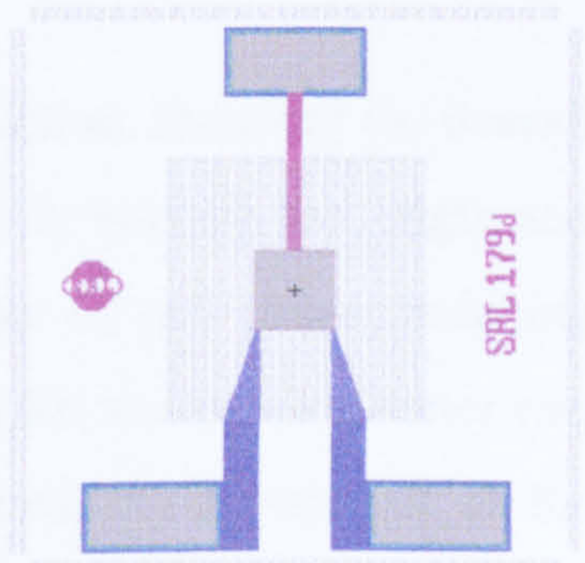

The only variant of this design is the SRL 179dx which is the gate-less version. This allows the effect of the catalyst to be isolated from the performance of the micro-hotplate. So that the characteristics of the bare micro-heater can be understood. This information can be compared against the simulation results for future development of micro-calorimeters.

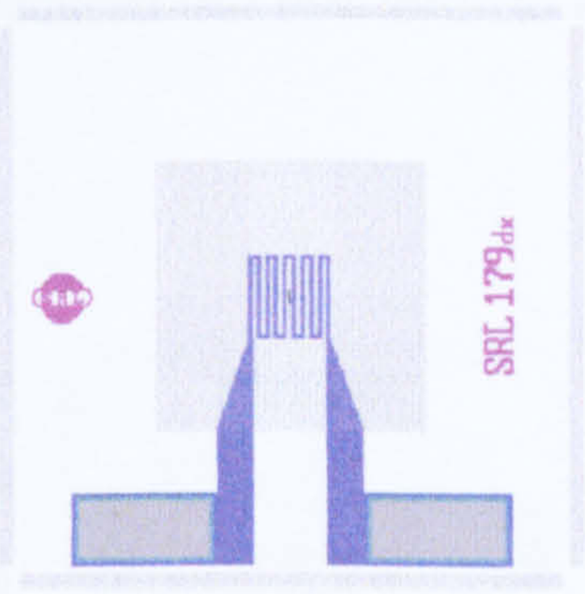

SRL 179e

This is a test structure which employed the some micro-heater as the SRL 136a and the size of the membrane was reduced. This provides another direct comparison for all the changes made.

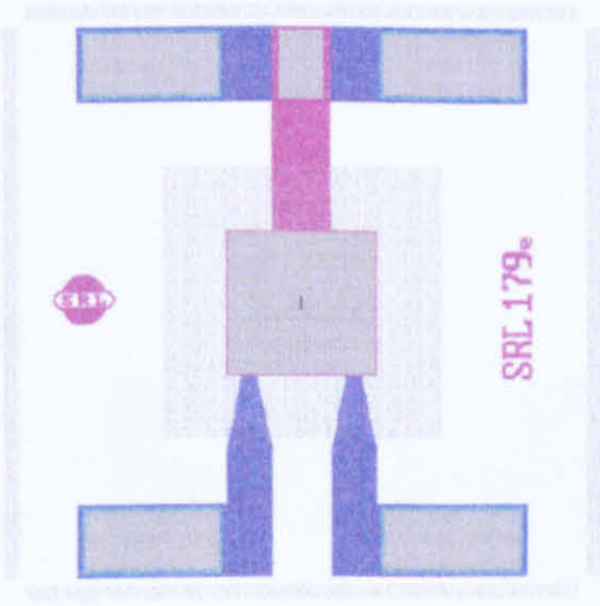

The only variant of this design is the SRL 179ex which is the gate-less version. This allows the isolation of the catalyst and the gate electrode which may cause complication to the investigation to the actual performance of the micro-hotplate. The data of micro-hotplate will be used in simulation and further study of the micro-pellistor designs.

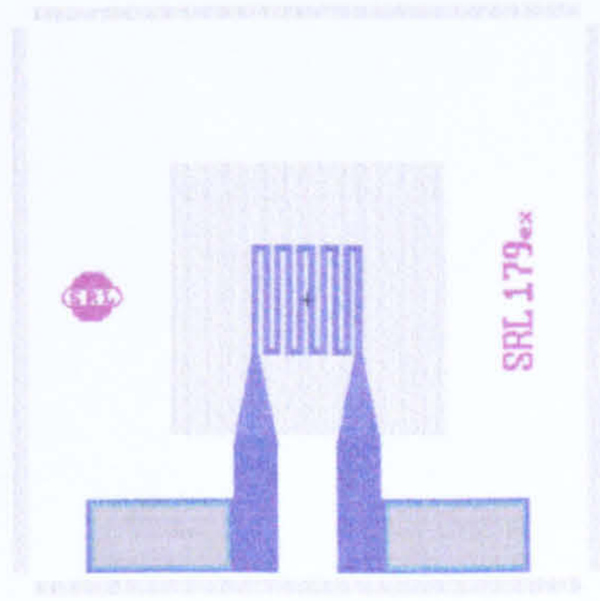

SRL 180 – The ultra small & robust family

As part of the research goal is about reducing the cost of production, reducing the overall area of the micro-calorimeter will carry this objective further. By halving the length and width of the 4 mm by 4 mm die will result in only a quarter of cell space; reducing production costs by 75%. Therefore, a batch of 2 mm by 2 mm die micro-calorimeter was designed. As the Span-to-width Ratio (*SWR*) has been reduced, the robustness of the device is expected to be higher. Though this batch of designs, the manufacturing difficulties and process variation can be assessed. Since the membrane had been decreased together with the overall geometry, the *MHR* was reduced and that leads to a higher estimated power consumption.

SRL 180a

This device employs the reduced size ultra-low resistance micro-heater. Similar to the other design using the ultra-low resistance micro-heater, the applied voltage will be lower than the specification. The purpose of this device is to examine the performance of the device and compare it with the SRL 177a which uses the same micro-heater. Therefore, the feasibility of reducing the overall die size can be investigated.

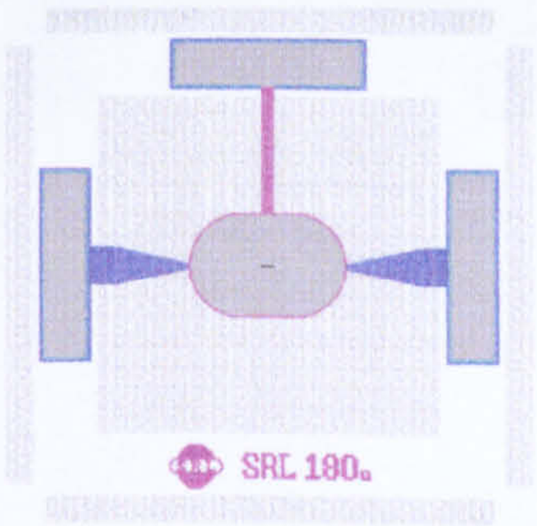

The variant of this design is the SRL 180ax. As the information about the micro-hotplate is equally important when developing future generation micro-calorimeter, this gate-excluded version is suitable for such purpose.

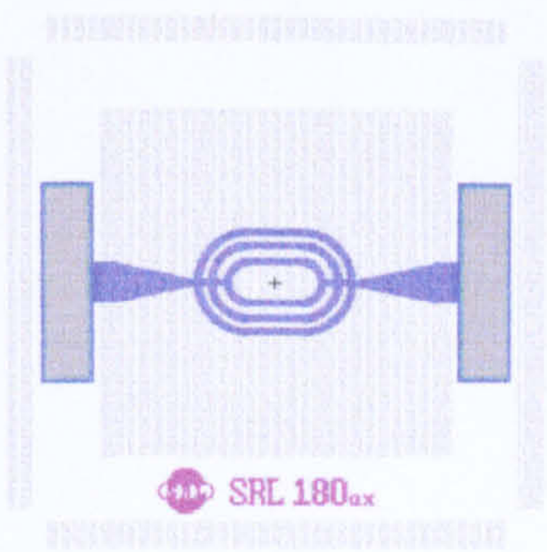

SRL 180b

This type of device employs the reduced size honeycomb micro-heater. With the same micro-heater as the SRL 177b, the performance will be examined and compared. Therefore, the potential of the size reduction can be investigated further.

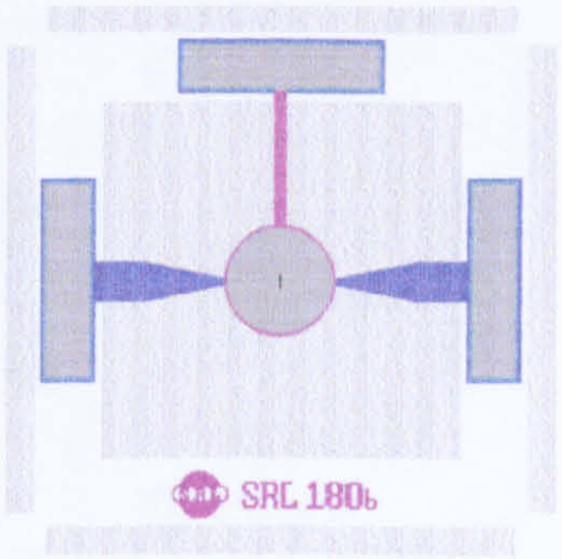

The gate-less version is the SRL 180bx. This test structure is used to enhance the understanding of the characteristics about the micro-heater and it is essential for future development of micro-calorimeter.

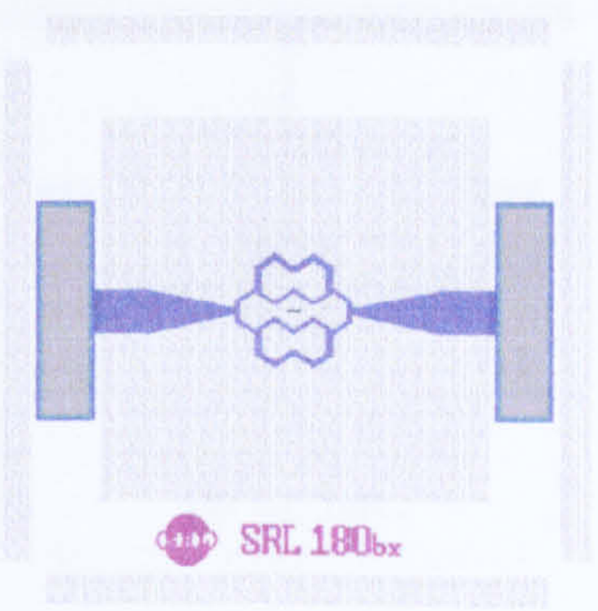

SRL 180c

This device employed the reduced size drive-wheel micro-heater design. As the SRL 177c uses an identical micro-heater design, SRL 180c will be used to evaluate the changes of the overall geometry in relation to the device performance. Moreover, it proves the potential of the overall die size reduction which should lead to lower production cost.

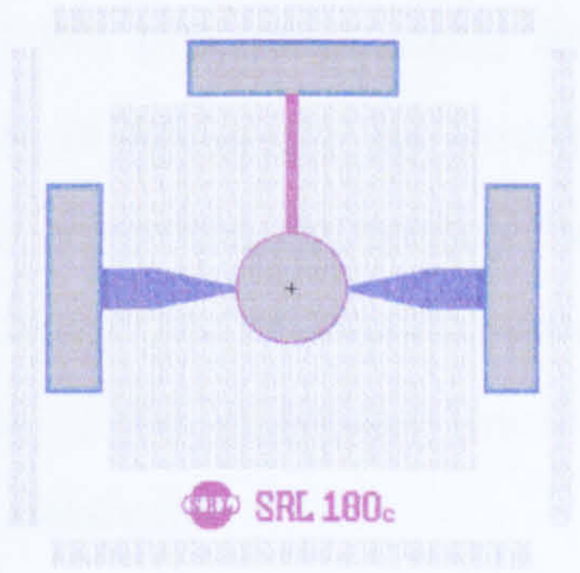

The common gate variant of this design is the SRL 180cs. The gate connection pad is replaced by the common gate connector which links the rest of the common gate devices on the reserved segment on the wafer. All the common gate connection is fed into the common gate contact pad on the edge of the wafer. Therefore, the potential for common gate deposition of catalyst can be evaluated.

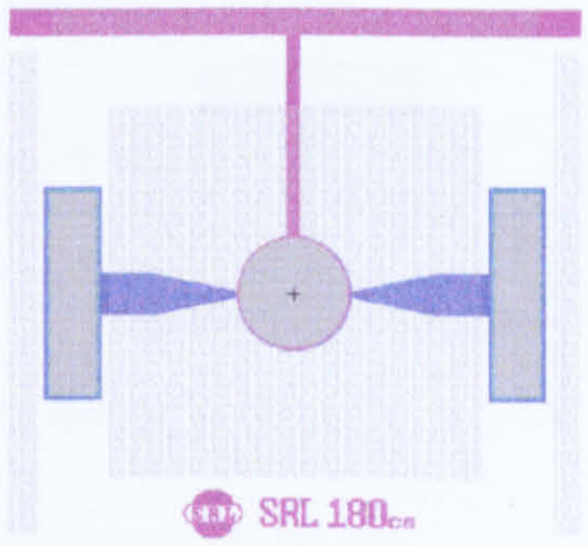

Another variant of the device is SRL 180cx which is the gate excluded version. The performance of this drive-wheel micro-heater on a smaller die is essential for the research on further reduction of the overall geometry.

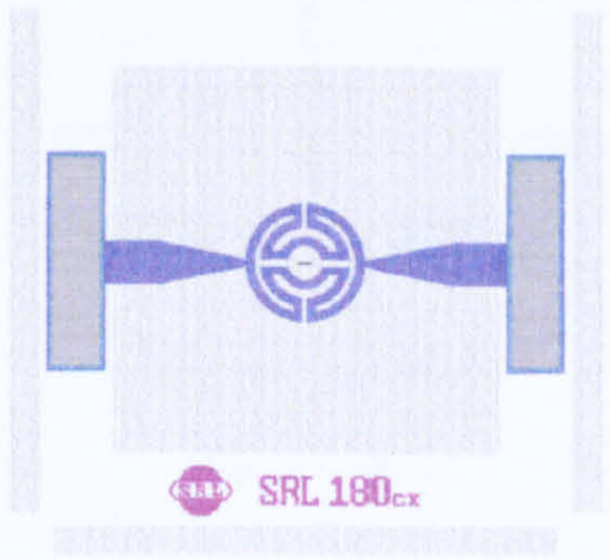

SRL 181 – The ultra small & low power family

Apart from exploring the overall die size which will affect the production cost, the minimum size of the micro-heater was another critical factor in designing the micro-pellistor and minimising the power consumption. This family of devices comprised the ultra-small micro-heater so as to enlarge the *MHR* and lead to lower power consumption. In addition, this family of device will assist the investigation of the minimum micro-heater size in order to achieve the required sensitivity from the catalyst.

SRL 181a

This device employs the miniature ultra-low resistance micro-heater design. The main purpose was to examine the difference in terms of performance compare with the larger devices. Furthermore, the life expectancy of the device was another essential area to look at since the heater track width had been reduce significantly. All these data will contribute to the development of future micro-calorimeter designs.

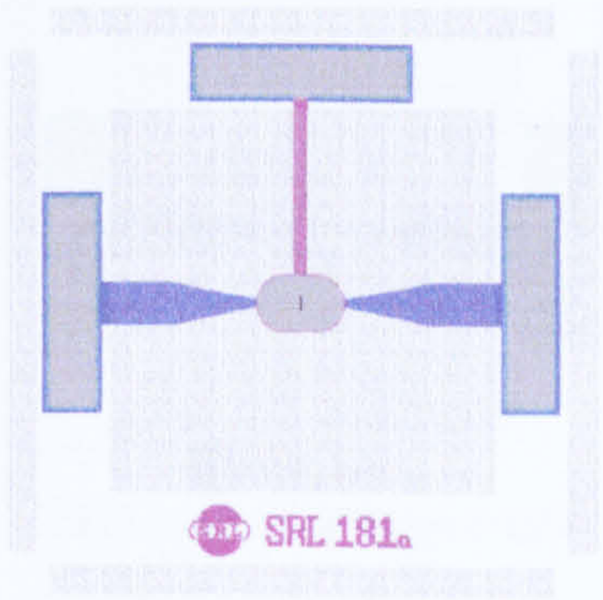

SRL 181as is the common gate version of this design and the main purpose is to explore the potential of the common gate deposition of the catalytic material with reduced active area.

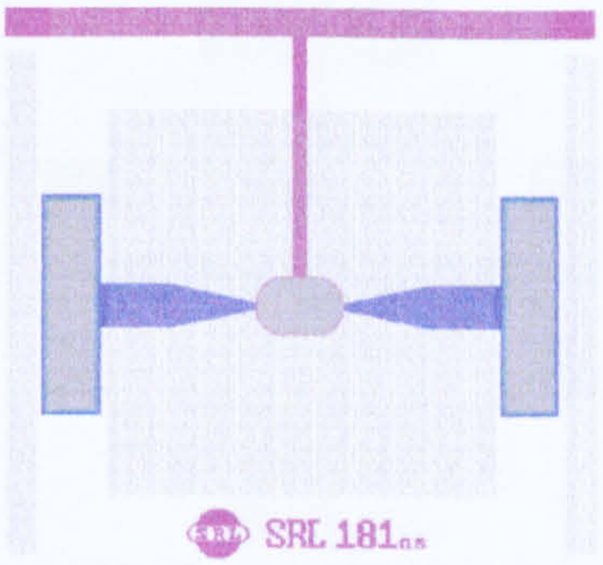

The gate-less version of this design is the SRL 181ax. The actual performance of the micro-heater should not be neglected. It will provide essential information for further development of ultra-small micro-heaters in the future.

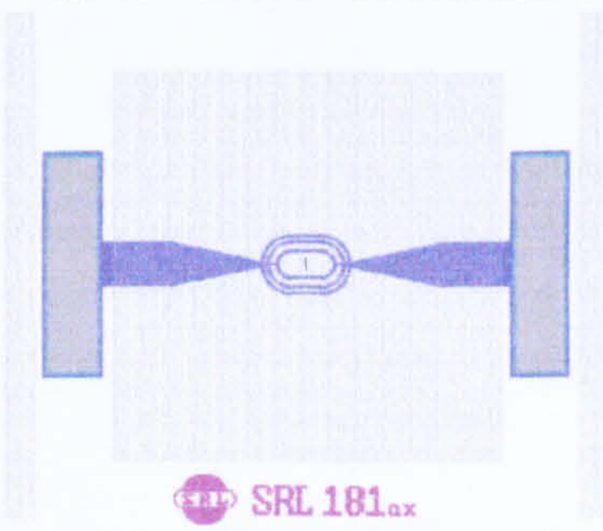

SRL 181b

This device employs the ultra-small honeycomb micro-heater design. This will provide the data required to investigate the performance as well as the life expectancy of the device. Comparing such data with the larger device, the potential of the die size reduction can be evaluated.

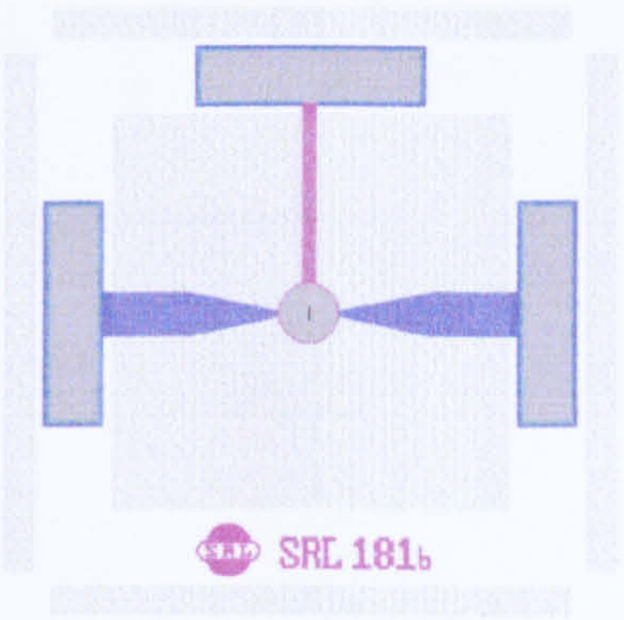

A variant of this design is the SRL 181bx where the gate electrode was excluded. Similar with the rest of gate-less devices, the information collected from it will be used for future development.

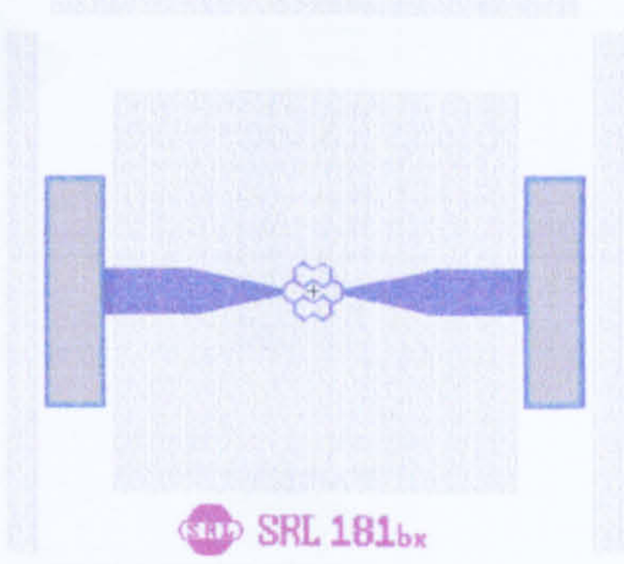

SRL 181c

This device employs the ultra-small drive-wheel micro-heater design. This device will provide additional data on how small the micro-heater can be made. At the same time, the sensitivity of the device can also be examined as the amount of catalyst and the active areas are significantly smaller than all the previous fabricated micro-calorimeters.

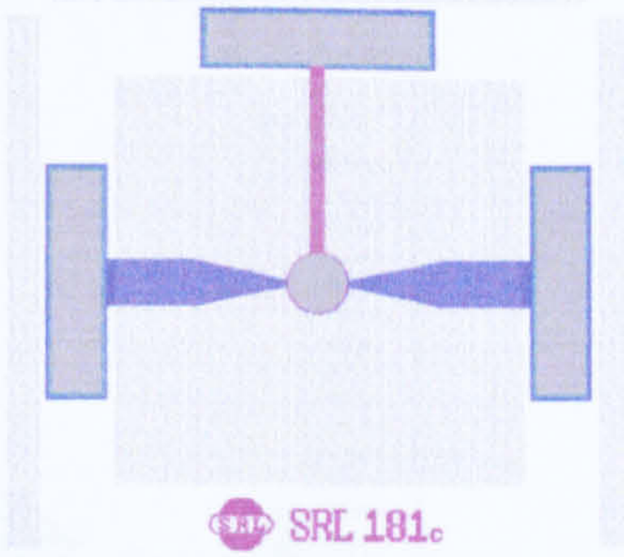

The SRL 181cx is the gate-less variant for this design. Along with the rest of gate-less devices, it will provide the thermal and stress profile of the micro-hotplate itself. Such information is useful for both simulation and future design of micro-calorimeters.

Appendix 2b

The SOLIDIS 3D simulation results

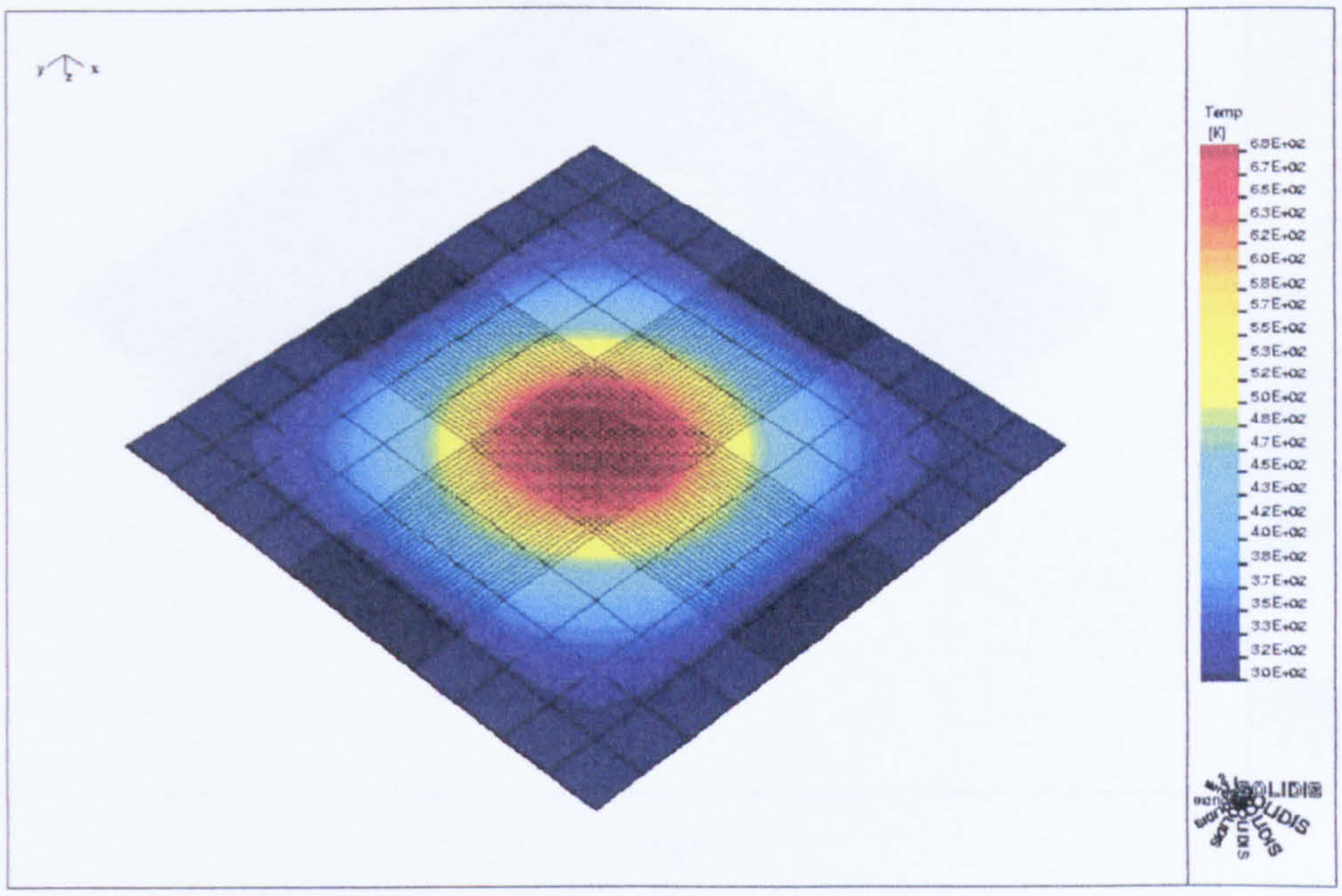

(a)

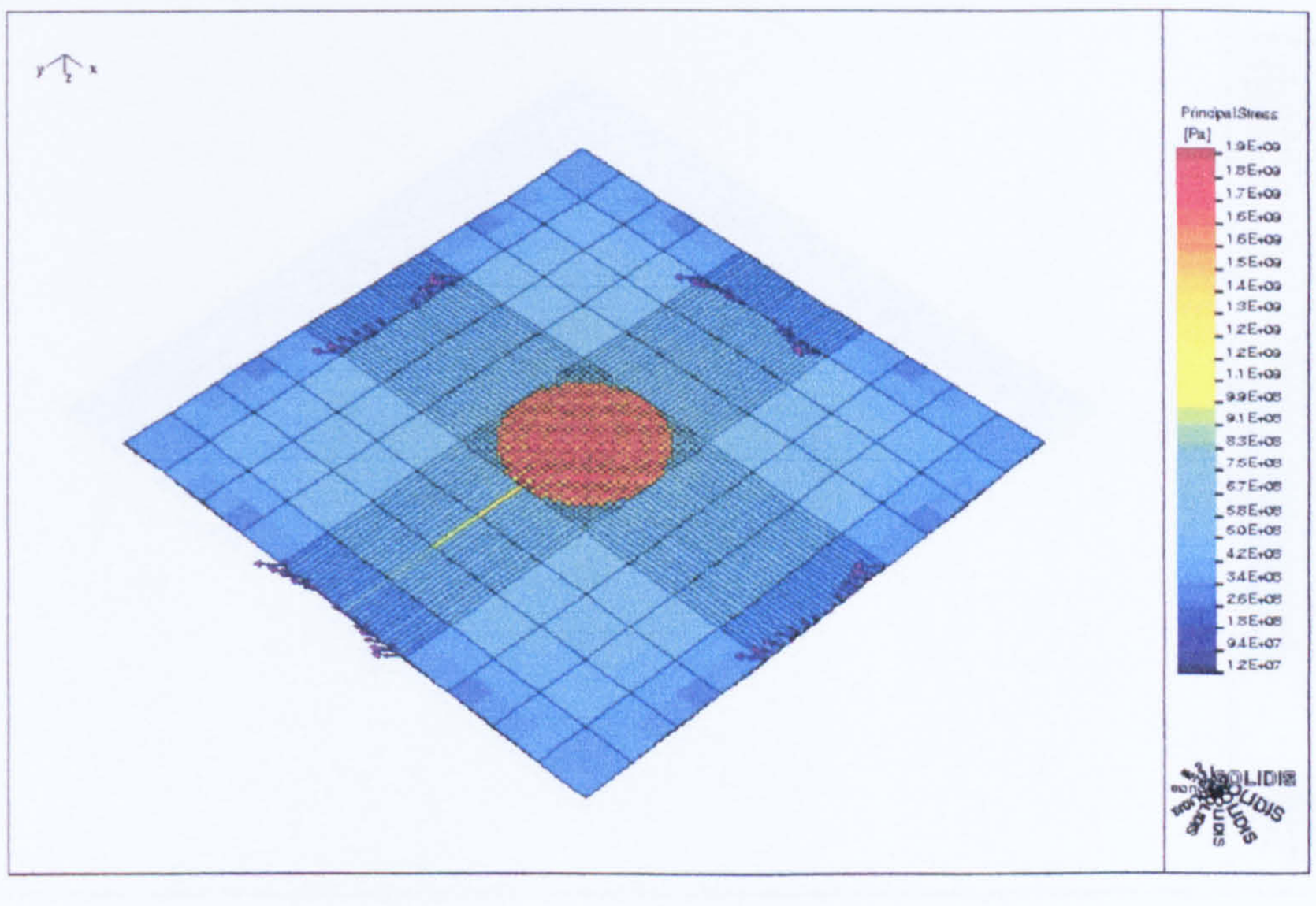

(b)

Simulation results for SRL 178c (a) The temperature profile at 100 mW. (b) The thermally induced stress.

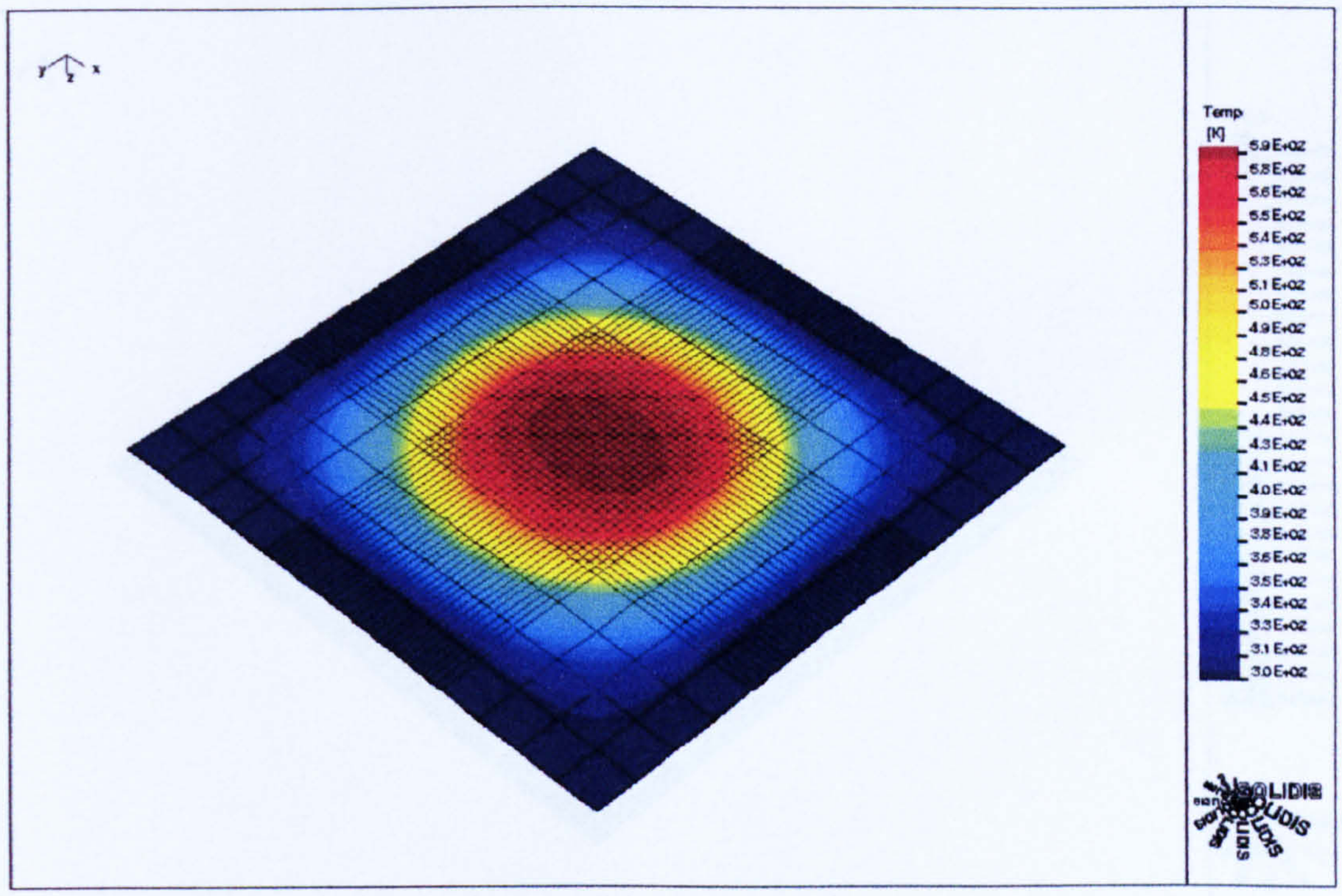

(a)

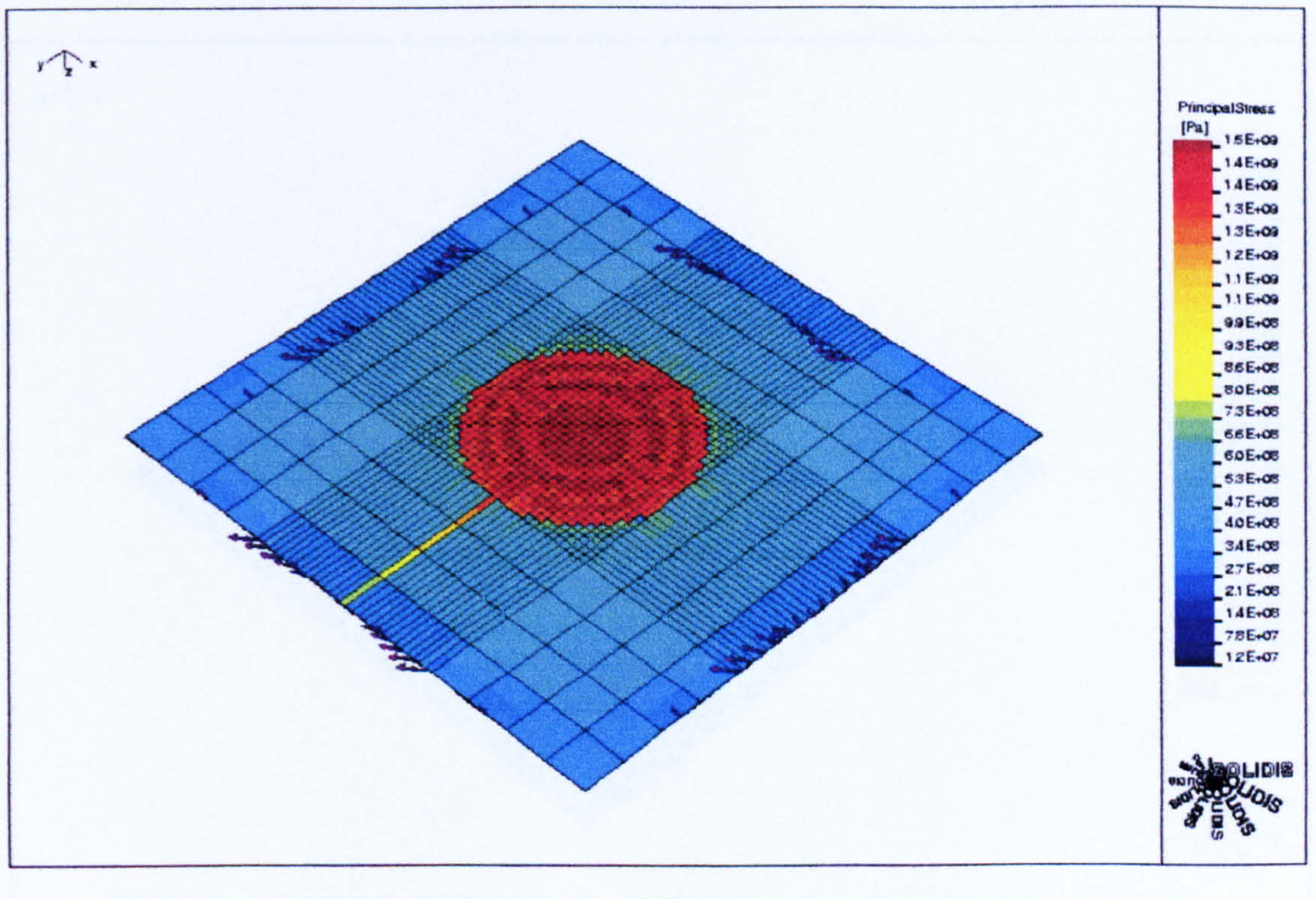

(b)

Simulation results for SRL 179c (a) The temperature profile at 100 mW. (b) The thermally induced stress.

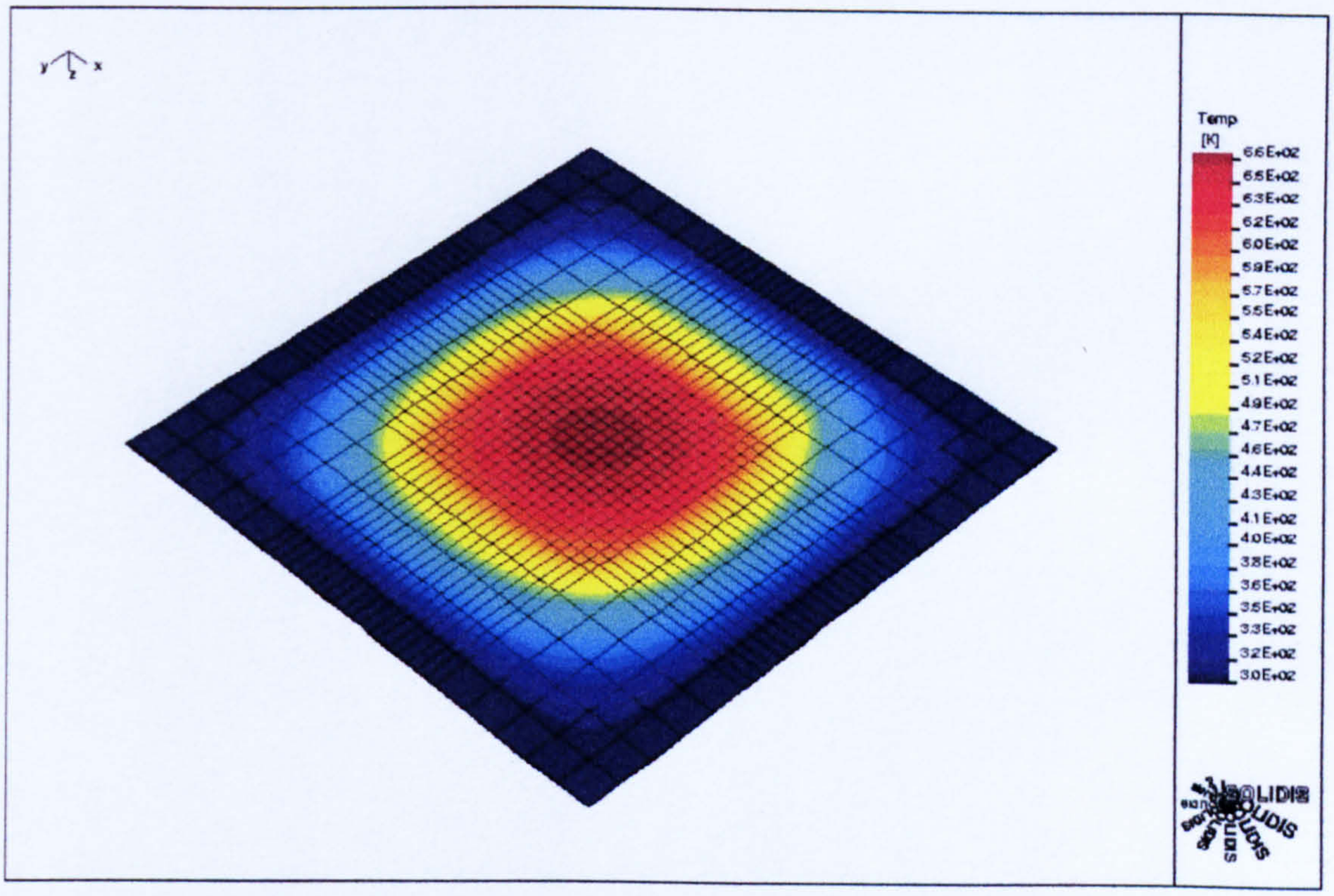

(a)

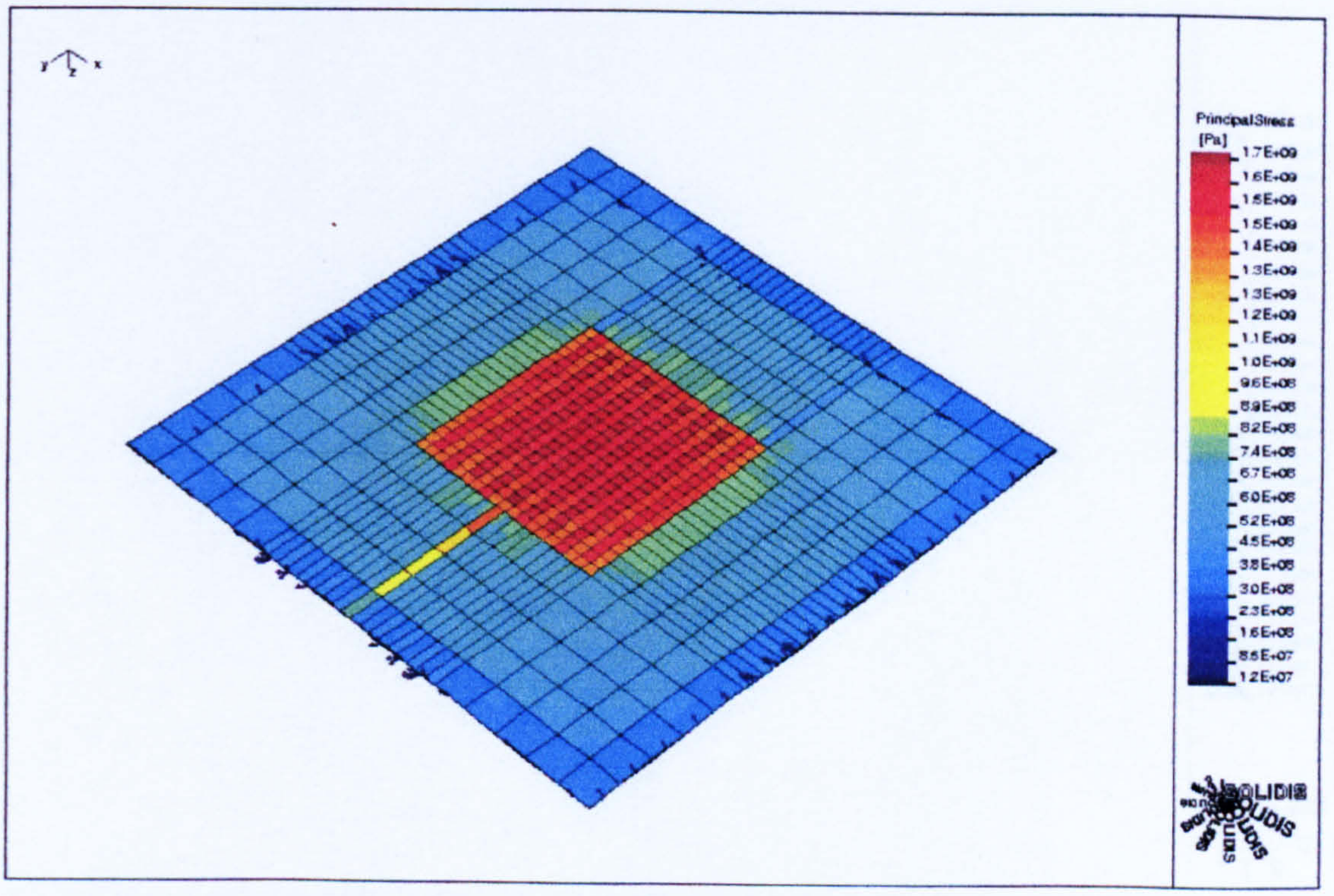

(b)

Simulation results for SRL 179d (a) The temperature profile at 100 mW. (b) The thermally induced stress.

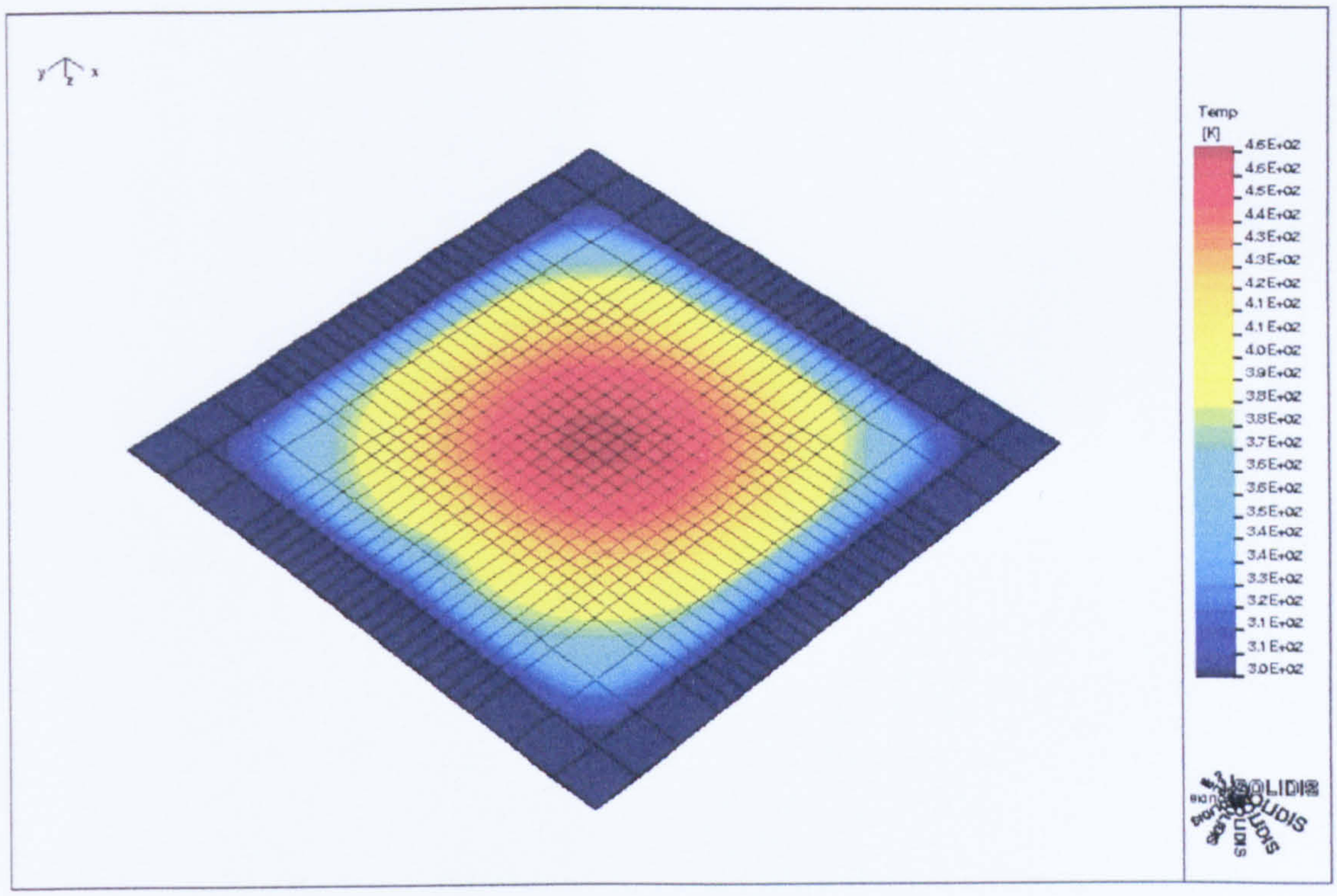

(a)

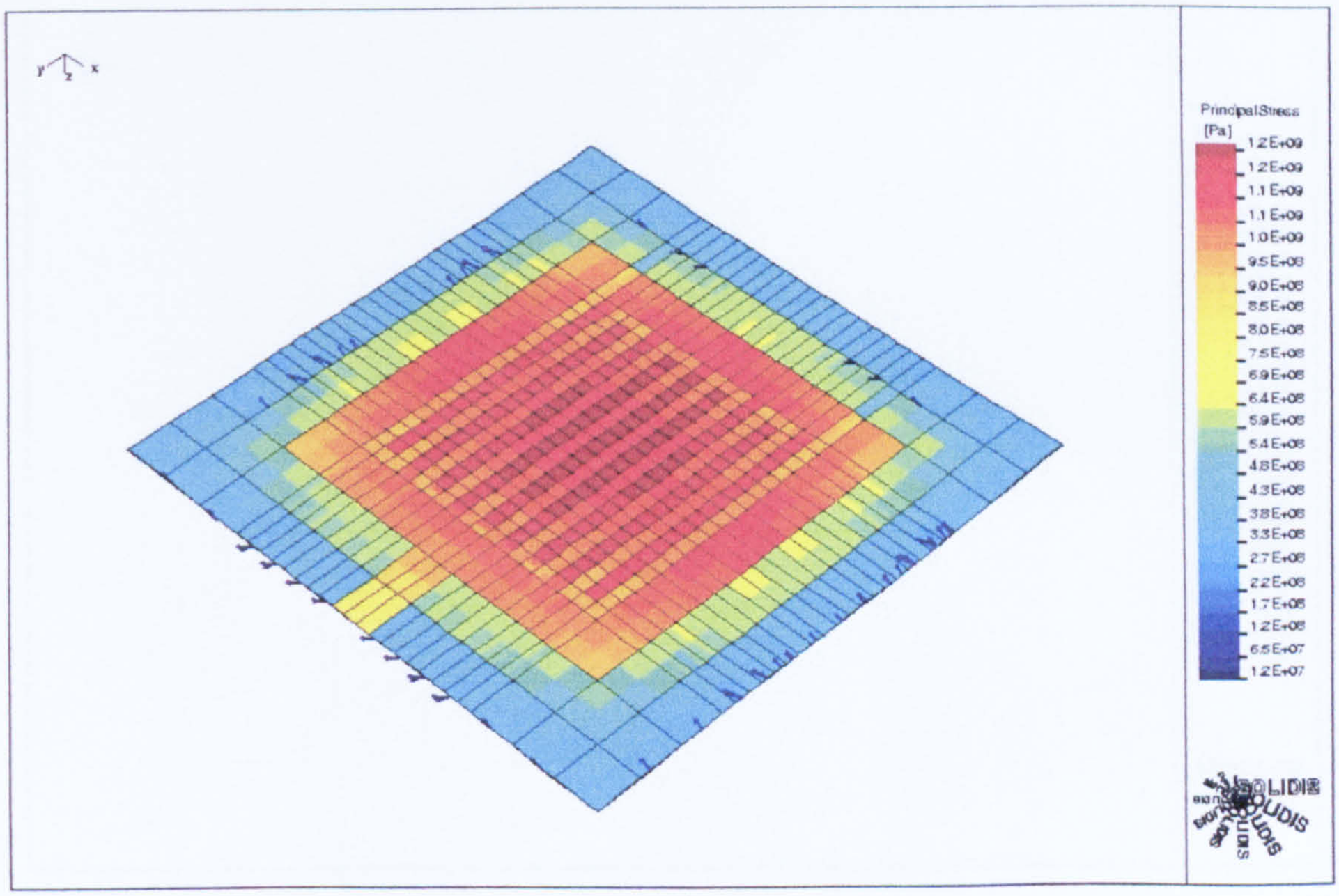

(b)

Simulation results for SRL 179e (a) The temperature profile at 100 mW. (b) The thermally induced stress.

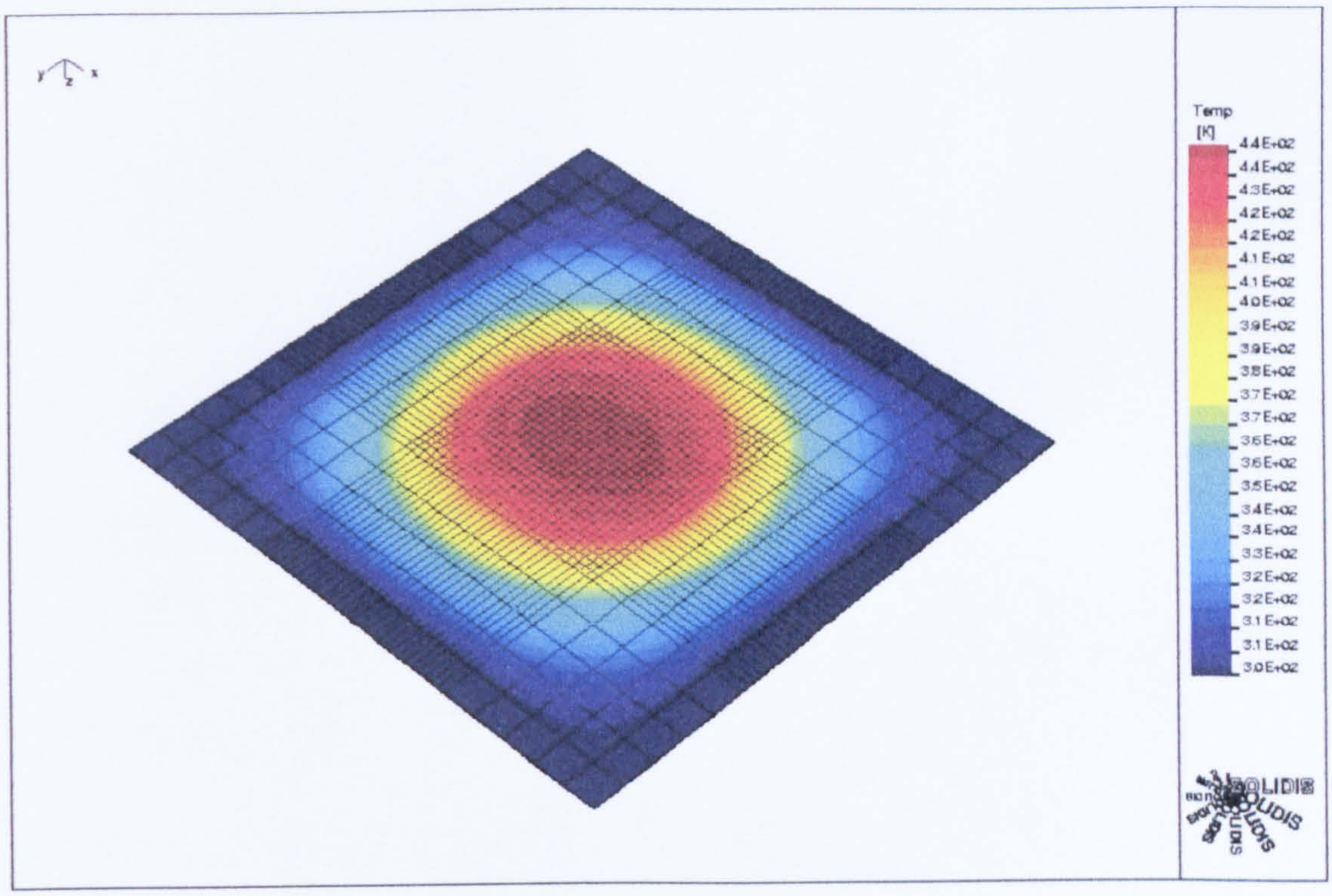

(a)

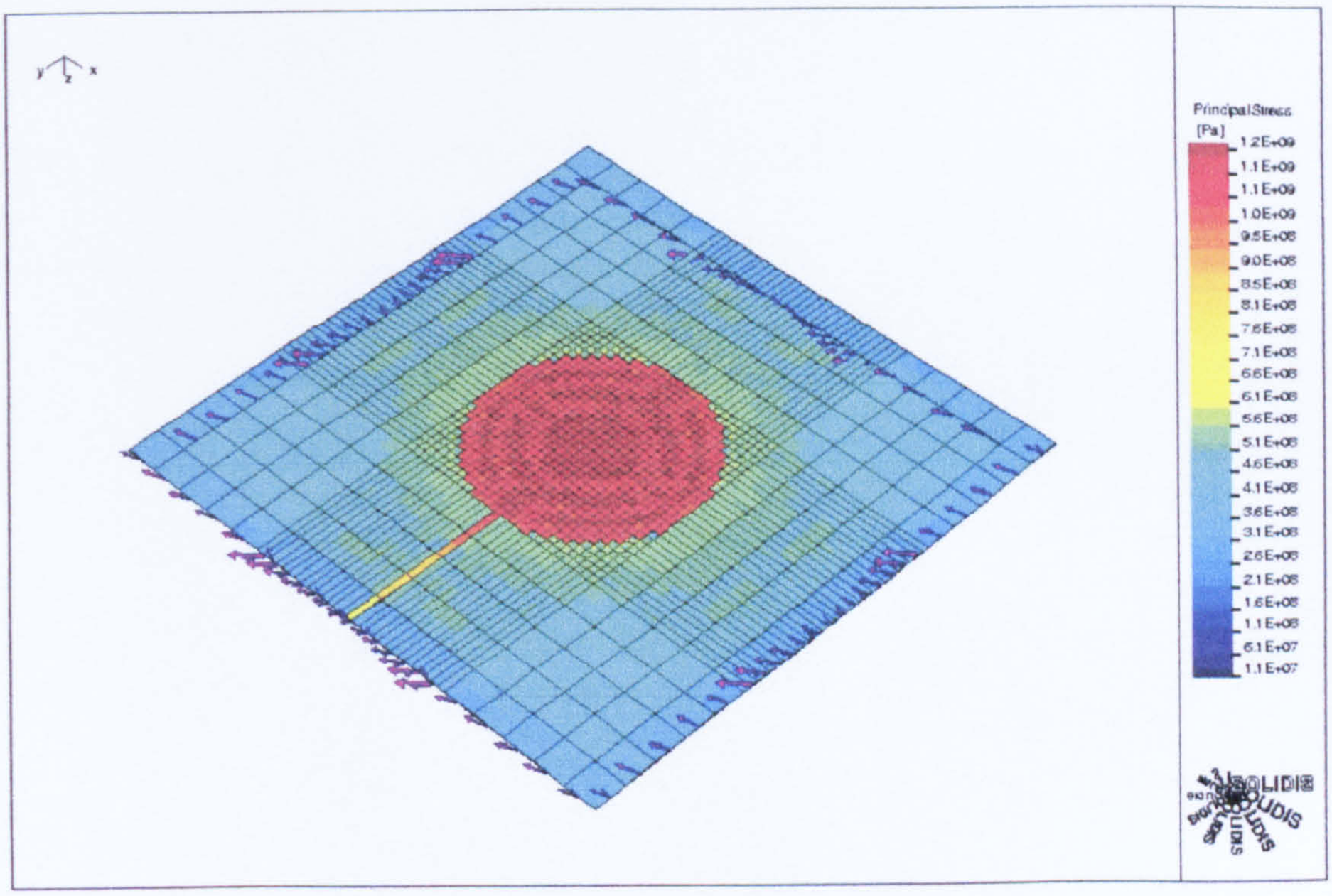

(b)

Simulation results for SRL 180c (a) The temperature profile at 100 mW. (b) The thermally induced stress.

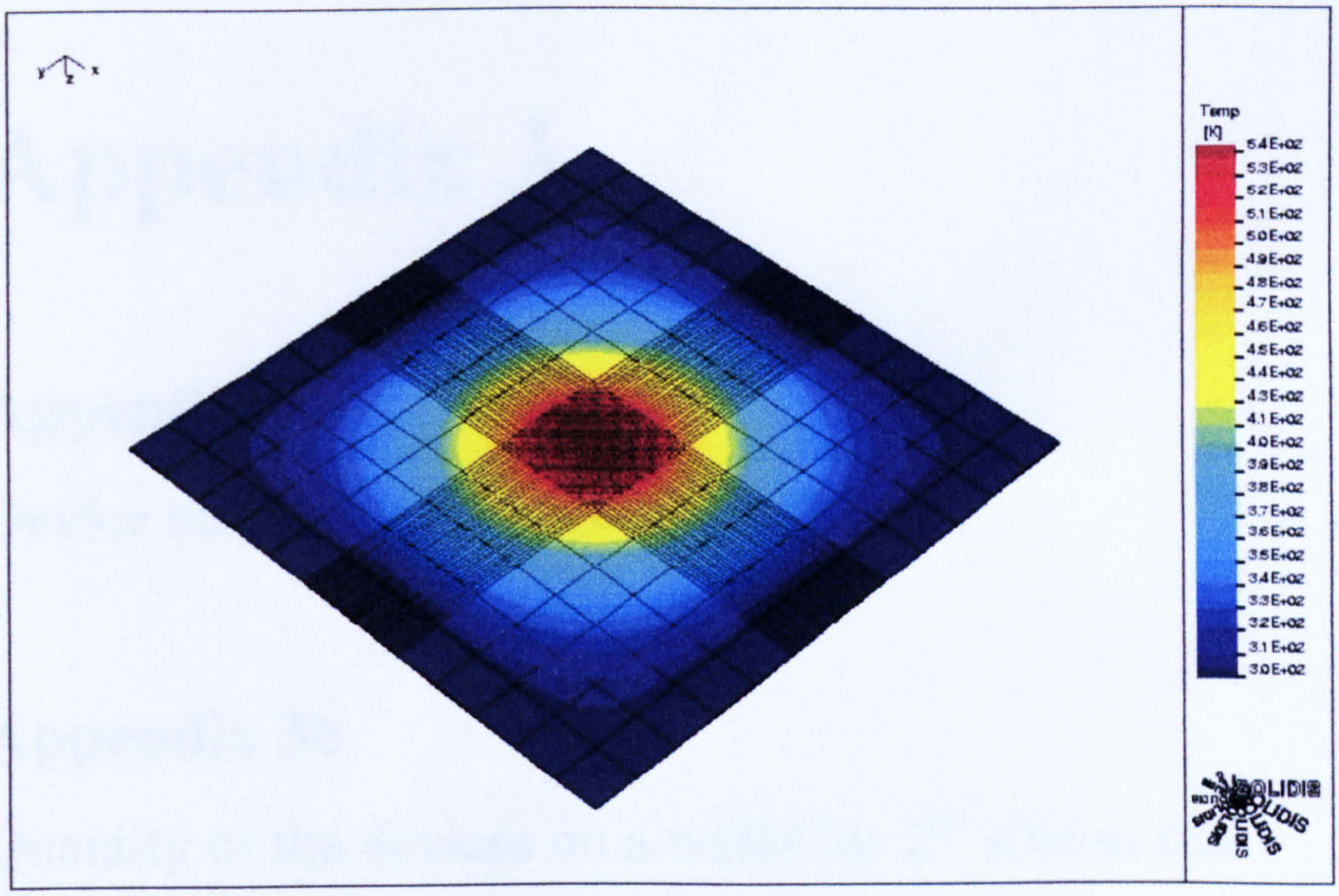

(a)

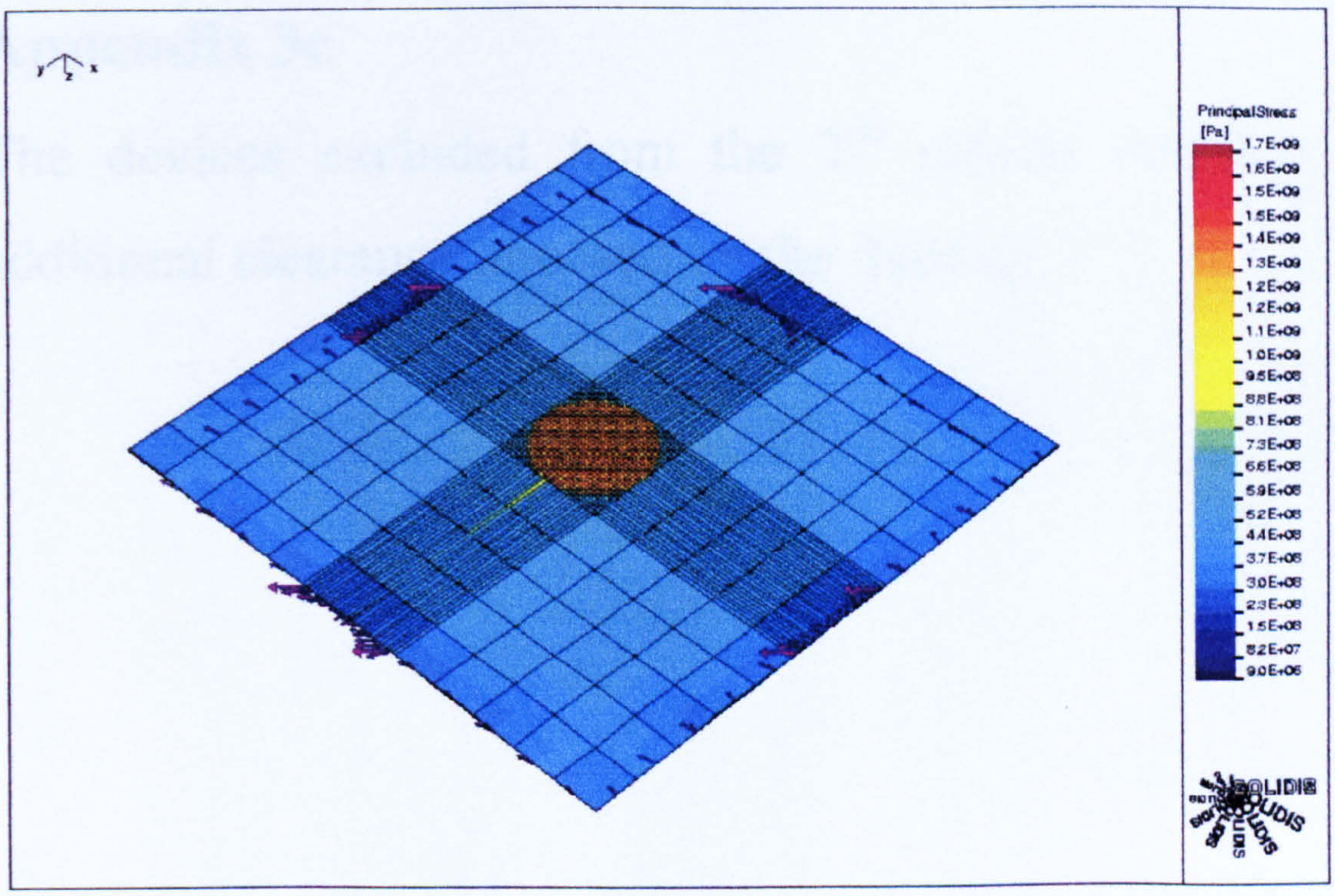

(b)

Simulation results for SRL 181c (a) The temperature profile at 100 mW. (b) The thermally induced stress.

Appendix 3

Appendix 3a

Device mapping of the second silicon run

Appendix 3b

Quantity of the devices on a wafer for 2nd silicon run

Appendix 3c

The devices excluded from the 2nd silicon run due to additional clearance imposed by the foundry

Appendix 3a: Device mapping for the second wafer run

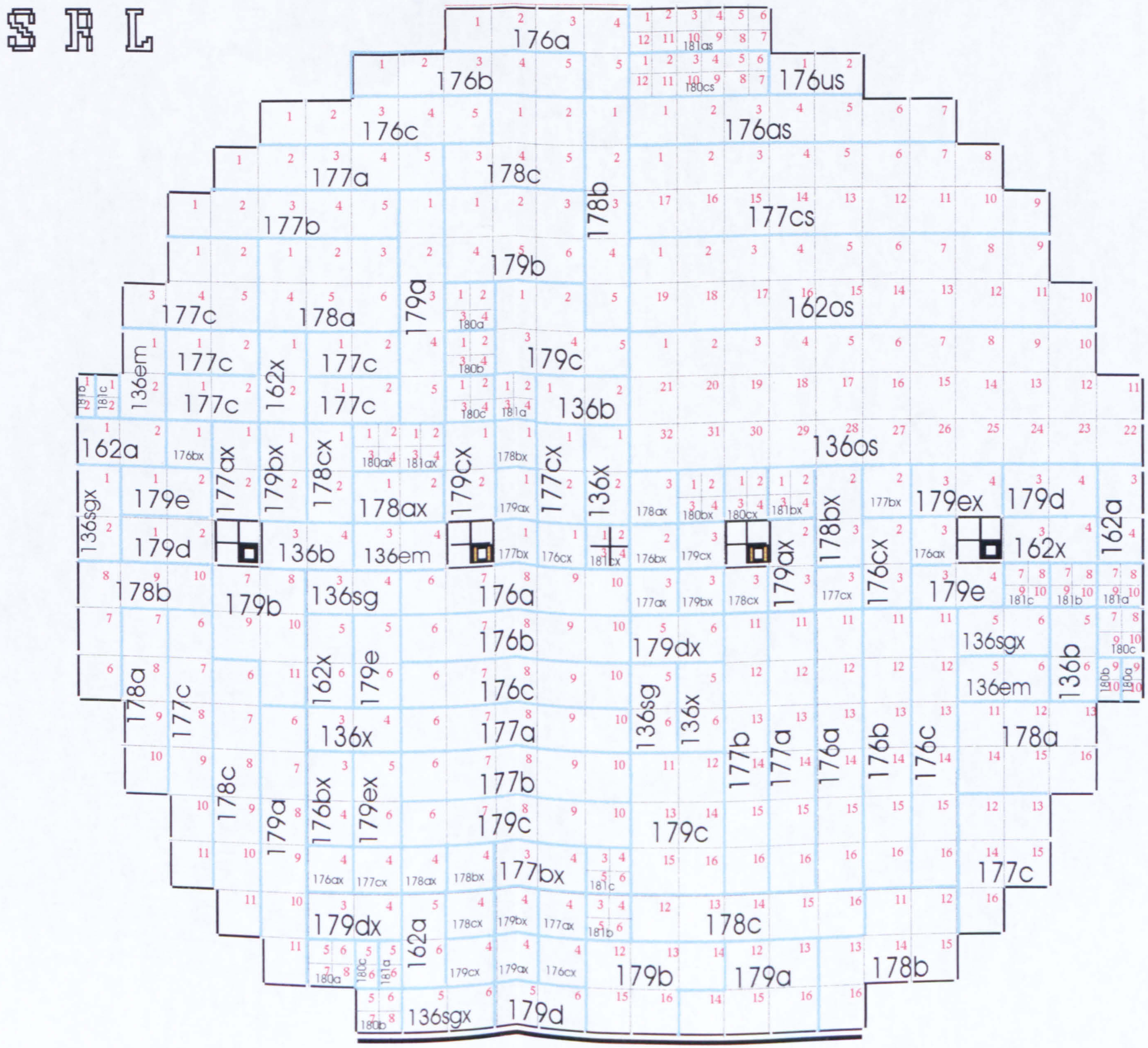

Appendix 3b

Quantity of the devices on a wafer for 2nd silicon run

Number of micro-calorimeter designs per Wafer													
	Individual Gate		Common Gate					Single Test Structures					
No.	*16 each*	*10 each*	*32 each*	*28 each*	*8 each*	*7 each*	*12 each*	*6 each*	*4 each*	*4 each*	*2 each*		
1	SRL 176a	SRL 180a	SRL 136os	SRL 162os	SRL 177cs	SRL 176as	SRL 180cs	SRL 136o	SRL 176ax	SRL 180ax	SRL 176us		
2	SRL 176b	SRL 180b					SRL 181as	SRL 136em	SRL 176bx	SRL 180bx			
3	SRL 176c	SRL 180c						SRL 136sg	SRL 176cx	SRL 180cx			
4	SRL 177a	SRL 181a						SRL 136sgx	SRL 177ax	SRL 181ax			
5	SRL 177b	SRL 181b						SRL 136x	SRL 177bx	SRL 181bx			
6	SRL 177c	SRL 181c						SRL 162o	SRL 177cx	SRL 181cx			
7	SRL 178a							SRL 162x	SRL 178ax				
8	SRL 178b							SRL 179d	SRL 178bx				
9	SRL 178c							SRL 179dx	SRL 178cx				
10	SRL 179a							SRL 179e	SRL 179ax				
11	SRL 179b							SRL 179ex	SRL 179bx				
12	SRL 179c								SRL 179cx				
Number of Devices	192	60	32	28	8	7	24	66	48	24	2	Total number of Devices	491
Number of (4x4)mm² Cells	192	15	32	28	8	7	6	66	48	6	2	Total number of Cells	410

Appendix 3c

The devices excluded from the 2nd silicon run due to additional clearance imposed by the foundry

Device Family	Device locator	Amount after modification	Original Amount
136os	10, 11, 22	29	32
136sgx	1, 2, 5, 6	2	6
162o	1, 3, 4, 6	2	6
162os	9, 10	26	28
176as	6, 7	5	7
176cx	4	3	4
176a	1, 2, 3, 4	12	16
176b	1, 2	14	16
176c	1, 2	14	16
177a	1, 2	14	16
177b	1, 2	14	16
177c	1, 3, 11, 15, 16	11	16
177cs	7, 8, 9, 10	4	8
178a	9, 10, 13, 16	12	16
178b	6, 7, 8, 13, 14, 15, 16	9	16
178c	11	15	16
179a	11, 12, 13, 14, 15, 16	10	16
179ax	4	3	4
179cx	4	3	4
179b	12, 13, 14, 15, 16	11	16
179d	5, 6	4	6
180a	5, 6, 7, 8, 9, 10	4	10
180b	5, 6, 7, 8	6	10
180c	5, 6, 8, 10	6	10
181a	5, 6, 8, 10	6	10
181as	1, 2, 3, 4, 5, 6	6	12
181b	1, 2	8	10
181c	1, 2	8	10
		Total: 92	

Appendix 4

Appendix 4a

Analysis of the potentiometer value for the micro-calorimeter interface circuit

Appendix 4b

Details of the micro-calorimeter interface circuit board

Appendix 4a

Analysis of the potentiometer value for the micro-calorimeter interface circuit

$$R_L = \frac{1}{\frac{1}{R} + \frac{1}{n\alpha R}} \qquad (1)$$

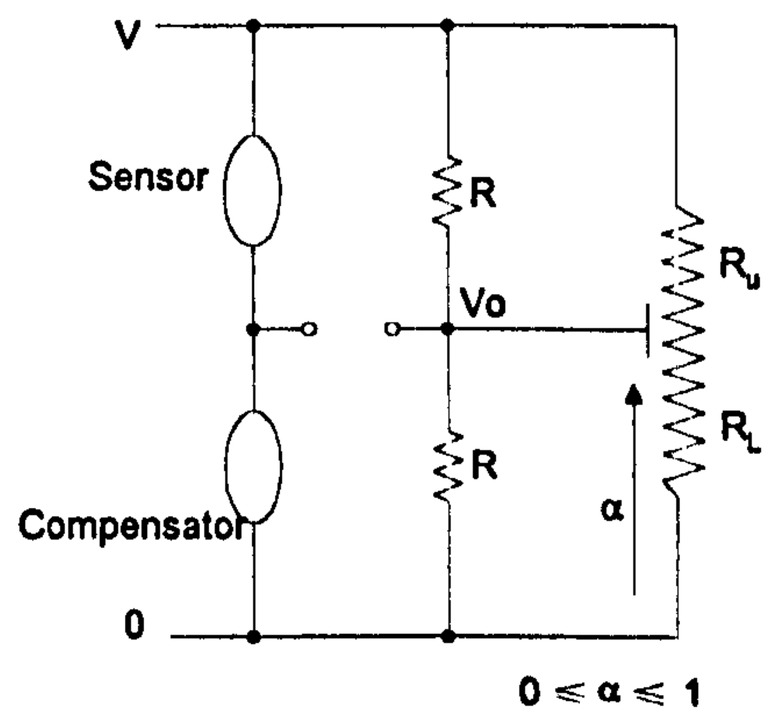

$$R_U = \frac{1}{\frac{1}{R} + \frac{1}{(1-\alpha)nR}} \qquad (2)$$

$$Vo = V\frac{R_L}{(R_L + R_U)} \qquad (3)$$

where α is the resistance ratio between R_u and R_L; n is ratio between the balance resistor, R, and the potentiometer ($R_U + R_L$).

Simplifying (1) and (2):

$$R_L = \frac{n\alpha R^2}{n\alpha R + R} = \frac{n\alpha R}{1 + n\alpha} \qquad (4)$$

$$R_U = \frac{(1-\alpha)nR^2}{(1-\alpha)nR + R} = \frac{(1-\alpha)nR}{1 + n(1-\alpha)} \qquad (5)$$

By substitute (4) and (5) into (3)

$$\frac{Vo}{V} = \frac{\alpha\left(1 + n(1-\alpha)\right)}{1 + 2n\alpha(1-\alpha)} \qquad (6)$$

The relationship between the α, and the n is plotted in figure A4.1.

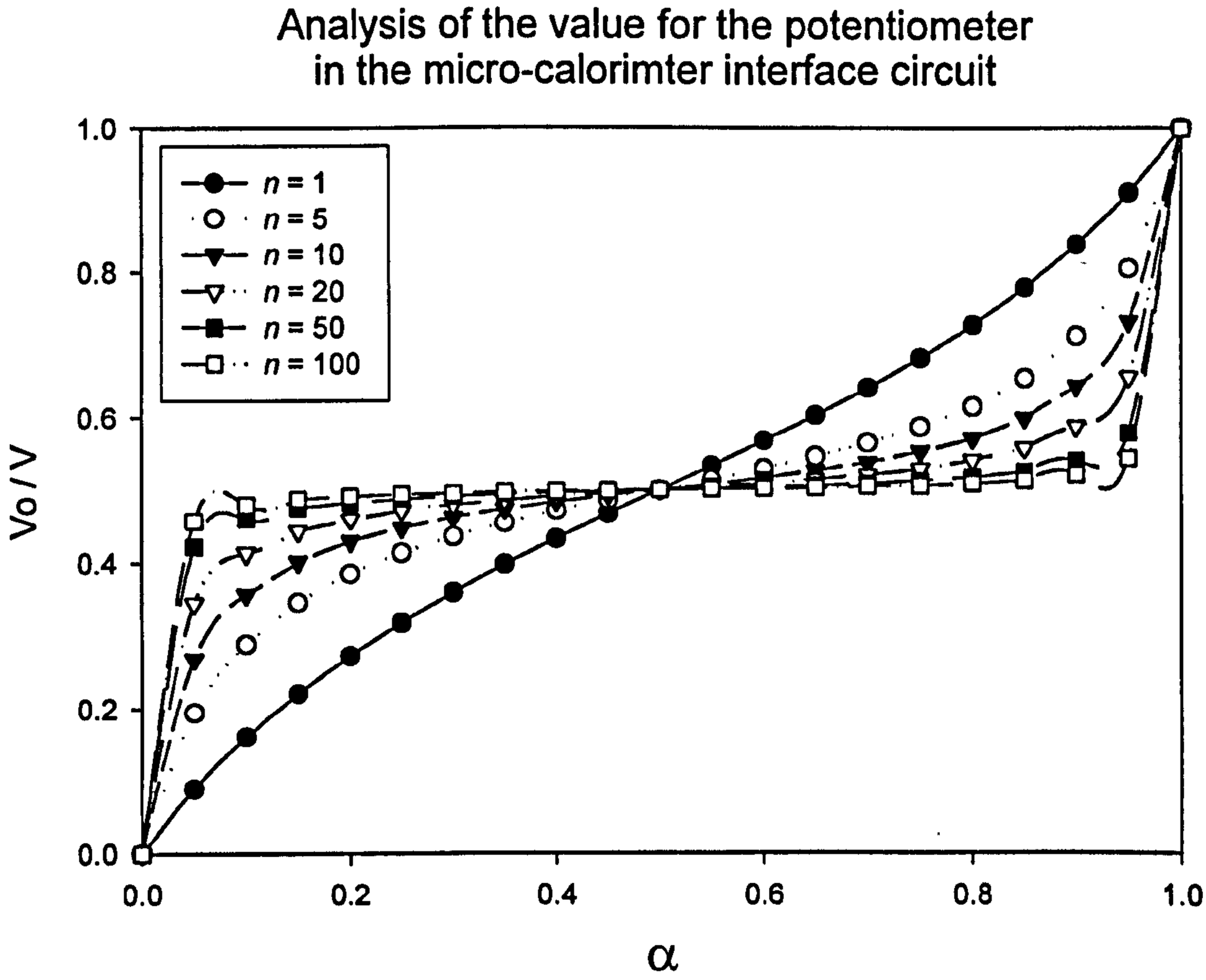

Figure A4.1: The relationship between the α and the *n*.

Therefore, when $n = 50$, it provides the most stable output with minimum ratio between the balance resistor and the potentiometer.

Appendix 4b

Details of the micro-calorimeter interface circuit board

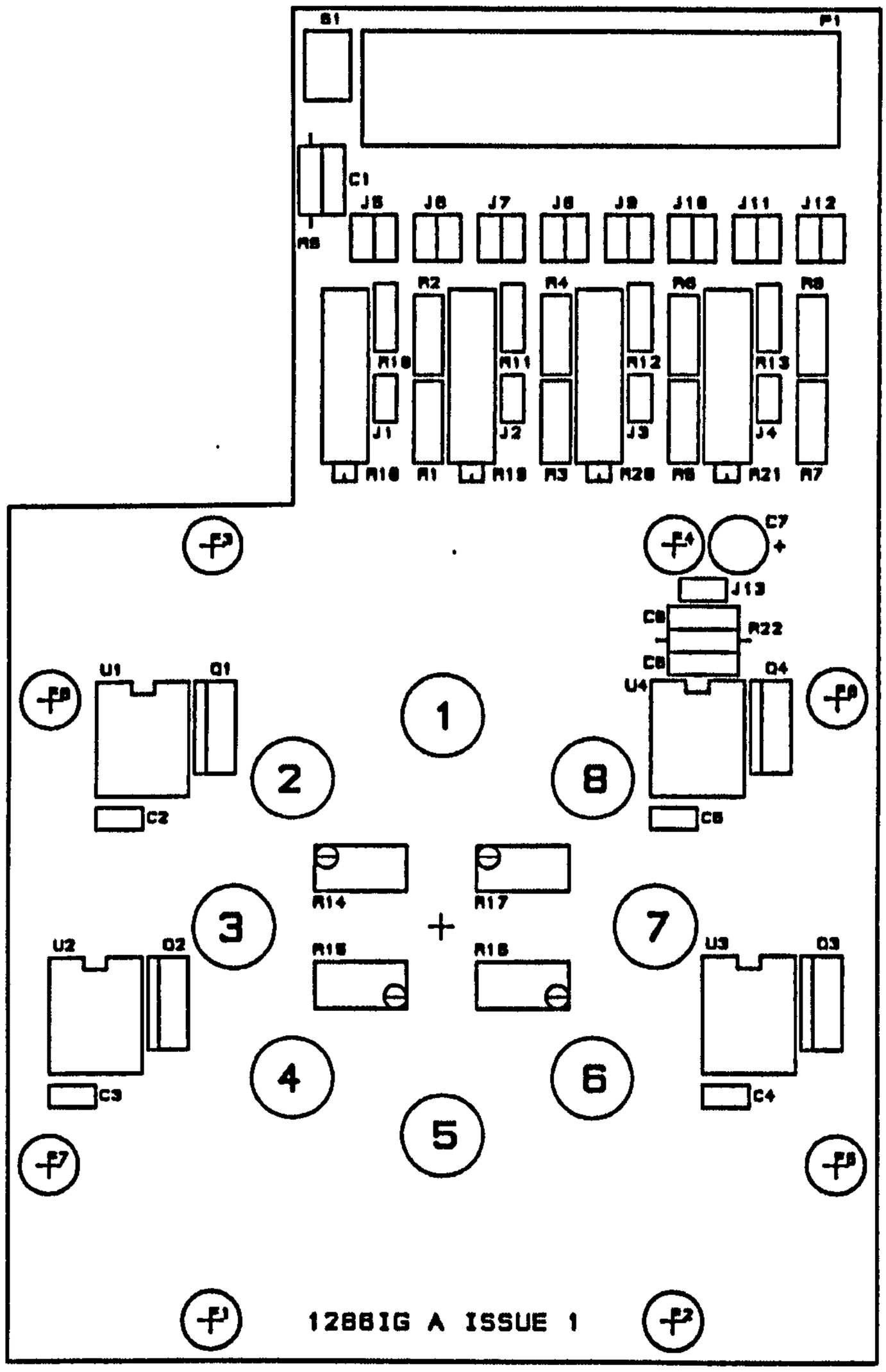

The component layer of the PCB.

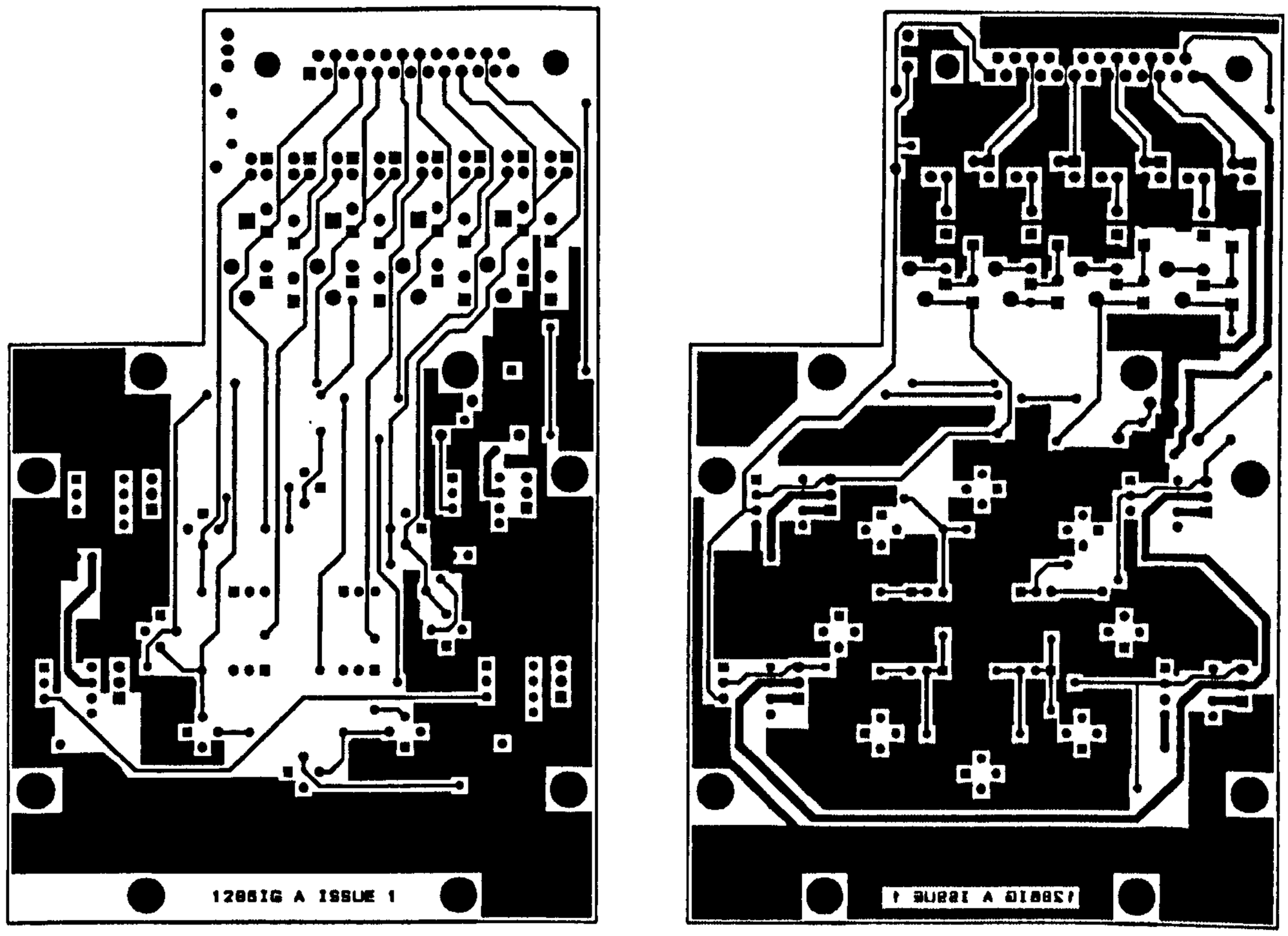

(a) (b)

The micro-calorimeter interface PCB. (a) The front-side and (b) the back-side.

Appendix 5

Appendix 5a

Numerical characterisation results for 1st generation devices

Appendix 5b

Numerical characterisation results for 2nd generation devices

Appendix 5c

Average temperature of the active area

Appendix 5d

Power curve coefficients for 1st and 2nd generation devices

Appendix 5a
Numerical characterisation results for 1st generation devices

Device: SRL 136a

Environment: Room	Sample Number					
	1	2	3	4	5	6
Constant current (mA)	Voltage Across sensor (V)					
10	2.04886	2.04317	2.05541	1.97840	2.05767	2.00098
15	3.53529	3.51546	3.54739	3.45680	3.53890	3.50672
20	5.57224	5.52595	5.59407	5.52964	5.58824	5.61374
25	8.34952	8.30624	8.41492	8.42110	8.36506	8.52929
26	9.06716	8.96956	9.09592	9.10437	9.09806	9.25288
28	10.38346	10.3293	10.44668	10.39151	10.41584	10.6427
26	9.07782	9.02510	9.13373	9.18267	9.09309	9.28386
25	8.45505	8.40921	8.50948	8.51937	8.48494	8.63036
20	5.70852	5.68557	5.74379	5.68115	5.73551	5.78238
15	3.62156	3.60917	3.63936	3.55250	3.63730	3.59732
10	2.08034	2.08064	2.09904	2.01930	2.09721	2.04303

Environment: Oven	Sample Number					
	1	2	3	4	5	6
	Heater Resistance (ohm)					
26.5	183.481	183.939	184.859	175.848	184.255	176.727
81	198.545	198.167	200.351	191.144	200.341	192.628
164	223.223	222.595	223.640	216.148	223.998	217.609

Device: SRL 136p

Environment: Room	Sample Number					
	1	2	3	4	5	6
Constant current (mA)	Voltage Across sensor (V)					
10	1.95857	1.94850	1.95313	1.96510	1.96682	2.03134
15	3.40565	3.37572	3.38951	3.41044	3.41982	3.48933
20	5.41794	5.35087	5.39230	5.41820	5.43295	5.47691
25	8.30535	8.12976	8.19120	8.21767	8.33129	8.27201
26	8.94360	8.79908	8.87357	8.91772	8.96648	8.83093
28	10.27185	10.12325	10.20648	10.25145	10.29044	10.22089
26	8.96412	8.83307	8.88496	8.93654	8.96485	8.95476
25	8.33440	8.21221	8.26465	8.31534	8.34161	8.35134
20	5.58557	5.50955	5.53702	5.56686	5.57964	5.64273
15	3.48473	3.45870	3.46613	3.48940	3.50342	3.58075
10	1.99152	1.97111	1.98425	1.98986	1.99762	2.09685

Environment: Oven	Sample Number					
	1	2	3	4	5	6
	Heater Resistance (ohm)					
26.5	173.354	172.968	173.336	173.860	174.333	182.234
81	190.114	188.336	188.768	190.425	190.237	197.585
164	214.742	213.016	213.749	214.599	215.149	218.453

Device: SRL 162g

Environment: Room	Sample Number					
	1	2	3	4	5	6
Constant current (mA)	Voltage Across sensor (V)					
10	2.96566	2.90309	2.94308	2.95547	2.91244	2.90226
15	5.75013	5.64926	5.71097	5.71816	5.64596	5.66450
16	6.46911	6.36543	6.41742	6.42059	6.48871	6.38251
18	8.06280	7.94238	7.98889	7.98586	8.00179	7.95831
19	8.90653	8.81134	8.85099	8.82618	8.83589	8.83554
20	9.87850	9.81437	9.86111	9.80688	9.76179	9.85719
19	8.98679	8.91387	8.96711	8.90266	8.85525	8.94871
18	8.13346	8.04461	8.09373	8.03778	8.01607	8.07184
16	6.57040	6.48660	6.54257	6.49113	6.47111	6.51184
15	5.85287	5.77851	5.81465	5.79303	5.75832	5.79783
10	3.03128	2.98046	3.02875	3.01818	2.98871	2.99241

Environment: Oven	Sample Number					
	1	2	3	4	5	6
	Heater Resistance (ohm)					
26.5	231.472	227.64	232.779	232.349	228.751	227.723
81	251.347	246.396	253.378	253.140	249.417	248.234
164	282.866	278.362	282.246	282.485	278.271	279.369

Device: SRL 162p

Environment: Room	Sample Number					
	1	2	3	4	5	6
Constant current (mA)	Voltage Across sensor (V)					
10	2.99345	2.92377	2.94135	2.89069	2.92676	2.92291
15	5.76197	5.66544	5.66783	5.62928	5.69742	5.64120
16	6.48342	6.36902	6.37617	6.34581	6.41318	6.35194
18	8.05888	7.93365	7.93148	7.95039	7.99655	7.89402
19	8.92471	8.79563	8.78333	8.81424	8.85558	8.79366
20	9.91555	9.75154	9.72604	9.78995	9.81622	9.72150
19	9.04100	8.86116	8.84733	8.88165	8.91605	8.92487
18	8.17600	8.01076	7.99802	8.00649	8.05502	8.06120
16	6.62040	6.46253	6.46577	6.44811	6.48965	6.52168
15	5.91622	5.75625	5.76131	5.74122	5.77724	5.80665
10	3.09546	2.98507	2.99497	2.96545	2.99330	3.01975

Environment: Oven	Sample Number					
	1	2	3	4	5	6
	Heater Resistance (ohm)					
26.5	237.732	228.907	231.124	225.541	228.233	232.226
81	257.251	248.993	250.059	245.961	248.744	252.526
164	287.739	279.054	281.441	276.201	279.262	282.543

Appendix 5b
Numerical characterisation results for 2nd generation devices

Characterisation of Micro-hotplate SRL 136o

Constant Current Characterisation using:
1) Knick DC-Calibrator J152
2) Thurlby digital multimeter 1503-HA, supplied by RS Component Ltd, stock no. 610-859
3) MHP Holder and T05 star-shape heatsink

Electrical Charactersiation

Constant Current	*Voltage across device (V)*			
(mA)	136o - 2 - w7	136o - 4 - w7	136o -1 - w8	136o - 5 - w10
10	1.794	1.798	1.732	1.751
15	3.214	3.165	3.024	3.062
20	5.249	5.101	4.864	4.945
25	7.968	7.804	7.431	7.589
26	8.609	8.439	8.083	8.249
25	8.003	7.852	7.507	7.667
20	5.277	5.201	4.952	5.023
15	3.226	3.212	3.065	3.100
10	1.798	1.811	1.744	1.762

Thermal characterisation using
1) Convection oven and mercury glass thermometer
2) Thurlby digital multimeter 1503-HA, supplied by RS Component Ltd, stock no. 610-859
3) Custom made thermal characterisation probe

Thermal Charactersiation

Temperature	*Micro-heater resistance (Ohm)*			
(deg. C)	136o - 2 - w7	136o - 4 - w7	136o -1 - w8	136o - 5 - w10
23.8	154.01	156.74	153.06	154.61
80	171.51	174.52	170.22	171.83
157	195.52	198.25	194.33	196.61

Siu Man Lee
Hotplate_char_rawdata.xls

Characterisation of Micro-hotplate SRL 162o

Constant Current Characterisation using:
1) Knick DC-Calibrator J152
2) Thurlby digital multimeter 1503-HA, supplied by RS Component Ltd, stock no. 610-859
3) MHP Holder and T05 star-shape heatsink

Electrical Charactersiation

Constant Current (mA)	*Voltage across device (V)*			
	162o - 2 - w7	162o - 5 - w7	162o - 5 - w8	162o - 2 - w10
10	2.657	2.652	2.669	2.725
15	5.289	5.220	5.304	5.472
16	5.977	5.889	5.995	6.201
18	7.518	7.382	7.543	7.838
19	8.375	8.218	8.415	8.739
18	7.551	7.421	7.592	7.870
16	6.029	5.943	6.066	6.257
15	5.340	5.273	5.374	5.531
10	2.676	2.672	2.695	2.746

Thermal characterisation using
1) Convection oven and mercury glass thermometer
2) Thurlby digital multimeter 1503-HA, supplied by RS Component Ltd, stock no. 610-859
3) Custom made thermal characterisation probe

Thermal Charactersiation

Temperature (deg. C)	*Micro-heater resistance (Ohm)*			
	162o - 2 - w7	162o - 5 - w7	162o - 5 - w8	162o - 2 - w10
23.9	200.51	202.45	201.05	203.58
92	228.15	229.69	229.23	231.89
161	256.08	257.15	257.04	260.83

Siu Man Lee
Hotplate_char_rawdata.xls

Characterisation of Micro-hotplate SRL 176a

Constant Current Characterisation using:
1) Knick DC-Calibrator J152
2) Thurlby digital multimeter 1503-HA, by RS Component Ltd, stock no. 610-859
3) MHP Holder and T05 star-shape heatsink

Electrical Characterisation

Constant Current (mA)	***Voltage across device (V)***				
	176a - 6 -w7	176a - 10 - w7	176a - 15 - w7	176a - 5 - w8	176a - 6 - w10
20	0.3793	0.3763	0.3790	0.3747	0.3719
40	0.8958	0.8879	0.8969	0.8878	0.8801
50	1.2568	1.2445	1.2602	1.2505	1.2381
55	1.4713	1.4566	1.4767	1.4676	1.4518
66	2.0289	2.0188	2.0479	2.0426	2.0146
55	1.4733	1.4649	1.4834	1.4727	1.4561
50	1.2584	1.2513	1.2655	1.2544	1.2415
40	0.8968	0.8917	0.8999	0.8901	0.8820
20	0.3796	0.3773	0.3798	0.3750	0.3719

Thermal characterisation using
1) Convection oven and mercury glass thermometer
2) Thurlby digital multimeter 1503-HA, by RS Component Ltd, stock no. 610-859
3) Custom made thermal characterisation probe

Thermal Characterisation

Temperature (deg. C)	***Micro-heater resistance (Ohm)***				
	176a - 6 -w7	176a - 10 - w7	176a - 15 - w7	176a - 5 - w8	176a - 6 - w10
23.9	17.97	17.89	18.08	17.72	17.68
91	20.48	20.32	20.50	20.30	20.11
161	23.00	22.81	23.07	22.96	22.70

Siu Man Lee
Hotplate_char_rawdata.xls

Characterisation of Micro-hotplate SRL 176b

Constant Current Characterisation using:
1) Knick DC-Calibrator J152
2) Thurlby digital multimeter 1503-HA, supplied by RS Component Ltd, stock no. 610-859
3) MHP Holder and T05 star-shape heatsink

Electrical Charactersiation

Constant Current	***Voltage across device (V)***				
(mA)	176b - 5 - w7	176b - 10 - w7	176b - 16 - w7	176b - 5 - w8	176b - 5 - w10
20	0.4495	0.4524	0.4660	0.4495	0.4536
40	1.1343	1.1275	1.1606	1.1291	1.1431
50	1.6477	1.6258	1.6727	1.6406	1.6621
55	1.9567	1.9286	1.9845	1.9539	1.9817
59	2.2303	2.2118	2.2696	2.2459	2.2755
55	1.9597	1.9472	1.9987	1.9736	2.0003
50	1.6506	1.6440	1.6891	1.6596	1.6827
40	1.1356	1.1374	1.1708	1.1396	1.1548
20	0.4497	0.4536	0.4673	0.4504	0.4547

Thermal characterisation using
1) Convection oven and mercury glass thermometer
2) Thurlby digital multimeter 1503-HA, supplied by RS Component Ltd, stock no. 610-859
3) Custom made thermal characterisation probe

Thermal Charactersiation

Temperature	***Micro-heater resistance (Ohm)***				
(deg. C)	176b - 5 - w7	176b - 10 - w7	176b - 16 - w7	176b - 5 - w8	176b - 5 - w10
22.6	20.81	21.05	21.74	20.86	20.95
93	23.88	24.00	24.75	23.89	24.04
165	26.96	27.03	27.90	27.10	27.28

Siu Man Lee
Hotplate_char_rawdata.xls

Characterisation of Micro-hotplate SRL 176c

Constant Current Characterisation using:
1) Knick DC-Calibrator J152
2) Thurlby digital multimeter 1503-HA, supplied by RS Component Ltd, stock no. 610-859
3) MHP Holder and T05 star-shape heatsink

Electrical Charactersiation

Constant Current (mA)	*Voltage across device (V)*				
	176c - 5 - w7	176c - 10 - w7	176c - 16 - w7	176c - 5 - w8	176c - 5 - w10
20	0.7657	0.7642	0.8178	0.7592	0.7633
30	1.3667	1.3540	1.4362	1.3519	1.3618
40	2.2269	2.1894	2.3065	2.2102	2.2275
45	2.7633	2.7104	2.8525	2.7563	2.7792
50	3.366	3.297	3.471	3.387	3.406
45	2.7653	2.7132	2.8646	2.7723	2.7917
40	2.2275	2.1916	2.3209	2.2261	2.2422
30	1.3664	1.3539	1.4438	1.3605	1.3700
20	0.7654	0.7636	0.8198	0.7616	0.7658

Thermal characterisation using
1) Convection oven and mercury glass thermometer
2) Thurlby digital multimeter 1503-HA, supplied by RS Component Ltd, stock no. 610-859
3) Custom made thermal characterisation probe

Thermal Charactersiation

Temperature (deg. C)	*Micro-heater resistance (Ohm)*				
	176c - 5 - w7	176c - 10 - w7	176c - 16 - w7	176c - 5 - w8	176c - 5 - w10
24.3	32.98	33.03	35.64	32.71	32.87
95	37.83	37.82	40.82	37.77	37.87
162	42.32	42.18	45.44	42.43	42.53

Siu Man Lee
Hotplate_char_rawdata.xls

Characterisation of Micro-hotplate SRL 177a

Constant Current Characterisation using:
1) Knick DC-Calibrator J152
2) Thurlby digital multimeter 1503-HA, supplied by RS Component Ltd, stock no. 610-859
3) MHP Holder and T05 star-shape heatsink

Electrical Characterisation

Constant Current	***Voltage across device (V)***				
(mA)	177a - 4 - w7	177a - 10 - w7	177a - 15 -w7	177a - 5 -w8	177a - 4 -w10
20	0.3898	0.3864	0.3890	0.3832	0.3868
40	0.9488	0.9323	0.9429	0.9312	0.9402
50	1.3534	1.3223	1.3401	1.3279	1.3401
60	1.8688	1.8169	1.8455	1.8335	1.8495
65	2.1768	2.1184	2.1488	2.1389	2.1563
60	1.8818	1.8331	1.8585	1.8505	1.8656
50	1.3646	1.3351	1.3527	1.3416	1.3537
40	0.9551	0.9392	0.9501	0.9387	0.9476
20	0.3911	0.3874	0.3904	0.3843	0.3877

Thermal characterisation using
1) Convection oven and mercury glass thermometer
2) Thurlby digital multimeter 1503-HA, supplied by RS Component Ltd, stock no. 610-859
3) Custom made thermal characterisation probe

Thermal Characterisation

Temperature	***Micro-heater resistance (Ohm)***				
(deg. C)	177a - 4 - w7	177a - 10 - w7	177a - 15 -w7	177a - 5 -w8	177a - 4 -w10
24.30	18.36	18.22	18.33	18.10	18.21
93.5	20.99	20.77	20.91	20.67	20.80
158	23.45	23.12	23.24	23.06	23.20

Siu Man Lee
Hotplate_char_rawdata.xls

Characterisation of Micro-hotplate SRL 177b

Constant Current Characterisation using:
1) Knick DC-Calibrator J152
2) Thurlby digital multimeter 1503-HA, supplied by RS Component Ltd, stock no. 610-859
3) MHP Holder and T05 star-shape heatsink

Electrical Characterisation

Constant Current (mA)	*Voltage across device (V)*				
	177b - 5 - w7	177b - 9 - w7	177b - 16 - w7	177b - 5 - w8	177b - 5 - w10
20	0.4737	0.4703	0.4745	0.4697	0.4760
30	0.8006	0.7942	0.7992	0.7931	0.8076
40	1.2445	1.2324	1.2363	1.2329	1.2605
50	1.8458	1.8279	1.8265	1.8375	1.8845
55	2.2218	2.1920	2.1896	2.2118	2.2638
50	1.8614	1.8394	1.8388	1.8508	1.8951
40	1.2566	1.2465	1.2487	1.2479	1.2761
30	0.8056	0.8004	0.8043	0.7992	0.8145
20	0.4751	0.4718	0.4759	0.4710	0.4781

Thermal characterisation using
1) Convection oven and mercury glass thermometer
2) Thurlby digital multimeter 1503-HA, supplied by RS Component Ltd, stock no. 610-859
3) Custom made thermal characterisation probe

Thermal Characterisation

Temperature (deg. C)	*Micro-heater resistance (Ohm)*				
	177b - 5 - w7	177b -9 - w7	177b - 16 - w7	177b - 5 - w8	177b - 5 - w10
22.7	21.73	21.52	21.73	21.51	21.74
95	25.01	24.67	24.90	24.72	24.93
160	27.92	27.37	27.64	27.64	27.85

Siu Man Lee
Hotplate_char_rawdata.xls

Characterisation of Micro-hotplate SRL 177c

Constant Current Characterisation using:
1) Knick DC-Calibrator J152
2) Thurlby digital multimeter 1503-HA, supplied by RS Component Ltd, stock no. 610-859
3) MHP Holder and T05 star-shape heatsink

Electrical Characterisation

Constant Current (mA)	*Voltage across device (V)*				
	177c - 5 - w7	177c - 9 - w7	177c - 14 - w7	177c - 5 - w8	177c - 5 - w10
15	0.5343	0.5338	0.5747	0.5270	0.5317
30	1.4237	1.4006	1.4852	1.4028	1.4192
35	1.8594	1.8231	1.9249	1.8373	1.8607
40	2.3726	2.3238	2.4475	2.3569	2.3945
43	2.7175	2.6618	2.8024	2.7159	2.7598
40	2.3757	2.3262	2.4564	2.3719	2.4058
35	1.8614	1.8252	1.9366	1.8536	1.8772
30	1.4243	1.4011	1.4938	1.4150	1.4308
15	0.5340	0.5330	0.5756	0.5278	0.5327

Thermal characterisation using
1) Convection oven and mercury glass thermometer
2) Thurlby digital multimeter 1503-HA, supplied by RS Component Ltd, stock no. 610-859
3) Custom made thermal characterisation probe

Thermal Characterisation

Temperature (deg. C)	*Micro-heater resistance (Ohm)*				
	177c - 5 - w7	177c - 9 - w7	177c - 14 - w7	177c - 5 - w8	177c - 5 - w10
23.8	32.13	32.35	35.18	31.75	32.06
91	36.60	36.84	39.72	36.20	36.45
161	41.07	41.36	44.55	40.78	41.07

Siu Man Lee
Hotplate_char_rawdata.xls

Characterisation of Micro-hotplate SRL 178a

Constant Current Characterisation using:
1) Knick DC-Calibrator J152
2) Thurlby digital multimeter 1503-HA, supplied by RS Component Ltd, stock no. 610-859
3) MHP Holder and T05 star-shape heatsink

Electrical Charactersiation

Constant Current (mA)	*Voltage across device (V)*				
	178a - 5 - w7	178a - 8 - w7	178a - 15 - w7	178a - 1 - w8	178a - 5 - w10
20	0.3862	0.4028	0.4127	0.3801	0.3851
40	0.9122	0.9424	0.9632	0.8985	0.9120
50	1.2797	1.3152	1.3415	1.2628	1.2832
60	1.7427	1.7833	1.8139	1.7228	1.7527
67	2.1389	2.1838	2.2238	2.1277	2.1598
60	1.7568	1.7988	1.8328	1.7448	1.7728
50	1.2906	1.3277	1.3553	1.2785	1.2980
40	0.9180	0.9495	0.9706	0.9072	0.9200
20	0.3873	0.4043	0.4139	0.3814	0.3860

Thermal characterisation using
1) Convection oven and mercury glass thermometer
2) Thurlby digital multimeter 1503-HA, supplied by RS Component Ltd, stock no. 610-859
3) Custom made thermal characterisation probe

Thermal Charactersiation

Temperature (deg. C)	*Micro-heater resistance (Ohm)*				
	178a - 5 - w7	178a - 8 - w7	178a - 15 - w7	178a - 1 - w8	178a - 5 - w10
23.5	18.39	19.26	19.75	18.12	18.29
94	21.07	22.04	22.55	20.78	20.99
162	23.58	24.67	25.22	23.36	23.59

Siu Man Lee
Hotplate_char_rawdata.xls

Characterisation of Micro-hotplate SRL 178b

Constant Current Characterisation using:
1) Knick DC-Calibrator J152
2) Thurlby digital multimeter 1503-HA, supplied by RS Component Ltd, stock no. 610-859
3) MHP Holder and T05 star-shape heatsink

Electrical Characterisation

Constant Current (mA)	*Voltage across device (V)*				
	178b - 1 - w7	178b - 5- w7	178b - 10 - w7	178b - 5 - w8	178b - 1 - w10
20	0.4678	0.4667	0.4719	0.4659	0.4738
30	0.7836	0.7823	0.7876	0.7806	0.7949
40	1.2063	1.2051	1.2071	1.2022	1.2259
50	1.7766	1.7795	1.7695	1.7678	1.8075
56	2.2031	2.2046	2.1923	2.2052	2.2498
50	1.7905	1.7909	1.7854	1.7922	1.8276
40	1.2188	1.2181	1.2206	1.2193	1.2416
30	0.7892	0.7876	0.7936	0.7881	0.8016
20	0.4697	0.4682	0.4737	0.4680	0.4758

Thermal characterisation using
1) Convection oven and mercury glass thermometer
2) Thurlby digital multimeter 1503-HA, supplied by RS Component Ltd, stock no. 610-859
3) Custom made thermal characterisation probe

Thermal Characterisation

Temperature (deg. C)	*Micro-heater resistance (Ohm)*				
	178b - 1 - w7	178b - 5- w7	178b - 10 - w7	178b - 5 - w8	178b - 1 - w10
23.6	21.42	21.32	21.64	21.26	21.66
95	24.78	24.67	24.98	24.66	25.03
159	27.53	27.39	27.75	27.47	27.87

Siu Man Lee
Hotplate_char_rawdata.xls

Characterisation of Micro-hotplate SRL 178c

Constant Current Characterisation using:
1) Knick DC-Calibrator J152
2) Thurlby digital multimeter 1503-HA, supplied by RS Component Ltd, stock no. 610-859
3) MHP Holder and T05 star-shape heatsink

Electrical Charactersiation

Constant Current (mA)	*Voltage across device (V)*				
	178c - 2 - w7	178c - 6 - w7	178c - 16 - w7	178c - 2 - w8	178c - 2 - w10
15	0.5187	0.5292	0.5407	0.5189	0.5248
30	1.3589	1.3789	1.3981	1.3624	1.3797
35	1.7716	1.7891	1.8132	1.7775	1.7997
40	2.2658	2.2741	2.3087	2.2739	2.3009
45	2.8438	2.8346	2.8853	2.8535	2.8926
40	2.2784	2.2801	2.3194	2.2895	2.3202
35	1.7844	1.7936	1.8255	1.7934	1.8180
30	1.3681	1.3807	1.4074	1.3742	1.3929
15	0.5205	0.5295	0.5421	0.5211	0.5265

Thermal characterisation using
1) Convection oven and mercury glass thermometer
2) Thurlby digital multimeter 1503-HA, supplied by RS Component Ltd, stock no. 610-859
3) Custom made thermal characterisation probe

Thermal Charactersiation

Temperature (deg. C)	*Micro-heater resistance (Ohm)*				
	178c - 2 - w7	178c - 6 - w7	178c - 16 - w7	178c - 2 - w8	178c - 2 - w10
23.7	31.47	32.15	32.92	31.52	31.75
92	36.10	36.62	37.65	36.10	36.36
162	40.69	41.07	42.35	40.67	40.95

Siu Man Lee
Hotplate_char_rawdata.xls

Characterisation of Micro-hotplate SRL 179a

Constant Current Characterisation using:
1) Knick DC-Calibrator J152
2) Thurlby digital multimeter 1503-HA, supplied by RS Component Ltd, stock no. 610-859
3) MHP Holder and T05 star-shape heatsink

Electrical Charactersiation

Constant Current (mA)	*Voltage across device (V)*				
	179a - 1- w7	179a - 6 - w7	179a - 10- w7	179a - 1 - w8	179a - 1 - w10
20	0.3709	0.3649	0.3894	0.3681	0.3701
40	0.8473	0.8299	0.8814	0.8377	0.844
55	1.3557	1.3208	1.3946	1.3345	1.3462
65	1.7966	1.7473	1.8363	1.7655	1.7815
69	1.9988	1.9459	2.0429	1.9659	1.9845
65	1.7993	1.7529	1.8438	1.7712	1.7876
55	1.3582	1.3255	1.4006	1.3391	1.3511
40	0.8486	0.8314	0.8832	0.8397	0.8452
20	0.3712	0.3647	0.3893	0.3683	0.3698

Thermal characterisation using
1) Convection oven and mercury glass thermometer
2) Thurlby digital multimeter 1503-HA, supplied by RS Component Ltd, stock no. 610-859
3) Custom made thermal characterisation probe

Thermal Charactersiation

Temperature (deg. C)	*Micro-heater resistance (Ohm)*				
	179a - 1- w7	179a - 6 - w7	179a - 10- w7	179a - 1 - w8	179a - 1 - w10
22.2	17.92	17.66	18.87	17.81	17.83
107	20.85	20.50	21.86	20.71	20.74
156	22.81	22.43	23.93	22.70	22.72

Siu Man Lee
Hotplate_char_rawdata.xls

Characterisation of Micro-hotplate SRL 179b

Constant Current Characterisation using:
1) Knick DC-Calibrator J152
2) Thurlby digital multimeter 1503-HA, supplied by RS Component Ltd, stock no. 610-859
3) MHP Holder and T05 star-shape heatsink

Electrical Characterisation

Constant Current (mA)	*Voltage across device (V)*				
	179b - 1 - w7	179b - 4 - w7	179b - 9 - w7	179b - 1 - w8	179b - 1 - w10
20	0.4502	0.4454	0.4514	0.4437	0.4490
40	1.1078	1.0931	1.1015	1.0884	1.0998
50	1.5901	1.5676	1.5732	1.5603	1.5768
55	1.8792	1.8556	1.8599	1.8458	1.8683
60	2.2028	2.1953	2.1883	2.1853	2.2065
55	1.8827	1.8734	1.8732	1.8683	1.8854
50	1.5929	1.5837	1.5868	1.5802	1.5944
40	1.1094	1.1015	1.1086	1.0995	1.1096
20	0.4505	0.4468	0.4524	0.4455	0.4497

Thermal characterisation using
1) Convection oven and mercury glass thermometer
2) Thurlby digital multimeter 1503-HA, supplied by RS Component Ltd, stock no. 610-859
3) Custom made thermal characterisation probe

Thermal Characterisation

Temperature (deg. C)	*Micro-heater resistance (Ohm)*				
	179b - 1 - w7	179b - 4 - w7	179b - 9 - w7	179b - 1 - w8	179b - 1 - w10
22.2	21.03	20.87	21.13	20.79	20.99
95	24.25	24.05	24.33	24.00	24.21
161	27.11	26.93	27.24	26.88	27.13

Siu Man Lee
Hotplate_char_rawdata.xls

Characterisation of Micro-hotplate SRL 179c

Constant Current Characterisation using:
1) Knick DC-Calibrator J152
2) Thurlby digital multimeter 1503-HA, supplied by RS Component Ltd, stock no. 610-859
3) MHP Holder and T05 star-shape heatsink

Electrical Charactersiation

Constant Current (mA)	*Voltage across device (V)*				
	179c - 4 - w7	179c - 6 - w7	179c - 14 - w7	179c - 5 - w8	179c - 5 - w10
20	0.7539	0.7506	0.7555	0.7466	0.7566
30	1.3288	1.3164	1.3236	1.3133	1.3342
40	2.1432	2.1154	2.1244	2.1189	2.1555
45	2.6509	2.6178	2.6285	2.6285	2.6725
50	3.2218	3.1918	3.2044	3.2135	3.2638
45	2.6527	2.6258	2.6402	2.6431	2.6907
40	2.1445	2.1231	2.1378	2.1346	2.1733
30	1.3292	1.3198	1.3310	1.3210	1.3427
20	0.7539	0.7515	0.7578	0.7486	0.7588

Thermal characterisation using
1) Convection oven and mercury glass thermometer
2) Thurlby digital multimeter 1503-HA, supplied by RS Component Ltd, stock no. 610-859
3) Custom made thermal characterisation probe

Thermal Charactersiation

Temperature (deg. C)	*Micro-heater resistance (Ohm)*				
	179c - 4 - w7	179c - 6 - w7	179c - 14 - w7	179c - 5 - w8	179c - 5 - w10
22.3	32.81	32.76	33.10	32.54	32.85
91	37.55	37.52	37.82	37.38	37.69
161	42.27	42.28	42.52	42.15	42.45

Siu Man Lee
Hotplate_char_rawdata.xls

Characterisation of Micro-hotplate SRL 179d

Constant Current Characterisation using:
1) Knick DC-Calibrator J152
2) Thurlby digital multimeter 1503-HA, supplied by RS Component Ltd, stock no. 610-859
3) MHP Holder and T05 star-shape heatsink

Electrical Charactersiation

Constant Current (mA)	*Voltage across device (V)*			
	179d - 2 - w7	179d - 3 - w7	179d - 2 - w8	179d - 2 - w10
8	1.883	1.893	1.882	1.910
10	2.588	2.603	2.585	2.628
12	3.459	3.478	3.453	3.511
14	4.523	4.546	4.513	4.598
16	5.799	5.826	5.787	5.908
14	4.527	4.552	4.522	4.605
12	3.462	3.478	3.456	3.515
10	2.590	2.601	2.585	2.626
8	1.884	1.890	1.879	1.907

Thermal characterisation using
1) Convection oven and mercury glass thermometer
2) Thurlby digital multimeter 1503-HA, supplied by RS Component Ltd, stock no. 610-859
3) Custom made thermal characterisation probe

Thermal Charactersiation

Temperature (deg. C)	*Micro-heater resistance (Ohm)*			
	179d - 2 - w7	179d - 3 - w7	179d - 2 - w8	179d - 2 - w10
22.3	198.48	198.15	197.22	199.58
94	227.49	227.26	226.46	229.78
163	255.97	254.76	254.12	257.99

Siu Man Lee
Hotplate_char_rawdata.xls

Characterisation of Micro-hotplate SRL 179e

Constant Current Characterisation using:
1) Knick DC-Calibrator J152
2) Thurlby digital multimeter 1503-HA, supplied by RS Component Ltd, stock no. 610-859
3) MHP Holder and T05 star-shape heatsink

Electrical Charactersiation

Constant Current (mA)	*Voltage across device (V)*			
	179e - 2 - w7	179e - 3 - w7	179e - 2 - w8	179e - 2 - w10
10	1.766	1.737	1.708	1.728
14	2.774	2.728	2.658	2.697
18	4.107	4.036	3.901	3.970
20	4.928	4.838	4.663	4.755
22	5.863	5.753	5.531	5.652
20	4.930	4.837	4.665	4.755
18	4.110	4.032	3.902	3.970
14	2.776	2.724	2.657	2.696
10	1.767	1.734	1.706	1.728

Thermal characterisation using
1) Convection oven and mercury glass thermometer
2) Thurlby digital multimeter 1503-HA, supplied by RS Component Ltd, stock no. 610-859
3) Custom made thermal characterisation probe

Thermal Charactersiation

Temperature (deg. C)	*Micro-heater resistance (Ohm)*			
	179e - 2 - w7	179e - 3 - w7	179e - 2 - w8	179e - 2 - w10
22.4	155.93	152.94	152.41	153.85
94	178.47	175.31	174.90	177.06
161	199.75	196.68	195.73	198.71

Siu Man Lee
Hotplate_char_rawdata.xls

Characterisation of Micro-hotplate SRL 180a

Constant Current Characterisation using:
1) Knick DC-Calibrator J152
2) Thurlby digital multimeter 1503-HA, supplied by RS Component Ltd, stock no. 610-859
3) MHP Holder and T05 star-shape heatsink

Electrical Charactersiation

Constant Current (mA)	*Voltage across device (V)*			
	180a - 2 - w7	180a - 4 - w7	180a - 1 - w8	180a - 1 - w10
20	0.3485	0.3450	0.3420	0.3475
40	0.8567	0.8447	0.8400	0.8575
50	1.2381	1.2173	1.2128	1.2405
55	1.4717	1.4469	1.4423	1.4763
60	1.7385	1.7188	1.7079	1.7528
55	1.4758	1.4594	1.4518	1.4906
50	1.2414	1.2276	1.2212	1.2535
40	0.8586	0.8491	0.8442	0.8647
20	0.3488	0.3454	0.3425	0.3287

Thermal characterisation using
1) Convection oven and mercury glass thermometer
2) Thurlby digital multimeter 1503-HA, supplied by RS Component Ltd, stock no. 610-859
3) Custom made thermal characterisation probe

Thermal Charactersiation

Temperature (deg. C)	*Micro-heater resistance (Ohm)*			
	180a - 2 - w7	180a - 4 - w7	180a - 1 - w8	180a - 1 - w10
22.7	16.43	16.30	16.12	16.32
98	19.00	18.81	18.67	18.92
161	21.09	20.90	20.80	21.08

Siu Man Lee
Hotplate_char_rawdata.xls

Characterisation of Micro-hotplate SRL 180b

Constant Current Characterisation using:
1) Knick DC-Calibrator J152
2) Thurlby digital multimeter 1503-HA, supplied by RS Component Ltd, stock no. 610-859
3) MHP Holder and T05 star-shape heatsink

Electrical Charactersiation

Constant Current (mA)	***Voltage across device (V)***			
	180b - 3 - w7	180b - 10 - w7	180b - 4 - w8	180b - 3 - w10
20	0.4543	0.4817	0.4542	0.4581
30	0.7875	0.8256	0.7839	0.7927
40	1.2626	1.3071	1.2514	1.2673
45	1.5674	1.6188	1.5535	1.5738
50	1.9239	2.0034	1.9319	1.9525
45	1.5742	1.6432	1.5807	1.6009
40	1.2677	1.3285	1.2732	1.2900
30	0.7895	0.8348	0.7936	0.8022
20	0.4549	0.4847	0.4572	0.4611

Thermal characterisation using
1) Convection oven and mercury glass thermometer
2) Thurlby digital multimeter 1503-HA, supplied by RS Component Ltd, stock no. 610-859
3) Custom made thermal characterisation probe

Thermal Charactersiation

Temperature (deg. C)	***Micro-heater resIstance (Ohm)***			
	180b - 3 - w7	180b - 10 - w7	180b - 4 - w8	180b - 3 - w10
22.9	20.31	21.74	20.38	20.48
92	23.38	25.10	23.58	23.68
162	26.08	28.00	26.38	26.46

Siu Man Lee
Hotplate_char_rawdata.xls

Characterisation of Micro-hotplate SRL 180c

Constant Current Characterisation using:
1) Knick DC-Calibrator J152
2) Thurlby digital multimeter 1503-HA, supplied by RS Component Ltd, stock no. 610-859
3) MHP Holder and T05 star-shape heatsink

Electrical Charactersiation

Constant Current (mA)	*Voltage across device (V)*			
	180c - 3 - w7	180c - 7 - w7	180c - 3 - w8	180c - 3 - w10
10	0.3138	0.3319	0.3125	0.3169
20	0.7250	0.7627	0.7232	0.7339
30	1.3521	1.4113	1.3514	1.3721
38	2.0791	2.1556	2.0873	2.1144
42	2.5241	2.6115	2.5475	2.5738
38	2.0805	2.1588	2.0992	2.1260
30	1.3526	1.4125	1.3615	1.3811
20	0.7250	0.7630	0.7258	0.7365
10	0.3138	0.3319	0.3125	0.3168

Thermal characterisation using
1) Convection oven and mercury glass thermometer
2) Thurlby digital multimeter 1503-HA, supplied by RS Component Ltd, stock no. 610-859
3) Custom made thermal characterisation probe

Thermal Charactersiation

Temperature (deg. C)	*Micro-heater resistance (Ohm)*			
	180c - 3 - w7	180c - 7 - w7	180c - 3 - w8	180c - 3 - w10
22.9	30.13	31.92	29.90	30.25
97	34.85	36.83	34.67	35.06
158	38.53	40.67	38.47	38.92

Siu Man Lee
Hotplate_char_rawdata.xls

Characterisation of Micro-hotplate SRL 181a

Constant Current Characterisation using:
1) Knick DC-Calibrator J152
2) Thurlby digital multimeter 1503-HA, supplied by RS Component Ltd, stock no. 610-859
3) MHP Holder and T05 star-shape heatsink

Electrical Characterisation

Constant Current (mA)	*Voltage across device (V)*			
	181a - 1 - w7	180a - 9 - w7	181a - 1 - w8	181a - 4 - w10
20	0.4461	0.6973	0.4432	0.4477
30	0.7872	1.1372	0.7832	0.7930
40	1.2830	1.7266	1.2808	1.2978
44	1.5331	2.0220	1.5389	1.5585
47	1.7408	2.2651	1.7578	1.7802
44	1.5340	2.0193	1.5492	1.5682
40	1.2836	1.7221	1.2947	1.3113
30	0.7873	1.1114	0.7899	0.7995
20	0.4459	0.6604	0.4450	0.4493

Thermal characterisation using
1) Convection oven and mercury glass thermometer
2) Thurlby digital multimeter 1503-HA, supplied by RS Component Ltd, stock no. 610-859
3) Custom made thermal characterisation probe

Thermal Characterisation

Temperature (deg. C)	*Micro-heater resistance (Ohm)*			
	181a - 1 - w7	180a - 9 - w7	181a - 1 - w8	181a - 4 - w10
23.0	19.62	32.32	19.43	19.58
87	22.33	33.59	22.19	22.32
155	24.96	36.86	24.92	25.06

Siu Man Lee
Hotplate_char_rawdata.xls

Characterisation of Micro-hotplate SRL 181b

Constant Current Characterisation using:
1) Knick DC-Calibrator J152
2) Thurlby digital multimeter 1503-HA, supplied by RS Component Ltd, stock no. 610-859
3) MHP Holder and T05 star-shape heatsink

Electrical Charactersiation

Constant Current (mA)	*Voltage across device (V)*			
	181b - 6 - w7	181b - 9 - w7	181b - 6 - w8	181b - 6 - w10
15	0.3463	0.3452	0.3450	0.3456
25	0.6810	0.6766	0.6792	0.6846
32	1.0132	1.0053	1.0120	1.0246
38	1.3809	1.3746	1.3895	1.4118
42	1.6724	1.6786	1.6985	1.7248
38	1.3820	1.3863	1.4016	1.4232
32	1.0137	1.0154	1.0250	1.0383
25	0.6810	0.6815	0.6856	0.6917
15	0.3463	0.3464	0.3465	0.3475

Thermal characterisation using
1) Convection oven and mercury glass thermometer
2) Thurlby digital multimeter 1503-HA, supplied by RS Component Ltd, stock no. 610-859
3) Custom made thermal characterisation probe

Thermal Charactersiation

Temperature (deg. C)	*Micro-heater resistance (Ohm)*			
	181b - 6 - w7	181b - 9 - w7	181b - 6 - w8	181b - 6 - w10
23.0	21.13	21.22	21.05	21.03
91	24.18	24.27	24.23	24.17
156	26.80	26.97	27.00	26.91

Siu Man Lee
Hotplate_char_rawdata.xls

Characterisation of Micro-hotplate SRL 181c

Constant Current Characterisation using:
1) Knick DC-Calibrator J152
2) Thurlby digital multimeter 1503-HA, supplied by RS Component Ltd, stock no. 610-859
3) MHP Holder and T05 star-shape heatsink

Electrical Characterisation

Constant Current (mA)	*Voltage across device (V)*		
	181c - 8 - w7	181c - 4 - w8	181c - 4 - w10
10	0.4614	0.4721	0.4734
14	0.7271	0.7473	0.7512
18	1.0834	1.1172	1.1258
22	1.5578	1.6086	1.6230
26	2.1648	2.2385	2.2638
22	1.5597	1.6125	1.6316
18	1.0841	1.1178	1.1295
14	0.7273	0.7466	0.7522
10	0.4614	0.4714	0.4733

Thermal characterisation using
1) Convection oven and mercury glass thermometer
2) Thurlby digital multimeter 1503-HA, supplied by RS Component Ltd, stock no. 610-859
3) Custom made thermal characterisation probe

Thermal Characterisation

Temperature (deg. C)	*Micro-heater resistance (Ohm)*		
	181c - 8 - w7	181c - 4 - w8	181c - 4 - w10
23.1	40.93	41.58	41.55
96	47.26	47.89	47.92
156	52.16	52.87	53.05

Siu Man Lee
Hotplate_char_rawdata.xls

Appendix 5c

Average temperature of the active area

The temperature and resistance of the micro-heater can be expressed in the equation (1).

$$R(T) = R_o\,(1 + \alpha\,(T - T_o)) \tag{1}$$

where $R(T_o) = R_o$

α = Temperature coefficient of resistivity

T = Temperature

Assuming the thermal profile of the micro-heater is plotted in figure A5.1(a).

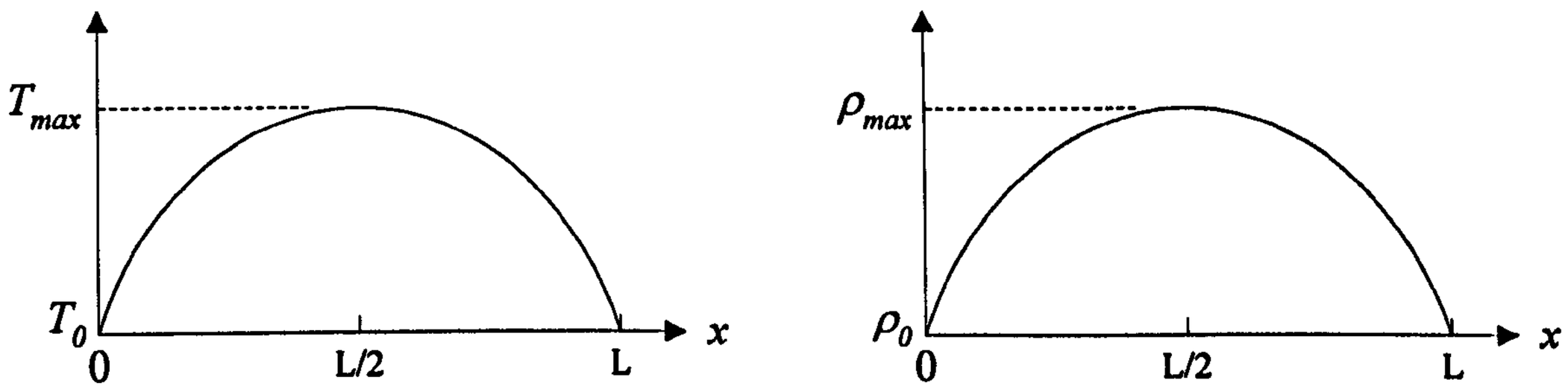

(a) (b)

Figure A5.1

The resistance per unit length can be defined as $\frac{dR}{dx}$. As the resistivity, ρ_o, of the platinum micro-heater is when $T = T_o$, and so $\rho_o = R_o/L$ and similarly ρ_m is when $T = T_m$ and $\rho_m = R_m/L$. So the thermal profile determines $\rho(x)$ is expressed into a function of x.

The resistance, R, can be found by integrating $\rho(x)$.

$$R = \int_{x=0}^{x=L} \rho(x)dx \tag{2}$$

Then assuming a linear model,

$$\rho(x) = \rho_o + (\rho_m - \rho_o)\frac{2x}{L}$$

Therefore,

$$R = \int_{x=0}^{x=L} \rho_o dx + \int_{x=0}^{\frac{L}{2}} (\rho_m - \rho_o)\frac{2x}{L} \tag{3}$$

Substituting into equation (3) for ρ_o and ρ_m:

$$R = \frac{R_o}{L}\int_0^L dx + \frac{4}{L^2}\int_0^{\frac{L}{2}} (R_m - R_o)x dx$$

$$R = Ro + \frac{1}{2}(R_m - R_o) = \frac{1}{2}(R_o + R_m) \tag{4}$$

Therefore,

$$R = \overline{R}$$

So for a linear function the total resistance is equal to the average resistance. Furthermore, According to equation (4), the maximum resistance, R_m,

$$R_m = 2R - R_o.$$

Then substituting R_m into equation (1), the peak temperature of the active area can be obtained from equation (5).

$$T_{\max} = T_o + \frac{2(R - R_o)}{\alpha R_o} \tag{5}$$

In addition, equation (3) can be solved with a known parametric equation, such as equation (6).

$$\rho(x) = \rho_o + (\rho_m - \rho_o)\left[a\frac{x}{\left(\frac{L}{2}\right)} + b\frac{x^2}{\left(\frac{L}{2}\right)^2} + c\frac{x^3}{\left(\frac{L}{2}\right)^3}\right] \tag{6}$$

where the coefficient a, b and c are obtained via simulation or IR imaging.

Appendix 5d

Power curve coefficients for 1st and 2nd generation devices

Coefficients of the Power model for 1st generation devices

	SRL 136a		SRL 136p		SRL 162g		SRL 162p	
	Coefficient	Std. Dev.	Coefficient	Std. Dev.	Coefficient	Std. Dev.	Coefficient	Std. Dev.
a	1.83E-01	7.22E-03	1.79E-01	4.96E-03	1.06E-01	5.89E-03	1.06E-01	4.24E-03
b	2.90E-04	5.89E-05	2.87E-04	4.29E-05	1.87E-04	4.76E-05	1.98E-04	7.57E-06
c	2.97E-11	2.57E-11	3.30E-11	2.18E-11	1.53E-11	1.68E-11	1.09E-11	3.67E-12

Coefficients of the Power model for 2nd generation devices

Standard family						
	SRL 176a		SRL 176b		SRL 176c	
	Coefficient	Std. Dev.	Coefficient	Std. Dev.	Coefficient	Std. Dev.
a	2.52E-01	1.82E-02	2.11E-01	1.51E-02	1.55E-01	1.32E-02
b	5.34E-04	1.09E-04	4.79E-04	9.03E-05	3.02E-04	7.91E-05
c	-1.18E-10	4.49E-11	-1.01E-10	3.71E-11	3.32E-11	3.25E-11

Low power family						
	SRL 177a		SRL 177b		SRL 177c	
	Coefficient	Std. Dev.	Coefficient	Std. Dev.	Coefficient	Std. Dev.
a	2.10E-01	1.52E-02	1.73E-01	1.32E-02	1.27E-01	9.65E-03
b	4.80E-04	9.09E-05	3.28E-04	7.93E-05	2.76E-04	5.78E-05
c	-8.76E-11	3.74E-11	-4.64E-11	3.26E-11	-2.30E-11	2.38E-11

Small-mem/ robust						
	SRL 178a		SRL 178b		SRL 178c	
	Coefficient	Std. Dev.	Coefficient	Std. Dev.	Coefficient	Std. Dev.
a	2.63E-01	1.87E-02	1.84E-01	1.35E-02	1.34E-01	1.02E-02
b	5.81E-04	1.12E-04	4.09E-04	8.08E-05	3.07E-04	6.12E-05
c	-1.45E-10	4.61E-11	-6.73E-11	3.33E-11	-1.96E-11	2.52E-11

Robust family						
	SRL 179a		SRL 179b		SRL 179c	
	Coefficient	Std. Dev.	Coefficient	Std. Dev.	Coefficient	Std. Dev.
a	3.43E-01	2.46E-02	2.53E-01	1.80E-02	1.73E-01	1.37E-02
b	6.69E-04	1.47E-04	5.33E-04	1.08E-04	3.82E-04	8.22E-05
c	-2.02E-10	6.06E-11	-1.43E-10	4.44E-11	-5.46E-14	3.38E-11

Meander designs								
	SRL 179d		SRL 179e		SRL 162o		SRL 136o	
	Coefficient	Std. Dev.	Coefficient	Std. Dev.	Coefficient	Std. Dev.	Coefficient	Std. Dev.
a	1.34E-01	1.07E-02	2.38E-01	1.74E-02	1.29E-01	1.17E-02	1.74E-01	1.45E-02
b	2.54E-04	6.38E-05	5.27E-04	1.04E-04	1.80E-04	7.03E-05	3.47E-04	8.71E-05
c	-1.51E-11	2.62E-11	-9.68E-11	4.28E-11	2.76E-11	2.89E-11	2.54E-11	3.58E-11

Ultra-small/ robust family						
	SRL 180a		SRL 180b		SRL 180c	
	Coefficient	Std. Dev.	Coefficient	Std. Dev.	Coefficient	Std. Dev.
a	2.03E-01	1.46E-02	1.36E-01	1.06E-02	1.18E-01	9.02E-03
b	3.83E-04	8.75E-05	2.44E-04	6.35E-05	2.52E-04	5.41E-05
c	-1.24E-10	3.60E-11	-2.98E-11	2.61E-11	-2.29E-11	2.22E-11

Ultra-small/ low power family						
	SRL 181a		SRL 181b		SRL 181c	
	Coefficient	Std. Dev.	Coefficient	Std. Dev.	Coefficient	Std. Dev.
a	1.10E-01	8.27E-03	9.87E-02	7.52E-03	6.02E-02	4.85E-03
b	2.27E-04	4.95E-05	1.86E-04	4.51E-05	1.07E-04	2.91E-05
c	-3.40E-11	2.04E-11	-3.00E-11	1.85E-11	-5.54E-12	1.20E-11

Appendix 6

Appendix 6a

The factor of the device resistance change

Appendix 6b

Specifications of the driving signal for small-signal mode

Appendix 6c

Specifications of the driving signal for power modulation

Appendix 6d

Experimental results for chemical dynamic response with square wave

Appendix 6a

The factor of the device resistance change

The relation of the Wheatstone bridge output and the resistors can be expressed in equation (1).

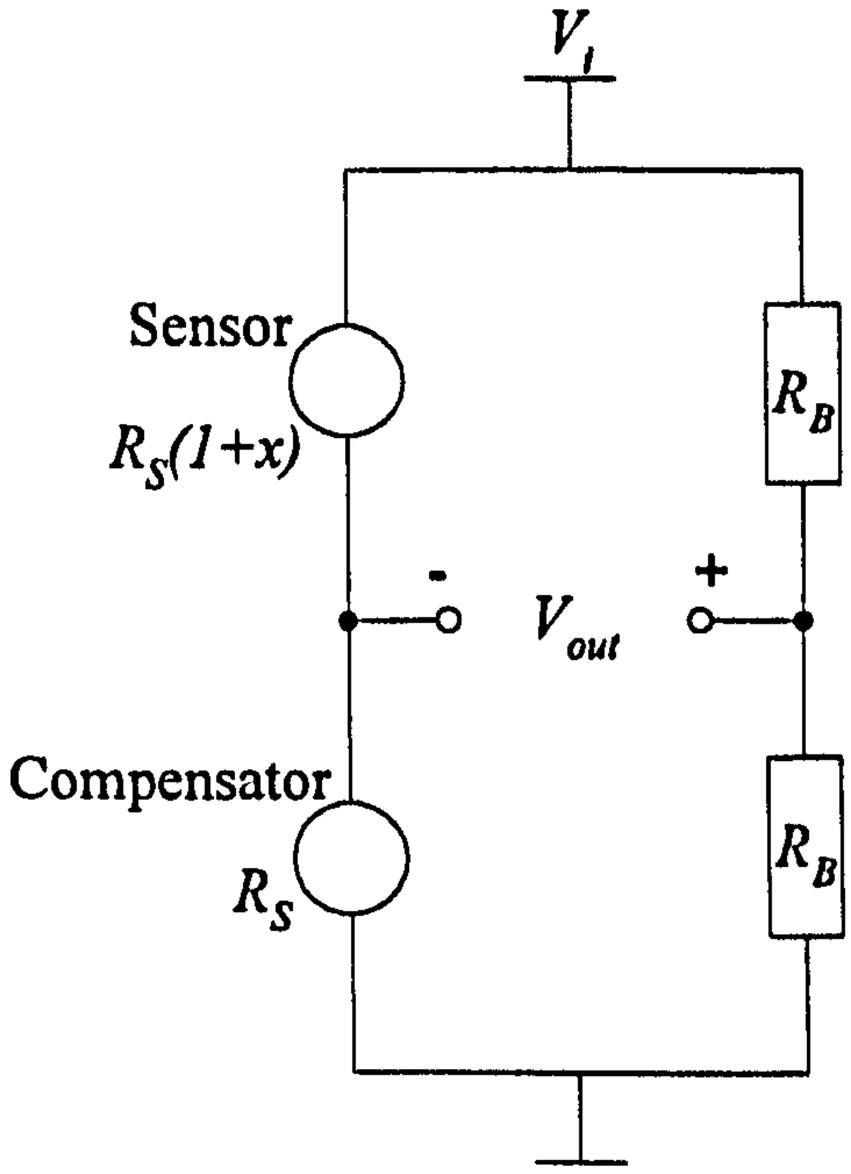

$$V_{out} = V_i\left[\frac{R_B}{2R_B} - \frac{R_s}{R_s + R_s(1+x)}\right] \qquad (1)$$

Simplifying equation (1) and the bridge gain is shown in equation 2.

$$\frac{V_{out}}{V_i} = \frac{x}{2(2+x)} \qquad (2)$$

since $x = \frac{\Delta R}{R_{500}}$, therefore, the change of the resistance can be obtained, as shown in equation (3).

$$\frac{\Delta R}{R_{500}} = \frac{4V_{out}}{V_i - 2V_{out}} \qquad (3)$$

Appendix 6b

Specifications of the driving signal for small-signal mode

SRL No.	SRL 136o				SRL 162o			
Operation temp. (deg.C)	500	400	300	200	500	400	300	200
Passivated (Y/N)	Yes				Yes			
Driving voltage (V)	7.5	6.8	5	3.6	6.34	5	3.8	2.7
Ripple Vp-p (mV)	500				500			
Frequency (Hz)	1				1			
At rising edge:								
DC-offset (V)	1.22	1.16	0.998	0.754	0.91	0.699	0.552	0.502
Voltage at 'H' (V)	1.26	1.21	1.05	0.822	0.94	0.764	0.603	0.557
Vp-to-final (mV)	40	39.2	42.4	40	32	30.6	32.8	30.4
t_{rise} (ms)	2.1	2.3	2.8	3.6	1.6	1.8	2.2	2.8
At falling edge:								
Vp-to-final (V)	36	36	37.6	36	28	29.6	29.6	27.2
t_{fall} (ms)	5.4	5.8	6.4	6.9	4.9	5.4	5.8	6.2

SRL No.	SRL 177c				SRL 180c			
Operation temp. (deg.C)	500	400	300	200	500	400	300	200
Passivated (Y/N)	Yes				Yes			
Driving voltage (V)	2.7	2.1	1.7	1.2	2.5	2	1.5	1
Ripple Vp-p (mV)	200				200			
Frequency (Hz)	1				1			
At rising edge:								
DC-offset (V)	2.02	1.85	1.72	1.32	2.05	1.85	1.59	1.19
Voltage at 'H' (V)	2.18	1.95	1.82	1.46	2.14	1.94	1.7	1.34
Vp-to-final (mV)	64	74	80	84	72	70	78	78
t_{rise} (ms)	1.25	1.5	1.8	2.2	1	1.2	1.5	1.8
At falling edge:								
Vp-to-final (V)	72	64	66	66	72	64	70	66
t_{fall} (ms)	3.96	4.6	5.4	6	2.8	3.4	4.1	4.9

SRL No.	SRL 181c			
Operation temp. (deg.C)	500	400	300	200
Passivated (Y/N)	Yes			
Driving voltage (V)	2	1.7	1.3	0.8
Ripple Vp-p (mV)	200			
Frequency (Hz)	1			
At rising edge:				
DC-offset (V)	1.26	1.15	1.01	0.708
Voltage at 'H' (V)	1.33	1.22	1.08	0.816
Vp-to-final m(V)	64	57.6	60	64
t_{rise} (ms)	0.52	0.62	0.8	1
At falling edge:				
Vp-to-final (V)	56	49.6	50.4	52
t_{fall} (ms)	1.4	2	2.4	3

Appendix 6c

Specifications of the driving signal for power modulation

	Idle voltage (V_{idle}) (V)	Operating voltage (V)	Frequency (Hz)	Duty-cycle (%)
SRL 136a	2.0	7.5	1	50
SRL 162g	2.5	6.3	1	50
SRL 176c	1.0	3.1	1	50
SRL 177c	0.8	2.7	1	50
SRL 178c	0.9	2.8	1	50
SRL 179c	1.1	3.2	1	50
SRL 180c	0.8	2.5	1	50
SRL 181c	0.7	2.0	1	50

Appendix 6d

Experimental results for chemical dynamic response with square wave

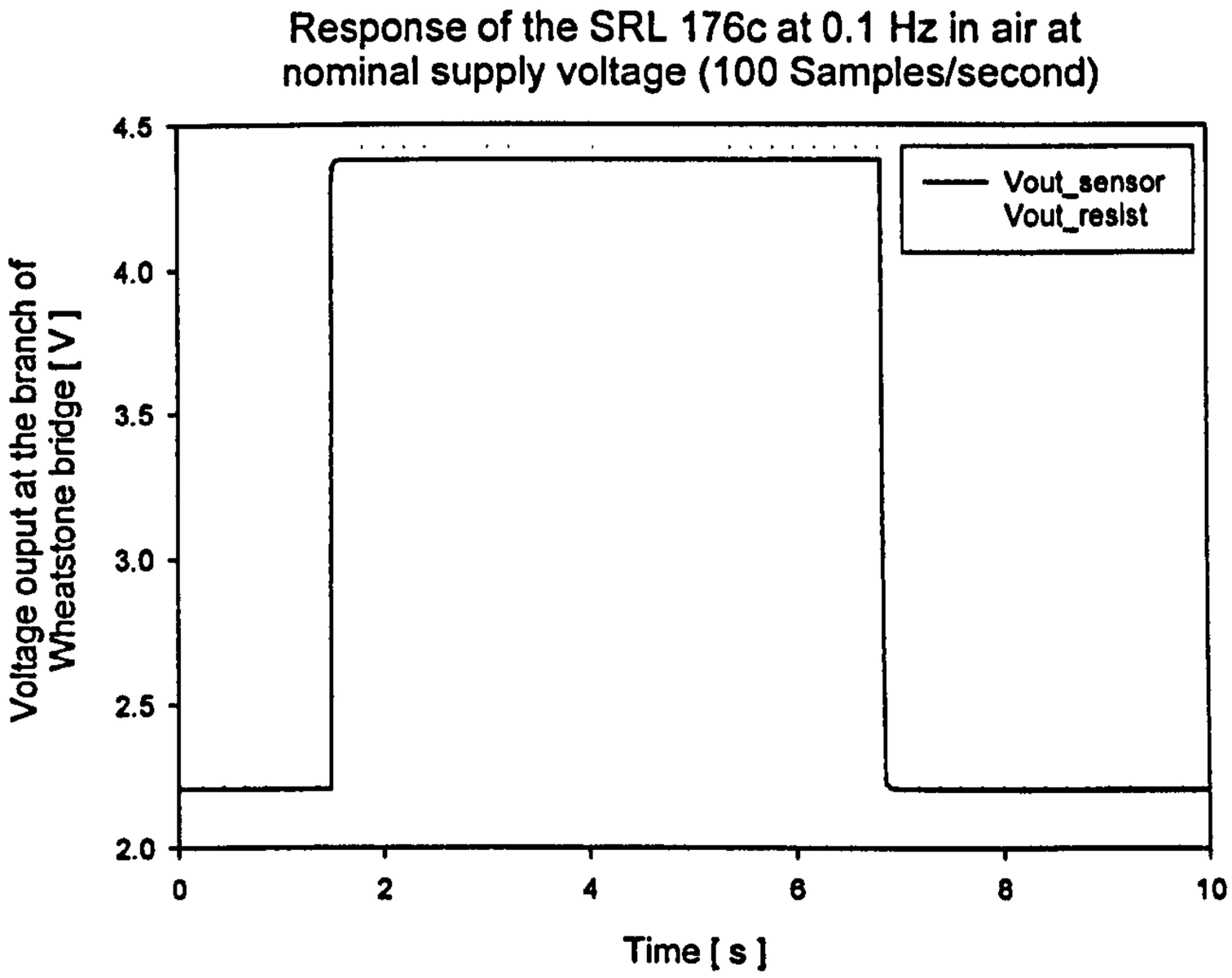

(a)

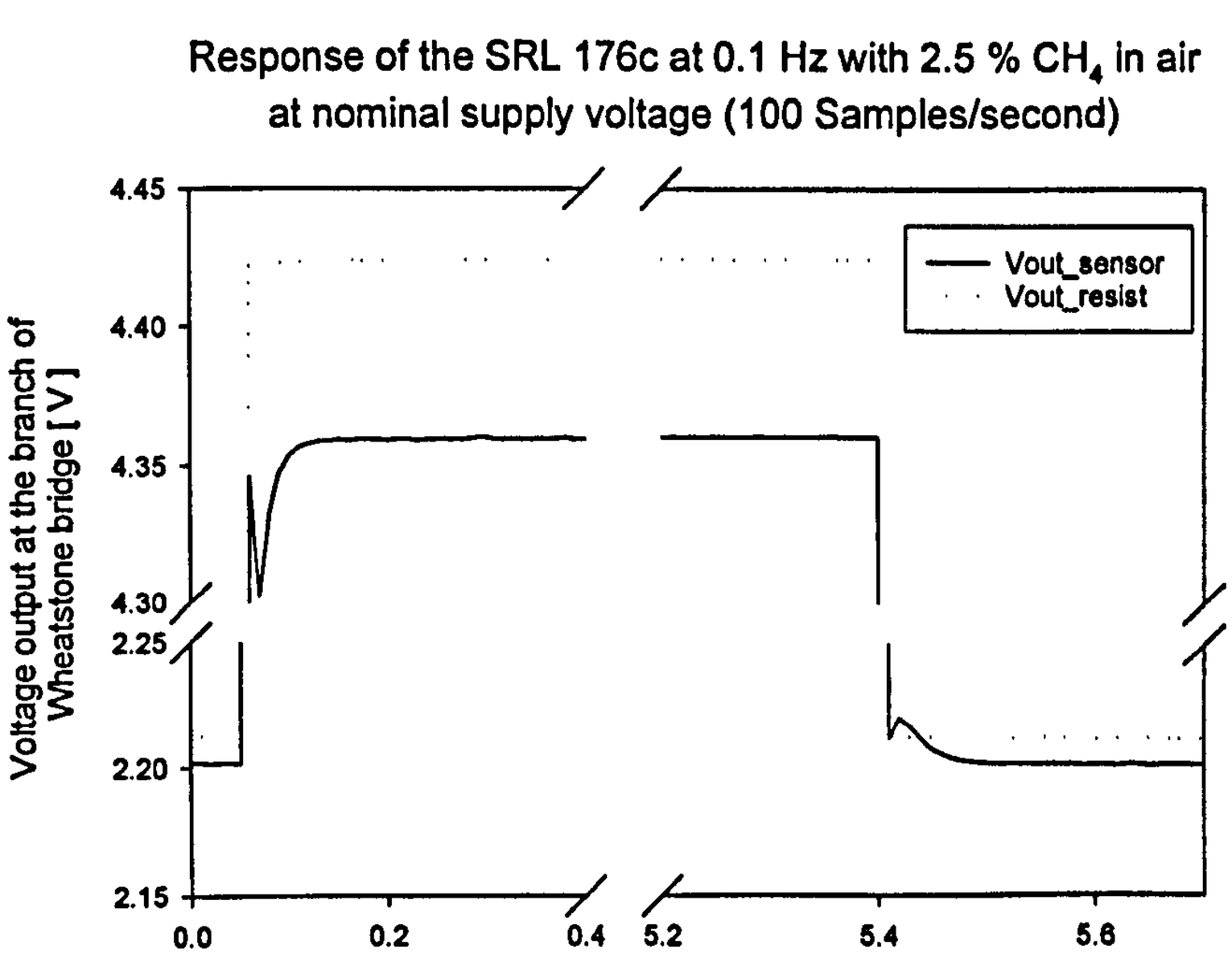

(b)

Figure A6.1: The responses of SRL 176c operated in air and 2.5% methane with nominal operating voltage at 0.1 Hz.

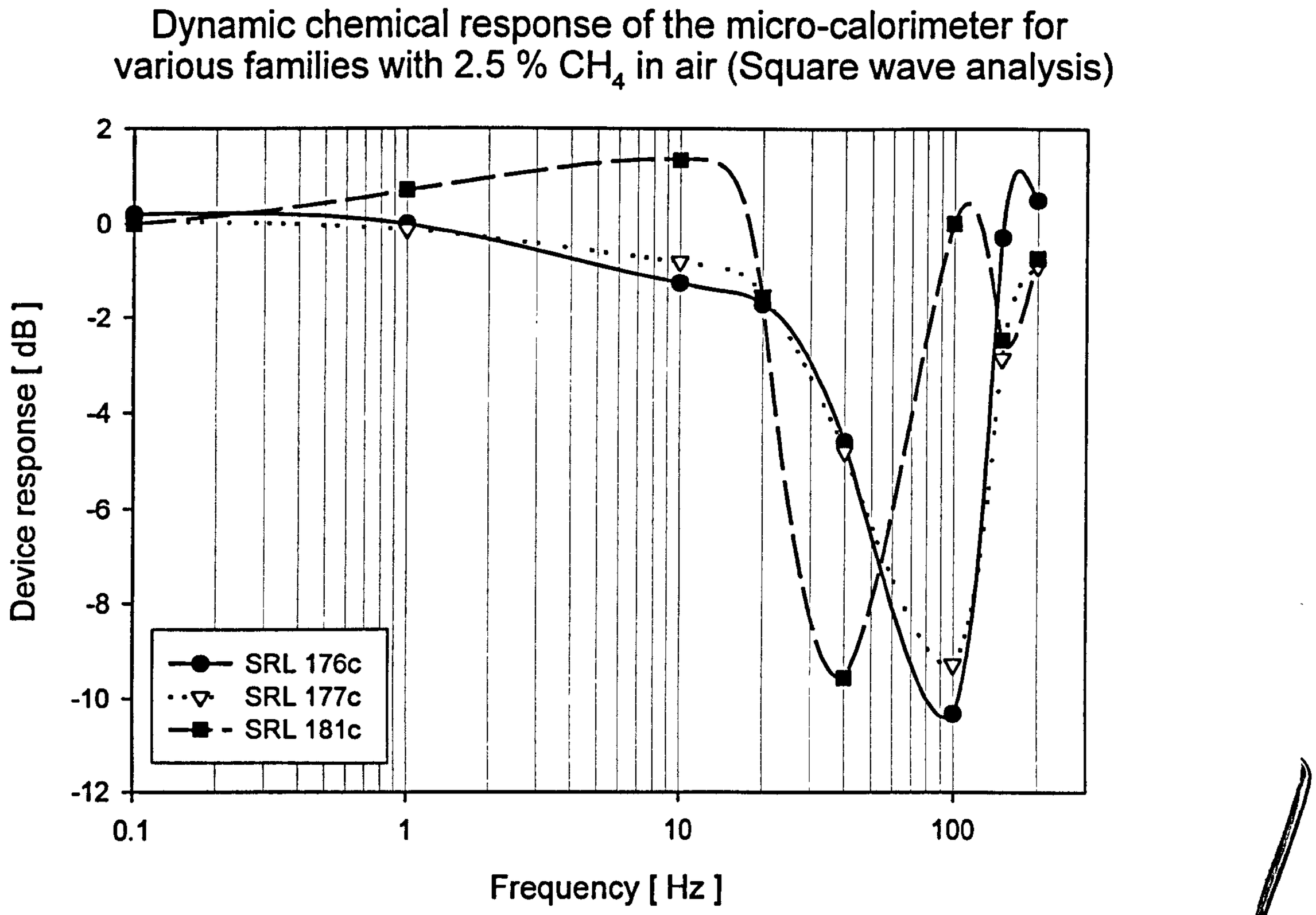

Figure A6.2: Chemical dynamic response for the micro-calorimeters with 2.5% methane in air by square wave analysis.

Appendix 7

Publications

[1] S.M Lee, J. W. Gardner, D. C. Dyer, Silicon planar pellistor employing nanostructured films and a micro-hotplate, *Proceeding the euspen nanotechnology workshop and joint Warwick-Tokyo Nanotechnology Symposium*, Warwick University, UK, 18th to 21st September 2000.

[2] S.M Lee, J. W. Gardner, D. C. Dyer, Silicon planar pellistor employing nanostructured films and a micro-hotplate, Poster Presentation in the euspen nanotechnology workshop and joint Warwick-Tokyo Nanotechnology Symposium, Warwick University, UK, 18th to 21st September 2000.

[3] J. W. Garnder, S. M. Lee, P. N. Bartlett, S. Guerin, D Briand and N. F. de Rooij, *Technical digest of Transducer'01 and EurosensorsXV*, The 11th international conference solid-state sensors and actuators, Munich, Germany, 10th to 14th June, 2001.

[4] S. A. A Leclerc, M. J Willett, S. M Lee, J. W Gardner, J Marwan, P. N Bartlett, Optimisation of mesoporous catalyst for combustible gas sensor application, *Proceeding of International Meeting on Chemical Sensors*, Boston, Massachusetts, USA, 7th – 10th July, 2002.

[5] S. A. A Leclerc, M. J Willett, S. M Lee, J. W Gardner, J Marwan, P. N Bartlett, Novel combustible gas sensors employing micromachined silicon substrates and nanostructured catalysts, *Proceeding of International Meeting on Chemical Sensors*, Boston, Massachusetts, USA, 7th – 10th July, 2002.

[6] P. N Bartlett, S. Guerin, J. Marwan, J. W. Gardner, S. M Lee, M. J Willett and S. A. A. Leclerc, A micromachined planar pellistor using an electrochemically deposited nanostructured catalyst, *Proceedings for the Symposium on Microfabricated Systems and MEMs – V*, Spring meeting of the Electrochemical Society, Philiadelphia, USA, 17th – 22nd May, 2002.

[7] S. A. A Leclerc, M. J Willett, S. M Lee, J. W Gardner, J Marwan, P. N Bartlett, Novel combustible gas sensors employing micromachined silicon substrates and nanostructured catalysts, submitted to *Sensors and Actuators B*.

[8] S. M Lee, D. C. Dyer, J. W Gardner, Design and optimisation of a high-temperature silicon micro-hotplate for nanoporous palladium pellistors, *Microelectronics Journal*, 34, pp115-126, 2003.

PAGES EXCLUDED UNDER INSTRUCTION FROM UNIVERSITY